Finite Element Modelling of GFRP Reinforced Concrete Beams

by

Joseph George Stoner

A thesis
presented to the University of Waterloo
in fulfillment of the
thesis requirement for the degree of
Master of Applied Science
in
Civil Engineering

Waterloo, Ontario, Canada, 2015

Author's Declaration

I hereby declare that I am the sole author of this thesis. This is a true copy of the thesis, including any required final revisions, as accepted by my examiners.

I understand that my thesis may be made electronically available to the public.

Abstract

The numerical modelling of twelve concrete beams reinforced with glass fibre reinforced polymer (GFRP) longitudinal and transverse bars was performed by the author using the finite element analysis (FEA) software ABAQUS. The experimental beam tests as performed by Krall (2014) were used to calibrate the Concrete Damaged Plasticity Model (CDPM) provided within ABAQUS. Recommendations were made regarding the modelling of concrete beams reinforced with and without GFRP stirrups.

The analyses of beams without stirrups are presented first. The Hognestad Parabola was effective in modelling the compressive behaviour of the concrete. A fracture mechanics approach was used to model the post-cracking tensile behaviour of the concrete, with a bilinear stress-displacement response and a fracture energy of $G_f = 90$N/m providing the strongest accuracy. The use of discrete truss sections and smeared membrane sections to model the GFRP longitudinal reinforcement were both studied; both methods were effective, but the truss approach is recommended.

Further modifications to the CDPM were necessary for the modelling of beams with stirrups. The presence of GFRP stirrups that do not exhibit the plastic behaviour that steel stirrups exhibit resulted in concrete-governed compression failures. To consider the confining effects that the stirrups had on the concrete, an increased dilation angle of $\psi = 50^\circ$ was used in combination with an increased maximum concrete compressive strain of $\varepsilon_{c,max} = 0.015$. Truss reinforcement was again used for the longitudinal reinforcement, whereas membrane sections are recommended for the stirrups.

A parametric study was performed by applying the proposed models to beams with slenderness ratios (a/d) ranging from 1.5 to 6.5. For a/d less than 2.5, further research is recommended to confirm the influence of the arch effect on the shear strength of deep members. For $a/d = 2.5$, the proposed ABAQUS models agree strongly with the shear model proposed by Nehdi et al. (2007). For larger ratios, the proposed models agree strongly with the flexural strength predictions. The proposed models are effective in accurately predicting the strength of beams with and without stirrups for various a/d ratios, and are able to produce reinforcement strain profiles and crack patterns that agree strongly with the experimental data.

Acknowledgements

I would like to first thank my supervisor and mentor, Dr. Maria Anna Polak. Dr. Polak has not only provided me with a wealth of technical knowledge, but has also ingrained in me the importance of networking and forming relationships; a refreshing perspective in the academic world that is essential for fostering future collaborations. Dr. Polak has always supported me, trusted my judgments, and believed in my abilities; for this I am truly grateful.

I would next like to thank my colleagues who have supported me throughout my studies: Martin Krall, my officemate whose research founded my own, for his creative insights and ability to provide critical feedback; Shayan Sepiani for providing me with my first ABAQUS tutorial that ultimately resulted in the success of this thesis; Aikaterini Genikomsou, who shared my struggles with numerical modelling, for being a constant source of support and advice; Paulina Arczewska for sharing her advanced knowledge of FRP materials and inspiring me to remain active in this field in the future; Georgios Balomenos for always making time if I needed help; Dritan Topuzi for continually acting as mentor for me and inspiring me to always further my professional development; and Adam Wosatko for sharing his knowledge of computational mechanics.

I would also like to thank the Ontario Centres of Excellence, Natural Sciences and Engineering Research Council of Canada, and Schoeck Canada for their financial contributions to this research.

Finally, to my family. The last few years have been a whirlwind of opportunities and accomplishments, but also obstacles and confusion. When I was at a loss with my research or anxious about my next steps in life, it was your everlasting support that allowed me to push forward.

Dedication

I dedicate this thesis to my sister, mother, and father.

Table of Contents

List of Figures

List of Tables

Chapter 1

Introduction

1.1 General

Many existing reinforced concrete structures experience deterioration as a result of the corrosion of internal steel reinforcement. The costs associated with repairing or replacing concrete structures that suffer from this deterioration consume a large portion of the owner's budget, and have prompted the development of solutions to impede the progression of corrosion. Alternatives to bare steel have been used including stainless steel, galvanized steel, epoxy-coated steel, and cathodic protection, with limited effectiveness. The use of fibre reinforced polymer (FRP) bars, an alternative to steel, as internal reinforcement for new concrete structures has become a topic of interest due to the material's high tensile strength, light weight, and inability to corrode. This material has been used successfully as internal reinforcement in concrete structures that are exposed to highly corrosive environments including bridge decks, barrier walls, parking garage slabs, and containment structures housing corrosive materials.

When a new material such as FRP is introduced, experimental testing is essential to observe the actual behaviour and failure mode of structures that utilize this material. However, this testing is often very expensive, time consuming, and may dictate the pace of research

progress. The testing of existing structures to ultimate failure is not possible, and the limitations of laboratory resources and testing equipment capabilities will often require experimental specimens of reduced scale. This therefore encourages the development and utilization of advanced analytical methods such as finite element analysis (FEA) to study the behaviour of structures (Nour et al., 2007).

The collaboration of numerical studies with an experimental program will not only yield time-consumption and financial benefits to the research, but will also improve the effectiveness of the experimental testing. For example, an alternative to testing 100 experimental specimens to study the influence of various design parameters on the structure's response, an exercise that may take a lifetime, one may test a much smaller sample of specimens and use these results to calibrate a numerical model. This model can then be used to propose future experiments that have been designed with a stronger technical understanding, thus providing more meaningful results.

This thesis presents the numerical analyses of concrete beams reinforced with internal FRP bars. The conclusions made from this research will allow for the effective design of future experimental tests and accurate prediction of beam responses. The knowledge gained from this research will be used to propose informed recommendations to design standards and codes to improve design procedures and encourage the use of FRP as a structural material.

1.2 Research Scope and Objectives

The primary objective of this research was to perform the finite element analysis (FEA) of concrete beams reinforced with glass fibre reinforced polymer (GFRP) bars. Twelve beams were constructed and tested at the University of Waterloo as presented by Krall (2014). These beams varied in terms of longitudinal bar diameter, longitudinal bar configuration,

stirrup spacing, and stirrup diameter. This research utilized the FEA software ABAQUS to perform the numerical simulations of these twelve beams. The Concrete Damaged Plasticity Model as provided by ABAQUS was used exclusively to model the concrete behaviour. The results of the experimental beams were used to calibrate and corroborate the Concrete Damaged Plasticity Model in order to propose recommendations regarding the accurate modelling of concrete members reinforced with internal FRP reinforcement. The specific objectives of this research are summarized as follows:

1. Perform numerical analyses of concrete beams reinforced with GFRP reinforcement.
2. Utilize the Concrete Damaged Plasticity Model (CDPM) as provided by ABAQUS to model the concrete behaviour.
3. Use the experimental beam data as presented by Krall (2014) to calibrate the CDPM.
4. Study the influence of the concrete model on the load-deflection response of each beam by modifying compression, tension, plasticity, and damage parameters.
5. Propose models to effectively simulate the response of concrete beams reinforced with and without stirrups.
6. Study the use of two methods to model the reinforcement: discrete truss sections and smeared reinforced membrane sections.
7. Study the reinforcement strain profiles provided by each model and compare to experimental data.
8. Study the concrete crack patterns provided by each model and compare to experimental observations.
9. Perform a parametric study by applying the proposed models to beams of varying shear span to effective depth (a/d) ratios.
10. Compare the FEA results with strength predictions as presented in current design standards and available literature.

11. Add to the limited literature regarding the numerical study of concrete structures reinforced with FRP materials.

1.3 Thesis Organization

This thesis is organized into seven chapters and four appendices:

- Chapter 2 presents a review of available background information and literature on the use of FRP materials in structural applications, finite element modelling of structures reinforced with FRP, the experimental tests performed on concrete beams reinforced with GFRP that were used to calibrate the models studied in this research, and current strength prediction models proposed for FRP reinforced concrete structures.
- Chapter 3 provides an overview of the Concrete Damaged Plasticity Model implemented by the FEA software ABAQUS that was used to perform the numerical simulations presented in this thesis.
- Chapter 4 provides an overview of the material properties, geometric details, and analytical parameters that were used to model all concrete beams studied in this research.
- Chapter 5 presents the analyses performed for beams reinforced with longitudinal bars only (beams with no stirrups).
- Chapter 6 presents the analyses performed for beams reinforced with both longitudinal and stirrup reinforcement (beams with stirrups).
- Chapter 7 presents the parametric study that was performed using the models proposed in Chapters 5 and 6.
- Appendix A provides the detailed drawings of the twelve reinforced concrete beams that were studied in this research, including the locations and nomenclature of the reinforcement strain gauges.

- Appendix B and Appendix C present the results of all ABAQUS modelling performed for beams without and with stirrups, respectively.
- Appendix D presents the results of the parametric study presented in Chapter 7.

Chapter 2

Background Information and Literature Review

2.1 Fibre Reinforced Polymers as Internal Reinforcement

Fibre reinforced polymer (FRP) materials were originally developed for the use in the aerospace and automotive industries due to their high strength and light weight. The use of FRP materials for civil engineering applications has been considered since the 1950s, but it was not until the 1970s that FRP was considered as a viable material for internal reinforcement for concrete structures (ISIS Canada, 2007). FRP composites have many civil engineering applications. One application includes all-FRP structures and components such as pultruded sections, pedestrian bridges, utility poles, and marine platforms. FRP can also be used as internal reinforcement for new concrete structures in the form of bars, rods, and prestressing tendons. The use of FRP materials for the strengthening and rehabilitation of existing structures has also been successful and is a field of extensive research. The focus of this thesis will be the use of FRP composites as internal reinforcement for new concrete structures.

2.1.1 FRP Constituents - Fibres

FRP products are composite materials that consist of high strength fibres embedded in a resin matrix. The fibres have high tensile strengths and provide the strength and stiffness of the FRP composite. The fibres have extremely large length-to-diameter ratios as they are considered continuous in length and have diameters in the range of 3 - 25 micrometres (ISIS Educational Committee, 2003). The two most common FRP materials used for structural applications include glass fibre reinforced polymers (GFRP) and carbon fibre reinforced polymers (CFRP), which utilize glass and carbon fibres, respectively. Aramid fibre reinforced polymers (AFRP) have also been developed, but are not used extensively in North America. Aramid fibres have been known to be susceptible to degradation due to ultraviolet exposure and moisture as well as sensitive to creep, thus limiting their desirability for structural applications (ISIS Educational Committee, 2006).

The selection of an appropriate fibre type for an FRP composite is dependent on the application. As the fibres provide the strength and stiffness to the composite, the mechanical properties of the composite are dependent on the type of fibres selected. Factors to be considered include the required tensile strength, the required stiffness, fatigue properties, durability, and cost. Table 2.1 provides a summary of the properties of the three main fibre types (ISIS Educational Committee, 2003).

Table 2.1: Comparison of Fibre Types

Criterion	Fibre Type		
	Carbon	Aramid	Glass
Tensile Strength	Very Good	Very Good	Very Good
Modulus of Elasticity	Very Good	Good	Adequate
Fatigue Behaviour	Excellent	Good	Adequate
Bulk Density	Good	Excellent	Adequate
Alkaline Resistance	Very Good	Good	Adequate
Price	Adequate	Adequate	Very Good

Glass fibres are the most commonly used fibres in structural engineering applications as they are the least expensive option and extensive research has been conducted using this type of reinforcement. Glass fibres are available in a variety of grades, with the most common being E-glass. FRP composites that utilize glass fibres have a typical modulus of elasticity of 40-65GPa, which is significantly lower than the modulus of elasticity of conventional steel reinforcement (200GPa).

Carbon fibres can be produced using one of three precursor fibre materials; polyacrylonitrile, rayon, or petroleum pitch. As the precursor material is variable, the mechanical properties of carbon fibres can vary significantly, thus these fibres are often differentiated into classes based on their elastic moduli. FRP composites that utilize carbon fibres are significantly more expensive than GFRP, however do exhibit properties that are very advantageous for structural engineering applications; CFRP materials have elastic moduli that are comparable to or higher than that of steel, outstanding durability properties, and excellent fatigue behaviour. These properties make CFRP ideal for prestressing tendons or rehabilitation and strengthening of existing structures (ISIS Educational Committee, 2003).

2.1.2 FRP Constituents - Resin

The high strength fibres are embedded into a polymeric resin matrix. The role of this matrix is to disperse and separate the individual fibres, to protect the fibres from abrasion and environmental degradation, to transfer externally applied stresses to the fibres through shear stresses that develop at the fibre-matrix interface, and to provide lateral support to the fibres against buckling when subjected to compressive loads (Amertrano, 2011).

The matrix materials used for FRP composites in structural engineering applications are often divided into two categories: thermoplastic resins and thermosetting resins. Ther-

moplastics are polymers that are composed of long-chain molecules with relatively weak secondary forces. This molecular structure allows the material to be repeatedly softened and hardened without causing degradation of the mechanical properties of the material. Conversely, thermosetting polymers are composed of long-chain molecules that are highly cross-linked. Therefore, the molecular structure of thermosets will experience irreversible deterioration if softened due to elevated temperatures, causing a severe reduction in strength. Thermosetting resins exhibit relatively good thermal stability under service temperatures and low creep and relaxation behaviour as compared to thermoplastic resins, therefore thermosetting resins are the preferred matrix material for structural engineering applications (ISIS Educational Committee, 2003).

Common thermosetting resins used include polyesters, vinyl esters, and epoxies. Vinyl esters are produced by the esterification between an epoxy resin and an unsaturated monocarboxylic acid. This means that vinyl esters are a class of polyesters that have been strengthened with epoxy molecules (Chimatech, 2014). Vinyl esters have been shown to have superior resistance to the ingress of moisture and alkalinity as compared to polyesters and epoxies, which makes this resin type advantageous for internal reinforcing bars that are exposed to highly alkaline concrete environments. Furthermore, vinyl esters appear to be tougher and more resistant to microcracking, thus minimizing the diffusion of potential acids and chemical solutions (ISIS Educational Committee, 2006). As a result of its superior durability, vinyl esters are a very common resin type for GFRP reinforcing bars and polyesters are not recommended (Micelli and Nanni, 2004).

2.1.3 FRP Constituents - Fillers and Additives

The final components of fibre reinforced polymers are materials known as fillers and additives. Fillers are inorganic compounds that are added to the polymer resin. Common filler

materials include calcium carbonate, aluminum silicate, alumina trihydrate and calcium sulphate. Fillers are used to reduce the final product cost by diluting the expensive resin material. Fillers also reduce the organic content of the composite, which improves the performance of the FRP under fire conditions by reducing its flammability and production of toxic smoke. Fillers can also be used to improve certain mechanical properties of the composite such as shrinkage, hardness, fatigue and creep performance. For pultruded sections such as unidirectional reinforcing bars, it is typical for less than 5% of the total weight to be filler in the resin matrix (Bai, 2013).

Additives are also incorporated into the resin material and serve to facilitate material processing, improve performance of the final product, and to modify certain mechanical properties of the composite. Certain additives are activated by heat and act as catalysts, or polymerization agents, to initiate the curing reaction of the resin. Additives may also be used to prevent the degradation of the FRP due to ultraviolet exposure, to ease the removal of the FRP from the molds (release agents), increase toughness, or to reduce flammability and smoke production (flame retardants). For reinforcing bars, it is typical for less than 1% of the resin weight to be additives (Bai, 2013).

2.1.4 Manufacture of FRP Internal Reinforcing Bars

There are many methods used to manufacture FRP materials used for structural engineering applications including, but not limited to, pultrusion, wet lay-up, filament winding, pull-winding, and injection molding. Pultrusion is the typical process used to manufacture straight internal reinforcement products such as bars, rods, and tendons, and will therefore be the focus of this discussion. The pultrusion process is an automated system which requires very little labour and is thus highly economical. It is an ideal process for products with a constant cross-section. Figure 2.1 depicts the typical steps involved in the

pultrusion process for FRP sections.

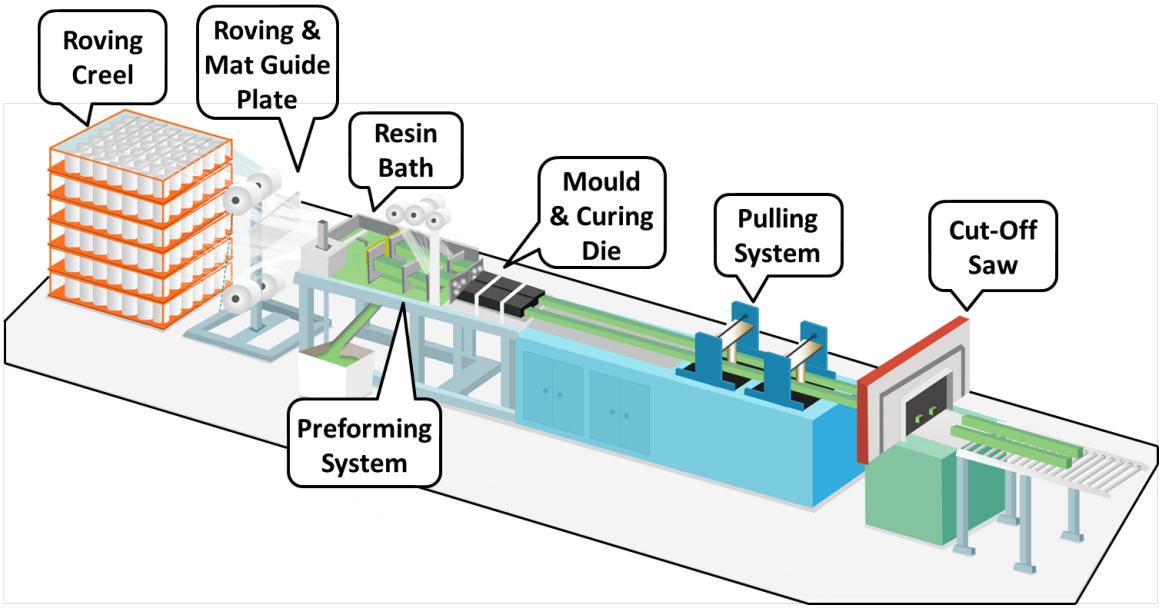

Figure 2.1: Pultrusion Process (Unicomposite Technology, 2014)

The process begins with the raw fibres stored in small spools called rovings which are kept on metal racks called creels. Guide plates are used to spread the fibre rovings as they travel through a bath of polymeric resins, thus allowing for maximum impregnation of the fibres into the resin. Upon exiting the resin bath, the fibres travel through a preforming system that continues to align the individual fibres while removing excess resin. The wet fibres are then pulled through a heated die with a predefined shape which molds the section and cures the resin. As a result of the elevated temperatures, the composite shrinks and separates from the internal walls of the die and exits as the finished product. The cured composite is typically pulled by means of urethane pads using a caterpillar belt. A cut-off saw is positioned at the end of the assembly to create products of set lengths. As the fibres and pultrusion system are continuous, any length of section is possible, but will be constrained by transportation and handling limitations (Bai, 2013).

The composite reinforcement that is produced in the pultrusion process will have a smooth surface. To improve the bond mechanisms between the reinforcing bar and concrete, man-

ufacturers will apply various surface treatments to the smooth bars. Figure 2.2 depicts reinforcing bar products with different surface treatments. A common treatment is to blast the surface of the bars with sand. Another treatment is to create ribbed bars by cutting grooves into the smooth bar or by using compression molding. Other manufacturers create bars that are helically wrapped with fibres and are then sand coated (Hollaway, 2009).

Figure 2.2: Various FRP Surface Treatments (Baena et al., 2009)

2.1.5 FRP Material Behaviour

The discussion presented here focuses on the properties and behaviour of FRP composites used as internal reinforcing bars for new concrete structures. When FRP materials are used for internal reinforcing bars, the fibres are continuous and oriented in the axis of the bar's length. This fibre orientation causes FRPs to be highly orthotropic composites with strength and stiffness properties much higher in the direction of the fibres than in the transverse direction. As the mechanical properties of FRP reinforcement are directionally dependent, the properties are typically specified by the manufacturer for the direction of the fibres. The tensile behaviour of FRP reinforcing bars is linear-elastic up to failure. Therefore, FRP bars rupture, and do not exhibit the plastic behaviour, or yielding, that is typical for conventional steel reinforcement. This has significant influence on the flexural

and shear behaviours and failure mechanisms of concrete structures reinforced with FRP.

In terms of compressive strength, steel is considered to be an isotropic material, and thus possesses compressive properties equal to its tensile properties. In doubly-reinforced sections, therefore, steel subjected to compressive stresses is considered to contribute to the resistance of the section. Conversely, FRP is an anisotropic material with a compressive strength that is significantly lower than its tensile strength. The lower compressive strength can be attributed to factors including fibre micro-buckling, transverse tensile stresses in the resin matrix material, and shear stresses (ISIS Educational Committee, 2003). In previous experimental work, the compressive strength was found to be 10%, 40% and 35% of the tensile strength for AFRP, CFRP and GFRP bars, respectively (Kobayashi and Fujisaki, 1995). Other studies have shown that the compressive strength of GFRP bars is approximately 80% of the tensile strength (Chaallal and Benmokrane, 1993). It is clear that this is a highly variable property for FRP products. Therefore, each design code or standard typically neglects the compressive strength of FRP bars as recommended by researchers (Almusallam et al., 1997).

The mechanical properties of FRP materials, such as ultimate tensile strength and tensile modulus of elasticity, will vary between products as these properties are highly dependent on factors including fibre type, resin matrix type, fibre volume fraction, manufacturing process, and varying uses of fillers and additives. Tables 2.2 and 2.3 present the material properties of commercially available GFRP and CFRP products, respectively. Figure 2.3 compares the stress-strain relationships of these products.

As shown in Figure 2.3, GFRP and CFRP reinforcing bars have ultimate tensile strengths that are significantly higher than conventional steel, but fail at much lower strains. It is also clear that the tensile modulus of elasticity of GFRP (42-66GPa) is significantly lower than that of steel (200GPa). As a result of the relatively low axial stiffness of FRP materials, the design of concrete structures reinforced with FRP bars will typically be governed by

Table 2.2: Available GFRP Products

	Bar Designation	Nominal Bar Diameter (mm)	Guaranteed Tensile Strength (MPa)	Tensile Modulus of Elasticity (GPa)	Ultimate Strain (%)
V-Rod - LM Grade I (Pultrall, 2013a)	#3	10	880	42.5	2.07
	#4	13	1000	42.5	2.35
	#5	16	940	42.5	2.21
	#6	19	940	42.5	2.21
	#8	25	960	42.5	2.26
V-Rod - Standard Grade II (Pultrall, 2013b)	#2	6	990	52.5	1.89
	#3	10	1100	52.5	2.10
	#4	13	1140	52.5	2.17
	#5	16	1130	52.5	2.15
	#6	19	1110	52.5	2.11
	#7	22	1100	52.5	2.10
	#8	25	800	52.5	1.52
V-Rod - HM Grade III (Pultrall, 2012a)	#3	10	1372	65.1	2.11
	#4	13	1312	65.6	2.00
	#5	16	1184	62.6	1.89
	#6	19	1105	63.7	1.73
	#7	22	1059	62.6	1.69
	#8	25	1000	66.4	1.51
	#10	32	1093	65.1	1.68
Aslan 100 (Hughes Brothers, 2011a)	#2	6	896	46.0	1.94
	#3	10	827	46.0	1.79
	#4	13	758	46.0	1.64
	#5	16	724	46.0	1.57
	#6	19	690	46.0	1.49
	#7	22	655	46.0	1.42
	#8	25	620	46.0	1.34
	#9	29	586	46.0	1.27
	#10	32	551	46.0	1.19
ComBAR (Schoeck, 2013)	-	8	>1000	>63.5	1.67
	-	12	>1000	>63.5	1.67
	-	16	>1000	>63.5	1.67
	-	25	>1000	>63.5	1.67

Table 2.3: Available CFRP Products

	Bar Designation	Nominal Bar Diameter (mm)	Guaranteed Tensile Strength (MPa)	Tensile Modulus of Elasticity (GPa)	Ultimate Strain (%)
V-Rod - Carbon (Pultrall, 2011a)	#2	6	1356	127.0	1.20
	#3	10	1431	120.0	1.33
	#4	13	1765	144.0	1.32
	#5	16	1532	140.0	1.18
Aslan 200 (Hughes Brothers, 2011b)	#2	6	2241	124.0	1.81
	#3	10	2172	124.0	1.75
	#4	13	2068	124.0	1.67

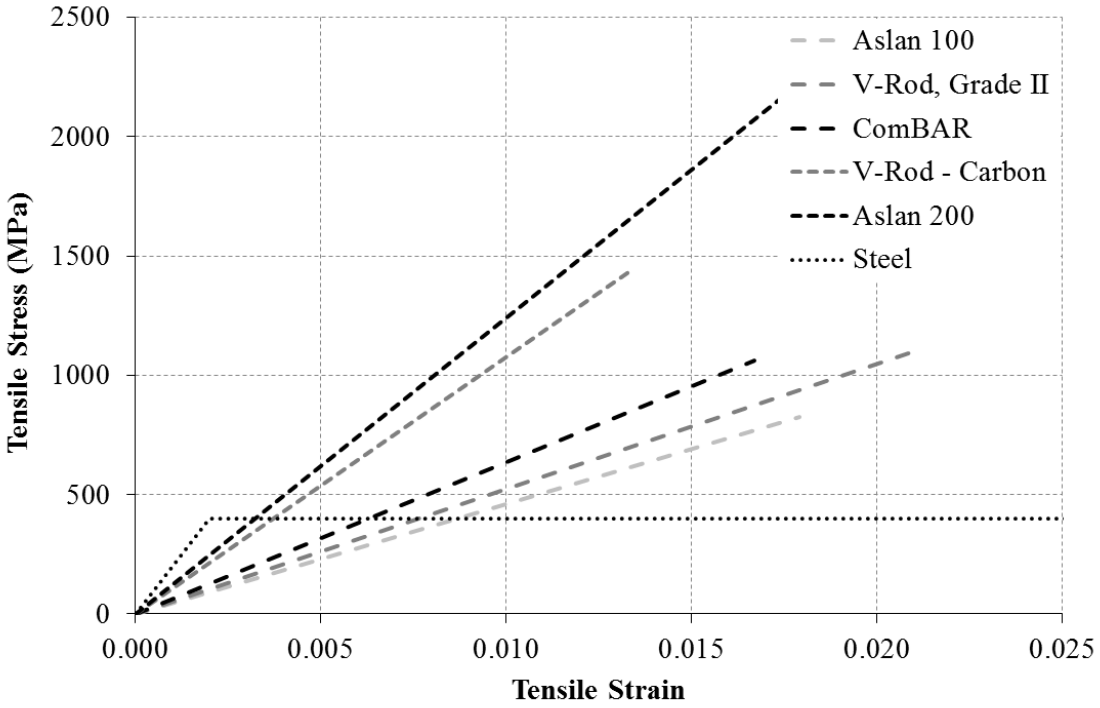

Figure 2.3: Stress-Strain Response for Various FRP Products

serviceability limits.

2.1.6 Advantages and Applications of Internal FRP Reinforcing Bars

FRP reinforcing bars have become a preferred alternative to conventional steel reinforcement in new concrete structures due to the superior durability properties of FRP composites. Steel reinforced concrete structures are susceptible to corrosion of the reinforcement. This corrosion induces tensile stresses within the concrete which often leads to spalling or delamination of the concrete. Corrosion also reduces the area of reinforcement available to provide strength, thus weakening the structure. Therefore, corrosion leads to deterioration that may be limited to aesthetic concerns only, or may progress to failure of the structure. FRP reinforcing bars do not corrode electrochemically, making this technology an attractive solution for structures in corrosive environments. Figure 2.4 presents four examples of reinforced concrete structures that are highly susceptible to corrosion and have successfully used FRP reinforcement.

Underground concrete storage tanks often contain highly corrosive liquids that may attack the reinforcement. Figure 2.4a depicts the use of Pultrall's V-Rod GFRP bars to reinforce the walls and foundation slab of a water treatment chlorination tank located in Thetford Mines, Quebec in 2012 (Pultrall, 2011a). Concrete bridge decks are also highly susceptible to corrosion due to the use of de-icing salts on roads in the winter months. Figure 2.4b depicts the use of Pultrall's V-Rod GFRP bars to reinforce the historic Bridgeport Bridge located in Kitchener, Ontario during a rehabilitation in 2009 (Pultrall, 2009). Concrete barrier walls are also exposed to splashing of corrosive de-icing salts from vehicles on roads and bridges, and are thus highly susceptible to corrosion. Figure 2.4c depicts the use of Schoeck's ComBAR GFRP bars to reinforce the concrete barriers on the Irvine Creek

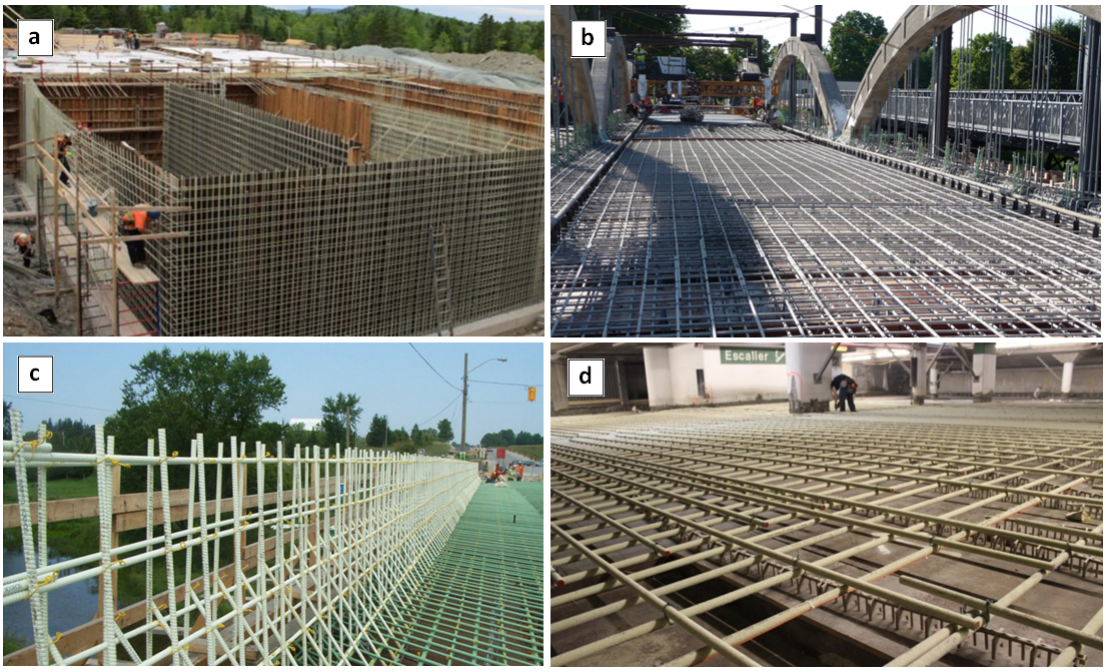

Figure 2.4: Various Applications of FRP Reinforcement

Bridge located near Fergus, Ontario in 2009 (Schoeck, 2009). Parking structures are also exposed to high levels of de-icing salts that fall off incoming vehicles. Figure 2.4d depicts the use of Pultrall's V-Rod GFRP bars to reinforce the floor slabs of the La Chanceliere Parking Garage located in Quebec City, Quebec in 2011 (Pultrall, 2012a).

FRP materials are also electromagnetically inert. This property is advantageous for structures that house equipment that use magnetic fields that are sensitive to the presence of steel. The functionality and precision of such equipment may be hindered by the mere presence of steel reinforcement in the concrete. Therefore, nano-technology laboratories, hospitals using magnetic resonance imaging (MRI), and toll booths are all applications that benefit from the use of FRP materials. The Mike and Ophelia Lazaridis Quantum-Nano Centre at the University of Waterloo is a local example where GFRP reinforcing bars have been used in the concrete floor slabs to prevent the interference of very sensitive equipment.

A further benefit of FRP reinforcing bars is their extremely high strength-to-weight ratio.

With tensile strengths that are significantly higher than the yield strength of steel, FRP bars are approximately one fifth the weight of steel (ISIS Educational Committee, 2003). As the weight of the reinforcement is minimal relative to the weight of the concrete, this lower reinforcement weight will not reduce the overall weight of the structure significantly. However, this lighter weight is advantageous as it will increase the ease of installation, handling, and shipping.

2.1.7 Limitations and Considerations for Internal FRP Reinforcing Bars

There are also disadvantages to using FRP reinforcing bars as an alternative to conventional steel bars. Although the cost of FRP bars continues to decrease as manufacturing processes are refined, the initial material cost of FRP reinforcement remains more expensive than steel. However, it has been shown that if a life-cycle analysis is performed to compare FRP reinforcement with other reinforcement alternatives (unprotected steel, cathodic protection, and epoxy-coated steel), the cost of the FRP design is significantly less (Eamon et al., 2012). This is a result of the superior durability of FRP reinforced structures that do not require the extensive rehabilitation work that is typical of steel reinforced structures.

A further disadvantage of FRP reinforcing bars, with GFRP most specifically, is their relatively low tensile modulus of elasticity as compared to steel. Concrete structures reinforced with FRP will experience larger reinforcement strains as a result of this lower axial stiffness, which will lead to the development of wider cracks, thus larger member deflections (Zhao, 1999). It is thus typical for the design of FRP reinforced concrete structures to be governed by serviceability limits as opposed to ultimate strength limits. Concrete members reinforced with FRP may then require more bars to satisfy serviceability requirements,

which may lead to highly congested formwork for cast-in-place concrete.

A further consideration that must be made when designing concrete structures reinforced with FRP materials is the potential of creep rupture. Polymeric resins are viscoelastic and their behaviour is characterized by time dependent factors including creep, stress relaxation, and load rate effects. Creep is the progressive deformation of a material with time under sustained loading. When FRP materials are subjected to constant elevated stress levels, sudden failure may occur; a failure mode referred to as creep rupture. To prevent failure of an FRP reinforced member due to creep rupture of the FRP reinforcement, design standards have specified limits on the maximum allowable stress to be carried by the reinforcement under service loading. These stress limits are typically expressed as a percentage of the ultimate tensile strength of the FRP.

Other factors to be considered when using FRP products include exposure to ultraviolet radiation, exposure to highly alkaline environments, exposure to elevated temperatures during a fire event, and exposure to moisture. The influence of these factors on the performance of internal FRP reinforcing bars remains a topic of research, and will not be discussed here. However, the use of bends in FRP internal reinforcement also introduces significant challenges in the design of FRP reinforced structures, and will be discussed next.

2.2 Bent FRP Reinforcement

Bent reinforcement in concrete structures is commonly required for shear reinforcement such as stirrups or to provide development to straight bars using hooks. Conventional steel reinforcement exhibits elasto-plastic behaviour, and can be easily formed to many shapes by cold bending, thus minimizing detailing costs. FRP reinforcement, however,

introduces challenges when compared to steel with regards to producing these bends. As discussed previously, thermosetting resins are the preferred resin material used for structural engineering applications and have highly cross-linked molecular structures. This molecular structure causes the material properties to be severely degraded if the composite is reheated. Therefore, once a thermoset FRP has cured and hardened, it cannot be bent. If a bend or hook is required, it must be produced during the manufacturing process before the resin has cured. As a result, unlike for steel reinforcement, this introduces a significant practical limitation as the modification or bending of FRP bars is not possible on a construction site.

A further concern with the use of bent FRP bars is the reduction of tensile strength that occurs at the bend. At a bend, in the corner portion of a stirrup for example, the FRP is subjected to the axial tensile stresses that are developed in the straight portion of the bar, the compressive transverse bearing stresses exerted by the confined concrete, and the bond stresses developed along the concrete-bar interface. This combination of transverse and axial stresses creates a multiaxial state of stress at the bend as shown in Figure 2.5.

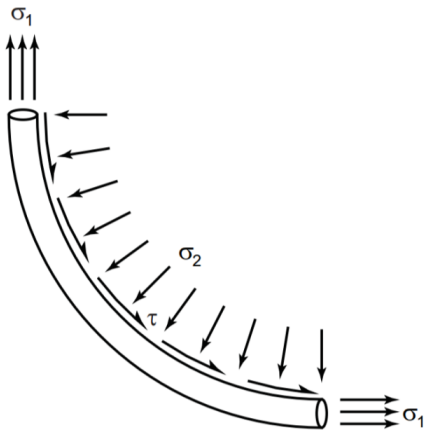

Figure 2.5: Multiaxial State of Stress at Bent Portion (International Federation for Structural Concrete, 2007)

Referring to Figure 2.5, σ_1 represents the axial tensile stress, σ_2 represents the transverse bearing stress, and τ represents the bond stresses. Researchers have shown that this state

of multiaxial stress can reduce the tensile strength of the FRP at the bend to as low as 40% of the tensile strength of the straight portion (Currier et al., 1994; Ueda et al., 1995; Ehsani et al., 1995; Morphy et al., 1997; Shehata et al., 2000). Consequently, if high stresses are developed in the reinforcement, premature failure is expected to occur at the bends prior to the full utilization of the straight portions.

It has been found that the bend strength is dependent on factors including the ratio of bend radius to bar diameter (r_b/d_b), concrete strength, and tail length (for hooks). The bend radius has been identified as a significant contributor to the strength of a bend, with larger radii yielding higher strengths (Imjai et al., 2007a). Equation 2.1 presents the design tensile strength of FRP bars at a bend as proposed by the Japan Society of Civil Engineers (JSCE, 1997):

$$f_{fb} = \left(0.05\frac{r_b}{d_b} + 0.3\right) f_{fu} \leq f_{fu} \tag{2.1}$$

where f_{fb} is the design tensile strength of the FRP at the bend, r_b is the radius of the bend (mm), d_b is the diameter of the bar (mm), and f_{fu} is the design ultimate tensile strength of the straight portion of the FRP. Imjai et al. (2007a) recommended an r_b/d_b value greater than 4 to guarantee a bend capacity of 40% of the ultimate strength of the straight portion. CSA S806-12 and ACI 440.1R-06 both require a minimum value of $r_b/d_b = 3$ for bent bars.

There may also be manufacturing defects present in the bent portion of the bar that influence the strength in this region. Fibres located at the inside of the bend radius may experience kinking or buckling. This results in fibres that are no longer oriented in the axis of the bar. Furthermore, distortion of the cross-section may occur at the bend, such as the collapse or flattening of the section as shown in Figure 2.6. These defects in combination with the multiaxial state of stress at the bend will significantly reduce the capacity of the bent bar.

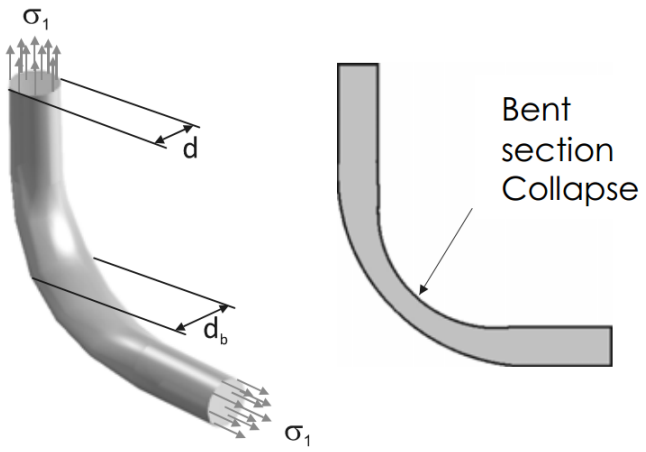

Figure 2.6: Flattening of Cross-Section at Bend (Imjai et al., 2007b)

2.3 Tests on Concrete Beams with GFRP Flexural and Shear Reinforcement

An experimental test program was conducted at the University of Waterloo by graduate student Martin Krall and his supervisor Dr. Maria Anna Polak. Three-point bending tests were performed on simply-supported concrete beams reinforced with glass fibre reinforced polymer (GFRP) longitudinal bars and GFRP stirrups. The results of this test program form the basis for the finite element analysis (FEA) performed for this thesis. The experimental results were used to develop, calibrate, and corroborate the FEA models presented by the author, thus the intent of this section is to provide an overview of this testing. This section provides an overview of the following: the test program objectives, the beam specimens tested, the design considerations used to construct the beams, and the observations recorded during testing. For further details regarding this testing, the reader is directed to the thesis of Martin Krall (Krall, 2014).

2.3.1 Objectives of Beam Testing

The original objective of the experimental beam testing was to investigate the influence of GFRP longitudinal reinforcing bar arrangements on the effective strength of GFRP stirrups. As discussed previously, it has been identified in the literature that the ultimate strength of FRP at bends is significantly less than the strength of the straight portion. Therefore, the strength of a GFRP stirrup will be governed by the strength at the corners. It was therefore the objective to determine how the longitudinal bar arrangement influenced the utilization of the stirrup bend strength, thus the influence on the strength of the stirrups. Unfortunately, the tested beams behaved more like deep beams as opposed to slender beams, and no stirrups ruptured during the testing. It was therefore not possible to make conclusions regarding the strength of the stirrups, thus a modified hypothesis was necessary.

The modified objective of the experimental beam testing was to investigate the influence of flexural and transverse reinforcement arrangements on the shear strength and failure mode of GFRP reinforced beams. Parameters that were varied included the longitudinal bar configuration, longitudinal bar diameter, stirrup diameter, and stirrup spacing. The influence of these parameters on the failure mode, peak load, and reinforcement strains was studied.

2.3.2 Overview of Beam Specimens

The experimental program consisted of the testing of a total of twelve concrete beams. Three longitudinal bar core diameters were considered, including 12mm, 16mm, and 25mm. Note that the term "core diameter" will be used throughout this thesis and refers to the diameter of the bar excluding the ribs. When calculating tensile strength properties of an FRP ribbed bar, it is typical to utilize only the material within the core and not the ribs.

For each longitudinal bar diameter, a different bar layout was used. Four stirrup spacings were considered, including 150mm, 220mm, 230mm and INF (INF refers to an infinite spacing, meaning no stirrups were used). Two stirrup core diameters were considered, including 12mm and 20mm. The following naming convention was used for all beams:

BM XX-(s)YYY

XX is a two digit value that is equal to the core diameter of the longitudinal bars in millimetres. YYY is a three digit value that is equal to the spacing of the stirrups within the shear span in millimetres. The inclusion of 's' in front of the stirrup spacing YYY means that the beam uses stirrups with a larger diameter of 20mm; the absence of 's' in front of YYY means that the beam uses stirrups with a diameter of 12mm. To demonstrate this naming convention, BM 12-150 has GFRP longitudinal bars with core diameters of 12mm and GFRP stirrups with core diameters of 12mm and spaced at 150mm; BM 16-s230 has GFRP longitudinal bars with core diameters of 16mm and GFRP stirrups with core diameters of 20mm and spaced at 230mm. Table 2.4 summarizes the beam specimens tested.

Table 2.4: Beam Specimen Naming Convention

Stirrup Spacing	Longitudinal Bar Core Diameter (mm)			Stirrup Core
(mm)	12	16	25	Diameter (mm)
INF	BM 12-INF	BM 16-INF	BM 25-INF	12
150	BM 12-150	BM 16-150	BM 25-150	12
220	BM 12-220	BM 16-220	BM 25-220	12
230	BM 12-s230	BM 16-s230	BM 25-s230	20

The configuration of the longitudinal bars was dependent on the bar diameters. Beams with 12mm bars used three layers of four bars (12 bars total). Beams with 16mm bars used two layers of three bars (6 bars total). Beams with 25mm bars used one layer of two bars (2 bars total). Bar configurations were chosen to create test groups which corresponded to

having one, two, or three layers of bars. The size and number of bars in each layer were selected such that the moment resistance of each beam configuration would be similar. Figure 2.7 presents the longitudinal bar configurations and reinforcement core diameters for all beams tested.

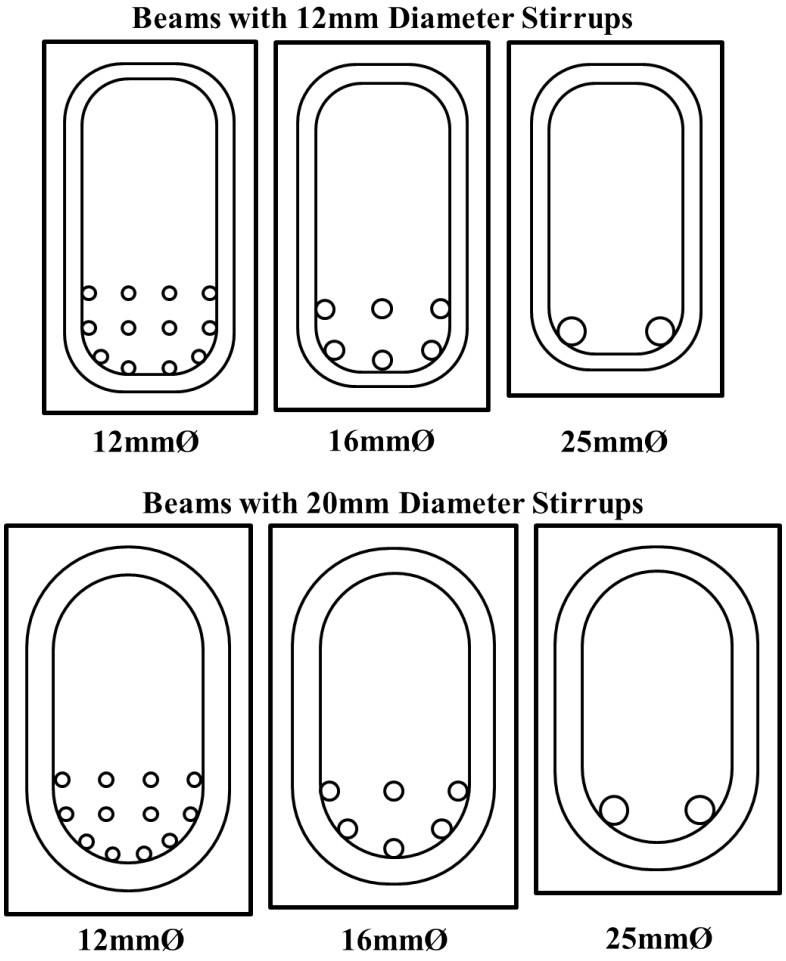

Figure 2.7: Bar Configurations for Tested Beams

For all twelve beams, the shear span to effective depth ratio (a/d) was fixed at 2.5. This is the limit between beam action and deep-beam action failure modes. Larger ratios were initially considered, but increased the probability of flexural failure which did not satisfy the objectives of the testing. The height of each beam, h, was altered in order to maintain a constant effective depth to the longitudinal tensile reinforcement, d, of 270mm for all beams. As the a/d ratio and d were equal for all beams, the shear span, a, was also constant

for all beams at 675mm. A constant shear span allowed a single pedestal configuration to be used for the testing of all twelve beams, thus reducing the labour required for testing. The width of the beam, b, was dependent on the stirrup diameter; beams with 12mm diameter stirrups had a designed beam width of 200mm, and beams with 20mm diameter stirrups had a designed beam width of 230mm.

The longitudinal reinforcing bars used in the beam specimens were ComBAR, glass fibre reinforced polymer bars provided by Schoeck Canada. The longitudinal bars were produced using the pultrusion process with ribs cut into the surface to improve the bar's bond properties. Closed-loop stirrups were also provided by Schoeck Canada. These stirrups were manufactured by enveloping the fibres and resin using a corrugated polypropylene conduit pipe. This pipe is flexible in the bending direction but stiff in the radial direction. This manufacturing technique was aimed to increase the strength of the stirrups in the bend regions. Table 2.5 provides a summary of the mechanical properties of the GFRP reinforcement used in the beam designs as specified by Schoeck Canada at the time of testing and Figure 2.8 depicts the products used for the longitudinal and transverse reinforcement. Referring to Table 2.5, E_f is the tensile modulus of elasticity, A_f is the cross-sectional area, $f_{fu,straight}$ is the ultimate tensile strength of the FRP in the straight portion, $f_{fu,bend}$ is the ultimate tensile strength of the FRP in the bent region, and r_{bend} is the radius of the stirrup corners. It is important to note that the strength and stiffness properties presented are applicable to the direction of the fibres only; FRP is significantly weaker in the transverse direction.

The beams and reinforcement were outfitted with a series of instrumentation to record strains and displacements during testing. Strain gauges were used to measure the axial strains of the longitudinal reinforcing bars. Gauges were positioned at mid-span on the middle bars of each reinforcing layer for the BM 12-YYY and BM 16-YYY series and at mid-span on both bars for the BM 25-YYY series. Strain gauges were also used to

Table 2.5: Properties of GFRP Reinforcement Used in Beam Testing

	Longitudinal Bars			Stirrups				
Beam	$f_{fu,straight}$ (MPa)	E_f (GPa)	A_f (mm^2)	$f_{fu,straight}$ (MPa)	$f_{fu,bend}$ (MPa)	E_f (GPa)	A_f (mm^2)	r_{bend} (mm)
12-INF								
12-150	1000	60	113	1000	700	50	113	42
12-220								
16-INF								
16-150	1000	64	201	1000	700	50	113	42
16-220								
25-INF								
25-150	1000	60	491	1000	700	50	113	42
25-220								
12-s230		60	113					
16-s230	1000	64	201	900	550	50	314	70
25-s230		60	491					

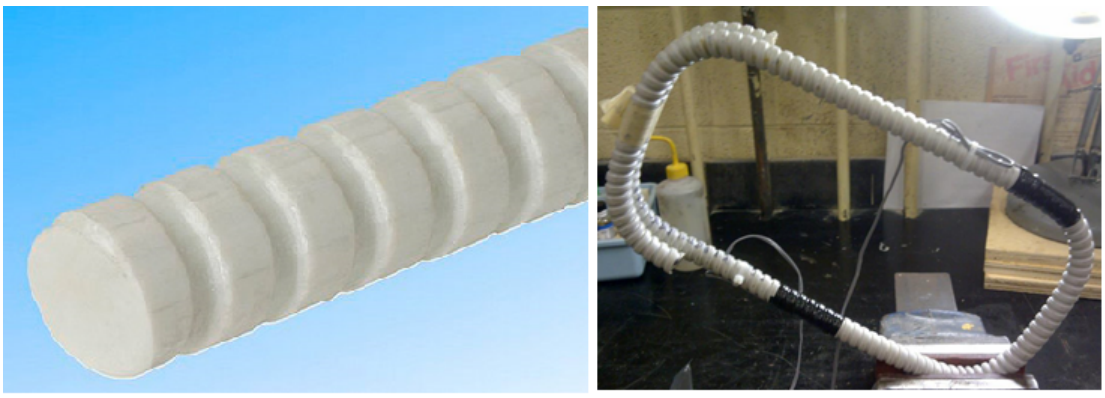

Figure 2.8: Reinforcement used in Testing: (a) Longitudinal GFRP Bar; (b) GFRP Stirrup

measure the axial strains of the stirrups. For beams with stirrups, one gauge was placed on the straight portion of the stirrup at mid-height, while a second gauge was positioned immediately above the bend region on the opposite leg of the stirrup. Beam displacements

were measured at mid-span and at the two quarter-span locations using linear variable displacement transformers (LVDTs). Appendix A presents the detailed drawings of each beam, as well as the location and labeling convention for all reinforcement strain gauges.

2.3.3 Beam Design Considerations

The maximum load permitted by the testing frames at the University of Waterloo was 500kN at the time of testing. Beams were therefore designed to have modest cross-sections in order to fail at a load within the 500kN limit. The next challenge was to design beams that had varying bar configurations and that would fail due to shear. The design became an exercise of decreasing the beam dimensions to satisfy the load testing limits without creating a beam that failed due to flexure.

A further design consideration was the required width of the beams to accommodate the stirrups. Ideally, all beams would have a constant width for comparison purposes. A width of 200mm was found to be acceptable for the beams that used 12mm diameter stirrups. However, as shown in Table 2.5, the 20mm diameter stirrups that were used in beams BM 12-s230, BM 16-s230, and BM 25-s230 required a larger radius at the bends as specified by the manufacturer. Manufacturers and design standards specify minimum limits on the bend radius to bar diameter ratio for reasons discussed previously. Therefore, it was necessary to increase the width of the beams to 230mm where larger stirrups were used to accommodate the larger bend radii.

CSA S806-12 - *Design and Construction of Building Structures with Fibre-Reinforced Polymers* was used to design the concrete beams for shear and flexure. The models proposed by Nehdi et al. (2007) were also utilized in the prediction of shear strengths. Maximum deflections were predicted using CSA S806-12 assuming a maximum load of 500kN. These deflection predictions were necessary to estimate the operating ranges of the LVDTs that

were used to measure beam deflections. Deflection predictions also provided a basis to determine an appropriate displacement-controlled load rate for the testing frame.

In order to keep the strength of the beams within testing limits, it was necessary to deviate from the provisions of CSA S806-12 when designing the concrete cover and bar spacing. The requirements for minimum bar spacing and minimum cover were relaxed for the purposes of this experimental investigation in order to accommodate the required number of bars. With the reduced bar spacing, some beams became highly congested, specifically the BM 12-YYY series (beams with twelve longitudinal bars with diameters of 12mm) as shown in Figure 2.7. It was therefore necessary to use a concrete mix design that was highly workable to ensure that all voids around the congested reinforcing bars were filled in order to prevent honeycombing. To achieve this, a mix with 3/8 inch (9.5mm) pea-stone aggregate and a slump of 200mm-250mm was specified. The mix also utilized plasticizer to encourage a workable batch.

2.3.4 Experimental Results and Observations

As discussed previously, no stirrups ruptured during testing, which prompted the revision of the testing objectives. Failure modes were very consistent amongst each beam series. Beams with no stirrups experienced shear-tension failures, while beams with stirrups experienced shear-compression / strut crushing failures. Cracking of all beams initiated with vertical flexural cracking at the mid-span. As loading increased, additional flexural cracks developed. For beams with stirrups, these flexural cracks typically developed at the stirrup locations. With further loading, diagonal shear cracks developed. All beams, except BM 25-INF, ultimately failed along a crack plane that ran from the point of load application to the support bearing plate. Figures 2.9 and 2.10 depict the typical failure mode of beams without and with stirrups, respectively.

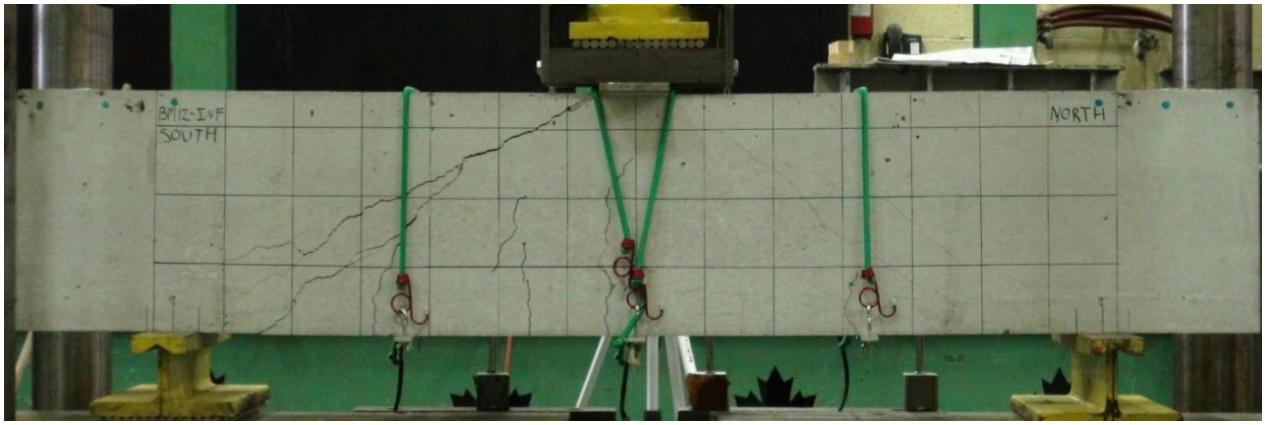

Figure 2.9: Typical Failure Mode for Beams with No Stirrups

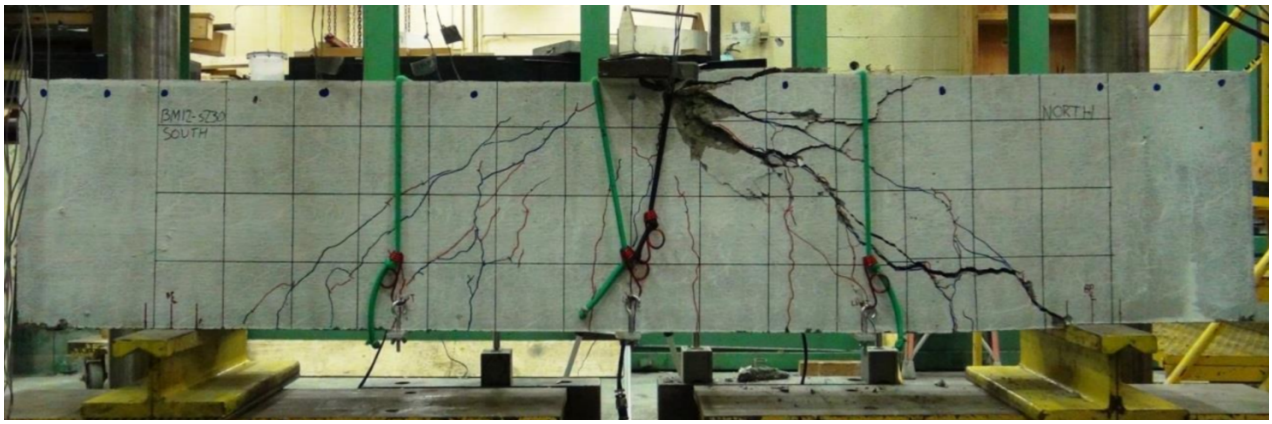

Figure 2.10: Typical Failure Mode for Beams with Stirrups

Figure 2.9 depicts BM 12-INF after testing and represents the typical failure mode of beams with no stirrups. It can be seen that the major crack ran from the load plate to the support plate. At failure, the cracks tended towards the three layers of reinforcement indicating tensile splitting. Figure 2.10 depicts BM 12-s230 after testing and represents the typical failure mode of beams with stirrups. It can be seen that the shear crack is significantly larger than for the beams with no stirrups. There is also a region of crushed concrete adjacent to the load plate, indicating a shear-compression failure.

Reinforcement strains were also analyzed. Longitudinal bar strains were found to be initially stiff before cracking. After cracking, the response softened significantly but remained linear until the beam's peak load was reached, as expected. Figure 2.11 depicts the ap-

plied load vs. axial strain plot for the longitudinal reinforcement within BM 25-150; this response was typical for all beams.

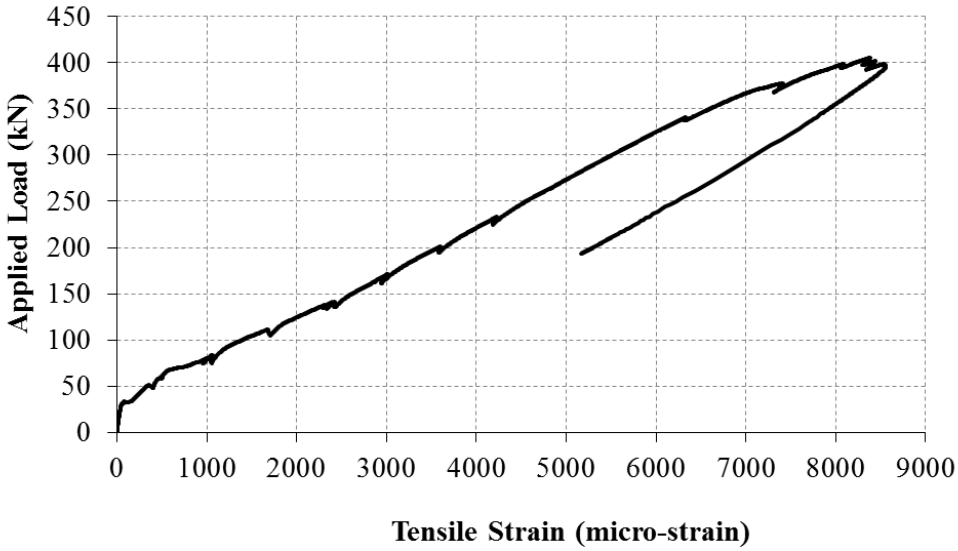

Figure 2.11: Typical Load-Strain Response of Longitudinal Reinforcing Bars

For beams with longitudinal bar diameters of 16mm and stirrups with diameters of 12mm (BM 16-YYY), strain gauges were positioned on the longitudinal bars at multiple positions along the beam's length. The motivation behind this was to study the development of strains in each bar at different locations. Figure 2.12 depicts the positions of the six strain gauges used for BM 16-220, as well as the axial strains at each gauge location under varying load levels.

Each curve in Figure 2.12 represents a different load level during the beam testing as a percentage of the peak load. At lower loads, only the strain gauges closest to the mid-span experienced significant strains. As loading increased, sections closer to the support began to experience larger strains. This plot is significant as it shows that the three gauges closest to the mid-span, Gauges 4, 5 and 6, experienced similar strains at peak load. This observation indicates that the bar had debonded in this region. Furthermore, the fact that Gauge 1 experienced negligible strains at all load levels indicates that the bar was adequately anchored at the ends. These observations of a tied-arch mechanism indicate

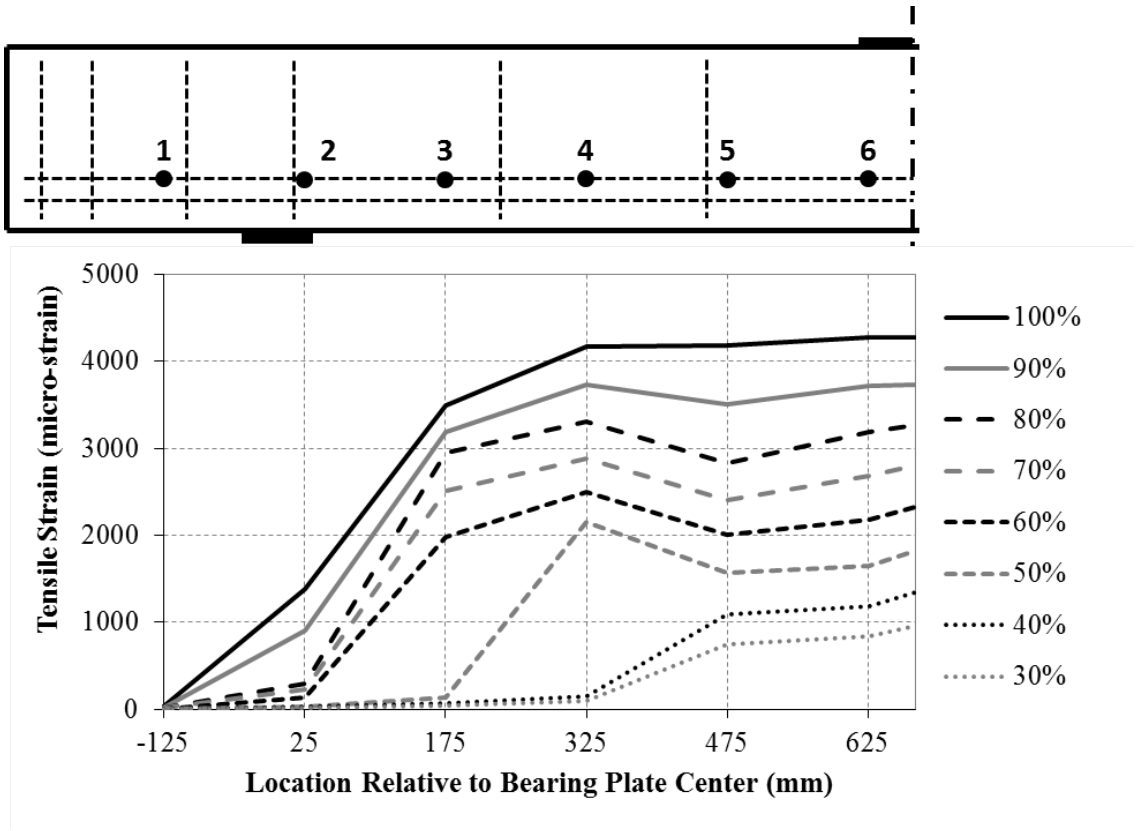

Figure 2.12: Strain Development in Reinforcing Bars - BM 16-220

that BM 16-220 experienced arch-action, which was reflected in the observed failure mode. Similar strain behaviour was observed for BM 16-150, which also experienced arch-action failure, but was not observed for BM 16-INF which experienced a shear-tension failure.

The strain behaviour of the stirrups was also analyzed. It was found that the strains within the straight portion of the stirrup were significantly larger than the strains in the regions near the stirrup bends. It was also found that stirrups in the middle of the shear span experienced larger strains than the stirrups closest to the supports and load location. This is to be expected, as the middle stirrups intersect the diagonal shear cracks that formed between the load application point and the support bearing plate.

Using the beam displacement data, load-displacement relationships were created for each beam. Figure 2.13 presents the load-displacement responses for all beams, with beams

organized with respect to stirrup spacing.

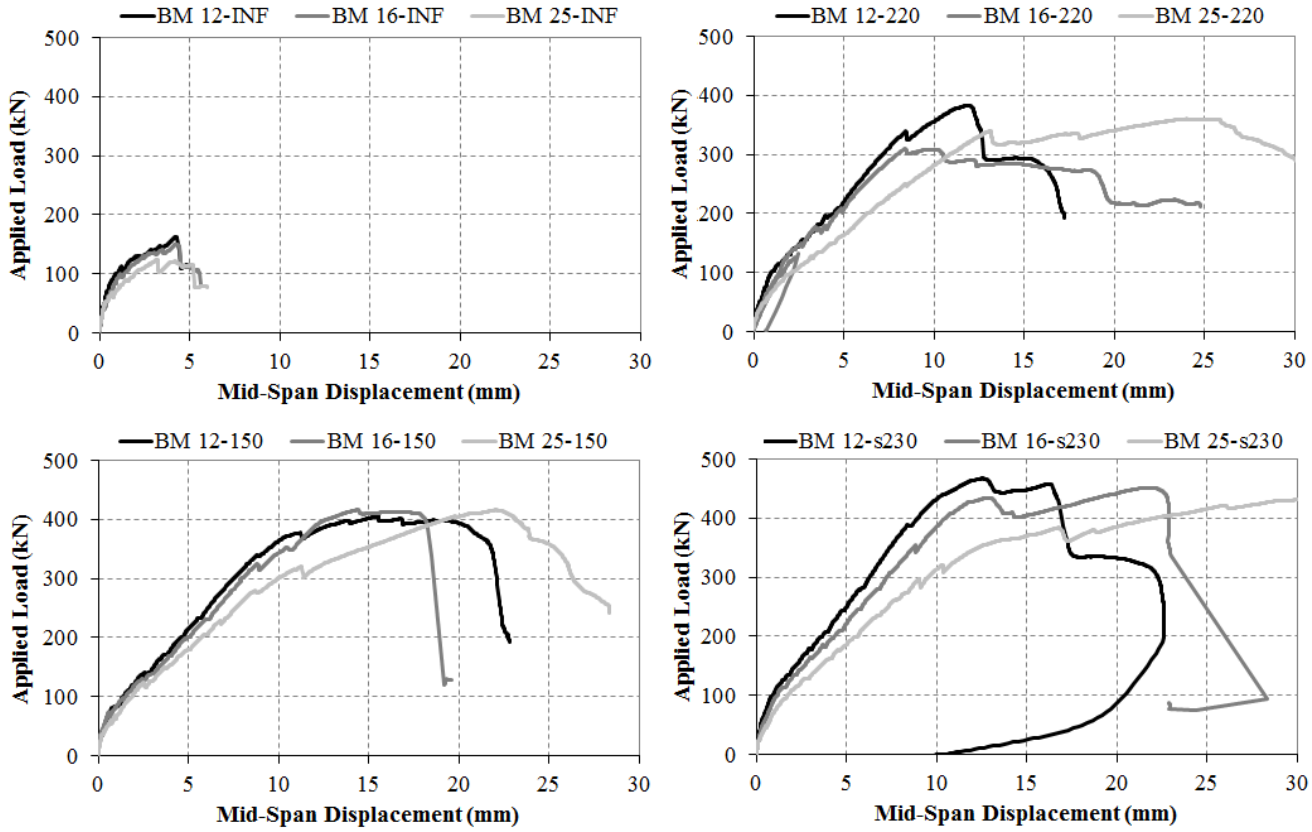

Figure 2.13: Comparison of Load-Displacement Responses

It was found that beams with higher flexural reinforcement ratios displayed stiffer load-displacement responses than those with lower flexural reinforcement ratios. For beams with no stirrups, an increase in flexural reinforcement ratio correlated to both an increase in peak load and mid-span deflection at peak load. For beams with stirrups, beams that had the same shear reinforcement ratio (same stirrup spacing) had similar peak loads. For beams with 12mm diameter stirrups, an increase in shear reinforcement ratio correlated to both an increase in peak load and mid-span deflection at peak load. It was also observed that as the shear reinforcement ratio increased, the crack sizes at peak load also increased. The plots also show that beams reinforced with GFRP reinforcing bars and stirrups are able to exhibit some post-peak ductility.

2.4 Strength Prediction of FRP Reinforced Beams

The experimental data and observations as collected by Krall (2014) were used to calibrate the numerical models proposed in this thesis. The model output will also be compared to the shear strength predictions as provided by CSA S806-12 - *Design and Construction of Building Structures with Fibre-Reinforced Polymers*, as well as the shear strength model proposed by Nehdi et al. (2007). An overview of these two models is presented in this section.

2.4.1 Shear Strength of FRP Reinforced Beams - CSA S806-12

The approach used by CSA S806-12 to determine the factored shear resistance of a concrete section reinforced with FRP longitudinal and transverse reinforcement follows the traditional approach used for steel reinforced sections where the contribution of the concrete and stirrups are summed. The provisions for the design of members for shear is found in Clause 8.4.4. The factored shear resistance, V_r, is determined using Equation 2.2 as specified in Clause 8.4.4.4.

$$V_r = V_c + V_{sf} \tag{2.2}$$

where V_c is the factored shear resistance provided by the concrete and V_{sf} is the factored shear resistance provided by the FRP shear reinforcement. For non-prestressed members, the ultimate shear resistance must not exceed the following:

$$V_{r,max} = 0.22\phi_c f_c^{'} b_w d_v \tag{2.3}$$

where ϕ_c is the material resistance factor for concrete (0.65), $f_c^{'}$ is the compressive strength of concrete, b_w is the width of the member web, and d_v is the effective shear depth. The effective shear depth, d_v, is taken as the greater of $0.9d$ or $0.72h$, where d is the depth to

the centroid of the longitudinal tensile reinforcement and h is the height of the member.

Clause 8.4.4.5 provides the shear resistance contribution provided by the concrete, V_c, and can be determined using Equations 2.4 and 2.5. These equations are applicable to members with an $f_c^{'}$ less than 60MPa and an effective depth less than 300mm.

$$V_c = 0.05\lambda\phi_c k_m k_r (f_c^{'})^{1/3} b_w d_v \tag{2.4}$$

where:

$$k_m = \sqrt{\frac{V_f d}{M_f}} \leq 1.0 \tag{2.5a}$$

$$k_r = 1 + (E_f \rho_{fw})^{1/3} \tag{2.5b}$$

In the above equations, λ accounts for concrete density (typically taken as 1.0 for normal density concrete), V_f and M_f are the factored shear force and bending moment at the section of interest, E_f is the modulus of elasticity of the FRP, and ρ_{fw} is the longitudinal FRP reinforcement ratio. The term k_m is a factor to account for the influence of the bending moment on the shear resistance, and the term k_r is a factor to account for the influence of the reinforcement rigidity on the shear resistance. Equation 2.6 specifies the limitations imposed on the concrete shear resistance:

$$V_c < 0.22\phi_c \sqrt{f_c^{'}} b_w d_v \tag{2.6a}$$

$$V_c > 0.11\phi_c \sqrt{f_c^{'}} b_w d_v \tag{2.6b}$$

Clause 8.4.4.6 provides the shear modification due to the arch effect. For sections that are located within a distance of $2.5d$ from the face of a support reaction that causes compression in the beam, the value of V_c as calculated using Equations 2.4 to 2.6 shall be multiplied

by the factor k_a as given in Equations 2.7 and 2.8:

$$k_a = \frac{2.5}{\frac{M_f}{V_f d}} \tag{2.7}$$

where:

$$1.0 \leq k_a \leq 2.5 \tag{2.8}$$

Clause 8.4.4.7 provides the shear modification due to member size. For members with an effective depth greater than 300mm and with less transverse shear reinforcement than required in Clause 8.4.5.2, the value of V_c as calculated using Equations 2.4 to 2.6 shall be multiplied by the factor k_s as given in Equation 2.9. If the member has an effective depth greater than 300mm but satisfies the minimum shear reinforcement requirement, a k_s value of 1.0 shall be used.

$$k_s = \frac{750}{450 + d} \leq 1.0 \tag{2.9}$$

Clause 8.4.4.9 provides the shear resistance contribution provided by the FRP stirrups, V_{sf}. For members with transverse reinforcement perpendicular to the longitudinal axis, V_{sf} shall be determined using Equation 2.10:

$$V_{sF} = \frac{0.4\phi_f A_{fv} f_{fu} d_v}{s}\ cot\theta \tag{2.10}$$

where ϕ_f is the material resistance factor for FRP (0.75), A_{fv} is the area of FRP shear reinforcement perpendicular to the axis of the member, and s is the spacing of the shear reinforcement. f_{fu} is the ultimate tensile strength of the straight portion of the FRP transverse reinforcement and shall not exceed a value of $0.005E_f$. The angle of the diagonal compressive strut, θ, shall be determined as:

$$\theta = 30^\circ + 7000\varepsilon_l \tag{2.11}$$

where ε_l is the longitudinal strain of the section at mid-depth as determined using Equation 2.12:

$$\varepsilon_l = \frac{M_f/d_v + (V_f - V_p) + 0.5N_f - A_p f_{po}}{2(E_f A_f + E_p A_p)} \geq 0 \tag{2.12}$$

where V_p is the component of the effective prestressing force in the direction of the applied shear, N_f is the factored axial load acting normal to the member's cross-section, A_p is the area of prestressing tendons, f_{po} is the stress in the prestressing tendons when the stress in the surrounding concrete is zero, A_f is the area of the FRP longitudinal tensile reinforcement, and E_p is the modulus of elasticity of the prestressing tendons. When evaluating Equation 2.12, V_f and M_f shall be taken as positive values, and M_f shall not be taken less than $(V_f - V_p)d_v$. The resulting value of θ shall satisfy the following limitation:

$$30^\circ \leq \theta \leq 60^\circ \tag{2.13}$$

2.4.2 Shear Strength of FRP Reinforced Beams - Nehdi et al., 2007

An extensive literature review was conducted by Krall (2014) to investigate current models proposed to predict the shear capacity of FRP reinforced concrete members. It was concluded that the model proposed by Nehdi et al. (2007) was both the simplest formulation as well as the most accurate among available research. The objective of the work proposed by Nehdi et al. (2007) was to develop simple yet accurate design equations to predict the shear strength of FRP reinforced concrete members with and without FRP stirrups. The genetic algorithm approach was used to develop the equations using the experimental results of 168 FRP reinforced concrete beams (68 of which had no shear reinforcement, and 100 of which were reinforced with FRP stirrups). The beams considered were all rectangular, simply supported, and exhibited shear failure. The genetic algorithm approach is

an advanced global optimization technique used for very complex and nonlinear problems. This approach was used to search for an optimum set of coefficients to be used in the proposed equations such that the difference between the predicted shear capacities and the experimental capacities is minimized.

The proposed model consists of two components; one to consider the shear resistance contribution of the concrete (V_{cf}) and the other to consider the shear resistance contribution of the FRP stirrups (V_{fv}). Therefore, the shear resistance as proposed by Nehdi et al. (2007) is as follows:

$$V_r = V_{cf} + V_{fv} \tag{2.14}$$

The shear resistance as contributed by the concrete is dependent on the ratio of a/d as follows:

For a/d $>$ 2.5:

$$V_{cf} = 2.1 \left(\frac{f_c' \rho_{fl} d}{a} \frac{E_{fl}}{E_s} \right)^{0.23} b_w d \tag{2.15}$$

For a/d $<$ 2.5:

$$V_{cf} = 2.1 \left(\frac{f_c' \rho_{fl} d}{a} \frac{E_{fl}}{E_s} \right)^{0.23} b_w d \left(\frac{2.5d}{a} \right) \tag{2.16}$$

The shear resistance as contributed by the FRP stirrups is as follows:

$$V_{fv} = 0.74(\rho_{fv} f_{fv})^{0.51} b_w d \tag{2.17}$$

In the above equations, f_c' is the compressive strength of the concrete, ρ_{fl} is the longitudinal FRP reinforcement ratio, d is the effective depth to the tensile reinforcement, E_{fl} is the modulus of elasticity of the FRP, E_s is the modulus of elasticity of steel, a is the length of the shear span, b_w is the width of the section, ρ_{fv} is the transverse FRP reinforcement ratio, and f_{fv} is the ultimate tensile capacity of the FRP shear reinforcement. These proposed equations were found to accurately predict the shear strength of beams reinforced with

and without FRP stirrups, and were found to be more accurate than existing equations provided by current shear design guidelines and codes.

2.5 Finite Element Modelling of Beams Reinforced with FRP

Ferreira et al. (2001) formulated a model for the finite element analysis of concrete beams reinforced with GFRP longitudinal reinforcing bars. The proposed model utilized two-dimensional degenerated concrete shell elements based on a first-order shear deformation theory. This shell element allowed for a layered discretization of the laminate materials. The compressive behaviour of concrete was modelled using two unidirectional approaches: Elastic-perfectly plastic and strain-hardening. A dual criterion for yielding and crushing conditions in terms of stresses and strains was considered. To model the tensile behaviour of concrete, a smeared crack approach was used. This approach assumes that the cracked concrete remains a continuum with degraded material properties. The tensile response of concrete was assumed to be linear-elastic up to peak stress, at which point there is a sudden and complete loss of stress carrying capacity. Once cracking has occurred, the elastic modulus is reduced to zero in the direction perpendicular to the cracked plane, and a reduced shear modulus is used. The GFRP tensile reinforcing bars were modelled as elastic-brittle layers of equivalent thickness, with strength and stiffness properties in the bar direction only. Several experiments of concrete beams were performed to validate the model, and strong correlation between the proposed model and the experimental results was observed. Although beam experiments were used for validation, the model is generally applicable to plates or shells of arbitrary shape.

Nour et al. (2007) performed finite element modelling of concrete structures reinforced with

internal FRP materials. Bouzaiene and Massicotte (1997) developed a three-dimensional hypoelastic constitutive model that can simulate the behaviour of concrete under multiaxial stress conditions. This model considers the elastic modulus degradation under loading-unloading, the transition between brittle and ductile behaviour under confinement, and the increase in concrete volume as the ultimate strength is approached. Massicotte et al. (2007) later introduced a tension stiffening model for steel reinforced concrete members to the original model proposed by Bouzaiene and Massicotte (1997). This model integrates variable tension stiffening factors defined as a function of the member strain to account for the steel-concrete interaction as proposed by Fields and Bischoff (2004). The post-cracking modelling of concrete uses the smeared crack approach as proposed by Rashid (1968). This new model was made portable, meaning the constitutive model can be implemented as a user-defined subroutine at Gauss integration point within finite element software. Nour et al. (2007) implemented this model into the general-purpose finite element software ABAQUS/Standard and ABAQUS/Explicit to analyze slender rectangular beams internally reinforced with GFRP longitudinal bars and steel stirrups. As a result of the lower modulus of elasticity of FRP reinforcement as compared to steel, the revised tension-stiffening relationship applicable to GFRP proposed by Bischoff and Paixao (2004) was used in the models performed by Nour et al. (2007). Concrete was modelled using 8-noded three-dimensional solid elements. The internal reinforcement, including longitudinal bars and stirrups, were modelled using 2-noded truss elements that were embedded into the solid concrete elements. Experimental testing performed by Grace et al. (1998) was used to validate the proposed model, and strong correlation between the model and the tests was observed.

Rafi et al. (2007) performed a two-dimensional non-linear finite element analysis of simply supported concrete beams reinforced with carbon fibre reinforced polymer (CFRP) bars. The constitutive model that was used for concrete in compression was proposed by Popovics (1973) and later modified by Thorenfeldt et al. (1987). The uniaxial stress-strain

relationship for compression includes an ascending branch until the ultimate compressive strength, followed by a gradual descending branch representing strain-softening. Further recommendations for the variables within this model as proposed by Collins and Mitchell (1991) were used for this analysis. The tensile behaviour of the concrete was modelled using a smeared crack approach. The uncracked concrete was considered isotropic, while the cracked concrete was considered orthotropic. The cracking criterion was based on fracture energy (G_f), where G_f was calculated using the relationship proposed by Wittmann (2002) as shown in Equation 2.18:

$$G_f = a\Phi_{max}^n \tag{2.18}$$

where $a = 80.6$, $n = 0.32$, and Φ_{max} is the maximum aggregate size. A fracture energy of 0.168N/mm was used for this study. The rotating crack model (RCM) was used to simulate the formation and propagation of cracks. The FRP reinforcing bars were modelled as linear-elastic up to failure with a von Mises yield criterion, associated flow and isotropic hardening. The concrete was modelled as two-dimensional isoparametric quadrilateral plane stress elements with eight nodes. The FRP reinforcement was modelled as uniaxial bar elements with strength and stiffness properties in the bar direction only. These bar elements were embedded into the quadrilateral concrete elements. The non-linear analysis was performed by incorporating the material models and element formulation into the finite element analysis software DIANA. Excellent convergence and numerical stability was observed, and strong agreement between the recorded experimental data and model was found.

Rafi et al. (2008) performed a three-dimensional finite element analysis of concrete beams reinforced with CFRP under elevated temperatures. This publication was the first to consider the numerical simulation of concrete structures reinforced with FRP under combined thermal and mechanical loading up to failure. The material formulations used for the concrete in compression and tension and for the reinforcing bars was identical to the for-

mulations used by Rafi et al. (2007). The concrete was modelled using three-dimensional isoparametric solid brick elements with 20 nodes and three translational degrees of freedom per node (translation in the three orthogonal directions). Only longitudinal tensile reinforcement was considered, and was modelled using uniaxial bar elements embedded in the concrete brick elements. The nonlinear analysis was performed using the finite element software DIANA. Thermal properties such as thermal conductivity, thermal capacitance and coefficient of thermal expansion were also considered, as well as the influence of elevated temperatures on the mechanical properties of concrete such as the reduction of compressive strength and reduction of modulus of elasticity.

Zhang and Lin (2013) proposed the use of a novel composite beam element for the nonlinear finite element analyses of FRP reinforced concrete beams. The proposed element is a one-dimensional two-noded layered composite beam element with two degrees of freedom per node (transverse displacement w, and rotation θ) as shown in Figure 2.14.

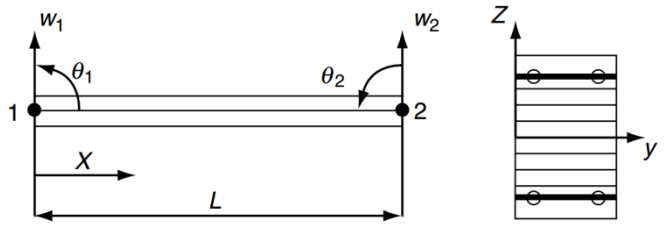

Figure 2.14: Two-Noded Composite Beam Element

As depicted in Figure 2.14, the cross-section of the element is divided into a number of layers in order to capture the nonlinear properties of concrete, with the reinforcing bars represented by a smeared layer of equivalent thickness. Each layer is assumed to be in a state of plane stress, and the material properties are constant throughout the thickness of each layer. The phenomenon of shear-locking in finite element analysis is a common concern when elements used to analyze deep beams are used to analyze slender beams. In previous studies, elements formulated using the Timoshenko beam theory have been found to prevent this phenomenon. In this study, the Timoshenko composite beam functions formulated in

Zhang and Kim (2006) were further developed to avoid shear-locking naturally within the one-dimensional layered element. This formulation allows the proposed element to be used for both slender and moderately deep beams. The nonlinear constitutive model proposed by Nitereka and Neale (1999) was used to model the compression behaviour of concrete. The stress-strain relationship consists of a quadratic ascending branch and a linear descending branch. For concrete in tension, the concrete is assumed to be isotropic and linear-elastic before cracking and orthotropic after cracking. The tension stiffening model proposed by Nour et al. (2007) was employed, which utilizes a tension-stiffening factor, β, which is a function of the reinforcing bar properties. The FRP reinforcement was modelled as linear-elastic up to failure. The numerical results were compared to experimental test data and it was demonstrated that the proposed composite element is able to accurately reproduce the response of both slender and moderately deep beams.

Lin and Zhang (2013) then extended this proposed model to analyze FRP reinforced concrete beams under fire conditions. Using the same one-dimensional composite beam element, a two-dimensional non-linear heat transfer analysis was performed to determine the temperature distribution throughout the element cross-section. A simplified method was then used to transfer the two-dimensional analysis into a one-dimensional result in order to carry out the one-dimensional structural analysis. A parametric study was performed to determine the influence of the concrete cover, type of FRP reinforcement, and the level of load on the flexural response of FRP reinforced concrete beams under elevated temperatures.

Demenico et al. (2014) proposed a finite element-based limit analysis approach to predict the peak load and failure mechanism of concrete members reinforced with FRP bars. The proposed methodology combines the use of the Linear Matching Method (LMM) and the Elastic Compensation Method (ECM). The LMM was originally conceived by Ponter and Carter (1997) and involves the kinematic approach of limit analysis and thus provides a

prediction of the upper bound to the peak load. The ECM was proposed by Mackenzie and Boyle (1993) and involves the static approach of limit analysis and thus provides a prediction of the lower bound to the peak load. The implementation of the LMM and ECM was carried out using the finite element analysis software ADINA. The concrete was modelled using three-dimensional 8-noded solid elements. The longitudinal reinforcement and stirrups were modelled using one-dimensional 2-noded truss elements that were embedded into the solid concrete elements. Test results for six beam sets with varying amounts of GFRP longitudinal reinforcement and steel stirrups were used to validate the proposed approach. The upper bound and lower bound peak load predictions were compared to the experimentally observed peak loads. It was found that the model was able to provide accurate ranges for the upper and lower limits on the peak load. However, it was also found that the model provided poor predictions for under-reinforced beams (beams that fail due to the rupture of the FRP bars as opposed to the crushing of concrete). This was to be expected, as the rupture of FRP bars represents a brittle failure and the proposed procedure focuses on the plastic behaviour of concrete. This limitation to the model was found to be acceptable as the brittle failure mode of under-reinforced concrete members is typically not considered in practical designs.

2.6 Nonlinear Fracture Mechanics of Concrete

Fracture mechanics is the study of the response and failure of structures as a consequence of crack initiation and propagation. In terms of concrete structures, fracture mechanics can be used to explain the various mechanisms by which cracks occur and to evaluate the damaging effects that these cracks have on the structure (Shi, 2009). The concepts discussed in this section, with emphasis on the tension-softening law and fracture energy of cracked concrete, will be used in the finite element modelling presented in this thesis.

2.6.1 Cracking Behaviour of Concrete

Concrete is a heterogeneous composite material that consists of cement, fine aggregate, coarse aggregate, and water (other admixtures and supplementary cementitious materials may also be present). Concrete can be considered to be a two-phase material consisting of a cement matrix and aggregates. These two phases are bonded together at the interface. Cracking at the interface between the aggregate and the matrix may occur due to bleeding or segregation of fresh concrete. Cracking may also occur due to the non-uniform distribution of strains that result from the shrinkage of the cement matrix during the hardening of the concrete. Therefore, many internal flaws and cracks exist in the concrete prior to loading (Shah et al., 1995). The mechanical behaviour of concrete is governed by the initiation and propagation of these internal cracks during loading.

Experimental evidence from uniaxial tension tests on concrete specimens have been collected from multiple researchers, including Hughes and Chapman (1966) and Evans and Marathe (1968), and have been used to formulate many of the fundamental concepts of concrete fracture mechanics. To demonstrate these key concepts, the uniaxial tension testing of concrete plates performed by Li et al. (1993) will be discussed. Four linear variable differential transducers (LVDTs) were used to measure displacements at various locations on the plates. Figure 2.15a shows the positions of the four LVDTs, Figure 2.15b shows the displacements as measured by each LVDT, and Figure 2.15c shows the stress-displacement response for LVDT-3 and LVDT-4.

Referring to Figure 2.15b and Figure 2.15c, four distinct stages of crack development are identified. In the first stage, prior to Point A, an acoustic emission detection system indicated that there were negligible internal cracks, which is reflected in the similar responses of all four LVDTs. Within the second stage, between Point A and Point B, differences in the displacements measured by each LVDT are observed, indicating the initiation of

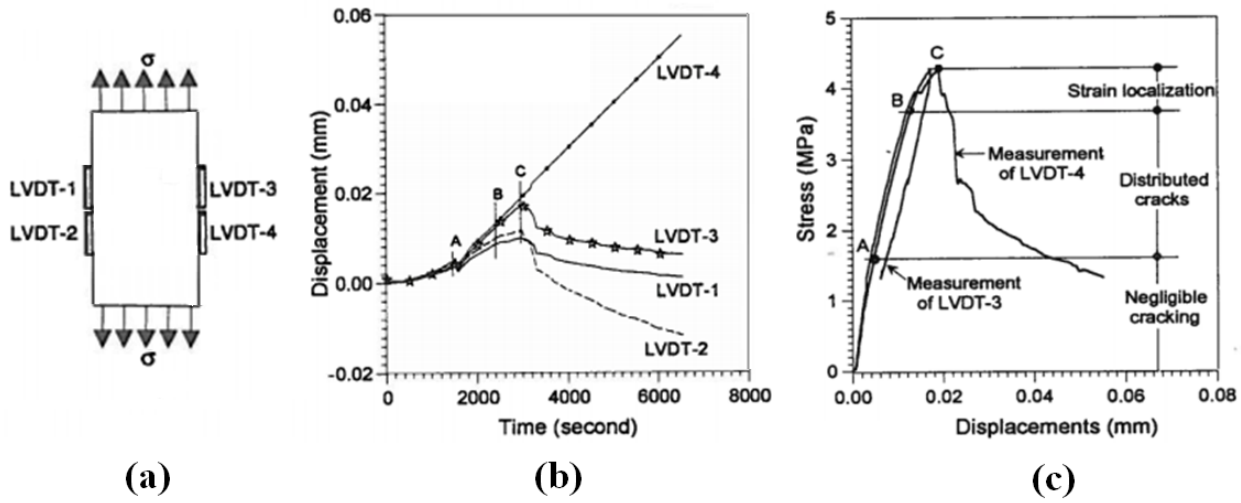

Figure 2.15: Tension Testing of Concrete Plates (Shah et al., 1995)

internal cracks. Within this stage the cracks are isolated and generally uniformly distributed. Within the third stage, between Point B and Point C, a narrow band of internal cracks was observed in the region of LVDT-4, which is reflected in the increased rate of displacement experienced by LVDT-4. This band of cracks indicates that the damage had begun to localize, and that the internal microcracks were beginning to form a major crack that was stable and propagated only with increasing load. This phenomenon is referred to as "strain localization". The fourth stage is beyond the peak load at Point C, at which point the displacement of LVDT-4 continued to increase while the displacement of all other LVDTs decreased. This phenomenon indicates that the major crack is no longer stable, and continues to propagate even with decreasing load. It also indicates that the regions of concrete beyond the localized area of damage had begun to unload. In summary, concrete under tensile loading experiences strain localization prior to the obtainment of the peak load, which results in the development of a major crack. The specimen will experience a strain-softening response as this major crack propagates and the rest of the specimen unloads (Shah et al., 1995).

2.6.2 Fracture Process Zone

Linear elastic fracture mechanics allows the stress to approach infinity at a crack tip. Since this phenomenon is not possible in real materials, an inelastic zone must exist at the crack tip. When performing a numerical analysis using the discrete crack approach, this inelastic zone around the crack tip is referred to as the Fracture Process Zone (FPZ). The FPZ is a tension zone that forms ahead of the pre-existing crack tip and is dominated by complicated toughening mechanisms that exist when a crack propagates. These mechanisms, as depicted in Figure 2.16, include: (a) microcrack shielding; (b) crack deflection; (c) aggregate bridging; (d) cracked surface interlock; (e) crack tip blunting; and (f) crack branching.

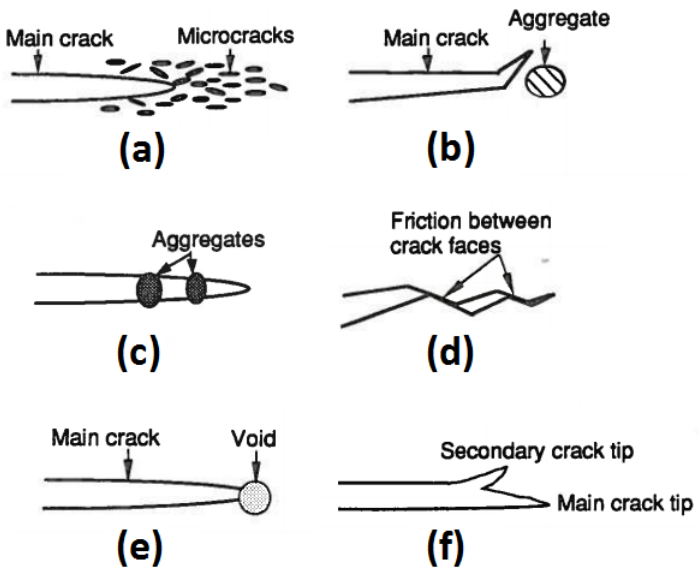

Figure 2.16: Fracture Process Zone Toughening Mechanisms (Shah et al., 1995)

Microcrack shielding refers to the formation of microcracks at flaws near the crack tip as a result of the high stress state. Crack deflection occurs when the path of least resistance is around a relatively large particle or along a weak interface. Aggregate bridging occurs when a crack has advanced beyond an aggregate that continues to carry stress across the crack. Cracked surface interlock refers to the friction that occurs between two cracked faces

which causes energy to be dissipated. Crack tip blunting is when a crack tip is terminated by an internal void, resulting in a blunted crack tip that requires an increased amount of energy to propagate. Crack branching is when a crack propagates into multiple branches; a process that consumes more energy to achieve (Shah et al., 1995).

The FPZ consumes a significant amount of energy from the applied external loads, thus the propagation of cracks is stable prior to the peak load. Furthermore, the toughening mechanisms present in the FPZ are responsible for the quasi-brittle fracture response of the concrete after peak load. Whereas brittle materials are linear elastic up to the peak stress followed by a catastrophic and complete loss of strength, quasi-brittle materials exhibit nonlinearity prior to the peak load, followed by strain-softening. As regions of the crack surfaces may still be in contact, mechanisms such as friction and aggregate interlock prevent catastrophic failure immediately after the peak load and results in a gradually decreasing, softening type response. The presence of these complex mechanisms deters the use of linear elastic fracture mechanics for concrete and necessitates the use of nonlinear fracture mechanics (Shah et al., 1995).

2.6.3 Fictitious Crack Model

The presence of the FPZ in front of an open crack poses an analytical challenge to the modelling of concrete fracture. The FPZ cannot be characterized as a continuous region nor as a discontinuous region. This region represents a partially damaged zone with some remaining stress-transferring capabilities through the toughening mechanisms discussed previously. This region functions as a transition zone between the open crack that is completely discontinuous and the intact concrete material that is completely continuous. Fracture of concrete originates in this region, thus the analysis of cracking necessitates the modelling of the FPZ (Shi, 2009). Hillerborg et al. (1976) proposed the first nonlinear the-

ory of fracture mechanics in the form of the Fictitious Crack Model (FCM). This approach models the fracture process zone as a fictitious crack that extends ahead of the physical, traction free, crack. This fictitious crack is subjected to closure stresses, $\sigma(w)$, as depicted in Figure 2.17 (Karihaloo, 2003).

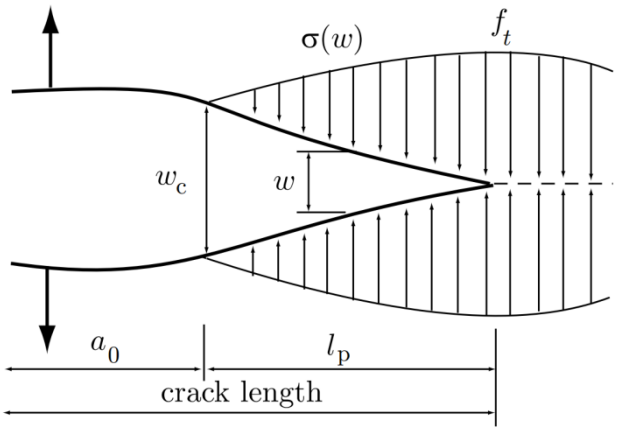

Figure 2.17: Fictitious Crack Model (Malm, 2006)

Referring to Figure 2.17, a_o represents the length of the open crack; l_p is the length of the fracture process zone; and w is the crack-opening-displacement within the FPZ. As can be seen, the closure stresses, often referred to as cohesion stresses, are not constant and are a function of the crack-opening-displacement. The closure stresses are equal to zero at the tip of the pre-existing open crack, which is the location of the critical crack-opening-displacement, w_c. These stresses then increase to the full uniaxial tensile strength of the material, f_t, at the location of the fictitious crack tip (extent of the FPZ). Figure 2.18 is also useful for the demonstration of the tension softening behaviour within the FPZ.

Prior to the peak load, Region AB, the concrete experiences micro-cracking but is not yet subject to the fracture process zone. Within the post peak region, BC, toughening mechanisms within the FPZ provide closure stresses that are a function of the crack-opening-displacements, w. The crack-opening-displacements continue to grow until Point D is reached, at which point zero stress is transferred and the crack-opening-displacement has reached the critical value, w_c (Karihaloo, 2003).

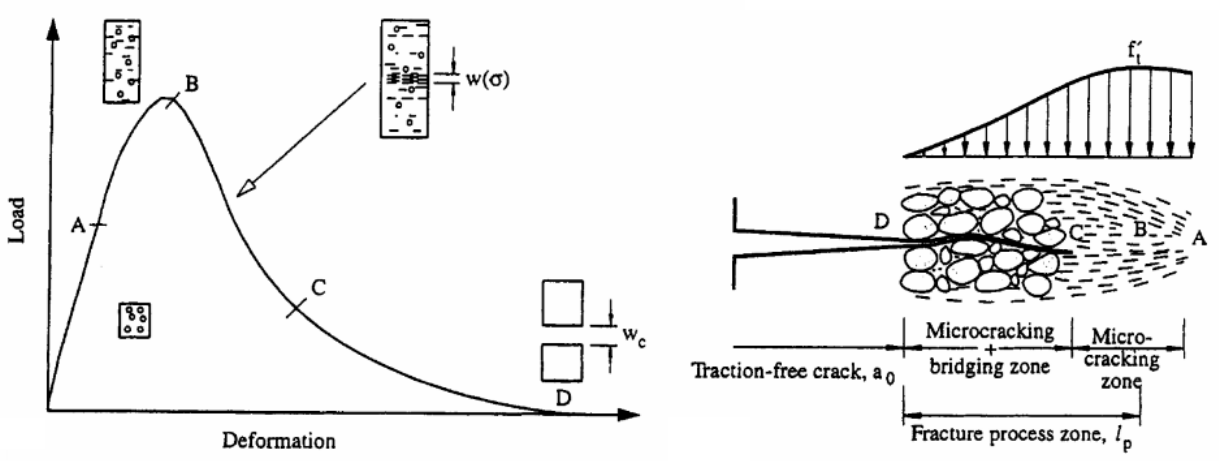

Figure 2.18: Tension Softening Response within the FPZ (Karihaloo, 2003)

2.6.4 Fracture Energy and Tension-Softening Law

Recalling the experiments of Li et al. (1993) discussed previously, portions of a concrete member under tension will experience strain localization at peak load while the remainder of the section will experience unloading. Figure 2.19a depicts a generalized stress-deformation response of a member under tension.

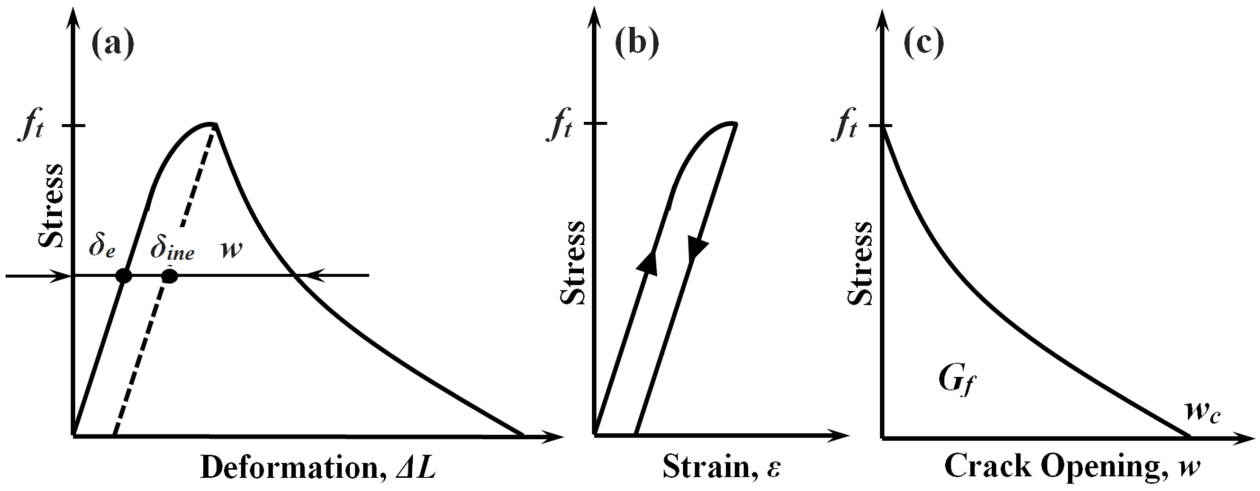

Figure 2.19: Derivation of Fracture Energy (Shah et al., 1995)

The total deformation of a member of length L can be expressed using Equation 2.19:

$$\Delta L = \delta_e + \delta_{ine} + w \tag{2.19}$$

where δ_e is the elastic deformation, δ_{ine} is the inelastic deformation, and w is the crack-opening-displacement of the fictitious crack (Shi, 2009). Figure 2.19a can be divided into two separate curves; Figure 2.19b depicts the stress-strain response of the uncracked section which undergoes linear-elastic unloading at peak load (strain is equal to the deformation divided by the original gauge length), and Figure 2.19c depicts the stress-elongation response for the additional deformation, w, within the damaged section (Hillerborg, 1985). The area under the stress-deformation curve (Figure 2.19c) represents the energy absorbed by the damaged concrete. This quantity represents the amount of energy required to overcome the resistance of various toughening mechanisms in order to create a crack of unit area. This property is referred to as the Mode-I fracture energy, or simply the fracture energy, and is denoted by G_f. The relationship between the stress-elongation response and the fracture energy can be expressed mathematically using Equation 2.20:

$$G_f = \int_0^{w_c} \sigma(w) dw \tag{2.20}$$

where w_c is the critical crack-opening-displacement when the softening stress is equal to zero. The relationship between the decreasing tensile stresses with increasing crack-opening-displacements as depicted in Figure 2.19c is referred to as the tension-softening law. The tension-softening law used to define the tensile response within the fracture process zone, $\sigma(w)$, and the fracture energy, G_f, are two fundamental parameters required for the Fictitious Crack Model. These parameters are material properties that are independent of structural geometry or size (Shah et al., 1995). The softening curve, $\sigma(w)$, requires only three parameters to be completely defined: the ultimate tensile strength of the material f_t, the fracture energy G_f (area under the curve), and the shape of the curve. Many shapes of

the softening curve have been proposed in the literature as shown in Figure 2.20, including linear, bilinear and exponential relationships. Specific models will be discussed in more detail in Section 3.3.2.

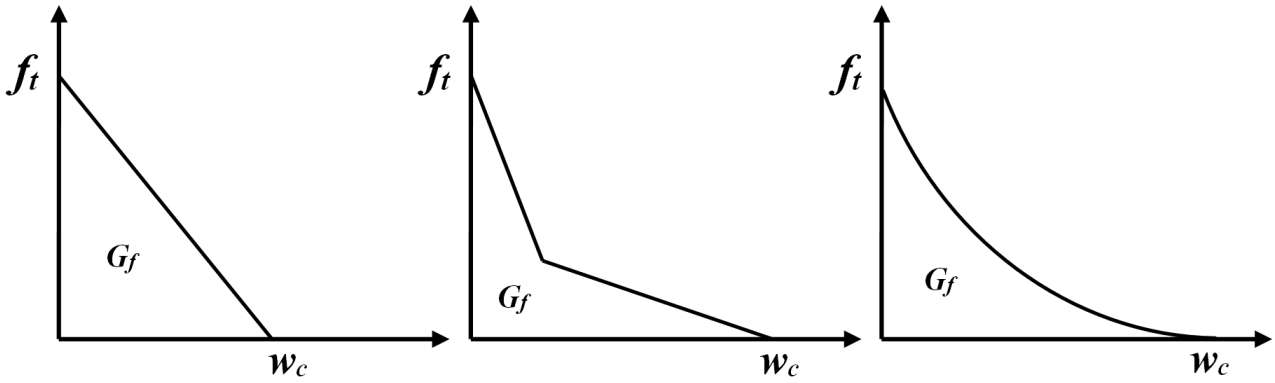

Figure 2.20: Various Tension-Softening Laws

2.7 Plasticity of Reinforced Concrete

The theory of plasticity is a necessary extension to the theory of elasticity and is required to study the stresses and strains of ductile materials that exhibit irrecoverable plastic deformations. The classical theory of plasticity was originally developed to model metals which exhibit significantly different deformation mechanisms as compared to concrete; however, there are similarities. Concrete does exhibit a nonlinear stress-strain response during loading and develops significant irreversible strains upon unloading. Concrete also exhibits ductility under compression loading and confining pressures. Therefore, the theory of plasticity can be used to model this behaviour of concrete (Chen and Han, 1988). The theory of plasticity has been used successfully to model many problems involving reinforced concrete and other similar materials that are subjected primarily to compressive stresses. In problems in which tension plays a significant role, such as shear failure, the plasticity theory may be applied to the compression zones while a fracture mechanics approach may be applied to the tension zones (Lubliner et al., 1989). There are three requirements for

any plasticity model:

1. Initial yield criterion
2. Hardening/softening rule
3. Flow rule

The plasticity models that have been proposed in the literature will typically differ from each other with regards to the shape of the yield surface, the hardening/softening rule and the flow rule. Aspects of each of these features is discussed next.

2.7.1 Initial Yield Criterion

A generalized stress-strain response of concrete subjected to uniaxial compression is shown in Figure 2.21.

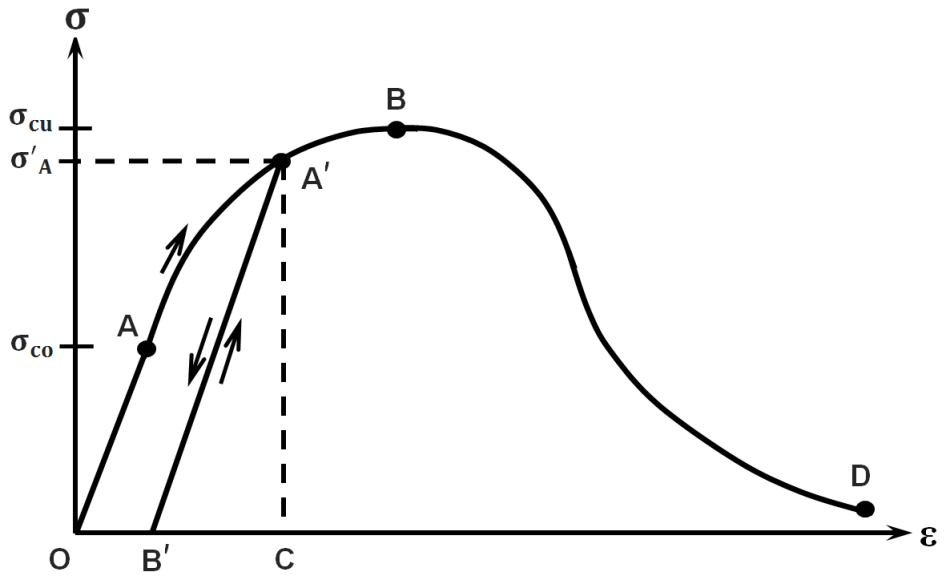

Figure 2.21: Unloading Response of Concrete under Compression (Chen and Han, 1988)

Under uniaxial compression, the stress-strain response is linear-elastic up to the initial yield stress σ_{co}, which corresponds to point A on the curve. Increased loading beyond point A

causes the concrete to behave plastically. The stress continues to increase with further straining, which is referred to as work-hardening or strain-hardening. Work-hardening is exhibited up to the ultimate stress σ_{cu}, which corresponds to point B on the stress-strain curve. Loading beyond the peak stress at point B causes the slope of the stress-strain curve to become negative; a phenomenon referred to as strain-softening.

Consider a case where a specimen is loaded monotonically to a stress of $\sigma_A^{'}$ (point $A^{'}$), a stress state beyond the initial yield point. If the specimen then experiences unloading, the response will follow the linear-elastic unloading path $A^{'}B^{'}$, which is parallel to the initial loading path OA (the unloading stiffness of concrete actually undergoes degradation, or damage, which will be discussed in more detail later). When the stress is again zero at the end of unloading, a residual strain will remain, $OB^{'}$. This irreversible strain is referred to as plastic strain while the recoverable strain, $B^{'}C$, is the elastic strain. If the specimen is then reloaded, the stress-strain curve will follow the reloading path $B^{'}A^{'}$, which is identical to the unloading path $A^{'}B^{'}$. The material is therefore elastic until the previous maximum stress at point $A^{'}$ is reached again. The stress $\sigma_A^{'}$ is then regarded as the new yield stress. Increased loading beyond point $A^{'}$ will lead to further plastic deformation and the stress-strain response will follow the original monotonic loading path $A^{'}D$ (Chen and Han, 1988). When using the theory of plasticity to model this work-hardening plasticity behaviour, it is necessary to define the initial yield surface and the failure surface within the stress space as shown in Figure 2.22.

The initial yield surface represents the limit of elastic behaviour and the initiation of plastic behaviour. When a state of stress falls within the initial yield surface, the material is assumed to be linear-elastic. When the material is stressed beyond the initial yield surface, the material behaves plastically and a new subsequent yield surface is developed. This new surface replaces the initial yield surface and is referred to as a loading surface. If the specimen is unloaded and reloaded within the new loading surface, no additional plastic

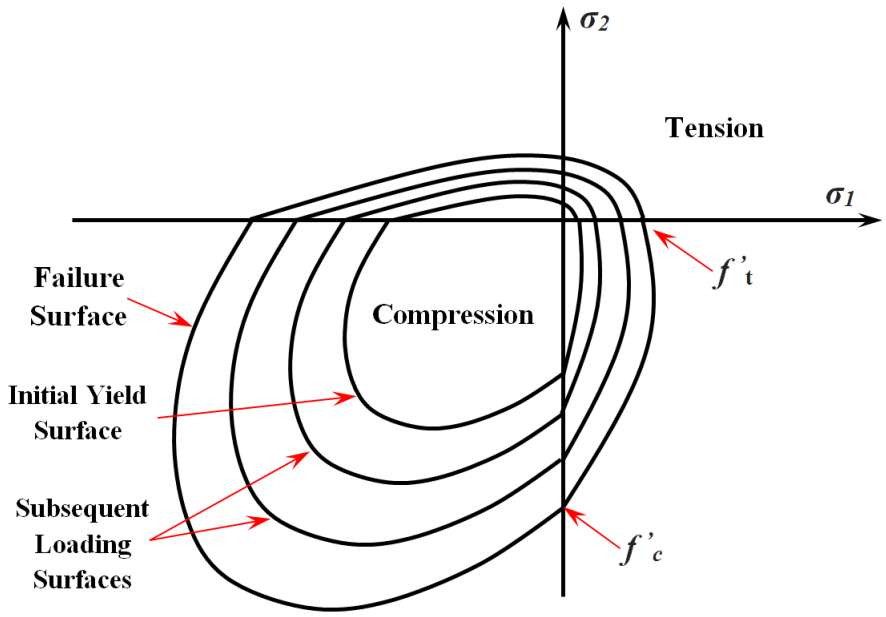

Figure 2.22: Loading Surfaces for Biaxially Stressed Concrete (Chen, 1982)

strain will occur until the specimen is reloaded beyond the new loading surface. If the specimen is loaded beyond the new loading surface, the loading surface will again expand and the specimen will experience an increase in plastic strain (Chen, 1982). Therefore, subsequent loading surfaces act as yield functions for the deformed material. This is identical to the scenario discussed in Figure 2.21. The failure surface represents the state of stress associated with failure (peak stress). The failure surface remains unchanged during loading and encloses all loading surfaces. Once loading has exceeded the initial yield surface and hardening occurs, the loading surface expands and changes its shape from the initial yield surface to the final shape that matches the ultimate failure surface (Chen and Han, 1988).

Many failure (or yield) criteria have been developed for concrete materials, including von Mises, Mohr-Coulomb, Drucker-Prager, Bresler-Pister, Hsieh-Ting-Chen, and Willam-Warnke. Figure 2.23 presents these failure models in both the meridional plane (left) and in the deviatoric plane (right).

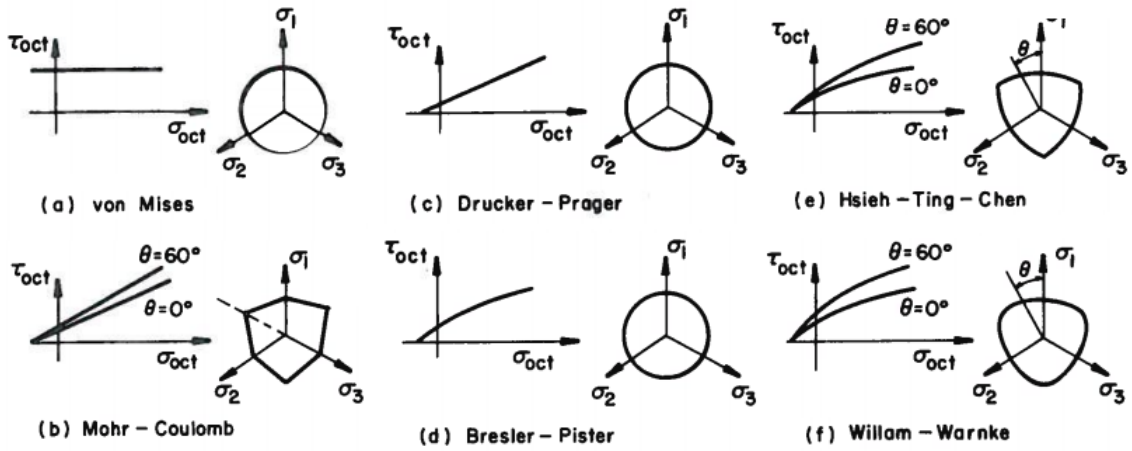

Figure 2.23: Common Failure Criteria for Concrete (Chen and Han, 1988)

The Drucker-Prager and Mohr-Coulomb criteria are the most commonly used yield criteria for concrete (Malm, 2006). However, it was concluded that these criteria require modifications to better represent concrete. As will be discussed in Section 3.3.4, a modified hyperbolic Drucker-Prager yield function as proposed by Lubliner et al. (1989) is implemented in ABAQUS.

2.7.2 Hardening Rule

The theory of plasticity allows the material strain to be dependent on its load history through the introduction of an internal scalar variable, κ, referred to as the hardening parameter. This parameter describes the irreversible material behaviour and is expressed by means of rate equations which are functions of the plastic strain rate: $d\kappa = f(d\epsilon^p)$ (Karihaloo, 2003). A significant challenge in the theory of plasticity is to determine the nature of the subsequent loading surfaces that develop during plastic loading. The hardening rule defines the motion of the subsequent loading surfaces and is responsible for how these surfaces evolve (Chen, 1982). A number of hardening rules have been proposed to describe the growth of the subsequent loading surfaces for work-hardening materials.

Three examples of hardening rules include isotropic hardening, kinematic hardening, and independent hardening.

Before these three examples of hardening rules can be discussed, it is first necessary to define the "Bauschinger effect". The Bauschinger effect refers to a type of directional anisotropy induced by plastic deformation. This effect is evident when a specimen that initially undergoes plastic deformation of one sign then exhibits a reduced yield stress when subsequently loaded in the opposite sign. For example, if a rod is subjected to a tensile stress that exceeds its yield strength and induces plastic deformation, subsequent compression of the same rod will lead to a compressive yield value that is noticeably lower than the initial tensile yield point. Therefore, the load history of a specimen is considered by the Bauschinger effect (Chen, 1982).

Isotropic hardening applies mainly to models in which the plastic deformation develops well beyond the initial yield surface and where the material is subjected to mainly monotonic and proportional loading. This rule therefore neglects completely the Bauschinger effect during load reversals. Isotropic hardening assumes that the loading surfaces can only expand in the stress space, but cannot translate or rotate. Conversely, kinematic hardening considers the Bauschinger effect and is more appropriate for problems with cyclic and reversed-type loading. Kinematic hardening assumes that the loading surface translates as a rigid body in stress space, maintaining its size, shape and orientation. A third rule, independent hardening, assumes that the hardening experienced in compression is independent of the hardening experienced in tension. This final hardening rule is best suited for concrete, and is a combination of the isotropic and kinematic hardening rules (Chen and Han, 1988). The independent hardening rule is implemented in the plasticity model used by ABAQUS, and is discussed further in Section 3.3.4.

2.7.3 Flow Rule

Up until this point, the initial yield surface has been discussed, as well as the use of hardening rules to determine the shape of subsequent loading surfaces at any given stress level. The flow rule represents the connection between the yield surface and the stress-strain relationship. For the purpose of this discussion, the yield surface will be denoted as f (Chen, 1982).

Concrete exhibits non-linear volume change when subjected to severe inelastic stress states during hardening. Experimental results indicate that under compressive loading, the concrete experiences inelastic volume contraction at initial yielding and volume dilation at stress levels of 75-90% of the ultimate stress (Kupfer et al., 1969). Figure 2.24 shows this phenomenon for concrete under uniaxial and biaxial compression.

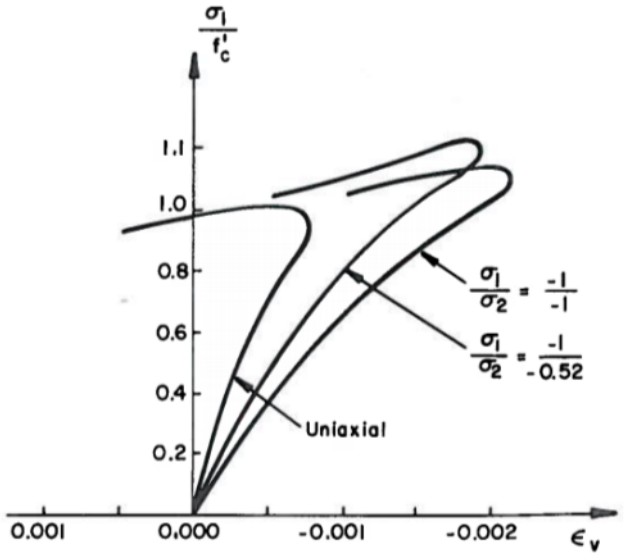

Figure 2.24: Volumetric Strain of Concrete under Compression (Kupfer et al., 1969)

The dilation that results from plastic deformation can be reproduced well using a plastic potential function G. The flow rule can be defined using Equation 2.21:

$$d\epsilon^p = d\lambda \frac{\partial G}{\partial \sigma} \tag{2.21}$$

where $d\lambda$ is a scalar hardening parameter that can vary throughout the straining process. This parameter uses positive values, and is nonzero only when plastic deformations occur. The gradient of the plastic potential function, $\partial G/\partial \sigma$, defines the direction of the plastic strain increment $d\epsilon^p$, while the length is determined by the hardening parameter $d\lambda$ (Chen, 1982). Figure 2.25 presents the flow rule for the classical linear Drucker-Prager model in the meridional plane.

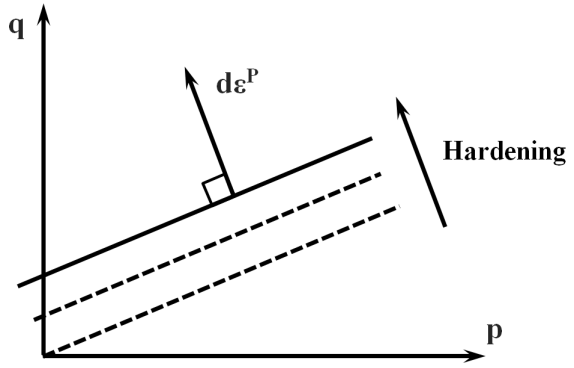

Figure 2.25: Drucker-Prager Flow Rule (DSS, 2012)

If the plastic potential surface has the same shape as the current yield or loading surface ($G = f$), the flow is considered "associated", meaning the plastic flow is connected or associated with the yield criterion. If the associated flow rule is utilized, the plastic flow develops normal to the loading surface, f. If two separate functions are used for the plastic potential surface and the yield surface ($G \neq f$) and the two surfaces do not coincide, the flow is considered "non-associated". If the non-associated flow rule is utilized, the plastic flow develops normal to the plastic potential surface, G (Malm, 2006).

As discussed previously, the initial contraction followed by dilation exhibited by concrete under compression yields an inflection point within the stress versus volumetric-strain curve as shown in Figure 2.24. This behaviour violates the associated flow rule. It has also been shown that the associated flow rule tends to overestimate the plastic volume expansion of concrete. Therefore, the non-associated flow rule is typically recommended to control dilatancy when modelling concrete (Chen and Han, 1988).

Chapter 3

Overview of Concrete Modelling using ABAQUS

3.1 ABAQUS Overview

Many commercial finite element analysis (FEA) software packages are available for the analysis of concrete structures. Examples include: ADINA (Automatic Dynamic Incremental Nonlinear Analysis) developed by ADINA R&D Inc. located in Watertown, Massachusetts, USA (ADINA R&D, 2014), DIANA (Displacement Analyzer) developed by TNO DIANA BV located in Delft, Netherlands (TNO DIANA BV, 2014), and ATENA developed by Cervenka Consulting located in Czech Republic (Cervenka Consulting, 2014). The FEA software ABAQUS was used for the simulations performed for this thesis (DSS, 2012).

ABAQUS was developed by Hibbitt, Karlsson and Sorensen, Inc. which was established in 1978. In 2005, this company was acquired by Dassault Systemes Simulia Corp. (DSS) based out of Providence, Rhode Island, USA. ABAQUS is a finite element analysis software that has become popular in academic and research institutions due to its extensive library of materials and elements and its ability to be customized for one-, two-, and three-dimensional problems. The ABAQUS product suite includes three core products, including

ABAQUS/CAE, ABAQUS/Standard, and ABAQUS/Explicit (DSS, 2012).

ABAQUS/CAE, referring to Complete ABAQUS Environment, is software that allows users to create, analyze, and visualize model output all in one environment using a customizable graphical user interface (GUI). ABAQUS/CAE allows users to create geometries using the GUI or by importing CAD models for meshing. Users can then analyze models and use the comprehensive visualization options to interpret and communicate the analysis results. ABAQUS/Standard is a finite element analysis product that utilizes solution techniques that are ideal for static and low-speed dynamic simulations. ABAQUS/Explicit is a finite element analysis product that utilizes solution techniques that are ideal for transient dynamic and highly nonlinear simulations. Both ABAQUS/Standard and ABAQUS/Explicit are supported within the CAE modelling environment for both pre-processing and post-processing activities (DSS, 2012). ABAQUS/Standard was used within the CAE modelling environment for all simulations performed for this thesis. Literature provided by DSS (2012), including the ABAQUS Analysis User's Manual, ABAQUS/CAE User's Manual, and ABAQUS Theory Manual, were used to prepare the concepts presented in this chapter.

3.2 Concrete Constitutive Models in ABAQUS

ABAQUS offers three constitutive models for concrete, including:

1. Smeared Crack Model (SCM)
2. Brittle Cracking Model (BCM)
3. Concrete Damaged Plasticity Model (CDPM)

All three models provide a general capability for modelling typical concrete structures such as beams, trusses, shells and solids. All models can be used for plain concrete, or other

quasi-brittle materials, but are intended primarily for the analysis of reinforced concrete structures.

The Smeared Crack Model (SCM) can be implemented in ABAQUS/Standard and is intended for applications in which the concrete is subjected to primarily monotonic loadings at low confining pressures. Cracking of the concrete is treated as the most important aspect of the concrete behaviour, thus cracking and post-cracking behaviour dominate the modelling. A crack detection surface is utilized to determine if an integration point has failed by tensile cracking. A smeared crack approach is used to represent the discontinuous brittle behaviour of cracked concrete. This approach does not track the formation of macrocracks, but instead modifies the stress and stiffness material properties to account for the presence of cracks. The SCM uses an associated flow rule with isotropic hardening which generally over-predicts the inelastic volumetric strain. When stresses are dominantly compressive, a simplified elastic-plastic yield surface is used. This yield surface is a function of only the first and second stress invariants; a simplification that leads to output that does not match all data accurately (inclusion of the third stress invariant in the yield surface would be required to achieve higher accuracy). The simplifications and limitations placed in this model are an attempt to increase computational efficiency.

The Brittle Cracking Model (BCM) can be implemented in ABAQUS/Explicit and is intended for applications in which the behaviour of the material is dominated by tensile cracking. This model can be used for materials such as ceramics and brittle rock, but is usually intended for plain concrete. The compressive behaviour is assumed to be linear-elastic, a significant simplification of the actual compressive behaviour of concrete. Therefore, the BCM is only adequate if brittle tensile behaviour dominates the material behaviour such that the linear-elastic compression model assumption is acceptable. The BCM only considers the brittle aspects of concrete behaviour; when microcracks coalesce to form discrete macrocracks representing regions of highly localized deformation. This model also utilizes

the smeared crack approach to represent the discontinuous brittle behaviour as discussed previously.

The Concrete Damaged Plasticity Model (CDPM) can be implemented in both ABAQUS/Standard and ABAQUS/Explicit and can be used to analyze concrete and other quasi-brittle materials. This model assumes that the two main failure mechanisms of concrete include tensile cracking and compressive crushing. The CDPM is effective for monotonic, cyclic, and dynamic loading under low confining pressures. Isotropic tensile plasticity and isotropic compressive plasticity are used to represent the inelastic behaviour of concrete. A non-associated flow rule with a multi-variable hardening plasticity is implemented in combination with a scalar isotropic damaged elasticity to describe the irreversible damage that occurs during the fracture process. Viscoplastic regularization may also be implemented to improve the convergence rate in tensile softening regions.

It is clear that the Concrete Damaged Plasticity Model is highly versatile in modelling concrete under various loading conditions. For this reason, the CDPM was used for all analyses performed in preparation of this thesis, and will be discussed in further detail in the next section.

3.3 Concrete Damaged Plasticity Model

3.3.1 Compression Modelling

In the Concrete Damaged Plasticity Model, the uniaxial compressive behaviour of concrete is assumed to follow the general stress-strain response as shown in Figure 3.1.

Under uniaxial compression, the stress-strain response is linear within the elastic region until the initial yield σ_{co}. Beyond this point, the concrete becomes plastic and experiences

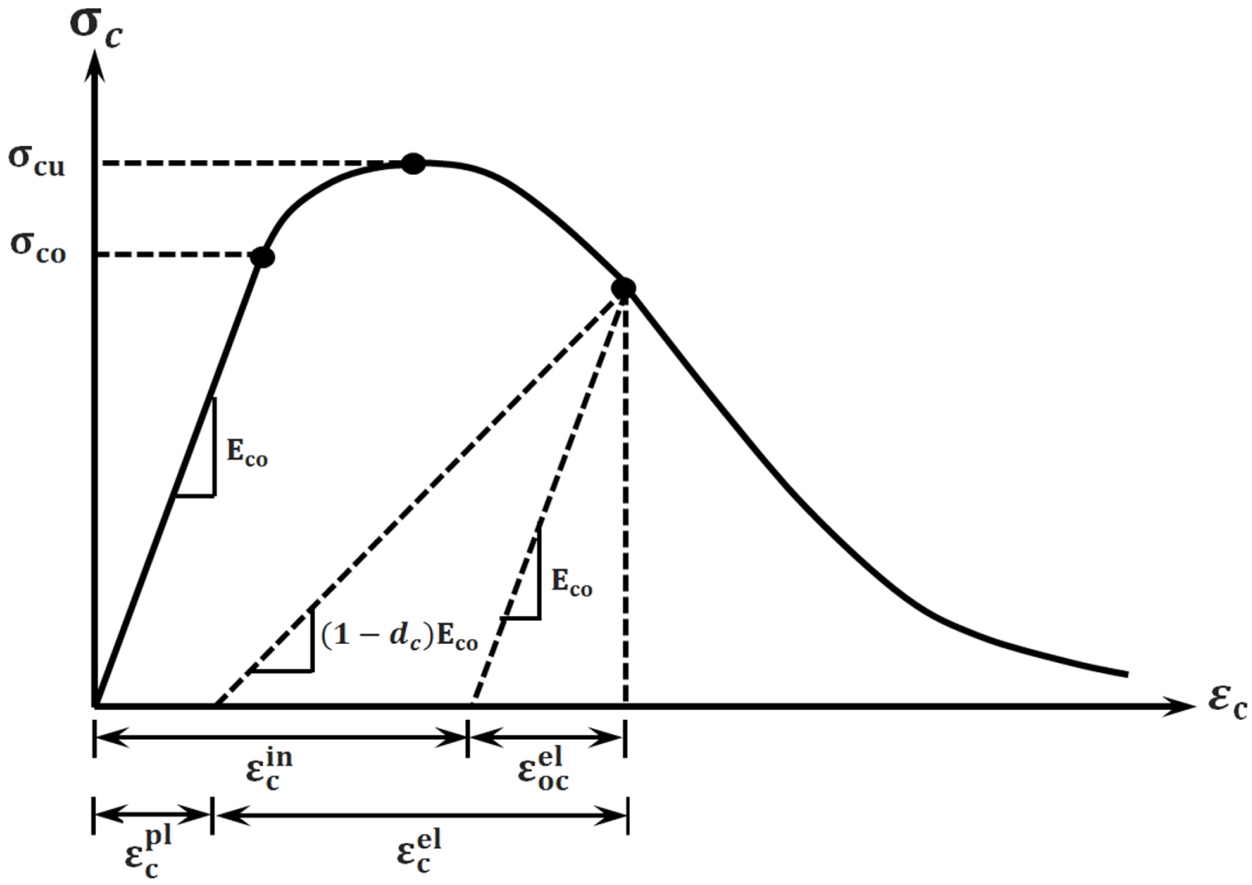

Figure 3.1: Stress-Strain Response for Concrete in Compression (DSS, 2012)

work-hardening up to the ultimate stress σ_{cu}, followed by strain-softening. To model the elastic compression behaviour, the user provides the initial undamaged modulus of elasticity, E_{co}. For the response beyond the elastic range, compressive stress data are provided in a tabular form as a function of the inelastic strain, ε_c^{in}. The inelastic strain, as shown in Figure 3.1, is expressed in Equation 3.1:

$$\varepsilon_c^{in} = \varepsilon_c - \varepsilon_{oc}^{el} = \varepsilon_c - \frac{\sigma_c}{E_{co}} \tag{3.1}$$

where ε_c^{in} is the inelastic strain, ε_c is the total compressive strain, ε_{oc}^{el} is the elastic compressive strain corresponding to the undamaged material, σ_c is the compressive stress, and E_{co} is the initial undamaged modulus of elasticity. The inelastic strain values inputted are pos-

itively increasing values, with the first value being zero (corresponding to the initial yield point). The specific stress-strain relationships used to model the concrete in compression will be presented in Section 5.1.

3.3.2 Tension Modelling

The uniaxial tensile behaviour of concrete is assumed to follow the general stress-strain response as shown in Figure 3.2.

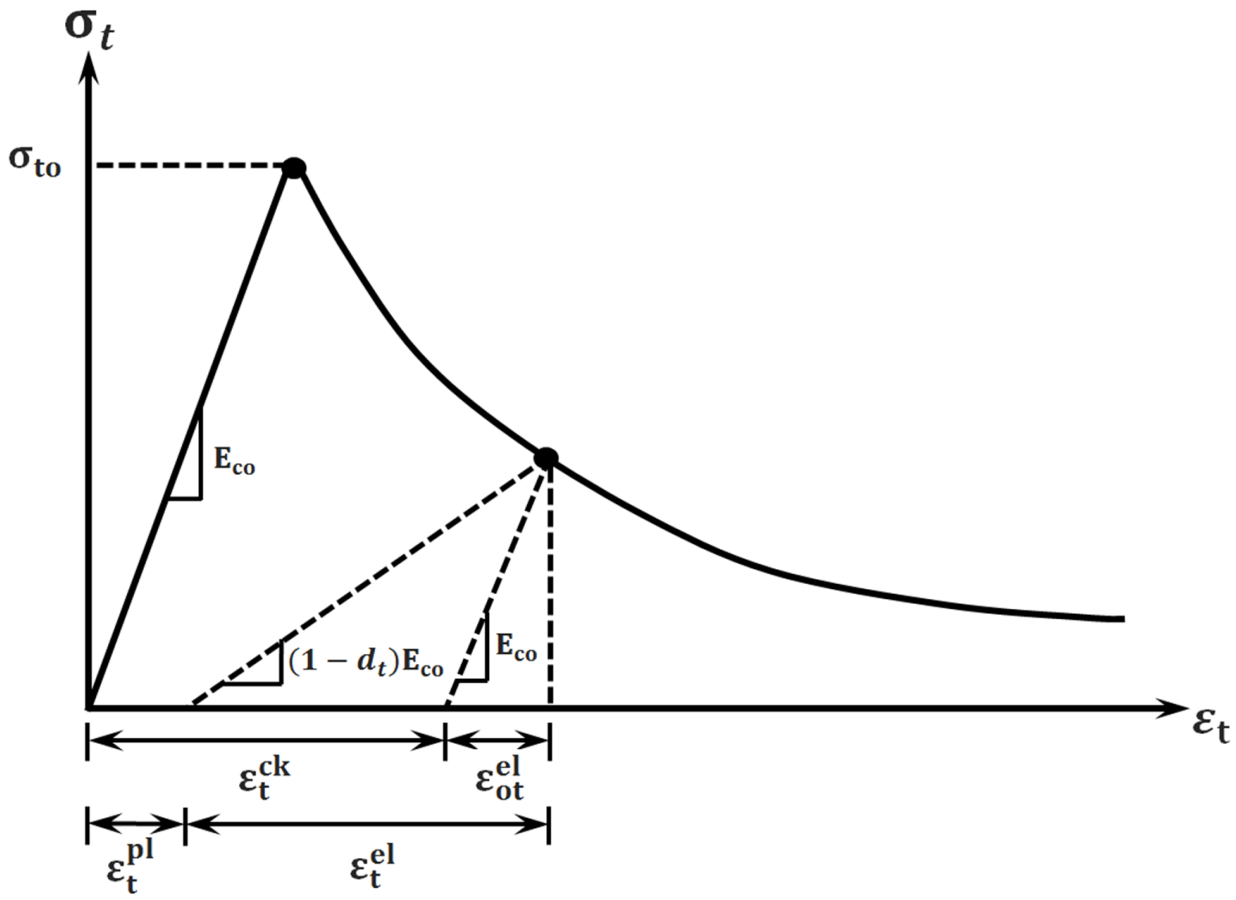

Figure 3.2: Stress-Strain Response for Concrete in Tension (DSS, 2012)

Under uniaxial tension, the stress-strain response is linear-elastic until the peak stress σ_{to}. As discussed previously, the peak tensile stress corresponds to the coalescing of microcracks which induces strain localization. This leads to the unstable propagation of a major crack,

the unloading of regions beyond the strain localization, and a strain-softening post-peak response. As concrete is a quasi-brittle material and is bonded to the reinforcement, the concrete between cracks continues to carry tensile loads even after cracking. The ability of the concrete between cracks to carry tension, a phenomenon which helps control the deformation of a member and the development of crack widths, is referred to as "tension stiffening". To account for this phenomenon, ABAQUS requires the user to define a post-peak response of the concrete in tension to simulate the interaction between the concrete and the reinforcing bars. There are three methods that can be used to define the post-peak uniaxial tensile response of concrete in the Concrete Damaged Plasticity Model within ABAQUS:

1. Provide the tensile stress in a tabular form as a function of the cracking strain, ε_t^{ck}.

2. Provide the tensile stress in a tabular form as a function of the crack-opening-displacement, w.

3. Prescribe a value for fracture energy, G_f.

The first method to define the post-peak tensile response of concrete allows the user to input a stress-strain curve similar to the one shown in Figure 3.2. The post-failure behaviour is provided as a function of the cracking strain ε_t^{ck}, as expressed in Equation 3.2:

$$\varepsilon_t^{ck} = \varepsilon_t - \varepsilon_{ot}^{el} = \varepsilon_t - \frac{\sigma_t}{E_{co}} \tag{3.2}$$

where ε_t^{ck} is the cracking strain, ε_t is the total tensile strain, ε_{ot}^{el} is the elastic tensile strain corresponding to the undamaged material, σ_t is the tensile stress, and E_{co} is the initial undamaged modulus of elasticity. To ensure numerical convergence, the Concrete Damaged Plasticity Model enforces the following lower limit on the post-peak tensile stresses specified

by the user:

$$\sigma_t \geq \frac{\sigma_{to}}{100} \tag{3.3}$$

where σ_{to} is the peak tensile stress. This method allows the user to control the shape of the post-peak curve, thus allowing the interaction between the concrete and reinforcing bars to be modelled and adjusted to suit the specific application. The specific post-peak stress-strain responses that were considered in the modelling performed for this thesis are presented in Section 5.2.1.

The second method to define the post-peak tensile response of concrete allows the user to input the tensile stress as a function of the crack-opening-displacement, w. This approach implements the concept of fracture energy as proposed by Hillerborg et al. (1976). Fracture energy, G_f, is a material parameter used in brittle fracture mechanics to define the energy required to open a crack of unit area. With this approach, the brittle behaviour of concrete is characterized by a stress-displacement response as opposed to a stress-strain response. Similar to the first approach, this method allows the user to customize the tension stiffening behaviour of the member by modifying the curve to fit the application. Examples of stress-displacement curves proposed in the literature are depicted in Figure 3.3.

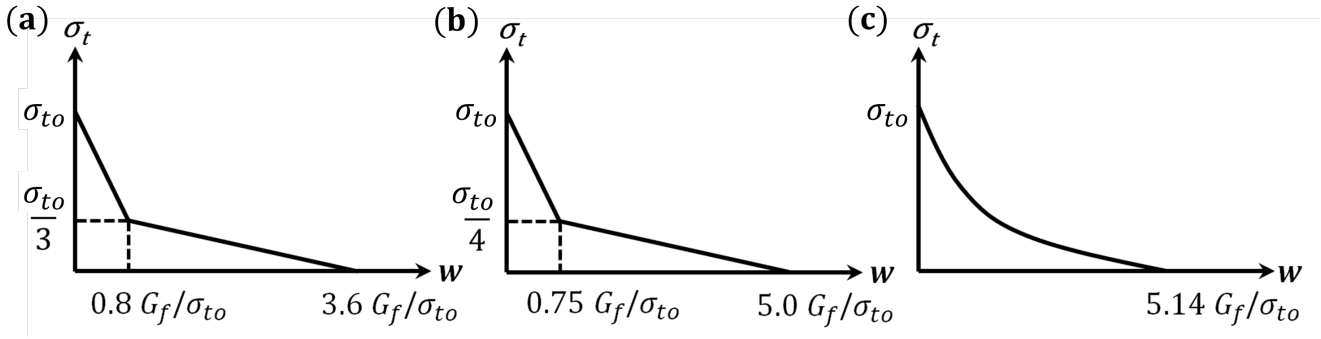

Figure 3.3: Examples of Stress-Displacement Curves

The bilinear stress-displacement response presented in Figure 3.3a was found to fit the tension-softening response for concrete by Petersson (1981). Figure 3.3b presents a bilinear

response with slightly modified parameters as found by Rokugo et al. (1989). Cornelissen et al. (1986) found that the exponential response in Figure 3.3c fits well with experimental data. As the area under these curves is equal to the material's fracture energy, this approach not only allows the user to define the rate of strength loss upon cracking but also the fracture energy of the material. The application and comparison of different proposed models will be presented in Chapters 5 and 6.

The third method to define the post-peak tensile response of concrete requires the user to simply prescribe a value for the fracture energy, G_f, as a material property. The only inputs required are the tensile peak stress, σ_{to}, and the fracture energy. This method assumes a linear stress-displacement post-peak response as shown in Figure 3.4.

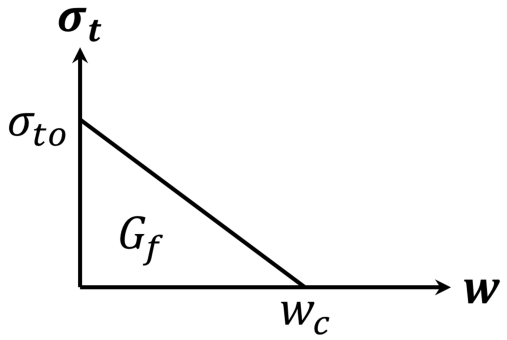

Figure 3.4: Linear Stress-Displacement Curve

As the peak stress is defined and the area under the linear curve is equal to the fracture energy provided by the user, the maximum crack displacement corresponding to a complete loss of strength, w_c, is given by Equation 3.4:

$$w_c = \frac{2G_f}{\sigma_{to}} \tag{3.4}$$

The selection of the optimal fracture energy value and stress-displacement curve is studied in further detail in Sections 5.2.3 and 6.2.1.

3.3.3 Damage Modelling

When concrete is unloaded from any point within the work-hardening or strain-softening regions of the compression and tension stress-strain curves (post-elastic regions), the unloading response becomes weakened and a degraded, or damaged, elastic modulus is used. As shown in Figures 3.1 and 3.2, the degradation of the elastic stiffness during unloading is characterized by two damage variables, d_c and d_t, for uniaxial compression and tension responses, respectively. These damage parameters are functions of the plastic strains ε_c^{pl} and ε_t^{pl}, temperature θ, and other predefined field variables f_i. The damage parameters can take values ranging from zero to one, with a value of zero corresponding to the undamaged material and a value of one corresponding to a material with a complete loss of strength (Equation 3.5).

$$d_t = d_t(\varepsilon_t^{pl}, \theta, f_i); \qquad 0 \leq d_t \leq 1.0 \tag{3.5a}$$

$$d_c = d_c(\varepsilon_c^{pl}, \theta, f_i); \qquad 0 \leq d_c \leq 1.0 \tag{3.5b}$$

As the damage parameters are a function of the plastic strains, ABAQUS will automatically convert the user defined inelastic or cracking strain values to plastic values. For uniaxial compression damage, damage parameter values are provided as a function of the inelastic strains, ε_c^{in}, which are converted to plastic strains using Equation 3.6:

$$\varepsilon_c^{pl} = \varepsilon_c^{in} - \frac{d_c}{1 - d_c}\frac{\sigma_c}{E_{co}} \tag{3.6}$$

where E_{co} is the initial undamaged modulus of elasticity. For uniaxial tension, if Method 1 is used to define the post-peak response as discussed previously, damage parameter values are provided as a function of the cracking strains, ε_t^{ck}, which are converted to plastic strains using Equation 3.7:

$$\varepsilon_t^{pl} = \varepsilon_t^{ck} - \frac{d_t}{1 - d_t}\frac{\sigma_t}{E_{co}} \tag{3.7}$$

If Method 2 or 3 is used to define the post-peak tensile response as discussed previously, damage parameter values are provided as a function of the cracking displacements, u_t^{ck} (previously referred to as w), which are converted to plastic displacements using Equation 3.8:

$$u_t^{pl} = u_t^{ck} - \frac{d_t}{1 - d_t}\frac{\sigma_t l_o}{E_{co}} \tag{3.8}$$

where l_o is the specimen length which is assumed to be equal to 1.0. It is important to note that when defining the damage parameters, excessive damage may cause the model to experience convergence issues. It is recommended to avoid using damage variables greater than 0.99, representing 99% reduction of the elastic stiffness.

If E_{co} is the initial undamaged modulus of elasticity of the concrete, the stress-strain responses for uniaxial tension and compression behaviour with consideration of the degradation of the elastic stiffness can be expressed using Equation 3.9:

$$\sigma_t = (1 - d_t)E_{co}(\varepsilon_t - \varepsilon_t^{pl}) \tag{3.9a}$$

$$\sigma_c = (1 - d_c)E_{co}(\varepsilon_c - \varepsilon_c^{pl}) \tag{3.9b}$$

A concrete member subjected to uniaxial load will experience the development and propagation of cracks. This phenomenon will cause the reduction of the available load carrying area, thus increasing the effective stresses that the concrete experiences. Therefore, ABAQUS considers this effect by automatically calculating these effective stresses, $\bar{\sigma}_t$ and $\bar{\sigma}_c$, for tension and compression, respectively. These effective stresses, as expressed in Equation 3.10, are referred to as uniaxial effective cohesion stresses and are used to determine the size of the yield and loading surfaces within the plasticity modelling of the concrete.

$$\bar{\sigma}_t = \frac{\sigma_t}{1 - d_t} = E_{co}(\varepsilon_t - \varepsilon_t^{pl}) \tag{3.10a}$$

$$\bar{\sigma}_c = \frac{\sigma_c}{1 - d_c} = E_{co}(\varepsilon_c - \varepsilon_c^{pl}) \tag{3.10b}$$

To further demonstrate the concept and influence of elastic stiffness degradation of concrete, a simple model was created using ABAQUS/Standard. A cube of concrete with dimensions 1.0x1.0x1.0mm was subjected to a uniaxial compressive load. The concrete was modelled using the Concrete Damaged Plasticity Model with a compressive strength of 54MPa and an initial undamaged modulus of elasticity of 36,742MPa. A displacement-controlled test was performed by imposing a downwards vertical displacement boundary condition to the top surface of the cube. This test method was selected so that the post-peak behaviour of the concrete could be studied. Figure 3.5 presents the uniaxial compressive stress-strain responses for a variety of tests performed.

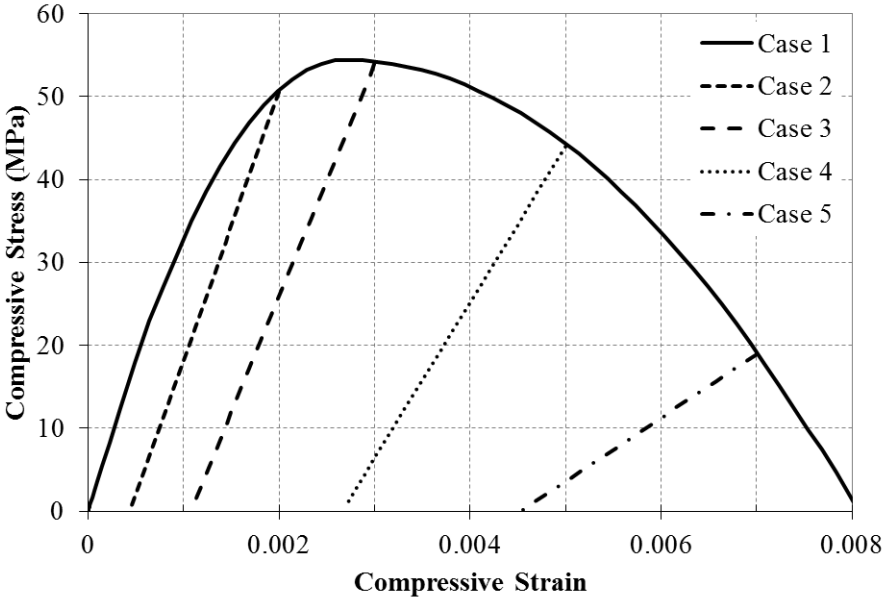

Figure 3.5: Elastic Stiffness Damage

In Case 1, the displacement was applied until a complete loss of strength was achieved (Load Only). For Cases 2, 3, 4 and 5, the load was applied to different strain levels, at which point the cube was unloaded completely (Load-Unload). As can be seen, the slope of the unloading curve for Cases 2, 3, 4 and 5 are no longer equal to the slope of the initial elastic loading curve. It is also shown that the slope of each unloading curve is dependent on the strain level at the initiation of unloading. Models that were unloaded later in

the stress-strain curve, Case 4 and 5 for example, experienced larger plastic strains, thus larger damage parameters, which resulted in a larger reduction in the unloading stiffness. Therefore, when concrete is unloaded from a state of stress that is beyond the elastic range, it will experience a reduction in stiffness, and the magnitude of this reduction depends on the strain level at the time of unloading. Table 3.1 presents further details of this modelling.

Table 3.1: Elastic Stiffness Damage Modelling

Case	Load Pattern	Total Stress at Unloading (MPa) σ_c	Total Strain at Unloading ε_c	$E_{reduced}$ (MPa)	d_c	ε_c^{pl}	ε_c^{el}	ε_c^{in}	ε_{oc}^{el}
1	Load Only	-	-	-	-	-	-	-	-
2	Load-Unload	50.6	0.002	32,362	0.119	0.0004	0.0016	0.0006	0.0014
3	Load-Unload	53.9	0.003	27,975	0.239	0.0011	0.0019	0.0015	0.0015
4	Load-Unload	44.0	0.005	18,800	0.488	0.0027	0.0023	0.0038	0.0012
5	Load-Unload	18.9	0.007	7,674	0.791	0.0045	0.0025	0.0065	0.0005

For each unloading case, σ_c and ε_c have been recorded, which are the total compressive stress and total compressive strain at the initiation of unloading, respectively. The reduced modulus of elasticity was calculated based on the slope of each unloading curve. Using this reduced stiffness, the compressive damage parameter, d_c, was found using Equation 3.11:

$$E_{reduced} = (1 - d_c)E_{co} \qquad \therefore d_c = 1 - \frac{E_{reduced}}{E_{co}} \tag{3.11}$$

Table 3.1 shows that Case 2 experienced an 11.9% reduction in stiffness, while Case 5 experienced a 79.1% reduction. The elastic compressive strain, ε_c^{el}, and the plastic compressive strain, ε_c^{pl}, were found using Equations 3.12a and 3.12b, respectively. Note that the sum of these two strains is equal to the total compressive strain, ε_c. Furthermore, the plastic strain

corresponds to the permanent strain level after complete unloading considering damage, and can be determined directly from the stress-strain curves in Figure 3.5. As can be seen, the values from the plots match the values calculated.

$$\varepsilon_c^{el} = \frac{\sigma_c}{(1-d_c)E_{co}} \tag{3.12a}$$

$$\varepsilon_c^{pl} = \varepsilon_c - \varepsilon_c^{el} = \varepsilon_c - \frac{\sigma_c}{(1-d_c)E_{co}} \tag{3.12b}$$

The elastic compressive strain corresponding to the undamaged concrete, ε_{oc}^{el}, and the inelastic compressive strain, ε_c^{in}, were calculated using Equations 3.13a and 3.13b, respectively. Note that the sum of these two strains is equal to the total compressive strain, ε_c.

$$\varepsilon_{oc}^{el} = \frac{\sigma_c}{E_{co}} \tag{3.13a}$$

$$\varepsilon_c^{in} = \varepsilon_c - \varepsilon_{oc}^{el} = \varepsilon_c - \frac{\sigma_c}{E_{co}} \tag{3.13b}$$

The intent of this modelling exercise was to demonstrate elastic degradation, as well as the calculation of the various concrete strains that ABAQUS uses. These calculations, however, required the unloading curves to be known in order to determine the damage parameters. The relationships used to define the damage parameters used in the modelling performed for this thesis are discussed in detail in Chapter 5.

3.3.4 Plasticity Modelling

As discussed in Section 2.7, the requirements of a plasticity model include the definition of an initial yield surface, a hardening rule, and a flow rule. The specific aspects of the plasticity model used by the Concrete Damaged Plasticity Model within ABAQUS are discussed here.

Yield Function

The Concrete Damaged Plasticity Model uses the yield condition proposed by Lubliner et al. (1989) with the modifications proposed by Lee and Fenves (1998) to account for the differences in strength evolution under tension and compression loading. In terms of the effective cohesion stresses, the yield function is expressed in Equation 3.14:

$$F(\bar{\sigma}, \tilde{\varepsilon}^{pl}) = \frac{1}{1-\alpha}\left[\bar{q} - 3\alpha\bar{p} + \beta(\tilde{\varepsilon}^{pl})\left\langle\hat{\bar{\sigma}}_{max}\right\rangle - \gamma\left\langle-\hat{\bar{\sigma}}_{max}\right\rangle\right] - \bar{\sigma}_c(\tilde{\varepsilon}_c^{pl}) = 0 \tag{3.14}$$

$$\alpha = \frac{(\sigma_{bo}/\sigma_{co}) - 1}{2(\sigma_{bo}/\sigma_{co}) - 1} \tag{3.15a}$$

$$\beta = \frac{\bar{\sigma}_c(\tilde{\varepsilon}_c^{pl})}{\bar{\sigma}_t(\tilde{\varepsilon}_t^{pl})}(1-\alpha) - (1+\alpha) \tag{3.15b}$$

$$\gamma = \frac{3(1-K_c)}{2K_c - 1} \tag{3.15c}$$

where:

- $\bar{\sigma}_t(\tilde{\varepsilon}_t^{pl})$ and $\bar{\sigma}_c(\tilde{\varepsilon}_c^{pl})$ are the effective tensile cohesion stress and effective compressive cohesion stress, respectively. These are both functions of the equivalent plastic strains, $\tilde{\varepsilon}_t^{pl}$ and $\tilde{\varepsilon}_c^{pl}$, respectively;
- σ_{bo} is the initial equibiaxial compressive yield stress;
- σ_{co} is the initial uniaxial compressive yield stress;
- $\bar{q}$ is the Mises equivalent stress, where $\bar{q} = \sqrt{\frac{3}{2}\bar{S} : \bar{S}} = \sqrt{3J_2}$; J_2 is the second deviatoric stress invariant;
- $\bar{p}$ is the effective hydrostatic pressure stress, where $\bar{p} = -I_1/3$; I_1 is the first stress

invariant;

- $\hat{\bar{\sigma}}_{max}$ is the maximum principal effective stress.

The terms α and γ represent material constants. The term α is a function of the ratio of initial equibiaxial and uniaxial compressive yield stresses, σ_{bo} and σ_{co}, respectively. Experimental values of this ratio lie between 1.10 and 1.16, yielding values of α between 0.09 and 0.12 (Lubliner et al., 1989). Testing performed by Kupfer et al. (1969) showed that specimens subjected to equal biaxial compression yielded a 16% higher strength than uniaxially loaded specimens. Therefore, the default value of σ_{bo} / σ_{co} used by ABAQUS is 1.16.

The term γ only appears under states of triaxial compression, corresponding to a stress state where $\sigma_{max}<0$, and is a function of the parameter K_c. K_c is the ratio of the second stress invariant on the tensile meridian (T.M.) to the second stress invariant on the compression meridian (C.M.) at initial yield for any given pressure invariant value. As shown in Figure 3.6, K_c is used to define the shape of the failure surface within the deviatoric plane.

When K_c takes a value of 1.0, the failure surface within the deviatoric plane becomes a circle, corresponding to the classical Drucker-Prager hypothesis. It has been shown in the literature that the shear strength of concrete under equal biaxial compression (the case where equal stresses act in two principal axes and zero stress acts in the third) is different than the shear strength of concrete under triaxial compression. These two stress states represent different positions within the deviatoric plane. Therefore, the failure surface which aims to reflect the experimental behaviour of concrete should take into account the influence of the third deviatoric stress invariant and adopt a non-circular failure surface within the deviatoric plane (Yu et al., 2010). Furthermore, the original model proposed by Lubliner et al. (1989) states that constant values of K_c ranging from 0.64 - 0.80 are

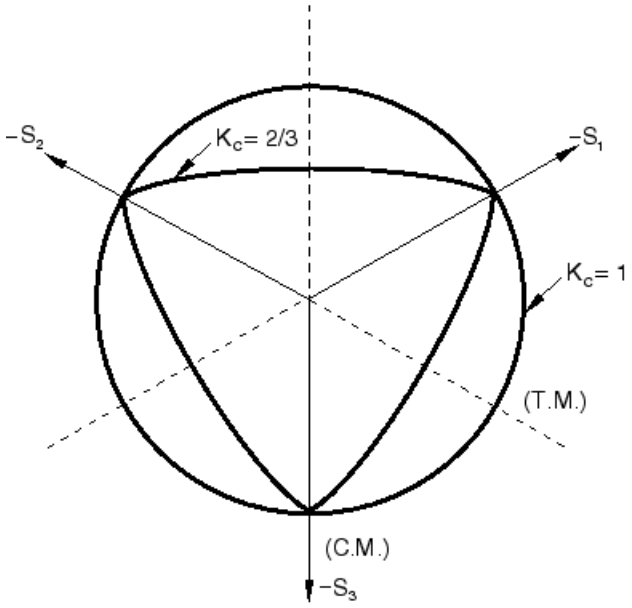

Figure 3.6: Influence of K_c on the Failure Surface in the Deviatoric Plane (DSS, 2012)

acceptable. The Concrete Damaged Plasticity Model in ABAQUS recommends a default value of 2/3 for K_c, and limits the permissible values to $0.5 < K_c \leq 1.0$.

Hardening

In the original plasticity model proposed by Lubliner et al. (1989), isotropic hardening was used. This hardening rule provides good results for monotonic loading, but is not appropriate for modelling the cyclic behaviour of concrete. Under cyclic loading, the evolution of one strength (compression or tension) does not influence the evolution of the other strength. Therefore, the modifications proposed by Lee and Fenves (1998) incorporated a two-variable hardening rule; one variable to control compression and the second to control tension. Recalling the hardening rules discussed in Section 2.7.2, this approach follows the independent hardening rule, where the material is assumed to harden independently in both tension and compression. In the Concrete Damaged Plasticity Model, the evolution of the yield and loading surfaces is controlled by two hardening variables, $\tilde{\varepsilon}_t^{pl}$ and $\tilde{\varepsilon}_c^{pl}$, referred to as the tensile and compressive equivalent plastic strains, respectively.

Plastic Flow Rule

It has been found that the use of the associated flow rule for concrete is not valid for the full range of the concrete response spectrum, and leads to significant discrepancies between the predicted and experimental responses (Hu and Schnobrich, 1989). As concrete is a material that experiences significant volume changes under loading, a non-associated flow rule is necessary to control dilatancy in the modelling (Lee and Fenves, 1998). Therefore, the Concrete Damaged Plasticity Model utilizes a non-associated plastic potential flow rule, which can be expressed in the effective stress space using Equation 3.16:

$$\dot{\varepsilon}^{pl} = \dot{\lambda}\frac{\partial G(\bar{\sigma})}{\partial \bar{\sigma}} \tag{3.16}$$

where $\dot{\varepsilon}^{pl}$ is the plastic strain rate, G is the flow potential function and λ is a non-negative scalar hardening parameter. The flow potential function, G, used in this model is a hyperbolic Drucker-Prager function and is expressed in the $p-q$ plane (meridional plane) using Equation 3.17:

$$G = \sqrt{\epsilon\sigma_{to}tan\psi + \bar{q}^2} - \bar{p}tan\psi \tag{3.17}$$

where ψ is the dilation angle, σ_{to} is the uniaxial tensile stress of the concrete at failure as defined by the user, and ϵ is a parameter referred to as the plastic potential eccentricity. This flow potential curve gives the relation between the plastic flow direction and the plastic strain rate. The curve is continuous and smooth, thus ensuring that the flow direction is always uniquely defined. The flow potential curve is defined in the $p-q$ plane as shown in Figure 3.7.

The function approaches the classic linear Drucker-Prager flow potential asymptotically as the confining pressure increases, and intersects the hydrostatic pressure axis at 90°. The shape of the hyperbola is adjusted through the eccentricity parameter, ϵ. The eccentricity is

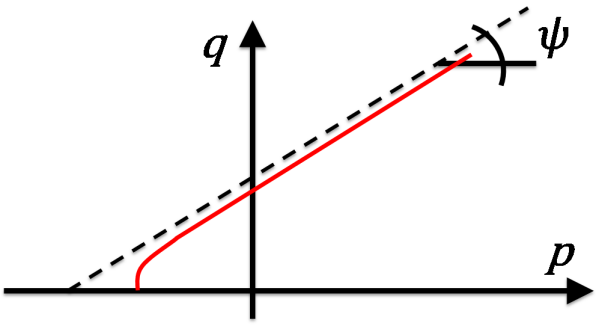

Figure 3.7: Hyperbolic Drucker-Prager Flow Potential Function (DSS, 2012)

a small positive value which defines the rate that the plastic potential function approaches the asymptote. The default value for the eccentricity is 0.1. This value implies that the material has a relatively constant dilation angle over a wide range of confining pressures. If a larger eccentricity is used, the function will have a greater curvature, thus the dilation angle will increase more rapidly as the confining pressure is decreased. Using eccentricity values that are significantly less than the default value may lead to convergence issues when modelling low confining pressures due to the tight curvature of the function at the intersection with the p-axis.

The flow potential function is also dependent on the dilation angle, ψ. This angle is a material property that is a measure of the inclination of the flow potential function within the meridional plane relative to the hydrostatic pressure axis at high confining pressures (Figure 3.7). A small dilation angle will produce a brittle behaviour, while higher values will produce a more ductile behaviour (Malm, 2009). The physical meaning of this angle and its influence on the behaviour of concrete will be discussed in further detail in Sections 5.4.1 and 6.4.1.

Viscoplastic Regularization

The softening behaviour exhibited in the post-peak response of concrete may cause numerical convergence problems in the model. This is especially significant for the uniaxial tensile stress-strain curve that displays a drastic change in slope at peak stress. A com-

mon technique to overcome these convergence issues is to use viscoplastic regularization of the constitutive equations. The Concrete Damaged Plasticity Model utilizes a generalization of the Devaut-Lions approach which allows the stresses to be outside of the yield surface. Within the plasticity material definition of the concrete model, users may input a value for the viscosity parameter, μ. The default value of μ that ABAQUS/Standard uses is zero, which corresponds to no viscoplastic regularization. A model that does not utilize viscoplastic regularization yields the inviscid solution, or the solution that considers zero viscosity of the concrete. If a viscosity parameter greater than zero is specified, the viscoplastic strain rate, $\dot{\varepsilon}_v^{pl}$, is defined using Equation 3.18:

$$\dot{\varepsilon}_v^{pl} = \frac{1}{\mu}(\varepsilon^{pl} - \varepsilon_v^{pl}) \tag{3.18}$$

where μ is the viscosity parameter that represents the relaxation time of the viscoplastic system, ε^{pl} is the plastic strain evaluated in the inviscid solution, and ε_v^{pl} is the viscoplastic strain. As a viscoplastic strain is now used, the viscous stiffness damage variable, d_v, is utilized and is defined using Equation 3.19:

$$\dot{d}_v = \frac{1}{\mu}(d - d_v) \tag{3.19}$$

where d is the stiffness damage variable of the inviscid solution. If viscoplastic regularization is specified, model output will be based on plastic strain and elastic stiffness degradation values, ε_v^{pl} and d_v, respectively. The use of a small value for the viscosity parameter relative to the iteration time increment will result in improvements to the solution convergence rate without compromising the accuracy of the results. As μ decreases towards zero, the solution becomes the plastic solution. If μ becomes significantly larger than the iteration time increment, the solution approaches the elastic solution. The selection of an appropriate viscosity parameter is discussed in detail in Sections 5.4.2 and 6.4.2.

Chapter 4

Beam Modelling Parameters

This chapter presents an overview of the model parameters that were used in the numerical simulations that apply to all twelve beams studied. The material properties of concrete and glass fibre reinforced polymer (GFRP) that were used for all beam simulations are presented. This chapter then focuses on the geometric and analytical details used to model the concrete beams and GFRP reinforcement, including beam dimensions, section assignments, boundary conditions, element selection, and time step incrementation.

4.1 Material Properties used in Modelling

4.1.1 Concrete - Compressive Strength

Concrete compressive strength testing was performed by Krall (2014) on 100x200mm cylinders to determine the actual properties of the concrete used in the experimental beams. After 28 days of being cast, 3 cylinders were tested and yielded an average compressive strength of 47.3MPa. After 101 days of being cast, 28 cylinders were tested and yielded an average compressive strength of 58.1MPa. The average compressive strength of all cylinders tested, regardless of age, was 56.5MPa. The twelve concrete beams were tested

over a span of 55 days; the first beam was tested 43 days after the concrete was cast, while the final beam was tested 98 days after the concrete was cast. Therefore, to increase the accuracy of the finite element modelling, it was necessary to predict the compressive strength of each beam at the time of testing. The model as proposed by ACI 209R-92 was considered, which correlates the compressive strength of concrete with the age of the concrete as shown in Equation 4.1:

$$f_{cmt} = \left(\frac{t}{a + bt}\right) f_{cm28} \tag{4.1}$$

where f_{cmt} is the compressive strength of concrete at time t, t is the age of the concrete in days, a and b are constants, and f_{cm28} is the concrete mean compressive strength at 28 days with units of MPa. The constants a and b are functions of the type of cement used and the method of curing. The ranges of these constants for normal weight concrete are 0.05 - 9.25 for a and 0.67 - 0.98 for b. Table 4.1 presents typical recommended values for a and b.

Table 4.1: ACI 209R-92 Concrete Age Model

Type of	Moist-Cured Concrete		Steam-Cured Concrete	
Cement	a	b	a	b
I	4.00	0.85	1.00	0.95
III	2.30	0.92	0.70	0.98

It was determined through trial-and-error that values of $a = 7.140$ and $b = 0.743$ are effective in replicating the strength development observed in the tested concrete and are able to accurately predict the measured 28-day and 101-day strengths. Figure 4.1 compares the relationship between compressive strength and time using the proposed constants and using the recommended constants for a Type I cement that has been moist cured ($a = 4.0$, $b = 0.85$).

Using the proposed model, the compressive strength was predicted for each beam. Table 4.2

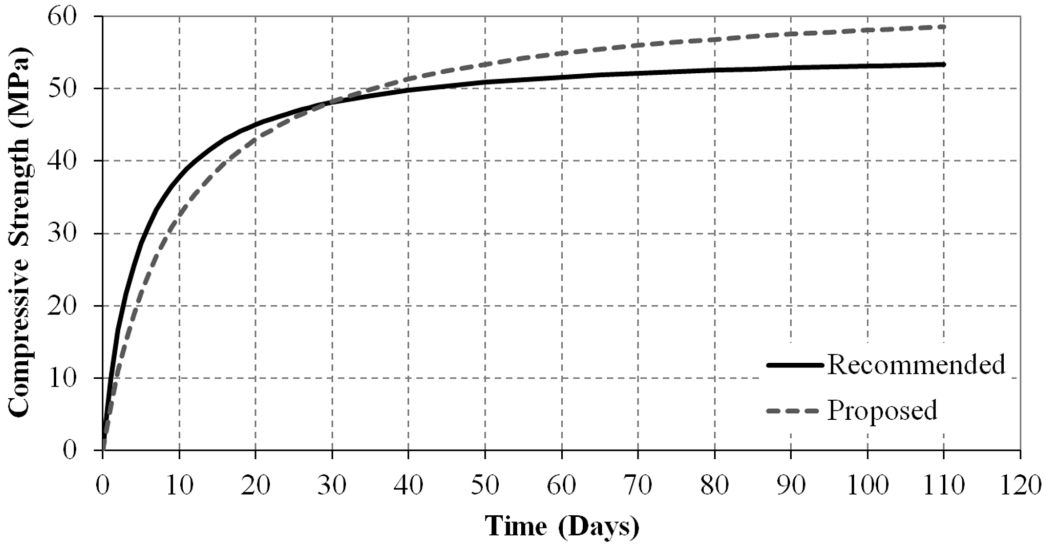

Figure 4.1: Proposed Concrete Age Model

presents the age of each beam at the time of testing, the compressive strength as predicted using the proposed model, and the percent difference between the predicted strength and the average experimental compressive strength of 56.5MPa.

As shown in Table 4.2, the beams with no stirrups (BM XX-INF) were tested first while the beams with the increased stirrup diameter (BM XX-s230) were tested last. As a result, the beams with no stirrups had the lowest predicted concrete compressive strengths and had the largest percent difference with the average compressive strength. For this reason, the compressive strength as predicted by the model was used for all beams with no stirrups. Conversely, the predicted concrete strength for all beams with stirrups matched very closely to the average tested strength. Therefore, the average compressive strength of 56.5MPa was used for all beams with stirrups to simplify the analyses, as shown in Table 4.2.

4.1.2 Concrete - Tensile Strength

The tensile strength of concrete typically ranges from 8 to 15% of the compressive strength. The tensile strength is strongly influenced by the type of aggregates, compressive strength

Table 4.2: Selection of Concrete Compressive Strength

Beam	t (Days)	f_c' Predicted (MPa)	% Difference	f_c' Used (MPa)
12-INF	54	54.0	4.3	54.0
16-INF	50	53.4	5.5	53.4
25-INF	43	52.0	7.9	52.0
12-220	72	56.2	0.6	56.5
16-220	68	55.8	1.3	56.5
25-220	56	54.3	3.8	56.5
12-150	91	57.6	1.9	56.5
16-150	86	57.3	1.3	56.5
25-150	84	57.1	1.1	56.5
12-s230	98	58.0	2.6	56.5
16-s230	96	57.9	2.4	56.5
25-s230	92	57.6	2.0	56.5

of the concrete, and the stress acting transversely to the tensile stress. The tensile strength is also strongly affected by the type of test used to determine it (MacGregor and Wight, 2005). Figure 4.2 presents three common experimental tests used to determine the tensile strength of concrete.

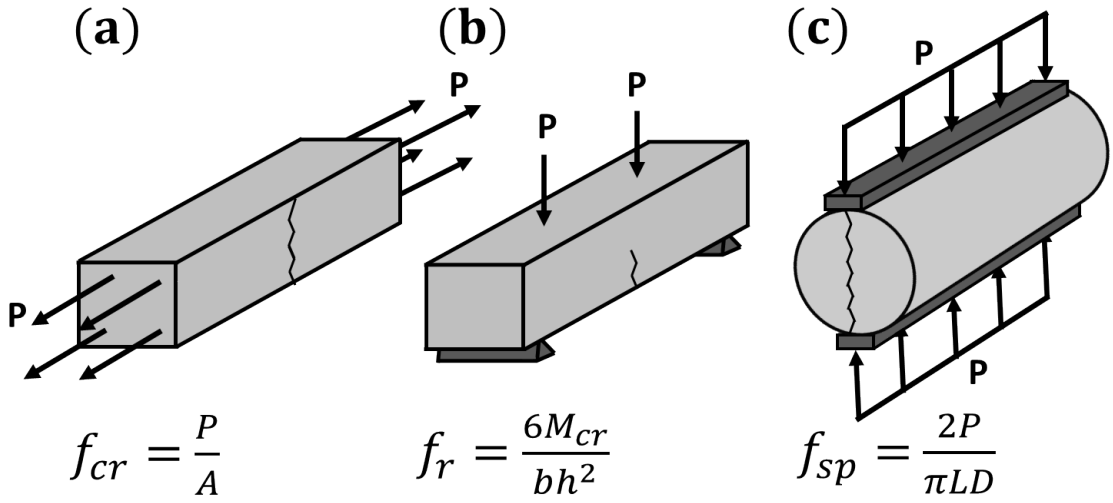

Figure 4.2: Common Tensile Strength Test Methods

The first tensile test is the "direct test" as shown in Figure 4.2a. Although this method is

less common as it is difficult to apply a tensile load directly to a concrete specimen, it is an effective means to determine the tensile capacity directly. The cracking stress, f_{cr}, can be determined from the test using the equation shown in Figure 4.2. In absence of this test, the cracking stress can be predicted as follows:

$$f_{cr} = 0.33\lambda\sqrt{f'_c} \tag{4.2}$$

where λ accounts for the concrete density. As it is difficult to apply tensile loads directly, indirect test methods have become standard practice. The "modulus of rupture" or flexure test involves the four-point loading of a concrete prism as shown in Figure 4.2b. This creates a region of pure bending between the load points where the shear force is zero. The applied moment that induces fracture within this region, M_{cr}, can be used to indirectly calculate the ultimate tensile stress, or modulus of rupture f_r. As the tensile strength of concrete under flexure is a primary concern, the modulus of rupture is typically used in design. CSA A23.3-04 specifies the following approximation to f_r:

$$f_r = 0.6\lambda\sqrt{f'_c} \tag{4.3}$$

Another common test is the "split-cylinder test". This test involves the application of a compressive load to the side of a standard test cylinder as shown in Figure 4.2c. This compressive load induces indirect tensile stresses transverse to the applied loading due to Poisson's effect, causing the cylinder to eventually split into two halves. Split-cylinder testing was performed by Krall (2014) on the experimental concrete to determine the splitting tensile strength f_{sp}, and yielded strengths ranging from 3.56MPa to 5.06MPa, with an average strength of 4.2MPa.

To accurately model the uniaxial behaviour of concrete under direct tensile loads, it was concluded that the estimation of the tensile strength using the direct test formulation was

the most appropriate. Therefore, Equation 4.2 was used for all beams. This resulted in a tensile strength of 2.42MPa, 2.41MPa, and 2.38MPa for beams 12-INF, 16-INF, and 25-INF, respectively, and 2.48MPa for all beams with stirrups.

4.1.3 Concrete - Modulus of Elasticity

The initial modulus of elasticity of concrete, E_{co}, is dependent on factors including the concrete compressive strength, properties of the aggregates and cement paste, and the rate of loading. Various relationships have been derived to estimate the modulus of elasticity of concrete. CSA A23.3-04 recommends the following relationship for concrete with densities between 1500 and 2500kg/m^3:

$$E_{co} = (3300\sqrt{f'_c} + 6900)\left(\frac{\gamma_c}{2300}\right)^{1.5} \tag{4.4}$$

where γ_c is the density of the concrete in kg/m^3. The density of each concrete cylinder used for compressive testing was determined by Krall (2014), and it was found that the average density of the concrete used in the beam specimens was 2417kg/m^3, which falls within the applicable range for Equation 4.4. CSA A23.3-04 also presents a simplified relationship as shown in Equation 4.5 which is applicable for normal density concrete with compressive strengths between 20 and 40MPa:

$$E_{co} = 4500\sqrt{f'_c} \tag{4.5}$$

ACI 318-11 provides the following empirical equations for computing the modulus of elasticity for concrete with unit weights varying between 90 and 155pcf (1442 and 2483kg/m^3):

$$E_{co} = 33 w_c^{1.5} \sqrt{f'_c} \qquad (Imperial\ Units) \tag{4.6a}$$

$$E_{co} = 0.0427 w_c^{1.5} \sqrt{f'_c} \qquad (SI\ Units) \tag{4.6b}$$

where w_c is the unit weight of concrete. For normal weight concrete with a density of 145pcf (2323kg/m^3), Equation 4.6 can be simplified to:

$$E_{co} = 57000 \sqrt{f'_c} \qquad (Imperial\ Units) \tag{4.7a}$$

$$E_{co} = 4700 \sqrt{f'_c} \qquad (SI\ Units) \tag{4.7b}$$

The average compressive strength of the concrete used in the beam testing was found to be 56.5MPa, thus Equation 4.5 is not applicable. Therefore, to consider the higher stiffness of high strength concrete and to maintain the simplicity of Equations 4.5 and 4.7, the following relationship was used to calculate the concrete modulus of elasticity for all beams:

$$E_{co} = 5000 \sqrt{f'_c} \tag{4.8}$$

This resulted in a modulus of elasticity of 36,742MPa, 36,538MPa, and 36,056MPa for beams 12-INF, 16-INF, and 25-INF, respectively, and 37,583MPa for all beams with stirrups.

4.1.4 Concrete - Poisson's Ratio

When using ABAQUS/CAE, the Poisson's ratio for concrete, υ, is inputed when defining the elastic properties. The Poisson's ratio of concrete as recommended by Model Code 2010 ranges from 0.14 to 0.26. This range is applicable for compressive stresses ranging from -$0.6 f_{ck}$ to $0.8 f_{ck}$, where f_{ck} is the characteristic compressive strength equal to approximately

f_c' minus 1.6MPa (Reineck et al., 2003). For the purposes of design, Model Code 2010 states that a value of $\upsilon = 0.20$ is sufficiently accurate. Chen (1982) states that the Poisson's ratio for concrete ranges from 0.15 to 0.22, with a representative range being 0.19 to 0.20. Therefore, a value of 0.20 was selected for all beam simulations performed for this thesis. The influence of the Poisson's ratio on the beam responses is presented in Appendix B and C, and was found to be negligible.

4.1.5 GFRP - Modulus of Elasticity and Tensile Strength

Fibre reinforced polymer (FRP) materials are linear-elastic until failure. This sudden and brittle rupture mode is regarded as a disadvantageous material characteristic as there is little warning of impending failure as compared to steel reinforcement which exhibits plastic deformation upon yielding. However, as it is only necessary to prescribe the tensile modulus of elasticity and the ultimate strength of the FRP material, this material behaviour is very simple to model. ComBAR, glass fibre reinforced polymer (GFRP) bars manufactured by Schoeck Canada, were used for both the longitudinal and transverse reinforcement within the experimental beams. The material properties used for the GFRP were taken from technical literature provided by the manufacturer at the time of testing, and have been previously summarized in Table 2.5. For the GFRP stirrups, the ultimate tensile strength of only the straight portion of the stirrup was specified in the modelling (the reduced strength at the stirrup corners was not considered). As no stirrups ruptured during testing, the reduced strength in the bent regions of the stirrups was not critical, therefore this simplification is acceptable.

4.2 Concrete Beam Modelling

4.2.1 Beam Dimensions

The considerations used to design the experimental beams were discussed previously, including the process used to select the width (b), height (h), effective reinforcement depth (d), shear span (a), longitudinal reinforcement ratio (ρ_F), and the transverse reinforcement ratio (ρ_V) for each beam. Table 4.3 presents the designed dimensions of the experimental beams that were used in the ABAQUS modelling. As can be seen, the shear span to effective depth ratio (a/d) remained constant for all beams, thus simplifying the analyses.

Table 4.3: Beam Dimensions

Beam	b (mm)	h (mm)	d (mm)	a/d	ρ_F (%)	ρ_V (%)
12-INF						0.00
12-150	200	350	270	2.5	2.51	0.75
12-220						0.51
16-INF						0.00
16-150	200	345	270	2.5	2.23	0.75
16-220						0.51
25-INF						0.00
25-150	200	330	270	2.5	1.82	0.75
25-220						0.51
12-s230		365			2.18	
16-s230	230	360	270	2.5	1.94	1.19
25-s230		345			1.58	

Due to the symmetry of the beams and applied loading, only one-half of each beam was analyzed to reduce the computational effort. Each beam was split at the mid-span such that only one shear span and one support were analyzed.

4.2.2 Beam Parts and Section Assignments

Each beam geometry was modelled in three-dimensions using the ABAQUS/CAE interface. The model is constructed by creating "Parts". Parts represent the building blocks of any ABAQUS model, and are assembled to create the final model. Each part is an independent geometry that is assigned a "Section". A section contains the information about the properties of a part or region of a part. The properties of this section are dependent on the type of part being considered. For example, for a deformable wire part, the section will define the cross-sectional area of the wire; for beam parts, the section will assign the profile of the part, thus defining cross-sectional properties such as moment of inertia. The section also assigns the desired material to the part. Each material that is created is assigned its own name and is independent of any specific section. Therefore, the user may assign a particular material to as many sections as necessary. Similarly, each section is assigned its own name and is independent of any specific part. Therefore, the user may assign a section to as many parts as necessary. In summary, the following procedure is used to assign properties to a part:

1. Create material
2. Create section
3. Assign the material to the section
4. Assign the section to the part

For the modelling performed for this thesis, three parts were necessary. The first part was the rectangular geometry of the beam consisting of concrete elements. The second part was the longitudinal tensile GFRP reinforcement. The third part was the transverse shear GFRP reinforcement (for beams with stirrups). Each of these parts was created independently, given section and material properties, and then assembled to create the

final model as shown in Figure 4.3.

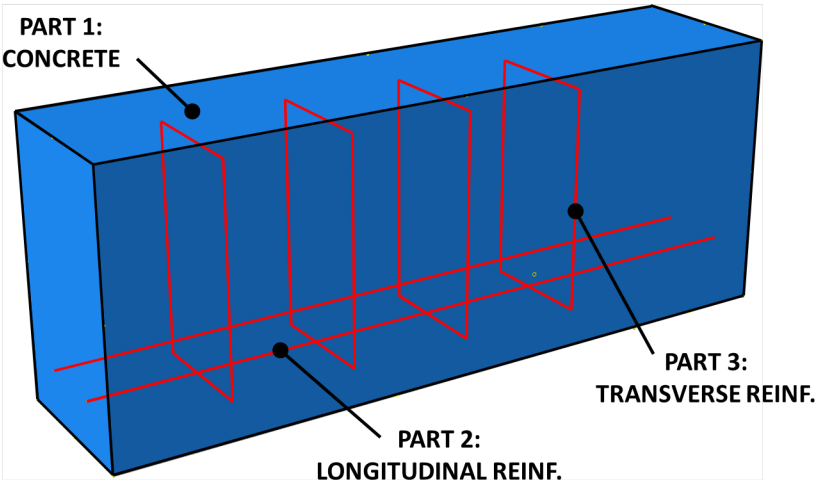

Figure 4.3: Beam Modelling Parts

The concrete part was defined as a three-dimensional "Deformable" body, meaning it is a part that can be of arbitrary shape and that can deform under mechanical, thermal, or electrical loading (as opposed to a "Discrete Rigid" body which is assumed to remain rigid during the analyses). To create the rectangular concrete region of the beam, the Extrusion formulation was used. This method allows the user to create a three-dimensional geometry by defining a two-dimensional cross-section profile and extruding this profile to the required length.

To define the properties of the concrete part, a "homogeneous solid" section was applied to it. This section is used to define a single material for solid regions. Other section options are available for different analysis types including "composite solid" sections for layered regions or "generalized plane strain" sections for two-dimensional planar regions.

The definition of the remaining two parts (longitudinal and transverse reinforcement) will be discussed in Section 4.3.

4.2.3 Concrete Element Selection

The use of ABAQUS software has become increasingly popular among researchers due to the extensive element library that is available. A discussion of the elements selected to model the concrete is presented here. The selection of elements for the GFRP reinforcement is discussed in Section 4.3.

The geometry that an element assumes is dependent on its "family". The element families that this thesis will focus on include continuum, membrane, and truss elements as shown in Figure 4.4.

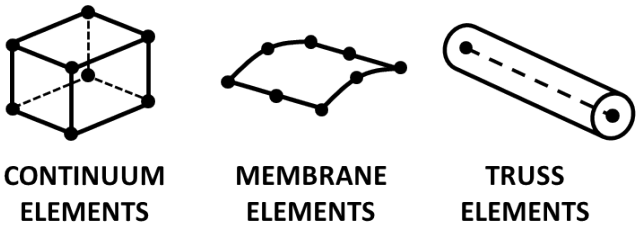

Figure 4.4: Element Families (DSS, 2012)

The concrete in all analyses performed in this thesis was modelled using continuum elements. Continuum, or solid, elements are the standard volume element offered by ABAQUS. These elements are advantageous for modelling three-dimensional nonlinear problems involving plasticity and large deflections. In three-dimensions, continuum elements may take the form of tetrahedra, triangular prisms, or hexahedra bricks. Tetrahedral elements are geometrically versatile and are advantageous for meshing complex shapes. Tetrahedra are also less sensitive to initial element shape; hexahedra elements are effective if their shape is approximately rectangular, and become less accurate if they are initially distorted. A mesh of undistorted hexahedral elements will often provide a solution of equivalent accuracy to tetrahedral elements, but with less computational effort. Hexahedral elements are more efficient and have a higher convergence rate. As the concrete beams modelled in this thesis were rectangular, hexahedral continuum elements were selected to improve the efficiency

of the analyses.

For a stress analysis, the degrees of freedom of interest are the translations of the element nodes. Interpolation of these nodal values is performed to determine the displacement at all other points within the element. The order of the interpolation (linear, quadratic, cubic, etc.) is dependent on the number of nodes per element. For example, the 8-node continuum element shown in Figure 4.4 uses linear interpolation and is referred to as a first-order element, whereas a 20-node continuum element uses quadratic interpolation and is referred to as a second-order element. Although second-order elements will provide results of higher accuracy with fewer elements as compared to linear elements in theory, higher-order elements will experience convergence issues when analyzing highly nonlinear problems. For this reason, a sufficient number of linear elements was deemed acceptable for all analyses.

"Shear locking" is a common phenomenon that occurs with first-order elements that are subjected to bending. Consider a block of material subjected to pure bending as shown in Figure 4.5a with the expected deformation shown in Figure 4.5b. If a two-dimensional, 4-noded, quadrilateral, linear element with 4 integration points is used to model this material, it would exhibit the deformation shown in Figure 4.5c.

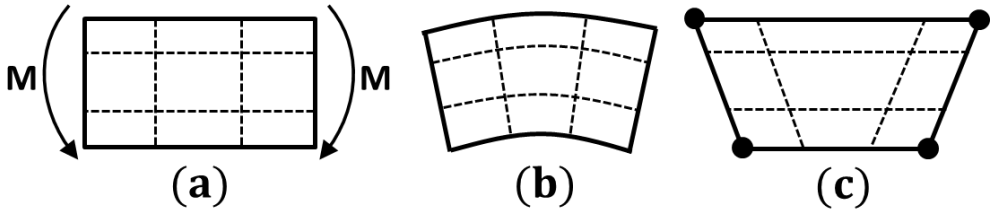

Figure 4.5: Shear Locking of First-Order Elements (DSS, 2012)

As can be seen, the dotted lines in the deformed shape of the element are no longer perpendicular at each integration point. This indicates that the shear stress at these points is nonzero, which is not true for a material under pure bending. This is a consequence of the inability of linear elements to have curved edges. This phenomenon means that strain

energy is creating shearing deformation as opposed to the expected bending deformation. This causes the element to be too stiff, and overall deflections to be underpredicted. A common technique to overcome this behaviour is through the use of "reduced integration". Reduced integration reduces the number of integration points per element in order to avoid excessive restraint. Consider the two-dimensional quadrilateral elements shown in Figure 4.6.

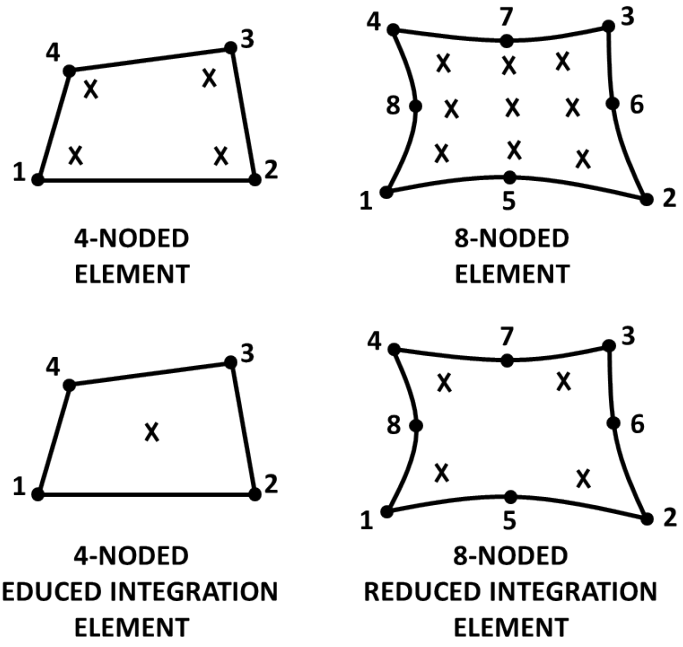

Figure 4.6: Full Integration vs. Reduced Integration Elements (DSS, 2012)

Reduced integration also decreases the time of analyses, which is especially beneficial for three-dimensional problems. For example, a C3D8 element is an 8-noded continuum element with 8 integration points (full integration), whereas a C3D8R element is an 8-noded continuum element with only 1 integration point (reduced integration). Although reduced integration is recommended to avoid shear locking of linear elements, this solution leads to the issue of "hourglassing". Consider the use of a single reduced integration element to model the previously discussed material as shown in Figure 4.7a.

With reduced integration, the linear quadrilateral element has only 1 integration point (as

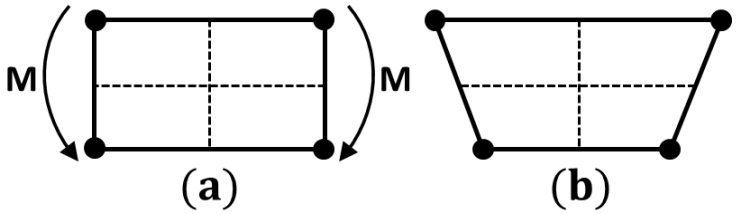

Figure 4.7: Hourglassing of Reduced Integration Element (DSS, 2012)

opposed to the fully integrated element with 4 integration points). Under pure bending, neither of the dotted lines at the integration point has changed length and the angle between them has not changed as shown in Figure 4.7b. Therefore, all components of stress at the element's only integration point are zero. This means that the strain energy in the element is zero, thus the element will be unable to resist this type of deformation as it has no stiffness under this loading. As a result, hourglassing may lead to uncontrolled distortions of the mesh. ABAQUS provides elements with hourglass control to minimize this effect.

In summary, C3D8R elements were used to model all concrete regions. These elements are hexahedral continuum elements (C), three-dimensional (3D), 8-noded linear bricks (8), reduced integration (R), with hourglass control.

4.2.4 Beam Boundary Conditions

The boundary conditions used for all beams are shown in Figure 4.8. As can be seen, the boundary conditions are in terms of the directional axes 1, 2, and 3 ('1' represents the out-of-plane direction, '2' represents the direction transverse to the beam's longitudinal axis, and '3' represents the direction parallel to the beam's longitudinal axis).

For the purposes of this discussion, "U" will represent displacements while "UR" will represent rotations. Therefore, U1 refers to the displacement in the 1-axis while UR2 refers to the rotation about the 2-axis.

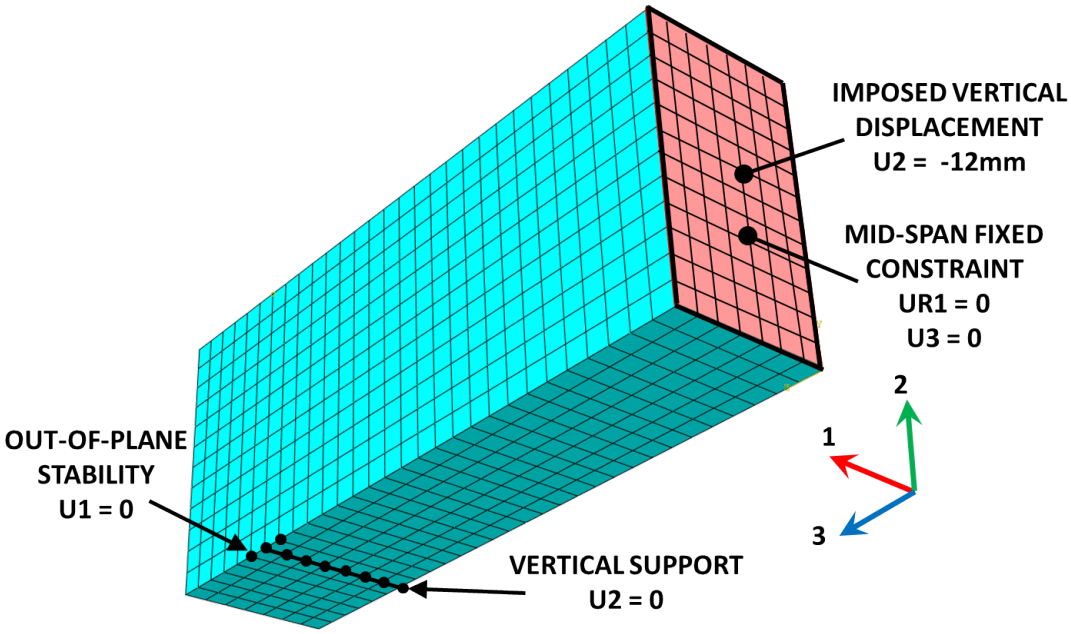

Figure 4.8: Boundary Conditions

As shown in Figure 2.9, the beams were tested with simple supports. One support provided restraint to both vertical and longitudinal displacements (directions 2 and 3) while allowing rotations about the out-of-plane axis (pin support). The second support provided restraint to only vertical displacements (direction 2) while allowing longitudinal displacements and rotations about the out-of-plane axis (roller support). To model these conditions, a displacement of zero was prescribed in the 2-axis to a line of nodes at the support (U2 = 0), thus allowing for rotations and longitudinal displacements.

Furthermore, as only one-half of each beam was modelled, it was necessary to apply boundary conditions to the mid-span section. To provide the continuity of the beam at the mid-span, the rotations about the 1-axis and the displacements in the 3-axis were restrained at all nodes at the mid-span while allowing for vertical displacements in the 2-axis (UR1 = 0, U3 = 0).

To ensure stability of the model and to avoid singularity, the out-of-plane translations were restrained at three nodes at the support (U1 = 0).

The models were analyzed using displacement-controlled loading. This method was used in order to study the post-peak response of the load-displacement behaviour of each beam. To do this, a downwards vertical displacement boundary condition was applied to all nodes at the mid-span. The magnitude of this displacement was set large enough to ensure that failure of each beam occurred. For example, a boundary condition of U2 = -12mm was used for all beams with no stirrups (BM XX-INF).

To study the behaviour of each beam under loading, Applied Loading vs. Mid-span Deflection curves were constructed for each proposed model. As the loading was applied as an imposed vertical displacement, it was necessary to calculate the applied loading for each simulation using the support reaction forces. As the beams were simply-supported, Equation 4.9 can be used to calculate the reaction forces:

$$R = \frac{P}{2} \qquad \therefore P = 2R \tag{4.9}$$

where R is the vertical component of the reaction force at each support and P is the total applied load. As the simulations were performed on three-dimensional beams, the reaction forces were distributed to multiple nodes (line of nodes at the support with prescribed boundary condition). Therefore, the reaction forces outputted at each support node were summed and multiplied by 2 to determine the total applied loading at any given time.

4.2.5 Time Step Incrementation

When creating an ABAQUS model for analysis, it is necessary to define one or more analysis "steps". The sequence of steps allows the user to capture changes in the loading and boundary conditions of the model, changes to the interaction between parts in the model, changes to the analysis procedure, or any other changes to the model that may occur during the analysis (DSS, 2012). For the models created in preparation of this

thesis, only one analysis step was required to capture the monotonic loading conditions.

ABAQUS/Standard uses the Newton's method to solve nonlinear equilibrium equations within each step. The solution is obtained through a series of increments, with iterations to obtain equilibrium occurring within each increment. ABAQUS allows the user to use Automatic Incrementation, where the analysis will select increment sizes automatically based on computational efficiency. With this type of solution technique, it is necessary to input the minimum increment size, the maximum increment size, and the maximum number of increments. If ABAQUS requires a smaller time increment than the value specified to reach convergence, the analysis will be terminated. Therefore, the required lower limit size may become quite small for highly nonlinear problems. Similarly, if ABAQUS requires more increments than the maximum value specified, the analysis will be terminated. Finally, when using Automatic Incrementation, ABAQUS will select the largest increment size possible to increase efficiency, but will not exceed the maximum size specified by the user.

The selection of the maximum increment size plays a critical role in the accuracy of the analysis. To demonstrate this point, ABAQUS/Standard was used to analyze a cube of concrete under uniaxial compression. The Hognestad Parabola was used to define the uniaxial stress-strain behaviour of the concrete, with a compressive strength of 56.5MPa. The model was analyzed using various values for the maximum time increment size as shown in Figure 4.9.

As can be seen, with a maximum increment size of 0.01, the analysis results are able to correlate strongly with the expected response (the expected response is omitted here for clarity, but is identical to the model response). With larger increment sizes, such as 0.1 and 1.0, the analyses are able to match the pre-peak behaviour that exhibits negligible change to the curvature, but fail to capture the large curvatures in the post-peak region. Therefore, to maximize the accuracy of the modelling, a maximum time increment size of

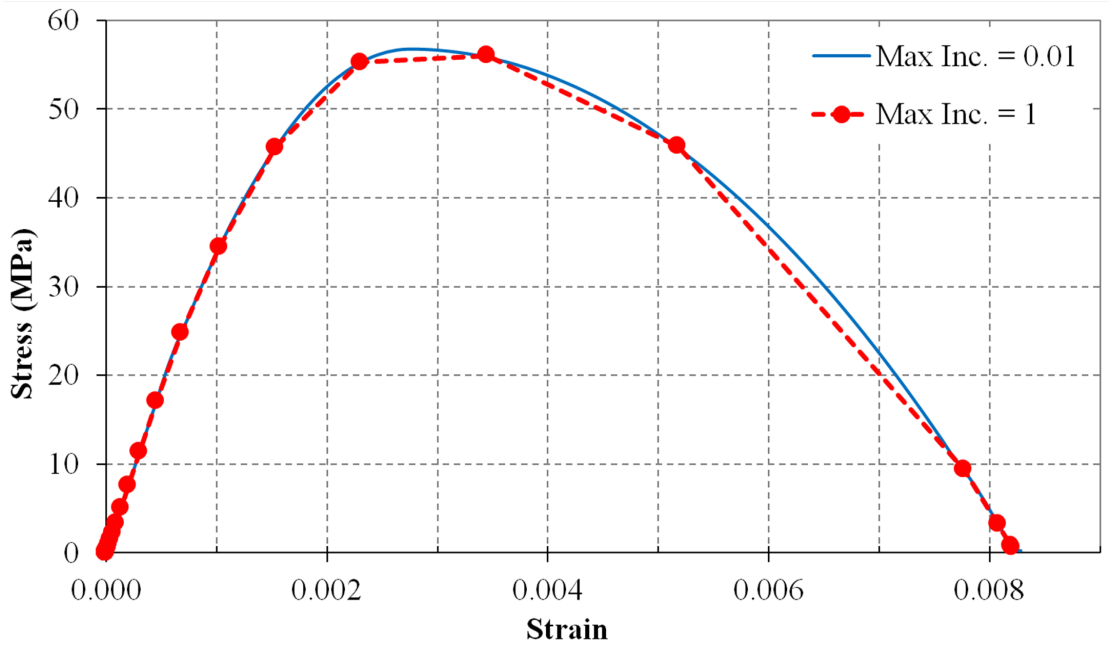

Figure 4.9: Influence of Maximum Time Increment Size

0.01 was used for all models to ensure that the full spectrum of the concrete response is captured.

4.3 GFRP Reinforcement Modelling

As discussed previously, an ABAQUS model is created by assembling one or more parts. The first part of the proposed model, the concrete beam, has been discussed. This section will now focus on the modelling of the remaining parts: the GFRP longitudinal and GFRP transverse reinforcement. Two methods of providing reinforcement to concrete were studied in this research:

1. Discrete, one-dimensional truss sections
2. Smeared, reinforced membrane sections

Each method will be presented separately, with each discussion to include the part and section properties, element selection, and assembly constraints.

4.3.1 Reinforcement Method 1 - Truss Sections

The first method used to model the reinforcement was the use of discrete truss sections. For the longitudinal bars, each individual bar was modelled as a discrete one-dimensional rod. For the transverse reinforcement, each stirrup was constructed using four discrete rods to create rectangular, closed-loop stirrups. The reinforcing bars were defined as deformable "wire" type parts. A wire is depicted as a line in ABAQUS/CAE, and is used to model a solid that has a thickness and depth that are significantly smaller relative to its length. To assign properties to this wire part, a "beam" section or a "wire" section can be assigned to it. Beam sections provide both axial and bending stiffness and define the cross-section profile (I-section, box section, circular section, etc.). Truss sections provide only axial stiffness and define the material properties and cross-sectional area. As the axial stiffness and cross-sectional area were the only two parameters of interest for each reinforcing bar, the truss section was applied to each wire part. The cross-sectional area of each bar was set equal to the values presented in Table 2.5 as specified by the manufacturer.

Using this method to model reinforcement, truss elements were used to mesh the discrete rods. Truss elements are slender structural elements that can only transmit axial force and do not transmit moments or transverse loads. ABAQUS provides 2-noded truss elements as shown in Figure 4.4 that perform linear interpolation of the nodal displacement values and carry constant strains. 3-noded truss elements are also available which use quadratic interpolation, thus allowing for curved elements and linear, non-constant, strain distributions within the element. It was concluded that a sufficient number of linear elements was adequate to capture the strain distribution within each reinforcing bar. Therefore, T3D2

elements were selected to model the truss sections: Truss elements (T), three-dimensional (3D), and 2-nodes per linear element (2).

These individual bars are then incorporated into the model by being embedded into the concrete through the "Embedded Region" constraint. With this constraint, the truss elements are referred to as the "embedded region" and the continuum concrete elements are referred to as the "host region". If a node of an embedded element lies within a host element, the translational degrees of freedom of the embedded node become constrained to the values of the corresponding degrees of freedom of the host element. With this modelling approach, the concrete behaviour is considered independently of the reinforcement. The influence of the interaction between the concrete and reinforcing bars on the member response, such as bond slip and dowel action, are not considered. However, these factors that influence the phenomenon of tension stiffening are simulated approximately through modifications made to the post-peak tensile response within the concrete model as discussed in Section 3.3.2. Therefore, the interaction between the concrete and the reinforcement is considered in the modelling of the concrete, not the reinforcement.

4.3.2 Reinforcement Method 2 - Membrane Sections

The second method studied to provide reinforcement to the concrete involved the use of embedded reinforced membrane sections. ABAQUS allows the user to define one or multiple layers of reinforcement within membrane sections. Once reinforcement has been specified for the membrane section, the membrane can be embedded into the continuum concrete elements using the Embedded Region constraint as discussed previously for the truss section method. For the longitudinal reinforcement, each membrane section represents a single layer of reinforcing bars. For the transverse reinforcement, each membrane section represents a single stirrup.

Each membrane was defined by first creating a three-dimensional, deformable "shell" part. A shell part is a planar representation of a solid that has a thickness that is significantly smaller relative to its width and length. To assign material properties and reinforcing layers to the shell part, a "membrane" section was assigned to it. Membrane sections represent thin surfaces that offer strength in the plane of the surface only, do not provide bending stiffness, and have negligible stresses in the thickness direction.

Using this method to model reinforcement, membrane elements were used to mesh the membrane sections. ABAQUS provides 4-noded quadrilateral membrane elements that perform linear interpolation of the nodal displacement values. Similar to the 8-noded hexahedral continuum elements that were used to model the concrete, the fully-integrated 4-noded membrane element also suffers from the phenomenon of shear locking, and thus requires reduced integration in combination with hourglass control. Alternatively, 8-noded quadrilateral membrane elements with quadratic interpolation as shown in Figure 4.4 could be used to avoid these issues, but may introduce numerical convergence issues. Therefore, M3D4R elements were selected to model the membrane sections: Membrane elements (M), three-dimensional (3D), 4-noded linear quadrilaterals (4), reduced integration (R), with hourglass control.

To define a layer of reinforcing bars within the membrane section, the user must specify the following: cross-sectional area of a single reinforcing bar (A_{bar}), spacing of the reinforcing bars (S), material of the reinforcing bars, and the orientation of the reinforcing bars within the membrane. The individual reinforcing bars within the membrane are treated as a smeared layer of reinforcement with an equivalent thickness. The equivalent thickness of this layer is determined using Equation 4.10:

$$t_{eq} = \frac{A_{bar}}{S} \tag{4.10}$$

where t_{eq} is the equivalent thickness of the reinforcement layer within the membrane section. Figure 4.10 presents the cross-sectional view of a reinforced membrane.

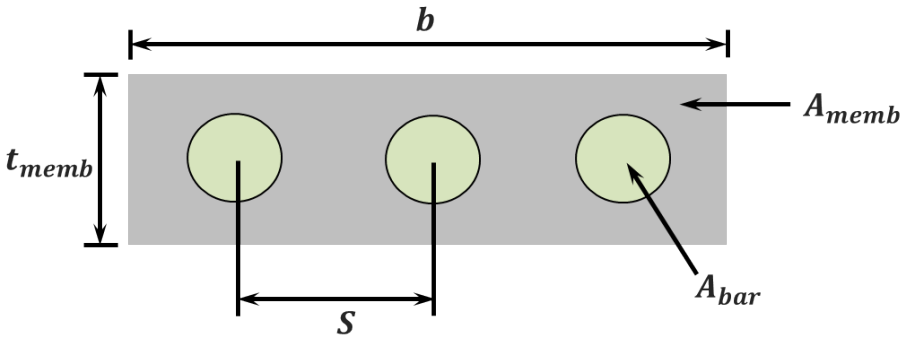

Figure 4.10: Reinforced Membrane Cross-Section

Referring to Figure 4.10, b is the width of the membrane, t_{memb} is the thickness of the membrane, and A_{memb} is the area of the membrane. When the reinforced membrane is embedded into the solid concrete elements and subjected to tensile loads, the area of the membrane and the area of the smeared reinforcement will contribute to the tensile carrying capacity and stiffness of the assembly. Therefore, the total area of material resisting tensile loading can be expressed using Equation 4.11:

$$A_{memb} = (b)(t_{memb}) \tag{4.11a}$$

$$A_{reinf} = (Number\ of\ bars)(A_{bar}) = \frac{A_{bar}b}{S} \tag{4.11b}$$

$$A_{total} = A_{memb} + A_{reinf} \tag{4.11c}$$

It is important to note that the area that the bars occupy within the membrane is double counted when calculating the tensile load in the reinforced membrane. This means that the full area of the membrane is used; the area that the bars occupy is not subtracted from the membrane area. For example, the total area is *not* calculated as follows:

$$A_{total} \neq (A_{memb} - A_{reinf}) + A_{reinf} \tag{4.12}$$

To demonstrate this point, an ABAQUS model was created of a single reinforced membrane. For simplicity, glass fiber reinforced polymer (GFRP) was used for both the membrane material and the reinforcing bar material. The membrane had a width of 200mm, a height of 350mm, and was fixed at the base. The membrane was reinforced with GFRP bars that had individual cross-sectional areas of 113mm^2 and spaced at 100mm. The membrane was put into a state of tension by applying a 3mm upwards vertical displacement to the top boundary of the membrane. As GFRP is a linear-elastic material and a single material was used for both the membrane and the reinforcing bars, the relationship expressed in Equation 4.13 was used to predict the applied load required to create the imposed vertical deformation.

$$\Delta = \frac{PL}{AE}; \qquad P = \frac{\Delta AE}{L} \tag{4.13}$$

where Δ is the applied displacement, A is the total area of the material resisting the applied displacement, E is the modulus of elasticity of the membrane/reinforcement materials, and L is the initial length of the membrane. For the analyses performed, Δ = 3mm, E = 63,500MPa, L = 350mm, b = 200mm, A_{bar} = 113mm^2, S = 100mm. The total area of reinforcement was equal to $A_{reinf} = A_{bar}b/S$ = 226mm^2. The area of the membrane, $A_{memb} = b * t_{memb}$, was a function of the membrane thickness, therefore the influence of various membrane thicknesses was studied. Ideally, the membrane material will provide zero contribution to the tensile carrying capacity of the reinforced membrane; it is the reinforcement *within* the membrane that should carry the loading. Table 4.4 presents the analysis for various membrane thicknesses.

Referring to Table 4.4, Case 1 represents the ideal scenario where only the reinforcement contributes to the strength (A_{memb} = 0). This case has a theoretical load of P_{theor} = 123.009kN. However, we cannot specify a membrane thickness of zero in ABAQUS, so this case was not modelled. Table 4.4 shows that with the same membrane reinforcement but an increased membrane thickness of 1mm, the ABAQUS model yielded a load of P_{model} =

Table 4.4: Reinforced Membrane Analysis

	CASE 1 Reinf. Only	CASE 2 Membrane + Reinf.	CASE 3 Membrane + Reinf.	CASE 4 Membrane + Reinf.	CASE 5 Membrane + Reinf.
t_{memb} (mm)	0	0.000001	0.001	1	10
ΔL (mm)	3	3	3	3	3
L (mm)	350	350	350	350	350
b (mm)	200	200	200	200	200
A_{memb} (mm^2)	0	0.0002	0.2	200	2,000
E_{frp} (MPa)	63,500	63,500	63,500	63,500	63,500
S (mm)	100	100	100	100	100
A_{bar} (mm^2)	113	113	113	113	113
A_{reinf} (mm^2)	226	226	226	226	226
A_{total} (mm^2)	226.0	226.0002	226.2	426.0	2226.0
P_{theor} (kN)	123.009	123.009	123.117	231.866	1,211.580
P_{model} (kN)	-	123.009	123.117	231.866	1,211.581
% Increase	-	0.00002%	0.09%	88.50%	884.96%

231.866kN, an 88.5% over-prediction of the load required in Case 1. Conversely, a membrane thickness of 0.000001mm is able to predict the load to within 0.00002% error. This analysis shows that it is possible to achieve accurate results using reinforced membranes.

A further observation is that the load predicted by the model strongly agrees with the theoretical load. This proves that the total area of material that ABAQUS uses to resist the tensile load, A_{total}, is the summation of A_{memb} and A_{reinf}. Therefore, the area that the bars occupy is double counted as demonstrated in Equations 4.11 and 4.12.

To model the longitudinal reinforcement, each truss section in Method 1 represents a single reinforcing bar, whereas each membrane section in Method 2 represents a single layer of

reinforcing bars. Beams BM 12-YYY have 3 layers of longitudinal bars, therefore 3 membrane sections were used to model this reinforcement configuration. Similarly, 2 membrane sections were used for beams BM 16-YYY, and 1 membrane section for beams BM 25-YYY. Each membrane section was embedded at the depth corresponding to the reinforcement layer. Within each membrane section, the reinforcement inputs were modified to yield a smeared layer of reinforcement with an area equivalent to the single layer of interest. Table 4.5 presents the inputs specified when defining the membrane sections that were used to model the three longitudinal reinforcement configurations for beams with 12mm diameter stirrups (beams with 20mm diameter stirrups used a different beam width, thus require different inputs).

Table 4.5: Membrane Details - Longitudinal Reinforcement

Beam	Area per Bar (mm^2)	Spacing (mm)	t_{eq} (mm)	Area/Layer (mm^2)	# of Layers	Total Area (mm^2)
12-YYY	113	50.00	2.26	452	3	1356
16-YYY	201	66.67	3.02	603	2	1206
25-YYY	491	100.00	4.91	982	1	982

Table 4.5 shows that the area of each bar matches the area provided by the manufacturer for each beam. It is important to note that the spacing specified is not equal to the actual spacing of the physical bars. This spacing was selected such that the product of the equivalent thickness, $t_{eq} = A/S$, and the beam width, $b = 200$mm, is equal to the required area of reinforcement per layer. To model the stirrups, each membrane section represented a single stirrup. Therefore, it was necessary for the reinforcement inputs to yield a smeared layer of reinforcement with an area equivalent to the area of two stirrup legs (closed loop stirrups). Table 4.6 presents the inputs specified when defining the membrane sections that were used to model the two stirrup types (12mm diameter and 20mm diameter).

Note that for beams with the larger stirrups, BM XX-sYYY, the beam width was increased

Table 4.6: Membrane Details - Transverse Reinforcement

Beam	Area per Bar (mm^2)	Spacing (mm)	t_{eq} (mm)	Total Area of Two Legs (mm^2)
XX-YYY	113	100.00	1.13	226
XX-sYYY	314	115.00	2.73	628

to $b = 230$mm. Figure 4.11 depicts the longitudinal reinforcement arrangements for the three types of beams using both truss sections and membrane sections. Note that the membrane sections span the entire width and length of each beam. Figure 4.12 depicts a typical transverse reinforcement arrangement using both truss and membrane sections.

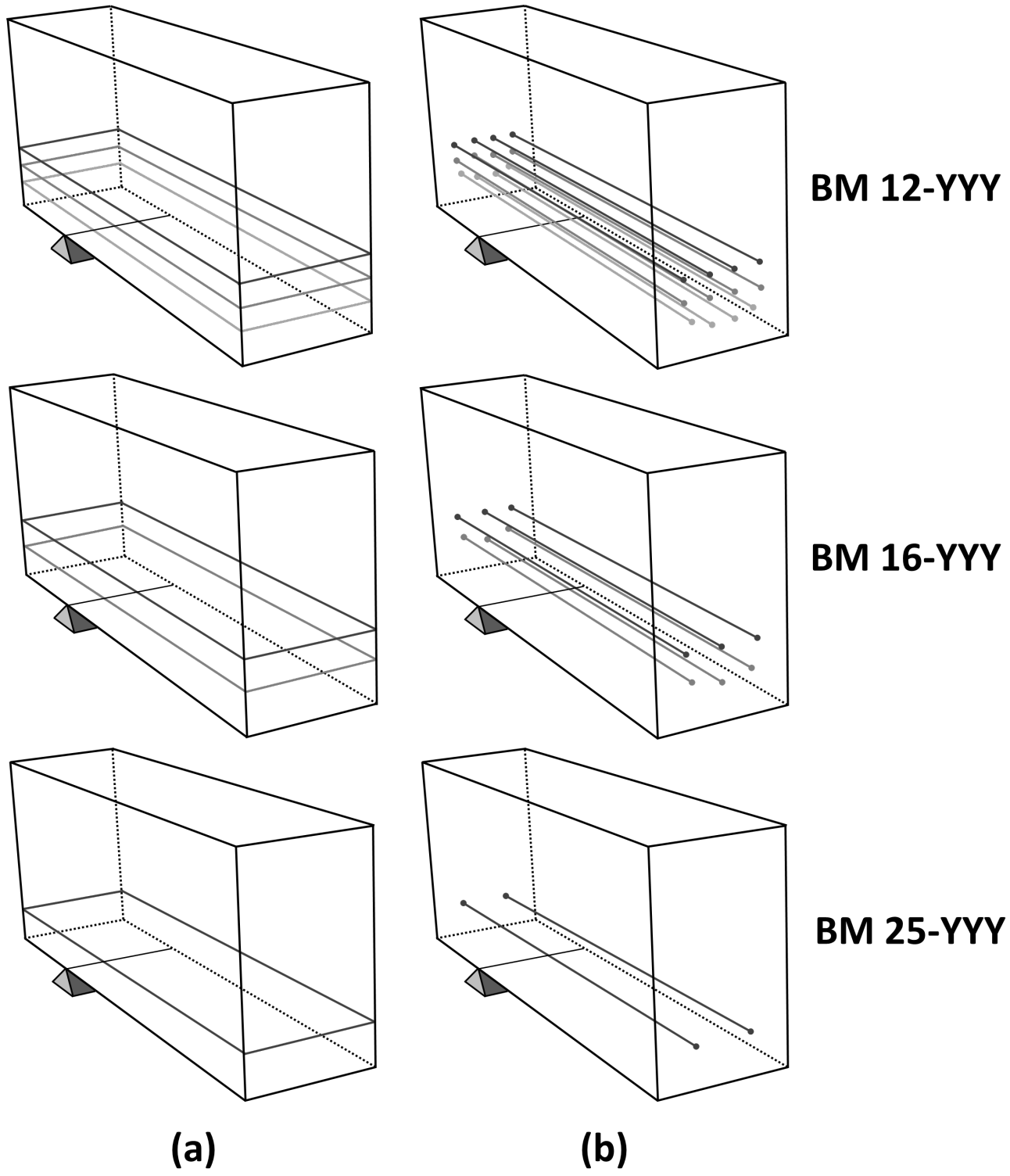

Figure 4.11: Modelling of Longitudinal Reinforcement: (a) Membrane Sections (b) Truss Sections

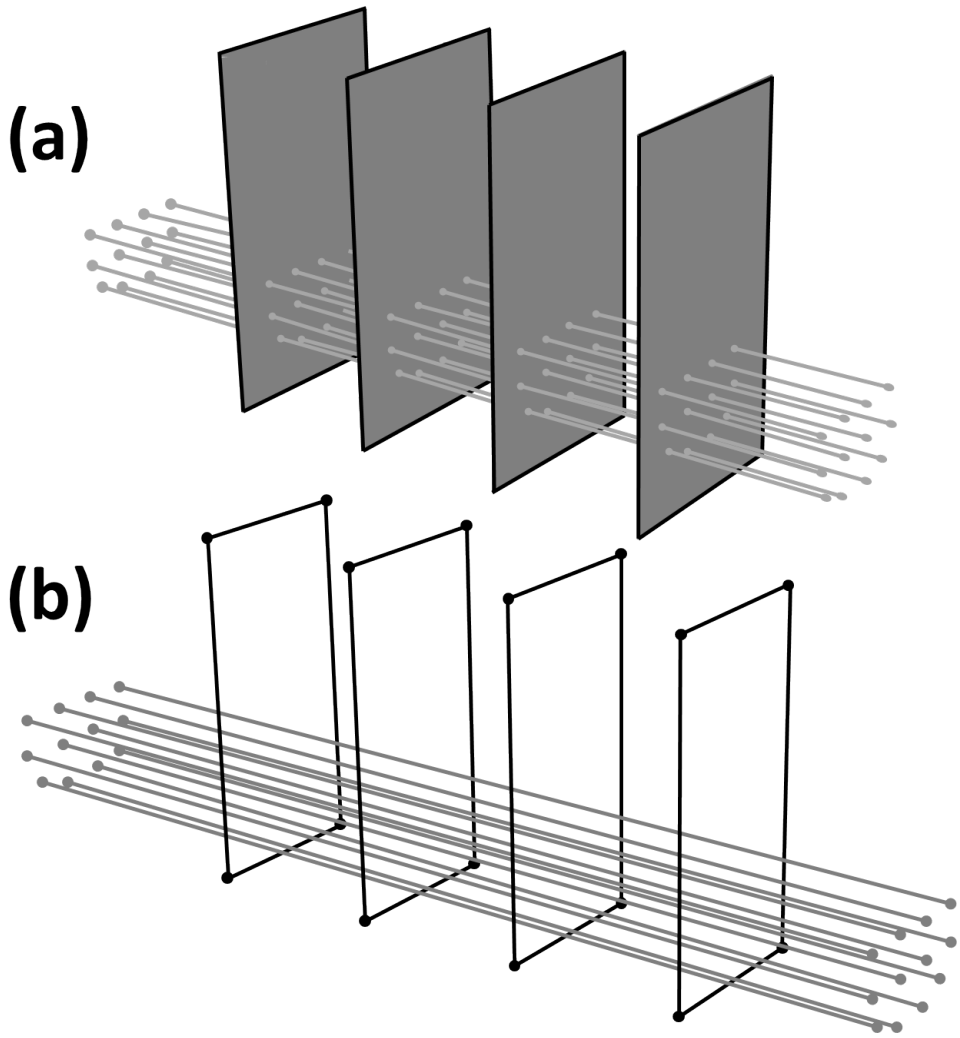

Figure 4.12: Modelling of Transverse Reinforcement: (a) Membrane Sections (b) Truss Sections

Chapter 5

Modelling of Beams with No Stirrups

Section 2.3 provided an overview of the experimental tests performed by Krall (2014) on concrete beams reinforced with glass fibre reinforced polymer (GFRP) bars. Three-point bending tests were performed on twelve rectangular beams. Three beams were reinforced with GFRP longitudinal bars and no transverse reinforcement (BM XX-INF). The remaining nine beams were reinforced with both GFRP longitudinal bars and GFRP transverse reinforcement (BM XX-(s)YYY). This chapter focuses on the finite element modelling of the beams with no stirrups, including BM 12-INF, BM 16-INF, and BM 25-INF.

5.1 Compression Modelling

The Hognestad Parabola constitutive equations were utilized to model the uniaxial concrete compressive behaviour for all beams with no stirrups as shown in Equation 5.1:

$$\sigma_c^{(1)} = E_{co}\varepsilon_c \qquad for \quad \sigma_c \leq 0.4f_c^{'} \tag{5.1a}$$

$$\sigma_c^{(2)} = f_c^{'}\left[2\left(\frac{\varepsilon_c}{\varepsilon_c^{'}}\right) - \left(\frac{\varepsilon_c}{\varepsilon_c^{'}}\right)^2\right] \qquad for \quad \varepsilon_c/\varepsilon_c^{'} \leq 1.0 \tag{5.1b}$$

$$\sigma_c^{(3)} = f_c^{'}\left[1 - \left(\frac{\frac{\varepsilon_c}{\varepsilon_c^{'}} - 1}{2}\right)^2\right] \qquad for \quad \varepsilon_c/\varepsilon_c^{'} > 1.0 \tag{5.1c}$$

where:

$$\varepsilon_c^{'} = \frac{2f_c^{'}}{E_{ct}} \tag{5.2a}$$

$$E_{co} = 5000\sqrt{f_c^{'}} \tag{5.2b}$$

$$E_{ct} = 5500\sqrt{f_c^{'}} \tag{5.2c}$$

In Equations 5.1 and 5.2, ε_c is the concrete compressive strain, $\varepsilon_c^{'}$ is the concrete strain at peak stress, E_{co} is the initial modulus of elasticity, and E_{ct} is the modified modulus of elasticity in the second region. These equations capture three regions of the uniaxial compressive behaviour of concrete as shown in Figure 5.1.

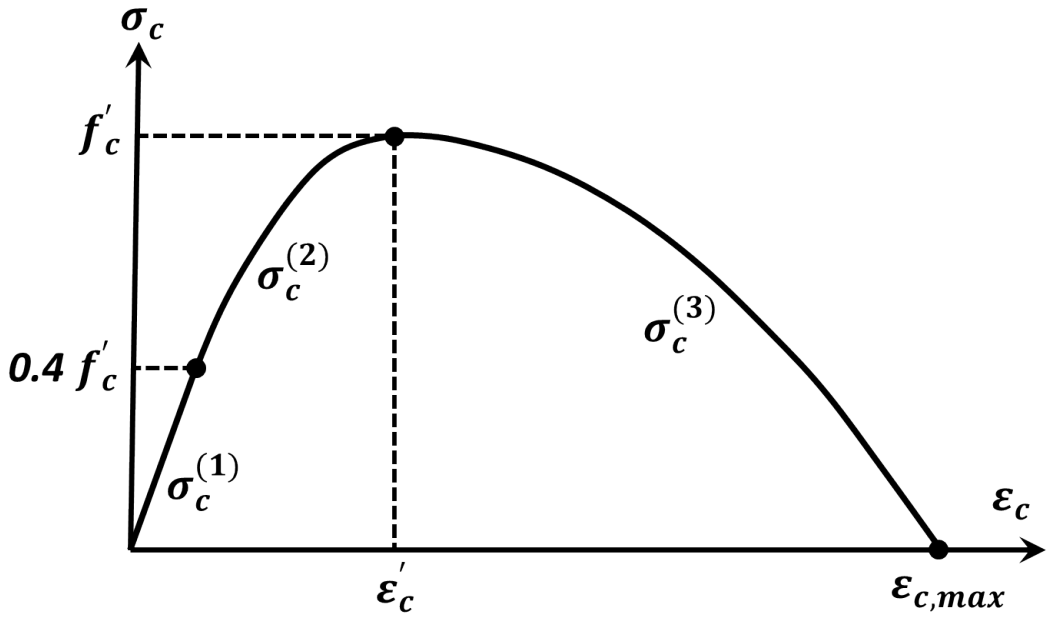

Figure 5.1: Hognestad Parabola Uniaxial Compression Model

The first region, $\sigma_c^{(1)}$, represents the linear-elastic region up to a stress level of $0.4f_c^{'}$. The second region, $\sigma_c^{(2)}$, represents the nonlinear ascending region up to the peak stress, $f_c^{'}$. The third region, $\sigma_c^{(3)}$, represents the post-peak strain-softening region that extends from the peak stress to a complete loss of strength. These equations were used in the compression modelling for all beams with no stirrups.

The compressive strength used for BM 12-INF, BM 16-INF and BM 25-INF was 54.0MPa, 53.4MPa, and 52.0MPa, respectively, as previously summarized in Table 4.2. Table 5.1 shows the calculated values for the strain at peak stress, $\varepsilon_c^{'}$, and the maximum strain corresponding to a complete loss of strength, $\varepsilon_{c,max}$, for all beams with no stirrups.

Table 5.1: Concrete Compressive Strains for Beams with No Stirrups

Beam	$f_c^{'}$ (MPa)	$\varepsilon_c^{'}$	$\varepsilon_{c,max}$
12-INF	54.0	0.00267	0.00802
16-INF	53.4	0.00266	0.00797
25-INF	52.0	0.00262	0.00787

The influence of this maximum compressive strain on each beam's behaviour was studied. To accomplish this, the expression for region 3 of the uniaxial compression curve, Equation 5.1c, was modified to become a function of the maximum strain as shown in Equation 5.3. This expression maintains the same peak stress and parabolic shape, but allows the maximum strain to be prescribed easily.

$$\sigma_c^{(3)} = f_c^{'} + \frac{f_c^{'}(\varepsilon_c - \varepsilon_c^{'})^2}{(\varepsilon_{c,max} - \varepsilon_c^{'})^2} \tag{5.3}$$

Various maximum compressive strain values were utilized to study the influence that this variable had on each beam's behaviour. Figure 5.2 presents the modified uniaxial compression curves as provided by Equation 5.3 for BM 12-INF using various values of $\varepsilon_{c,max}$. Figure 5.3 shows the influence of various maximum strain values on the load vs. mid-span deflection response for BM 12-INF.

As can be seen, for maximum compressive strain values ranging from 0.008 (original Hognestad Parabola value) to 0.0125, there is no change to the pre-peak response for BM 12-INF. This result was similar for the other beams with no stirrups. This behaviour is to be expected, as the beams with no stirrups all experienced shear-tension failures during the experimental testing. Therefore, failure modes were not dependent on the compressive

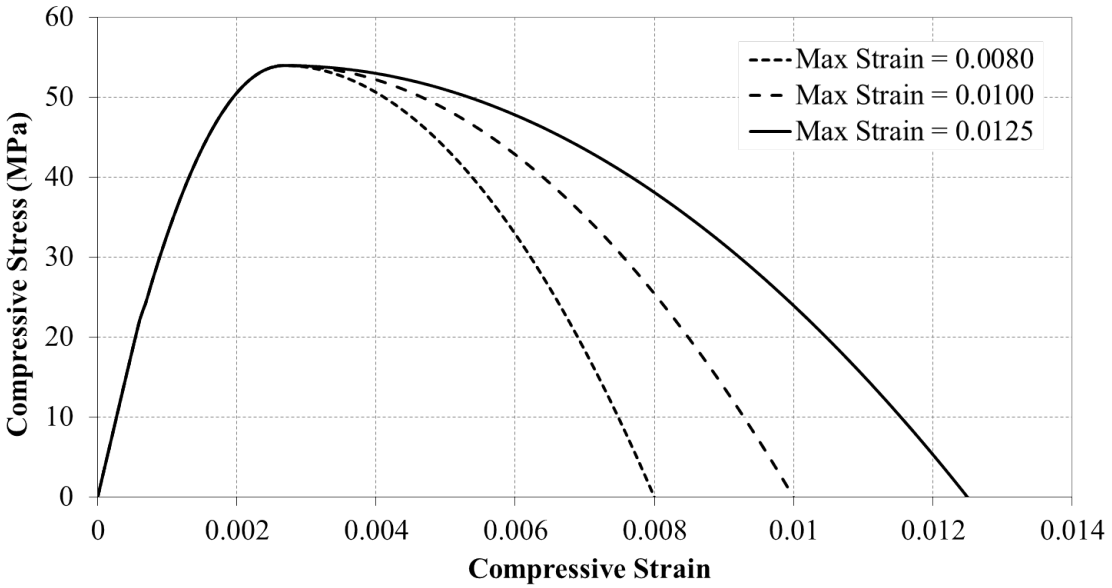

Figure 5.2: Modified Hognestad Parabola Curves for BM 12-INF

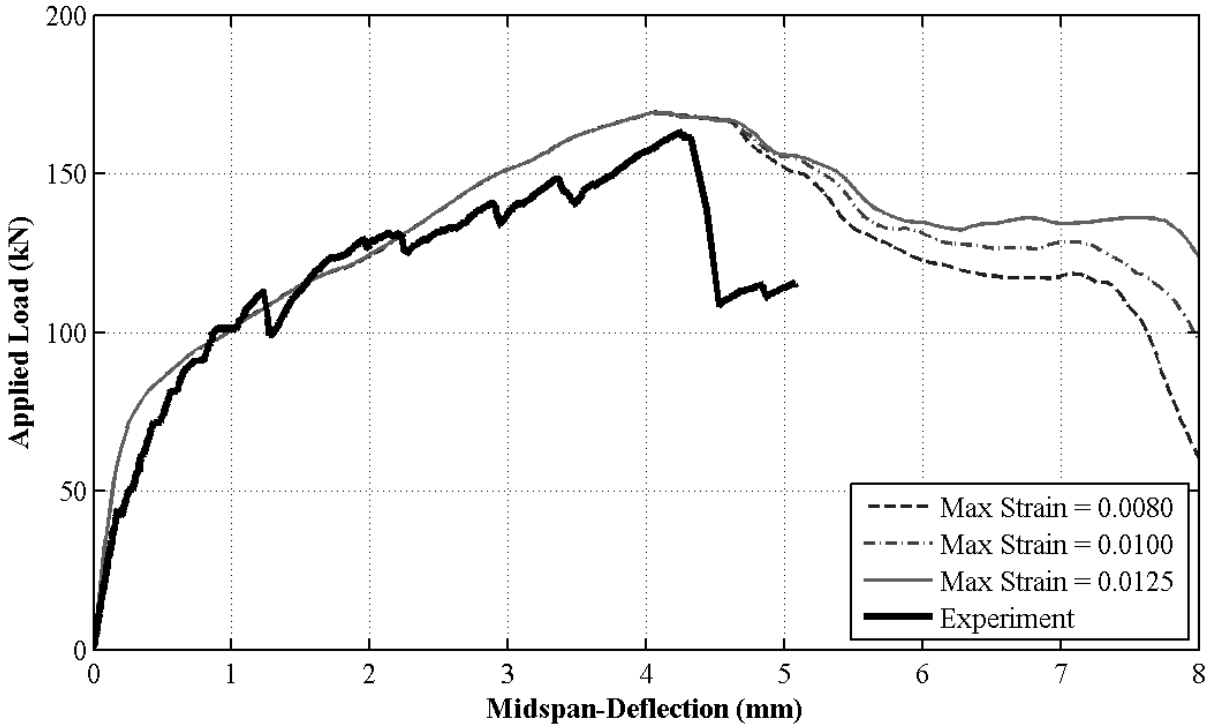

Figure 5.3: Influence of Maximum Compressive Strain - BM 12-INF

crushing of concrete. The influence of this maximum strain was found to be significant for the modelling of beams with stirrups as will be discussed in Chapter 6.

5.2 Tension Modelling

Section 3.3.2 introduced three methods to define the uniaxial post-peak tensile response of concrete in the Concrete Damaged Plasticity Model: 1) Stress-strain approach, 2) Fracture energy approach, and 3) Crack-opening-displacement approach. The intent of this section is to provide an overview of the analyses performed for each method, compare the effectiveness of each method, and propose recommendations as to the most beneficial approach.

5.2.1 Stress-Strain Approach

The first approach to model the post-cracking response of concrete under uniaxial tensile loads is to specify stress-strain data. It is common for design standards to assume that concrete can support zero tensile stresses after cracking. However, as a result of the bond between the concrete and the reinforcing bars, concrete is in fact capable of carrying tensile stresses between cracks. This additional strength and stiffness that is associated with the concrete-bar interaction is known as "tension stiffening", and can be simulated by utilizing a gradually descending post-peak tensile response. To consider this effect, the following stress-strain constitutive equations were considered:

$$\sigma_t^{(1)} = E_{co}\varepsilon_t \qquad for \quad \varepsilon_t \leq \varepsilon_{cr} \tag{5.4a}$$

$$\sigma_t^{(2)} = f_t' \left(\frac{\varepsilon_{cr}}{\varepsilon_t}\right)^{0.4} \qquad for \quad \varepsilon_t > \varepsilon_{cr} \tag{5.4b}$$

where:

$$E_{co} = 5000\sqrt{f_c'} \tag{5.5a}$$

$$\varepsilon_{cr} = \frac{f_t'}{E_{co}} \tag{5.5b}$$

$$f_t' = 0.33\sqrt{f_c'} \tag{5.5c}$$

In Equations 5.4 and 5.5, ε_t is the concrete tensile strain, E_{co} is the initial modulus of elasticity, ε_{cr} is the concrete strain at peak stress (at cracking), and f_t' is the tensile strength of the concrete (peak stress). These equations capture two regions of the uniaxial tensile behaviour of concrete as shown in Figure 5.4.

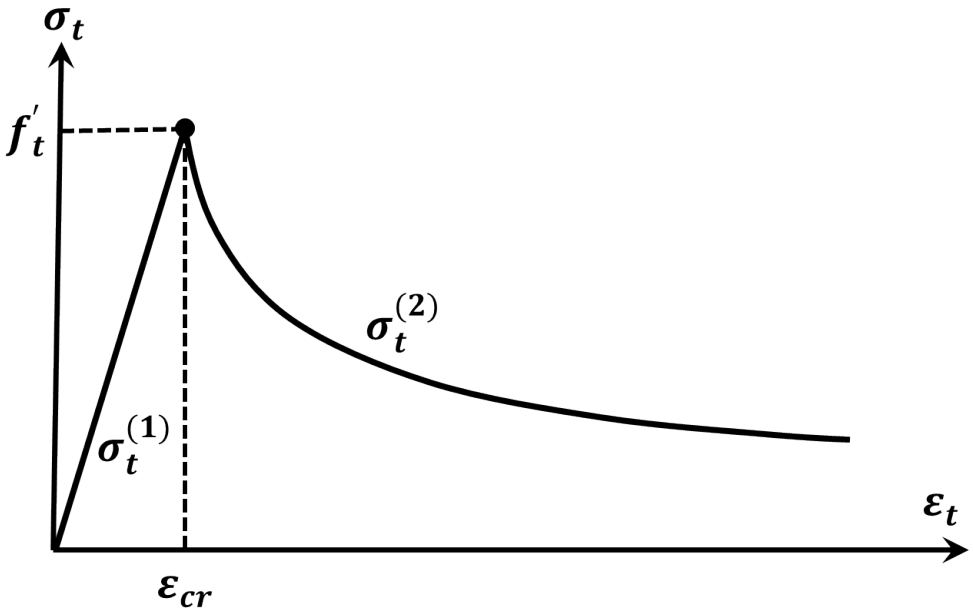

Figure 5.4: Uniaxial Stress-Strain Tension Model

The first region, $\sigma_t^{(1)}$, represents the linear-elastic region up to the cracking stress f_t'. The second region, $\sigma_t^{(2)}$, represents the nonlinear descending post-peak region that attempts to simulate the tension stiffening phenomenon. The post-peak relationship presented in Equation 5.4b was first proposed by Tamai (1988), and has since been used by many researchers including Belarbi and Hsu (1994), Hsu and Zhang (1996), and Wang and Hsu

(2001). As the magnitude of the tension stiffening that occurs will significantly influence the response of a reinforced structure, Kmiecik and Kaminski (2011) utilized a modified version of the post-peak response:

$$\sigma_t^{(2)} = f_t' \left(\frac{\varepsilon_{cr}}{\varepsilon_t} \right)^n for \quad \varepsilon_t > \varepsilon_{cr} \tag{5.6}$$

Equation 5.6 allowed Kmiecik and Kaminski (2011) to study various post-peak responses by introducing a variable, n, to control the rate of strength degradation. Values of n ranging from the original value, 0.4, to 1.5 were studied. As n increases, the rate of decay of the tensile capacity increases, representing less tension stiffening as shown in Figure 5.5.

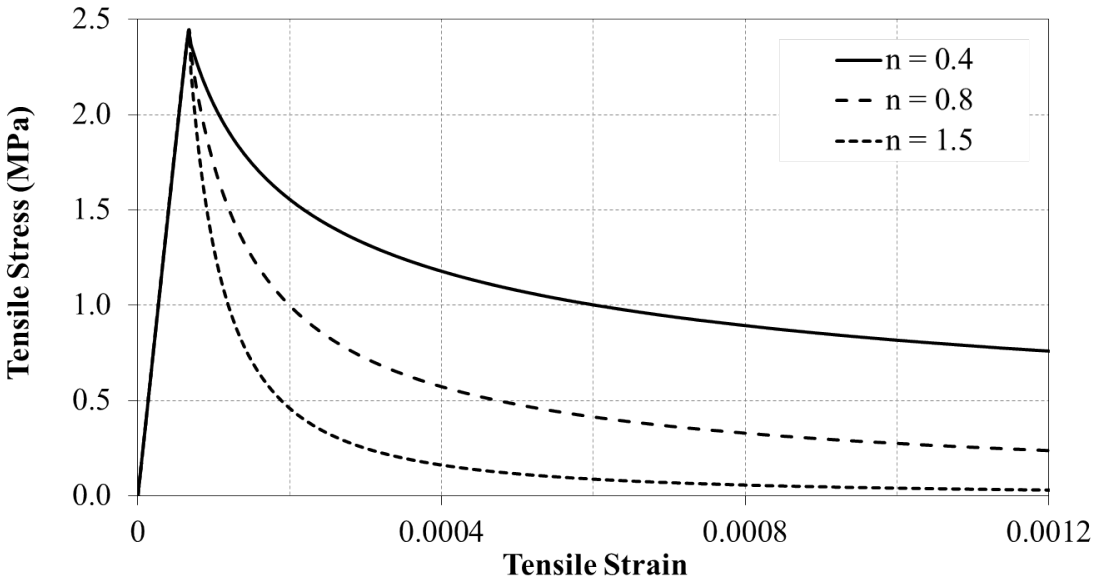

Figure 5.5: Modified Uniaxial Stress-Strain Tension Model

When using the stress-strain approach to define the tensile behaviour of the concrete, it was found that the simulations were terminated early in the analysis due to significant convergence issues. With these numerical difficulties, no useful results were produced. Wang and Hsu (2001) also encountered this issue, and suggested that the sharp change in curvature at the peak stress was responsible. Potential solutions to this issue were studied by the author, including the use of a plateau at the peak stress or the use of a higher

viscosity parameter, with no success.

In addition to the numerical issues encountered when using the uniaxial stress-strain approach, this approach may also introduce unreasonable mesh sensitivity into the results if significant regions of the concrete contain little or no reinforcement (DSS, 2012). This applies particularly to the beams with no stirrups, as significant strains and deformations associated with the shear-tension failures occur in elements that do not contain reinforcement. This issue can be addressed through the use of the fracture energy concept as proposed by Hillerborg et al. (1976), which will be discussed next.

5.2.2 Fracture Energy Approach

The second approach studied to define the tensile behaviour of the concrete was the use of fracture energy. As discussed in Section 3.3.2, fracture energy, G_f, is a material property as proposed by Hillerborg et al. (1976) to define the energy required to open a crack of unit area. This approach defines the brittle nature of concrete through a stress vs. crack-opening-displacement relationship as opposed to the previously discussed stress vs. strain relationship.

For normal strength concrete, the fracture energy is dependent on factors including the water-to-cement ratio, maximum aggregate size, curing conditions, and age of the concrete. For high strength concrete, the type and quantity of aggregate become more influential than the size of the aggregate. High strength aggregates are tougher to fracture and will cause the crack orientations to change and multiply, thus will consume more energy during the fracture process. The influence of all these factors has led to a significant scatter of experimental G_f values presented in the literature. However, it is clear that there is a direct correlation between a concrete's compressive strength and fracture energy (International Federation for Structural Concrete, 2013).

Model Code 1990 estimates the fracture energy using the following expression:

$$G_f = G_{Fo}\left(\frac{f_{cm}}{f_{cmo}}\right)^{0.7} \tag{5.7}$$

where $f_{cmo} = 10\text{MPa}$. f_{cm} is the mean value of the concrete compressive strength, and is a function of the characteristic compressive strength, f_{ck}, as shown in Equation 5.8:

$$f_{cm} = f_{ck} + \Delta f \tag{5.8a}$$

$$\Delta f = 8MPa \tag{5.8b}$$

Reineck et al. (2003) proposed the following relationship between the characteristic compressive strength, f_{ck}, and the cylinder strength, $f_c^{'}$:

$$f_{ck} = f_c^{'} - 1.6MPa \tag{5.9}$$

The final variable of Equation 5.7 is the base value of the fracture energy, G_{Fo}, which is a function of the maximum aggregate size, d_{max}, as found in Table 5.2.

Table 5.2: Base Values of Fracture Energy - Model Code 1990

d_{max} (mm)	G_{Fo} (Nmm/mm^2)
8	0.025
16	0.030
32	0.058

When compared with experimental data, Model Code 1990 appears to over-emphasize the influence of compressive strength on the fracture energy, causing significant underestimation of G_f for concrete with strengths below 120MPa. Trunk and Wittmann (1998) proposed the following relationship between fracture energy and the maximum aggregate size, d_{max}:

$$G_f = ad_{max}^n \tag{5.10}$$

where $a = 80.6$ and $n = 0.32$ as obtained from experimental data. *fib* Bulletin 42 (2008) derived an improved approximation based on experimental data as shown in Equation 5.11:

$$G_f = G_{Fo}\left(1 - 0.77\frac{f_{cmo}}{f_{cm}}\right) \tag{5.11}$$

where $G_{Fo} = 0.18$N/mm, $f_{cmo} = 10$MPa, and f_{cm} is calculated using Equations 5.8 and 5.9. It has been found that Equation 5.11 provides the best fit to experimental data, but becomes inconsistent for very low concrete strengths ($f_{ck} < 15$MPa). In the absence of experimental data, it is recommended to use the following expression specified by Model Code 2010 for normal weight concrete due to its simplicity and consistency over the full spectrum of concrete strengths (International Federation for Structural Concrete, 2013):

$$G_f = 73(f_{cm})^{0.18} \tag{5.12}$$

where f_{cm} is calculated using Equations 5.8 and 5.9. Table 5.3 provides a summary of the predicted values for G_f for each beam using the presented models.

Table 5.3: Fracture Energy Predictions for Beams with No Stirrups

Beam	f_c' (MPa)	f_{ck} (MPa)	f_{cm} (MPa)	G_f (N/m) Model Code 1990	Trunk and Wittmann 1998	fib Bulletin 42 2008	Model Code 2010
12-INF	54.0	52.4	60.4	91.3	165.7	157.1	152.7
16-INF	53.4	51.8	59.8	90.7	165.7	156.8	152.5
25-INF	52.0	50.4	58.4	89.2	165.7	156.3	151.8

As expected, Model Code 1990 predicted the lowest fracture energy values with an average of 90.4N/m, whereas Trunk and Wittmann (1998) predicted the highest values of 165.7N/m. To prescribe a fracture energy to the Concrete Damaged Plasticity Model, the user must select the "GFI" tension type. This approach requires the user to input the

tensile strength of the concrete and the desired fracture energy. This method assumes a linear stress-displacement post-peak response as depicted in Figure 3.4.

The influence of various fracture energy values was studied for each beam with no stirrups. Figure 5.6 shows the load-displacement responses for BM 12-INF. The designation "Linear" for each curve in Figure 5.6 refers to the shape of the stress-displacement curve used. This classification will become necessary in the next section.

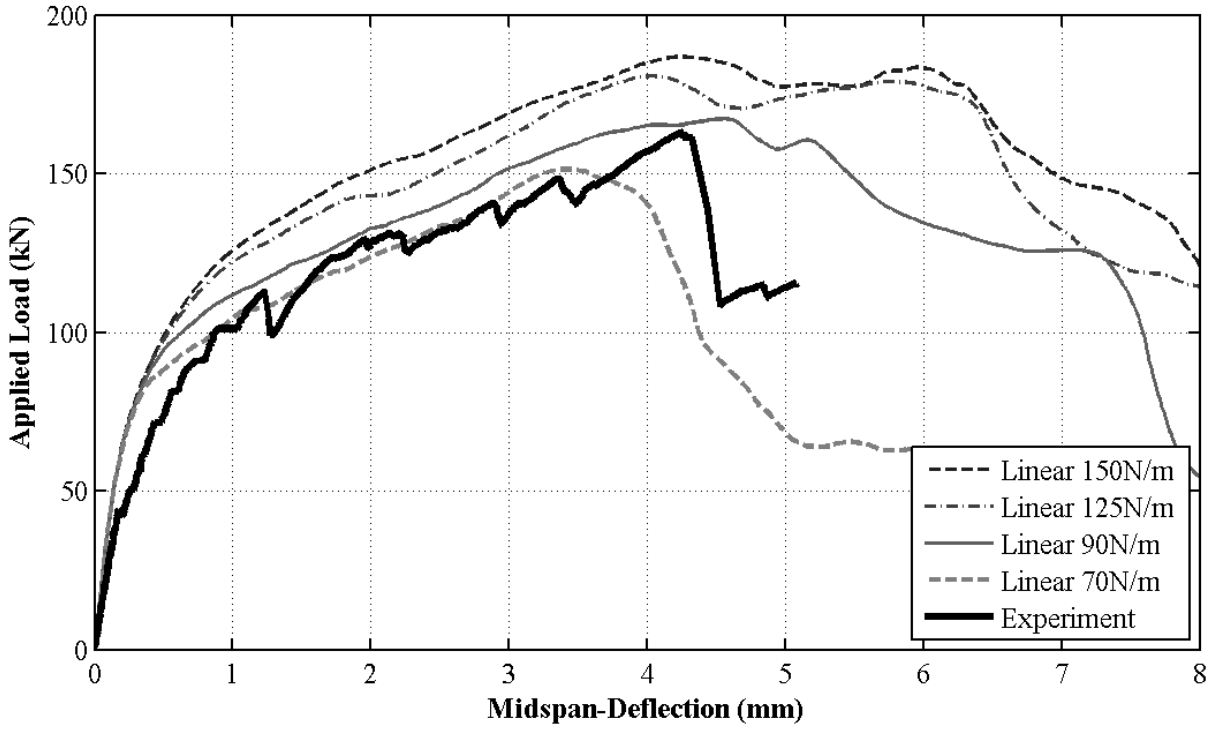

Figure 5.6: Influence of Fracture Energy - BM 12-INF

Figure 5.6 shows the influence of fracture energy values ranging from 70N/m to 150N/m. For BM 12-INF, each curve begins to diverge at a load of approximately 80kN. This is the point at which the formation of major cracks initiate, thus reducing the stiffness of the beam response. As the concrete fracture energy increased, so did the stiffness of the beam response within the post-cracking region. At a given crack-opening-displacement, an element of concrete with a larger fracture energy will carry larger tensile stresses, thus stiffening the response. With low fracture energies, 70N/m specifically, the beams experienced

sudden and brittle failures. With larger fracture energies, the beams failed at larger peak loads and experienced larger mid-span deflections. Using the linear stress-displacement method to model the tension, a fracture energy of 90N/m produced the strongest agreement to the experimental data for all beams with no stirrups.

5.2.3 Crack-Opening-Displacement Approach

The use of the "GFI" tension modelling discussed previously implements the concept of fracture energy, but enforces a linear stress-displacement curve. To utilize a custom stress-displacement curve, the "Displacement" tension modelling approach can be used in ABAQUS. The user is able to input the post-cracking tensile stress as a function of the crack-opening-displacement, w. Examples of stress-displacement curves proposed in the literature were presented in Figure 3.3. The bilinear curve proposed by Petersson (1981) and the exponential curve proposed by Cornelissen et al. (1986) were each studied using various values of fracture energy. Figure 5.7 presents the three stress-displacement relationships studied for BM 12-INF ($f_c^{'} = 54$MPa) with a fracture energy of $G_f = 90$N/m, and Table 5.4 summarizes the maximum crack-opening-displacements, w_c, associated with each curve.

Table 5.4: Maximum Crack Displacements for BM 12-INF

Method	w_c (mm)
Linear	0.074
Bilinear	0.134
Exponential	0.191

The curves used for BM 16-INF and BM 25-INF were similar to those shown in Figure 5.7; however, these beams used slightly different compressive strengths, resulting in different tensile strengths and maximum crack-opening-displacements. As each curve in Figure 5.7

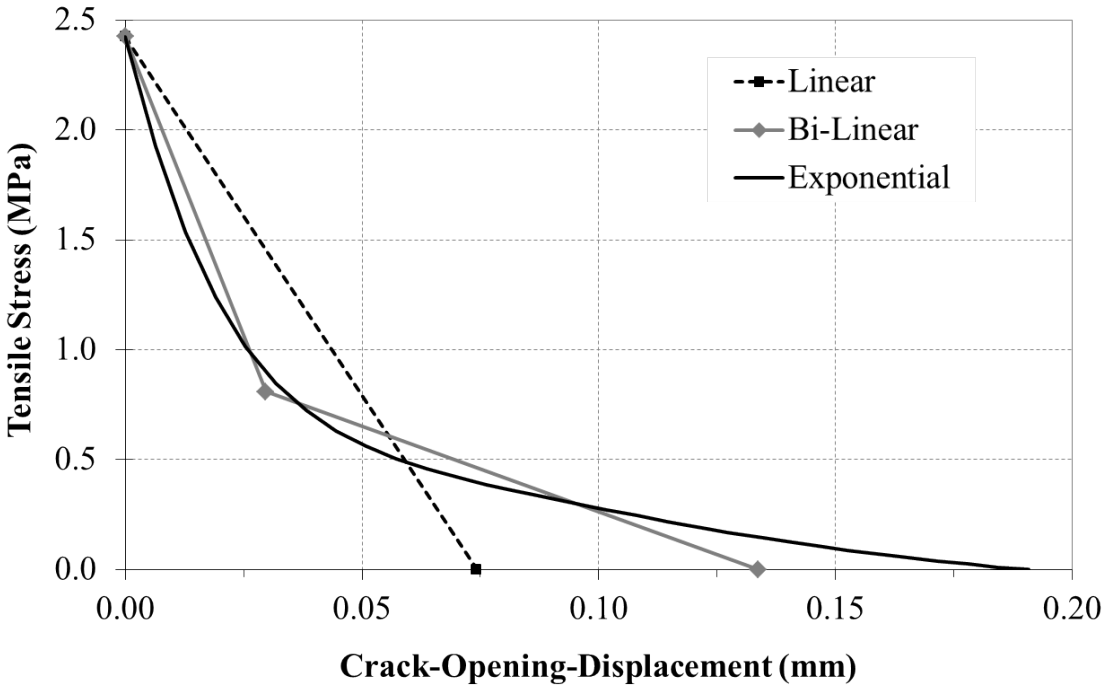

Figure 5.7: Stress-Displacement Curves for BM 12-INF

represents a fracture energy of 90N/m, the area under all three curves is equal to 90N/m. Therefore, as the tensile stress associated with a displacement of zero is equal to the tensile strength of the concrete, $f_t^{'}$, and is a material constant, a larger fracture energy will result in a larger maximum displacement, w_c. Figure 5.8 shows the influence of various fracture energies using the bilinear stress-displacement approach on the load-displacement response of BM 16-INF.

The responses presented in Figure 5.8 show a similar behaviour as provided by the GFI method discussed previously. Larger fracture energies, 125N/m and 150N/m, yielded beams that were much stronger and more ductile than the experimental beams. Lower fracture energies, 70N/m and 90N/m, yielded beams that experienced brittle failures that matched closely with the experiment. Again, a fracture energy of 90N/m yielded the most accurate and consistent results for all beams with no stirrups.

The tensile strains experienced by the longitudinal reinforcement were then studied to

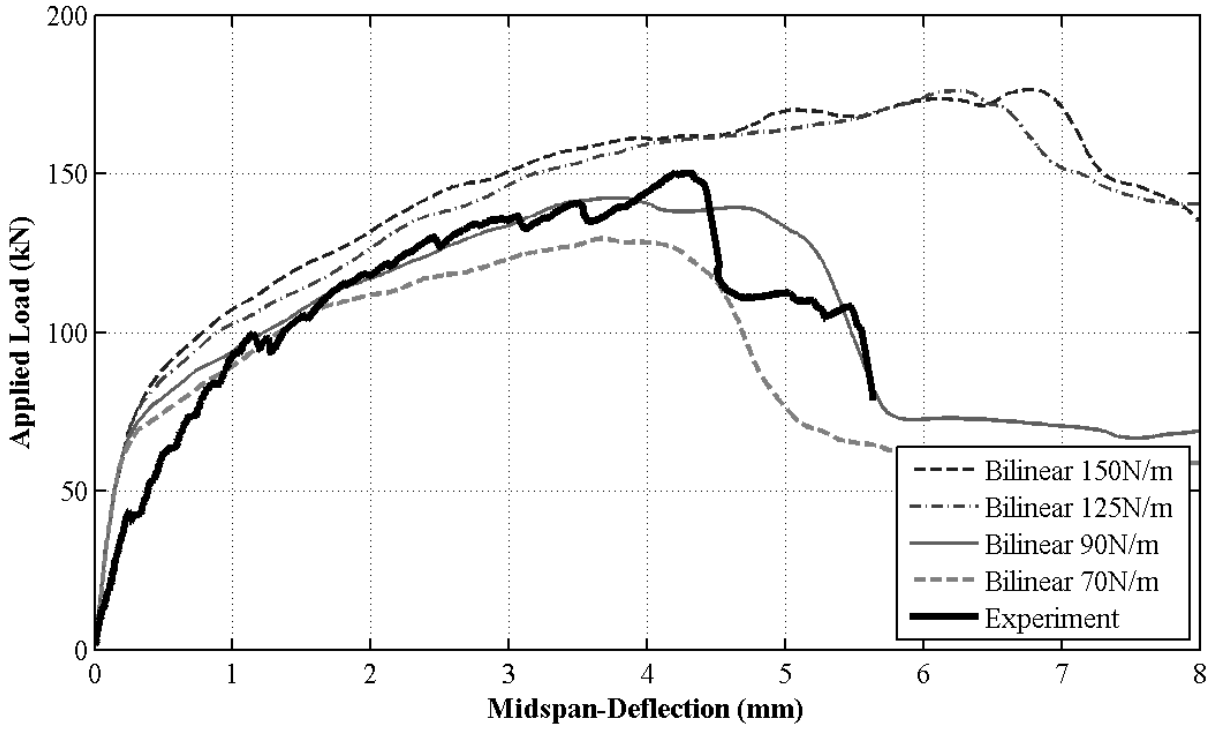

Figure 5.8: Influence of Fracture Energy - BM 16-INF

further demonstrate the influence of fracture energy. Strain gauges were used on the reinforcing bars to monitor the development of tensile strains at various locations during the experimental testing. Appendix A depicts the locations and nomenclature of the strain gauges used during testing. For the purposes of this discussion, all models presented in this section utilized truss elements to model the longitudinal reinforcement. The tensile strains of the longitudinal reinforcement as measured during testing were compared with the strains predicted by the ABAQUS analyses for various fracture energies. Figure 5.9 compares the tensile strains at the L-1A-C strain gauge location for BM 25-INF. Figure 5.10 compares the tensile strains at the L-1-C strain gauge location for BM 16-INF. The bilinear stress-displacement function was used for all models presented.

Referring to Figure 5.9, it can be seen that the bilinear stress-displacement relationship with a fracture energy of 90N/m provided results that agreed strongly with the experimental strain profiles. With an increased fracture energy of 150N/m, the strain curves were shifted

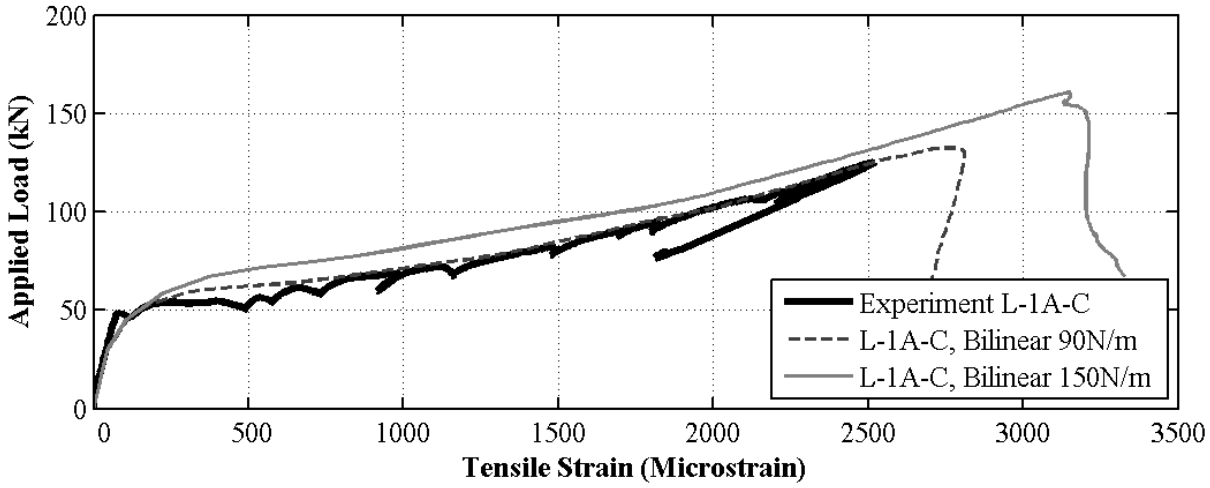

Figure 5.9: Influence of Fracture Energy on Reinforcement Strains - BM 25-INF

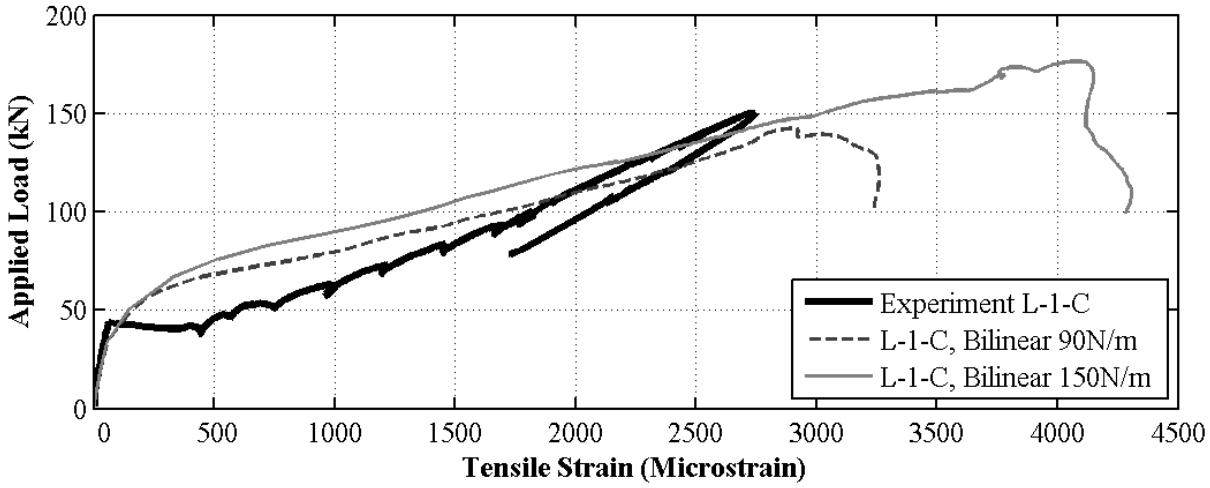

Figure 5.10: Influence of Fracture Energy on Reinforcement Strains - BM 16-INF

upwards, indicating a stiffer response. When a higher fracture energy is specified, more energy is required to overcome the toughening mechanisms as discussed in Section 2.6.2, thus requiring more energy to be consumed to crack the concrete. This increased energy reflects a stronger "bond" between the concrete and the reinforcing bars. This stronger interaction, simulating the effects of tension stiffening, allows the concrete to carry more load after cracking, thus creating a stronger and stiffer structure. Further discussion of the reinforcement modelling is discussed in Section 5.6.

5.2.4 Comparison of Tension Modelling Approaches

It was shown that the use of a stress-strain tension model was not an appropriate alternative for the modelling of the beams presented in this thesis. In the analyses to determine the influence of fracture energy, a fracture energy of $G_f = 90$N/m was found to produce the strongest agreement with the experimental data for beams with no stirrups. This value correlates best with the fracture energy prediction provided by Model Code 1990. Figures 5.11 and 5.12 compare the use of the three stress-displacement curves studied (linear, bilinear, and exponential), with a fracture energy of 90N/m for beams BM 12-INF and BM 25-INF, respectively.

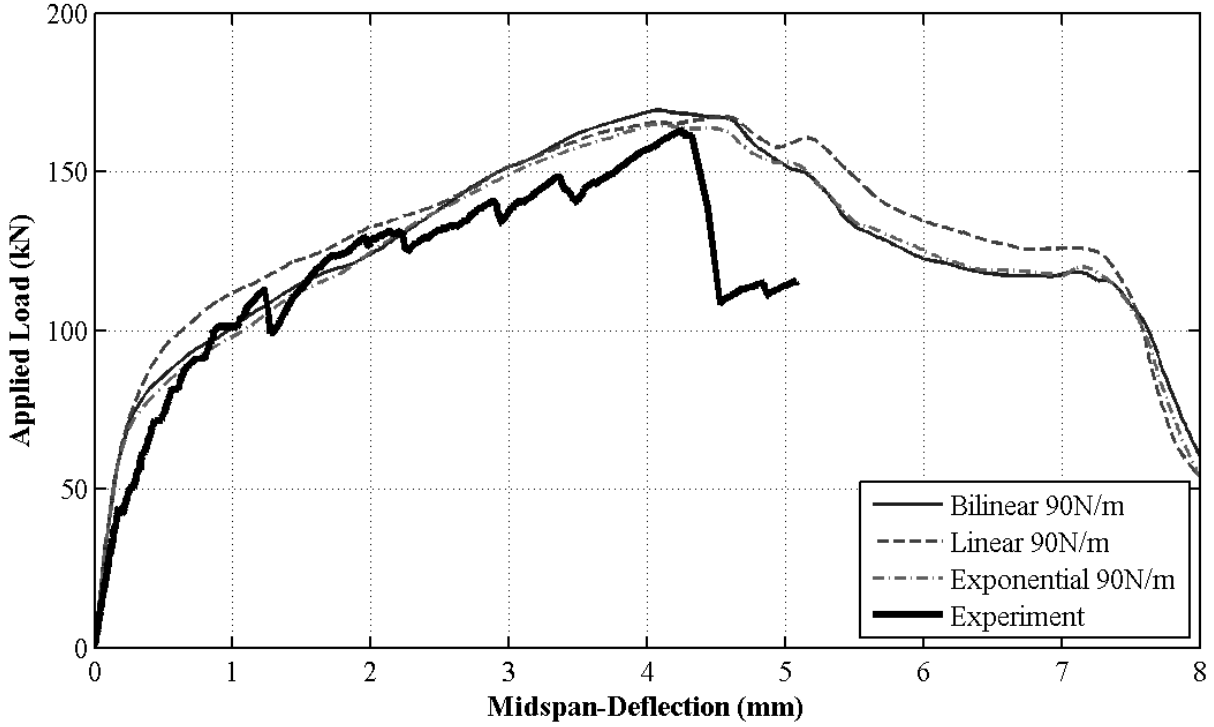

Figure 5.11: Influence of Stress-Displacement Model - BM 12-INF

For BM 12-INF, all three methods produced similar peak loads of 169.4kN, 167.3kN, and 164.8kN for the bilinear, linear, and exponential functions, respectively. However, the difference between each method is observed in the deflection response within the post-cracking region prior to the obtainment of the peak load. At a load of approximately 70kN,

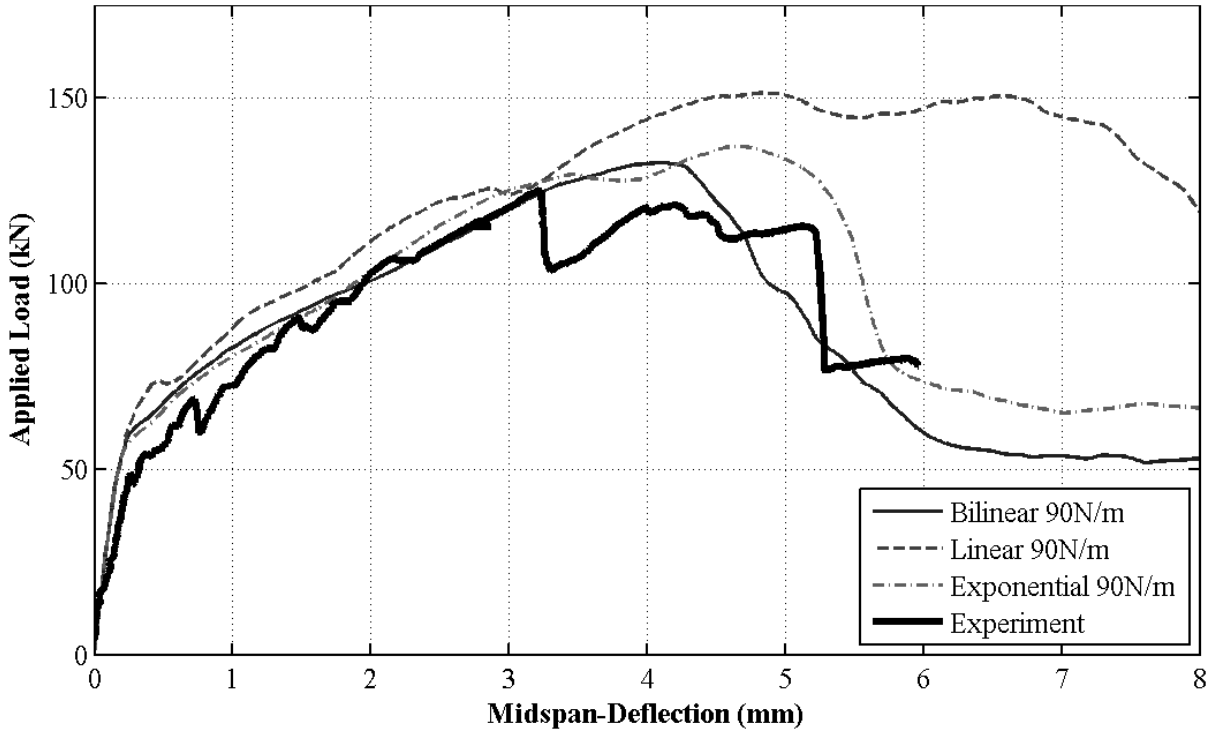

Figure 5.12: Influence of Stress-Displacement Model - BM 25-INF

the three curves begin to diverge. Although the beams using the bilinear and exponential functions continue to match closely, the linear stress-displacement function produces a stiffer response after the major cracking occurs. This can be explained by referring to Figure 5.7. For a given crack displacement that is less than 0.055, the linear function will provide the largest tensile stress capacity. Alternatively, the slope of the linear function is far less than the initial slopes of the bilinear and exponential functions. This means that after cracking, the bilinear and exponential functions will experience a reduction in tensile carrying capacity at an initial rate much faster than the linear function. Therefore, although the fracture energy of all three methods is equal, thus the area under each curve is equal, the shape of the function will dictate the rate at which the concrete loses its tensile stress carrying ability. This behaviour was also observed for BM 16-INF and BM 25-INF.

Figures 5.13 and 5.14 compare the influence of the tension model on the longitudinal reinforcement strain profile for BM 12-INF and BM 25-INF, respectively. Again, the

fracture energy remained constant at 90N/m for all three models presented.

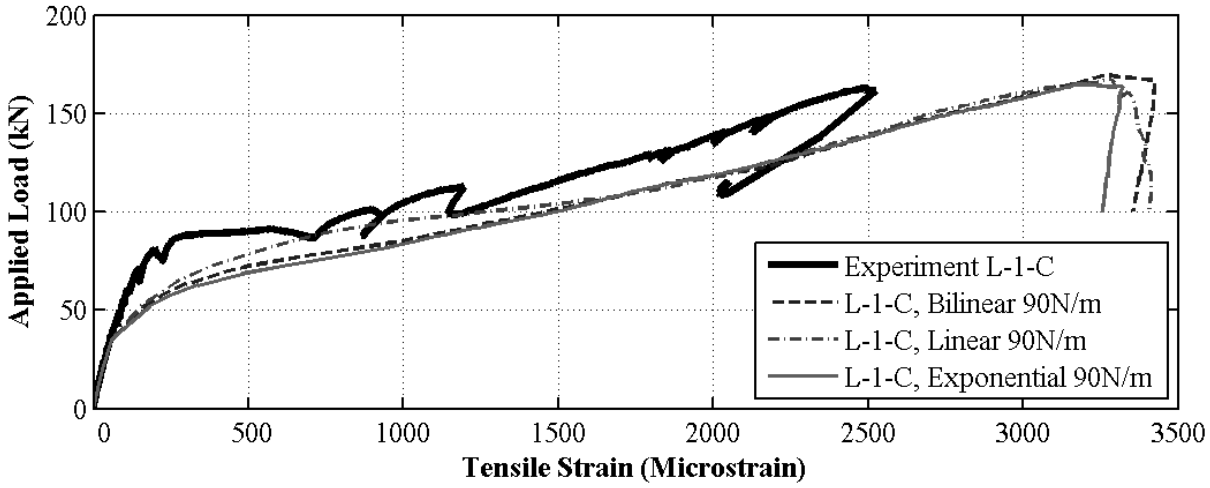

Figure 5.13: Influence of Stress-Displacement Model on Reinf. Strains - BM 12-INF

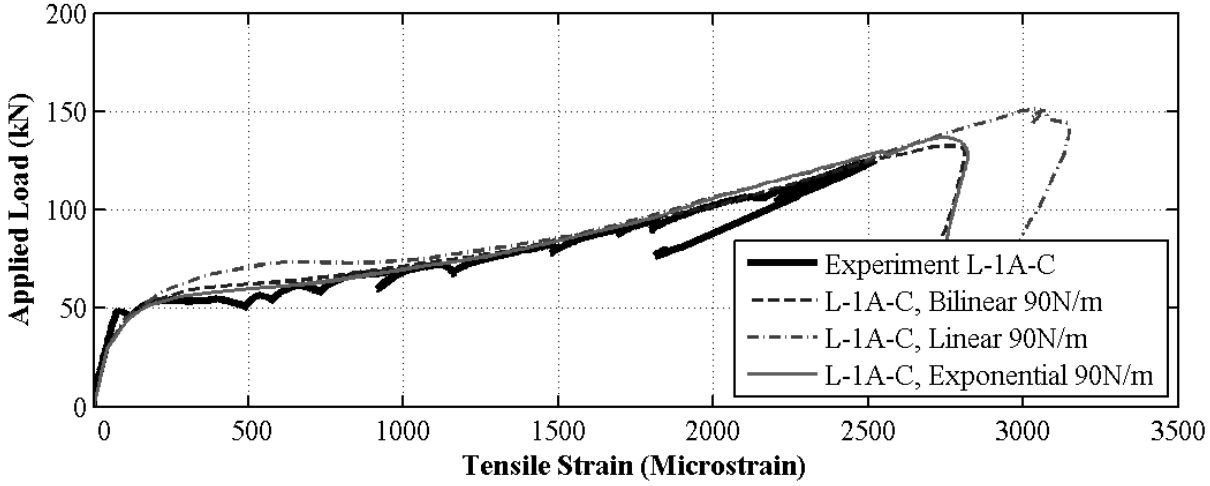

Figure 5.14: Influence of Stress-Displacement Model on Reinf. Strains - BM 25-INF

It is clear that the reinforcement strains in the beams that used the bilinear tension model agree strongly with the beams that used the exponential tension model; a result of the similar shape that these stress-displacement models take. The linear approach, however, consistently produced responses that exhibited additional strength immediately after cracking before converging to the solution of the bilinear and exponential models at higher load levels. Again, this is a result of the shape of the stress-displacement curve that favours a more gradual reduction of strength loss. As the bilinear and exponential tension models

yield identical results, the bilinear approach is recommended due to its simplicity. Furthermore, the bilinear model is favoured over the linear tension model as it is more able to capture the rapid loss of tension capacity after cracking that was observed in the experimental beams.

5.3 Damage Modelling

When concrete is stressed beyond the elastic region and develops plastic strains, subsequent unloading of this concrete will exhibit a degraded or damaged elastic modulus. Therefore, to increase the accuracy of the concrete modelling, damage parameters d_t and d_c may be specified for both tension and compression, respectively.

To incorporate compression damage, the user specifies compressive damage parameters in a tabulated form as a function of the inelastic strains, ε_c^{in}. Referring to the uniaxial compression response shown in Figure 3.1, the compressive damage parameter, d_c, is a function of the plastic strain and elastic strain corresponding to the damaged concrete, ε_c^{pl} and ε_c^{el}, respectively. Restating Equation 3.1, the inelastic concrete strain can be found as follows:

$$\varepsilon_c^{in} = \varepsilon_c - \varepsilon_{oc}^{el} = \varepsilon_c - \frac{\sigma_c}{E_{co}} \tag{5.13}$$

where ε_c and σ_c are determined using the specified constitutive equations. To approximate the plastic strain associated with a given total strain, the model proposed by Polling (2001) was used:

$$\varepsilon_c^{pl} = b_c \varepsilon_c^{in} \tag{5.14}$$

For concrete under compression, the recommended value for b_c is 0.7. Therefore, the elastic

strain corresponding to the damaged concrete can be found using Equation 5.15:

$$\varepsilon_c^{el} = \varepsilon_c - \varepsilon_c^{pl} = \varepsilon_c - b_c \varepsilon_c^{in} \tag{5.15}$$

Using the calculated elastic strain, the compression damage parameter at any given strain level can be estimated as:

$$d_c = 1 - \frac{\frac{\sigma_c}{\varepsilon_c^{el}}}{E_{co}} \tag{5.16}$$

In summary, to define the damage parameters at a given strain level for concrete under compression, Equations 5.13 to 5.16 were used.

To incorporate tension damage, the tensile damage parameters may be specified in a tabulated form as a function of either the cracking strain, ε_t^{ck}, or the crack-opening-displacement, w. If the damage parameters are to be defined using the strain method, an approach similar to the one used to find the compressive damage parameters may be used to calculate d_t. For concrete under tension loading, Polling (2001) recommends a b_t value of 0.1.

$$\varepsilon_t^{ck} = \varepsilon_t - \varepsilon_{ot}^{el} = \varepsilon_t - \frac{\sigma_t}{E_{co}} \tag{5.17a}$$

$$\varepsilon_t^{pl} = b_t \varepsilon_t^{ck} \tag{5.17b}$$

$$\varepsilon_t^{el} = \varepsilon_t - \varepsilon_t^{pl} = \varepsilon_t - b_t \varepsilon_t^{ck} \tag{5.17c}$$

$$d_t = 1 - \frac{\frac{\sigma_t}{\varepsilon_t^{el}}}{E_{co}} \tag{5.17d}$$

If the crack-opening-displacement method is used to specify d_t, the values of w can be defined using the approaches discussed in Section 5.2.2 and 5.2.3 including linear, bilinear, or exponential formulations. The damage parameter associated with each displacement value can then range from $d_t = 0$ at a crack opening of 0 to $d_t = 1.0$ at the maximum crack opening, w_c. It is important to note, however, that excessive damage may have a critical

effect on the rate of convergence of the ABAQUS analyses. Therefore, it is recommended to avoid the use of damage parameters greater than 0.99, corresponding to 99% reduction of the elastic modulus. For all analyses performed for this thesis, the damage parameters were limited to 0.9, or 90% reduction of the elastic modulus, to avoid such issues.

The influence of incorporating damage into the beam models was studied. The following four cases were considered:

1. Compression and tension damage included
2. No damage included
3. Compression damage only
4. Tension damage only

Figure 5.15 shows the influence of each of the four cases on the load-displacement response for BM 16-INF.

First compare Cases 1 and 2; the use of both damage parameters versus the omission of both damage parameters, respectively. It can be seen that the beam response in the service loading region is similar regardless if damage is included or not. However, the beam that considered both compression and tension damage failed at a load very close to that of the experimental beam, whereas a larger peak load and higher degree of ductility are observed when damage is omitted. This behaviour is identical for all beams with no stirrups. As the damaged response is different than the no-damage response, it proves that unloading occurred within the damaged zones of the concrete during the analyses as a result of the coalescing of localized cracks, even though the loading was monotonic. When damage is considered, the unloaded concrete will have a degraded capacity, thus will respond differently than if no damage is used.

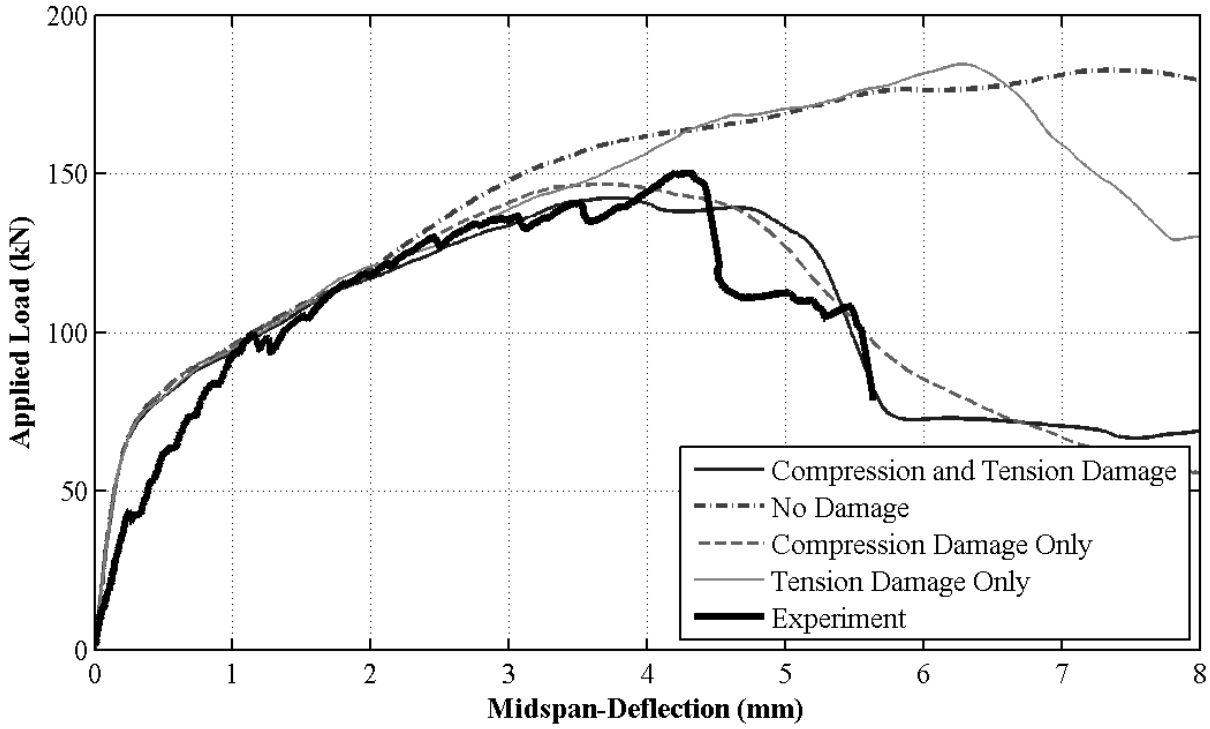

Figure 5.15: Influence of Damage - BM 16-INF

Now compare Cases 2 and 4; the omission of both damage parameters versus the use of tension damage only, respectively. For all beams with no stirrups, these two responses matched strongly. This means that the use of tension damage alone has negligible influence on the modelling of beams with no stirrups. Alternatively, consider Cases 1 and 3; the use of both damage parameters versus the use of compression damage only. Again, these two curves match strongly. This further shows that if tensile damage is removed such that only compression damage is used, the response remains unchanged. It can therefore be concluded that tension damage had minimal influence on the behaviour of beams with no stirrups (slight variations were noted for BM 12-INF). Conversely, the comparison of Case 2 with Case 3 or Case 1 with Case 4 demonstrates the large influence of compression damage.

In summary, the use of both compression and tension damage parameters yielded accurate responses for all beams with no stirrups. Compression damage proved to play a significant

role in replicating the shear failures of the experimental beams, whereas tension damage played a lesser role.

5.4 Plasticity Modelling

The plasticity modelling within the Concrete Damaged Plasticity Model is controlled by five parameters as introduced in Section 3.3.4: ψ, ϵ, σ_{bo}/σ_{co}, K_c, and μ. The parameters σ_{bo}/σ_{co} and K_c directly influence the yield function as presented in Equations 3.14 and 3.15. The default value of 1.16 was used for σ_{bo}/σ_{co} for all beam simulations, which represents the ratio of the initial equibiaxial compressive yield stress to the initial uniaxial compressive yield stress. The default value of 2/3 was used for K_c for all beam simulations, which represents the ratio of the second stress invariant on the tensile meridian to the second stress invariant on the compressive meridian. ϵ represents the plastic potential eccentricity and is a parameter that controls the flow potential function, G, as expressed in Equation 3.17. The default value of 0.1 was used for ϵ for all beam simulations. The purpose of this section is to study the influence of the remaining two parameters, ψ and μ, on the modelling of beams with no stirrups.

5.4.1 Dilation Angle

The dilation angle of concrete, ψ, is a material parameter in the Concrete Damaged Plasticity Model used to control the plastic flow potential function, G. This angle is a measure of the inclination of the plastic flow potential function within the meridional plane relative to the hydrostatic pressure axis at high confining pressures (Figure 3.7). Malm (2006) performed finite element modelling of shear critical beams subjected to four-point bending using ABAQUS to determine the influence of the dilation angle. It was found that small

dilation angles (10°) produced very brittle beam responses, whereas larger angles (> 40°) produced responses that exhibited higher ductility and achieved larger peak loads. Malm (2006) found that dilation angles between 30° and 40° provided the best agreement with experimental data. In the material model proposed by Lee and Fenves (1998), the dilation angle for both uniaxial tension and compression is defined as 31°. Jankowiak and Lodygowski (2005) proposed a dilation angle of 38° based on the minimization of error between the biaxial failure envelope of Kupfer et al. (1969) and the yield surface used by ABAQUS. Therefore, typical values for the dilation angle of normal grade concrete range from 30° to 40° as presented in the literature.

The influence of various dilation angles, ranging from 20° to 50°, on the load-deflection response was studied for all beams with no stirrups. Figure 5.16 shows the results for BM 16-INF.

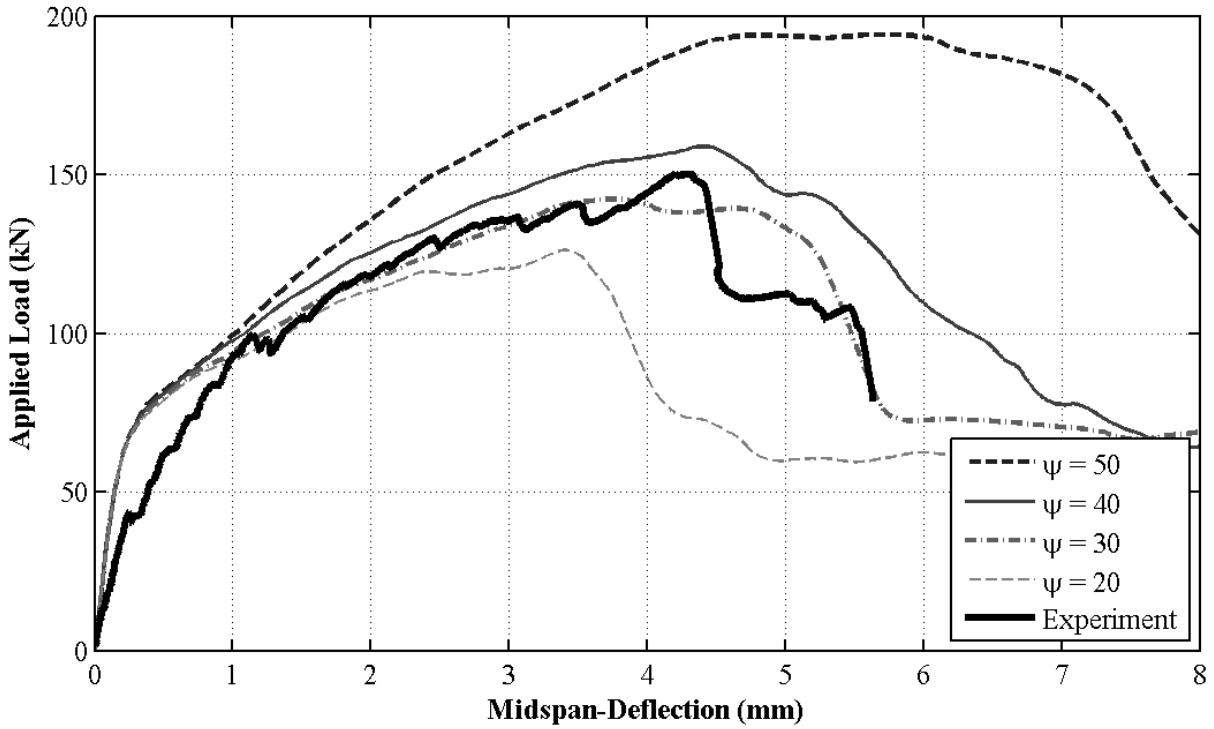

Figure 5.16: Influence of Dilation Angle - BM 16-INF

Figure 5.16 shows a similar pattern as observed by Malm (2006). As the dilation angle

increased, the beam's response became more ductile and failed at higher loads and larger mid-span deflections. Furthermore, with larger dilation angles, the post-cracking response became much stiffer. These stiffer responses were much less pronounced in the modelling performed by Malm (2006). It was found that for all beams with no stirrups, a dilation angle of 40° and 50° led to the overprediction of the member stiffness and peak load, most notably for BM 25-INF. An angle of 20° provided an improvement to the post-cracking behaviour, however an angle of 30° provided the strongest and most consistent agreement with the experimental data. For this reason, a dilation angle of $\psi = 30°$ was used for the modelling of all beams with no stirrups.

5.4.2 Viscoplastic Regularization

The Concrete Damaged Plasticity Model allows the user to perform viscoplastic regularization of the constitutive equations to overcome numerical convergence issues associated with the post-peak response of concrete as discussed in Section 3.3.4. Viscoplastic regularization is provided through the viscosity parameter, μ. The default value of μ is zero, which means no viscoplastic regularization is used. The influence of various values of μ on the behaviour of beams with no stirrups is demonstrated in Figure 5.17 for BM 16-INF.

When a value of zero was used for the viscosity parameter for BM 16-INF, the model encountered convergence issues and aborted the analysis prematurely at an applied load of 107kN (71% of the experimental peak load). Therefore, a non-zero input for μ was required to model the full spectrum of the beam response. An increased value of 0.00001 was then used, which resulted in an accurate estimation of the load-deflection response. This analysis, however, remained significantly computationally inefficient. Increasing μ to 0.0001 provided a more accurate representation of the response, and was significantly less computationally demanding. Further increases to μ provided responses with significant

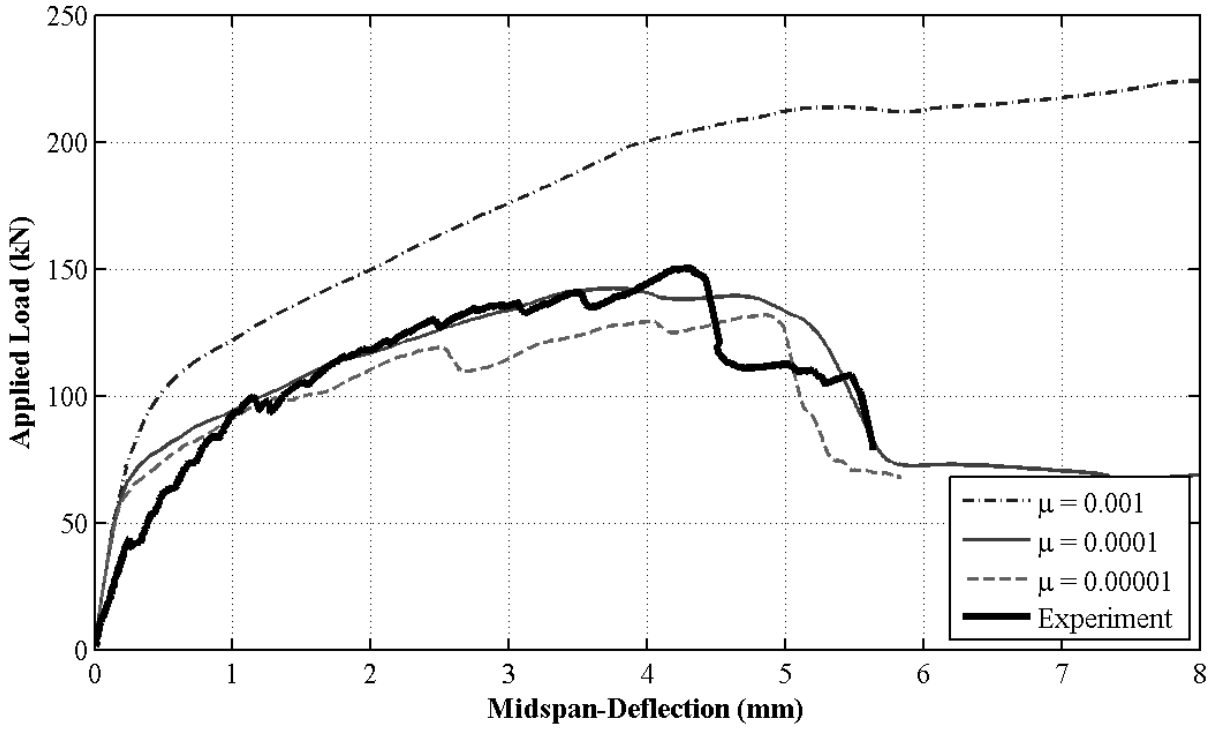

Figure 5.17: Influence of Viscoplastic Regularization - BM 16-INF

deviations from the experimental data. As this value becomes large relative to the iteration time increment, the response approaches the elastic solution, which is inappropriate for a concrete model. This behaviour is consistent for all three beams with no stirrups as shown in Appendix B. A value of $\mu = 0.0001$ was found to produce the most accurate results for all three beams, and was used for all further modelling of beams with no stirrups. This small, non-zero value introduces viscoplastic regularization that overcomes the numerical solution issues, improves computational efficiency, and does not compromise the accuracy of the results.

5.5 Mesh Refinement

The influence of mesh refinement of the concrete region on the beam response was studied for all beams with no stirrups. Table 5.5 presents the mesh alternatives considered.

Table 5.5: Concrete Mesh Alternatives

Beam	H (mm)	B (mm)	L (mm)	Number of Elements			Total Number of Elements	Aspect Ratio
				Depth	Width	Length		
12-YYY	350	200	839.63	21	12	51	12,852	1.01
	350	200	855.00	16	9	38	5,472	1.03
	350	200	851.09	12	7	29	2,436	1.03
	350	200	843.75	8	5	20	800	1.09
	350	200	859.09	6	3	14	252	1.14
16-YYY	345	200	839.63	21	12	51	12,852	1.01
	345	200	855.00	16	9	38	5,472	1.04
	345	200	851.09	12	7	29	2,436	1.03
	345	200	843.75	8	5	20	800	1.08
	345	200	859.09	6	3	14	252	1.16
25-YYY	330	200	839.63	(20)	12	51	12,240	1.01
	330	200	855.00	(15)	9	38	5,130	1.02
	330	200	851.09	12	7	29	2,436	1.07
	330	200	843.75	8	5	20	800	1.05
	330	200	859.09	(5)	3	14	210	1.09

Table 5.5 presents the height (H), width (B) and total length (L) of each beam. The number of elements in each dimension of the beam are shown. For example, the coarsest mesh used for beams with 12mm diameter longitudinal bars, BM 12-YYY, was 6 elements deep, 3 wide, and 14 long. The total number of elements and the governing aspect ratio of the elements are also presented. When selecting the various mesh patterns and element sizes, effort was made to ensure that each option utilized elements with aspect ratios as close to 1.0 as possible. Three-dimensional hexahedral elements are sensitive to initial distortions, thus the use of square elements yields more stable analyses with higher accuracy and less numerical issues. It is important to note that beams 25-YYY have a significantly reduced height as compared to the other beams, therefore required modified mesh alternatives to

maintain aspect ratios close to 1.0. These modified mesh options will be referred to in brackets for this discussion. Figure 5.18 presents the various mesh alternatives studied.

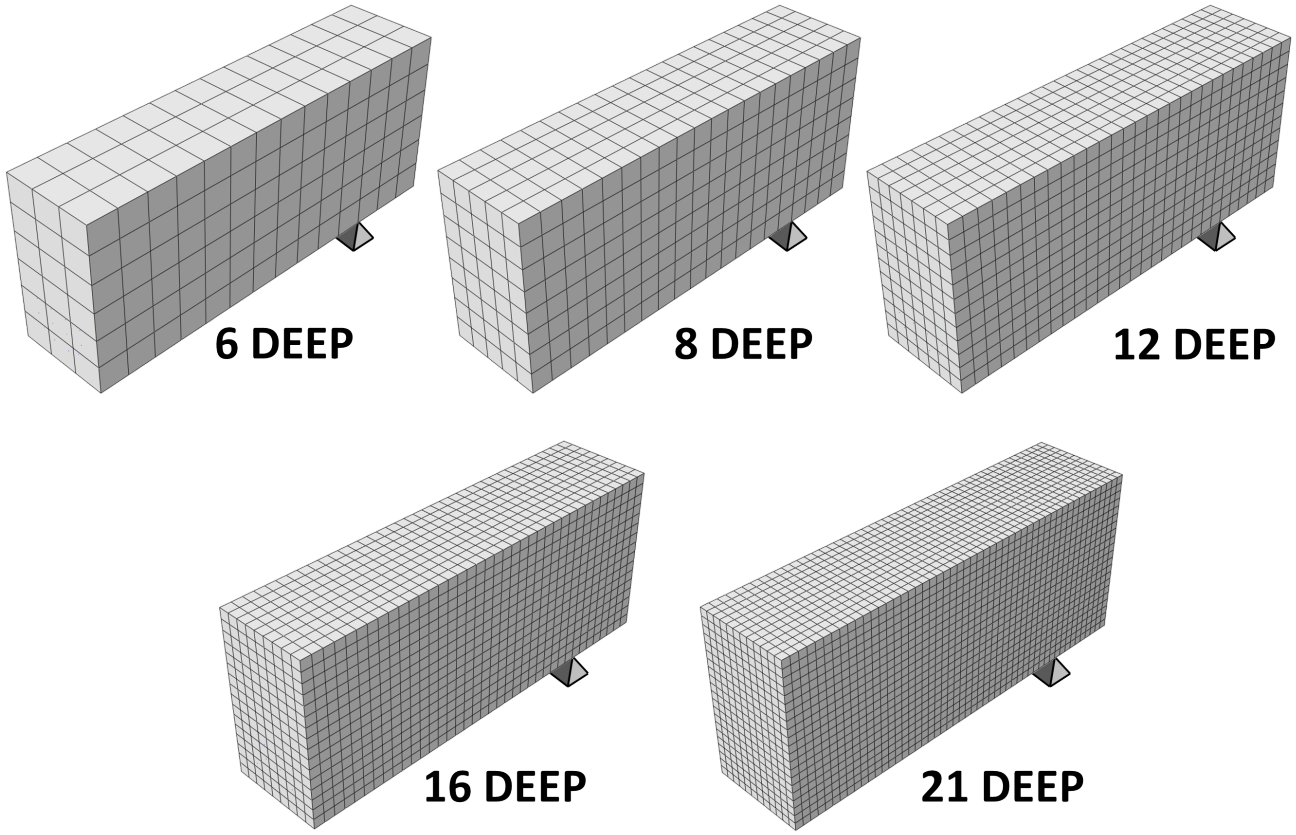

Figure 5.18: Mesh Alternatives

It is important to discuss the total length of each beam, L. Each beam studied had the same shear span of 675mm, which extended from the mid-span to the support. Additional elements were added to each model such that the beam extended beyond the support and created an overhang as depicted in Figure 5.18. The length of this overhang was dependent on the number of elements in the overhang and the length of each element within the overhang. As the size of each element varied between mesh refinements, the length of this overhang also varied. This explains the slight variation between the values of L shown in Table 5.5.

The various mesh refinement options are characterized by the number of elements in the

depth of the beam. The coarsest mesh used only 5 elements throughout the beam depth, while the finest mesh used 21 elements throughout the beam depth. To truly model the response of a beam subjected to bending, a model would need to be capable of capturing the curvature of the beam. Curvature is the second derivative of the deflected shape, meaning the shape functions within each element are required to be a minimum of second-order to produce continuous derivatives within and between elements. As first-order, linear concrete elements were used for all models to improve computational efficiency and to prevent numerical complications, a finer mesh is expected to yield a stronger approximation of the beam response. Furthermore, the strain within a linear element is constant, whereas the strain distribution of a beam cross-section subjected to bending is not constant. Therefore, to accurately capture the variation of strains throughout the depth of each beam, a sufficient number of element layers must be present.

Figure 5.19 shows the influence of each mesh refinement on the load-deflection response for BM 25-INF.

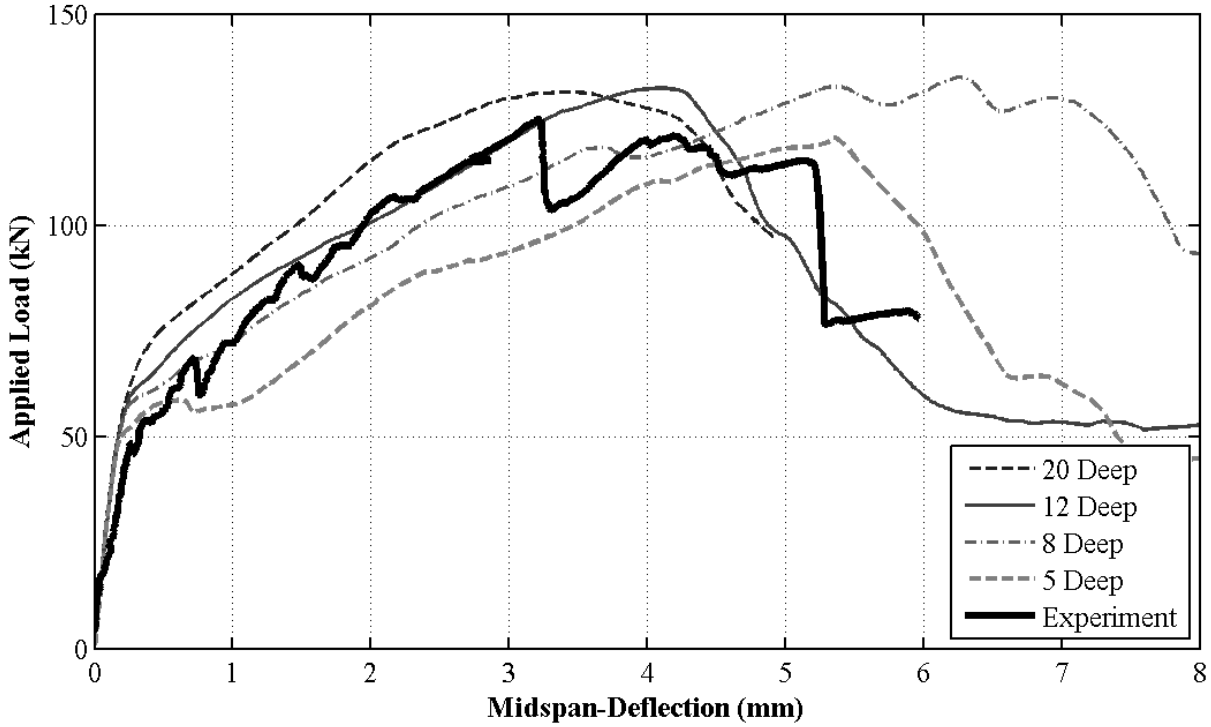

Figure 5.19: Influence of Mesh Refinement - BM 25-INF

Table 5.6 compares the peak load predicted by each mesh for all beams with no stirrups and the percent difference with the experimental values. Note that the mesh designations in brackets refer to the modified mesh alternatives used for BM 25-INF.

Table 5.6: Influence of Mesh Refinement on Peak Load

	BM 12-INF		BM 16-INF		BM 25-INF	
	Load (kN)	% Diff.	Load (kN)	% Diff.	Load (kN)	% Diff.
Experiment	163.1	-	150.2	-	125.1	-
21 (20) Deep	158.3	2.92%	160.0	6.51%	131.6	5.16%
16 (15) Deep	157.8	3.24%	149.3	0.63%	127.4	1.84%
12 Deep	169.4	3.87%	142.3	5.28%	132.5	5.92%
8 Deep	168.7	3.47%	144.5	3.83%	135.0	7.94%
6 (5) Deep	145.5	10.76%	152.6	1.58%	120.8	3.43%

Referring to Table 5.6, it can be seen that all mesh densities provided peak load predictions that were within 10% of the experimental results (with the exception of the 6-deep mesh used for BM 12-INF). However, as Figure 5.19 shows, it is the deflection responses that vary significantly within the service loading range. Figure 5.19 presents an interesting pattern that was consistent for all beams studied. As the mesh becomes finer, the pre-peak response of each beam becomes stiffer. This observation contradicts the typical behaviour of finite element models where a finer mesh provides less restraint to nodal displacements, thus yielding responses that are less stiff. This phenomenon was also observed in the ABAQUS modelling performed by Malm (2006). DSS (2012) attributes this mesh sensitivity to regions of the concrete with little or no reinforcement. In the absence of reinforcement, cracking failures are not distributed evenly and may lead to the localization of cracking. If no additional cracks are formed with mesh refinement, the crack bands will become narrower and more localized, thus preventing the model from converging to a unique solution as the mesh density is refined. Furthermore, DSS (2012) also theorizes that three-dimensional models have a higher susceptibility to mesh sensitivity as compared

to two-dimensional models due to the potential of cracking in the out-of-plane direction.

Figure 5.20 compares the crack patterns at failure associated with the five mesh refinements studied for BM 25-INF. The crack pattern observed at failure during the experimental testing is also shown. Note that the right end of each mesh represents the mid-span section of the beam (point of load application), and the left end of each mesh represents the location of the support

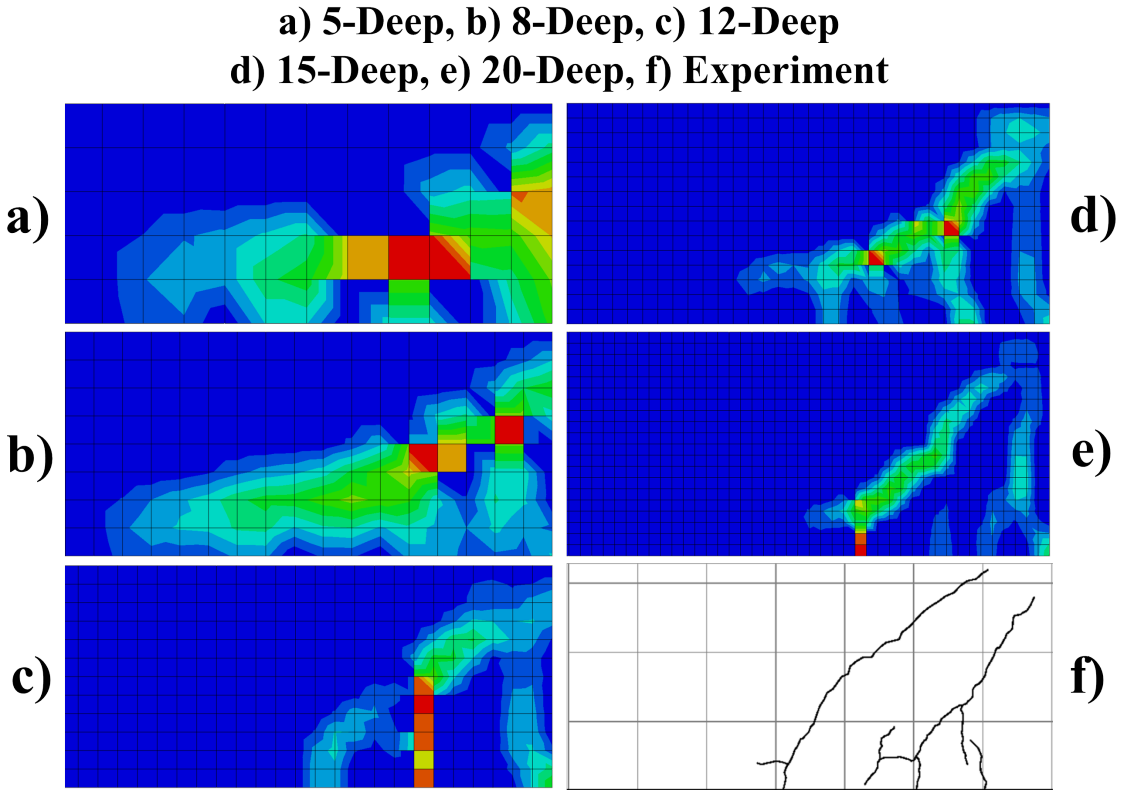

Figure 5.20: Influence of Mesh Refinement on Crack Pattern - BM 25-INF

It can be seen that all mesh densities accurately capture the presence of diagonal shear cracks, in the form of large plastic strains, originating from the load point. As the mesh is refined, the crack pattern remains similar, but the crack bands become narrower and better defined. The use of finer meshes, 12-deep to 20-deep, provide crack patterns that agree strongly with the experimentally observed pattern. These results are consistent for all other beams with no stirrups.

The use of a 16 (15) element deep mesh yielded the highest accuracy results in terms of peak load and deflection response. However, the 12-deep mesh was also able to provide accurate results that correlated well with the experimental data as shown in Figure 5.21. Furthermore, the 12-deep mesh was able to provide this accuracy with the use of less than one-half of the number of elements required for the 16 (15)-deep mesh. With the accuracy of the 12-deep mesh and the reduced computational effort required as compared to the 16 (15)-deep mesh, the 12-deep mesh was utilized for all modelling of beams with no stirrups.

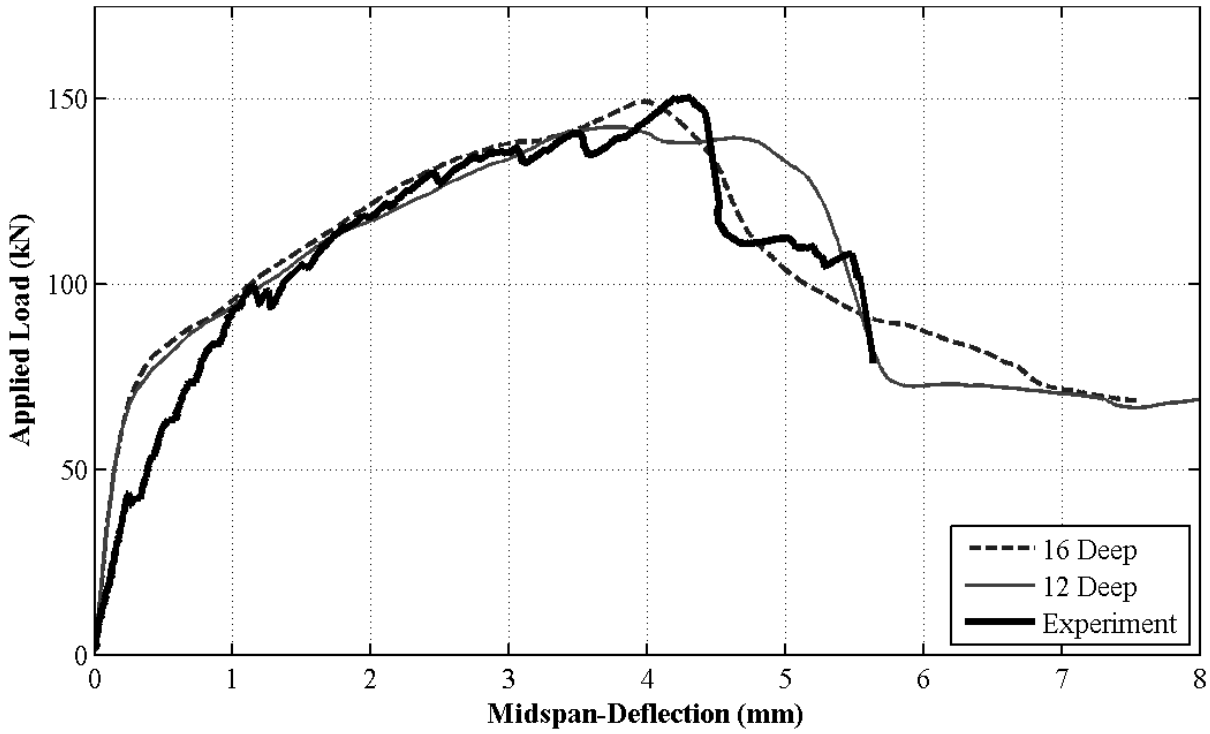

Figure 5.21: Influence of Mesh Refinement - BM 16-INF

5.6 Modelling of GFRP Reinforcement

Two methods of modelling the GFRP reinforcement were studied in this research: 1) Discrete, one-dimensional truss sections; and 2) Smeared, reinforced membrane sections. As this chapter focuses on beams with no stirrups, this section will concentrate on the modelling of the longitudinal reinforcing bars.

5.6.1 GFRP Longitudinal Reinforcement

Figures 5.22 to 5.24 compare the influence of the reinforcement modelling technique on the load-deflection responses for all beams with no stirrups.

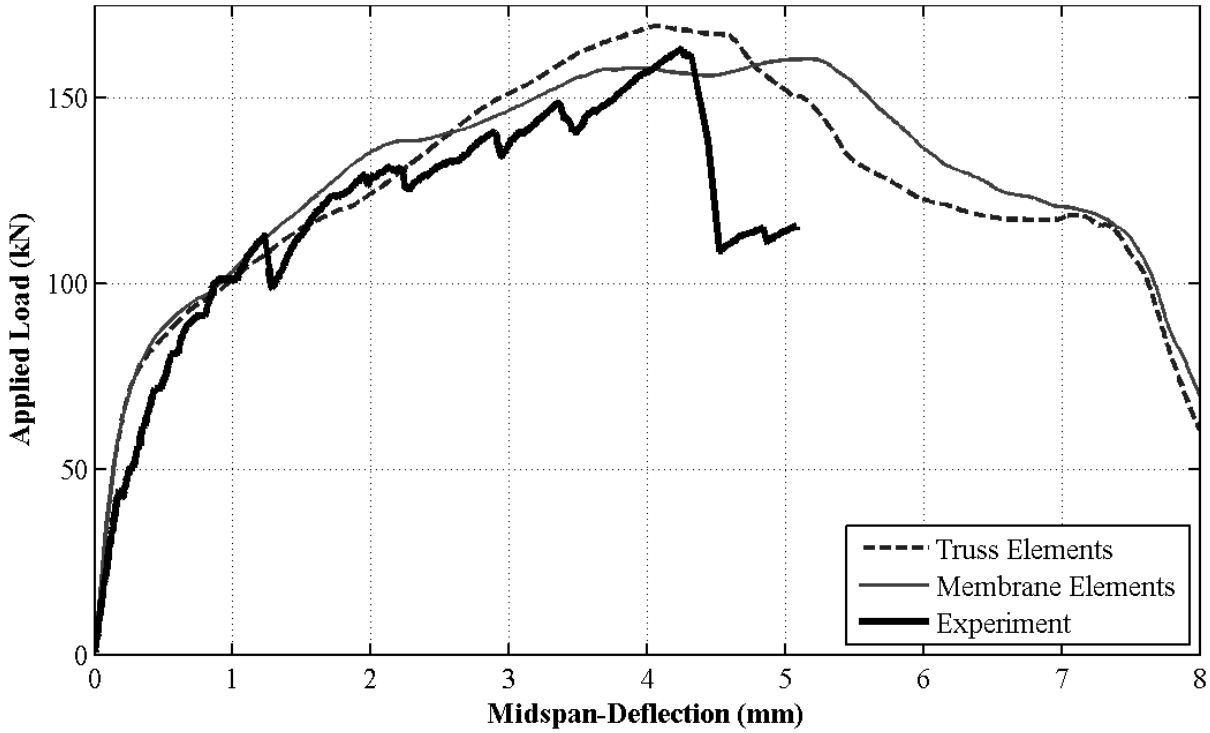

Figure 5.22: Influence of Longitudinal Reinforcement Modelling - BM 12-INF

For BM 12-INF, both methods of modelling the reinforcement produced similar responses over the complete spectrum of the analysis (both pre-peak and post-peak regions) that agree strongly with the experimental behaviour. For BM 16-INF and BM 25-INF, both methods provide similar post-cracking responses but result in different peak loads.

The load-strain behaviour of the reinforcing bars was then studied for each modelling method. As discussed in Section 2.3.2, strain gauges were used during the experimental testing to monitor the strain development of individual bars at various locations. For beams with 12mm or 16mm diameter longitudinal bars (BM 12-YYY and BM 16-YYY), a strain gauge was positioned on the middle bars of each reinforcing layer at the mid-span section.

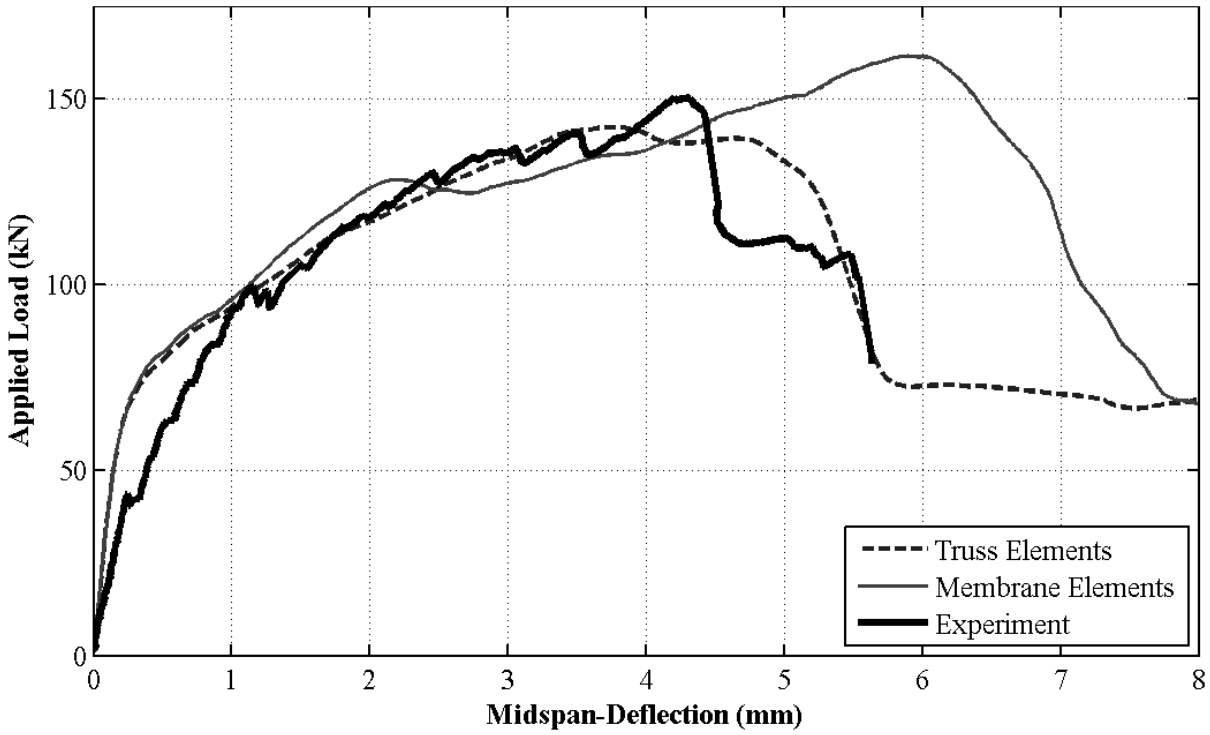

Figure 5.23: Influence of Longitudinal Reinforcement Modelling - BM 16-INF

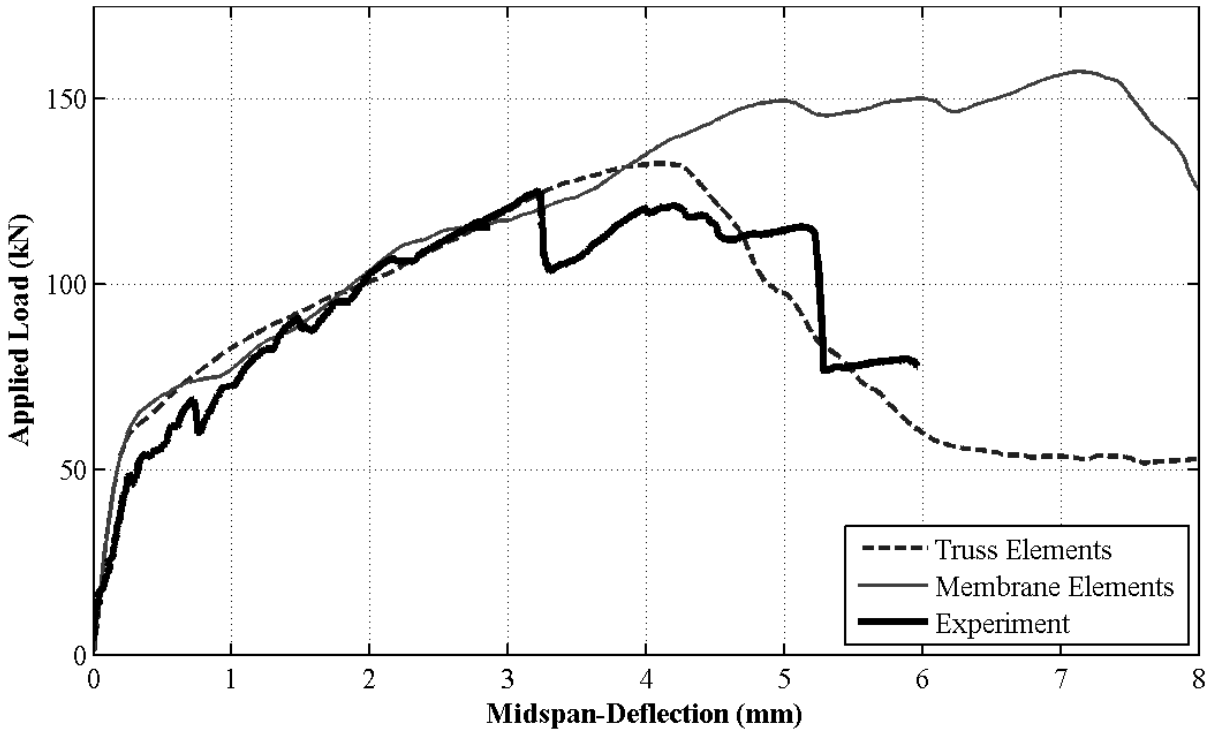

Figure 5.24: Influence of Longitudinal Reinforcement Modelling - BM 25-INF

For beams with 25mm diameter longitudinal bars (BM 25-YYY), gauges were placed on both bars at the mid-span section. Appendix A shows the locations and nomenclature of all strain gauges used. Figure 5.25 compares the experimental reinforcement strains for each of the three reinforcing layers in BM 12-INF with the model analyses for both truss and membrane approaches. Figure 5.26 presents the strain profiles for each of the two layers in BM 16-INF. Figure 5.27 presents the strain profiles for the single layer in BM 25-INF.

With the exception of the second layer of reinforcement in BM 12-INF (strain gauge L-2-C), the membrane strains agree strongly with the truss strains for all reinforcement layers in each beam. This proves that the smeared reinforcement within each membrane section is capable of providing the same stiffness properties as the discrete truss bars, and that the process used to define the membrane sections as presented in Section 4.3.2 was accurate. This validates the use of embedded membranes to model layers of reinforcement as an alternative to the traditional, discrete truss approach. However, the truss reinforcement provided a higher level of consistency and agreement with the experimental data, and allows for the easy visualization of the stress distribution within each individual bar. Therefore, it was concluded that the truss approach is the optimal solution to model the longitudinal bars.

The strain profiles for BM 16-INF were then studied. At a load of approximately 41kN, the experiment reinforcement experienced a sudden increase in strain while maintaining a constant load. This plateau suggests that the reinforcement debonded from the concrete at the location of the strain gauge, causing an immediate activation of the GFRP reinforcement. As can be seen in Figure 5.26, the analysis reinforcement became fully activated at a much more gradual rate and was unable to exhibit the rapid loss of bond. This is a result of the concrete tension model used. By incorporating a tension model that utilizes a post-cracking strain-softening region, the analysis assumes that the concrete is able to carry

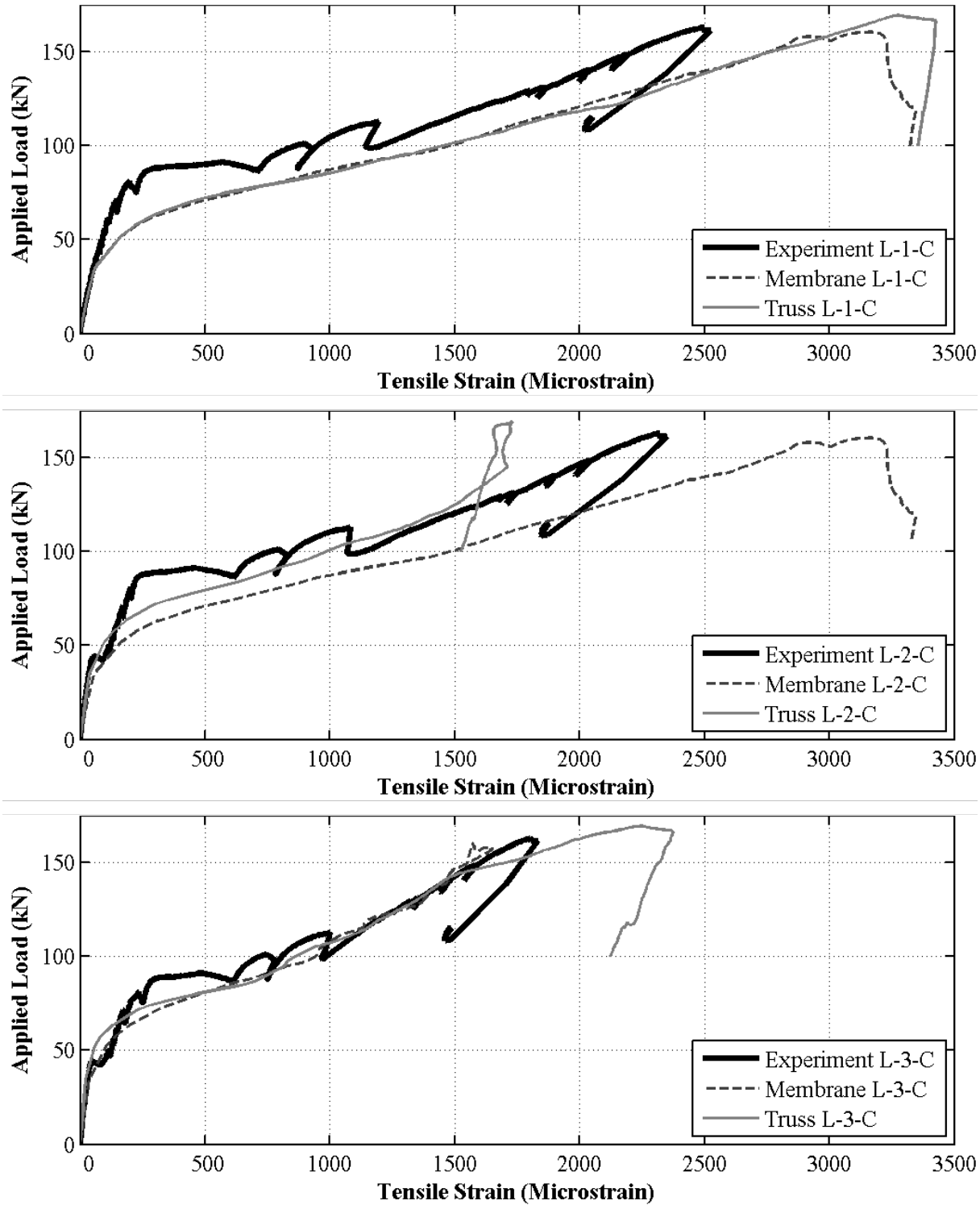

Figure 5.25: Longitudinal Reinforcement Strains - BM 12-INF

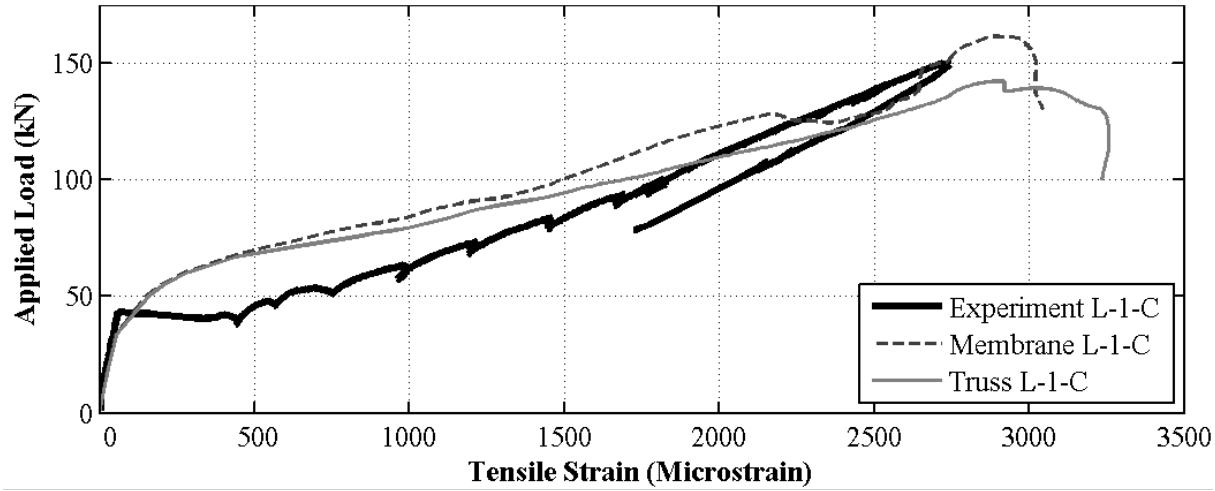

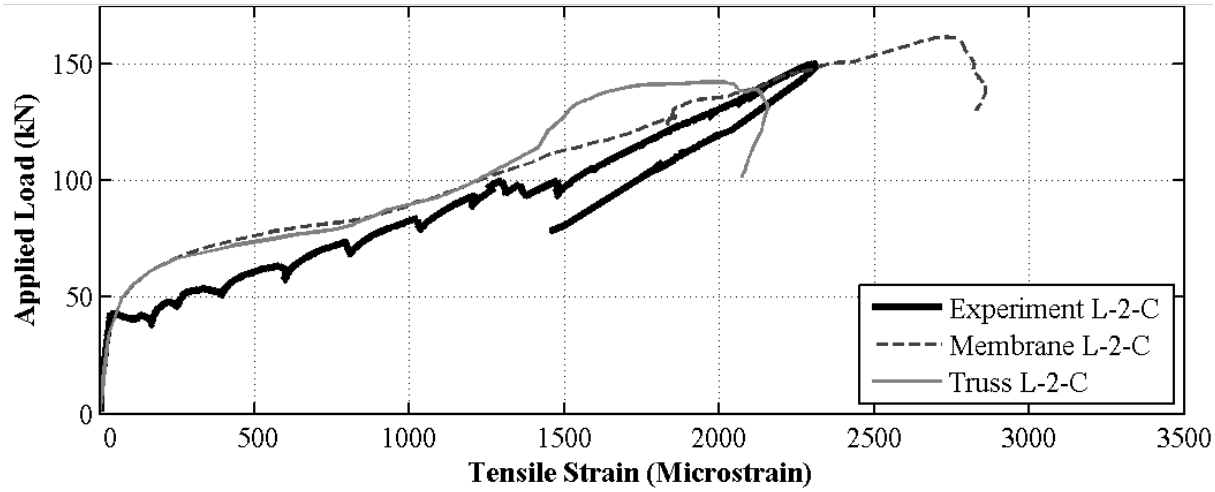

Figure 5.26: Longitudinal Reinforcement Strains - BM 16-INF

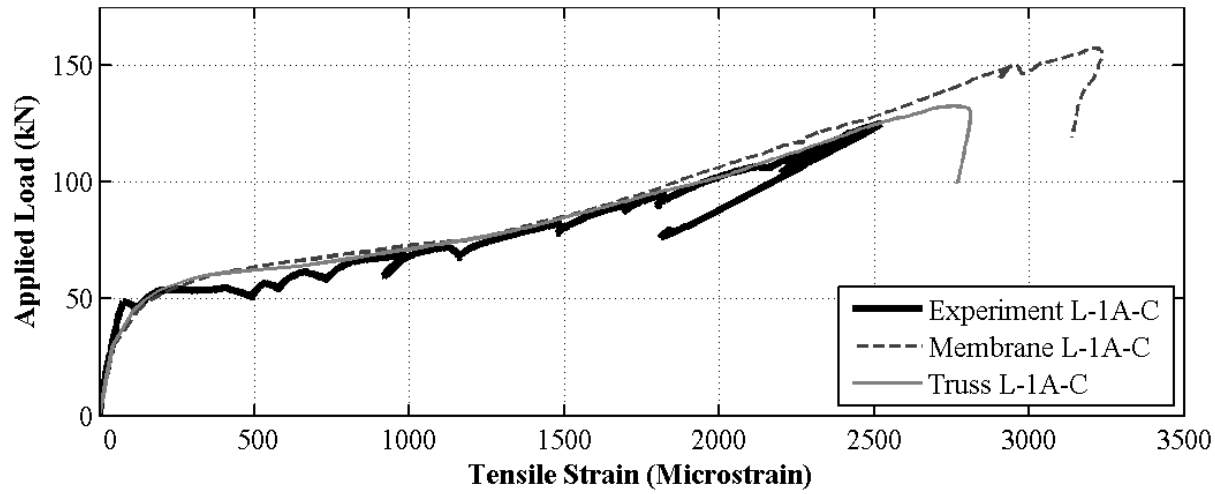

Figure 5.27: Longitudinal Reinforcement Strains - BM 25-INF

tensile loads immediately after cracking. Therefore, this tension model assumes a certain degree of bond between the reinforcement and the concrete. To more accurately replicate the experimental results, a modified post-cracking tension model can be used that introduces a more drastic reduction in tension carrying capacity upon cracking. Maintaining a constant fracture energy $G_f = 90\text{N/m}$, Figure 5.28 presents a possible modified version of the original bilinear stress-displacement model for BM 16-INF.

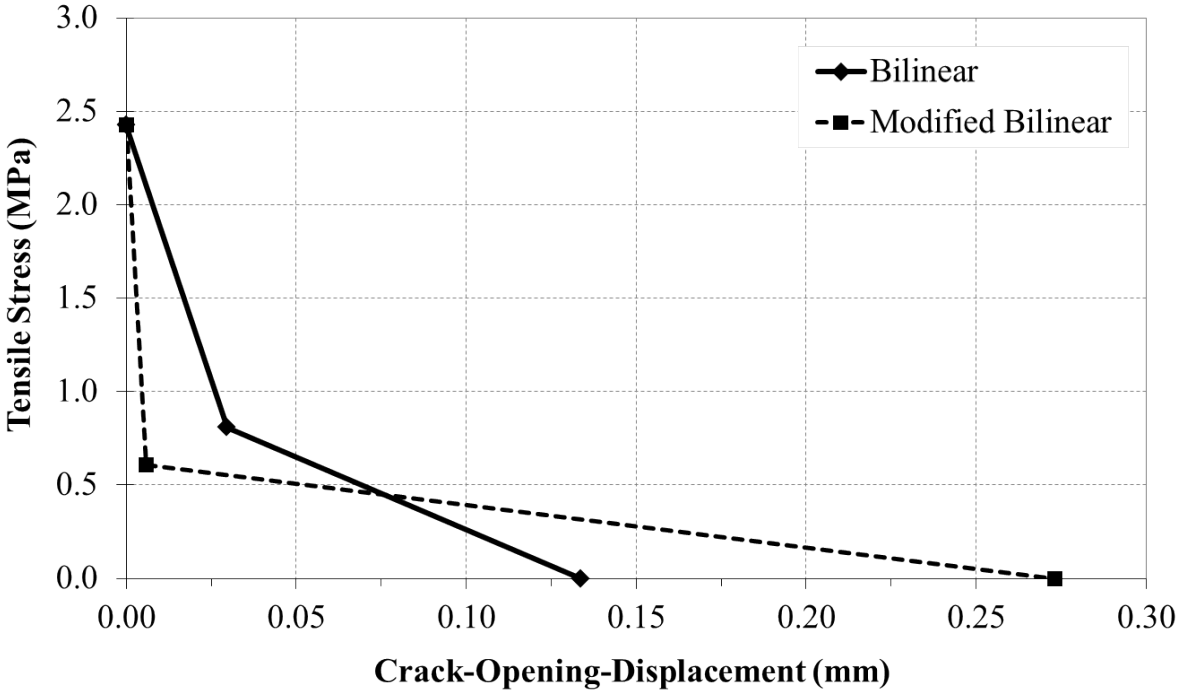

Figure 5.28: Modified Bilinear Tension Model - BM 16-INF

This modified curve represents the same fracture energy as the original bilinear curve; the area under both curves is equal. However, the modified curve implements a rapid decay of strength for very small crack displacements. The influence of this modified model on the beam response and on the tensile reinforcement strains is shown in Figures 5.29 and 5.30 for BM 16-INF, respectively.

The modified bilinear stress-displacement curve produces a beam response that is significantly less stiff after cracking as compared to the response with the original bilinear model.

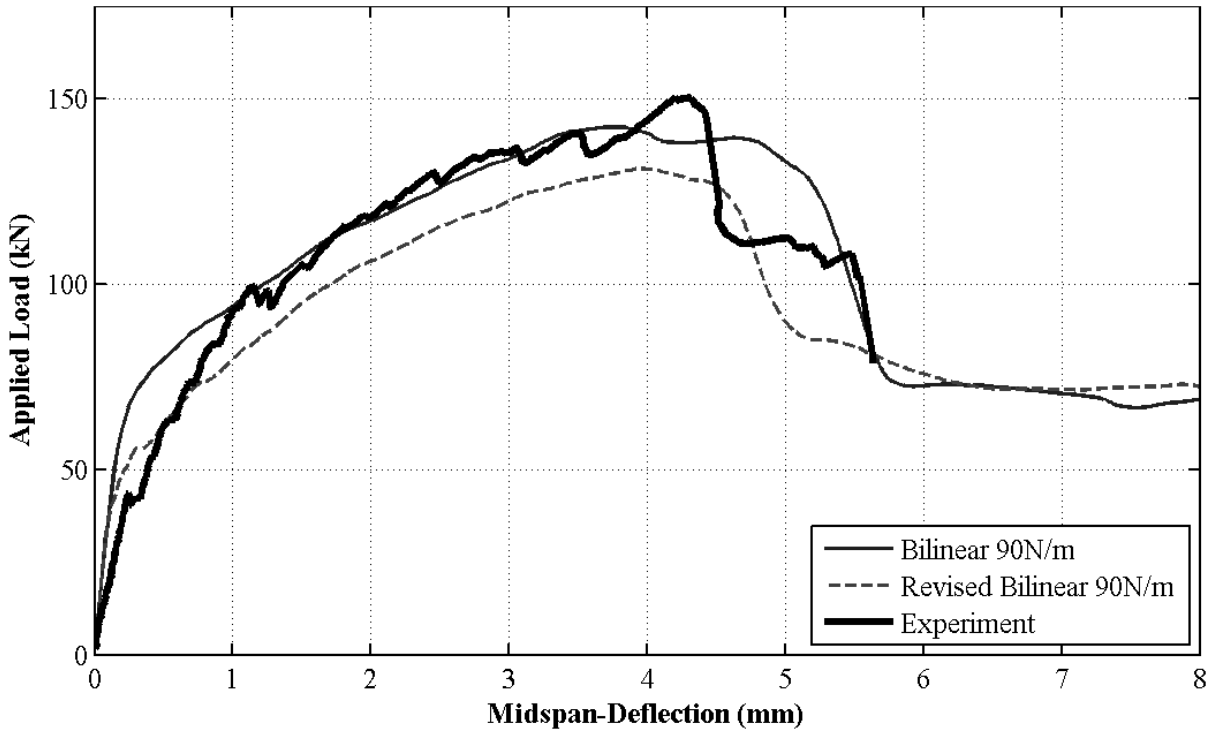

Figure 5.29: Influence of Modified Tension Model - BM 16-INF

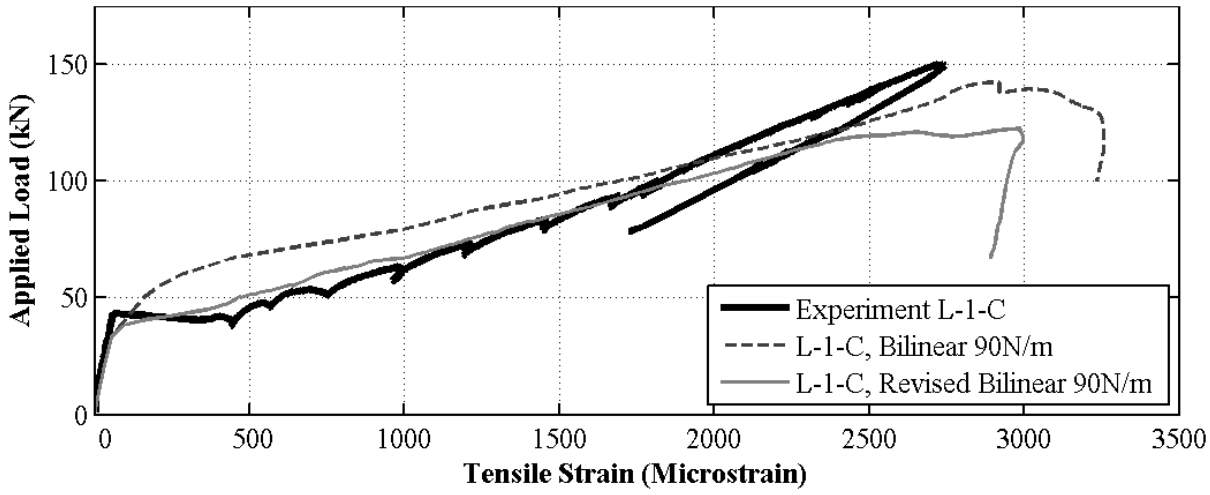

Figure 5.30: Influence of Modified Tension Model on Reinf. Strains - BM 16-INF

With the new curve, the concrete loses its tensile strength rapidly upon cracking, causing the beam to experience a brittle failure earlier. However, Figure 5.30 shows that the modified tension model was able to accurately replicate the experimental strains. This demonstrates that not only does the magnitude of the fracture energy influence the beam behaviour, but also the shape of the stress-displacement curve. By modifying this shape, one can control the amount of tension stiffening that the reinforcement experiences. With a rapid loss of tensile strength immediately after cracking, the model was able to replicate the debonding, or slippage, that the experimental beams experienced.

5.7 Final Recommendations and Comparison to Code Predictions

5.7.1 Proposed Model for Beams with No Stirrups

Table 5.7 summarizes the parameters recommended for the effective modelling of concrete beams reinforced with GFRP longitudinal bars and no stirrups.

Figure 5.31 compares the load-deflection responses for the beams with no stirrups as predicted using the proposed ABAQUS model with the responses measured during the experimental testing.

Figure 5.32 presents the crack patterns at failure as produced by the proposed model. The actual crack patterns at failure as observed during the experimental testing have been superimposed in white. Note that the top right corner of each diagram represents the point of load application at mid-span and the bottom left corner is the location of the support.

It can be seen that all models were able to accurately capture the crack patterns at failure.

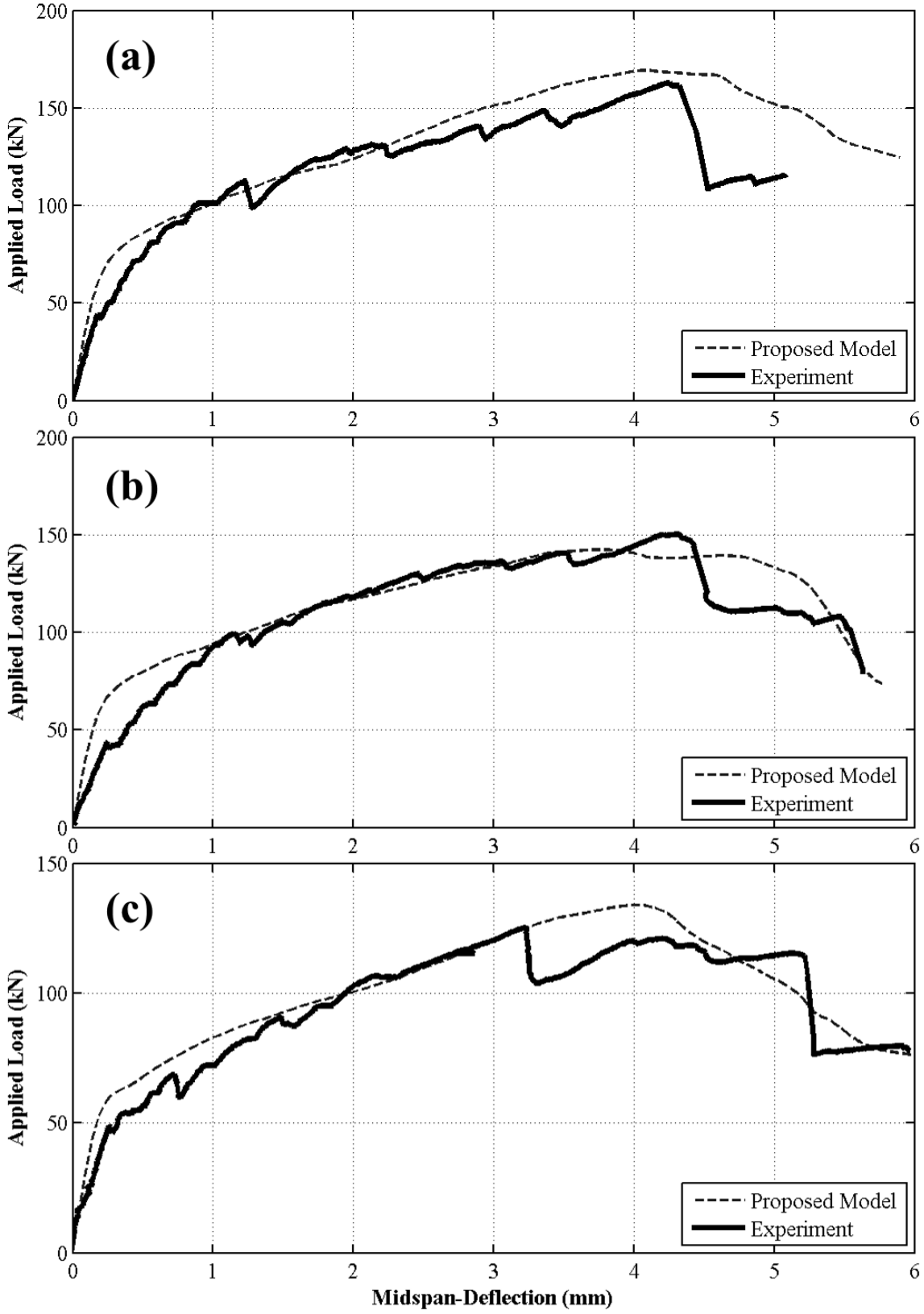

Figure 5.31: Proposed Model for BM XX-INF: (a) BM 12-INF (b) BM 16-INF (c) BM 25-INF

Table 5.7: Proposed Parameters for the Modelling of Beams with No Stirrups

Compression Model:	Hognestad Parabola
Maximum Compressive Strain, $\varepsilon_{c,max}$:	0.008
Tension Model:	Bilinear Stress-Displacement
Fracture Energy, G_f:	90 N/m
Damage:	Tension and Compression Included
Poisson's Ratio, v:	0.2
Dilation Angle, ψ:	30°
σ_{bo}/σ_{co}:	1.16
Eccentricity, ϵ:	0.1
K_c:	2/3
Viscosity Parameter, μ:	0.0001
Mesh Refinement:	12 Deep
Longitudinal Reinforcement:	Linear Truss Sections
Stirrup Reinforcement:	N/A

It is interesting to note that the diagonal crack developed in BM 12-INF originated near the support and propagated towards the load point. For BM 16-INF and BM 25-INF, however, the diagonal cracks originated further and further away from the support, resulting in cracks with steeper inclinations. This demonstrates the influence of the longitudinal reinforcement ratio and bar configuration on the concrete cracking. BM 12-INF had the largest reinforcement ratio and the smallest bars, thus allowing for a stronger interaction between the reinforcement and concrete. Although this resulted in a higher number of cracks, the cracks were more distributed and had smaller widths. Conversely, BM 25-INF had the smallest reinforcement ratio and used much larger bar diameters. With larger and fewer bars, there will be less interaction between the reinforcement and concrete, which will result in fewer and larger cracks. As these beams had no stirrups, these larger cracks resulted in a more drastic shear failure with fewer flexural cracks.

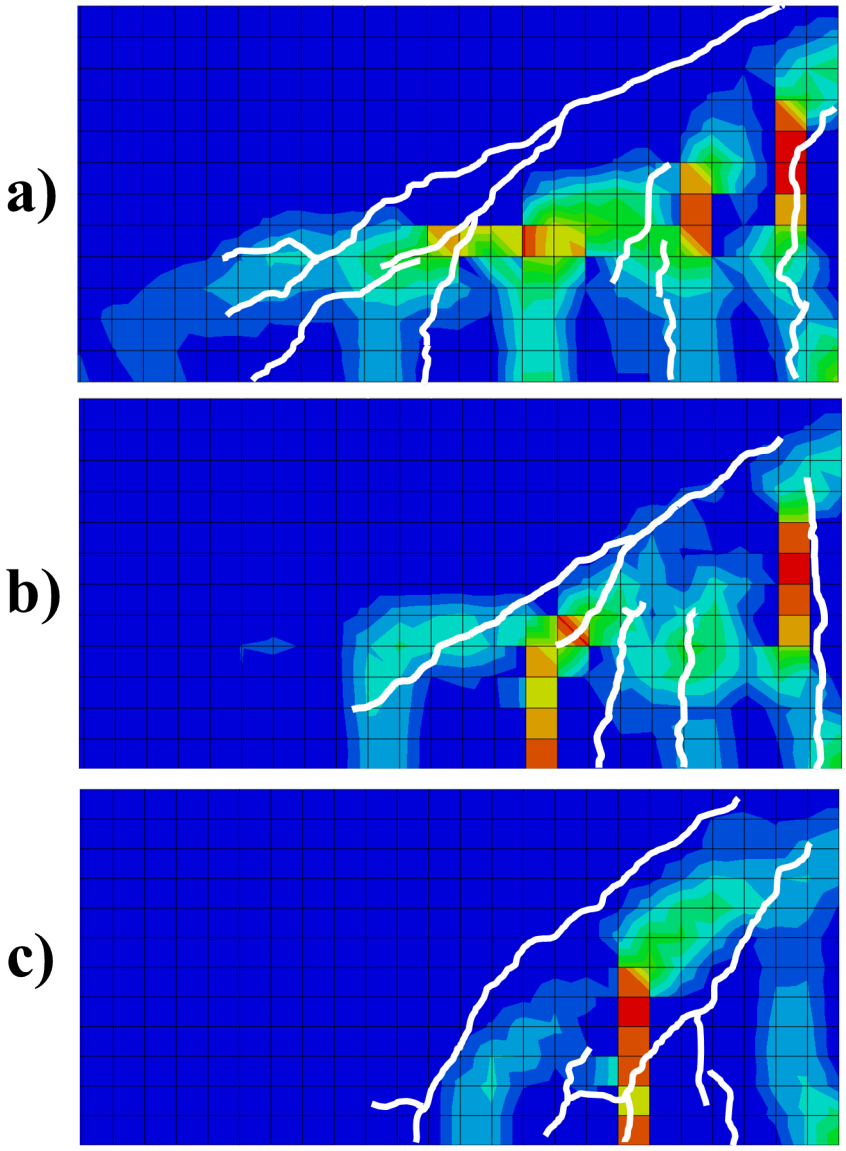

Figure 5.32: Comparison of Crack Patterns at Failure - BM XX-INF: (a) BM 12-INF, (b) BM 16-INF, (c) BM 25-INF

5.7.2 Comparison to Code Predictions

Table 5.8 presents the failure loads for each beam as provided by various flexure and shear resistance predictions and the proposed model. These predictions, P_P, are then compared to the experimental peak loads, P_E.

Referring to Table 5.8, the flexural strengths provided poor approximations to the exper-

Table 5.8: Comparison of Predicted and Experimental Peak Loads

Beam	Experiment	CSA S806-12 Flexure		CSA S806-12 Shear		Nehdi et al. Shear		ABAQUS Model	
	P_E (kN)	P_P (kN)	Ratio P_E/P_P	P_P (kN)	Ratio P_E/P_P	P_P (kN)	Ratio P_E/P_P	P_P (kN)	Ratio P_E/P_P
12-INF	163.1	431.9	0.38	152.8	1.07	151.3	1.08	169.4	0.96
16-INF	150.2	410.3	0.37	144.8	1.04	146.9	1.02	142.3	1.06
25-INF	125.1	372.5	0.34	131.8	0.95	139.3	0.90	132.5	0.94

imental peaks load; this is to be expected as all beams experienced shear failures. The shear strengths provided by CSA S806-12 were able to consistently predict the peak load to within 7% of the experimental loads. The shear strengths predicted by Nehdi et al. (2007) were all within 10% of the experimental strengths. Finally, the proposed ABAQUS model was able to accurately predict the peak loads to within 4%, 6%, and 6% of the experimental values for BM 12-INF, BM 16-INF, and BM 25-INF, respectively.

Table 5.9 presents the ratio of the peak load as predicted by the proposed ABAQUS model to the peak load as provided by the various strength prediction models and the experimental data. Note that a value less than 1.0 means that the proposed model underpredicted the peak load relative to the model of interest, whereas a ratio greater than 1.0 means the proposed model overpredicted the peak load.

Table 5.9: Comparison of Model Results Relative to Peak Load Predictions

Beam	Experiment	CSA S806-12 Flexure	CSA S806-12 Shear	Nehdi et al. Shear
12-INF	1.04	0.39	1.11	1.12
16-INF	0.95	0.35	0.98	0.97
25-INF	1.06	0.36	1.01	0.95

It is clear that the shear strength predictions of CSA S806-12 provided the strongest

agreement with the ABAQUS model output, with BM 16-INF and BM 25-INF providing strengths within 2% and 1%, respectively. The model proposed by Nehdi et al. (2007) also agreed strongly; it will be shown in the next chapters that this model is very effective in providing accurate shear strength predictions for FRP reinforced beams.

Chapter 6

Modelling of Beams with Stirrups

Chapter 5 presented the finite element analyses of three concrete beams with no stirrups as tested by Krall (2014). This chapter focuses on the remaining nine concrete beams that were reinforced with both glass fibre reinforced polymer (GFRP) longitudinal bars and stirrups. Similar to the beams with no stirrups, the beams with stirrups are characterized by three longitudinal reinforcement core diameters: 12mm, 16mm, and 25mm. Each core diameter corresponds to a different longitudinal reinforcement arrangement as presented in Figure 2.7. For each longitudinal reinforcement arrangement, three stirrup spacings were tested: 150mm, 220mm, and 230mm. The beams with stirrups spaced at 150mm and 220mm used stirrups with a core diameter of 12mm, whereas the beams with stirrups spaced at 230mm used stirrups with a core diameter of 20mm. This chapter therefore focuses on the modelling of beams BM XX-150, BM XX-220, and BM XX-s230.

6.1 Compression Modelling

The Hognestad Parabola constitutive equations used for the modelling of beams with no stirrups as introduced in Equations 5.1 and 5.2 were also considered for the modelling of beams with stirrups. The modification to the third region of the uniaxial compressive

response as expressed in Equation 5.3 was also utilized to control the maximum strain within the post-peak strain-softening region, $\varepsilon_{c,max}$. All concrete beams with stirrups were modelled using a compressive strength of $f_c^{'} = 56.5$MPa, resulting in a maximum concrete compressive strain of $\varepsilon_{c,max} = 0.0082$ when using the original Hognestad Parabola equations. It was concluded in Chapter 5 that a maximum strain value of 0.008 and a dilation angle of $\psi = 30°$ provided the best results for the modelling of beams with no stirrups. Using this model, Figure 6.1 presents the load-deflection response for BM 16-150 as determined using ABAQUS.

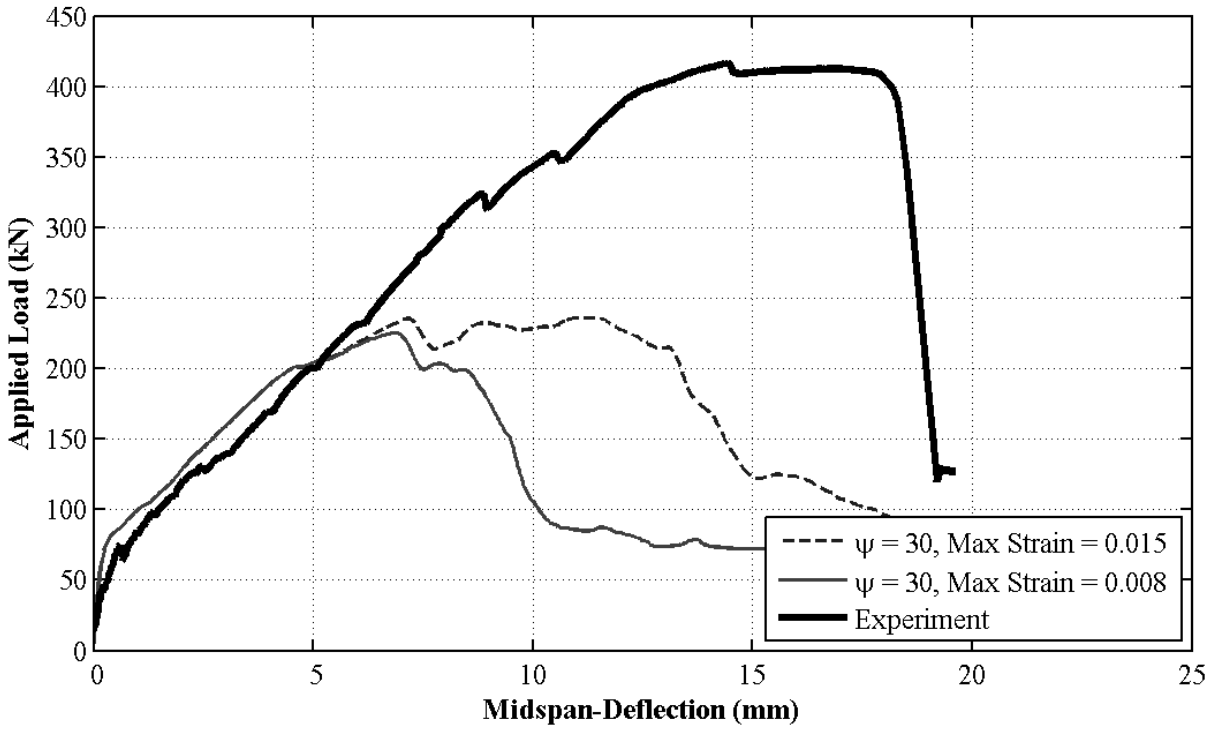

Figure 6.1: Influence of Maximum Compressive Strain with $\psi = 30°$ - BM 16-150

It can be seen that the model recommended for beams with no stirrups ($\varepsilon_{c,max} = 0.008$ and $\psi = 30°$) severely underpredicted the ultimate load of BM 16-150. This behaviour was observed for all other beams with stirrups. Also shown in Figure 6.1 is the influence of increasing the maximum compressive strain to 0.015 while maintaining a dilation angle of 30°. Similar to the beams with no stirrups, increasing the maximum strain had negligible influence on the beam strength. However, Figures 6.2 and 6.3 present the influence of

changing $\varepsilon_{c,max}$ on the load-deflection responses for BM 12-150 and BM 12-220, respectively, when an increased dilation angle of 50° is used.

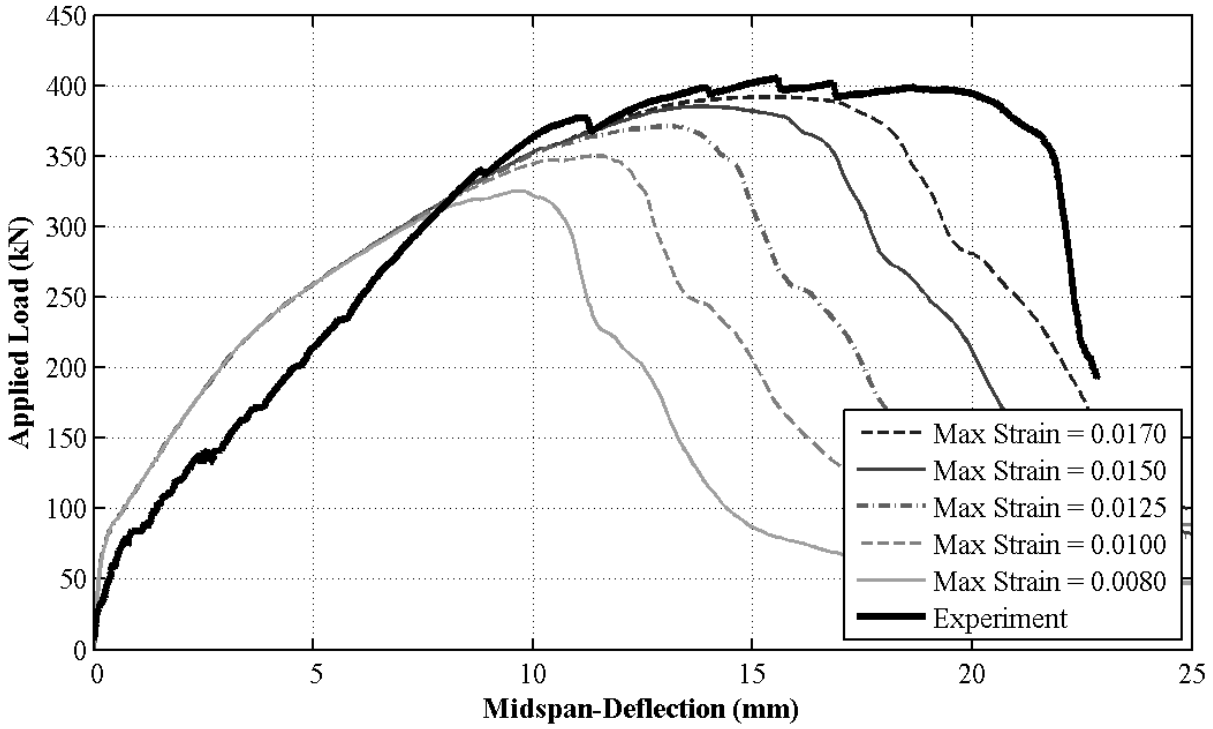

Figure 6.2: Influence of Maximum Compressive Strain with $\psi = 50°$ - BM 12-150

In the modelling of beams with no stirrups, the magnitude of $\varepsilon_{c,max}$ had no influence on the beam strength as these beams experienced shear-tension failures that were not governed by the crushing of concrete. Similarly, the modelling of beams with stirrups and a dilation angle of 30° also yielded brittle tension failures, thus $\varepsilon_{c,max}$ had no influence again. However, it can be seen that the maximum compressive strain has a significant influence on the response of beams with stirrups once the dilation angle is increased to 50°. As $\varepsilon_{c,max}$ increases, the peak load and deflection at failure both increase, providing a more ductile response. For BM 12-150, the original Hognestad Parabola caused the beam to fail at a load of 324.9kN and a mid-span deflection of 9.5mm, whereas the modified Hognestad Parabola with a maximum strain of 0.015 caused the beam to fail at 385.1kN and a mid-span deflection of 14mm. This dependence on the concrete compression model is ideal for the modelling of beams with stirrups, as the experimental beams experienced

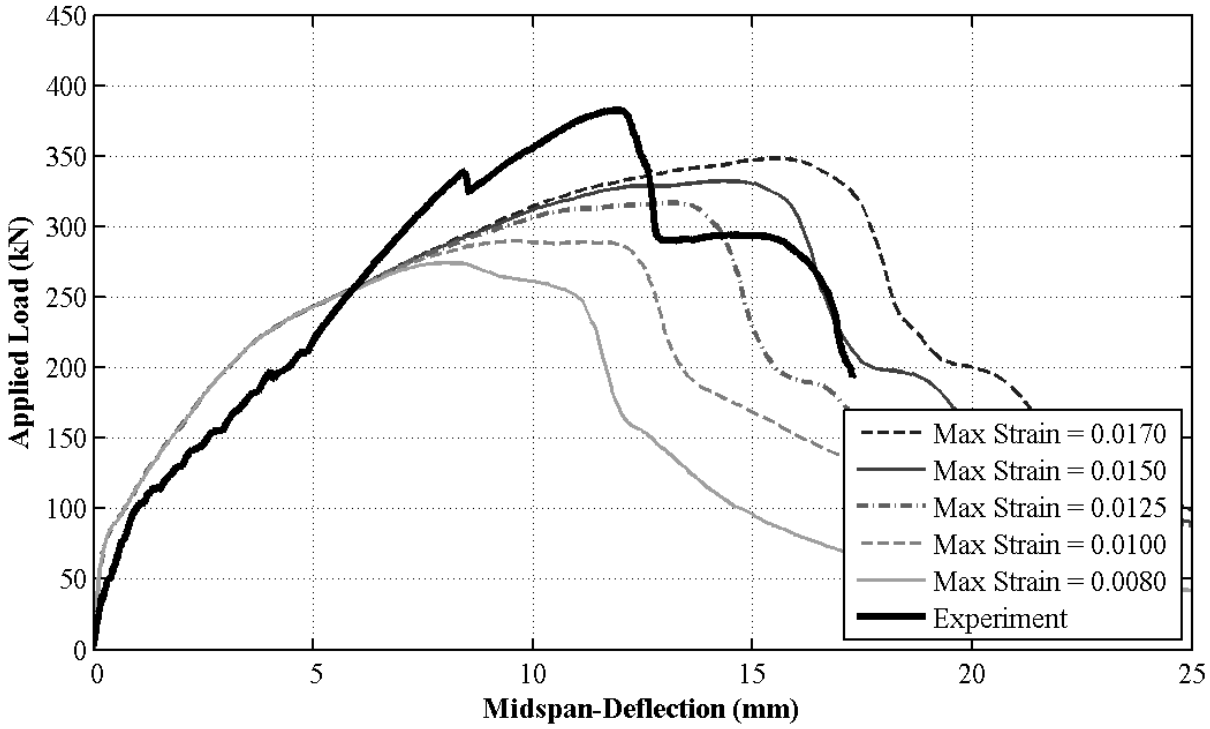

Figure 6.3: Influence of Maximum Compressive Strain with $\psi = 50°$ - BM 12-220

compression crushing of diagonal struts that extended from the point of load application to the support bearing plate. Therefore, a model that is able to capture the ductility of the concrete reinforced with stirrups and to shift the failure mode from a brittle tension fracture to a more ductile crushing failure is desired.

When modelling the tension behaviour of concrete, various post-peak models were used to recognize the ability of concrete to sustain loading after cracking as presented in Section 5.2 (stress-strain, fracture energy, stress-displacement). The manipulation of these post-cracking relationships simulated the effects of tension stiffening by controlling the rate at which the concrete lost its tensile carrying capacity. The influence of the concrete-reinforcement interaction that governs the effects of tension stiffening was therefore incorporated into the concrete modelling and not the reinforcement modelling. Similarly, the stirrups also interact with the concrete and significantly influence the structure's behaviour. These stirrups act to carry tensile loads across cracks, thus preventing brittle shear failures.

More significantly, these stirrups provide passive confinement to the concrete bound within the stirrups as a result of the inelastic expansion, or dilation, that concrete experiences under high compressive loading. This confinement strengthens the beam response by allowing the concrete to carry higher stresses. Similar to the impact of tension stiffening, the influence of confinement will not be captured by ABAQUS. Therefore, the manipulation of the concrete compression model, similar to the manipulation of the tension models, allows for the effects of confinement to be reflected in the simulation outputs.

Therefore, in order for the concrete compression model to simulate the failures observed during the experimental testing, the combined calibration of the maximum compressive strain, $\varepsilon_{c,max}$, and the dilation angle, ψ, was necessary. Further discussion of the influence of the dilation angle on the response of beams with stirrups is provided in Section 6.4.1.

6.2 Tension Modelling

Section 3.3.2 introduced three methods to define the uniaxial post-peak tensile response of concrete in the Concrete Damaged Plasticity Model: 1) Stress-strain approach, 2) Fracture energy approach, and 3) Crack-opening-displacement approach.

The use of the stress-strain tension model was considered in the modelling of beams with no stirrups. It was found that this approach led to significant numerical issues that forced the analyses to terminate prematurely, thus preventing the full beam response from being captured. This method may also lead to unreasonable mesh sensitivity in regions of concrete that contain little or no reinforcement. Therefore, this approach was not pursued in the modelling of beams with stirrups. Furthermore, the fracture energy approach is an extension of the crack-opening-displacement approach used in Section 5.2, thus both methods will be discussed together.

6.2.1 Crack-Opening-Displacement Approach

Section 5.2.2 provided an overview of the various models that have been proposed to predict the fracture energy of concrete, G_f. Table 6.1 provides a summary of the predicted G_f values for all beams with stirrups using the proposed models. As a concrete compressive strength of $f_c^{'} = 56.5$MPa was used for all beams with stirrups, the values presented are applicable to all beams studied in this chapter.

Table 6.1: Fracture Energy Predictions for Beams with Stirrups

Beam	$f_c^{'}$ (MPa)	f_{ck} (MPa)	f_{cm} (MPa)	G_f (N/m)			
				Model Code 1990	Trunk and Wittmann 1998	fib Bulletin 42 2008	Model Code 2010
ALL	56.5	54.9	62.9	94.0	165.7	158.0	153.8

As the concrete compressive strength used for the beams with stirrups was slightly higher than the strengths used for the beams with no stirrups, the predicted fracture energies are also slightly higher. The exception to this is the Trunk and Wittmann (1998) model which is a function of the maximum aggregate size, d_{max}, and not the compressive strength. To define the strain-softening behaviour of the concrete under tensile loading, it was concluded previously that specifying the tensile stress as a function of the crack-opening-displacement, w, provided both accurate and efficient solutions. Three stress-displacement curves were studied, including linear, bilinear, and exponential relationships. Figures 6.4 and 6.5 show the influence of various fracture energies using the bilinear stress-displacement approach on the load-displacement response of BM 16-150 and BM 25-220, respectively.

As shown in Figures 6.4 and 6.5, fracture energies ranging from 70N/m to 150N/m were considered. The influence of the fracture energy is most apparent in the service loading region after the formation of major cracks and prior to the obtainment of the peak load.

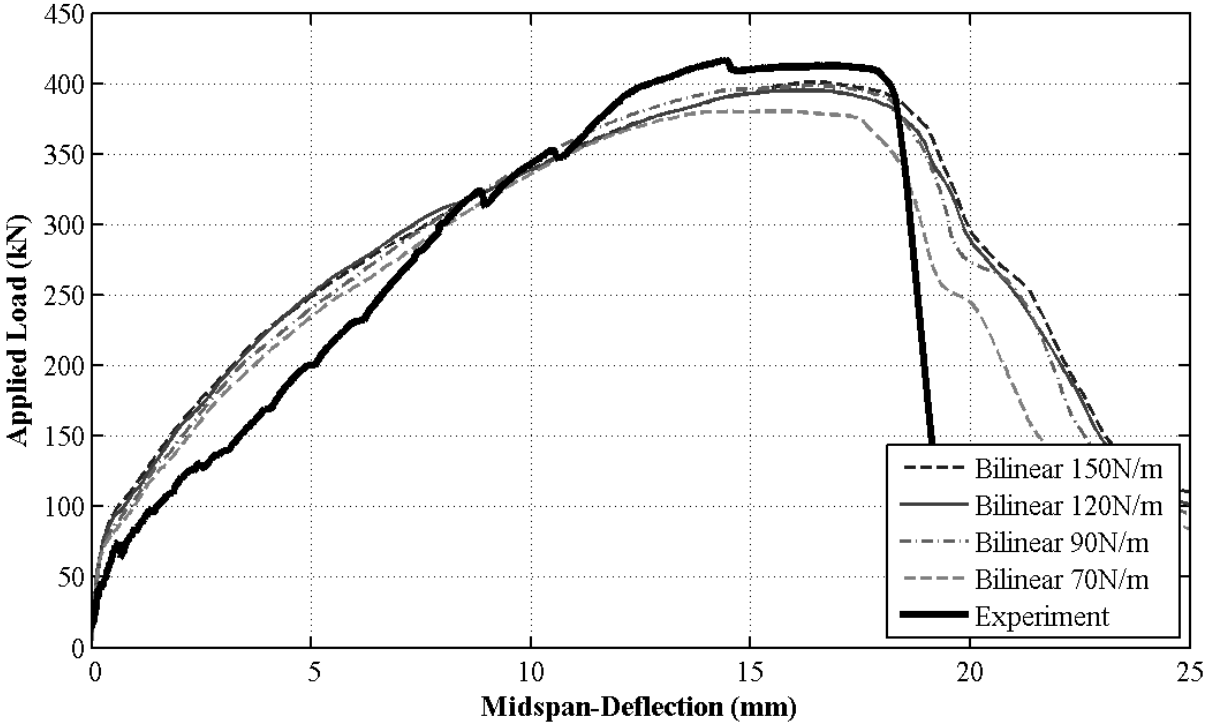

Figure 6.4: Influence of Fracture Energy - BM 16-150

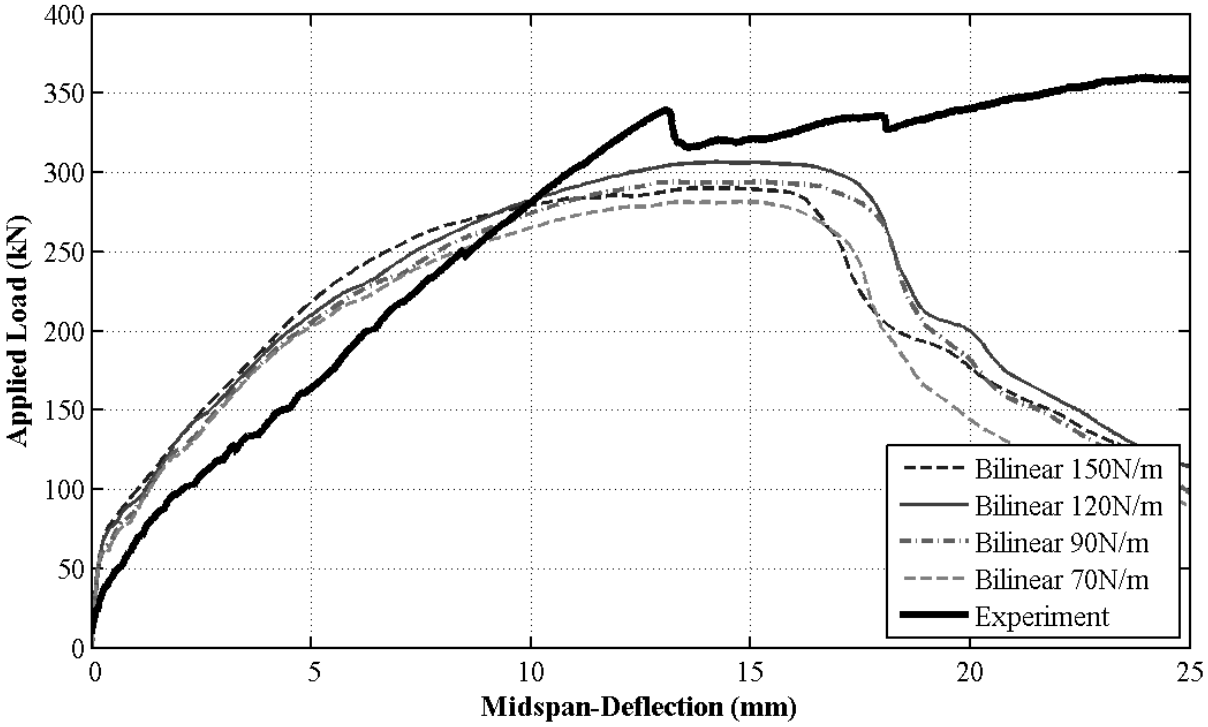

Figure 6.5: Influence of Fracture Energy - BM 25-220

As the fracture energy increased, more energy was required to crack the concrete, thus producing a stiffer member response. All fracture energies studied produced similar peak loads and failure modes. This is to be expected, as the definition of the concrete compression model and calibration of the dilation angle used in the modelling of beams with stirrups shifted the failure modes to compression-governed. Therefore, the post-peak tension modelling played a significantly lesser role in the modelling of beams with stirrups as compared to the modelling of beams with no stirrups. In some cases, BM 12-150 and BM 25-150 in particular, a larger fracture energy was able to produce higher peak loads that matched closer to the experimental results. However, these larger fracture energies also produced stiffer deflection responses. Therefore, similar to the modelling of beams with no stirrups, a lower fracture energy of $G_f = 90\text{N/m}$ was selected as the most appropriate value as a result of the consistency in results, strong accuracy of the peak load predictions, and superior agreement to the service-loading deflection responses.

Figures 6.6 and 6.7 present the influence of various fracture energy values on the longitudinal reinforcement tensile strains for BM 16-150 and BM 25-220, respectively. The bilinear stress-displacement relationship was used to model the concrete in tension, and truss sections were used to model the reinforcement.

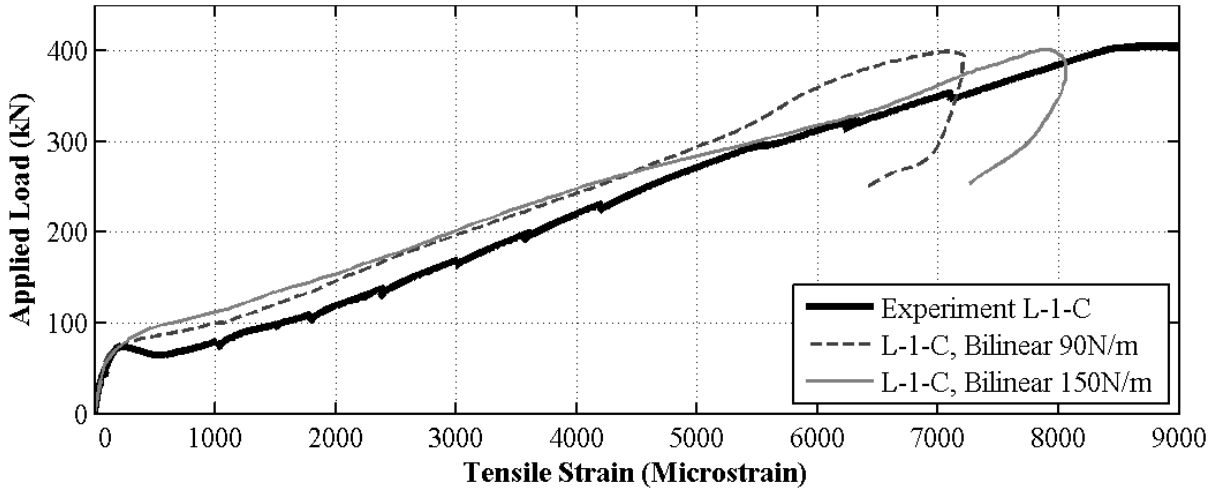

Figure 6.6: Influence of Fracture Energy on Reinforcement Strains - BM 16-150

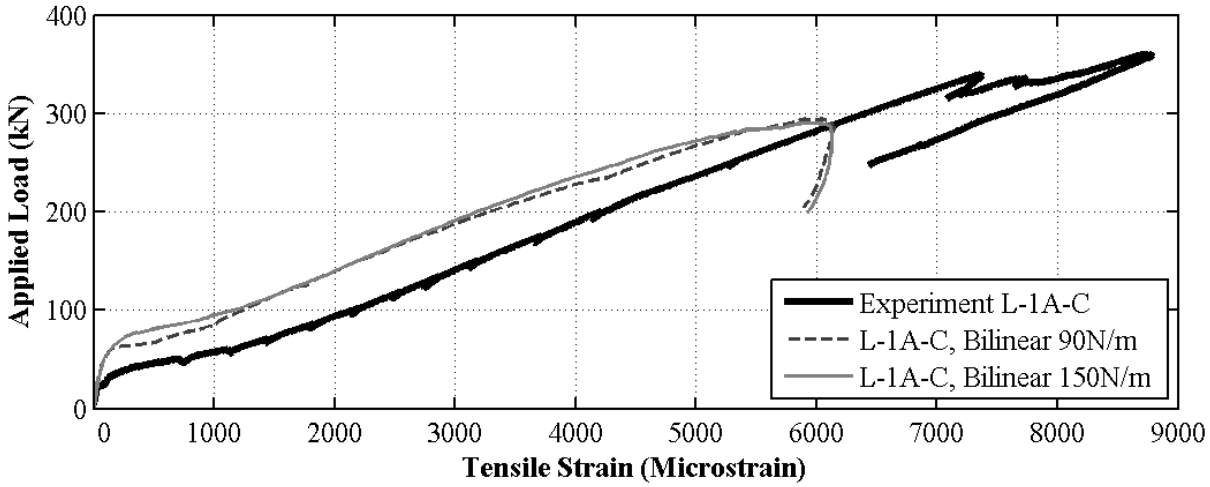

Figure 6.7: Influence of Fracture Energy on Reinforcement Strains - BM 25-220

It can be seen that the bilinear stress-displacement relationship with a fracture energy of 90N/m provided a strong agreement to the experimental strain profile at the L-1-C strain gauge location for BM 16-150. With an increased fracture energy of 150N/m, the reinforcement exhibited a modest increase in strength immediately after cracking before converging to the 90N/m response. With a larger fracture energy, the tensile strength of the concrete degrades at a slower rate upon cracking, thus will stiffen the reinforcement response. For the modelling of beams with stirrups, the influence of fracture energy on the reinforcement strains is only apparant immediately after cracking. This influence is far less pronounced than was observed in the modelling of beams with no stirrups (Figure 5.9, 5.10).

Figures 6.8 and 6.9 compare the influence of the three stress-displacement curves studied (linear, bilinear, and exponential) on the beam response for BM 16-150 and BM 25-220, respectively, with a constant fracture energy of 90N/m.

For each beam with stirrups, all three stress-displacement models produced similar peak loads. For BM 16-150, the bilinear, exponential, and linear functions yielded peak loads of 398.6kN, 389.4kN, and 372.6kN, respectively. However, the difference between each method was observed in the post-cracking region prior to the obtainment of the peak load.

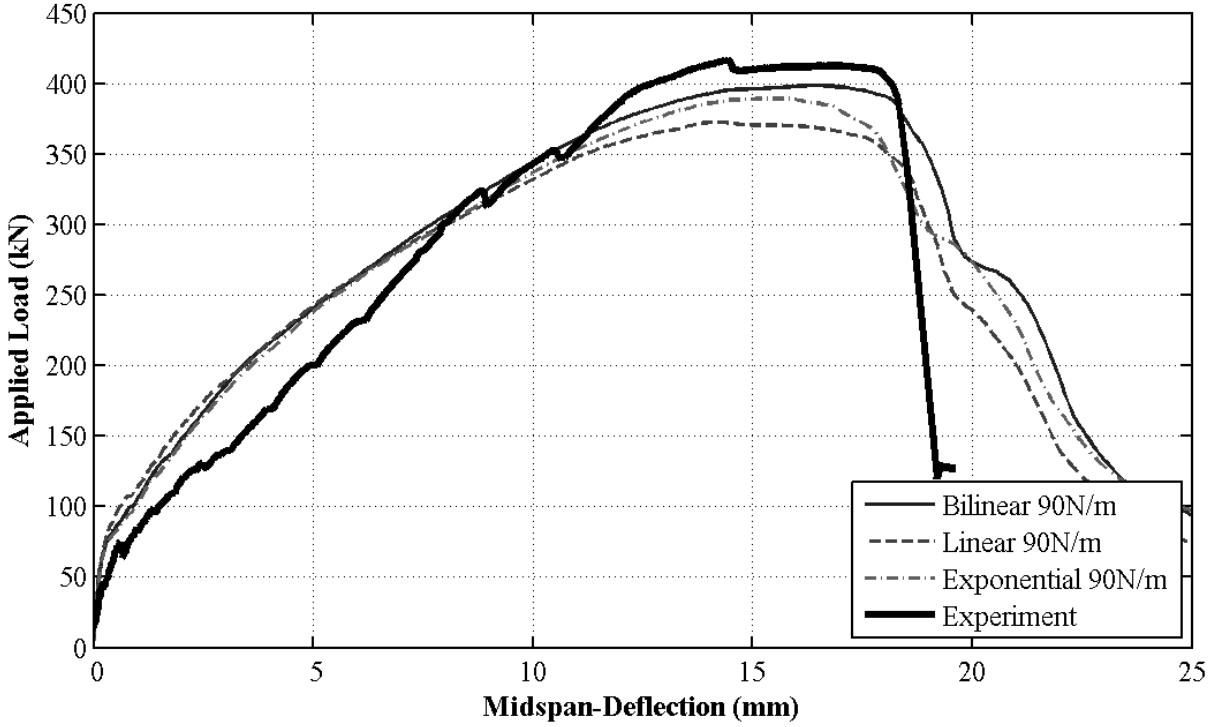

Figure 6.8: Influence of Stress-Displacement Model - BM 16-150

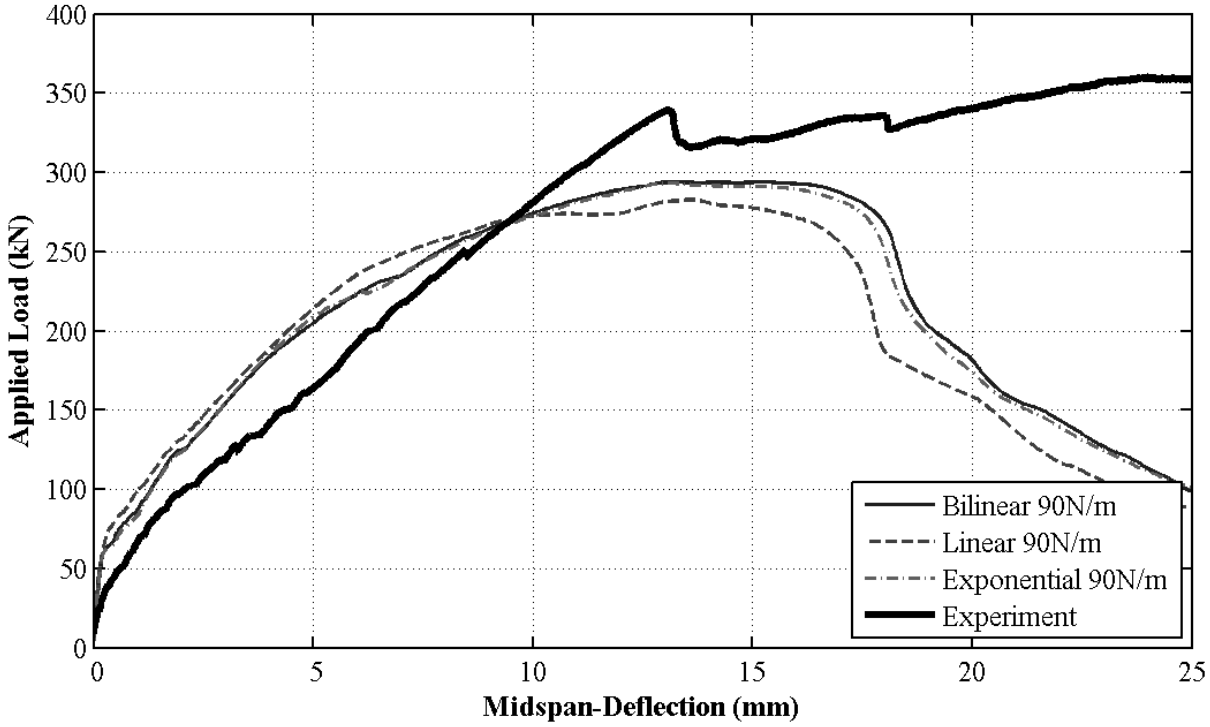

Figure 6.9: Influence of Stress-Displacement Model - BM 25-220

At a load of approximately 70kN, the three responses begin to diverge. Although the beams using the bilinear and exponential functions continued to match closely, the linear stress-displacement function produced a stiffer response after the major cracking occurred. This behaviour is consistent with the results presented for beams with no stirrups, and is a result of the rate of strength loss associated with the stress-displacement responses as discussed in Section 5.2.4.

Figures 6.10 and 6.11 compare the influence of the stress-displacement tension models on the longitudinal reinforcement strain profiles for BM 16-150 and BM 25-220, respectively, with a constant fracture energy of 90N/m. The use of the exponential stress-displacement model was omitted here for clarity as this function provided similar results to the bilinear approach for all beams.

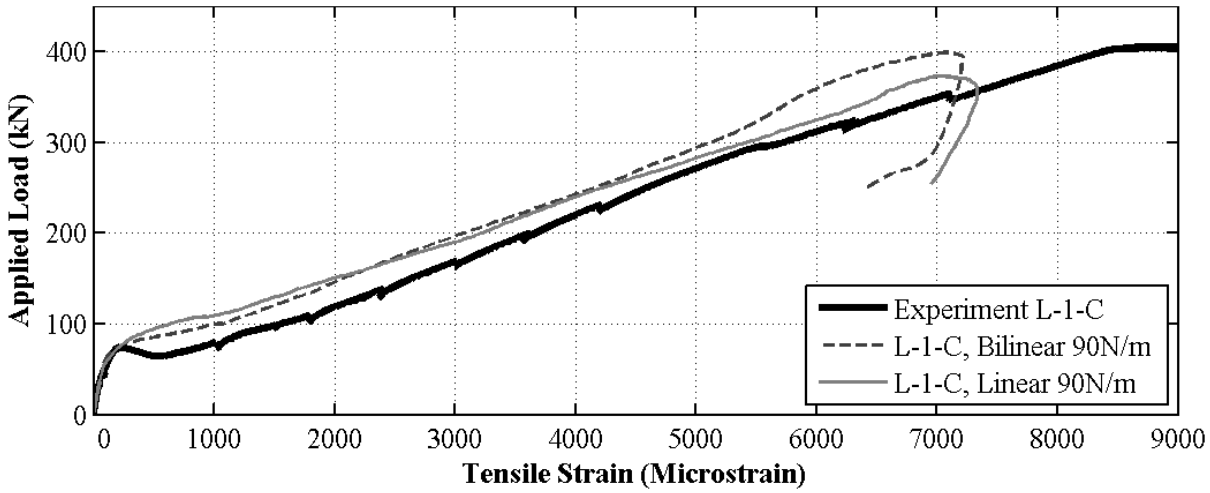

Figure 6.10: Influence of Stress-Displacement Model on Reinf. Strains - BM 16-150

Again, all tension models provided similar strain profiles. However, the linear function is able to sustain larger tensile stresses than the bilinear and exponential models for a wide range of crack-displacements, thus resulting in a slightly stiffer strain response immediately after cracking. Referring to Figures 6.6 and 6.7, the use of a higher fracture energy produced a similar effect as using the linear tension model.

It has been shown that a fracture energy of 90N/m is effective in modelling the beams

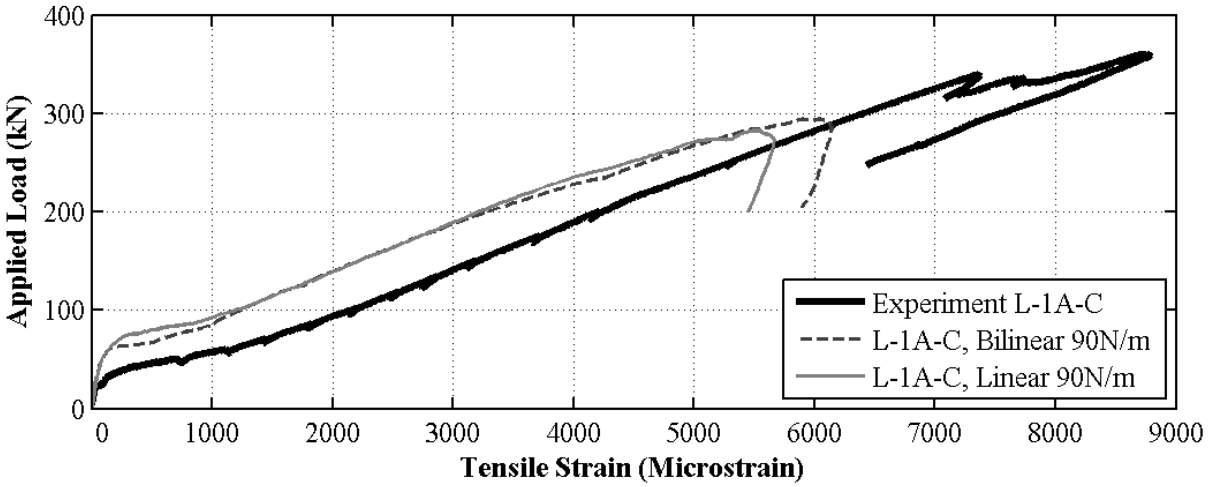

Figure 6.11: Influence of Stress-Displacement Model on Reinf. Strains - BM 25-220

with stirrups. The bilinear and exponential tension models produce similar results that agree strongly with the experimental data. The use of high fracture energies or the linear tension model also produce accurate results, but tend to over-stiffen the beam responses and reinforcement strain profiles within the service-loading range.

6.3 Damage Modelling

The influence of incorporating damage into the beam models was studied. Similar to the modelling of beams with no stirrups, the following four cases were considered:

1. Compression and tension damage included
2. No damage included
3. Compression damage only
4. Tension damage only

Figures 6.12 and 6.13 show the influence of each of the four cases on the load-displacement responses for BM 12-150 and BM 12-220, respectively.

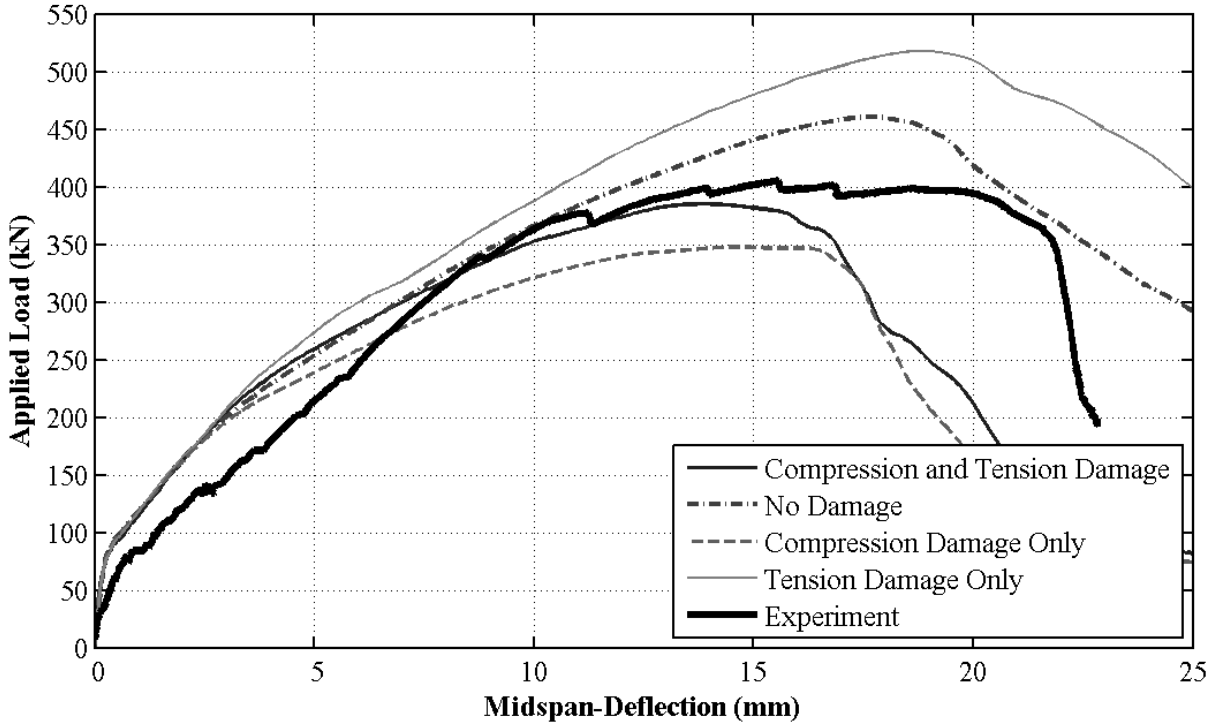

Figure 6.12: Influence of Damage - BM 12-150

The responses of the four cases presented were similar for all beams with stirrups, regardless of stirrup spacing or longitudinal bar arrangement. The following list is the order that each case consistently conformed to for each beam, ordered from strongest peak load to weakest peak load: Tension damage only, no damage, compression and tension damage, and compression damage only.

First compare Cases 2 and 3; the omission of both damage parameters versus the use of compression damage only, respectively. When compression damage is included, the peak load achieved by BM 12-150 was reduced significantly from 460.6kN to 347.8kN. Similar to the beams with no stirrups, this proves that the stiffness degradation of concrete under compressive loads plays a significant role in the structure's response, even under monotonic loading.

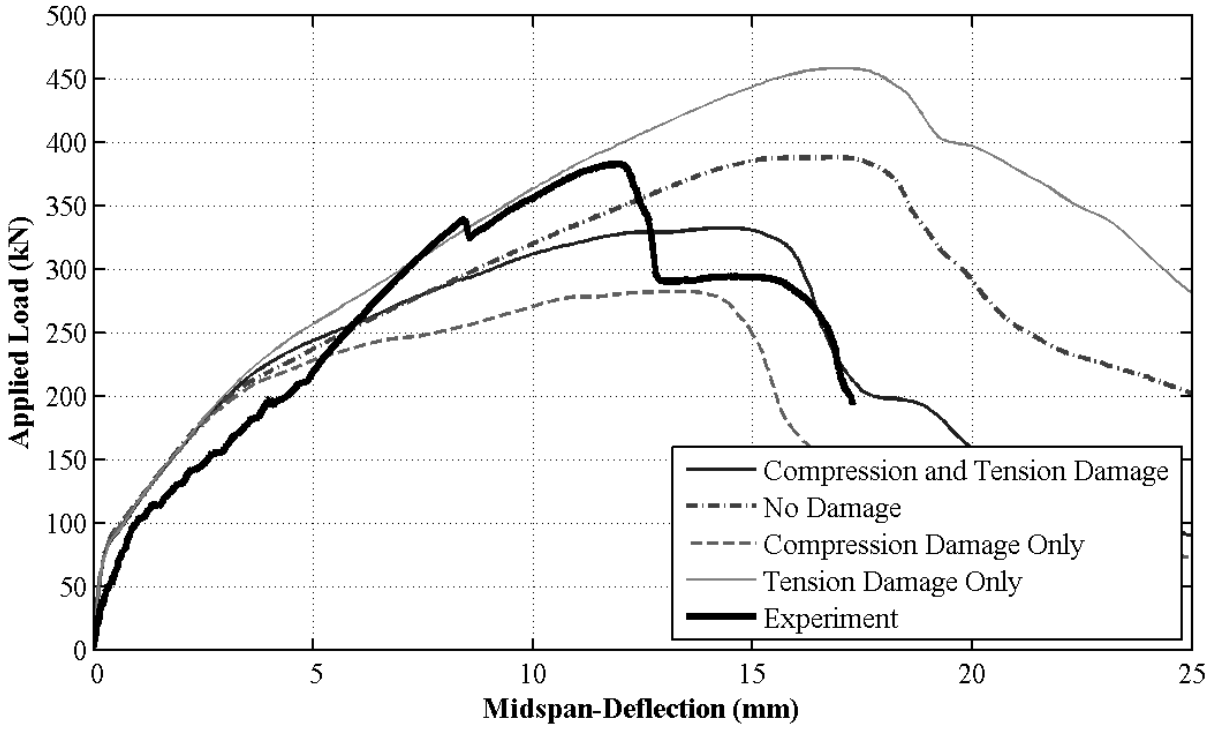

Figure 6.13: Influence of Damage - BM 12-220

Next compare Cases 2 and 4; the omission of both damage parameters versus the use of tension damage only, respectively. For beams with no stirrups, it was found that the inclusion of only tension damage produced no significant difference to the load-deflection responses as compared to the no-damage response. However, for all beams with stirrups, BM 25-220 most notably, the inclusion of tension damage resulted in the significant increase in beam stiffness and peak load. This means that the inclusion of tension damage produces a structure that is in fact stronger, not weaker, which is a counter-intuitive observation.

When starting with zero damage, the addition of compression damage or tension damage individually has been discussed. Now consider the alternative perspective by starting with both damage parameters and removing compression or tension damage individually. Compare Cases 1 and 3; the use of both damage parameters versus the use of compression damage only. When tension damage is removed, the peak load achieved by each beam is reduced. Next, compare Cases 1 and 4; the use of both damage parameters versus the use

of tension damage only. When compression damage is removed, the peak load is increased significantly. The following summary can be made regarding the influence of including tension and/or compression damage parameters on the peak load of beams with stirrups.

Start with No Damage:

Add Tension Damage: Peak Load $\uparrow$

Add Compression Damage: Peak Load $\downarrow\downarrow$

Add Tension and Compression Damage: Peak Load $\uparrow + \downarrow\downarrow = \downarrow$

Alternatively, start with Tension and Compression Damage:

Remove Tension Damage: Peak Load $\downarrow$

Remove Compression Damage: Peak Load $\uparrow\uparrow$

Remove both Tension and Compression Damage: Peak Load $\downarrow + \uparrow\uparrow = \uparrow$

It is clear that the use of compression damage parameters has a detrimental, or degrading, effect on the beam stiffness and failure load. Conversely, it appears that the use of tension damage parameters has a strengthening effect on the beam response. Similar to the beams with no stirrups, the degrading effects of the compression damage have shown to be stronger than the strengthening effects of the tension damage. Thus, the combined use of both compression and tension damage parameters leads to a weaker beam as compared to the no-damage case and is able to accurately replicate the experimental data.

6.4 Plasticity Modelling

The plasticity modelling within the Concrete Damaged Plasticity Model is controlled by five parameters as introduced in Section 3.3.4: ψ, ϵ, σ_{bo}/σ_{co}, K_c, and μ. Similar to the modelling of beams with no stirrups, the default values of 1.16, 2/3, and 0.1 were used for

the parameters σ_{bo}/σ_{co}, K_c, and ϵ, respectively, for the modelling of beams with stirrups. The purpose of this section is to study the influence of the remaining two parameters, ψ and μ, on the modelling of beams with stirrups.

6.4.1 Dilation Angle

As discussed in Section 5.4.1, typical dilation angles used for normal grade concrete range from 30° to 40°. The influence of various dilation angles, ranging from 30° to 50°, on the load-deflection response was studied for all beams with stirrups. Figures 6.14 and 6.15 show the results for BM 16-150 and BM 25-220, respectively. The responses presented here all used a maximum concrete compressive strain of $\varepsilon_{c,max} = 0.015$.

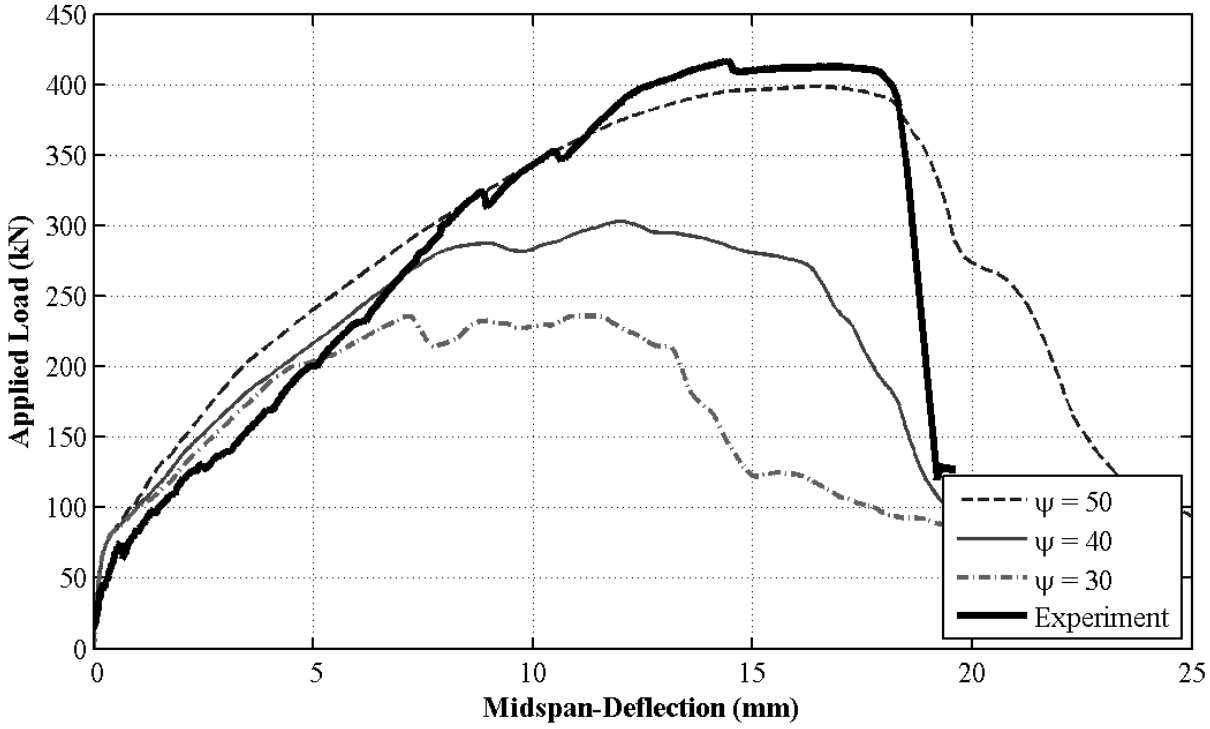

Figure 6.14: Influence of Dilation Angle - BM 16-150

Figures 6.14 and 6.15 show that the beam responses are highly dependent on the dilation angle when a maximum compressive strain of 0.015 is used. Similar to the beams with no stirrups, as the dilation angle increases, the beam's response becomes more ductile and

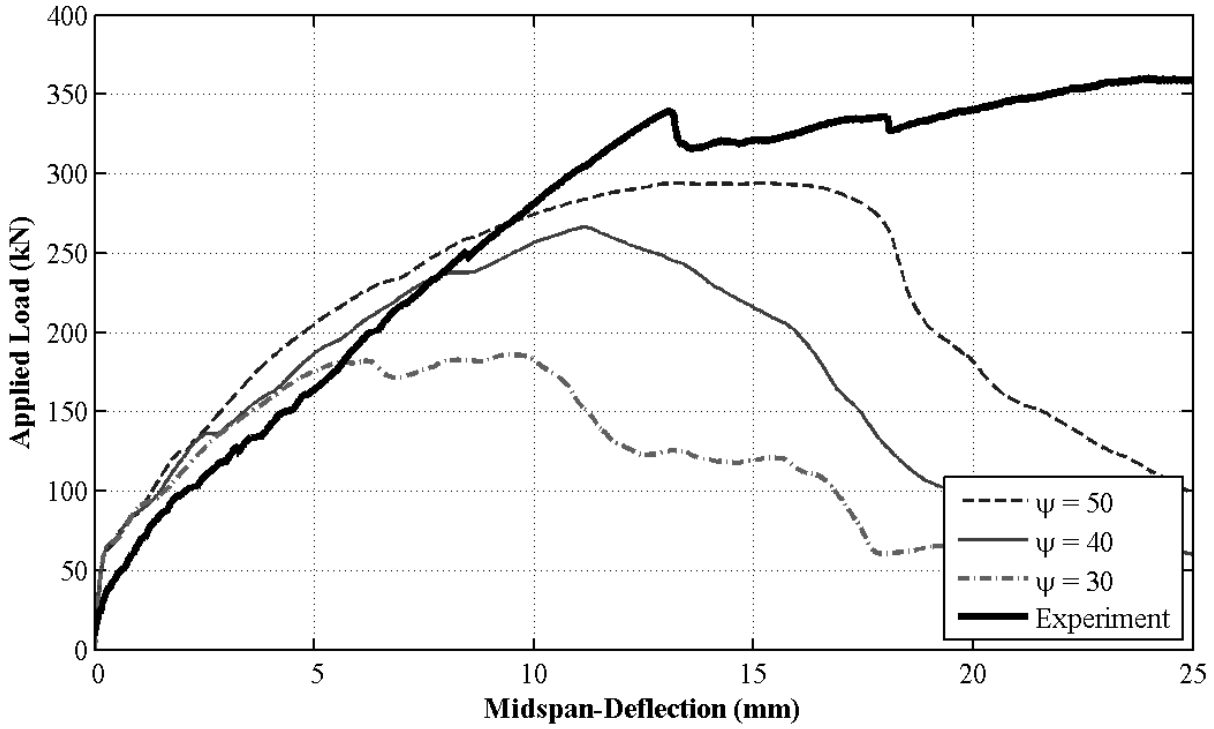

Figure 6.15: Influence of Dilation Angle - BM 25-220

fails at higher loads and larger mid-span deflections. Furthermore, with larger dilation angles, the post-cracking response becomes much stiffer. For the modelling of beams with no stirrups, a dilation angle of 30° provided the most accurate results while an angle of 50° led to the significant overprediction of the failure load. For the modelling of beams with stirrups, a dilation angle of 30° was found to severely underpredict the failure load while an angle of 50° provided a stronger agreement with experimental results. Considering BM 16-150, an angle of 30° resulted in a peak load of 236.0kN, while an increased angle of 50° resulted in a peak load of 398.6kN; a 69% increase.

Malm (2006) performed finite element modelling of wide-flanged concrete deep beams subjected to four-point bending using ABAQUS. The beams studied had very small shear span to effective depth ratios (a/d) of 1.25, thus experienced shear failures. The beams utilized stirrups in the flanges and in the web. Concrete experiences inelastic volume expansion, or dilation, under high compressive stresses. As concrete dilates, the stirrups will resist

this expansion and will exert passive confinement to the concrete. This confinement increases the ductility of the concrete by allowing the concrete to carry higher compressive stresses and undergo larger compressive strains. The ABAQUS modelling performed by Malm (2006), however, was unable to account for this confinement effect, thus resulted in beam responses that were significantly weaker than experimental data. To account for the effects of confinement, Malm (2006) used an associated plastic flow rule. This was achieved by equating the dilation angle, ψ, with the concrete material friction angle, β. The formulation used by Malm (2006) to find β was as follows:

$$\psi = \beta = arctan(3/2) = 56.3^{\circ} \tag{6.1}$$

The use of this higher dilation angle produced a more ductile material, thus simulating the effects of high confining stresses. Chen and Han (1988) stated that the use of the associated flow rule has been shown to overestimate the dilation of concrete, which is why the non-associated flow rule is typically used (the non-associated rule is used by ABAQUS). Therefore, by using a larger dilation angle that is close to the material friction angle, one can simulate the associated flow rule, thus allowing for the confinement effects to be considered. It is also interesting to note that the angle of 56.3° as used by Malm (2006) is the maximum dilation angle that ABAQUS will permit the user to input.

Section 6.1 discussed the combined influence of the dilation angle and the maximum compressive strain, $\varepsilon_{c,max}$. Figure 6.16 compares the use of maximum strain values of 0.008 and 0.015 and dilation angles of 30° and 50° for BM 25-220.

With a dilation angle of 30°, brittle failure occurs, thus the increase in maximum compressive strain has little influence. Conversely, with an increased dilation angle of 50°, the beam responses exhibit more ductility and a strong dependence on the maximum compressive strain. Alternatively, increasing only the maximum strain has negligible influence,

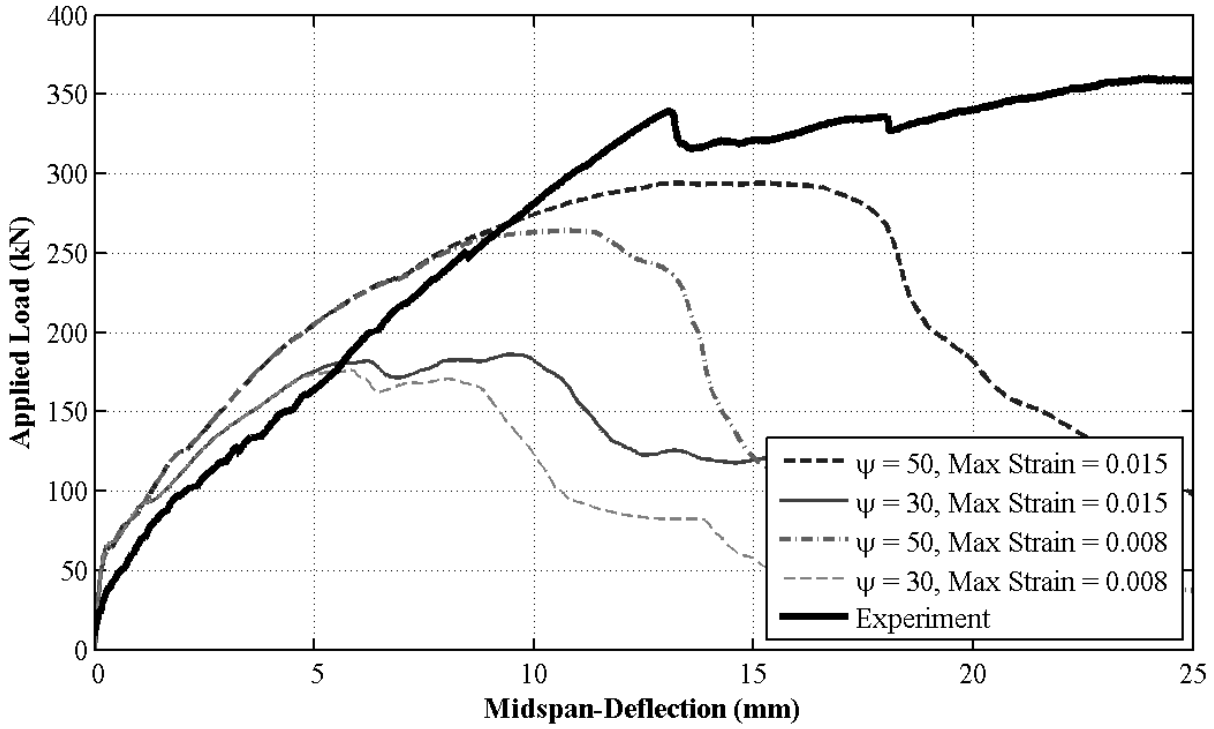

Figure 6.16: Influence of Dilation Angle and Maximum Compressive Strain - BM 25-220

while increasing only the dilation angle proves to strengthen the beam significantly. It is therefore necessary to increase both the dilation angle and the maximum compressive strain to simulate the behaviour as observed during the experimental testing.

In summary, it was concluded that the dilation angle used to model the beams with no stirrups, 30°, was not appropriate for the modelling of beams with stirrups. A larger angle was required to simulate the confinement of the concrete provided by the GFRP stirrups. It was found that an angle of 50° produced results that agreed strongly with the experimental data when used in combination with a larger maximum compressive strain.

6.4.2 Viscoplastic Regularization

Section 5.4.2 presented the influence of the viscoplastic regularization of the constitutive equations for beams with no stirrups by comparing the use of various viscosity parameters,

μ. The influence of various values of μ on the behaviour of beams with stirrups is presented in Figures 6.17 and 6.18 for BM 25-150 and BM 25-220, respectively.

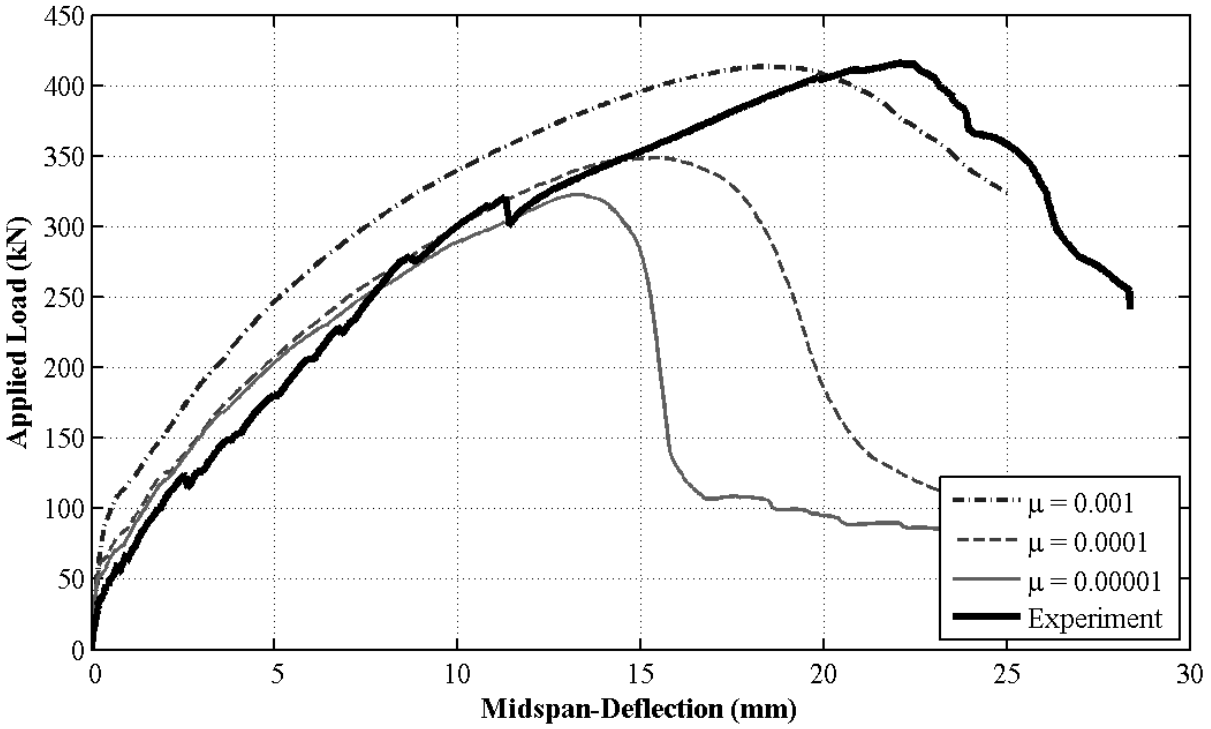

Figure 6.17: Influence of Viscoplastic Regularization - BM 25-150

Similar to the modelling of beams with no stirrups, the use of a viscosity parameter of $\mu = 0$ led to significant numerical issues that caused the analyses to terminate prematurely. Therefore, a non-zero input for μ was required to capture the full spectrum of the beam response. The use of non-zero viscosity parameters including 0.00001, 0.0001, and 0.001 were considered. Beams BM 25-150 and BM 25-220 are presented here as they demonstrate a common pattern found for all beams. When a large viscosity parameter of 0.001 was used, the models failed at peak loads that matched more closely with the experimental failure loads than the other viscosity parameters considered. For BM 25-150, the experimental beam failed at a load of 415.8kN. A viscosity parameter of 0.001 yielded a peak load of 413.3kN (0.6% difference), while a viscosity parameter of 0.0001 yielded a peak load of 348.6kN (16% difference). This would suggest that $\mu = 0.001$ is the most appropriate value. However, the deflection response associated with this viscosity param-

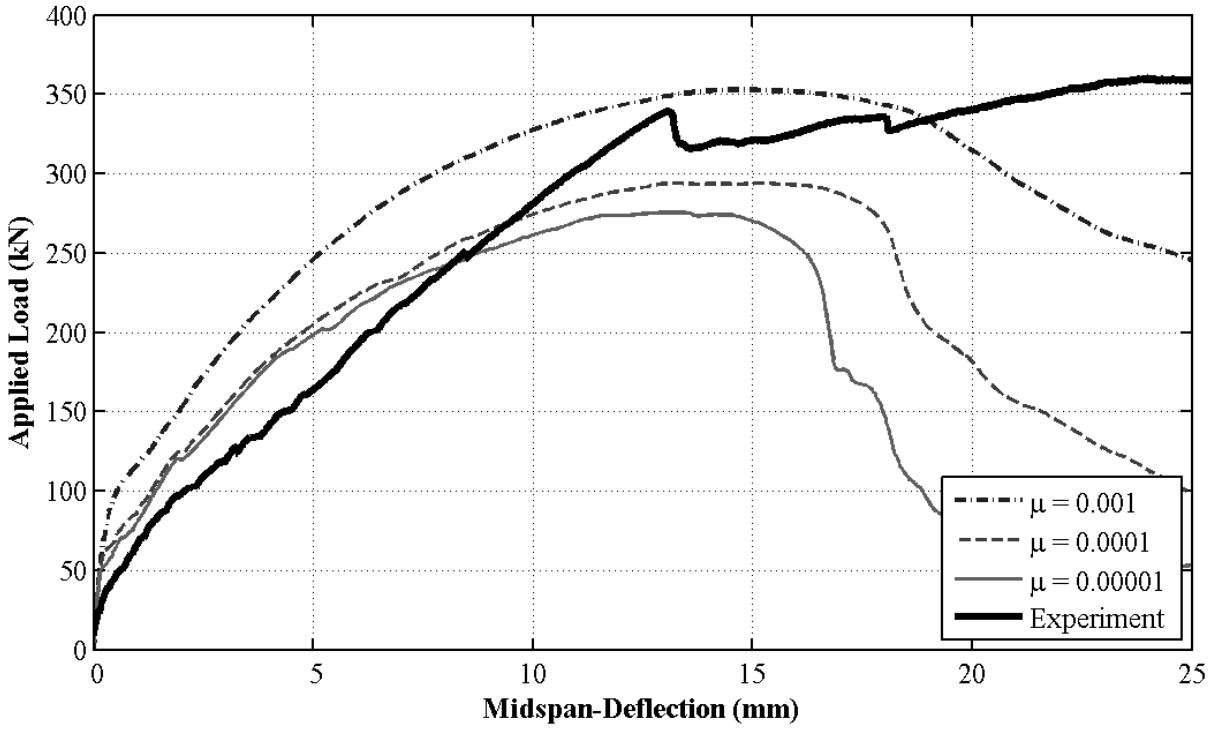

Figure 6.18: Influence of Viscoplastic Regularization - BM 25-220

eter is severely stiffer than the experimental response. With larger values of μ, the beam will behave more elastically, thus reducing the accuracy and legitimacy of the model. To remain consistent with the modelling of beams with no stirrups, a value of $\mu = 0.0001$ was selected for the modelling of all beams with stirrups. This small, non-zero value introduces viscoplastic regularization that overcomes the numerical solution issues, improves computational efficiency, and is able to produce accurate responses. Although this value of μ appears to severely underpredict the experimental peak load of BM 25-150, Section 6.8 will show that this model provides results that match closely to the shear strength predictions proposed by Nehdi et al. (2007).

6.5 Mesh Refinement

The concrete mesh alternatives studied for the modelling of beams with no stirrups as presented in Table 5.5 were also studied for the beams with stirrups. Recall that the beams with 25mm diameter longitudinal bars required modifications to the mesh alternatives (denoted using brackets) in order to maintain element aspect ratios close to 1.0. Figures 6.19 and 6.20 present the influence of mesh refinement on the load-deflection responses for BM 12-150 and BM 25-220, respectively.

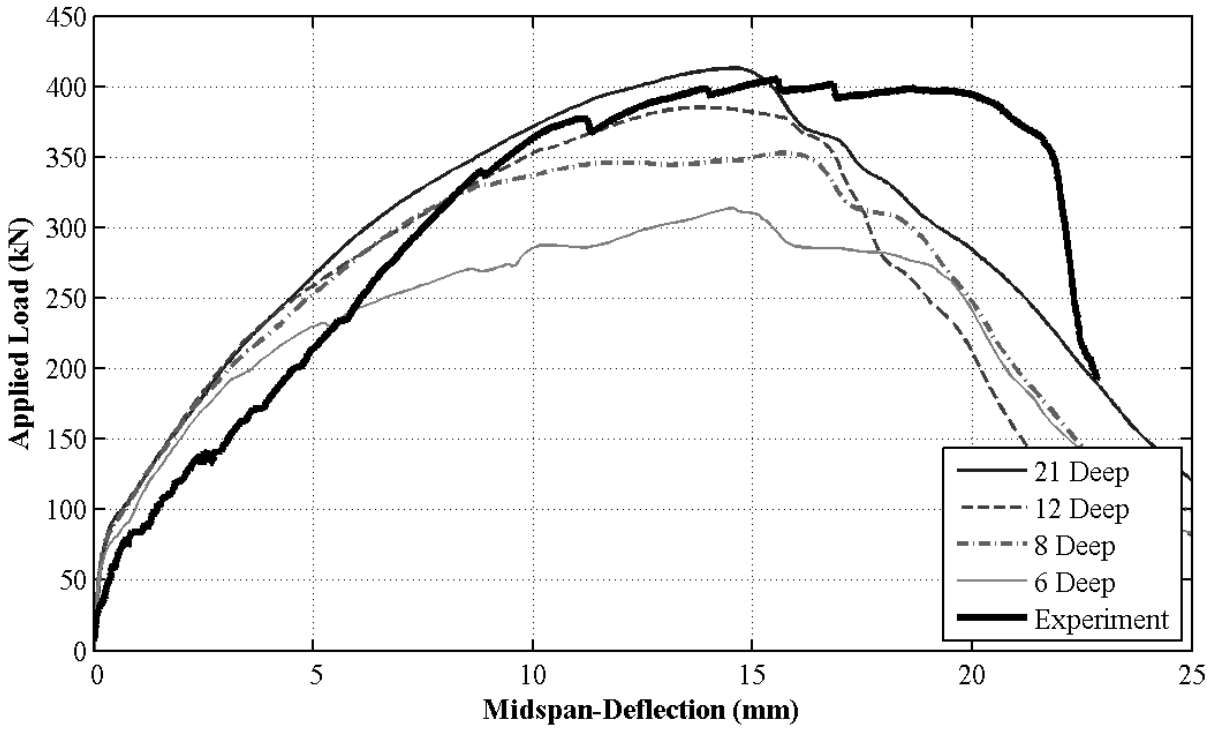

Figure 6.19: Influence of Mesh Refinement - BM 12-150

It can be seen that the influence of mesh refinement follows the same pattern as observed with the modelling of beams with no stirrups. As the mesh becomes finer, the pre-peak response of the beam becomes stiffer. This behaviour was consistent for all beams with stirrups. The 6 (5) element deep mesh proved to severely underpredict the ultimate load of each beam. For all beams, with the exception of BM 12-220, the 12-deep and 16 (15)-deep meshes agreed strongly and were able to provide the highest level of accuracy and

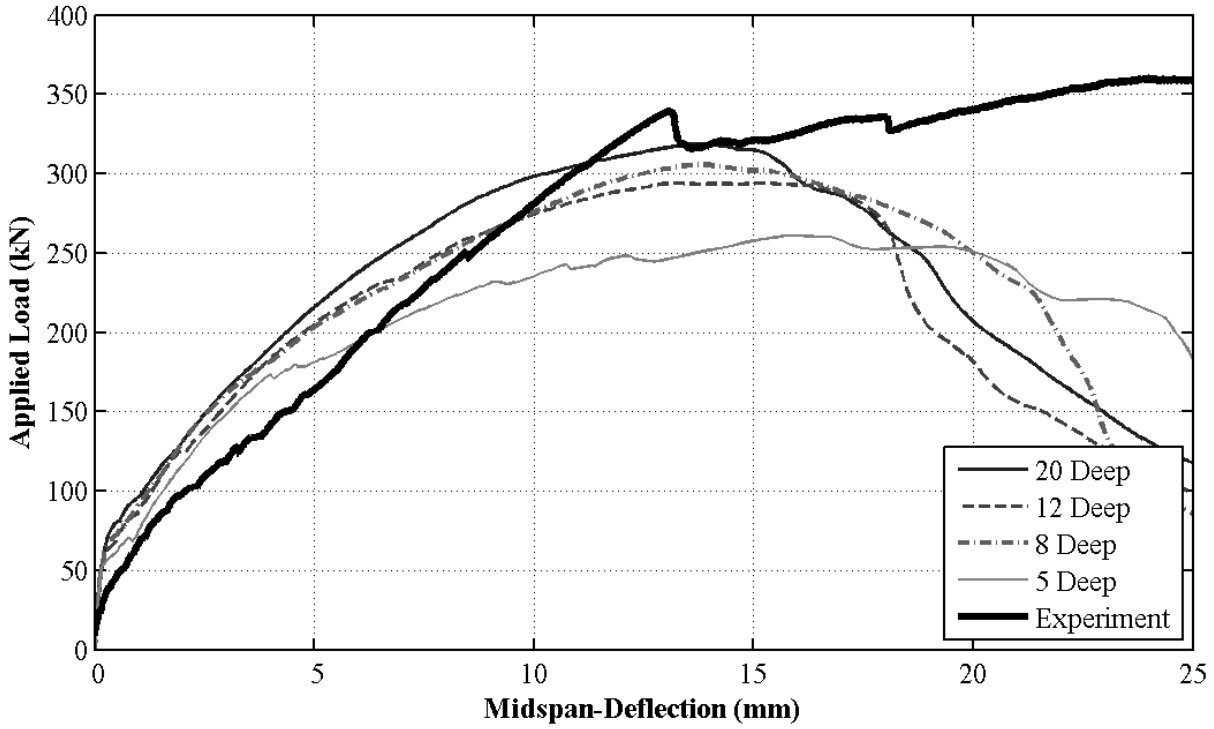

Figure 6.20: Influence of Mesh Refinement - BM 25-220

consistency with the experimental results. The 21 (20)-deep mesh either provided similar results to the 12-deep mesh or yielded responses that were far stiffer. Therefore, similar to the beams with no stirrups, it was concluded that a mesh utilizing 12 elements in the cross-section depth was the alternative that optimized both the accuracy of the model predictions and the computational effort required to achieve that accuracy.

Figure 6.21 compares the crack patterns at failure for each of the five mesh refinements studied for BM 12-150. The crack pattern observed at failure during the experimental testing is also shown. Note that the right end of each mesh represents the mid-span section of the beam (point of load application), and the left end of each mesh represents the location of the support.

It can be seen that all mesh densities accurately capture the presence of diagonal shear cracks, in the form of large plastic strains, spanning from the load point to the support point. As the mesh is refined, the crack pattern remains similar, but the crack bands

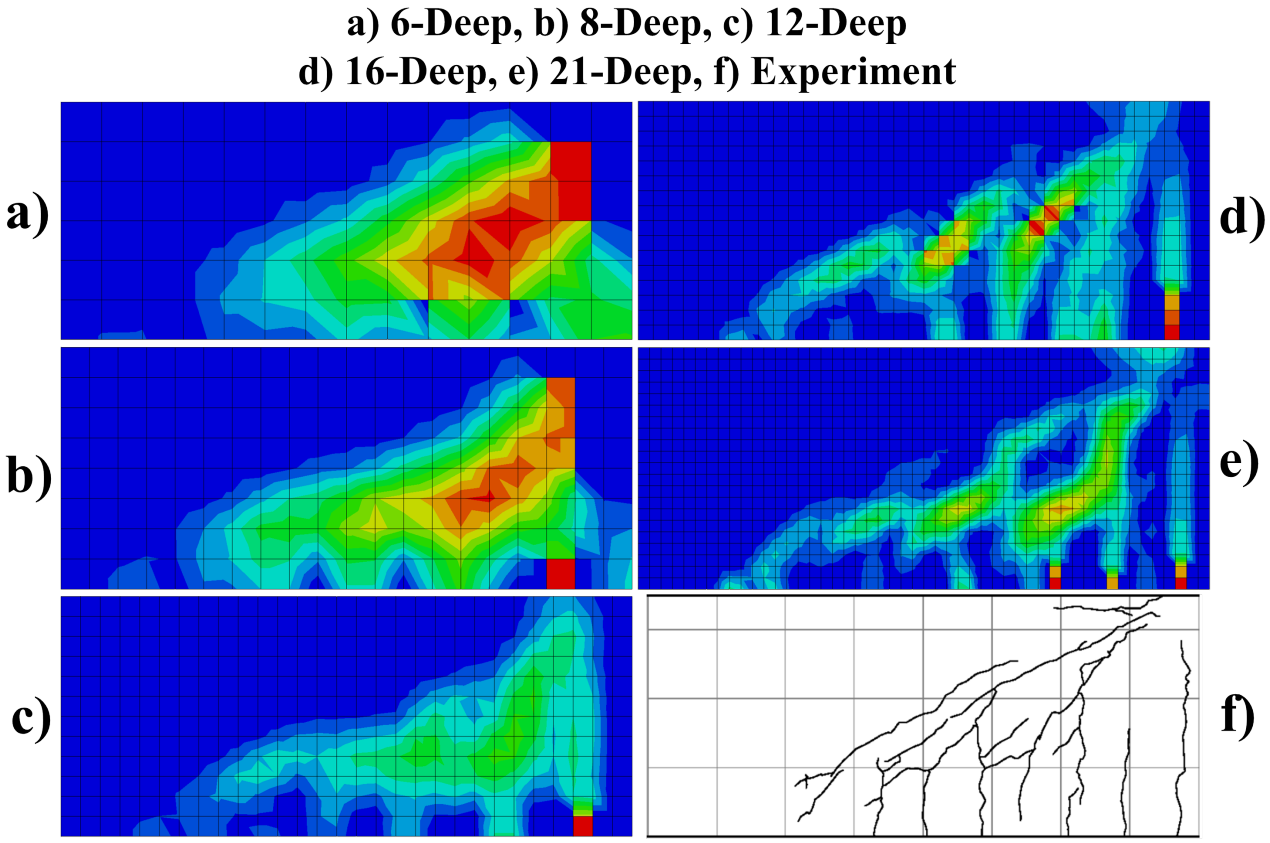

Figure 6.21: Influence of Mesh Refinement on Crack Pattern - BM 12-150

become narrower and better defined. The use of finer meshes, 16-deep and 21-deep, provide crack patterns that agree strongly with the experimentally observed pattern. These results are consistent for all other beams with stirrups.

6.6 Modelling of GFRP Reinforcement

Two methods of modelling the GFRP reinforcement were studied in this research: 1) Discrete, one-dimensional truss sections; and 2) Smeared, reinforced membrane sections. As this chapter focuses on beams with stirrups, this section will discuss the modelling of both the longitudinal and transverse reinforcement.

6.6.1 GFRP Longitudinal Reinforcement

Section 5.6 compared the use of discrete truss sections and reinforced membrane sections to model the longitudinal reinforcing bars in beams with no stirrups. It was demonstrated that both methods produced beam responses that agreed strongly with the experimental behaviour. The tensile strains in the reinforcement were also studied, and it was determined that both modelling methods provided similar strain profiles that matched strongly with the experimental strain gauge data. It was concluded that the use of truss sections was the preferred method of modelling the longitudinal reinforcement for beams with no stirrups. For this reason, discrete truss sections were used exclusively to model the longitudinal bars for all beams with stirrups.

Figures 6.22 and 6.23 show the longitudinal reinforcement strain profiles for BM 16-150 and BM 16-220, respectively. Truss sections were used for all longitudinal reinforcement, and membrane sections were used for the stirrups. A concrete dilation angle of 50° was used with a maximum concrete compressive strain of 0.015.

It can be seen that the truss sections provided accurate strain responses that matched closely with the experimental data. It is important to discuss BM 16-220. During the experimental testing of this beam, a thunderstorm caused the test-frame hydraulics to shut off, thus terminating the testing. The beam was loaded to approximately 43% of the ultimate load and was then unloaded completely due to the thunderstorm. Once power was restored, testing re-initiated. Therefore, all data presented here for BM 16-220 was collected after the unloading. As unloading occurred after the formation of many cracks, this beam underwent a load cycle. This load cycle is reflected in Figure 6.23. The experimental strain profile is approximately linear for the full response and does not exhibit the sharp decrease in stiffness at cracking that the ABAQUS model does. This is because cracking had already occurred due to the load cycle, and the reinforcement was activated

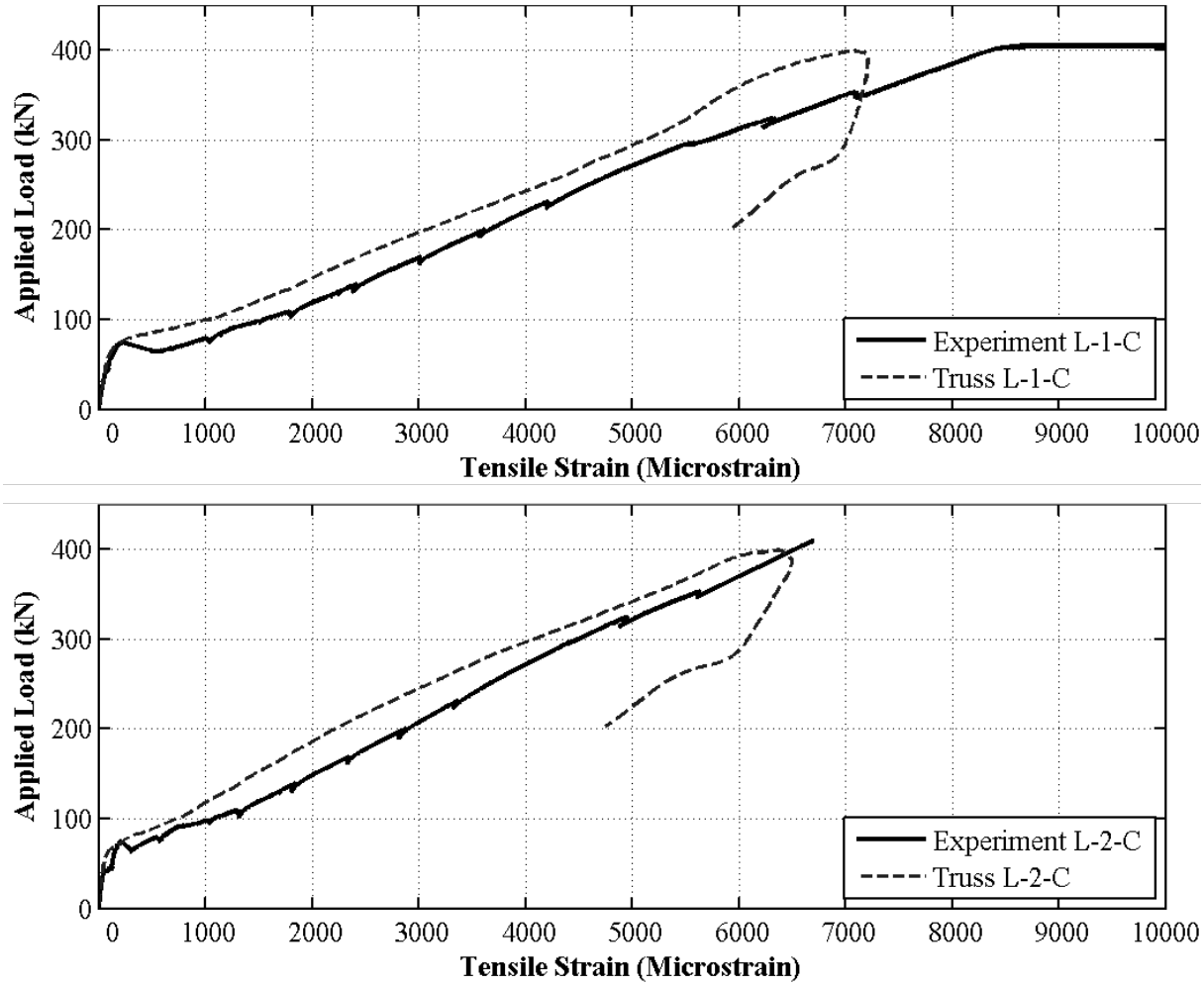

Figure 6.22: Longitudinal Reinforcement Strains - BM 16-150

immediately. However, the model response does converge to the experimental response after cracking.

6.6.2 GFRP Stirrup Reinforcement

Figure 6.16 presented the influence of the concrete dilation angle, ψ, and maximum concrete compressive strain, $\varepsilon_{c,max}$, on the load-deflection response of BM 25-220. It has been discussed that the combined calibration of these two parameters is necessary to capture the influence of the GFRP stirrups on the beam behaviour. The influence of the GFRP

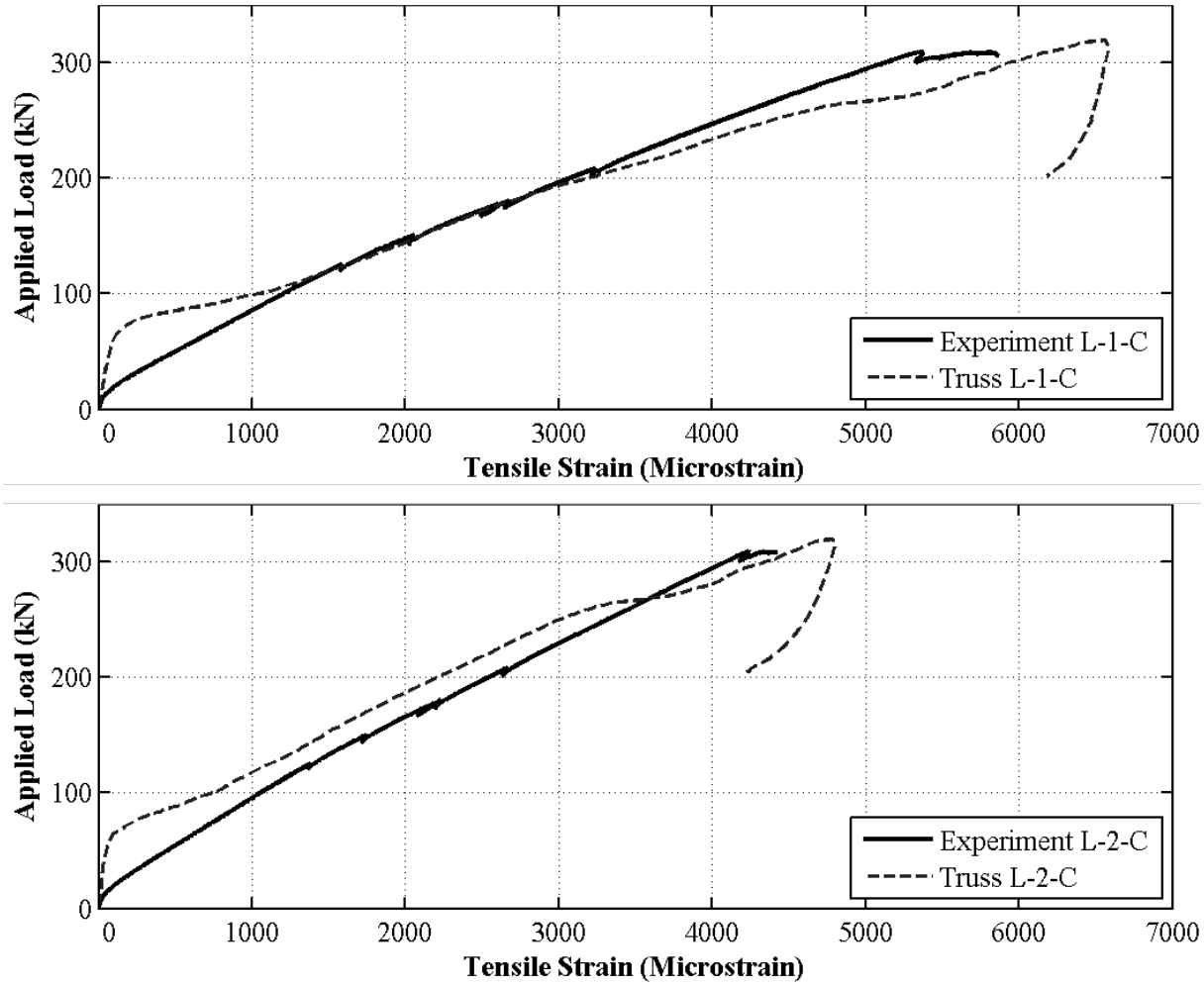

Figure 6.23: Longitudinal Reinforcement Strains - BM 16-220

stirrup modelling will now be considered by demonstrating the results of BM 12-150.

Figure 6.24 presents the influence of the stirrup modelling on the load-deflection response for BM 12-150. Models considered the use of truss-section stirrups, membrane-section stirrups, and no stirrups. The responses shown in Figure 6.24 utilized the concrete parameters as recommended in Chapter 5 for the modelling of beams with no stirrups ($\psi = 30°$ and $\varepsilon_{c,max} = 0.008$).

The experimental beam failed at a peak load of 405.2kN. When using the concrete model proposed for beams with no stirrups, peak loads of 232.0kN, 218.6kN, and 169.4kN were obtained by the truss-stirrup, membrane-stirrup, and no-stirrup models, respectively. Both

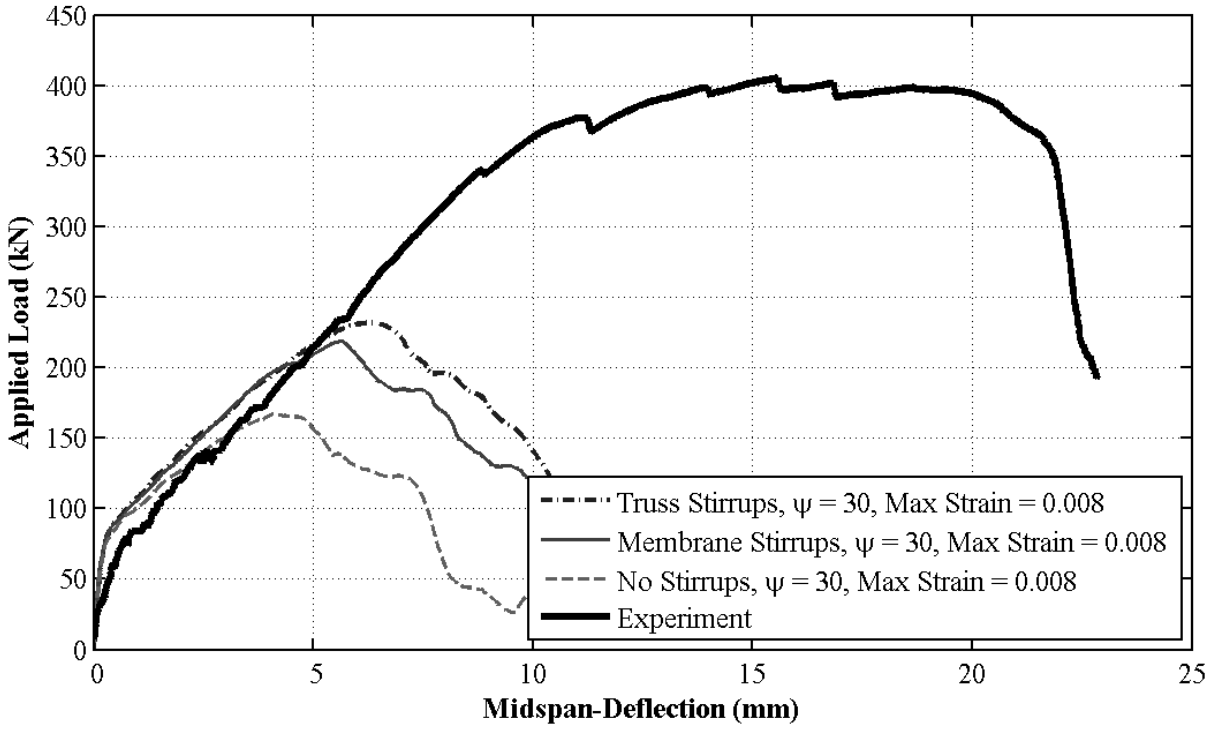

Figure 6.24: Influence of Stirrups ($\psi = 30°$ & $\varepsilon_{c,max} = 0.008$) - BM 12-150

methods of modelling the stirrups produced similar peak loads and identical deflection responses. However, the models experienced brittle failures and severely underpredicted the peak load as compared to the experiment. Furthermore, it can be seen that the models with stirrups produced responses similar to the model with no stirrups. This shows that the stirrup reinforcement was not utilized as expected. Modifications to the concrete model were therefore necessary to capture the effects of the stirrups.

Figure 6.25 presents the influence of the stirrup modelling on the load-deflection response of BM 12-150 with a concrete dilation angle of 30° and an increased maximum concrete compressive strain of 0.015.

With the increased compressive strain, peak loads of 237.9kN, 249.8kN, and 169.9kN were produced by the truss-stirrup, membrane-stirrup, and no-stirrup models, respectively. This increased strain had minimal influence on the peak loads of each beam. As discussed previously, a dilation angle of 30° produces brittle failures that are not dependent on

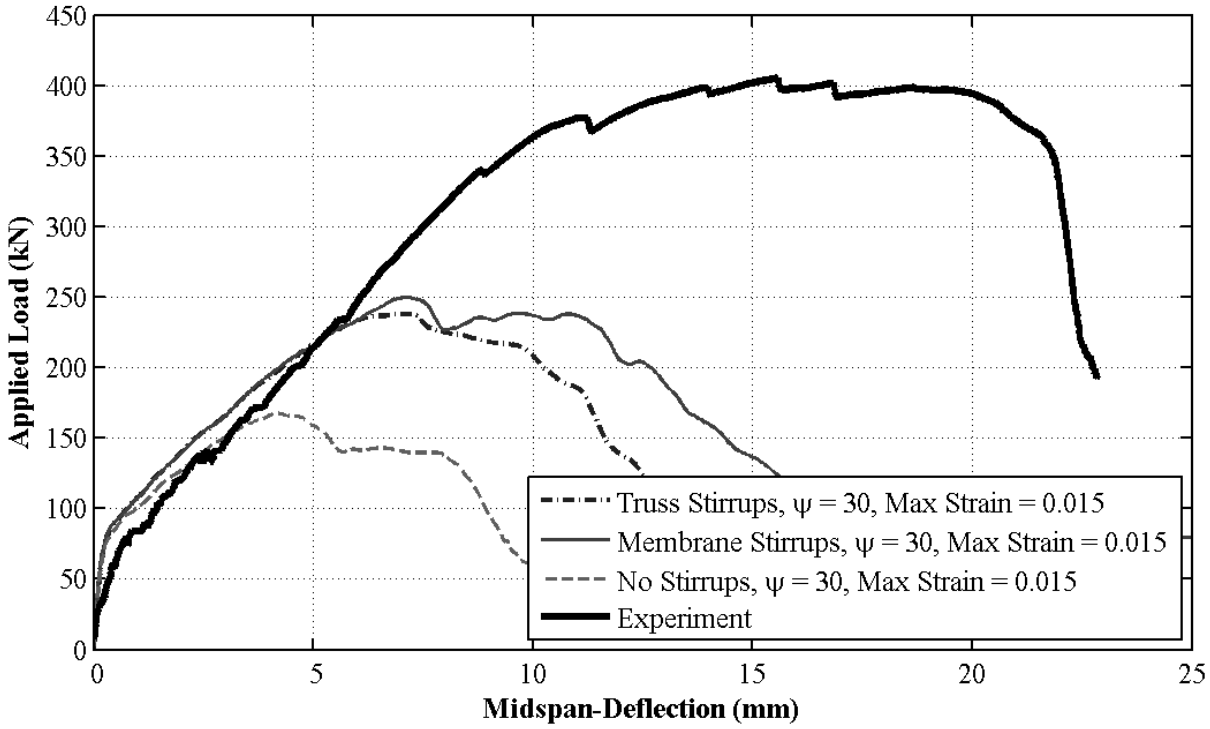

Figure 6.25: Influence of Stirrups ($\psi = 30°$ & $\varepsilon_{c,max} = 0.015$) - BM 12-150

the compressive crushing of concrete, therefore increasing $\varepsilon_{c,max}$ had minimal influence. However, the beams experienced a more gradual reduction in strength after the failure load when a larger maximum strain was used. Again, although the models with stirrups were not able to capture the strength and ductility of the experimental response, the truss-section model continued to match closely with the membrane-section model.

Figure 6.26 presents the influence of the stirrup modelling on the load-deflection response of BM 12-150 with an increased concrete dilation angle of 50° and the original maximum concrete compressive strain of 0.008.

With an increased dilation angle, peak loads of 310.5kN, 324.9kN, and 195.0kN were produced by the truss-section, membrane-section, and no-stirrup models, respectively. The larger dilation angle produced a significant increase in the peak load obtained by the models with stirrups, and also increased the strength of the beam with no stirrups. The beam with truss-stirrups continued to match closely with the beam with membrane-stirrups.

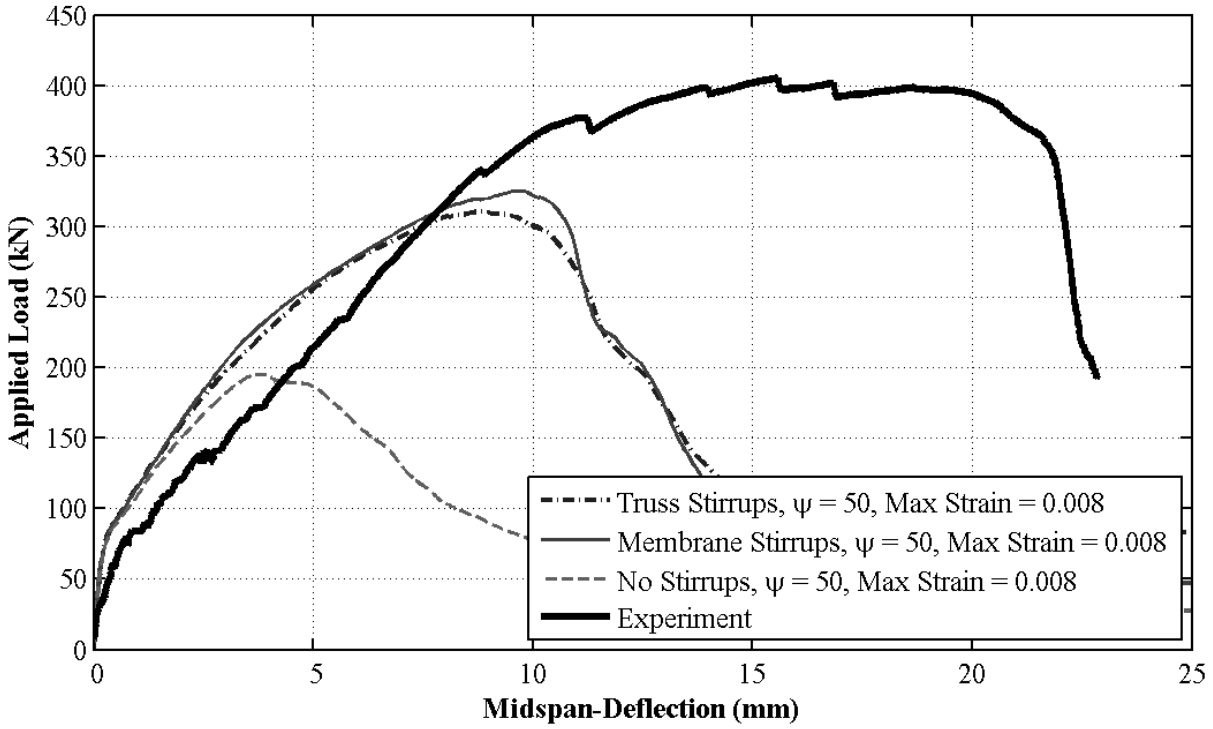

Figure 6.26: Influence of Stirrups ($\psi = 50°$ & $\varepsilon_{c,max} = 0.008$) - BM 12-150

Figure 6.27 presents the influence of the stirrup modelling on the load-deflection response of BM 12-150 with both an increased concrete dilation angle of 50° and an increased maximum concrete compressive strain of 0.015.

With both an increased dilation angle and an increased compressive strain, peak loads of 343.6kN, 385.1kN, and 195kN were produced by the truss-stirrup, membrane-stirrup, and no-stirrup models, respectively. This final case had the largest influence on the responses of beams with stirrups. Unlike the first three cases, the response of the membrane-stirrup model deviated significantly from the truss-stirrup model. It can be seen that the use of membrane-section stirrups provided the most accurate results when compared to the experimental response. Table 6.2 summarizes the peak loads predicted by each concrete model and stirrup modelling technique. This table also presents the percent difference between the peak load predicted by each model, P_P, and the peak load predicted by the original concrete model used for beams with no stirrups, P_1 ($\psi = 30°$ and $\varepsilon_{c,max} = 0.008$).

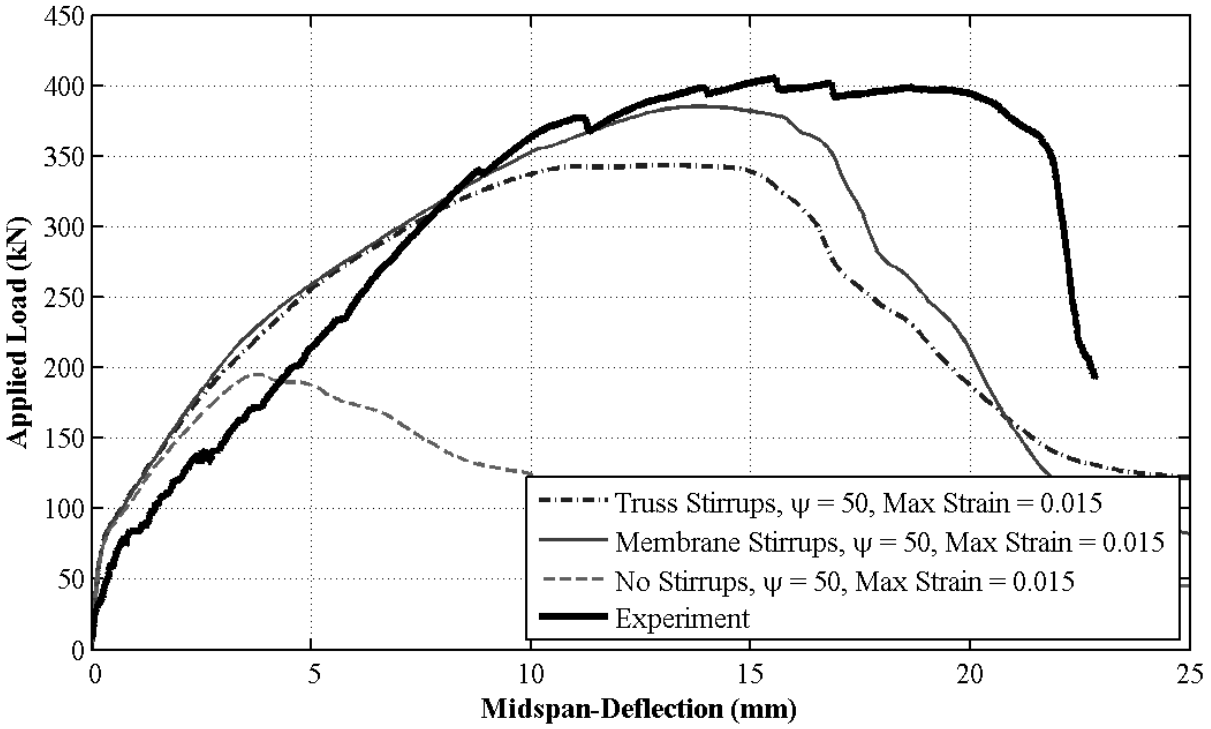

Figure 6.27: Influence of Stirrups ($\psi = 50°$ & $\varepsilon_{c,max} = 0.015$) - BM 12-150

Table 6.2: Influence of Stirrup Modelling and Concrete Model - BM 12-150

Stirrups	$\psi = 30°$ $\varepsilon_{c,max} = 0.008$	$\psi = 30°$ $\varepsilon_{c,max} = 0.015$		$\psi = 50°$ $\varepsilon_{c,max} = 0.008$		$\psi = 50°$ $\varepsilon_{c,max} = 0.015$	
	P_1 (kN)	P_P (kN)	% Diff.	P_P (kN)	% Diff.	P_P (kN)	% Diff.
Truss	232.0	237.9	2.5%	310.5	33.8%	343.6	48.1%
Membrane	218.6	249.8	14.3%	324.9	48.6%	385.1	76.2%
None	169.4	169.9	0.3%	195.0	15.1%	195.0	15.1%

Table 6.2 demonstrates the influence of changing the concrete parameters ψ and $\varepsilon_{c,max}$ on the beam peak loads. Considering the beams with stirrups first, increasing only the maximum concrete strain had minimal influence, resulting in a 2.5% and 14.3% increase to the peak load predicted by the truss and membrane models, respectively. Conversely, increasing only the dilation angle had a significant influence, resulting in a 33.8% and 48.6% increase for the truss and membrane models, respectively. The combined modification of

the dilation angle and the maximum strain resulted in further increases to the peak load, with the membrane stirrups yielding a strong correlation to the experimental results (P_P = 385.1kN, within 5% of experimental load). These observations were consistent for the modelling of all beams with stirrups.

Now considering the results for the models with no stirrups, increasing only the maximum concrete strain resulted in negligible change to the peak load (0.3%). However, increasing only the dilation angle increased the peak load by 15.1%. The combined modification of the dilation angle and the maximum strain also resulted in a 15.1% increase; the same result as increasing the dilation angle only. These results suggest that even with an increased dilation angle, the beams with no stirrups exhibit brittle tension-governed failures that are not influenced by $\varepsilon_{c,max}$.

The stirrup strains were then studied and compared to the data collected during the experimental testing. Appendix A provides information regarding strain gauge locations and nomenclature. Figure 6.28 presents the strain profiles for three stirrups within the shear span of BM 12-150 at strain gauge locations S-4-S, S-5-S, and S-6-S. Figure 6.29 presents the strain profiles for two stirrups within the shear span of BM 16-220 at strain gauge locations S-5-S and S-6-S. All gauges presented were located at the mid-height of each stirrup within the straight regions.

BM 12-150 and BM 16-220 were presented here as these beams were representative of all beams modelled. A consistent observation is that the truss-stirrup strains match closely with the membrane-stirrup strains initially. At failure, however, the truss-stirrups exhibited brittle responses, whereas the membrane-stirrups exhibited much higher ductility. It is clear that the use of membrane sections to model the stirrups allowed the stirrups to carry higher tensile strains. This higher utilization of the stirrups resulted in the increased strength of these beams as compared to the truss-stirrup models. Figures 6.30 and 6.31 compare the stirrup strains for BM 12-150 and BM 16-220, respectively, as produced using

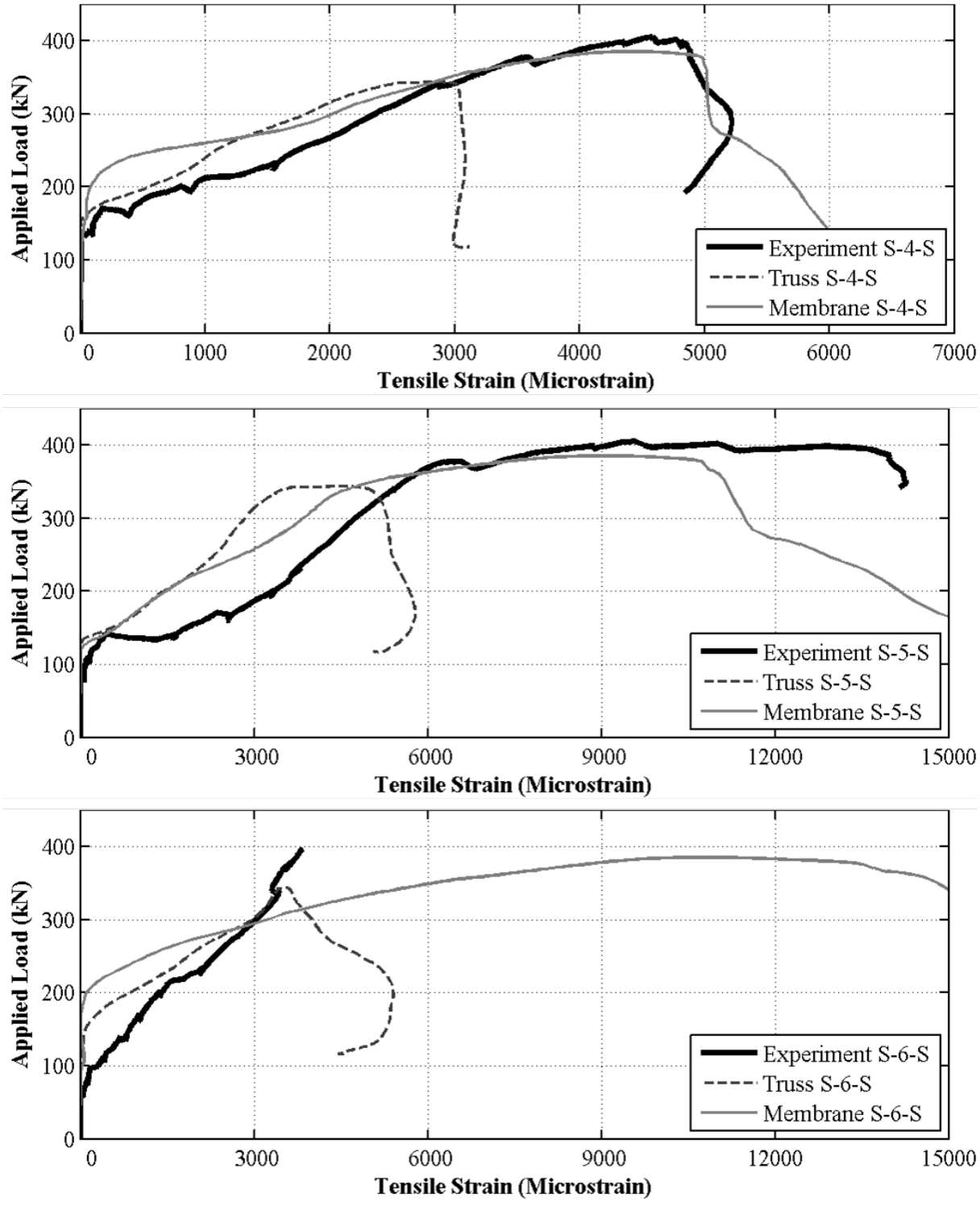

Figure 6.28: Influence of Stirrup Modelling on Strains - BM 12-150

the membrane-stirrup method.

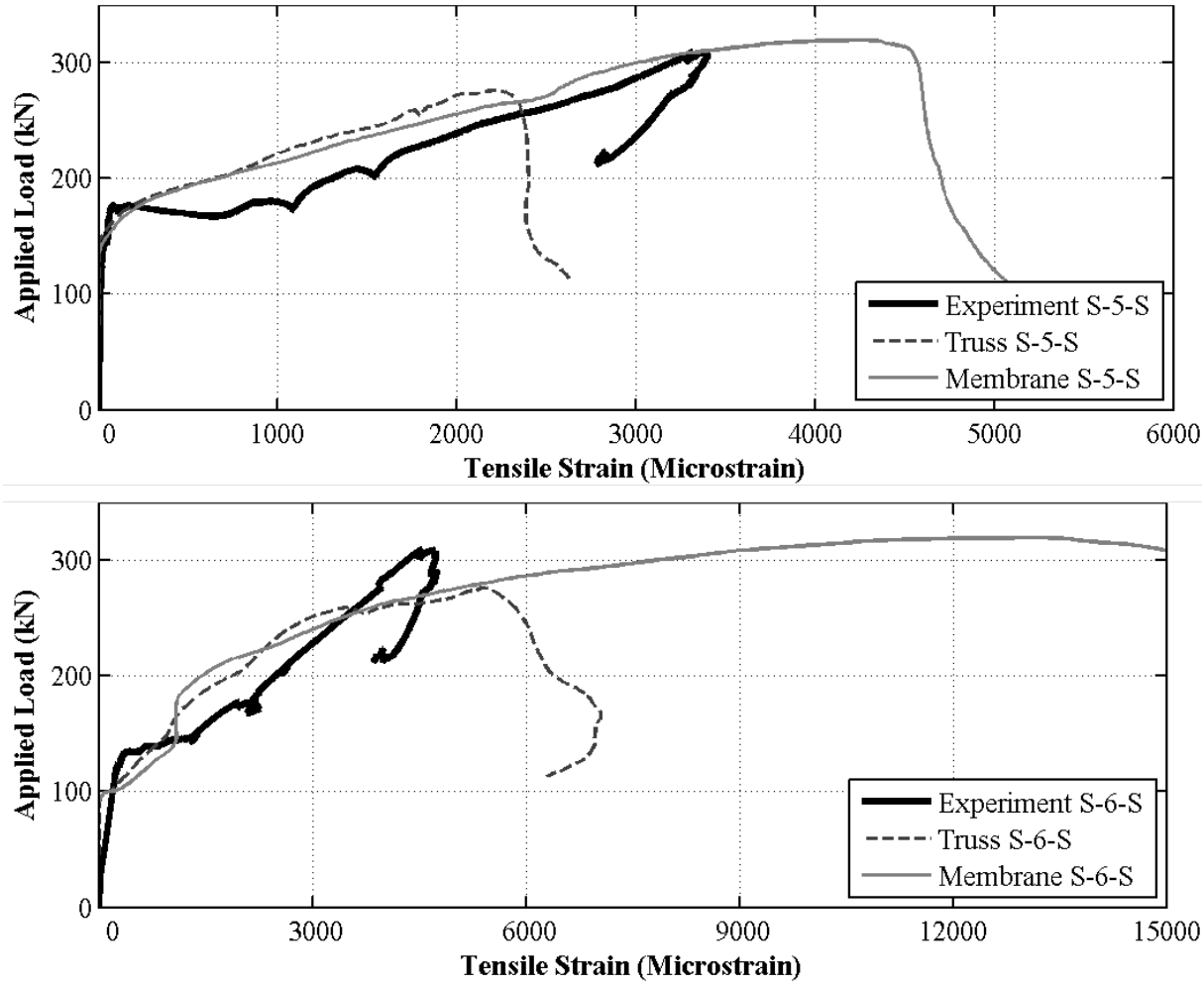

Figure 6.29: Influence of Stirrup Modelling on Strains - BM 16-220

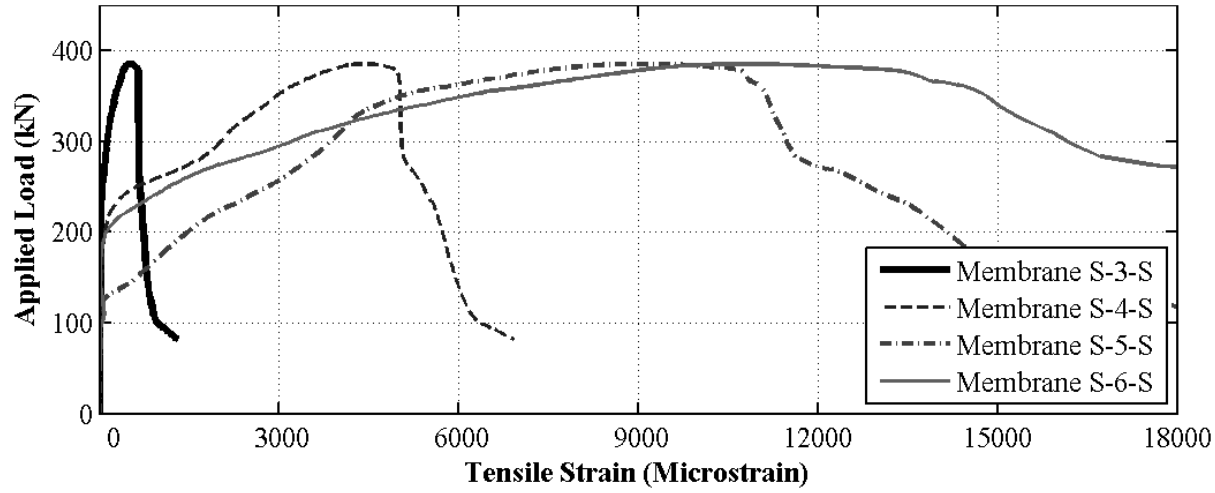

Figure 6.30: Membrane Stirrup Strains - BM 12-150

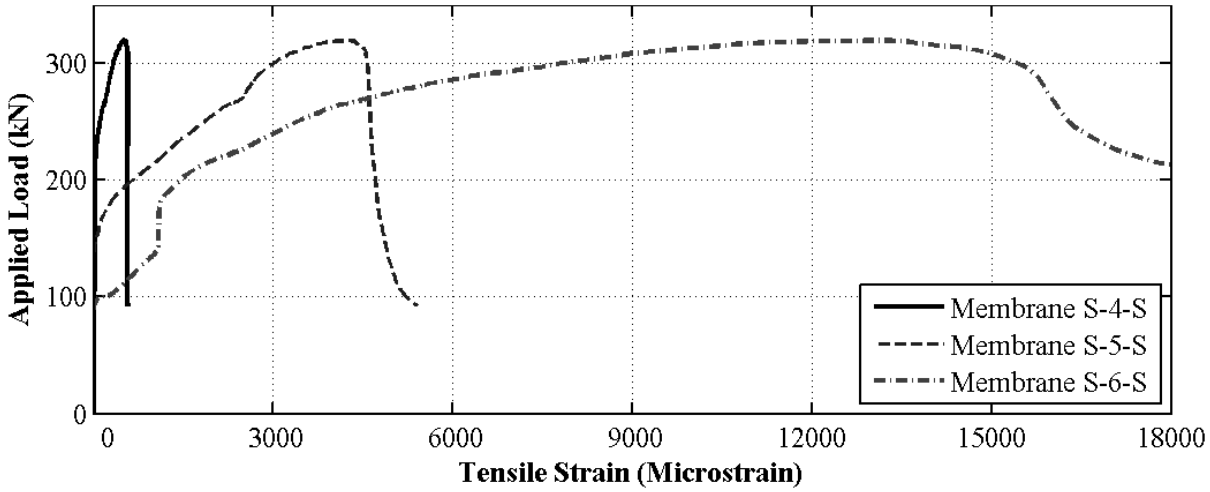

Figure 6.31: Membrane Stirrup Strains - BM 16-220

For BM 12-150, the membrane-stirrup model predicted the largest stirrup strains at the S-5-S and S-6-S locations. This is to be expected, as the experimental beams failed by the crushing of a diagonal strut running from the point of load application to the support plate. This failure surface intersects the S-5-S and S-6-S locations, thus activating these stirrups and causing larger strains. This is also reflected in the large strains measured at S-5-S during the experimental testing. It is important to note that the strain gauge at S-6-S failed prior to the peak load during the experimental testing, which explains the sudden loss of data as shown in Figure 6.28. However, it is reasonable to assume that this gauge would have experienced large strains matching the model output if it had not failed prematurely. Similarly for BM 16-220, the membrane-stirrup model predicted the largest strains at S-6-S as this location was intersected by the major shear crack.

The GFRP stirrups were defined using a modulus of elasticity of 50,000MPa and an ultimate tensile strength of 1000MPa, resulting in a rupture strain of 0.02 (20,000 microstrain). In all models of beams with stirrups, the rupture of the stirrups was not the cause of failure. However, as shown for S-6-S in both BM 12-150 and BM 16-220, the membrane stirrups experienced very large strains that approached the failure strain. Therefore, although the membrane elements were able to accurately capture the strain profile for most

stirrups, the strain predictions for stirrups that were intersected by major diagonal shear cracks experienced excessively large strains.

In conclusion, the comparison of the models with and without stirrups proved that the presence of stirrup members in the models provided significant contribution to the beam strength. These stirrups allowed tensile stresses to be carried in damaged regions and across cracks, thus preventing brittle shear failures of the beams. Furthermore, the use of membrane sections to model the stirrups, in conjunction with an increased concrete dilation angle and maximum concrete compressive strain, proved to produce accurate beam responses, and is the preferred method to model stirrups as compared to the traditional truss-stirrup alternative.

6.7 Influence of Stirrup Diameter

Thus far, the modelling of beams with stirrups spaced at 150mm and 220mm within the shear span have been discussed. This section will now apply the proposed model for beams with stirrups to the BM XX-s230 beam series: BM 12-s230, BM 16-s230, and BM 25-s230. These beams used stirrups that are spaced at 230mm within the shear span and have core diameters of 20mm (as opposed to 12mm as used for all other beams). With the larger stirrup diameters, these beams required larger cross-sections to accommodate the larger bend radii at the stirrup corners as previously summarized in Table 4.3. Figures 6.32 to 6.34 compare the experimental load-deflection responses with the proposed models for each beam with larger stirrups.

It can be seen that the proposed model was able to provide reasonable predictions for the load-deflection responses for each beam. It is interesting to note that the load-deflection response for each of the beams tested with larger stirrups exhibited two peaks. The first

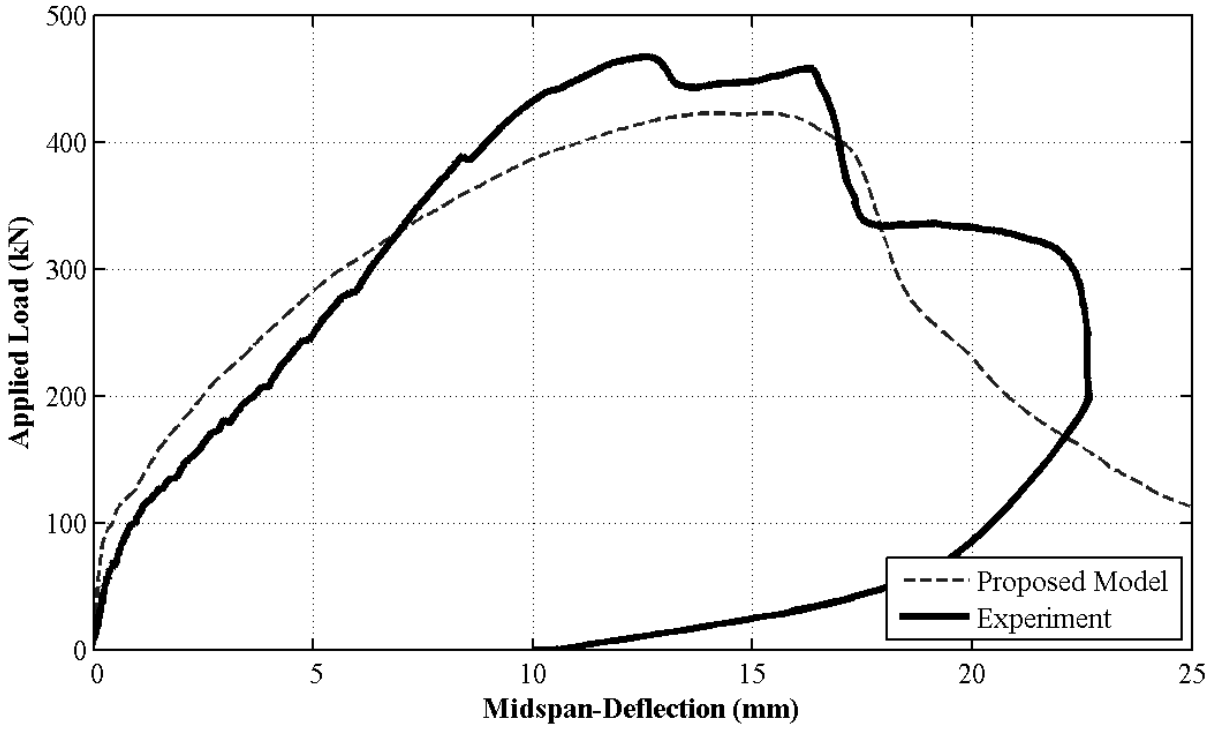

Figure 6.32: Load-Deflection Response - BM 12-s230

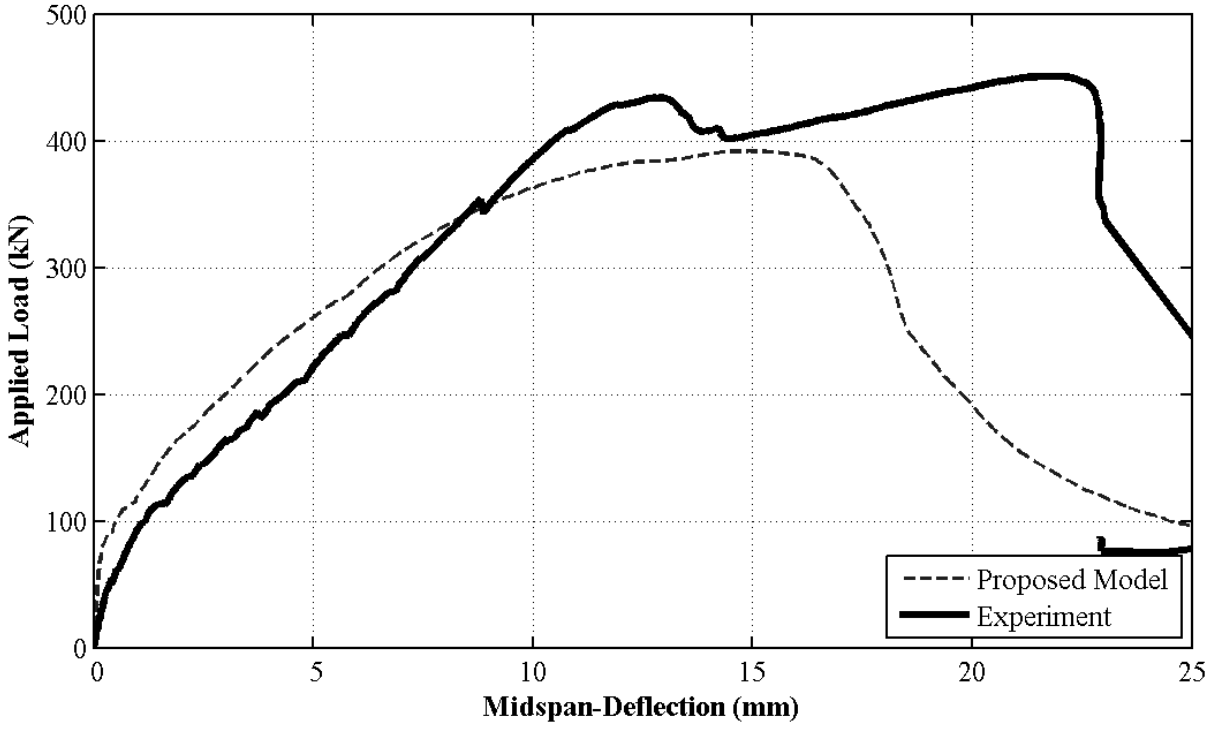

Figure 6.33: Load-Deflection Response - BM 16-s230

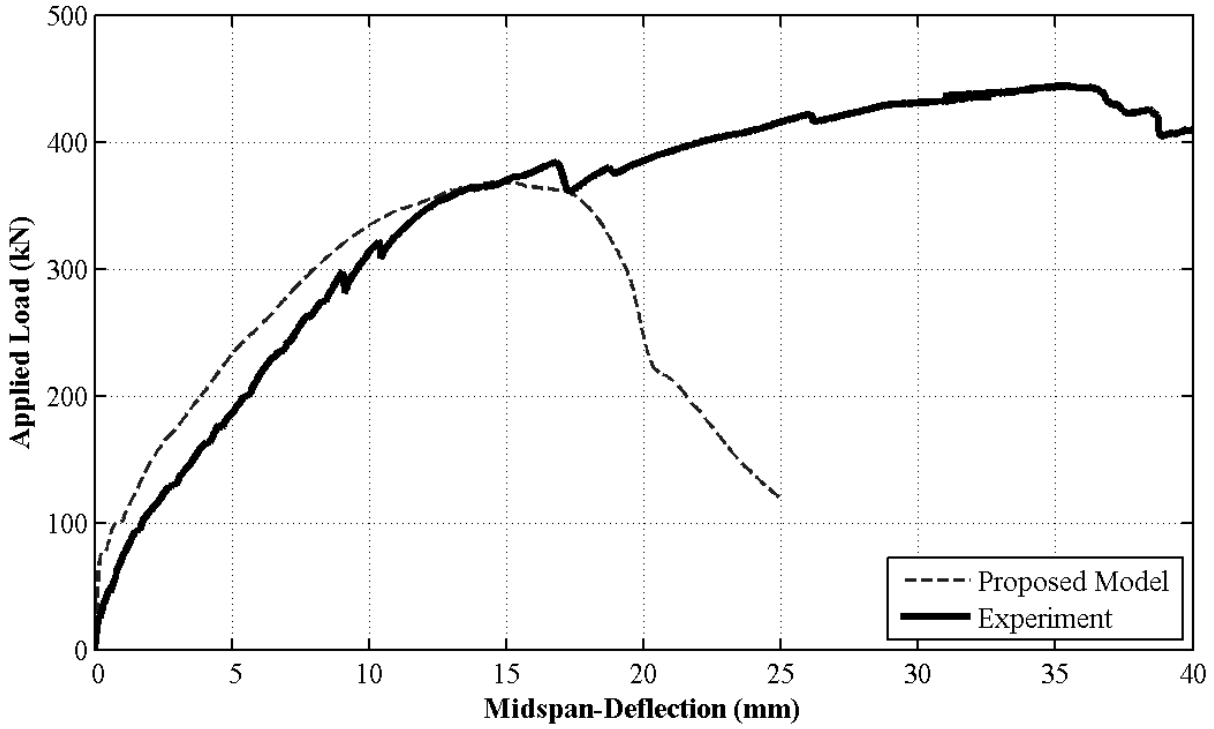

Figure 6.34: Load-Deflection Response - BM 25-s230

peak was observed at a mid-span deflection of 12.5mm, 13.0mm, and 17.0mm for BM 12-s230, BM 16-s230, and BM 25-s230, respectively. BM 25-s230 experienced a sudden drop in strength at a load of 388.7kN, however regained strength and continued to a second peak of 444.0kN at a mid-span deflection of 35mm. This beam continued to carry a load greater than 350kN for deflections greater than 60mm (not shown in Figure 6.34), thus exhibiting significant ductility. For BM 25-s230, the model matched closely with the first peak load. This first peak load also matched the peaks loads of BM 12-s230 and BM 16-s230. For this reason, the first peak exhibited by BM 25-s230 was used for all comparisons. Table 6.3 presents the failure loads provided by the experimental tests and the proposed model.

Figures 6.35 to 6.37 compare the crack patterns observed at failure during the experimental testing with the pattern produced by the ABAQUS modelling. All experimental crack patterns were provided by Krall (2014).

The crack patterns from each beam were similar, and consisted of diagonal shear cracks

Table 6.3: Comparison of Peak Loads for Beams with Larger Stirrups

Beam	Peak Load (kN)		% Diff.
	Experiment	Model	
12-s230	466.9	422.5	9.5%
16-s230	434.0	391.8	9.7%
25-s230	388.7	368.1	4.1%

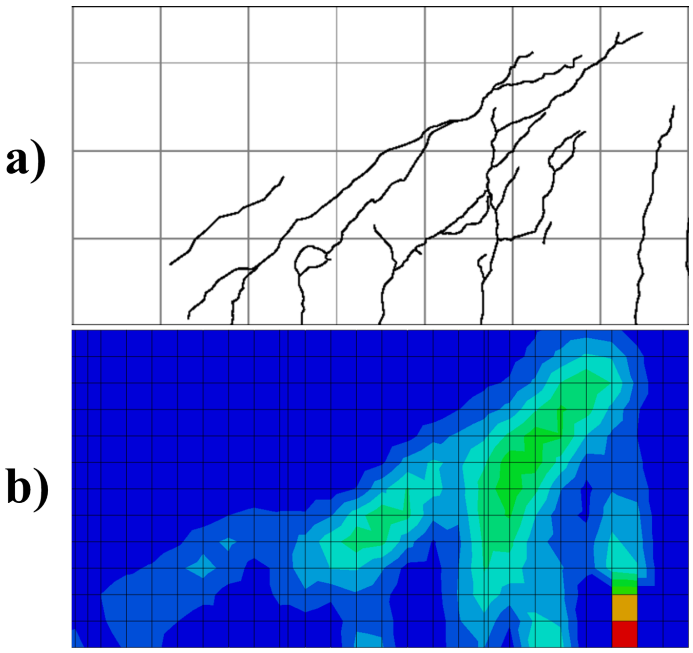

Figure 6.35: Crack Pattern at Failure - BM 12-s230: (a) Experiment (b) ABAQUS Model

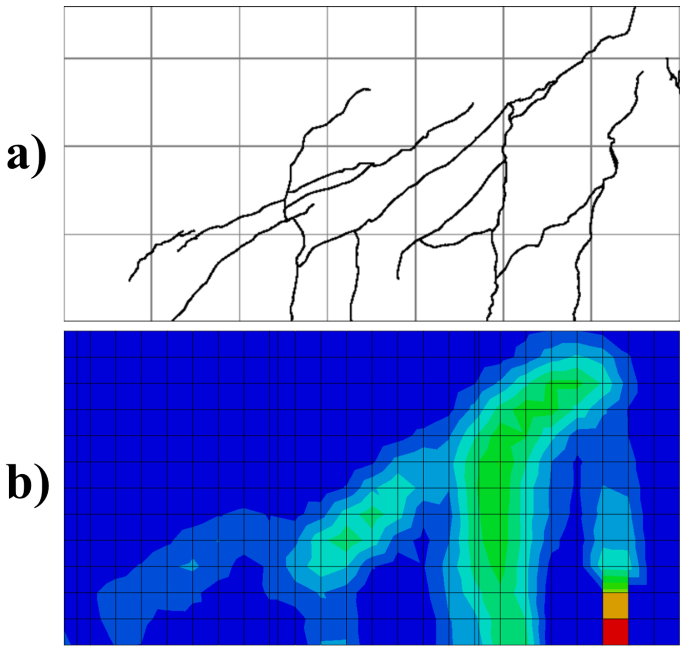

Figure 6.36: Crack Pattern at Failure - BM 16-s230: (a) Experiment (b) ABAQUS Model

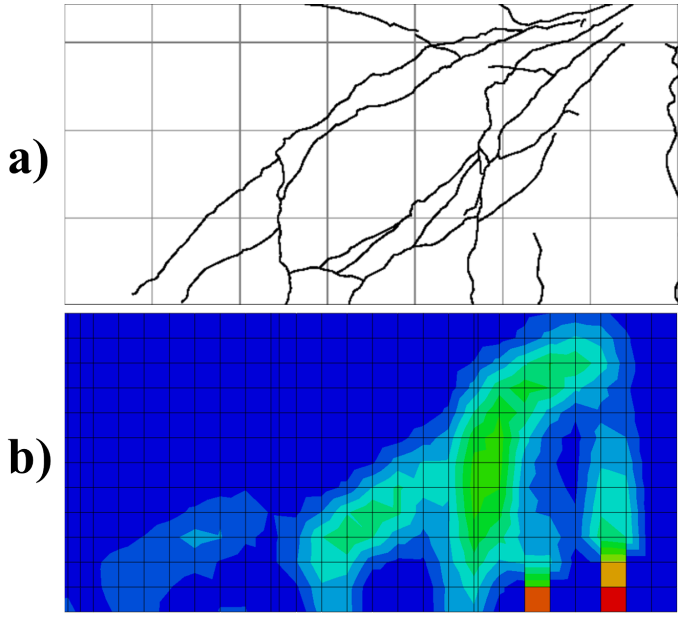

Figure 6.37: Crack Pattern at Failure - BM 25-s230: (a) Experiment (b) ABAQUS Model

extending from the point of load application (top right corner) towards the support bearing plate (bottom left corner). The model was able to accurately replicate these crack patterns.

6.8 Final Recommendations and Comparison to Code Predictions

6.8.1 Proposed Model for Beams with Stirrups

Table 6.4 summarizes the parameters recommended for the effective modelling of concrete beams reinforced with GFRP longitudinal bars and stirrups.

Table 6.4: Proposed Parameters for the Modelling of Beams with Stirrups

Compression Model:	Modified Hognestad Parabola
Maximum Compressive Strain:	0.015
Tension Model:	Bilinear Stress-Displacement
Fracture Energy, G_f:	90 N/m
Damage:	Tension and Compression Included
Poisson's Ratio, v:	0.2
Dilation Angle, ψ:	50°
σ_{bo}/σ_{co}:	1.16
Eccentricity, ϵ:	0.1
K_c:	2/3
Viscosity Parameter, μ:	0.0001
Mesh Refinement:	12 Deep
Longitudinal Reinforcement:	Linear Truss Sections
Stirrup Reinforcement:	Reinforced Membrane Sections

The final parameters proposed for the modelling of beams with GFRP stirrups utilizes a modified concrete compression model that has been calibrated to match the experimental results. From the experimental observations and ABAQUS simulations, it was clear that the beams tested experienced concrete-governed failures; the longitudinal and transverse reinforcement did not rupture. For concrete beams reinforced with traditional steel, the members are designed assuming that the steel will yield prior to the failure of the concrete.

When steel yields, it undergoes significant plastic straining which ultimately leads to the failure of the member. Therefore, as the reinforcement did not control the failure of these beams, it was necessary to focus on the concrete model in order to replicate the experimental results.

Furthermore, the confinement provided by the GFRP stirrups has been discussed. As GFRP does not yield and has a significantly higher tensile strength as compared to steel, the GFRP stirrups will be able to provide a higher level of passive confinement to the concrete as the concrete dilates under high compressive stresses, thus strengthening the concrete. To capture this additional degree of confinement, modifications to the concrete parameters were considered, including the maximum compressive strain, $\varepsilon_{c,max}$, and the dilation angle, ψ.

Figures 6.38 and 6.39 compare the load-deflection responses as predicted using the proposed model with the responses measured during the experimental testing for beams with stirrups spaced at 150mm and 220mm, respectively.

Figures 6.40 and 6.41 present the crack patterns at failure as produced by the proposed model. The actual crack patterns at failure as observed during the experimental testing have been superimposed in white. Note that the top right corner of each diagram represents the point of load application at mid-span and the bottom left corner is the location of the support.

It can be seen that all models were able to accurately capture the crack patterns at failure. All beams presented experienced diagonal shear cracks that extended from the load point towards the support.

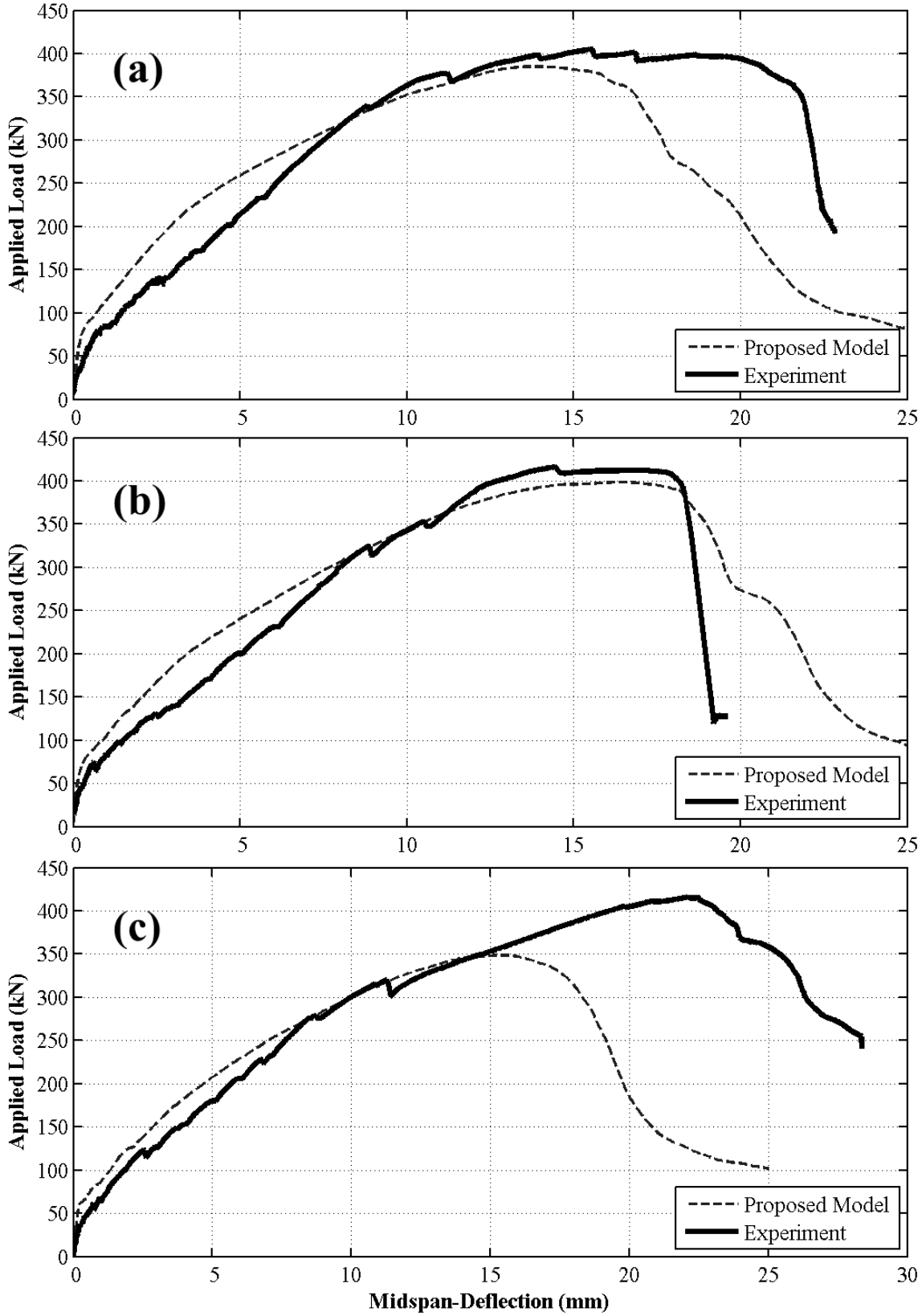

Figure 6.38: Proposed Model for BM XX-150: (a) BM 12-150 (b) BM 16-150 (c) BM 25-150

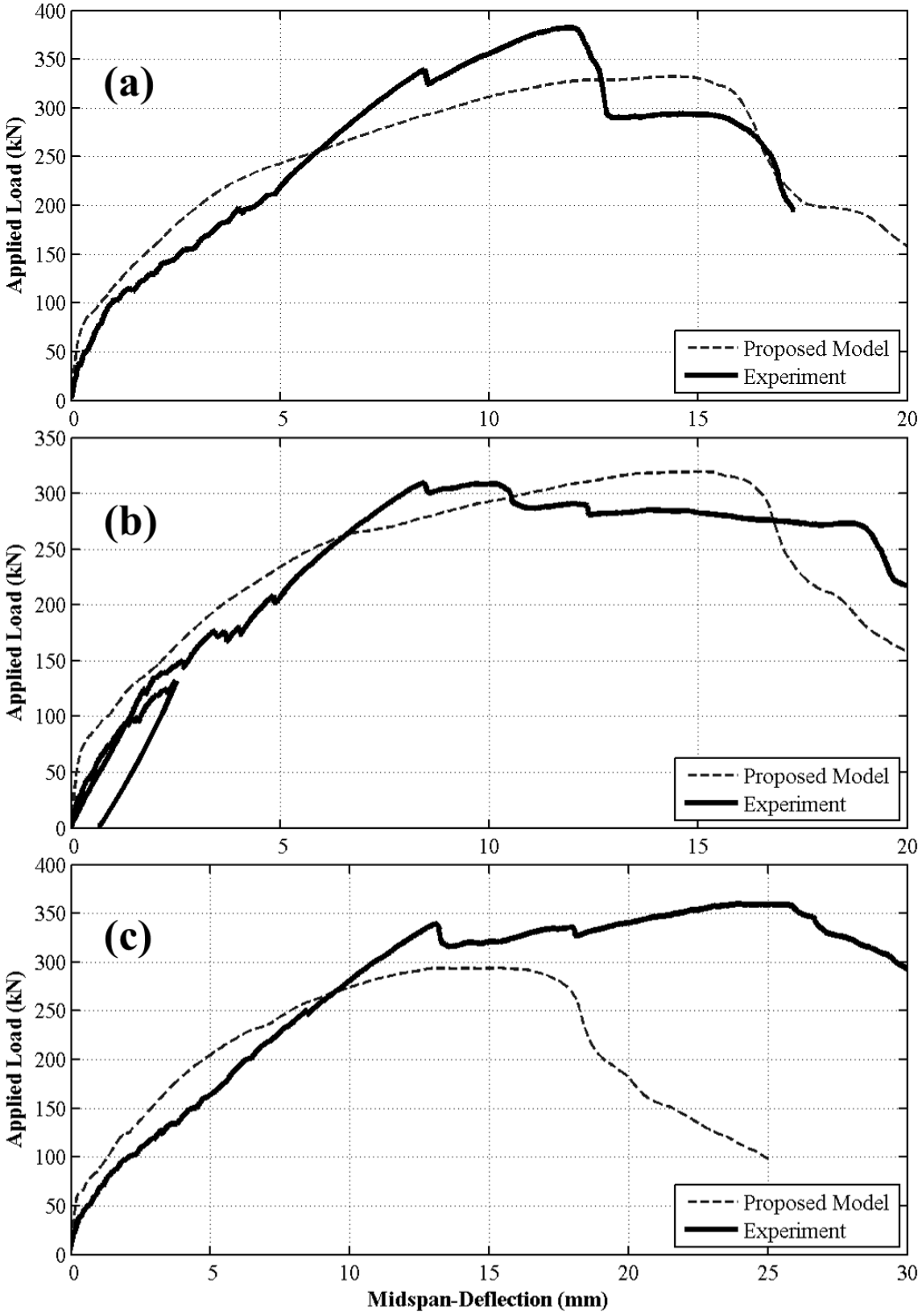

Figure 6.39: Proposed Model for BM XX-220: (a) BM 12-220 (b) BM 16-220 (c) BM 25-220

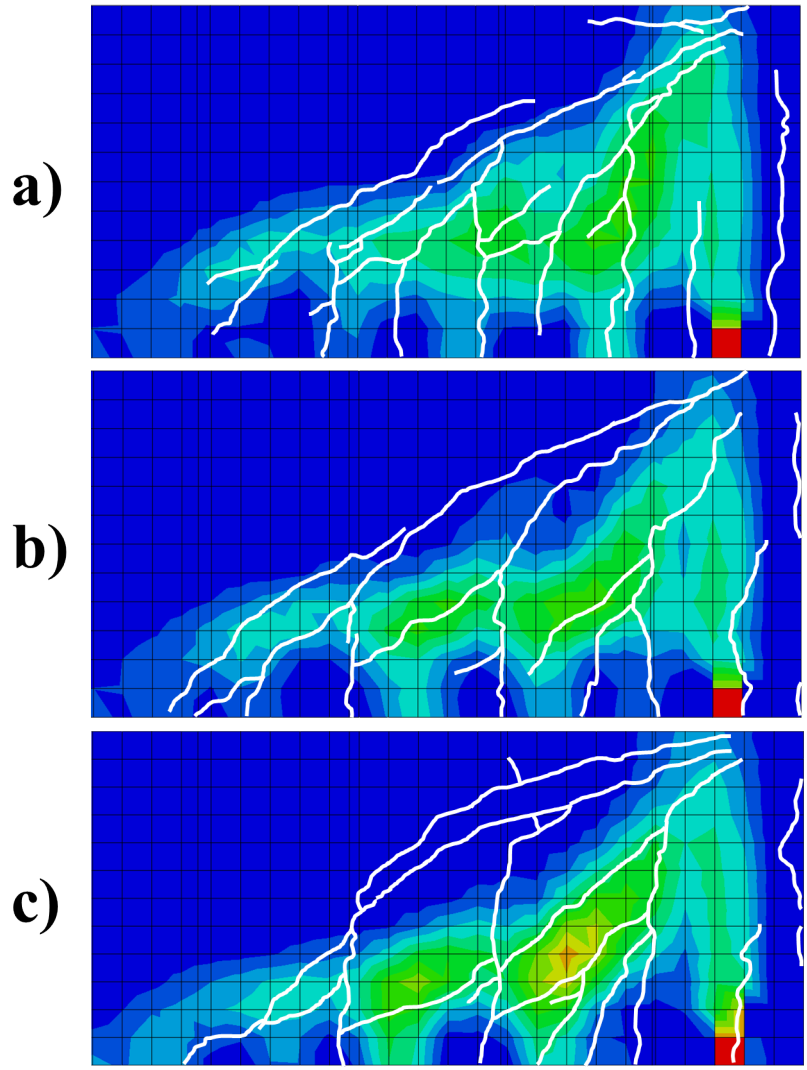

Figure 6.40: Comparison of Crack Patterns at Failure - BM XX-150: (a) BM 12-150, (b) BM 16-150, (c) BM 25-150

6.8.2 Comparison to Code Predictions

Table 6.5 presents the failure loads for each beam as provided by various flexure and shear resistance predictions and the proposed model. These predictions, P_P, are then compared to the experimental peak loads, P_E.

Table 6.6 presents the ratio of the peak load as predicted by the proposed ABAQUS model to the peak load as provided by the various strength prediction models and the experimental data. Note that a value less than 1.0 means that the proposed model underpredicted the

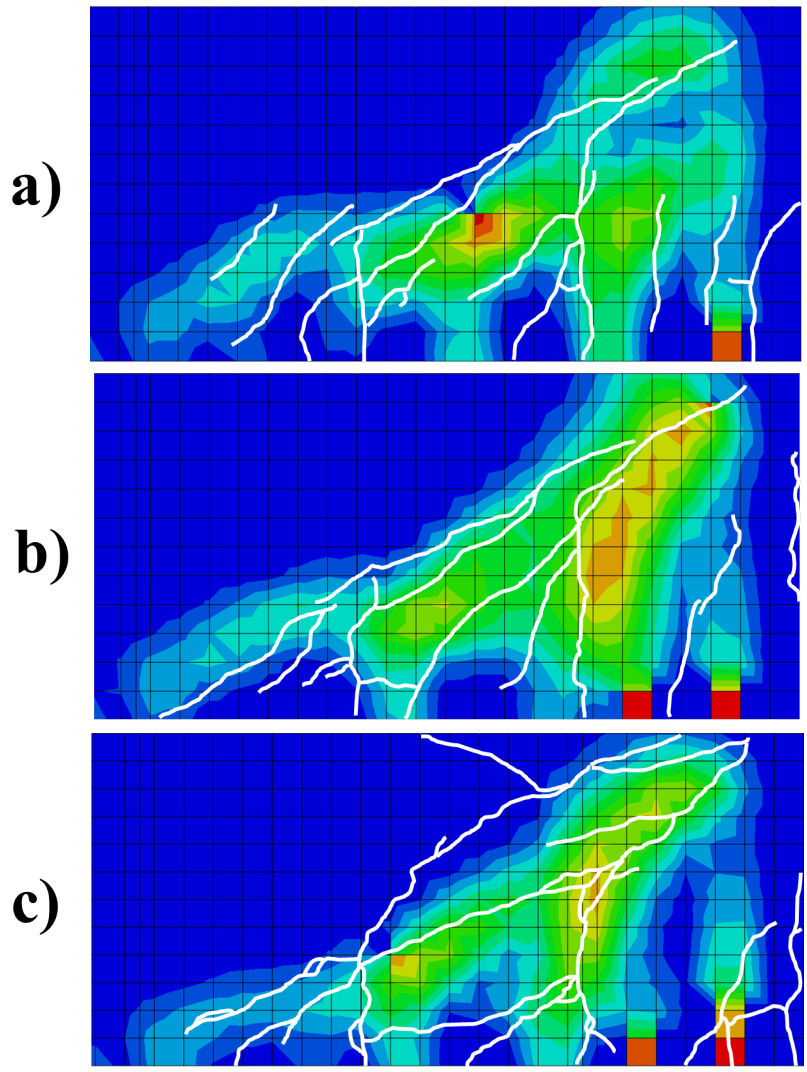

Figure 6.41: Comparison of Crack Patterns at Failure - BM XX-220: (a) BM 12-220, (b) BM 16-220, (c) BM 25-220

peak load relative to the model of interest, whereas a ratio greater than 1.0 means the proposed model overpredicted the peak load.

It is clear that the shear strength predictions of CSA S806-12 severely underestimated the shear strength of all beams and provided the weakest correlation with the model output and experimental data. The shear strength predictions proposed by Nehdi et al. (2007) provided the best agreement to the ABAQUS results for beams with stirrups at 150mm and 220mm, whereas the CSA flexure model provided better results for beams with stirrups at

Table 6.5: Comparison of Predicted and Experimental Peak Loads

Beam	Exper.	CSA S806-12 Flexure		CSA S806-12 Shear		Nehdi et al. Shear		ABAQUS Model	
	P_E (kN)	P_P (kN)	Ratio P_E/P_P	P_P (kN)	Ratio P_E/P_P	P_P (kN)	Ratio P_E/P_P	P_P (kN)	Ratio P_E/P_P
12-150	405.2	441.9	0.92	226.2	1.79	376.7	1.08	385.1	1.05
16-150	416.5	422.0	0.99	214.4	1.94	372.7	1.12	398.6	1.04
25-150	415.8	388.0	1.07	195.4	2.13	365.7	1.14	348.6	1.19
12-220	382.4	441.9	0.87	206.2	1.85	337.0	1.13	332.2	1.15
16-220	309.3	422.0	0.73	195.7	1.58	333.0	0.93	319.7	0.97
25-220	360.1	388.0	0.93	178.9	2.01	326.0	1.10	294.1	1.22
12-s230	466.9	484.0	0.96	293.3	1.59	477.9	0.98	422.5	1.11
16-s230	434.0	462.0	0.94	277.0	1.57	473.4	0.92	391.8	1.11
25-s230	388.7	424.0	0.92	245.5	1.58	465.7	0.83	368.1	1.06

Table 6.6: Comparison of Model Results Relative to Peak Load Predictions

Beam	Experiment	CSA S806-12 Flexure	CSA S806-12 Shear	Nehdi et al. Shear
12-150	0.95	0.87	1.70	1.02
16-150	0.96	0.94	1.86	1.07
25-150	0.84	0.90	1.78	0.95
12-220	0.87	0.75	1.61	0.99
16-220	1.03	0.76	1.63	0.96
25-220	0.82	0.76	1.64	0.90
12-s230	0.90	0.87	1.44	0.88
16-s230	0.90	0.85	1.41	0.83
25-s230	0.95	0.87	1.50	0.79

230mm. As will be discussed in Chapter 7, the beams with larger stirrups required larger sections, thus had shear strengths that matched closely with the flexural strengths.

Chapter 7

Parametric Study

Chapters 5 and 6 presented the ABAQUS analyses of concrete beams reinforced without and with stirrups, respectively. Recommendations were made regarding the parameters that were most effective in producing simulations that replicated the experimental observations. Two models were proposed: one for the analysis of beams without stirrups as presented in Table 5.7 and the other for the analysis of beams with stirrups as presented in Table 6.4. The proposed models specify parameters that influence the concrete model including the compression, tension, plasticity, and damage behaviour. The proposed models recommend the element types to be used for the glass fibre reinforced polymer (GFRP) longitudinal and stirrup reinforcement. The proposed models also suggest analytical parameters that optimize the accuracy and computational effort of each analysis including the mesh refinement and level of viscoplastic regularization. Using these proposed models, a parametric study was performed.

7.1 Scope of Study

The primary objective of the parametric study was to apply the proposed models to beams of various shear span to effective depth (a/d) ratios ranging from 1.5 to 6.5. This ratio,

hereafter referred to as the slenderness ratio, dictates the slenderness of the beam and will influence the governing mode of failure. All experimental beams and analytical models presented up to this point have utilized slenderness ratios of $a/d = 2.5$, effective depths of $d = 270$mm, and shear spans of $a = 675$mm. As all beams studied were loaded using three-point bending, the total span of each simply-supported beam was therefore $L = 2a = 1350$mm. Using the same effective depth $d = 270$mm, Table 7.1 presents the shear spans and total spans of the six slenderness ratios considered in the parametric study.

Table 7.1: Spans Considered in Parametric Study

a/d	a (mm)	L (mm)
1.5	405	810
2.5	675	1350
3.5	945	1890
4.5	1215	2430
5.5	1485	2970
6.5	1755	3510

All six slenderness ratios were studied for each of the twelve beams (BM XX-INF, XX-150, XX-220, XX-s230). For each analysis, the slenderness ratio was the only variable changed; all material parameters and mesh refinements remained constant.

The secondary objective of the parametric study was to analyze the influence of the slenderness ratio on each beam's behaviour and failure mode. This involved studying the load-deflection response, moment-deflection response, and crack patterns.

The final objective of the parametric study was to compare the failure loads as provided by the numerical models with the strength predictions as provided by design standards and available literature. Comparisons were limited to the flexural and shear strength predictions provided by CSA S806-12 and the shear strength prediction provided by Nehdi

et al. (2007) as introduced in Section 2.4.

7.2 Results and Analysis

Appendix D presents the load-deflection and moment-deflection responses that were modelled for slenderness ratios (a/d) ranging from 1.5 to 6.5 for each beam. Table D.1 from Appendix D presents the failure load, P, and corresponding bending moment, M, for each slenderness ratio for all twelve beams as determined using by ABAQUS. The results will now be separated for beams with and without stirrups.

7.2.1 Beams with No Stirrups

Figure 7.1 shows the load-deflection and moment-deflection responses for BM 16-INF.

It can be seen that as the slenderness ratio increased, the mid-span deflection at failure increased. This is to be expected, as the stiffness of a beam decreases as the slenderness is increased. Furthermore, as the slenderness ratio increased, the applied load at failure decreased. However, the bending moment at failure remained relatively similar, ranging from 40.1kNm to 61.4kNm. As will be shown later, these moments are far less than the flexural strength of this beam. Therefore, for even the most slender models, the absence of stirrups resulted in shear-governed failures that occurred at approximately similar bending moments and that were independent of the slenderness of the beam. This was consistent for all beams with no stirrups. This behaviour is also reflected in the crack patterns exhibited at failure as shown in Figure 7.2.

Referring to Figure 7.2, the top-right corner of each beam represents the point of load application at mid-span, and the bottom-left corner is the location of the support. For

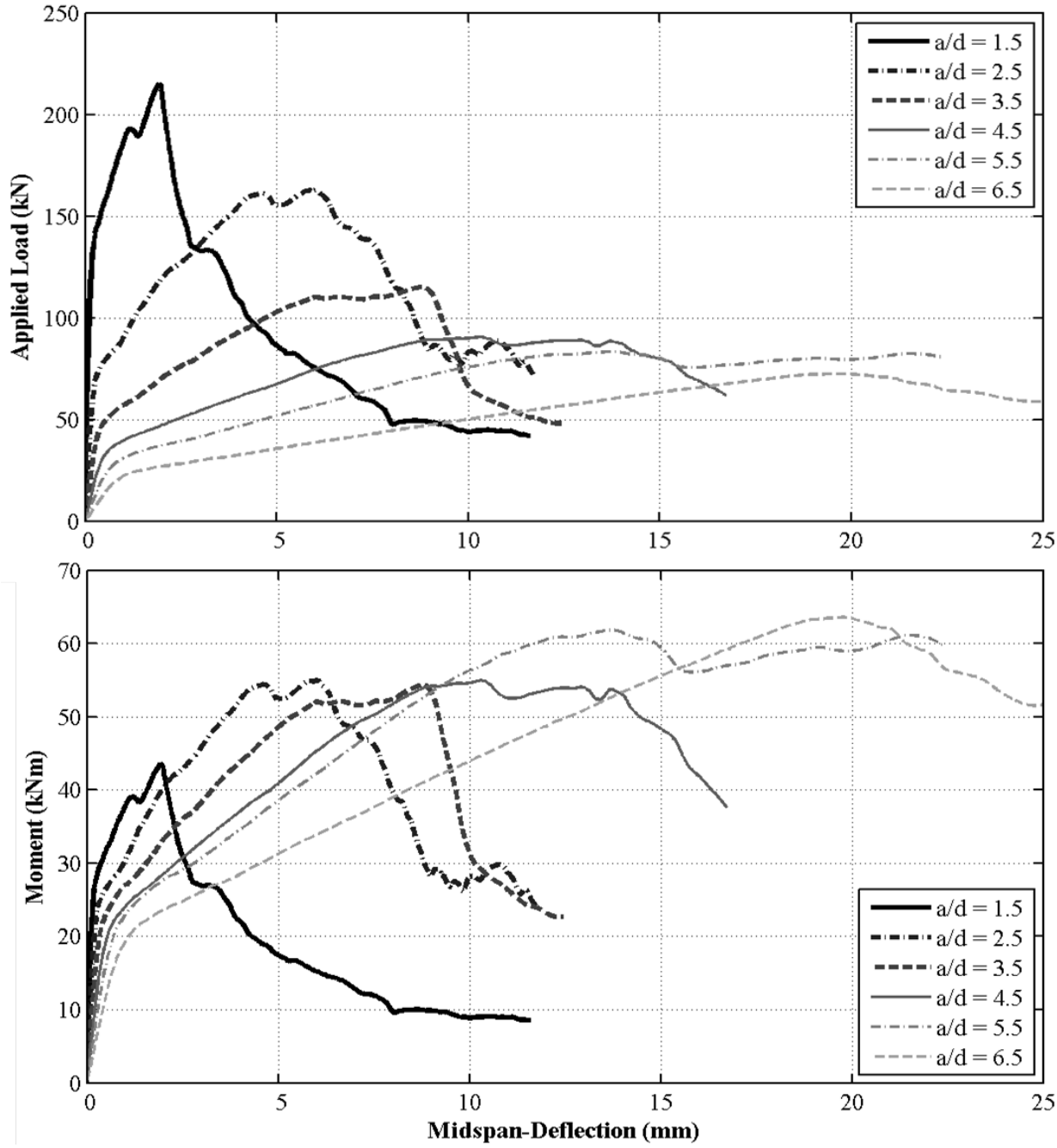

Figure 7.1: Influence of Slenderness Ratio - BM 16-INF

slenderness ratios of 1.5 to 3.5, a very distinct diagonal shear crack is apparent at failure that extends from the load point towards the support. Ratios of 4.5 and 5.5 show the distinct formation of vertical flexural cracks; however there are still regions within the mid-height of the beam that exhibited critically concentrated plastic strains, indicating

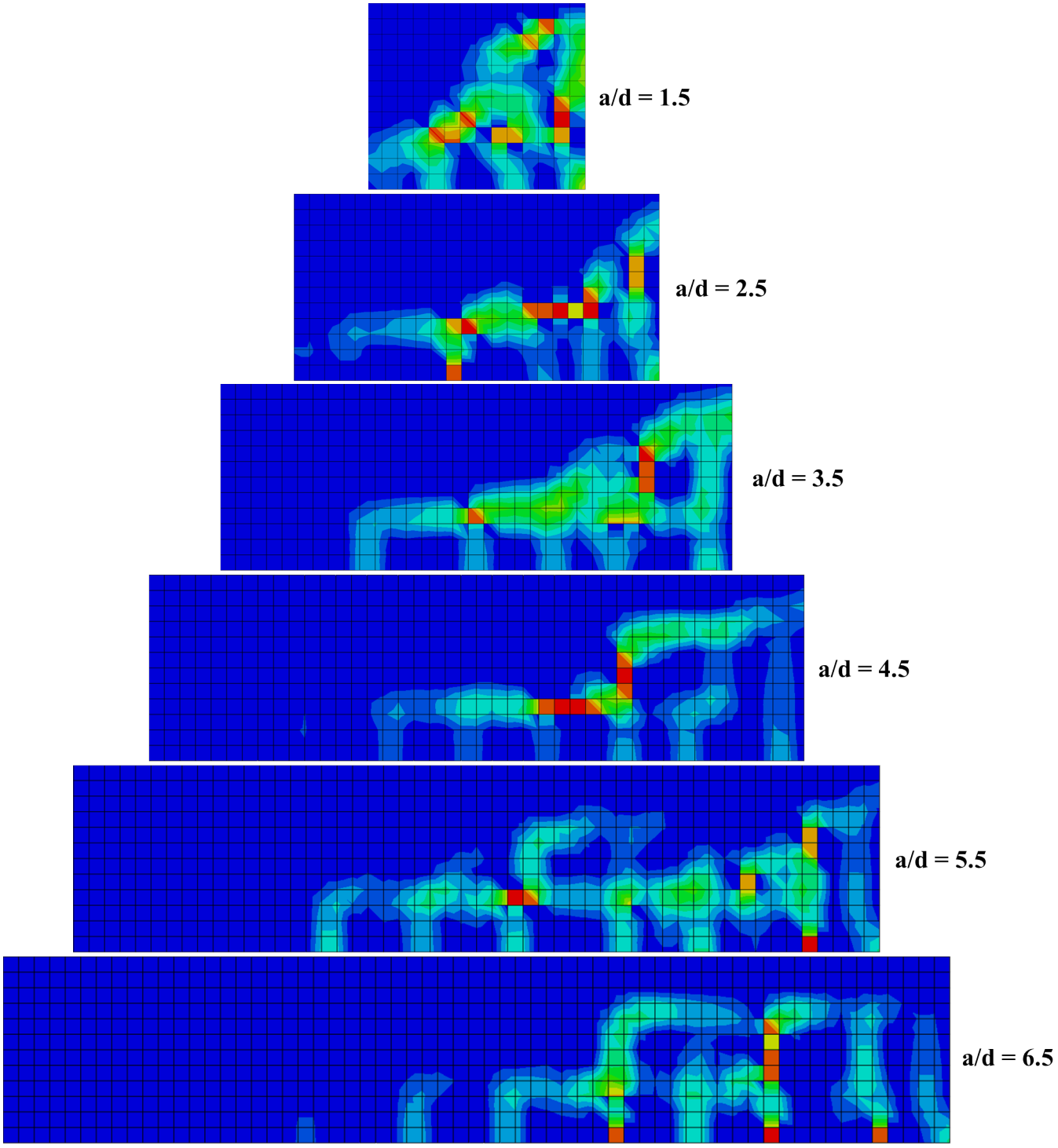

Figure 7.2: Influence of Slenderness Ratio on Crack Pattern at Failure - BM 16-INF

shear failures within these elements. The largest slenderness ratio of 6.5 exhibited very distinct vertical flexural cracks; this is to be expected as the flexural strength approaches

the shear strength with increasing slenderness. However, even this most slender beam with no stirrups showed concentrated plastic strains within the web of the beam, thus indicating shear failure. Furthermore, the crack patterns of this beam differ significantly from the flexural failures exhibited by beams with stirrups as will be discussed later.

Table 7.2 compares the peak loads obtained from the ABAQUS model with various strength predictions for all beams with no stirrups. Strength predictions include: (1) flexural strength as predicted by CSA S806-12; (2) shear strength as predicted by CSA S806-12; and (3) shear strength as predicted by Nehdi et al. (2007). Table 7.2 also provides the ultimate load as measured during the experimental testing (Exp.); applicable to $a/d = 2.5$.

Table 7.2: Comparison of Ultimate Loads for Beams with No Stirrups (kN)

Beam	a/d	CSA Flexure	CSA Shear	Nehdi et al.	ABAQUS Model	Exp.
12-INF	1.5	719.9	271.6	283.7	217.3	-
	2.5	431.9	152.8	151.3	169.4	163.1
	3.5	308.5	129.1	140.1	133.3	-
	4.5	240.0	113.9	132.2	100.0	-
	5.5	196.3	103.0	126.2	83.3	-
	6.5	163.6	94.8	121.5	85.8	-
16-INF	1.5	683.8	266.2	275.4	215.0	-
	2.5	410.3	144.8	146.9	142.3	150.2
	3.5	293.1	122.3	136.0	110.3	-
	4.5	227.9	107.9	128.4	90.5	-
	5.5	186.5	97.6	122.6	83.3	-
	6.5	155.4	89.8	117.9	72.5	-
25-INF	1.5	620.8	256.9	261.0	198.1	-
	2.5	372.5	131.8	139.3	132.5	125.1
	3.5	266.1	111.4	128.9	105.0	-
	4.5	206.9	98.2	121.6	83.8	-
	5.5	169.3	88.9	116.2	71.8	-
	6.5	141.1	81.7	111.8	69.9	-

For the purposes of this discussion, the shear model proposed by Nehdi et al. (2007) will

be referred to as the "Nehdi" model; the CSA S806-12 flexure prediction will be referred to as the "Flexure" model; and the CSA S806-12 shear prediction will be referred to as the "CSA Shear" model. Figure 7.3 plots the peak load predictions as a function of the slenderness ratio for BM 16-INF. The experimental failure load is also presented.

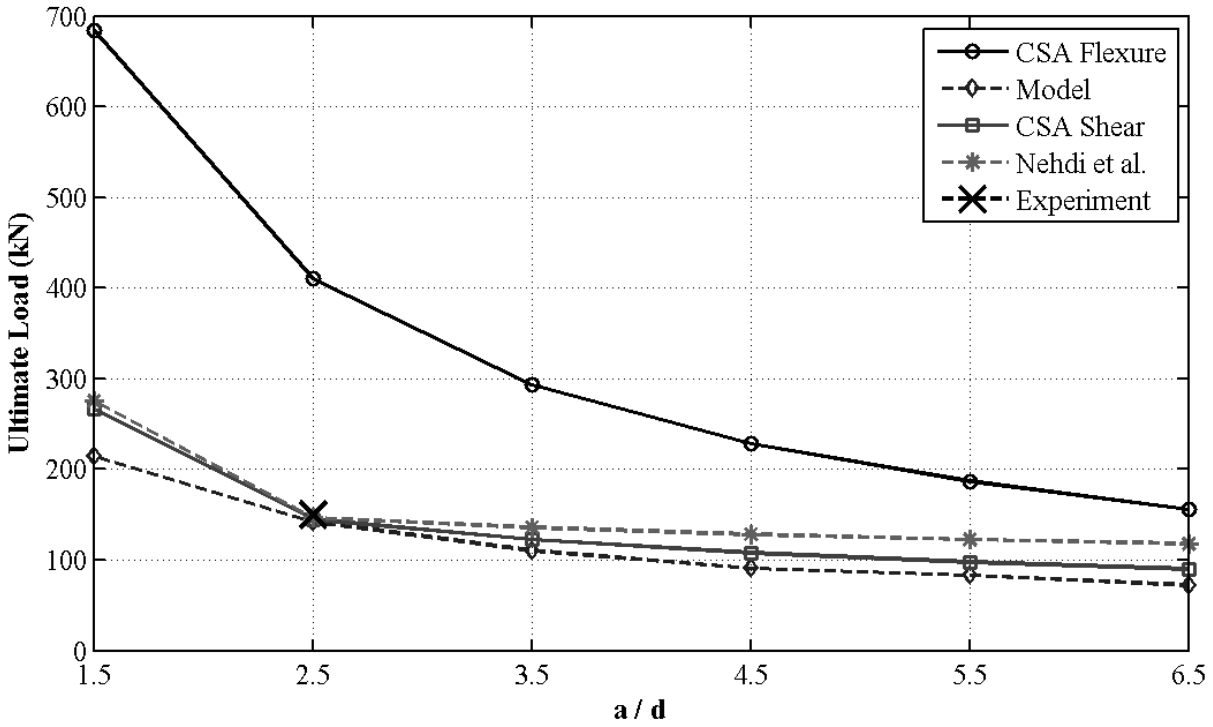

Figure 7.3: Failure Load Predictions - BM 16-INF

As shown in Table 7.2 and Figure 7.3, the Flexure model vastly overpredicted the failure load for all values of a/d as compared to the other strength predictions. This means that flexure never governed the failure; a pattern consistent for all beams with no stirrups. This is to be expected as these beams had no stirrups and will thus experience brittle shear failures; it would take a very slender beam with no stirrups to fail due to flexure (a/d > 6.5). It is also clear that the ABAQUS modelling agreed strongly with the shear predictions provided by the Nehdi model and CSA Shear model. Figure 7.4 focuses on these curves.

It can be seen that for $a/d = 1.5$, the Nehdi and CSA Shear models match closely with a peak load of 275.4kN and 266.2kN, respectively. However, the ABAQUS model predicted

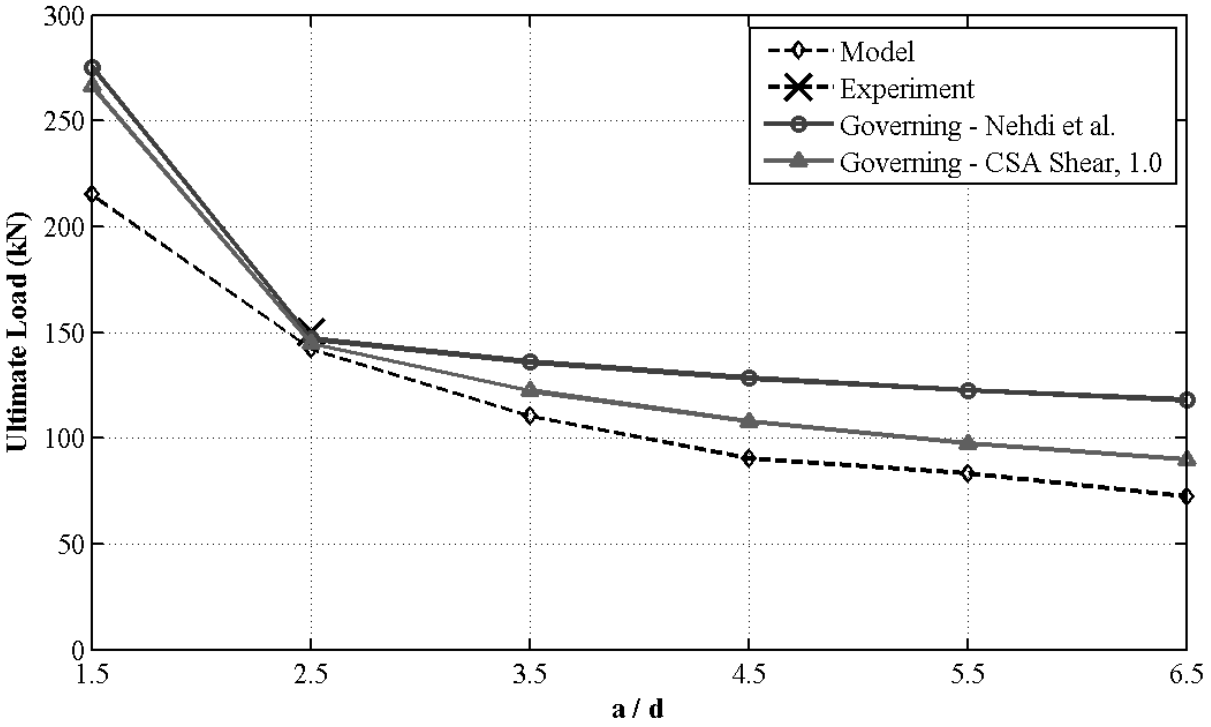

Figure 7.4: Governing Load Predictions - BM 16-INF

a lower load of 215kN. As discussed in Section 2.4.1, CSA S806-12 applies a k_a factor to the shear resistance provided by the concrete, V_c. This factor ranges from 1.0 to 2.5 and is multiplied with V_c to account for the additional strength provided by the arch effect in deep members. Using the shear strength predictions of CSA S806-12, the critical section of a simply-supported beam under three-point bending is the mid-span; this section has the lowest shear resistance. It was found that for all beams with slenderness ratios of 1.5, the k_a factor at mid-span was 1.67, whereas a factor of 1.0 was found for all other slenderness ratios. Similarly, the Nehdi model also considers the influence of the beam slenderness on the concrete shear strength. As shown in Equation 2.16, the shear resistance contribution of the concrete is multiplied by $(2.5d/a)$ if the slenderness ratio is less than 2.5. Again, it was found that this factor is equal to 1.67 for all beams with slenderness ratios of 1.5, whereas a factor of 1.0 was found for all other slenderness ratios. Therefore, both shear models used a factor of 1.67 to increase the concrete shear strength for beams with slenderness ratios less than 2.5. It is clear that the ABAQUS model was unable to consider the effects

of arch action as this additional strength was not captured.

For a slenderness ratio of 2.5, the proposed model agreed strongly with both shear strength prediction models. For all ratios greater than 2.5, the strengths predicted by the Nehdi model were consistently higher than the strengths of CSA S806-12, and the ABAQUS model results agreed best with the CSA Shear model. This was consistent for all beams with no stirrups.

7.2.2 Beams with Stirrups

Figure 7.5 shows the load-deflection and moment-deflection responses for BM 16-150.

It can be seen that the moment-deflection response for BM 16-150 was highly dependent on the slenderness ratio of the beam. For low ratios of 1.5 and 2.5, the beam failed at lower moments, 95.2kNm and 133.0kNm, respectively, whereas larger ratios of 3.5 to 6.5 caused the beam to fail at larger moments of 149.4kNm, 159.5kNm, 168.8kNm, and 168.7kNm, respectively. As the ratio increased, the failure moments converged to a relatively constant value that was significantly higher than the failure moments of the deeper beams. This suggests that the presence of stirrups allowed the beams to shift from shear-governed failures to flexure-governed failures with increasing slenderness. This was consistent for all beams with stirrups. This behaviour is also reflected in the crack patterns exhibited at failure as shown in Figure 7.6 for BM 16-150.

For slenderness ratios of 1.5 and 2.5, a very distinct diagonal shear crack is apparent at failure that extends from the load point towards the support. For ratios of 3.5 and greater, the formation of distinct vertical flexural cracks is evident, especially with $a/d = 6.5$. It is important to note the difference between the crack patterns shown in Figure 7.6 and the patterns shown in Figure 7.2 for BM 16-INF. Although the crack patterns for BM 16-INF

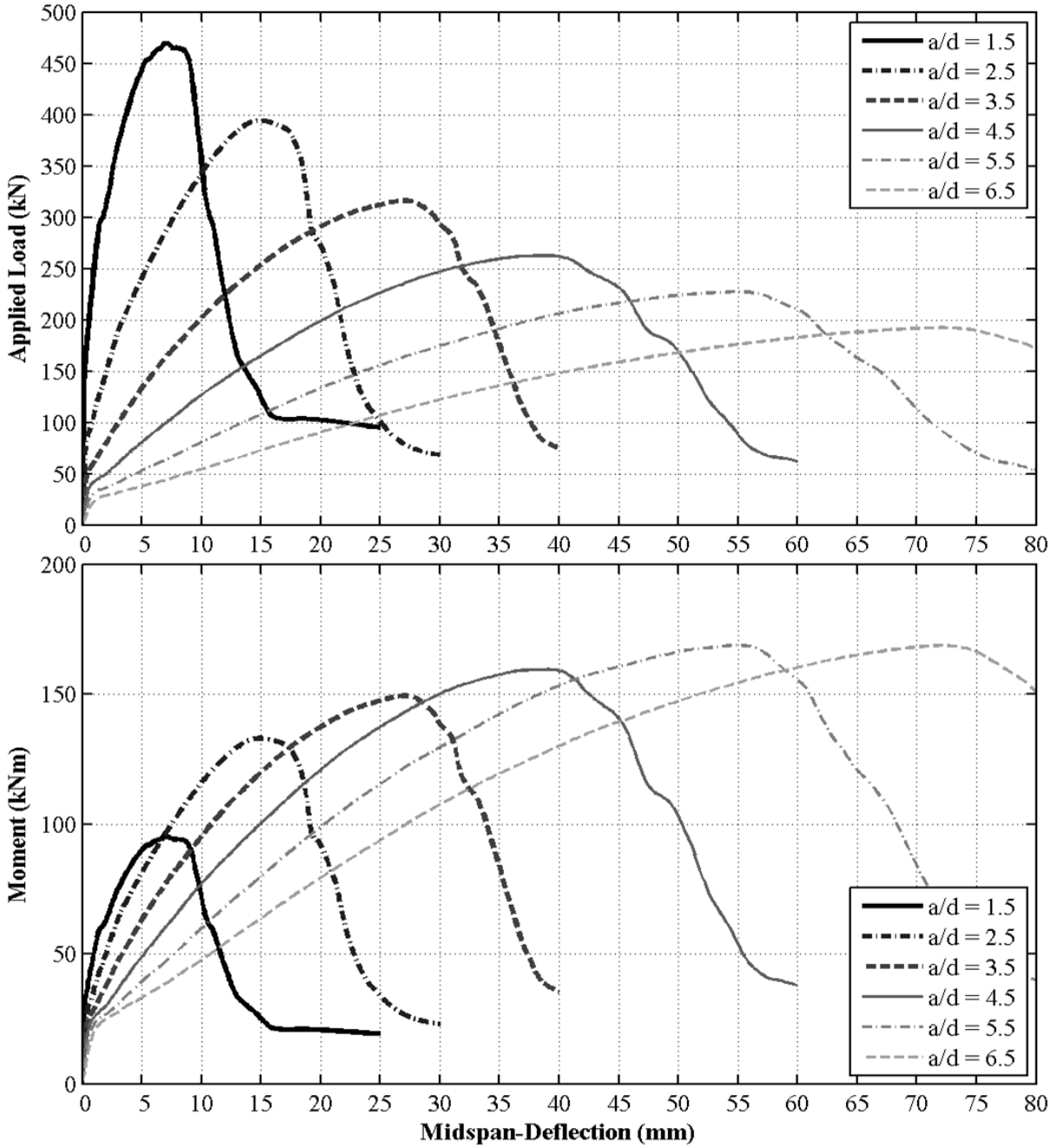

Figure 7.5: Influence of Slenderness Ratio - BM 16-150

also exhibited vertical flexural cracks, the failures were concentrated in elements within the web of the beam and resulted in shear failures. Conversely, the cracking of BM 16-150 shows that the plastic strains were distributed more evenly amongst elements, suggesting a more ductile failure mode. Furthermore, BM 16-150 exhibited distinct plastic strains

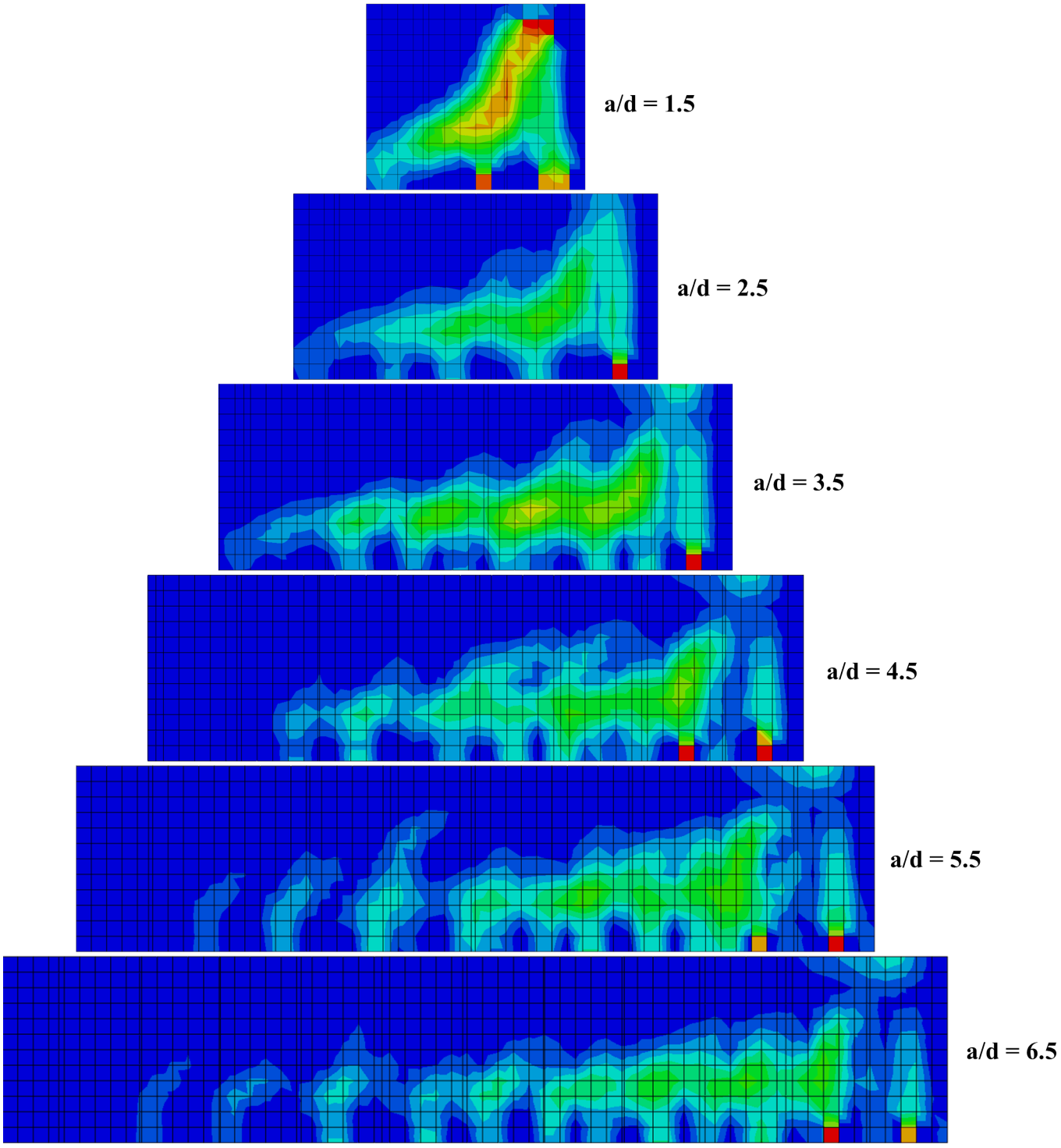

Figure 7.6: Influence of Slenderness Ratio on Crack Pattern at Failure - BM 16-150

in the vicinity of the load point (top-right corner) for a/d ratios of 3.5 and greater, thus indicating concrete crushing at the top of the beam; a further indication of flexural failure

of the section.

Table 7.3 compares the peak loads obtained from the ABAQUS model with various strength predictions for all beams with stirrups spaced at 150mm. This table also provides the ultimate load as measured during the experimental testing (Exp.); applicable to $a/d = 2.5$.

Table 7.3: Comparison of Ultimate Loads for Beams with Stirrups at 150mm (kN)

Beam	a/d	CSA Flexure	CSA Shear, 0.4	CSA Shear, 1.0	Nehdi et al.	ABAQUS Model	Exp.
12-150	1.5	736.4	345.5	446.9	510.5	478.1	-
	2.5	441.9	226.2	300.8	376.7	385.1	405.2
	3.5	315.6	196.9	262.4	365.4	325.0	-
	4.5	245.5	177.2	235.1	357.4	269.2	-
	5.5	200.8	162.3	214.2	351.4	234.1	-
	6.5	167.4	150.6	205.8	346.6	207.6	-
16-150	1.5	703.3	336.2	407.4	502.8	469.9	-
	2.5	422.0	214.4	283.2	372.7	393.9	416.5
	3.5	301.4	186.4	246.1	361.6	316.2	-
	4.5	234.4	167.3	219.8	353.9	262.5	-
	5.5	191.8	153.0	207.5	348.0	227.4	-
	6.5	159.8	141.7	199.5	343.3	192.3	-
25-150	1.5	646.6	320.9	380.2	489.8	369.7	-
	2.5	388.0	195.4	254.4	365.7	346.0	415.8
	3.5	277.1	169.2	220.2	355.1	271.7	-
	4.5	215.5	151.3	206.6	347.7	226.8	-
	5.5	176.4	137.9	197.0	342.1	213.5	-
	6.5	147.0	127.3	189.7	337.7	185.6	-

The results for the beams with stirrups spaced at 220mm and 230mm can be found in Appendix D. Figure 7.7 plots the peak load predictions as a function of the slenderness ratio for BM 16-150. The experimental failure load is also presented.

As shown in Table 7.3 and Figure 7.7, the Flexure model vastly overpredicted the failure load for $a/d = 1.5$ as compared to the other strength predictions. This is to be expected

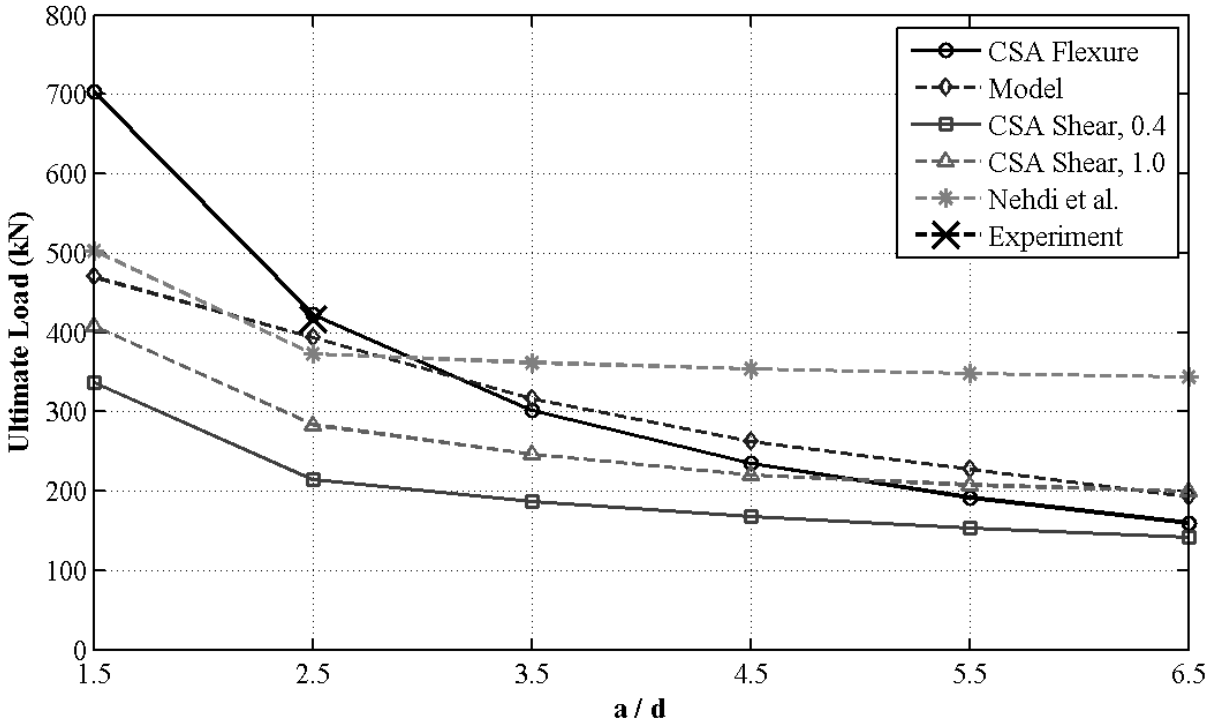

Figure 7.7: Failure Load Predictions - BM 16-150

as this low slenderness ratio represents a deep beam which will experience a brittle shear failure as opposed to a flexural failure. At a slenderness ratio of 2.5, the flexural strength prediction approached the shear strength determined by the Nehdi model. A ratio of 2.5 represents the theoretical boundary between deep-beam behaviour (shear-governed) and slender-beam behaviour (flexure-governed). Beyond this boundary ratio, the predicted flexural strength became less than the shear strength predicted by the Nehdi model and became the governing strength.

It is important to discuss the shear predictions provided by CSA S806-12. Referring back to Equation 2.10, the shear contribution provided by the GFRP stirrups is multiplied by a reduction factor of 0.4; a factor that is not applied when steel stirrups are used. This factor is used to consider the reduced strength of the FRP stirrups due to the bent regions. As no stirrups ruptured during the experimental tests or ABAQUS modelling, a factor of 1.0 was also considered in the presented comparisons (CSA Shear, 1.0). For all beams with stirrups,

the CSA shear predictions (factor of 0.4 and 1.0) significantly underestimated the shear strength as compared to the Nehdi model for all values of a/d. Although these models matched closely for the beams with no stirrups (concrete contribution only), it is clear that CSA S806-12 assumes that the stirrups provide a significantly smaller contribution to the shear resistance of the beam as compared to the Nehdi model. Alternatively, it is possible that the CSA model underestimates the influence that the FRP stirrups have on the concrete such as increased confinement as compared to steel.

As the failure mode shifted from shear-governed to flexure-governed with increases to the slenderness ratio, Figure 7.8 compares the ABAQUS model results for BM 16-150 with the governing strength predictions.

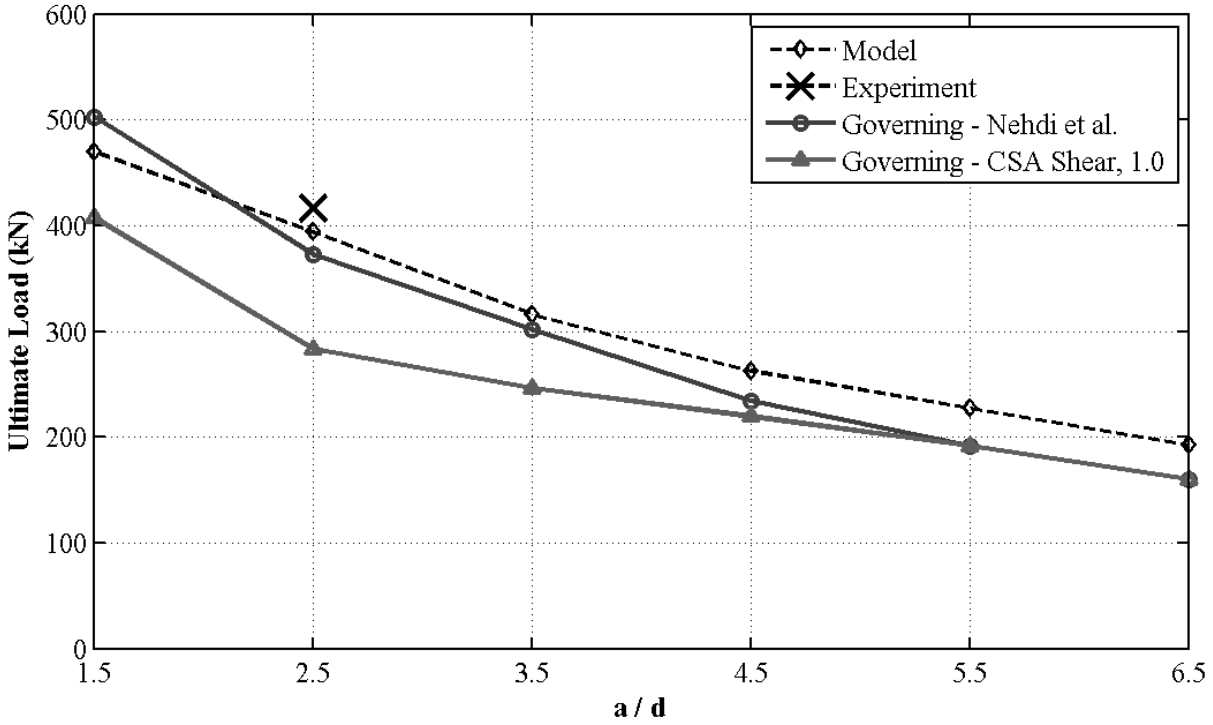

Figure 7.8: Governing Load Predictions - BM 16-150

The curve labeled "Governing - Nehdi et al." presents the minimum of the CSA flexural strength and the shear strength predicted by Nehdi et al. (2007). The curve labeled "Governing - CSA Shear, 1.0" presents the minimum of the CSA flexural strength and

the CSA shear strength with a factor of 1.0. For a slenderness ratio of 1.5 and 2.5, the ABAQUS model for BM 16-150 agreed strongly with the Nehdi model. For ratios of 3.5 and greater, the flexural strength of the beam governed and agreed strongly with the model.

The results for beams with stirrups spaced at 230mm (BM XX-s230) differed slightly from the results for beams with stirrups at 150mm and 220mm. The cross-sections of these beams were increased to accommodate the presence of larger stirrups. Figure 7.9 presents the peak loads as predicted for BM 16-s230 using various models, and Figure 7.10 presents the governing peak loads.

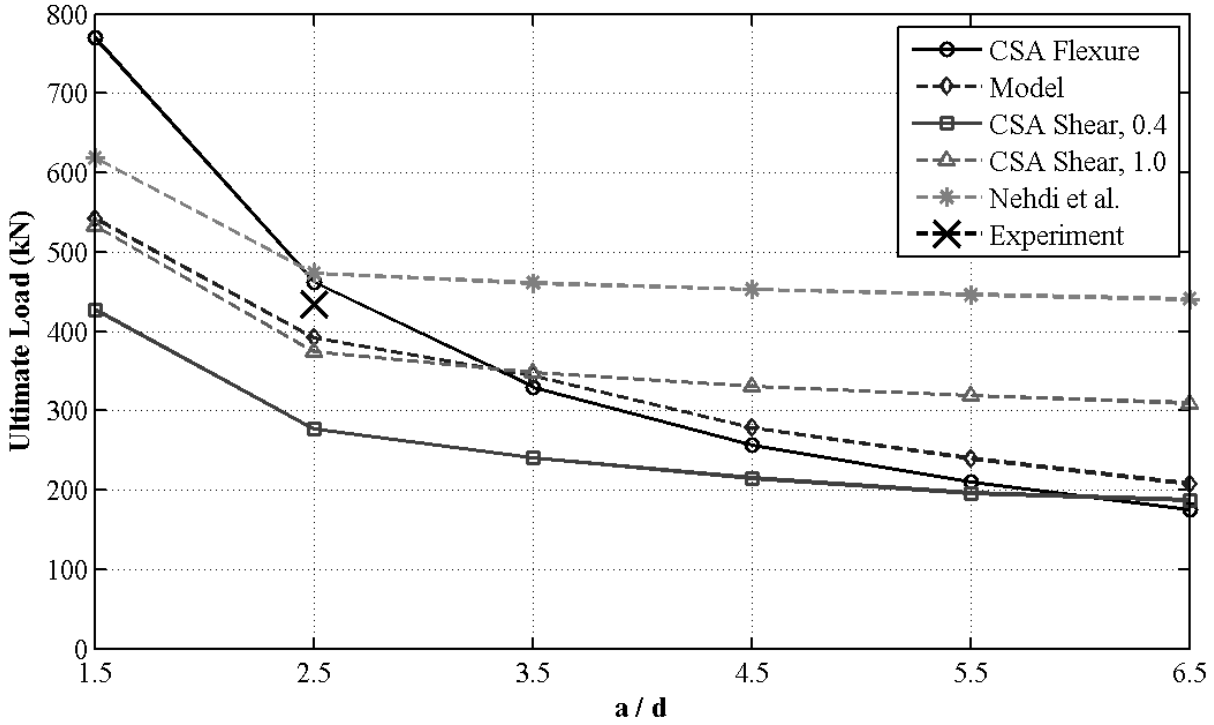

Figure 7.9: Failure Load Predictions - BM 16-s230

As BM 16-s230 had a larger height and width than all other beams with 16mm longitudinal bars, this section had a much higher shear capacity. As a result, the two governing curves converged much sooner ($a/d = 3.5$) as compared to the beams with stirrups at 150mm or 220mm that did not converge until ratios of 5.5 or 6.5. This means that the shift from shear-governed to flexure-governed failures occurred much sooner for beams with larger

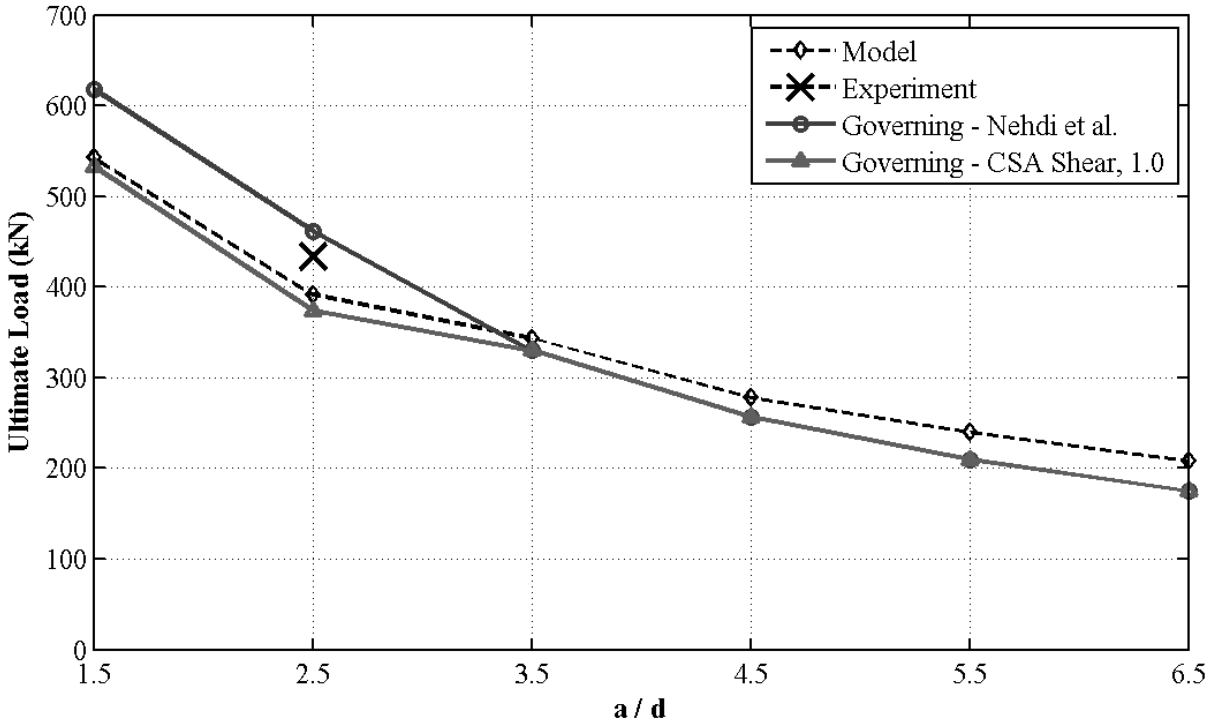

Figure 7.10: Governing Load Predictions - BM 16-s230

stirrups (at lower slenderness ratios).

7.2.3 Final Discussion

Beams with No Stirrups:

The study of the moment-deflection responses, crack patterns at failure, and various strength predictions demonstrated that the failure mode of each beam with no stirrups was shear governed, regardless of the slenderness ratio. Therefore, the Flexure model was not appropriate for these beams. It was found that for slenderness ratios of 1.5 and 2.5, the CSA Shear model and the Nehdi model matched closely. For $a/d = 1.5$, these shear models both predicted larger failure loads than the ABAQUS model to consider the influence of the arch effect in very deep beams. As this increased strength was not exhibited by the ABAQUS models, more research is required to study this effect.

For slenderness ratios greater than 2.5, the CSA Shear model and Nehdi model diverged, with the proposed ABAQUS model agreeing most strongly with the CSA Shear model. Therefore, when considering the contribution of only the concrete to the shear resistance of a beam (no stirrups present), both the Nehdi and CSA Shear models provide accurate results for $a/d \leq 2.5$, whereas the CSA Shear model is recommended for all $a/d > 2.5$.

Beams with Stirrups:

The study of the moment-deflection responses, crack patterns at failure, and various strength predictions demonstrated that each beam with stirrups experienced shear-governed failures for low slenderness ratios of 1.5 and 2.5, and shifted towards flexure-governed failures for ratios larger than 2.5. For beams with no stirrups, the shear predictions provided by Nehdi et al. (2007) and CSA S806-12 matched closely for all slenderness ratios. Conversely, the strength predictions provided by these two models diverged significantly for all beams with stirrups. For the CSA Shear model, a reduction factor of 0.4 is applied to the strength contribution of the FRP stirrups; this proved to severely underestimate the shear strength of each beam as compared to experimental and ABAQUS results. Even with the omission of this reduction factor, the CSA Shear model consistently predicted lower shear strengths than the Nehdi model for low slenderness ratios. However, when the reduction factor was omitted, the CSA Shear model provided the best correlation to the ABAQUS model for $a/d = 1.5$ whereas the Nehdi model produced much higher strengths. Therefore, one conclusion could be that the CSA Shear model with no reduction factor and the proposed ABAQUS model are both able to provide accurate shear predictions for beams with FRP stirrups and slenderness ratios of 1.5 while the Nehdi model overpredicts this strength; conversely, it is possible that the Nehdi model is the most accurate and is able to capture the arch effects of deep beams while the CSA Shear model and ABAQUS model are unable to. Therefore, more research is necessary to study very deep beams with $a/d = 1.5$ to conclude which model is most appropriate.

For a slenderness ratio of 2.5, the Nehdi model provided the best correlation with experimental results for all beams with stirrups. For beams with stirrups at 150mm and 220mm, the ABAQUS model matched closely with the experimental and Nehdi results. For the larger beams with stirrups at 230mm, however, the ABAQUS model agreed best with the CSA Shear model (with no reduction factor). Although the BM XX-s230 series did experience shear failures during the experimental testing, the larger sections of these beams increased the shear strengths such that the flexural strength matched closely with the shear predictions as shown in Figure 7.9. Therefore, it is possible that the Nehdi model was less effective for these larger beams as this model is applicable to shear-governed failures and these beams were close to the shear-flexure failure boundary.

For all values of a/d equal to and greater than 3.5, flexural failures were predicted. As a consequence, the Nehdi model became less and less accurate as compared to the ABAQUS model as this model was calibrated using shear-critical beams only. The ABAQUS model agreed strongly with the Flexure model for all beams with stirrups. It was found that the strengths predicted by the CSA Shear model (no reduction factor) converged with the Flexure model at large slenderness ratios of 5.5 and 6.5 for beams with stirrups at 150mm and 220mm, whereas the CSA Shear model with the reduction factor included converged with the Flexure model for beams with stirrups at 230mm.

Table 7.4 presents the final recommendations for the modelling and strength prediction of concrete beams reinforced with GFRP stirrups. This table presents whether each model is recommended ("Yes") or not recommended ("No") for various slenderness ratios.

Table 7.4: Model Recommendations for Beams with Stirrups

a/d	CSA Flexure	CSA Shear, 0.4	CSA Shear, 1.0	Nehdi et al.	ABAQUS Model
1.5	No	No	More research required		
2.5	No	No	No*	Yes	Yes
≥ 3.5	Yes	No	No	No	Yes

* Most accurate for BM XX-s230, but underpredicted all others

Chapter 8

Conclusions and Recommendations

Krall (2014) performed testing on twelve concrete beams reinforced with glass fibre reinforced polymer (GFRP) longitudinal bars and stirrups. Beams varied in terms of longitudinal bar diameter, longitudinal bar configuration, stirrup diameter, and stirrup spacing (or absence of stirrups). Beams were classified as having no stirrups (BM XX-INF), stirrups spaced at 150mm (BM XX-150), stirrups spaced at 220mm (BM XX-220), and stirrups spaced at 230mm (BM XX-s230).

This thesis presented the numerical modelling of these beams using the finite element analysis software ABAQUS. The Concrete Damaged Plasticity Model is a concrete constitutive model provided within ABAQUS and was used exclusively in this thesis. This model implements a non-associated plastic flow rule with a multi-variable hardening formulation. The use of a scalar isotropic damaged elasticity is possible and viscoplastic regularization may be used in tensile softening regions to improve convergence of the models. The Concrete Damaged Plasticity Model was calibrated using the experimental data for the modelling of beams with and without GFRP stirrups. The conclusions made regarding these analyses and recommendations for future work will now be presented.

8.1 Beam Modelling Parameters

Chapter 4 provided an overview of the selection of material properties and element formulations. The following conclusions were made:

- The concrete age model proposed by ACI 209R-92 was used to correlate the concrete compressive strength with the time after casting in order to increase the accuracy of the ABAQUS modelling with respect to the experimental testing. Using this analysis, compressive strengths of 54.0MPa, 53.4MPa, and 52.0MPa were used for BM 12-INF, 16-INF, and 25-INF, respectively, and a strength of 56.5MPa was used for all beams with stirrups.
- The tensile strength of the concrete was calculated using the direct cracking formulation, $f_{cr} = 0.33\lambda\sqrt{f'_c}$, which yielded tensile strengths ranging from 2.38MPa to 2.48MPa.
- All GFRP reinforcement used for the experimental beams was ComBAR as provided by Schoeck Canada. The mechanical properties of this material used in the ABAQUS modelling were taken from the technical literature provided by Schoeck Canada.
- Three "parts" were used to assemble the beam models: (1) concrete beam, (2) GFRP longitudinal reinforcement, and (3) GFRP stirrups. The concrete beam was modelled as a deformable, homogeneous solid. The concrete was discretized using hexahedral, first-order, continuum elements. Reduced integration and hourglass control were incorporated to prevent the phenomena of shear locking and hourglassing.
- Two methods of modelling the GFRP reinforcement were studied in this research: (1) discrete, one-dimensional truss sections, and (2) smeared, reinforced membrane sections. The truss members were defined as deformable wire sections which were discretized using first-order truss elements, thus providing axial stiffness only. The membrane members were defined as deformable membrane sections which were discretized using 4-noded quadrilateral membrane elements with reduced integration

and hourglass control. It was demonstrated that the modification of the membrane thickness and smeared reinforcement spacing allowed the reinforced membranes to provide the required stiffness.

- The Embedded Region constraint was used to embed the GFRP reinforcement into the continuum concrete elements.

8.2 Modelling of Beams with No Stirrups

Chapter 5 presented the ABAQUS analyses of the three concrete beams reinforced with GFRP longitudinal reinforcement and no stirrups, including BM 12-INF, BM 16-INF, and BM 25-INF. The following conclusions were made:

- The Hognestad Parabola was used to model the uniaxial compressive behaviour of the concrete. Using the original parabola, a maximum strain corresponding to a complete loss of strength of $\varepsilon_{c,max} = 0.008$ was used.
- The post-peak region of the Hognestad Parabola was modified to become a function of $\varepsilon_{c,max}$ in order to study the influence of this strain on the beam behaviour. It was concluded that this maximum strain had no influence on the pre-peak beam response, which was to be expected as the beams with no stirrups experienced brittle shear-tension failures that were not dependent on the crushing of concrete.
- Three methods of defining the post-cracking tensile behaviour of the concrete were studied: (1) stress-strain approach, (2) fracture energy approach, and (3) stress-displacement approach. It was found that the stress-strain approach created numerical difficulties that prevented any useful results from being produced. Therefore, it was concluded that this method is not appropriate for these analyses.
- The fracture energy approach and stress-displacement approach allow the user to define post-cracking tensile stresses as a function of the crack-opening-displacements.

Values of fracture energy, G_f, ranging from 70N/m to 150N/m were studied, and various stress-displacement curves were studied, including linear, bilinear, and exponential. With higher fracture energies, the beams exhibited stiffer post-cracking responses and failed at higher loads. It was concluded that a fracture energy of 90N/m as recommended by Model Code 1990 provided the most consistent and accurate results for all beams with no stirrups. Furthermore, the bilinear and exponential functions produced similar responses that agreed strongly with the experiments, while the linear model was unable to capture the sharp strength loss at cracking. Therefore, the bilinear model as proposed by Cornelissen et al. (1986) was recommended due to its simplicity. This curve was able to capture the displacement response and reinforcement strain profiles accurately.

- The use of concrete damage parameters was considered to account for the elastic degradation that occurs upon unloading. It was concluded that the tension damage parameters did not influence the beam responses, whereas the compression parameters significantly weakened the behaviour. The combined use of tension and compression damage parameters is recommended as it provides results that agree strongly with the experiments and is consistent with the model proposed for beams with stirrups.
- The influence of the concrete dilation angle, ψ, on each beam response was studied. The typical values for the dilation angle as recommended in the literature range from 30° to 40°. It was concluded that an angle of $\psi = 30°$ produced the strongest agreement with the experimental results.
- The Concrete Damaged Plasticity Model allows the user to specify a viscosity parameter, μ, to perform viscoplastic regularization in order to overcome numerical convergence issues. An analysis was performed to determine the optimal value of this parameter, and it was concluded that a value of $\mu = 0.0001$ improved the computational efficiency of the models without compromising the accuracy of the results.

- The influence of the concrete mesh refinement on each beam response was studied. Meshes were characterized by the number of elements in the depth of the beam which ranged from 5-deep to 21-deep. All mesh refinements produced similar peak loads and crack patterns. However, as the mesh became finer, the displacement response became stiffer within the service loading region. It was concluded that a mesh with 12 elements in the depth of the beam provided both accurate and consistent results while optimizing the computational effort required.
- The longitudinal reinforcement was modelled using both the truss and membrane reinforcement approaches. It was determined that both methods provided similar beam responses and both produced reinforcement strain profiles that agreed strongly with the experimental strain data. It was concluded that the traditional truss method was the optimal solution as this approach resulted in slightly higher accuracy and allowed for easy visualization of the stresses in the individual reinforcing bars. However, it was demonstrated that the reinforced membrane approach is a valid alternative that produces accurate results.
- The influence of a modified bilinear stress-displacement tension model on the beam response and reinforcement strain behaviour was presented. This modified relationship implemented a sharper decrease in strength at cracking while maintaining a constant fracture energy, thus allowing the reinforcement "slippage" or debonding to be modelled at cracking. This analysis demonstrated how the tension model may be modified to simulate the interaction between the reinforcement and concrete.
- It was found that with minor calibration of the Concrete Damaged Plasticity Model, ABAQUS was able to provide accurate load-deflection responses, reinforcement strain profiles, and crack patterns that agreed strongly with the experimental data for all beams with no stirrups.

8.3 Modelling of Beams with Stirrups

Chapter 6 presented the ABAQUS analyses of the nine concrete beams reinforced with GFRP longitudinal bars and GFRP stirrups, including the BM XX-150, BM XX-220, and BM XX-s230 beam series. The following conclusions were made:

- The use of the Hognestad Parabola was considered for the concrete uniaxial compressive model. Using the original parabola ($\varepsilon_{c,max} = 0.008$) and a dilation angle of $\psi = 30°$ as recommended for the modelling of beams with no stirrups, the ABAQUS results severely underpredicted the ultimate load of all beams with stirrups. With a dilation angle of 30°, the beams experienced brittle failures and modifications to $\varepsilon_{c,max}$ had no influence on the beam responses. With an increased dilation angle of 50°, the beam responses became more ductile and modifications to $\varepsilon_{c,max}$ had a significant influence on the beam behaviour. It was theorized that since the GFRP stirrups did not rupture during testing and are unable to exhibit the plastic yielding that steel stirrups undergo, GFRP stirrups provide a significant degree of passive confinement to the core concrete, thus increasing the strength and ductility of the beam. Therefore, it was concluded that the combined modification of the concrete dilation angle and the maximum compressive strain was necessary to simulate the effects of this confinement provided by the GFRP stirrups. Values of $\psi = 50°$ and $\varepsilon_{c,max} = 0.015$ were recommended for the modelling of all beams with stirrups.
- The influence of the post-cracking tensile response was studied. The stress-strain formulation was again found to be inappropriate as this approach led to significant numerical difficulties. The stress-displacement approach was studied using various values of fracture energy, G_f, and curve shapes (linear, bilinear, exponential). It was concluded that the amount of fracture energy had minimal influence on the peak load; this was to be expected as these failures were compression-governed. However, larger fracture energies resulted in stiffer post-cracking responses. Similar to the modelling

of beams with no stirrups, it was concluded that the bilinear model as proposed by Cornelissen et al. (1986) with a fracture energy of 90N/m provided the best results for all beams with stirrups.

- The use of concrete damage parameters was considered to account for the elastic degradation that occurs upon unloading. It was concluded that the incorporation of compression damage parameters had a detrimental, or weakening, effect on the beam response, as expected. Conversely, the incorporation of tension damage parameters had a strengthening effect. The degrading effects of the compression damage proved to be stronger than the strengthening effects of the tension damage. Therefore, the combined use of both parameters resulted in a weaker beam as compared to the no-damage case, and is recommended for the modelling of beams with stirrups.
- It was concluded that viscoplastic regularization of the constitutive equations was necessary for all beams with stirrups, and a viscosity parameter of $\mu = 0.0001$ was found to improve the computational efficiency while producing accurate results.
- Similar to the modelling of beams with no stirrups, it was concluded that a mesh refinement with 12 elements in the depth of the beam provided both accurate and consistent results while optimizing computational effort.
- It was concluded that truss elements were the preferred method of modelling the longitudinal reinforcing bars. The reinforcement strains outputted by ABAQUS agreed strongly with the experimental data.
- The stirrup reinforcement was modelled using both the truss and membrane reinforcement approaches. It was determined that when a dilation angle of 30° and a maximum compressive strain of 0.008 were used, the stirrups were not engaged and the beams behaved similar to the beams with no stirrups. As the experimental beams with stirrups experienced concrete-governed failures (no stirrups ruptures), modifications to the concrete model were necessary to strengthen the beam and utilize the stirrups. With these modifications, it was concluded that the membrane stirrups were

the preferred alternative as they were able to capture the load-deflection response of each beam and provide reasonable stirrup strain predictions.

- The proposed model was also applied to beams with larger stirrup diameters (BM XX-s230). It was found that the model was able to replicate the experimental crack patterns and predict the failure loads to within 10% of the experimental data.
- It was found that with proper calibration of the Concrete Damaged Plasticity Model, ABAQUS was able to provide accurate load-deflection responses, reinforcement strain profiles, and crack patterns that agreed strongly with the experimental data for all beams with stirrups.

8.4 Parametric Study

A parametric study was performed to study the effectiveness of the proposed ABAQUS models in simulating the behaviour of GFRP reinforced concrete beams with varying slenderness ratios, (a/d). The proposed models for beams with no stirrups and for beams with stirrups were applied to beams with slenderness ratios ranging from 1.5 to 6.5. The following conclusions were made:

- For the beams with no stirrups, the bending moment at failure was relatively constant for each beam as the slenderness ratio changed and remained well below the flexural strength of the section. This proved that the absence of stirrups resulted in shear-governed failures, regardless of the beam slenderness. With no stirrups, it would take a very slender beam ($a/d > 6.5$) to generate moments that govern the failure.
- For the beams with no stirrups, slenderness ratios of 1.5 to 3.5 resulted in distinct diagonal shear cracks that extended from the load point towards the support. Elements within the web of the beam experienced highly concentrated strains that resulted in brittle shear failures of the beams. With ratios larger than 3.5, vertical

flexural cracks developed, but failure was again governed by the tensile shear cracking of the concrete.

- For beams with stirrups, the bending moment at failure was highly dependent on the slenderness ratio. For a/d of 1.5 and 2.5, the beams experienced shear failures and failed at bending moments much lower than the flexural strength. For ratios of 3.5 and greater, the beams shifted towards flexural failures, thus failed at relatively similar bending moments. These failure modes were also reflected in the crack patterns. At low slenderness ratios, distinct diagonal shear cracks governed the failures. For ratios greater than 3.5, vertical flexural cracks were distributed evenly along the tensile face of the beams and no concentrated shear failures were observed. These beams also exhibited plastic strains in the compression zone at mid-span suggesting compression crushing; a further indication of flexural failure.
- The peak loads obtained from the ABAQUS modelling were compared with various strength prediction models. It was concluded that the flexural strength predictions for beams with no stirrups as provided by CSA S806-12 did not govern for any slenderness ratios. For beams with no stirrups, the shear strength for very deep beams ($a/d = 1.5$) as predicted by CSA S806-12 and Nehdi et al. (2007) considered the increased strength resulting from the arch effect. This increased strength was not captured by the ABAQUS model. For $a/d \geq 2.5$, the CSA shear model and the Nehdi model matched closely, however the CSA shear model agreed best with the ABAQUS results.
- For beams with stirrups, the CSA shear predictions diverged significantly from the Nehdi predictions. For $a/d = 1.5$, the predicted strengths were quite variable, thus it was concluded that more research is required to determine which model provides the most accurate strength prediction. For $a/d = 2.5$, the Nehdi model proved to be the most accurate as compared to the experimental and ABAQUS results. For all slenderness ratios greater than 2.5, flexural failures governed, and the ABAQUS model

provided results that matched strongly with the CSA flexural strength predictions.

- In conclusion, with the exception of $a/d = 1.5$, the proposed ABAQUS models were able to accurately simulate the failure load, mode of failure, and crack pattern at failure for all slenderness ratios up to 6.5.

8.5 Recommendations for Future Work

Aspects of the presented research require further investigation to provide a stronger understanding of the observations and conclusions made in this thesis. The following recommendations are made regarding future work:

- Further investigation is required to determine the physical meaning of the dilation angle, ψ. Studies should aim to explain why an increased dilation angle of 50° was able to better represent the concrete used for beams with stirrups
- Further investigation is required to study the influence of compression and tension damage parameters. Studies should aim to explain why compression damage has a detrimental effect on a beam's response, whereas tension damage has an apparent strengthening effect.
- Further investigation is required regarding the accuracy of the shear predictions provided by CSA S806-12. The parametric study demonstrated that this model consistently underestimated the strength as compared to the model proposed by Nehdi et al. (2007) (a model calibrated by actual shear-critical beam experiments) and the ABAQUS results.
- Further investigation is required regarding the strength prediction of very deep members ($a/d = 1.5$). Studies should aim to solve the inconsistencies that were observed between the shear prediction models regarding the influence of the "arch effect".
- Further experimental beam tests should be designed using the proposed ABAQUS

models. The ability of the proposed model to simulate these future experiments will further validate its accuracy. The combined knowledge gained from the future experiments and potential modifications made to the current model will provide the basis for recommendations to be made to current design standards. These recommendations are necessary, as it was shown, that the CSA shear predictions are currently far too conservative.

References

ACI Committee 209 (1997). Prediction of creep, shrinkage, and temperature effects in concrete structures, (ACI 209R-92).

ACI Committee 440 (2006). Guide for the design and construction of structural concrete reinforced with FRP bars, (ACI 440.1R-06), American Concrete Institute, Detroit, Michigan.

ADINA R&D (2014). ADINA. Watertown, MA, USA.

Almusallam, T., Al-Salloum, Y., Alsayed, S., and Amjad, A. (1997). Behaviour of concrete beams doubly reinforced by FRP bars. In *Proceedings of the Third International Symposium on Non-metallic (FRP) Reinforcement for Concrete Structures (FRPRCS-3)*, pages 471–478.

Amertrano, D. (2011). Bond characteristics of glass fibre reinforced polymer bars embedded in high performance and ultra-high performance concrete. Master's Thesis, Ryerson University.

Baena, M., Torres, L., Turon, A., and Barris, C. (2009). Experimental study of bond behaviour between concrete and FRP bars using a pull-out test. *Composites: Part B*, 40(8):784–797.

Bai, J. (2013). *Advanced fibre-reinforced polymer composites for structural applications*. Woodhead Publishing, Oxford.

Belarbi, A. and Hsu, T. (1994). Constitutive laws of concrete in tension and reinforcing

bars stiffened by concrete. *ACI Structural Journal*, 91(4):465–474.

Bischoff, P. and Paixao, R. (2004). Tension stiffening and cracking of concrete reinforced with glass fiber reinforced polymer (GFRP) bars. *Canadian Journal of Civil Engineering*, 31(4):579–588.

Bouzaiene, A. and Massicotte, B. (1997). Hypoelastic tridimensional model for nonproportional loading of plain concrete. *Journal of Engineering Mechanics*, 123(11):1111–1120.

Canadian Standards Association (2004). Design of concrete structures, (CAN/CSA A23.3-04), Canadian Standards Association, Mississauga, Ontario.

Canadian Standards Association (2012). Design and construction of building structures with fibre-reinforced polymers, (CAN/CSA S806-12), Canadian Standards Association, Mississauga, Ontario.

Cervenka Consulting (2014). ATENA [5]. Praha, Czech Republic.

Chaallal, O. and Benmokrane, B. (1993). Physical and mechanical performance of an innovative glass-fiber-reinforced plastic rod for concrete and grouted anchorages. *Canadian Journal of Civil Engineering*, 20(2):254–268.

Chen, W. F. (1982). *Plasticity in Reinforced Concrete*. McGraw Hill, New York.

Chen, W. F. and Han, D. J. (1988). *Plasticity for Structural Engineers*. Springer-Verlag, New York.

Chimatech (2014). Vinyl-ester resins. Retrieved November 20, 2014 from http://www.chimatech.bg/en/.

Collins, M. P. and Mitchell, D. (1991). *Material Properties: Prestressed Concrete Structures*. Prentice-Hall, New Jersey.

Cornelissen, H., Hordijk, D., and Reinhardt, H. (1986). Experimental determination

of crack softening characteristics of normalweight and lightweight concrete. *Heron*, 32(2):45–56.

Currier, J., Fogstad, C., Walrath, D., and Dolan, C. (1994). Bond development of thermoplastic FRP shear reinforcement stirrups. In *Infrastructure: New Materials and Methods of Repair*, pages 592–597. American Society of Civil Engineers.

Dassault Systemes Simulia (DSS) (2012). ABAQUS [6.12]. Providence, RI, USA.

Demenico, D. D., Pisano, A. A., and Fuschi, P. (2014). A FE-based limit analysis approach for concrete elements reinforced with FRP bars. *Composite Structures*, 107:594–603.

Eamon, C., Jensen, E., Grace, N., and Shi, X. (2012). Life-cycle cost analysis of alternative reinforcement materials for bridge superstructures considering cost and maintenance uncertainties. *Journal of Materials in Civil Engineering*, 24(4):373–380.

Ehsani, M., Saadatmanesh, H., and Tao, S. (1995). Bond of hooked glass fiber reinforced plastic (GFRP) reinforcing bars to concrete. *ACI Materials Journal*, 92(4):391–400.

Evans, R. and Marathe, M. (1968). Microcracking and stress-strain curves for concrete in tension. *Materials and Structures*, 1(1):61–64.

Ferreira, A. J. M., Camanho, P. P., Marques, A. T., and Fernandes, A. A. (2001). Modelling of concrete beams reinforced with FRP re-bars. *Composite Structures*, 53(1):101–116.

Fields, K. and Bischoff, P. (2004). Tension stiffening and cracking of high-strength reinforced concrete tension members. *ACI Structural Journal*, 101(4):447–456.

Grace, N. F., Soliman, A. K., Abdel-Sayed, G., and Saleh, K. R. (1998). Behavior and ductility of simple and continuous FRP reinforced beams. *Journal of Composites for Construction*, 2(4):186–194.

Hillerborg, A. (1985). The theoretical basis of a method to determine the fracture energy Gf of concrete. *Materials and Structures*, 18(4):291–296.

Hillerborg, A., Modeer, M., and Petersson, P. (1976). Analysis of crack formation and crack growth in concrete by means of fracture mechanics and finite elements. *Cement and Concrete Research*, 6(6):773–782.

Hollaway, L. C. (2009). Polymer composites in construction: a brief history. In *Proceedings of the Institution of Civil Engineers: Engineering and Computational Mechanics*, volume 162, pages 107–118.

Hsu, T. and Zhang, L. (1996). Tension stiffening in reinforced concrete membrane elements. *ACI Structural Journal*, 93(1):108–115.

Hu, H. and Schnobrich, W. (1989). Constitutive modeling of concrete by using nonassociated plasticity. *Journal of Materials in Civil Engineering*, 1(4):199–216.

Hughes, B. and Chapman, G. (1966). The complete stress-strain curve for concrete in direct tension. *RILEM Bulletin*, 30:95–97.

Hughes Brothers (2011a). Aslan 100 Glass Fibre Reinforced Polymer (GFRP) Rebar Product Data Sheet. Retrieved October 20, 2014 from http://aslanfrp.com.

Hughes Brothers (2011b). Aslan 200 Carbon Fibre Reinforced Polymer (CFRP) Bar Product Data Sheet. Retrieved October 20, 2014 from http://aslanfrp.com.

Imjai, T., Guadagnini, M., and Pilakoutas, K. (2007a). Mechanical performance of curved FRP rebars - Part I: Experimental study. In *Asia-Pacific Conference on FRP in Structures*, pages 333–338.

Imjai, T., Guadagnini, M., and Pilakoutas, K. (2007b). Mechanical performance of curved FRP rebars - Part II: Analytical study. In *Asia-Pacific Conference on FRP in Structures*, pages 339–344.

International Federation for Structural Concrete (2007). FRP Reinforcement in RC Structures - Bulletin 40, Laussanne, Switzerland.

International Federation for Structural Concrete (2008). Constitutive Modelling of High Strength/High Performance Concrete - Bulletin 42, Laussanne, Switzerland.

International Federation for Structural Concrete (2013). Code-Type Models for Structural Behaviour of Concrete - Laussanne, Switzerland.

ISIS Canada (2007). *Reinforcing Concrete Structures with Fibre Reinforced Polymers - Design Manual No. 3.* ISIS Canada, Intelligent Sensing for Innovative Structures, A Canadian Network of Centres of Excellence, University of Manitoba, Winnipeg, Manitoba, Canada.

ISIS Educational Committee (2003). *ISIS Educational Module 2: An Introduction to FRP Composites for Construction.* ISIS Canada, Intelligent Sensing for Innovative Structures, A Canadian Network of Centres of Excellence, University of Manitoba, Winnipeg, Manitoba, Canada.

ISIS Educational Committee (2006). *ISIS Educational Module 8: Durability of FRP Composites for Construction.* ISIS Canada, Intelligent Sensing for Innovative Structures, A Canadian Network of Centres of Excellence, University of Manitoba, Winnipeg, Manitoba, Canada.

Jankowiak, T. and Lodygowski, T. (2005). Identification of parameters of concrete damage plasticity constitutive model. *Foundations of Civil and Environmental Engineering.*

Japan Society of Civil Engineers (1997). Recomendation for design and construction of concrete structures using continuous fibre reinforcing materials. *Concrete Engineering Series*, (23).

Karihaloo, B. (2003). Failure of concrete. *Comprehensive Structural Integrity*, 2(10):475–546.

Kmiecik, P. and Kaminski, M. (2011). Modelling of reinforced concrete structures and com-

posite structures with concrete strength degradation taken into consideration. *Archives of Civil and Mechanical Engineering*, 11(3):623–636.

Kobayashi, K. and Fujisaki, T. (1995). Compressive behavior of FRP reinforcement in non-prestressed concrete members. In *Proceedings of the Second International Symposium on Nonmetallic (FRP) Reinforcement for Concrete Structures (FRPRCS-2)*, pages 267–274.

Krall, M. (2014). Tests on concrete beams with GFRP flexural and shear reinforcements & analysis method for indeterminate strut-and-tie models with brittle reinforcements. Master's Thesis, University of Waterloo.

Kupfer, H., Hilsdorf, H., and Rusch, H. (1969). Behavior of concrete under biaxial stresses. *ACI Journal Proceedings*, 66(8):656–666.

Lee, J. and Fenves, G. (1998). Plastic-damage model for cyclic loading of concrete structures. *Journal of Engineering Mechanics*, 124(8):892–900.

Li, Z., Kulkarni, S., and Shah, S. (1993). New test method for obtaining softening response of unnotched concrete specimen under uniaxial tension. *Experimental Mechanics*, 33(3):181–188.

Lin, X. and Zhang, Y. X. (2013). Nonlinear finite element analyses of steel/FRP-reinforced concrete beams in fire conditions. *Composite Structures*, 97:277–285.

Lubliner, J., Oliver, J., Oller, S., and Onate, E. (1989). A plastic-damage model for concrete. *International Journal of Solids and Structures*, 25(3):299–326.

MacGregor, J. and Wight, J. (2005). *Reinforced Concrete: Mechanics and Design*. Pearson Prentice Hall, Upper Saddle River, New Jersey, 4th edition.

Mackenzie, D. and Boyle, J. T. (1993). A method of estimating limit loads by iterative elastic analysis: Parts I, II, III. *International Journal of Pressure Vessels and Piping*, 53(1):77–142.

Malm, R. (2006). Shear cracks in concrete structures subjected to in-plane stresses. Thesis, Royal Institute of Technology, Stockholm, Sweden.

Malm, R. (2009). Predicting shear type crack initiation and growth in concrete with non-linear finite element method. Thesis, Royal Institute of Technology, Stockholm, Sweden.

Massicotte, B., Nour, A., Ftima, M. B., and Yildiz, E. (2007). EPM3D - A user-supplied constitutive model for the nonlinear finite element analysis of reinforced concrete structures.

Micelli, F. and Nanni, A. (2004). Durability of FRP rods for concrete structures. *Construction and Building Materials*, 18(7):491–503.

Morphy, R., Sheata, E., and Rizkalla, S. (1997). Bend effect on strength of CFRP stirrups. In *3rd International Symposium on Non-Metallic (FRP) Reinforcement for Concrete Structures*, pages 19–26.

Nehdi, M., Chabib, H. E., and Said, A. A. (2007). Proposed shear design equations for FRP-reinforced concrete beams based on genetic algorithms approach. *Journal of Materials in Civil Engineering*, 19(12):1033–1042.

Nitereka, C. and Neale, K. W. (1999). Analysis of reinforced concrete beams strengthened in flexure with composite laminates. *Canadian Journal of Civil Engineering*, 26(5):646–654.

Nour, A., Massicotte, B., Yildiz, E., and Koval, V. (2007). Finite element modelling of concrete structures reinforced with internal and external fibre-reinforced polymers. *Canadian Journal of Civil Engineering*, 34(3):340–354.

Petersson, P. (1981). Crack growth and development of fracture zones in plain concrete and similar materials. REPORT TVBM - 1006, Lund Institute of Technology, Lund, Sweden.

Polling, R. (2001). Eine praxisnahe, schdigungsorientierte materialbeschreibung fr stahlbeton. Dissertation, Ruhr-Universitt Bochum.

Ponter, A. R. S. and Carter, K. F. (1997). Limit state solutions, based upon linear elastic solutions with a spatially varying elastic modulus. *Computer Methods in Applied Mechanics and Engineering*, 140:237–258.

Popovics, S. (1973). A numerical approach to the complete stress-strain curve of concrete. *Cement and Concrete Research*, 3(5):583–599.

Pultrall (2009). Bridgeport Bridge, Ontario. Retrieved September 15, 2014 from http://www.vrod.ca.

Pultrall (2011a). Thetford Mines Water Treatment Plant, Quebec. Retrieved September 15, 2014 from http://www.vrod.ca.

Pultrall (2011b). V-Rod CARBON. Retrieved October 20, 2014 from http://www.vrod.ca.

Pultrall (2012a). Parking Garage. Retrieved September 15, 2014 from http://www.pultrall.com.

Pultrall (2012b). V-Rod HM. Retrieved October 20, 2014 from http://www.vrod.ca.

Pultrall (2013a). V-Rod LM. Retrieved October 20, 2014 from http://www.vrod.ca.

Pultrall (2013b). V-Rod STANDARD. Retrieved October 20, 2014 from http://www.vrod.ca.

Rafi, M. M., Nadjai, A., and Ali, F. (2007). Analytical modeling of concrete beams reinforced with carbon FRP bars. *Journal of Composite Materials*, 41(22):2675–2690.

Rafi, M. M., Nadjai, A., and Ali, F. (2008). Finite element modeling of carbon fiber-reinforced polymer reinforced concrete beams under elevated temperatures. *ACI Structural Journal*, 105(6):701–710.

Rashid, Y. R. (1968). Ultimate strength analysis of prestressed concrete pressure vessels. *Nuclear Engineering and Design*, 7(4):334–344.

Reineck, K., Kuchma, D., Kim, K., and Marx, S. (2003). Shear datadata for reinforced concrete members witwith shear reinforcement. *ACI Structural Journal*, 100(2):240–249.

Rokugo, K., Iwasa, M., Suzuki, T., and Koyanagi, W. (1989). Testing methods to determine tensile strain softening curve and fracture energy of concrete. In *Fracture toughness and fracture energy test method for concrete and rock*, pages 153–163.

Schoeck (2009). Rehabilitation of Irvine Creek Bridge. Retrieved September 15, 2014 from http://www.schoeck-combar.ca/.

Schoeck (2013). Schoeck ComBAR Product Data Sheet for Straight Bars. Retrieved October 20, 2014 from http://www.schoeck.ca/.

Shah, S., Swartz, S., and Ouyang, C. (1995). *Fracture Mechanics of Concrete: Applications of Fracture Mechanics to Concrete, Rock and Other Quasi-Brittle Materials*. Wiley, New York.

Shehata, E., Morphy, R., and Rizkalla, S. (2000). Fibre reinforced polymer shear reinforcement for concrete members: Behaviour and design guidelines. *Canadian Journal of Civil Engineering*, 27(5):859–872.

Shi, Z. (2009). *Crack Analysis in Structural Concrete - Theory and Applications*. Elsevier, Boston.

Tamai, S. (1988). Average stress-strain relationship in post yield range of steel bar in concrete. *Concrete Library, JSCE*, 11:117–129.

Thorenfeldt, E., Tomaszewicz, A., and Jensen, J. J. (1987). Mechanical properties of high-strength concrete and applications in design. In *Proceedings of the Symposium utilization of high-strength concrete*, pages 149–159.

TNO DIANA BV (2014). DIANA. Delft, The Netherlands.

Trunk, B. and Wittmann, F. (1998). Experimental investigation into the size dependence of fracture mechanics parameters. In *Third International Conference of Fracture Mechanics of Concrete Structures*, volume 3, pages 1937–1948.

Ueda, T., Sato, Y., Kakuta, Y., Imamura, A., and Kanematsu, H. (1995). Failure criteria for FRP rods subjected to a combination of tensile and shear forces. In *Proceedings of the Second International RILEM Symposium on Non-Metallic (FRP) Reinforcement for Concrete Structures*, pages 26–33.

Unicomposite Technology (2014). Pultrusion process. Retrieved September 5, 2014 from http://www.unicomposite.com/.

Wang, T. and Hsu, T. (2001). Nonlinear finite element analysis of concrete structures using new constitutive models. *Computers and Structures*, 79(32):2781–2791.

Wittmann, F. H. (2002). Crack formation and fracture energy of normal and high strength concrete. *Sadhana*, 27(4):413–423.

Yu, T., Teng, J., Wong, Y., and Dong, S. (2010). Finite element modeling of confined concrete-I: DruckerPrager type plasticity model. *Engineering Structures*, 32(3):665–679.

Zhang, Y. X. and Kim, K. S. (2006). Geometrically nonlinear analysis of laminated composite plates by two new displacement-based quadrilateral plate elements. *Composite Structures*, 72(3):301–310.

Zhang, Y. X. and Lin, X. (2013). Nonlinear finite element analyses of steel/FRP reinforced concrete beams by using a novel composite beam element. *Advances in Structural Engineering*, 16(2):339–352.

Zhao, W. (1999). *Crack and deformation behavior of FRP reinforced concrete structures.* PhD Thesis, University of Sheffiled, Sheffield, UK.

Appendix A

Beam Drawings

This Appendix provides the detailed drawings of the twelve concrete beams that were studied in this thesis. Drawings include cross-section dimensions, longitudinal bar arrangements, and stirrup layouts. The location and nomenclature of all reinforcement strain gauges are also presented.

BM 12-INF

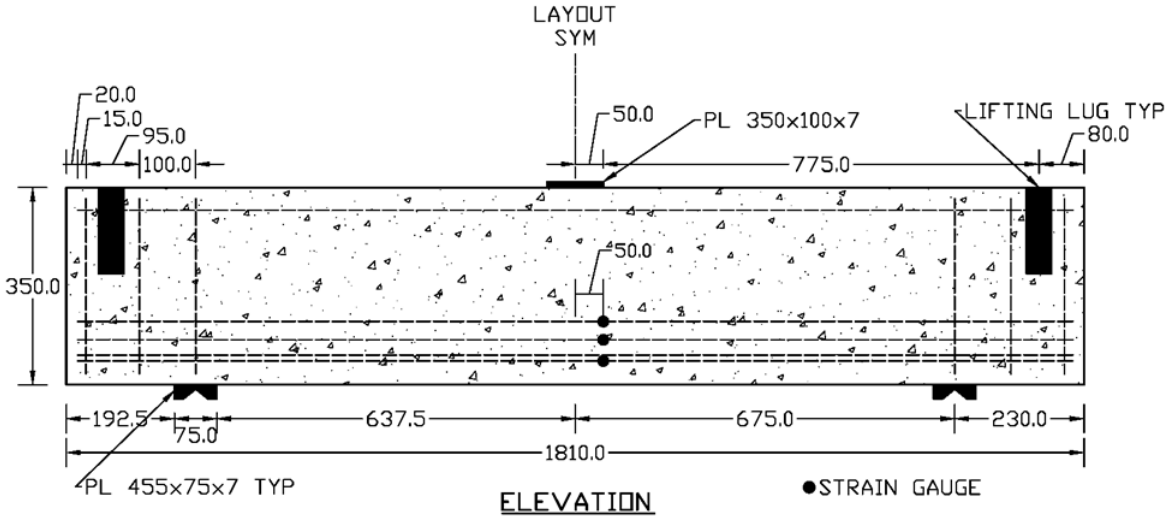
LAYOUT
SYM
20.0
15.0
95.0
100.0
50.0
PL 350x100x7
775.0
LIFTING LUG TYP
80.0
350.0
50.0
192.5
75.0
637.5
675.0
230.0
1810.0
PL 455x75x7 TYP
ELEVATION
●STRAIN GAUGE

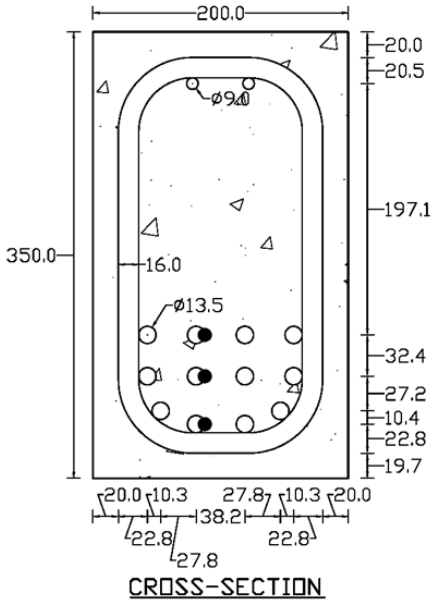
200.0
20.0
20.5
ø9.0
197.1
350.0
16.0
ø13.5
32.4
27.2
10.4
22.8
19.7
20.0
10.3
27.8
10.3
20.0
38.2
22.8
22.8
27.8
CROSS-SECTION

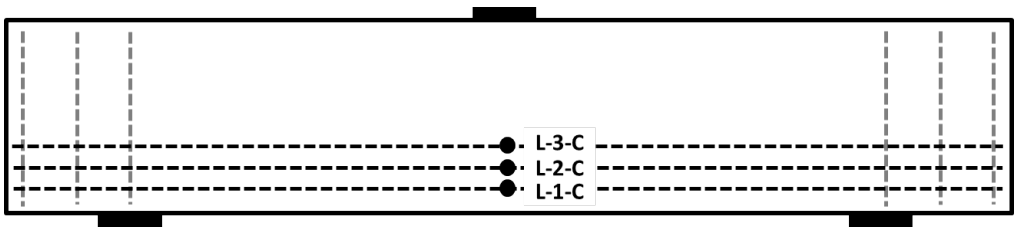
L-3-C
L-2-C
L-1-C

BM 12-150

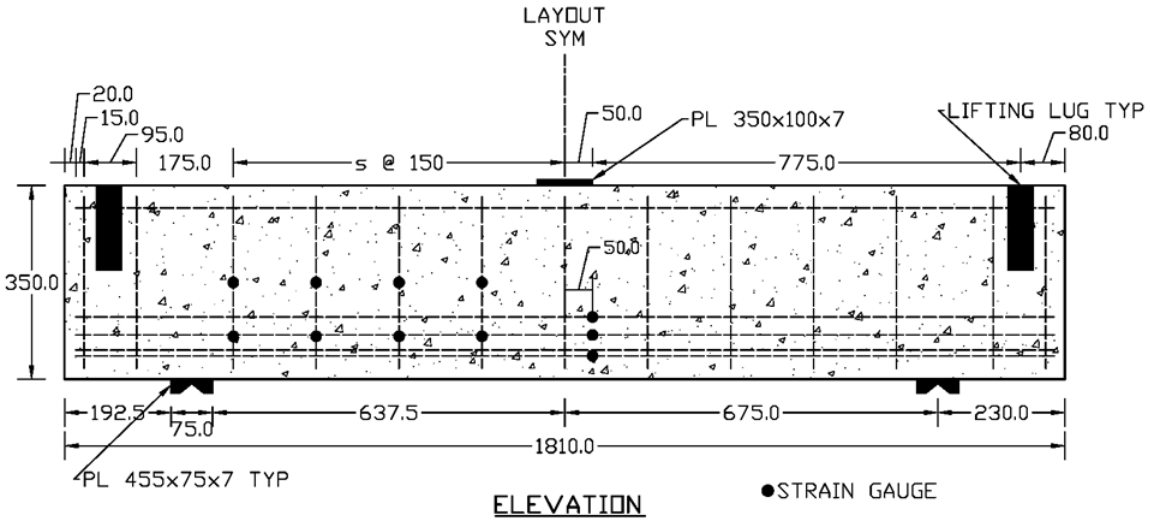

ELEVATION

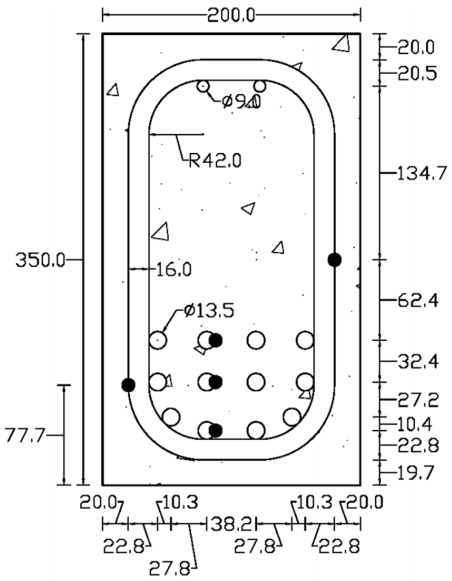

CROSS-SECTION

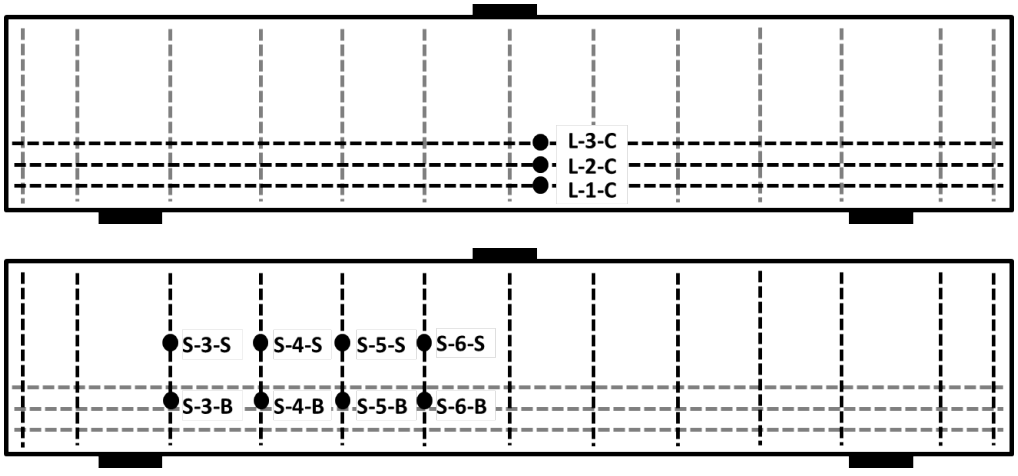

BM 12-220

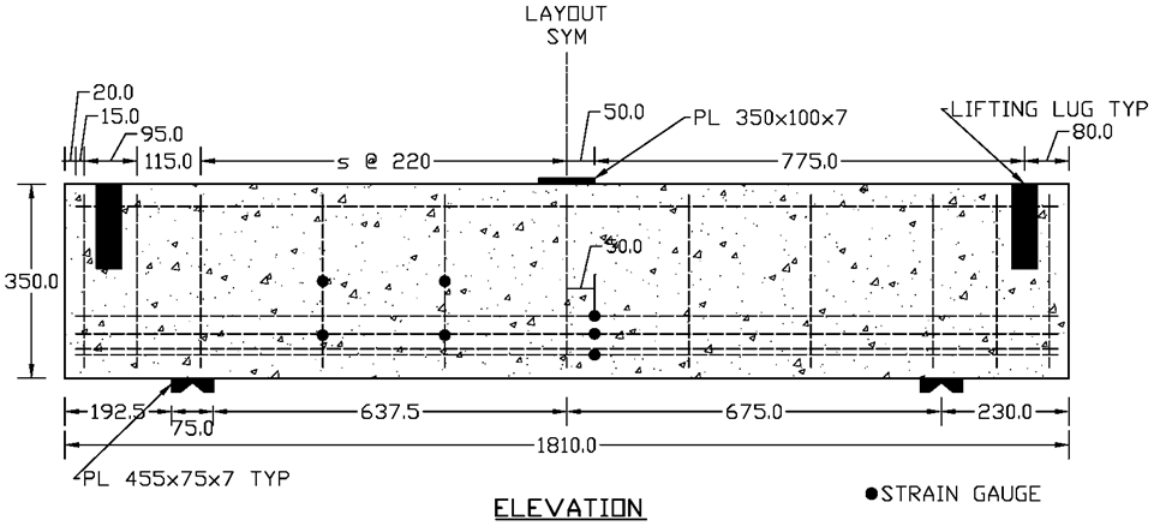

ELEVATION

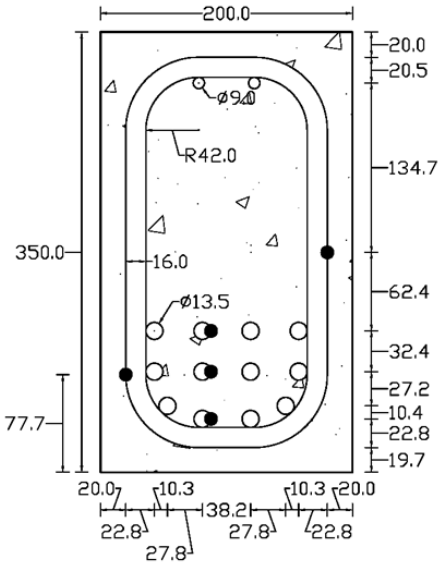

CROSS-SECTION

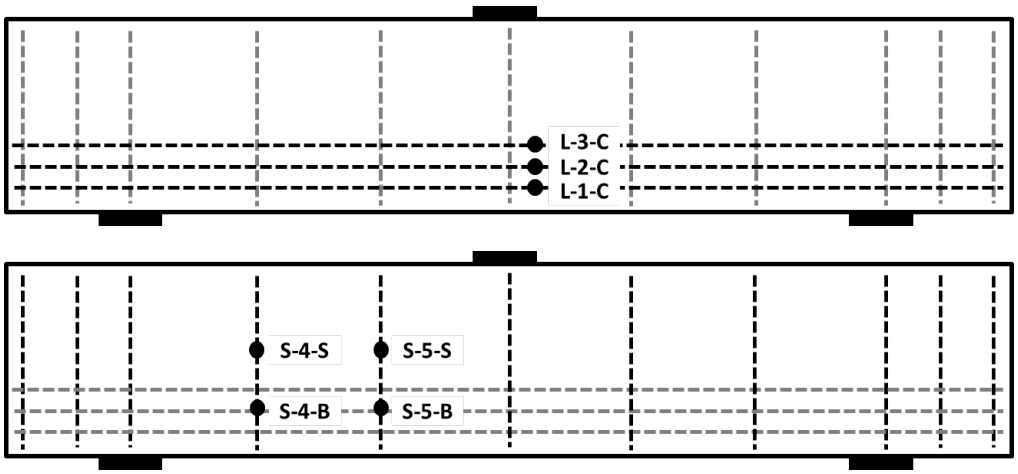

BM 12-s230

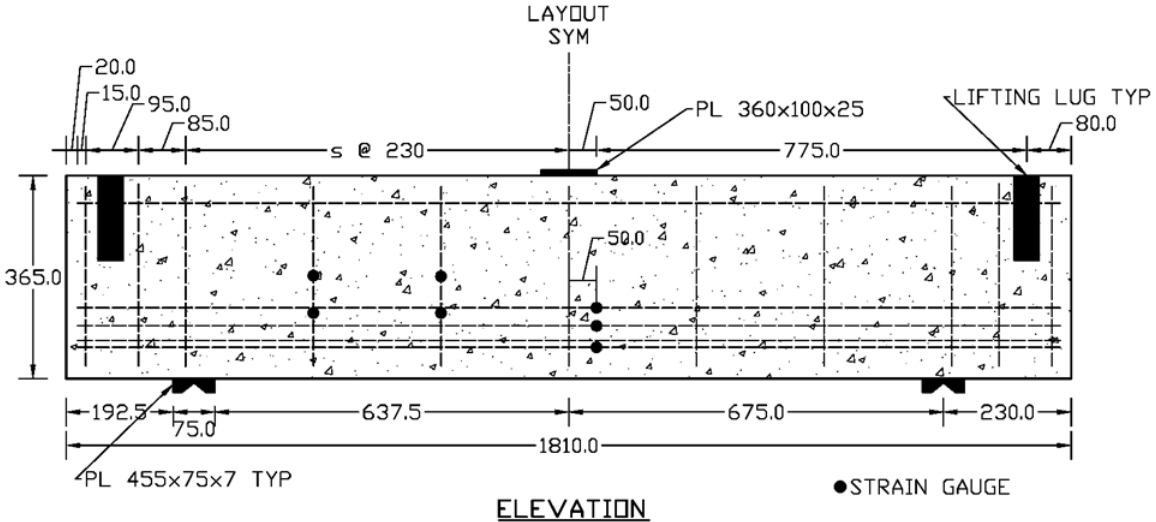

ELEVATION

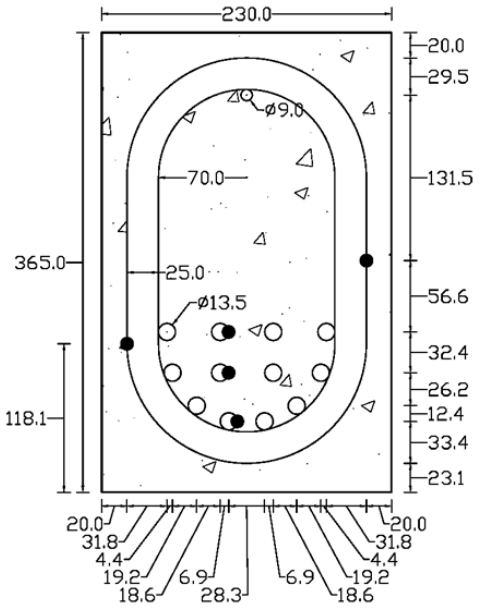

CROSS-SECTION

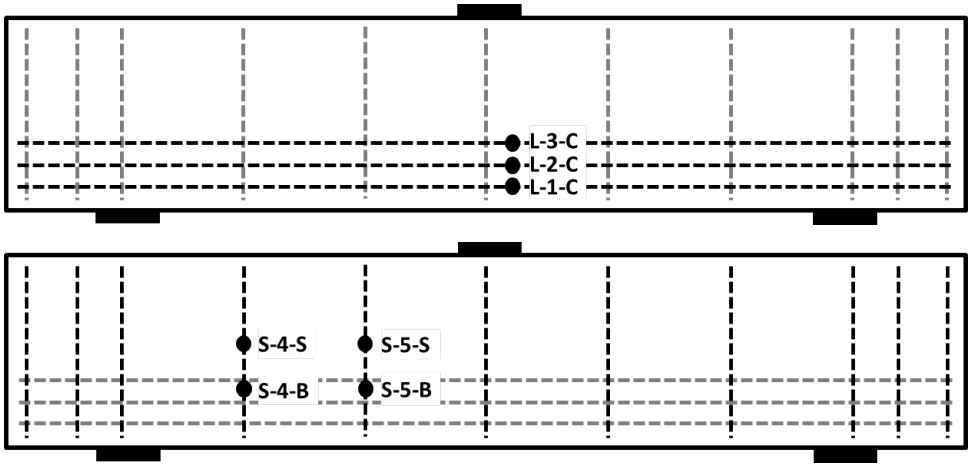

BM 16-INF

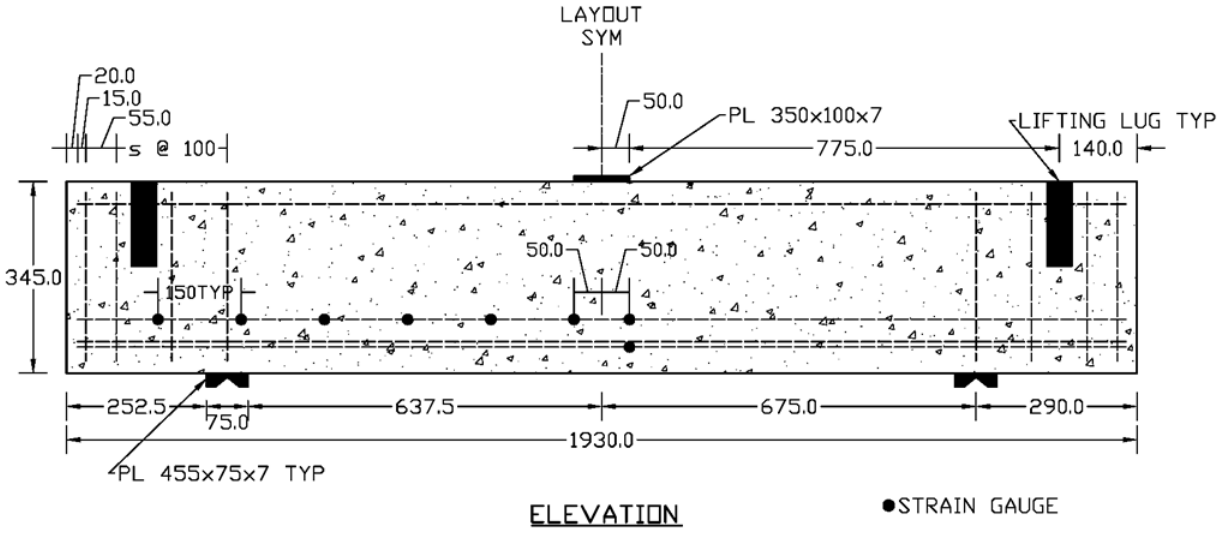
LAYOUT
SYM
20.0
15.0
55.0
s @ 100
50.0
PL 350x100x7
775.0
LIFTING LUG TYP
140.0
345.0
150TYP
50.0
50.0
252.5
75.0
637.5
675.0
290.0
1930.0
PL 455x75x7 TYP
ELEVATION
●STRAIN GAUGE

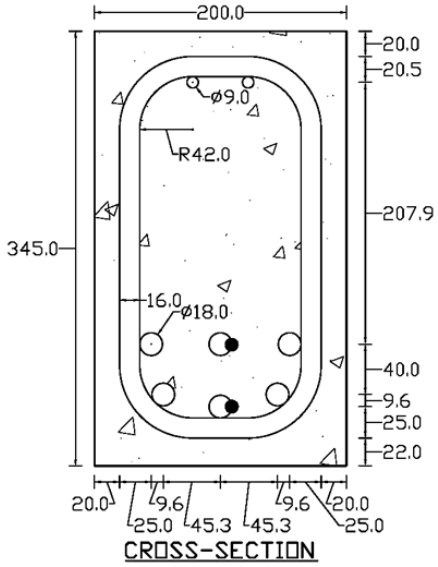
200.0
20.0
20.5
ø9.0
R42.0
207.9
345.0
16.0
ø18.0
40.0
9.6
25.0
22.0
20.0
9.6
25.0
45.3
45.3
9.6
20.0
25.0
CROSS-SECTION

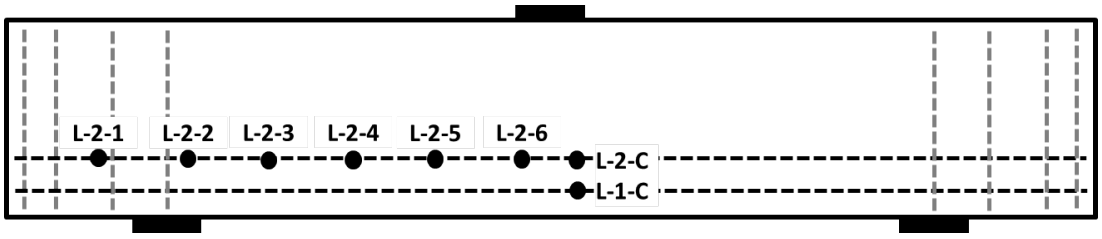
L-2-1
L-2-2
L-2-3
L-2-4
L-2-5
L-2-6
L-2-C
L-1-C

BM 16-150

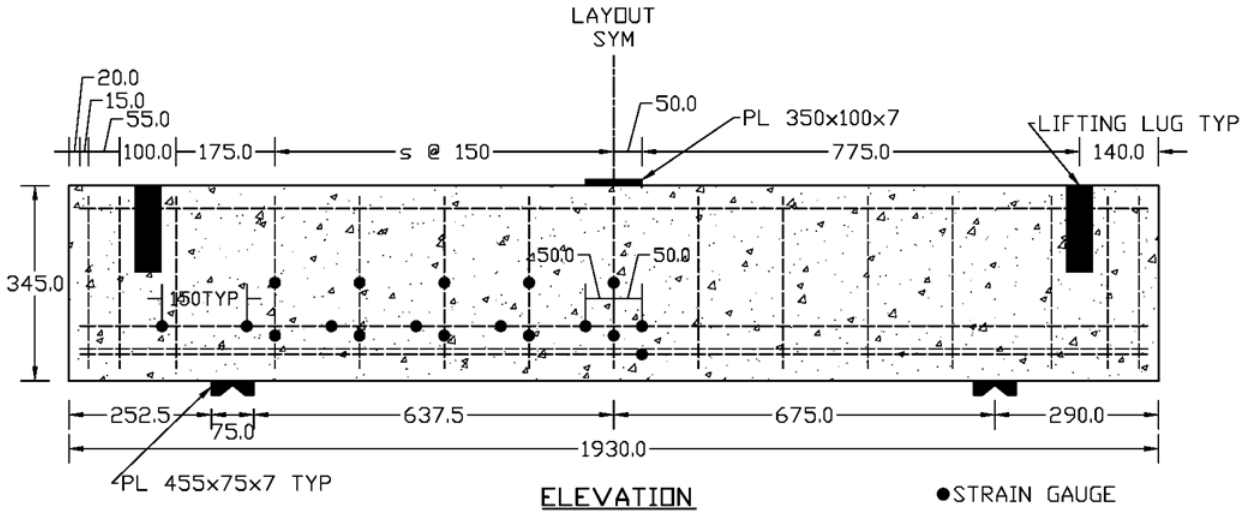
LAYOUT
SYM
20.0
15.0
55.0
100.0
175.0
s @ 150
50.0
PL 350x100x7
775.0
LIFTING LUG TYP
140.0
345.0
150TYP
50.0
50.0
252.5
75.0
637.5
675.0
290.0
1930.0
PL 455x75x7 TYP
ELEVATION
●STRAIN GAUGE

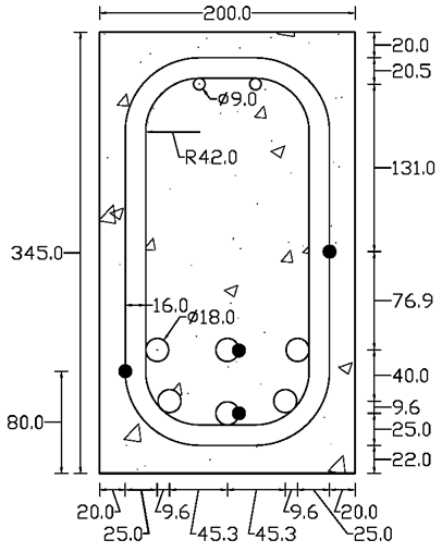
200.0
20.0
20.5
ø9.0
R42.0
131.0
345.0
16.0
ø18.0
76.9
40.0
80.0
9.6
25.0
22.0
20.0
25.0
9.6
45.3
45.3
9.6
20.0
25.0
CROSS-SECTION

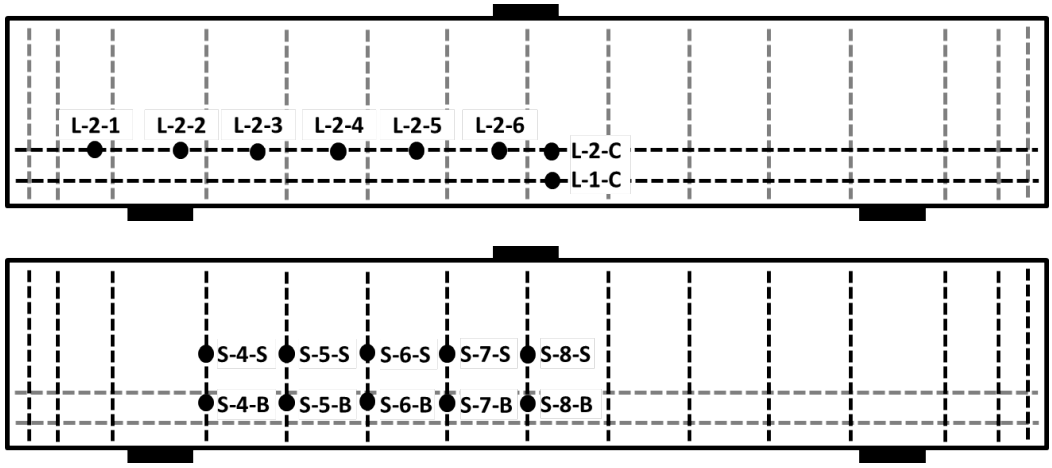
L-2-1
L-2-2
L-2-3
L-2-4
L-2-5
L-2-6
L-2-C
L-1-C
S-4-S
S-5-S
S-6-S
S-7-S
S-8-S
S-4-B
S-5-B
S-6-B
S-7-B
S-8-B

BM 16-220

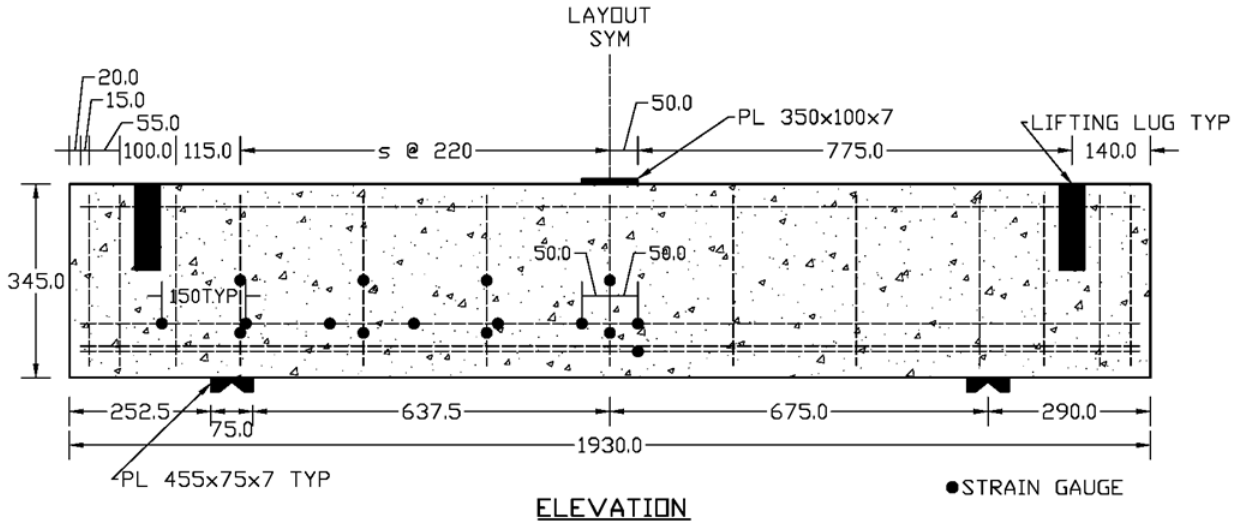

ELEVATION

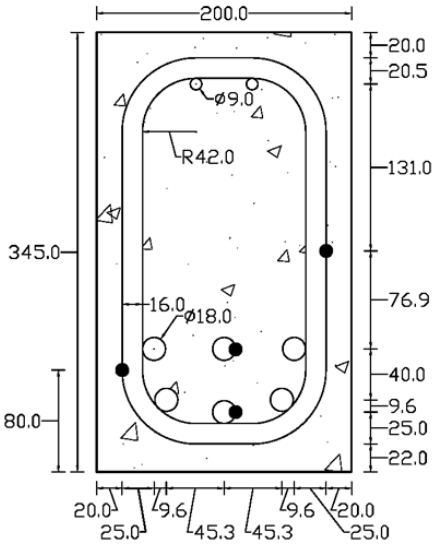

CROSS-SECTION

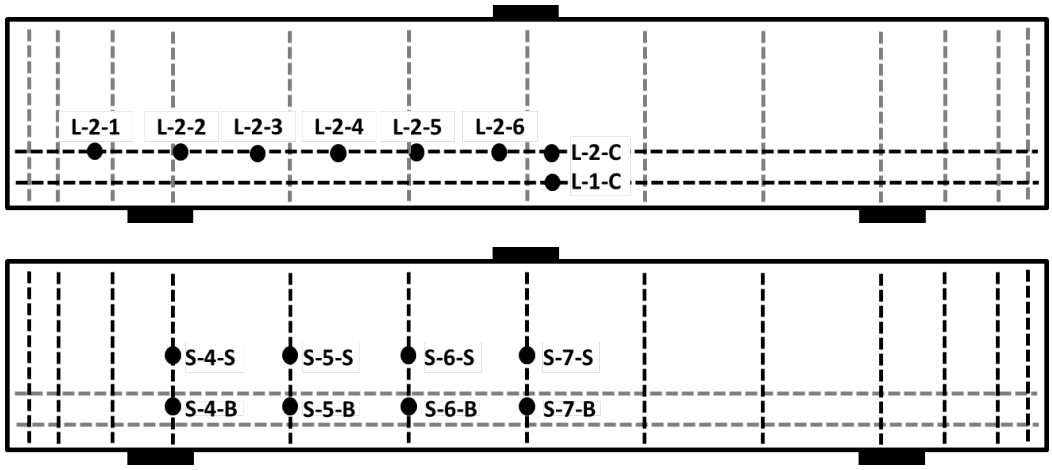

BM 16-s230

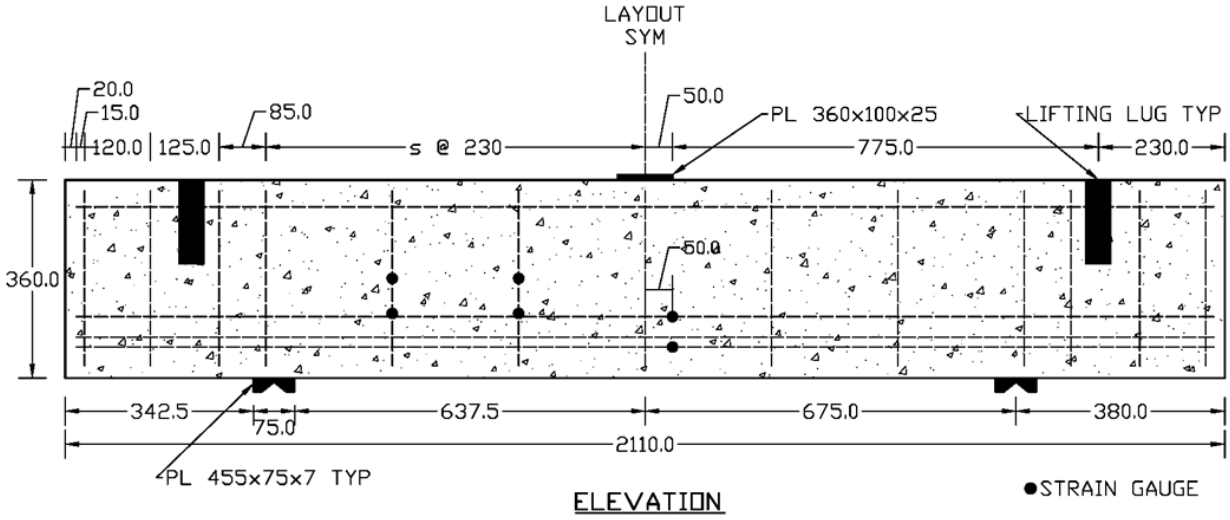

ELEVATION

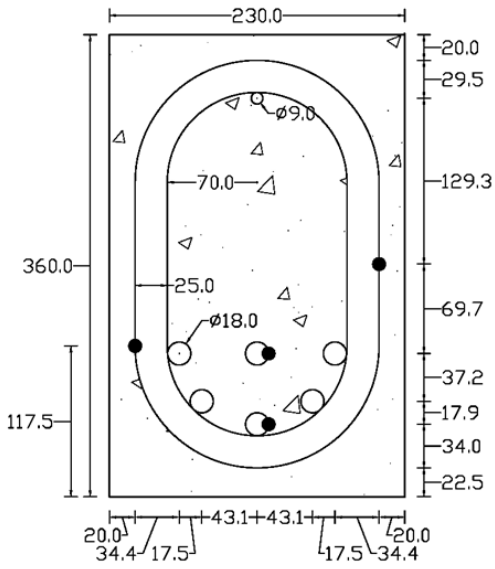

CROSS-SECTION

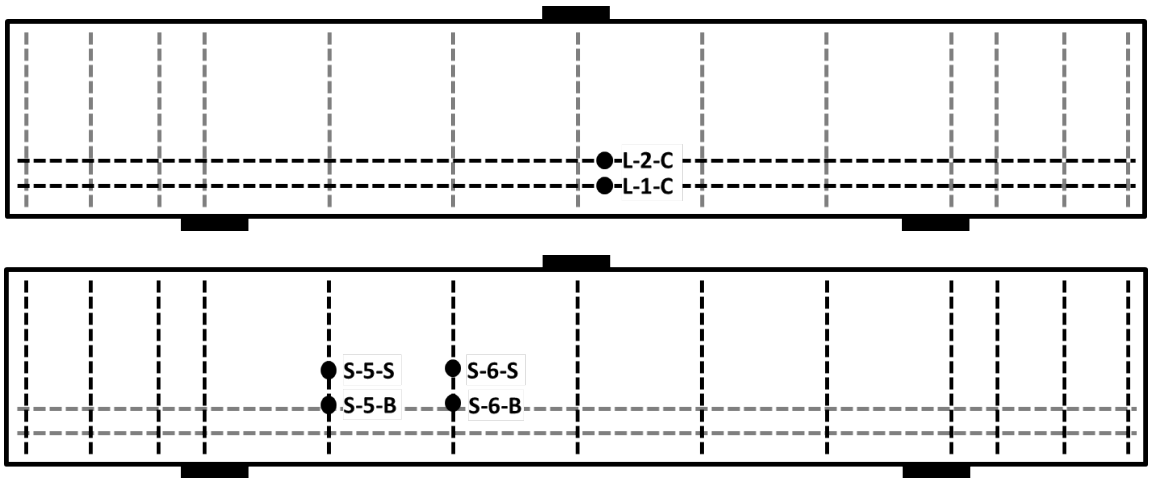

BM 25-INF

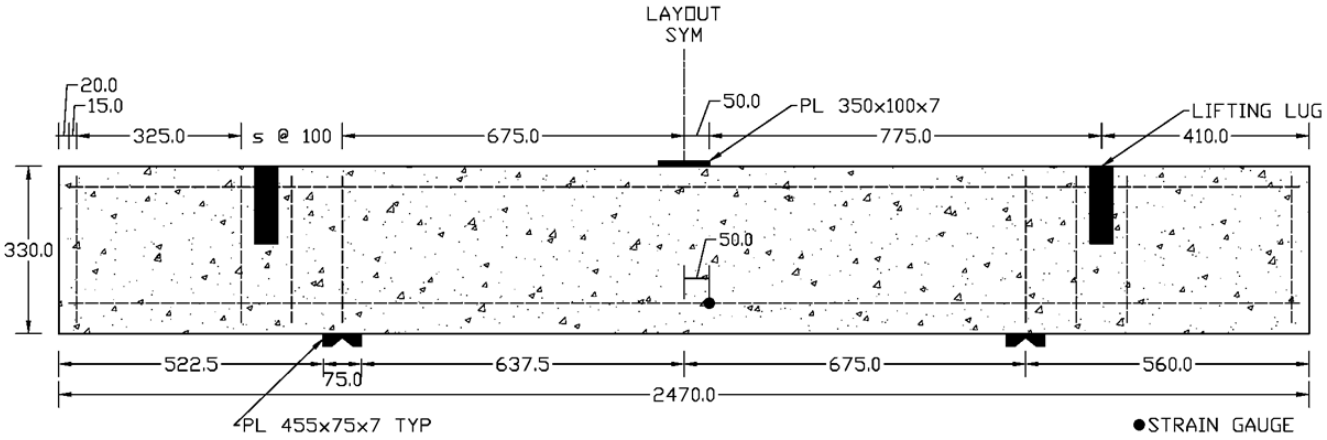

ELEVATION

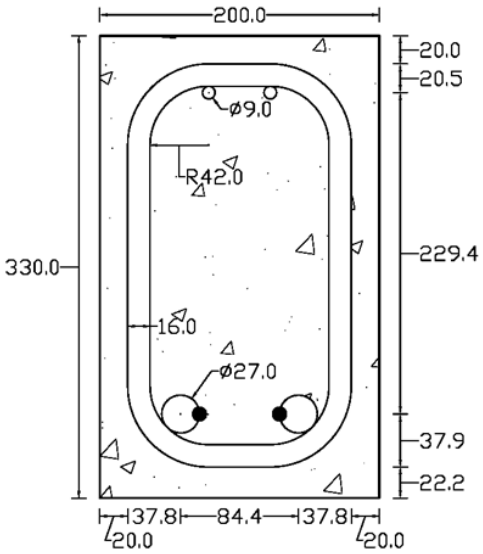

CROSS-SECTION

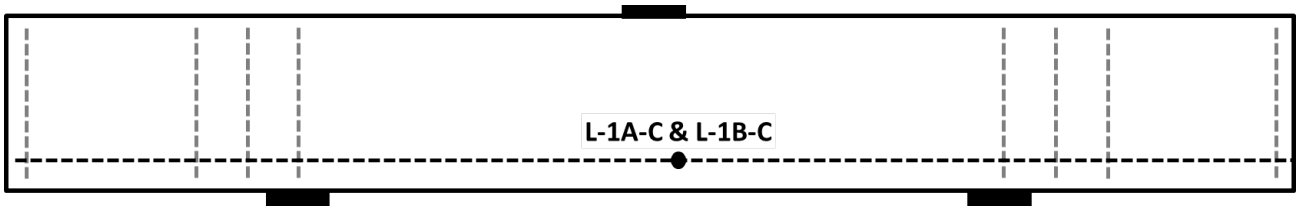

BM 25-150

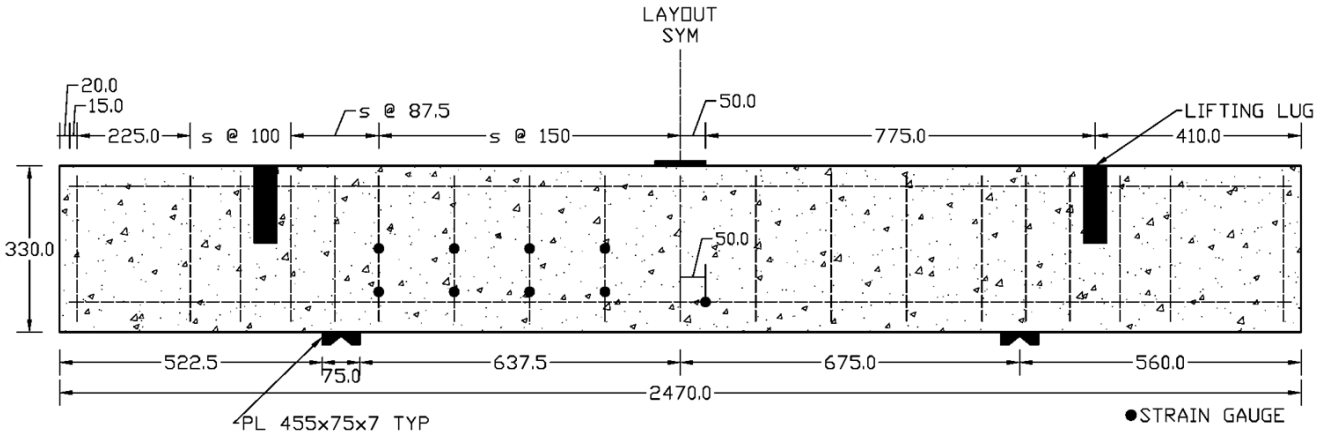

ELEVATION

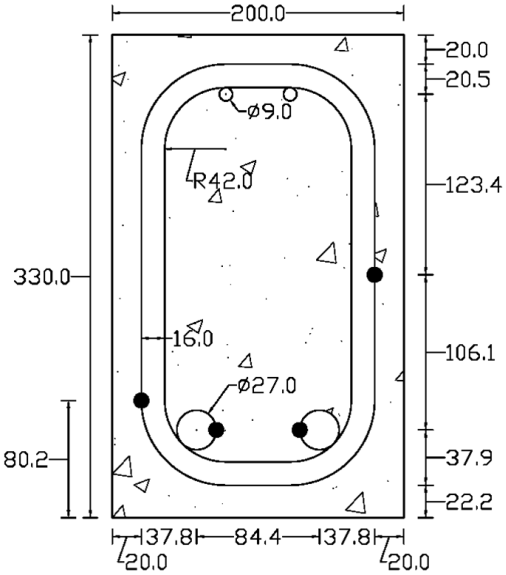

CROSS-SECTION

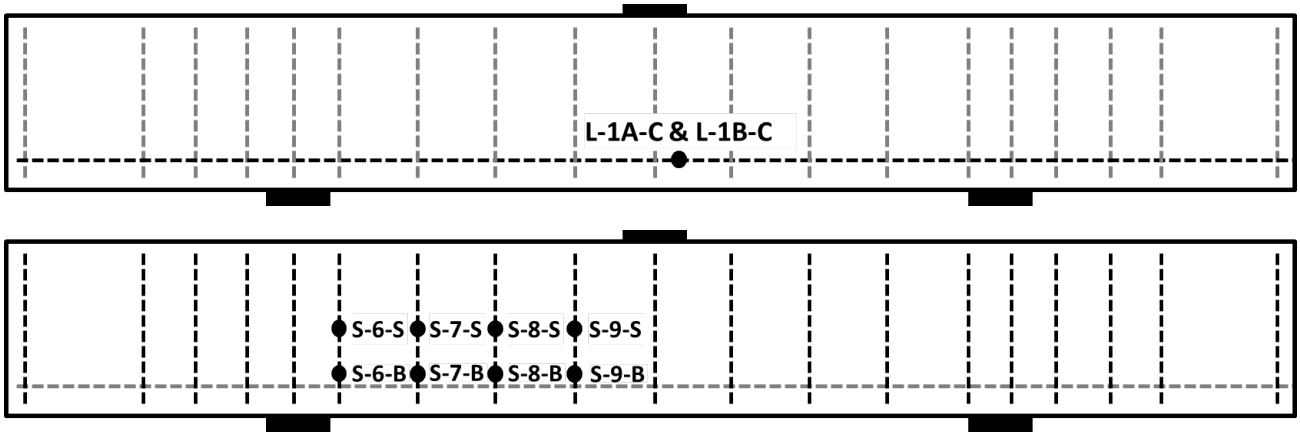

BM 25-220

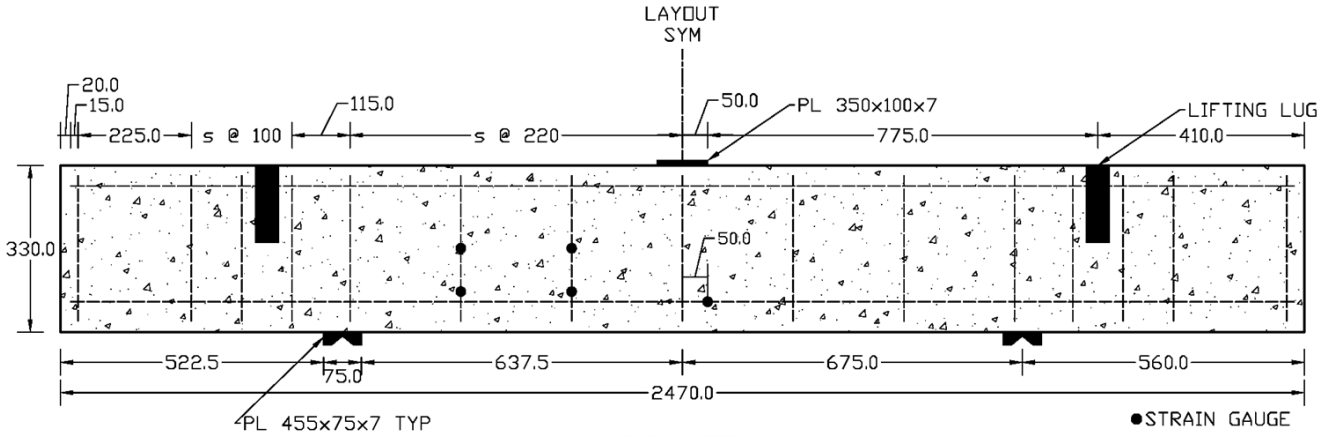

ELEVATION

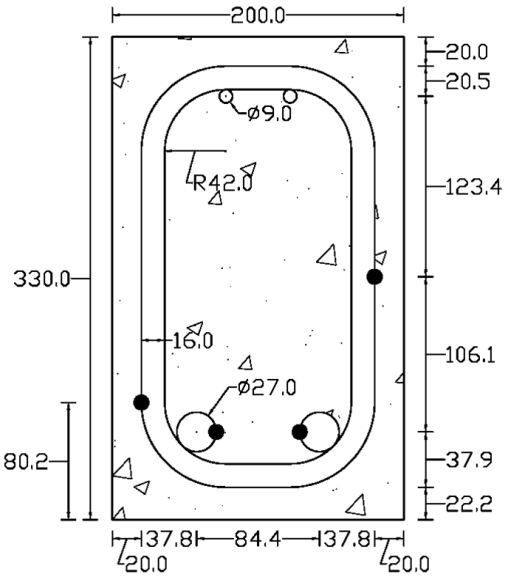

CROSS-SECTION

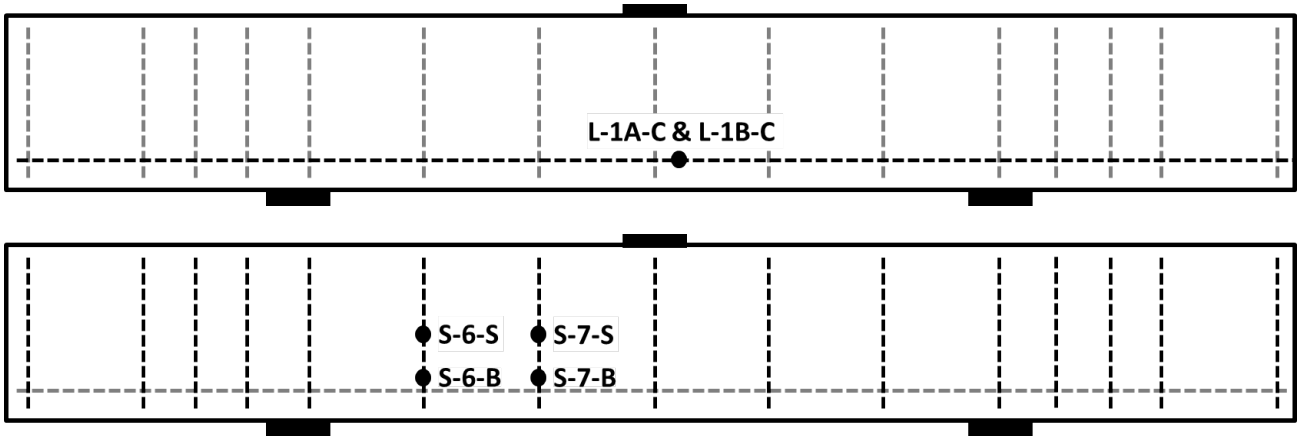

BM 25-s230

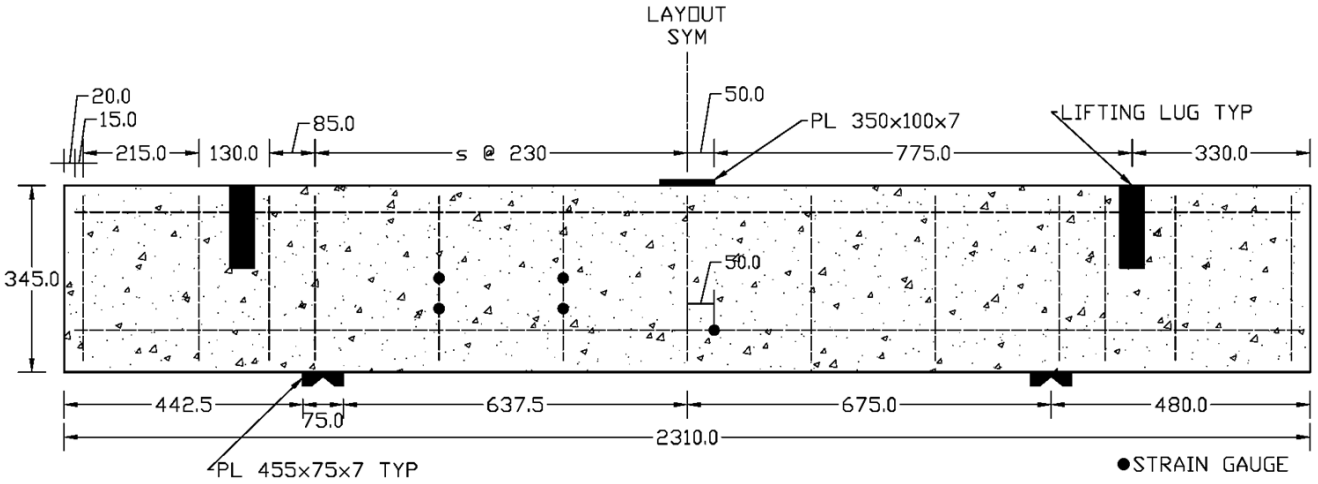

ELEVATION

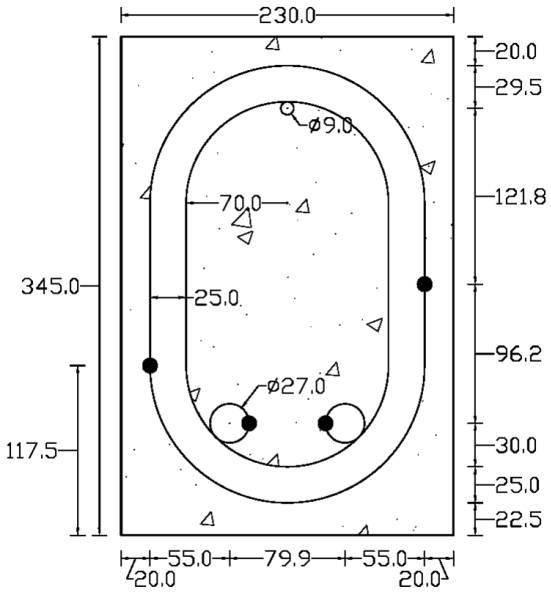

CROSS-SECTION

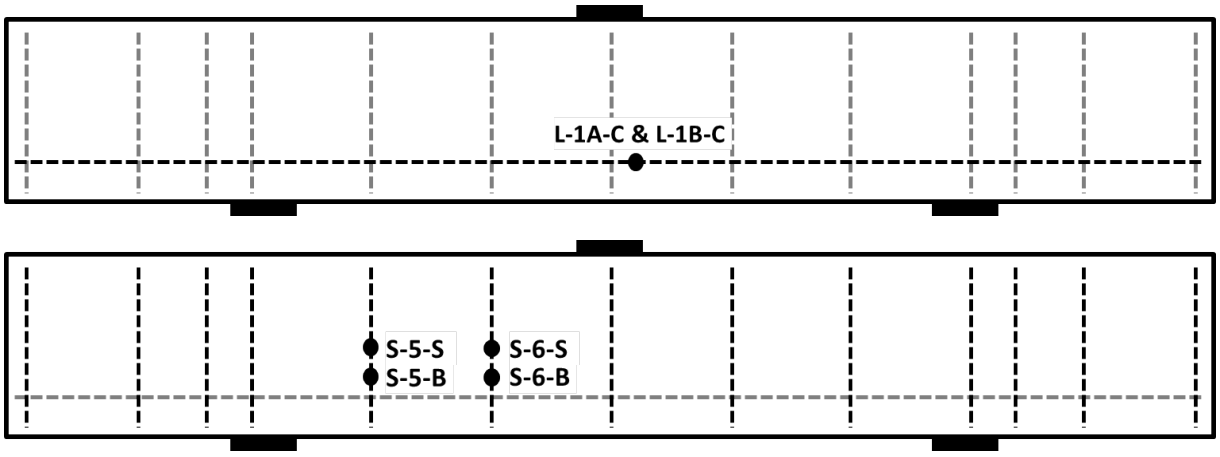

Appendix B

Beams with No Stirrups

This Appendix provides the results of all analyses performed for beams with no stirrups, including BM 12-INF, BM 16-INF, and BM 25-INF. Unless stated otherwise, the parameters summarized in Table B.1 were used in all analyses presented in this appendix.

Table B.1: Parameters Used for the Modelling of Beams with No Stirrups

Compression Model:	Hognestad Parabola
Maximum Compressive Strain:	0.008 (Hognestad)
Tension Model:	Bilinear Stress-Displacement
Fracture Energy, G_f:	90 N/m
Damage:	Tension and Compression Included
Poisson's Ratio, v:	0.2
Dilation Angle, ψ:	30°
σ_{bo}/σ_{co}:	1.16
Eccentricity, ϵ:	0.1
K_c:	2/3
Viscosity Parameter, μ:	0.0001
Mesh Refinement:	12 Deep
Longitudinal Reinforcement:	Linear Truss Sections
Stirrup Reinforcement:	N/A

BM 12-INF

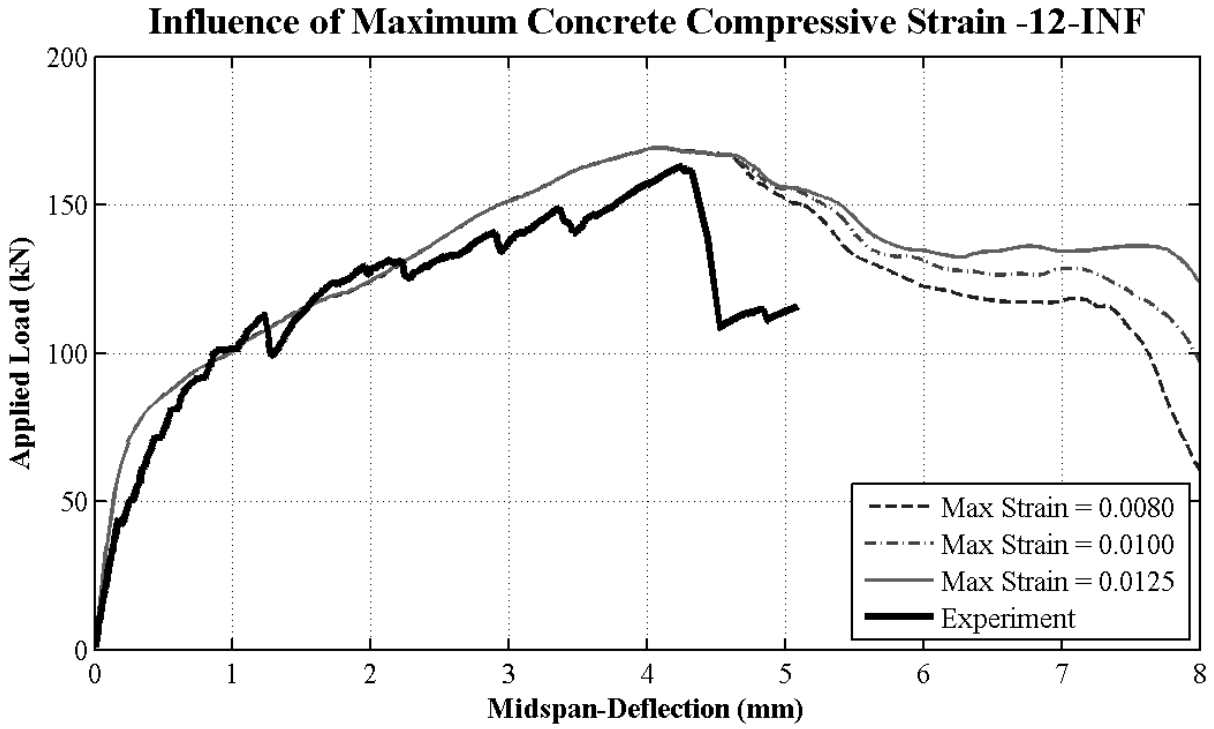
Influence of Maximum Concrete Compressive Strain -12-INF
Applied Load (kN)
Midspan-Deflection (mm)
Max Strain = 0.0080
Max Strain = 0.0100
Max Strain = 0.0125
Experiment

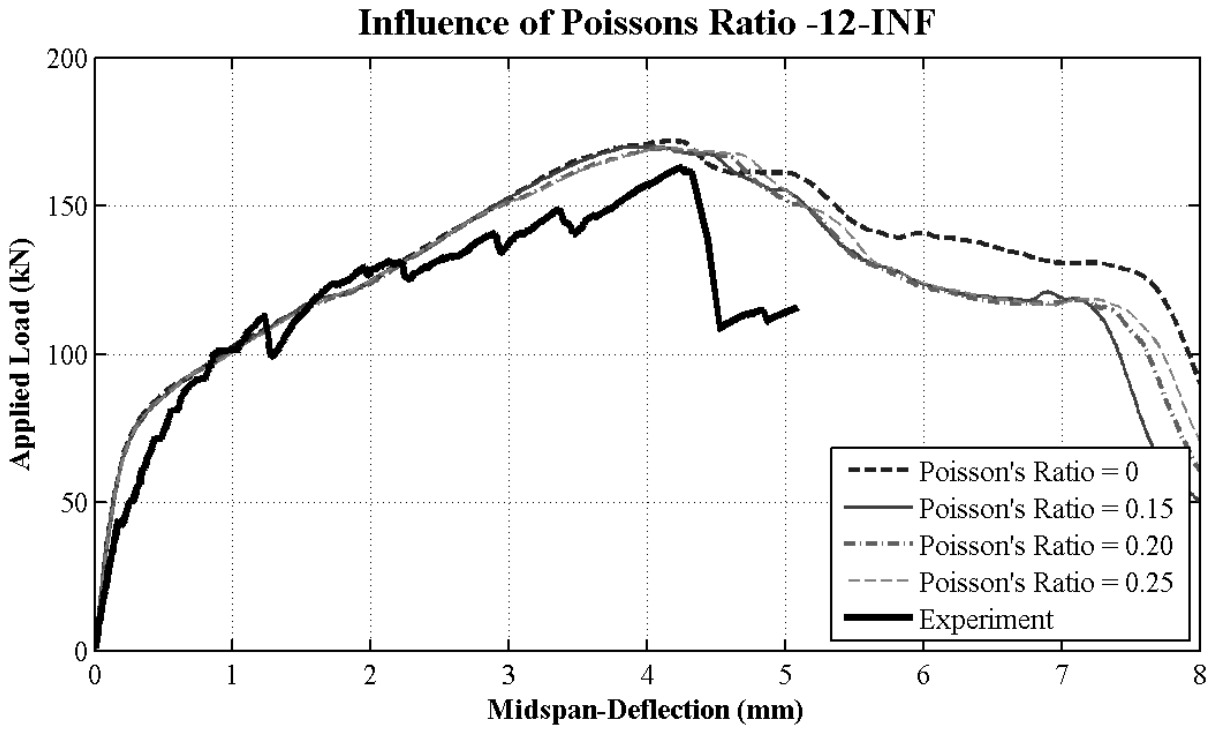
Influence of Poissons Ratio -12-INF
Applied Load (kN)
Midspan-Deflection (mm)
Poisson's Ratio = 0
Poisson's Ratio = 0.15
Poisson's Ratio = 0.20
Poisson's Ratio = 0.25
Experiment

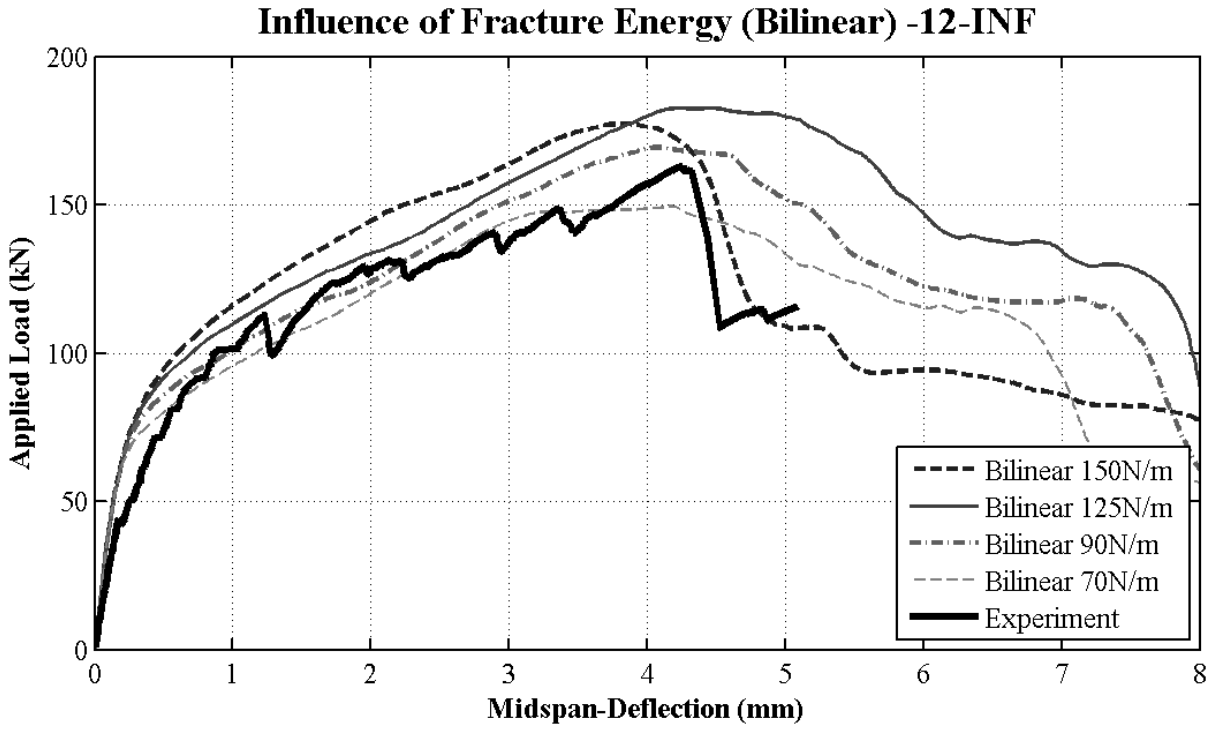
Influence of Fracture Energy (Bilinear) -12-INF
Applied Load (kN)
Midspan-Deflection (mm)
Bilinear 150N/m
Bilinear 125N/m
Bilinear 90N/m
Bilinear 70N/m
Experiment

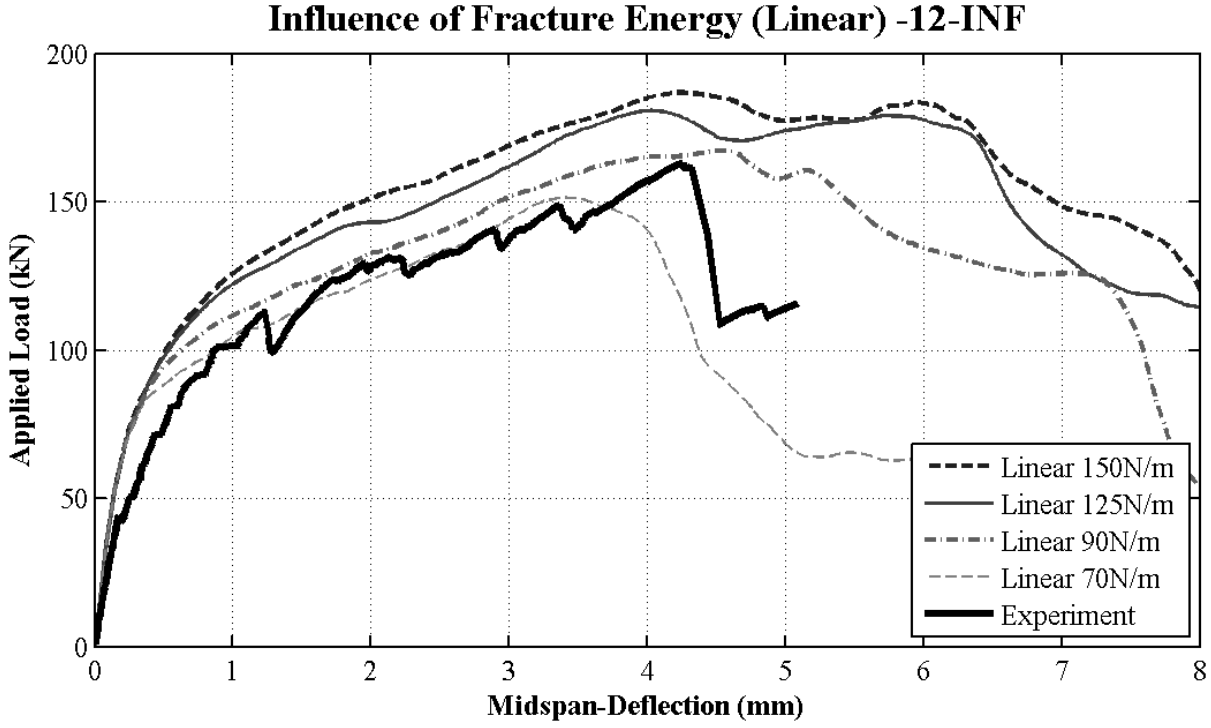
Influence of Fracture Energy (Linear) -12-INF
Applied Load (kN)
Midspan-Deflection (mm)
Linear 150N/m
Linear 125N/m
Linear 90N/m
Linear 70N/m
Experiment

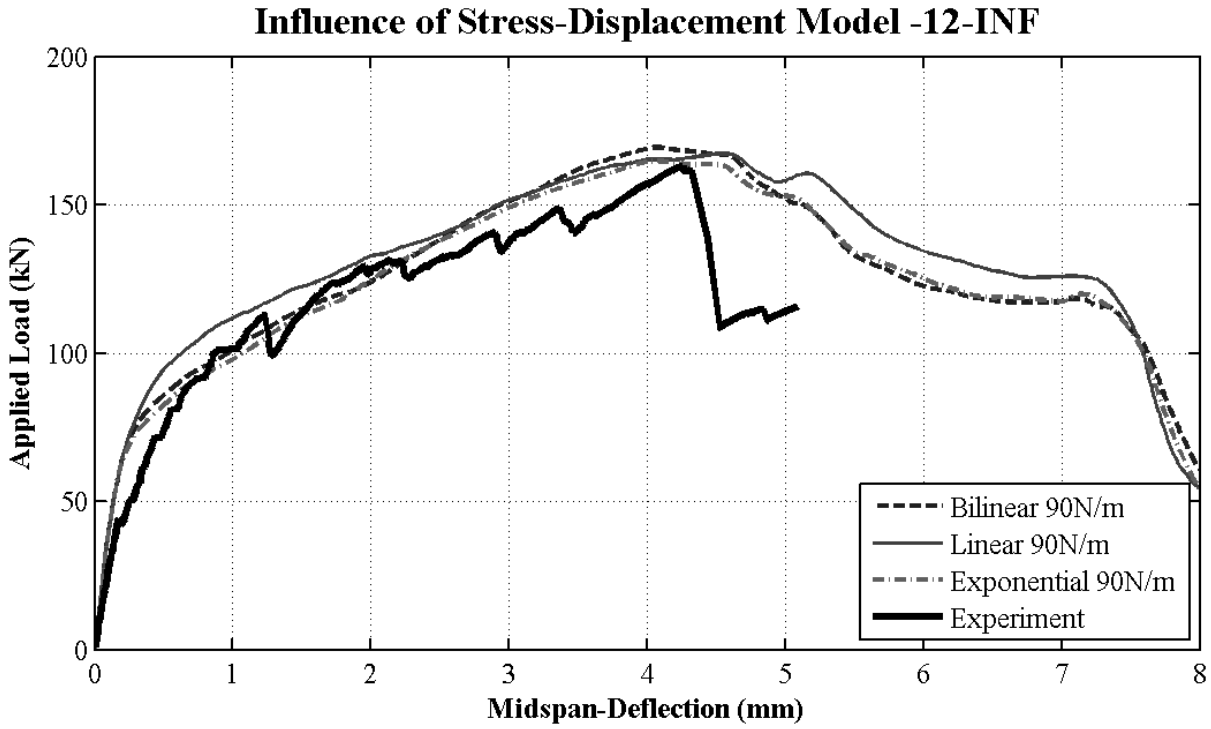
Influence of Stress-Displacement Model -12-INF
Applied Load (kN)
Midspan-Deflection (mm)
Bilinear 90N/m
Linear 90N/m
Exponential 90N/m
Experiment

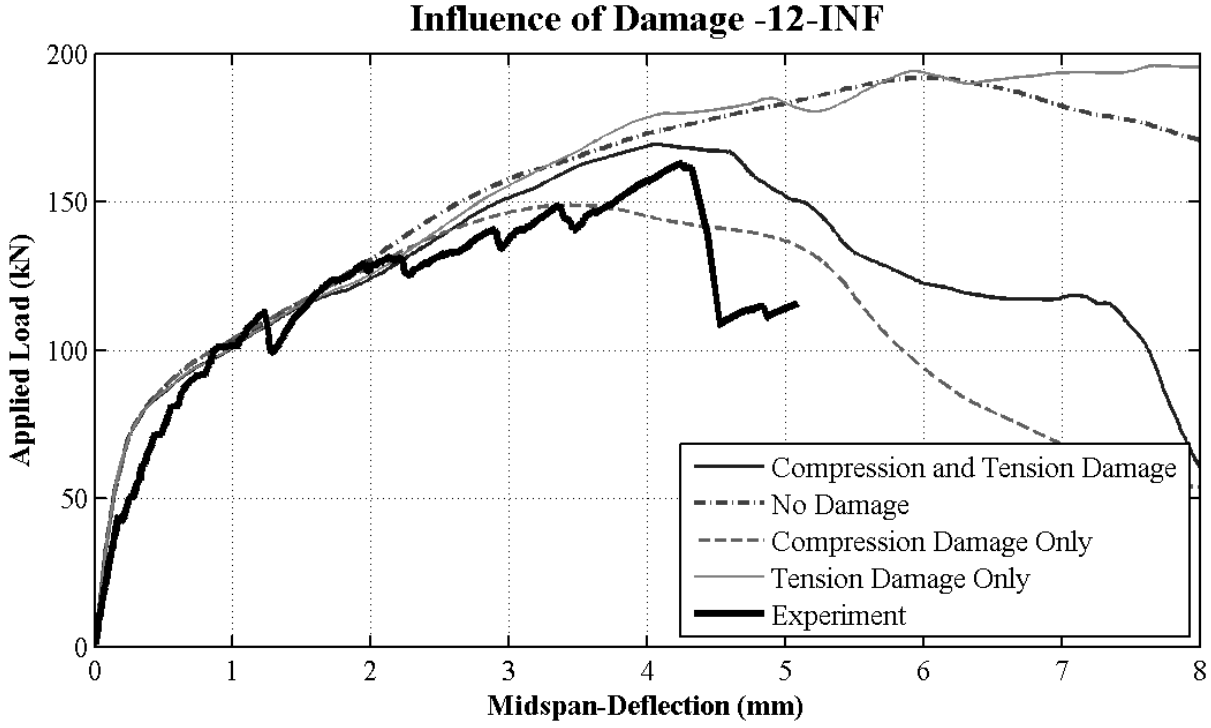
Influence of Damage -12-INF
Applied Load (kN)
Midspan-Deflection (mm)
Compression and Tension Damage
No Damage
Compression Damage Only
Tension Damage Only
Experiment

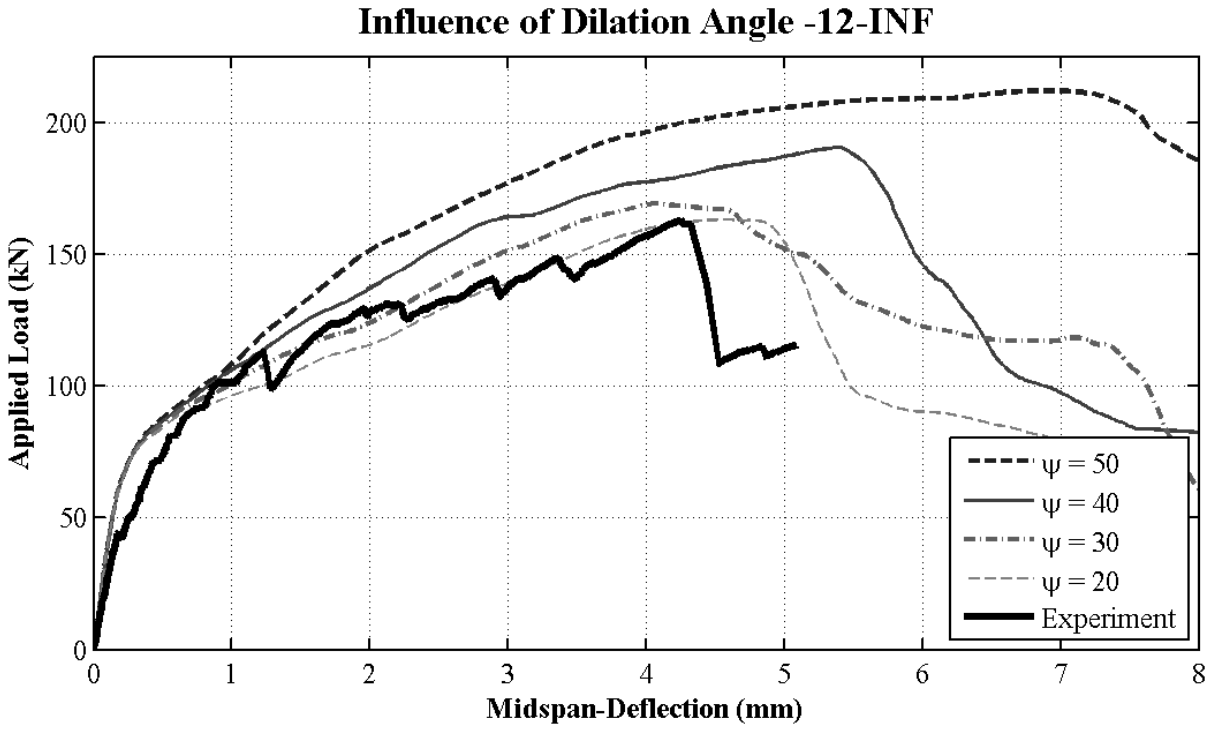
Influence of Dilation Angle -12-INF
Applied Load (kN)
Midspan-Deflection (mm)
ψ = 50
ψ = 40
ψ = 30
ψ = 20
Experiment

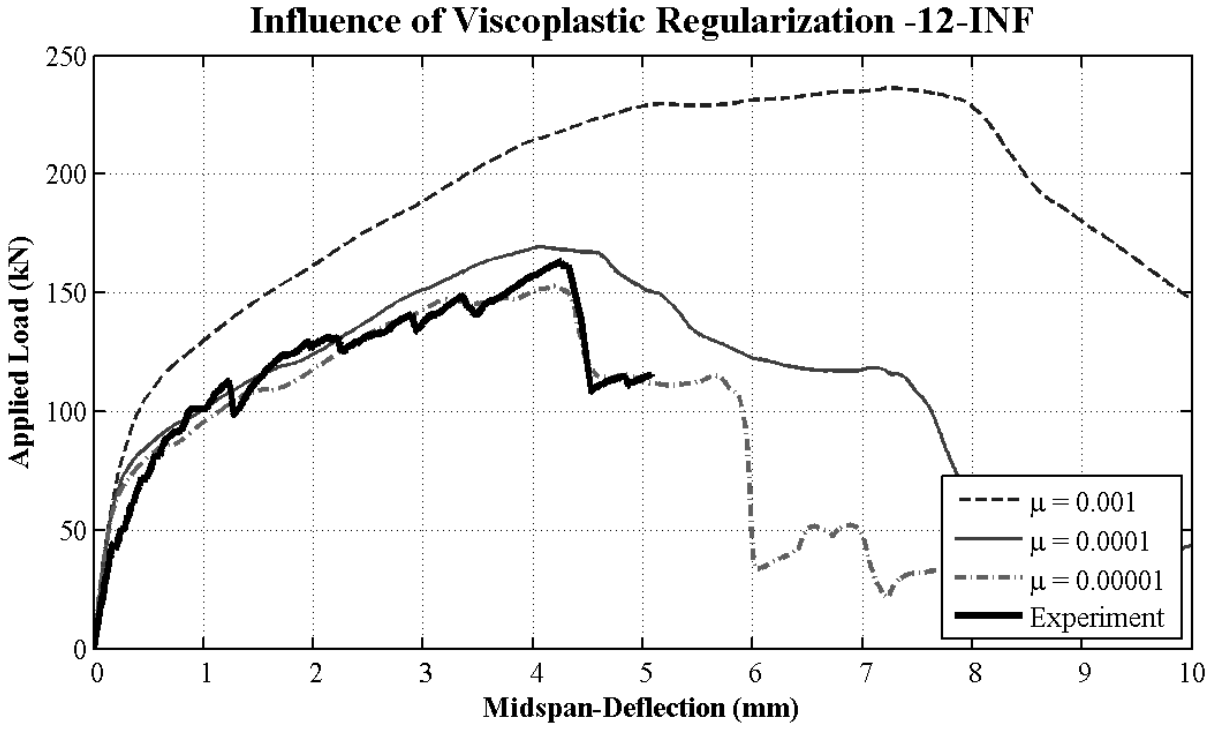
Influence of Viscoplastic Regularization -12-INF
Applied Load (kN)
Midspan-Deflection (mm)
μ = 0.001
μ = 0.0001
μ = 0.00001
Experiment

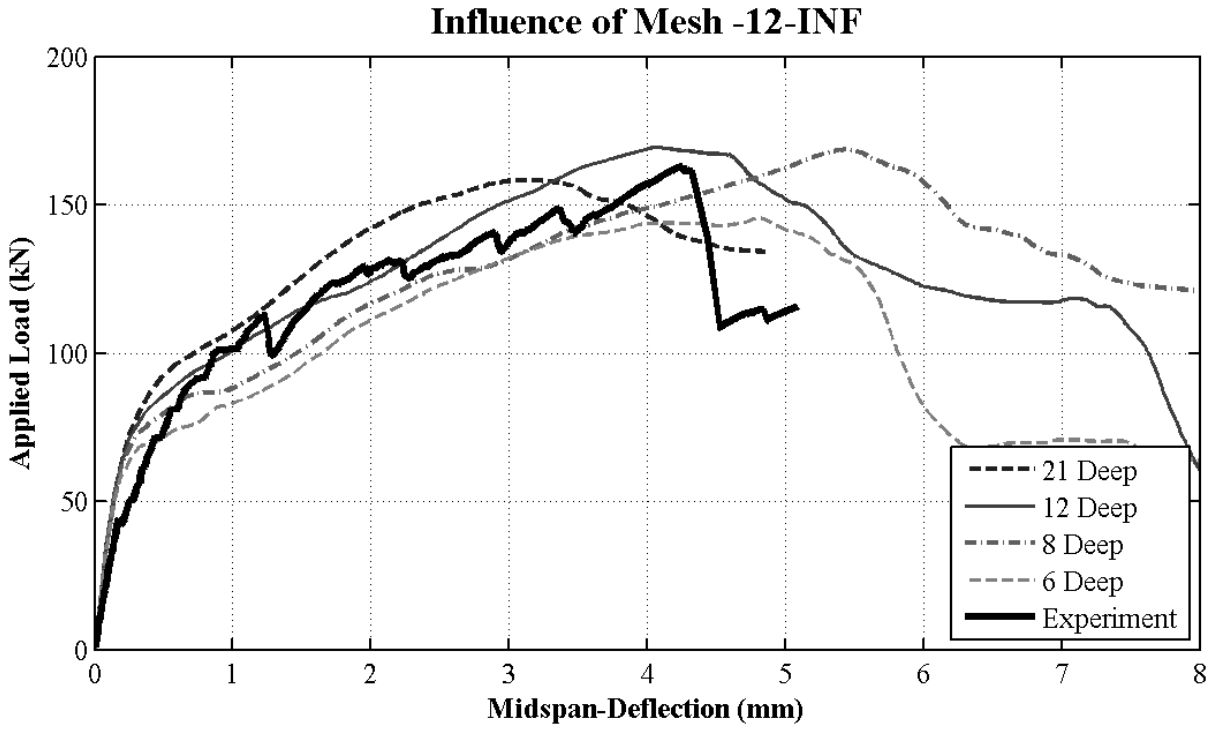
Influence of Mesh -12-INF
Applied Load (kN)
Midspan-Deflection (mm)
21 Deep
12 Deep
8 Deep
6 Deep
Experiment

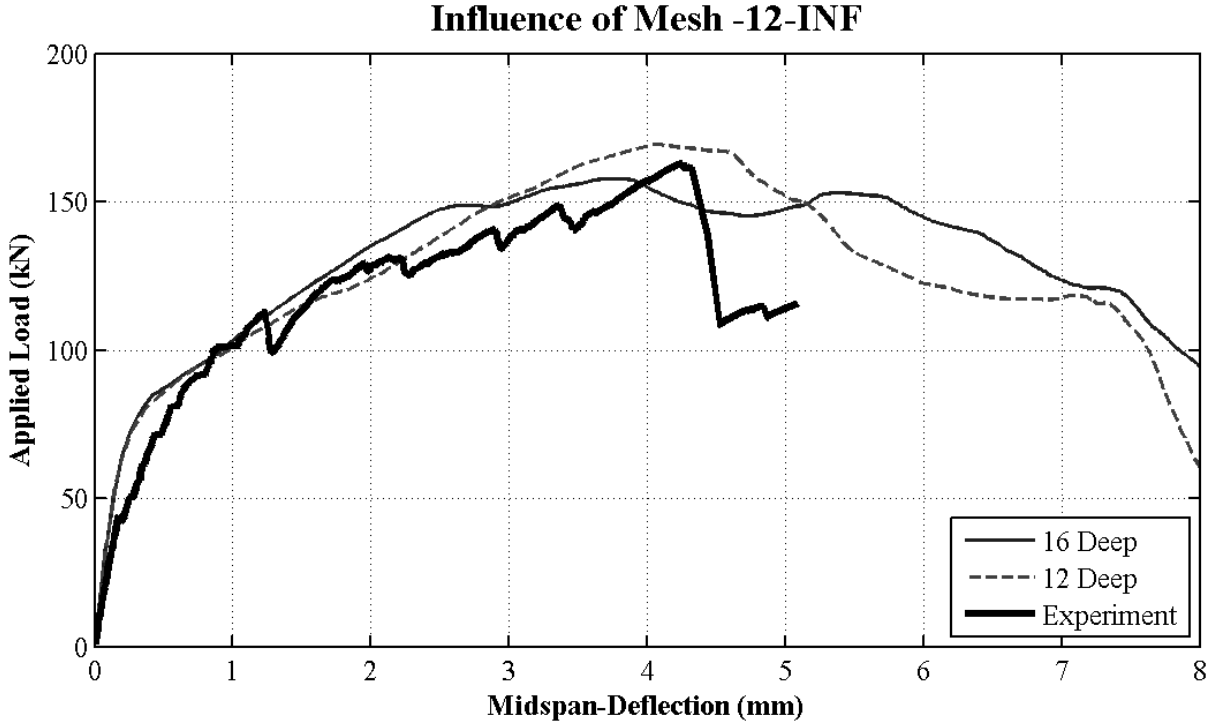
Influence of Mesh -12-INF
Applied Load (kN)
Midspan-Deflection (mm)
16 Deep
12 Deep
Experiment

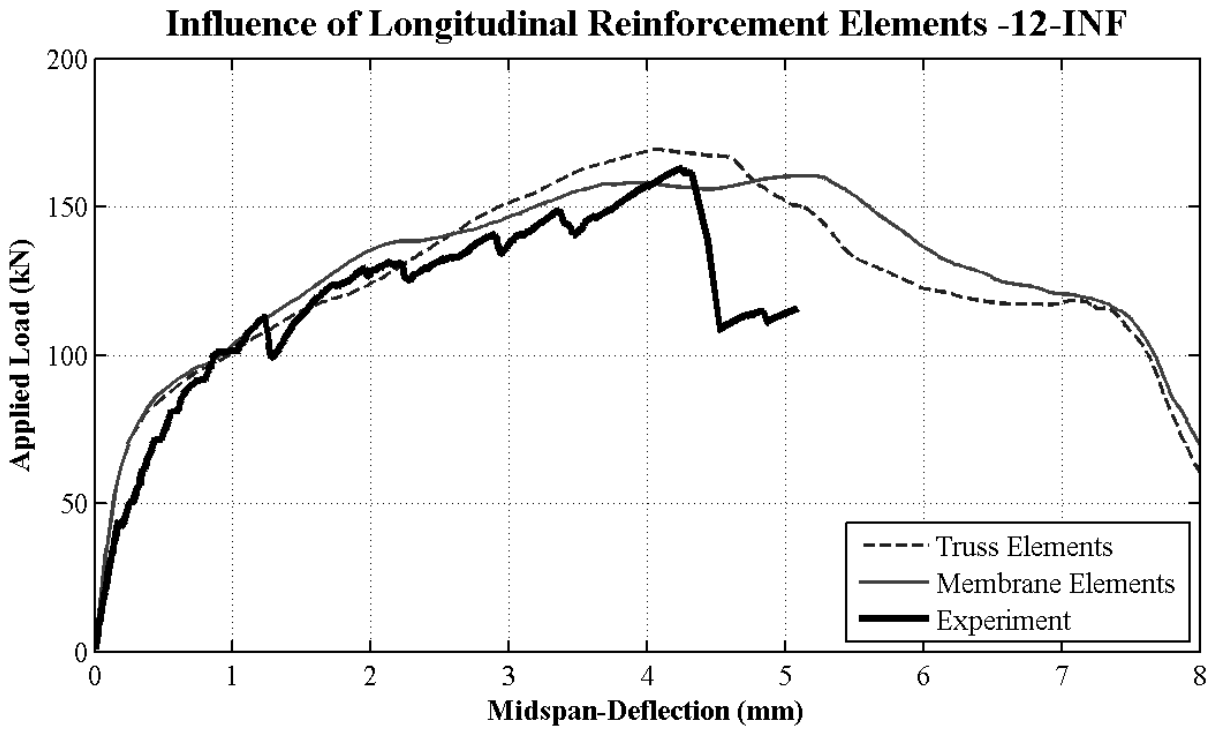
Influence of Longitudinal Reinforcement Elements -12-INF
Applied Load (kN)
Midspan-Deflection (mm)
Truss Elements
Membrane Elements
Experiment
0
50
100
150
200
0
1
2
3
4
5
6
7
8

BM 16-INF

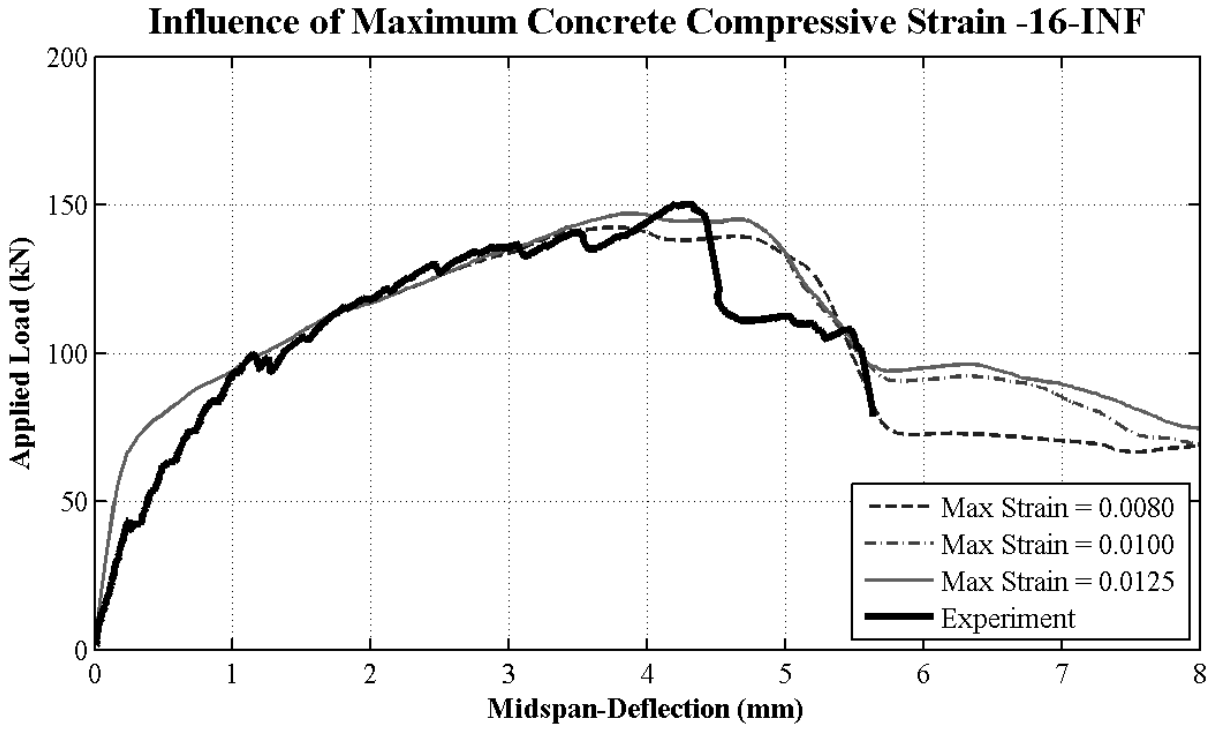
Influence of Maximum Concrete Compressive Strain -16-INF
Applied Load (kN)
Midspan-Deflection (mm)
Max Strain = 0.0080
Max Strain = 0.0100
Max Strain = 0.0125
Experiment

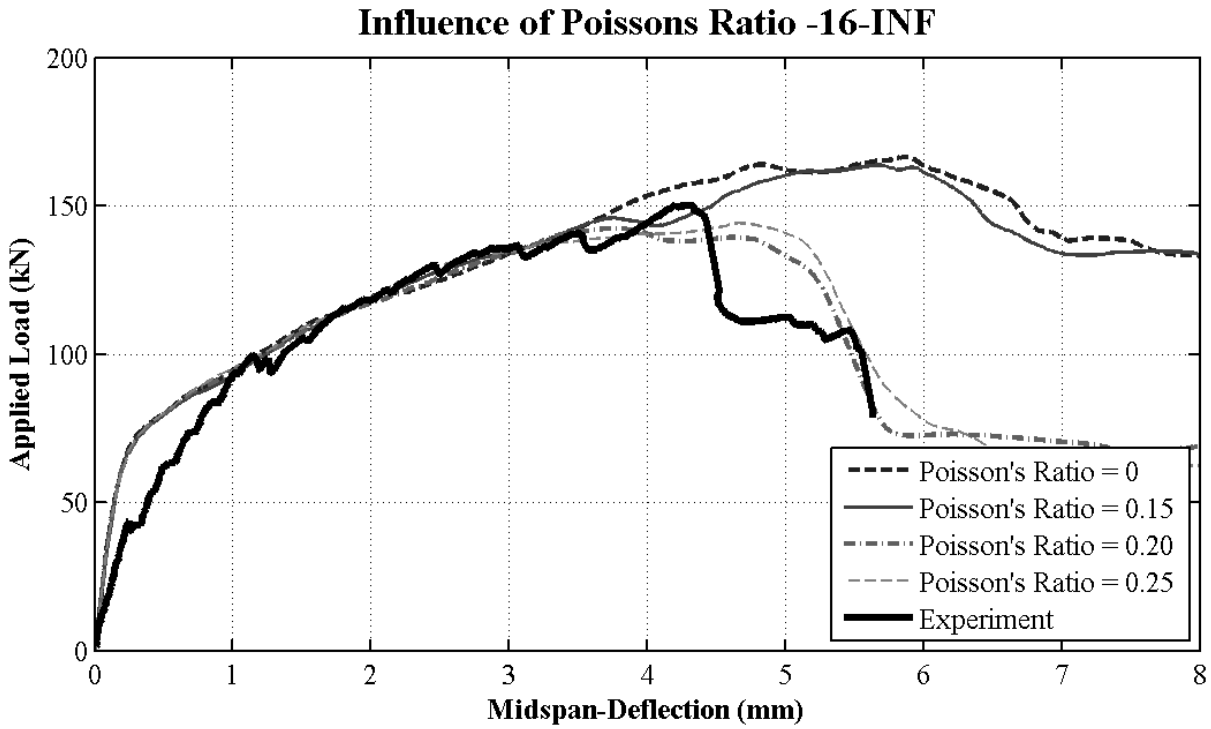
Influence of Poissons Ratio -16-INF
Applied Load (kN)
Midspan-Deflection (mm)
Poisson's Ratio = 0
Poisson's Ratio = 0.15
Poisson's Ratio = 0.20
Poisson's Ratio = 0.25
Experiment

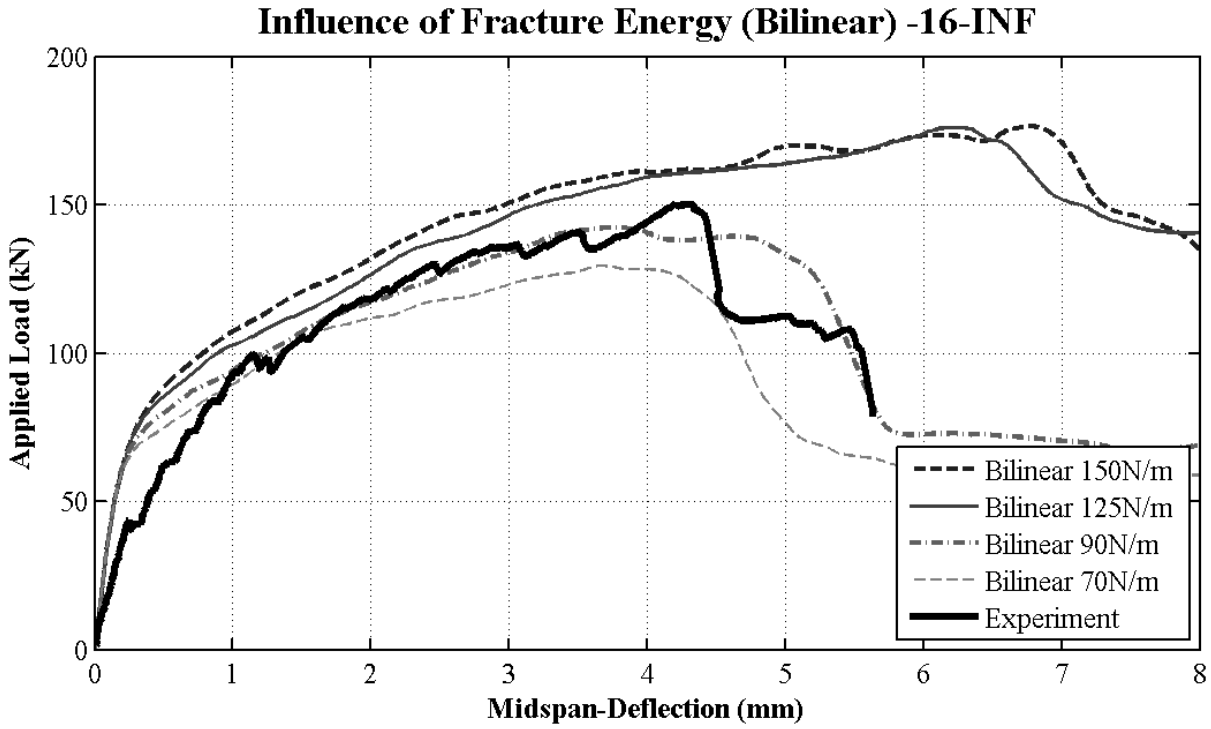
Influence of Fracture Energy (Bilinear) -16-INF
Applied Load (kN)
Midspan-Deflection (mm)
Bilinear 150N/m
Bilinear 125N/m
Bilinear 90N/m
Bilinear 70N/m
Experiment

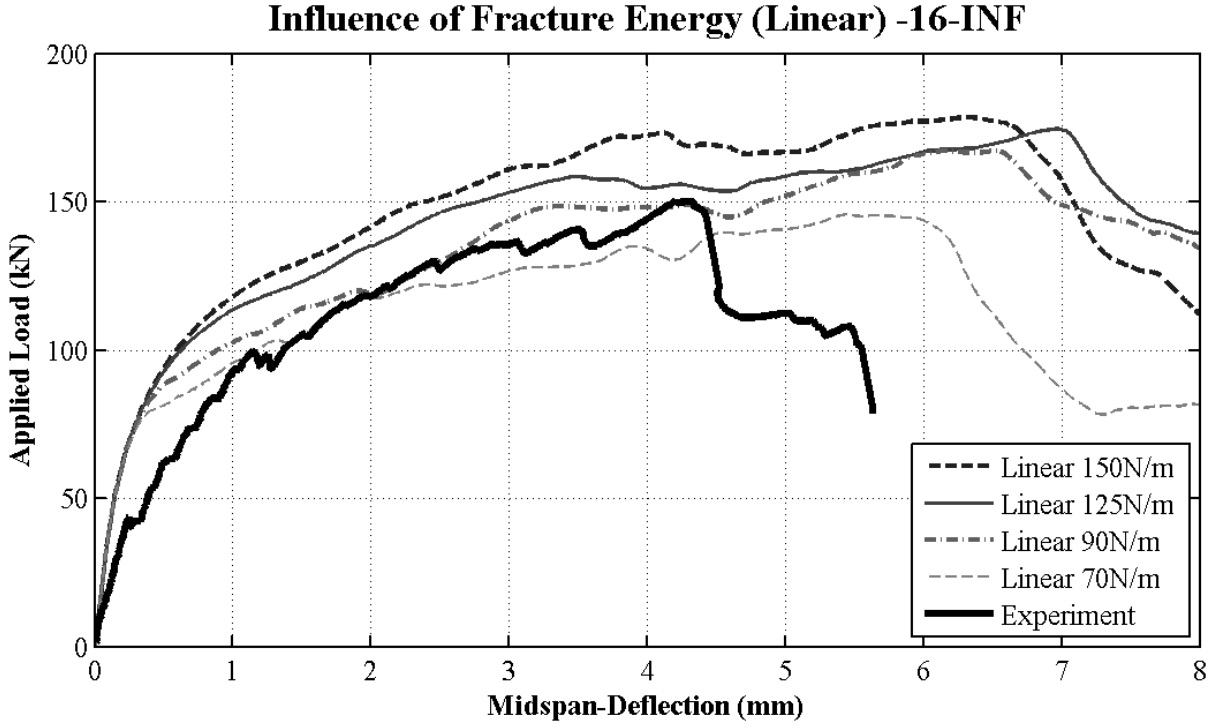
Influence of Fracture Energy (Linear) -16-INF
Applied Load (kN)
Midspan-Deflection (mm)
Linear 150N/m
Linear 125N/m
Linear 90N/m
Linear 70N/m
Experiment

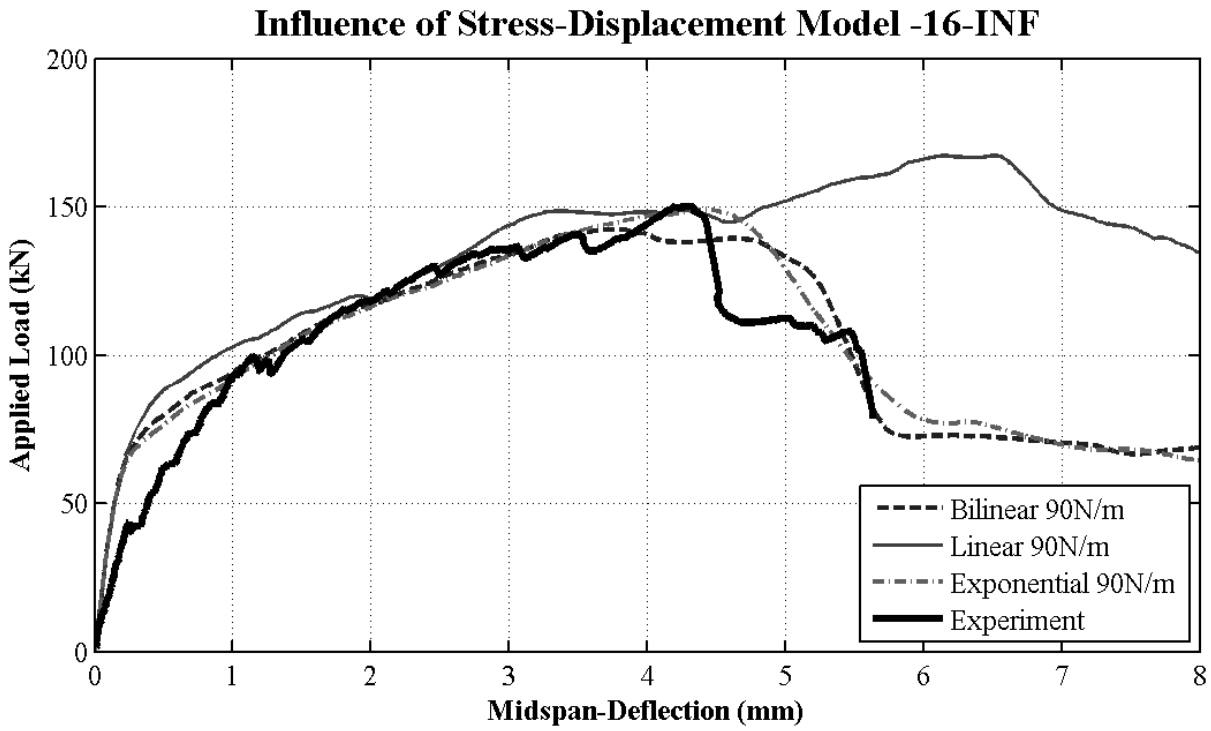
Influence of Stress-Displacement Model -16-INF
Applied Load (kN)
Midspan-Deflection (mm)
Bilinear 90N/m
Linear 90N/m
Exponential 90N/m
Experiment

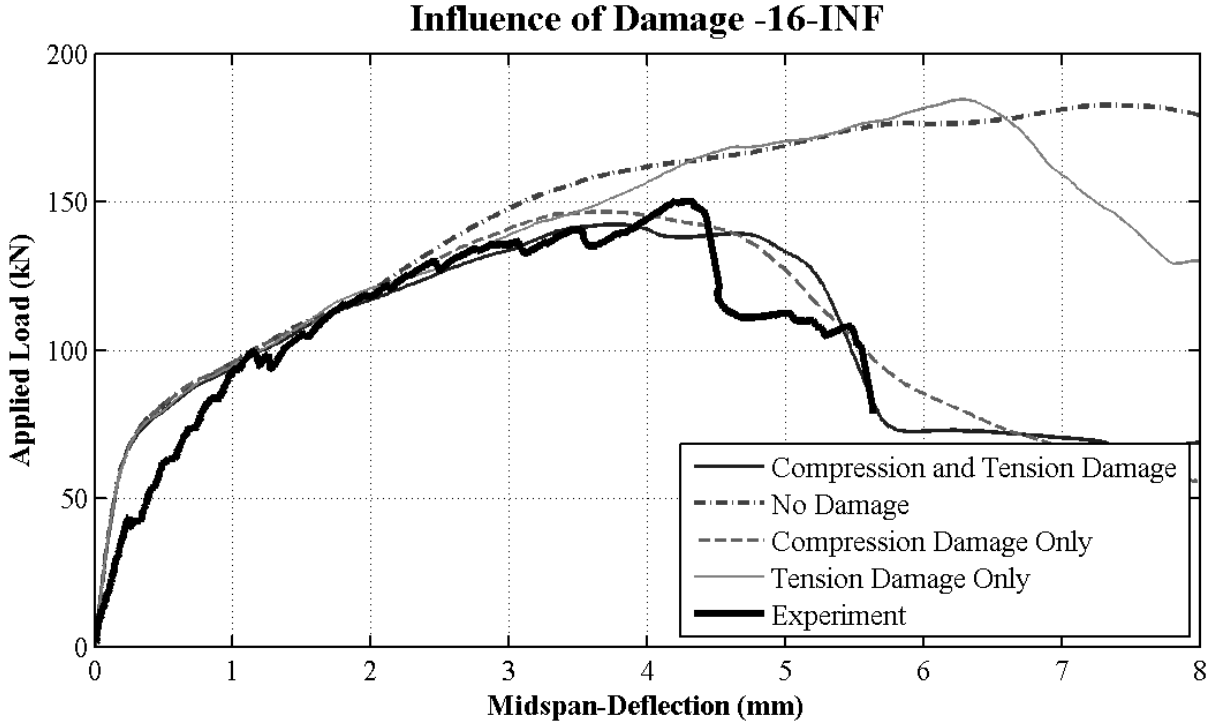
Influence of Damage -16-INF
Applied Load (kN)
Midspan-Deflection (mm)
Compression and Tension Damage
No Damage
Compression Damage Only
Tension Damage Only
Experiment

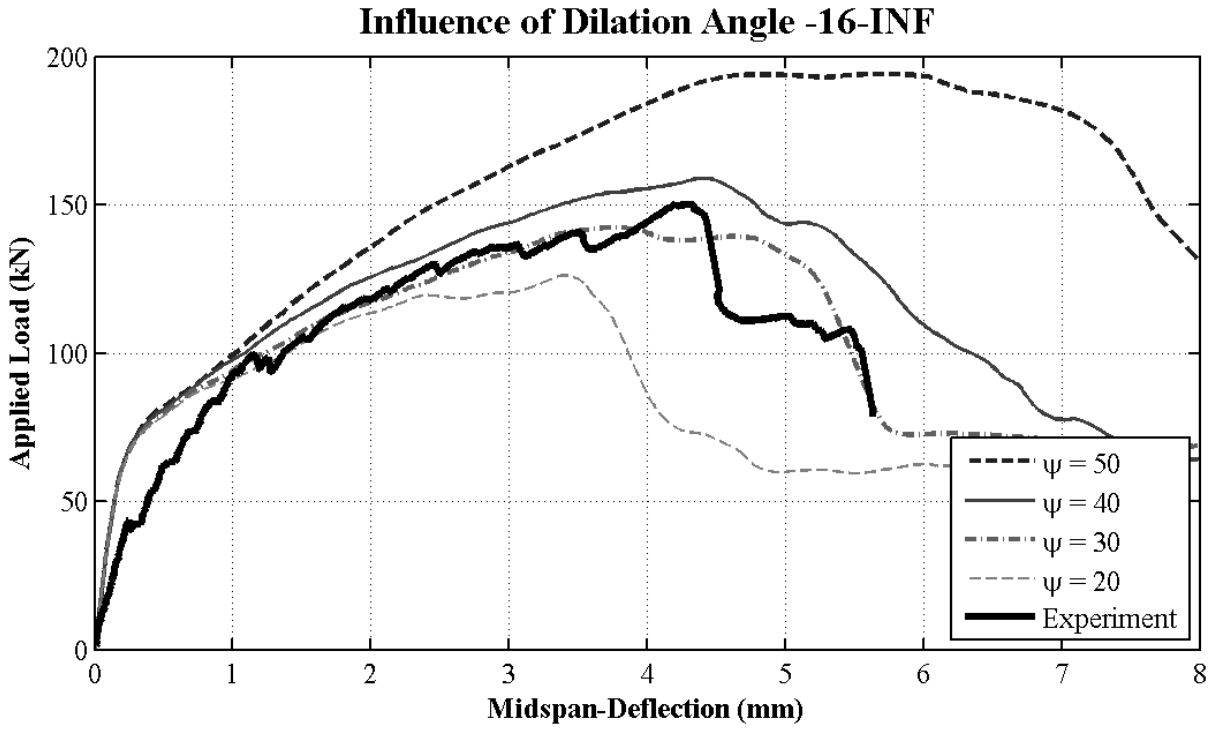
Influence of Dilation Angle -16-INF
Applied Load (kN)
Midspan-Deflection (mm)
ψ = 50
ψ = 40
ψ = 30
ψ = 20
Experiment

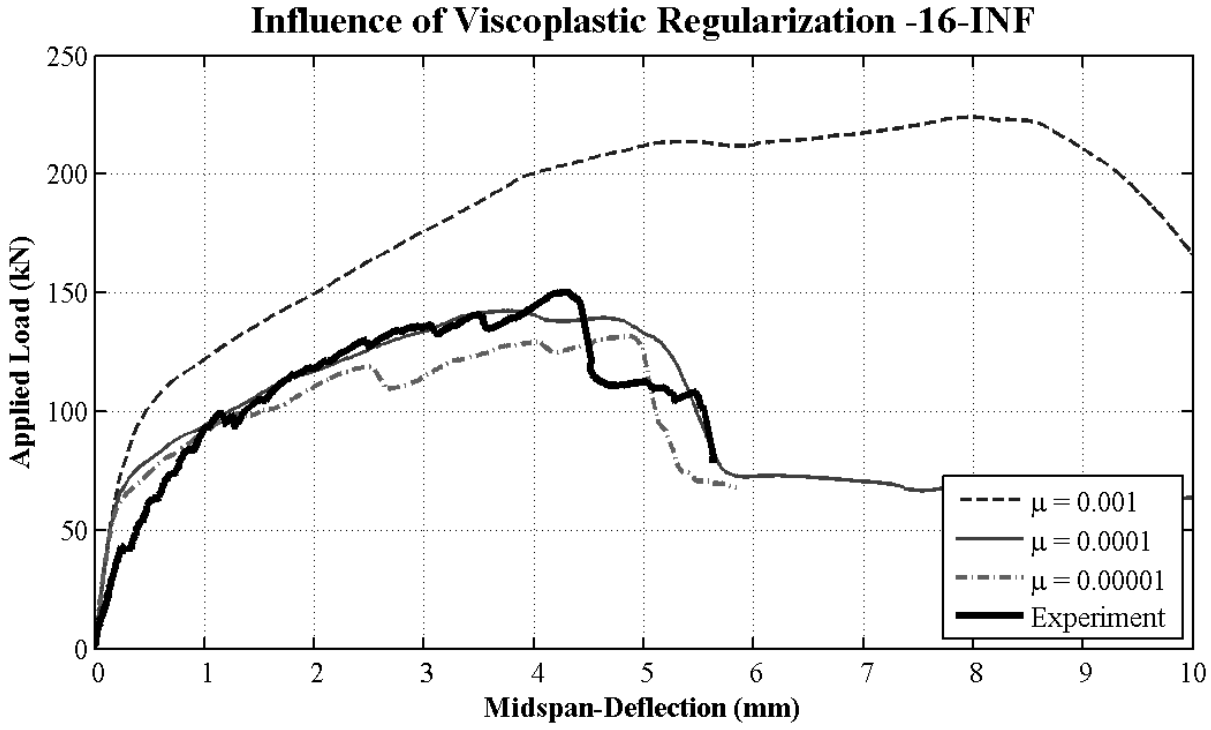
Influence of Viscoplastic Regularization -16-INF
Applied Load (kN)
Midspan-Deflection (mm)
μ = 0.001
μ = 0.0001
μ = 0.00001
Experiment

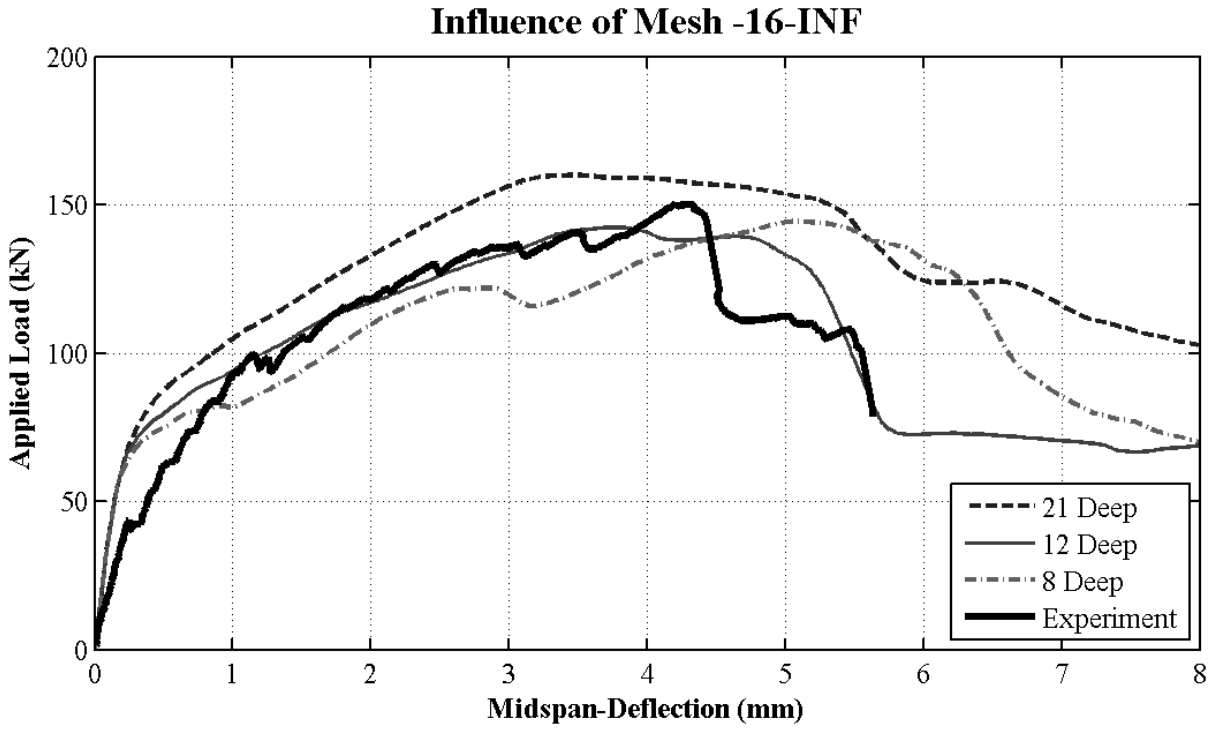
Influence of Mesh -16-INF
Applied Load (kN)
Midspan-Deflection (mm)
21 Deep
12 Deep
8 Deep
Experiment

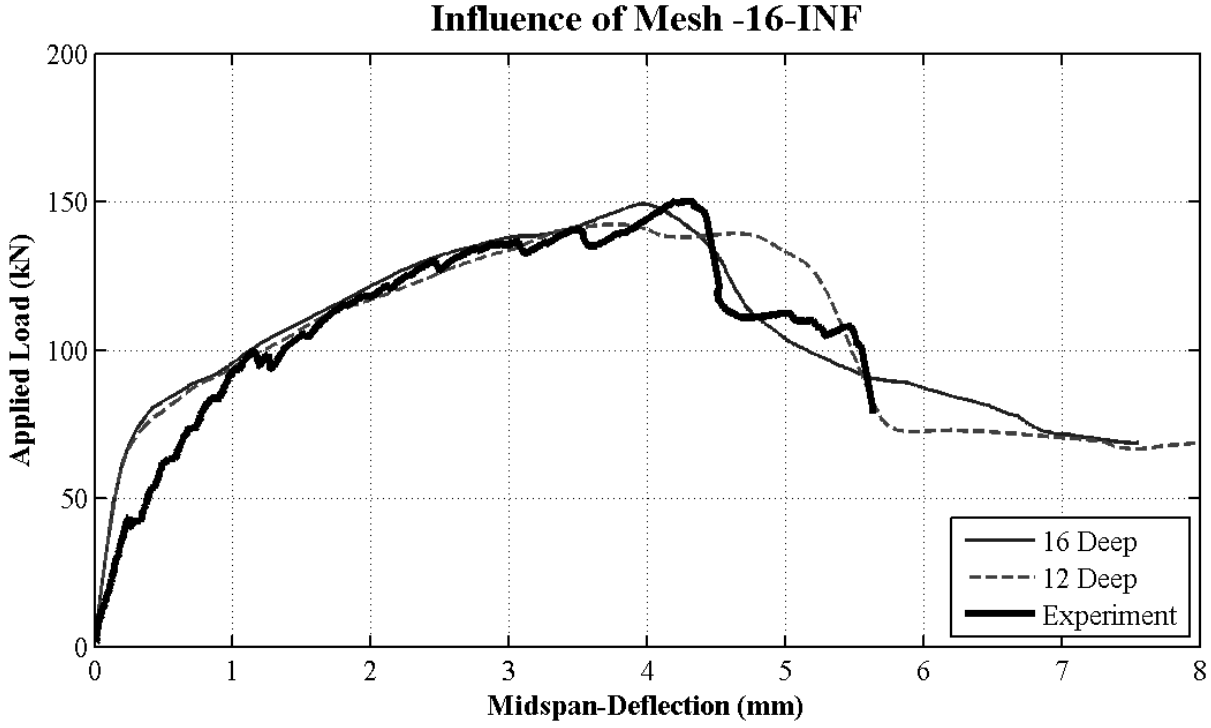
Influence of Mesh -16-INF
Applied Load (kN)
Midspan-Deflection (mm)
16 Deep
12 Deep
Experiment

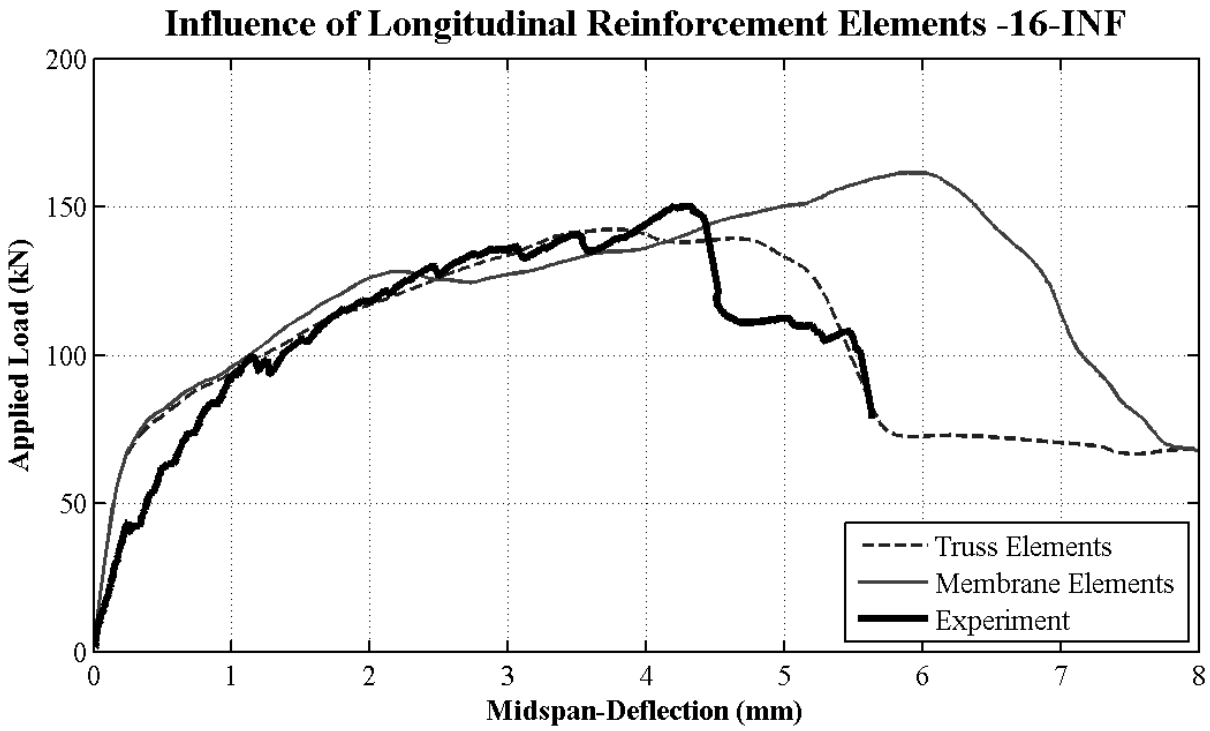
Influence of Longitudinal Reinforcement Elements -16-INF
Applied Load (kN)
Midspan-Deflection (mm)
Truss Elements
Membrane Elements
Experiment
0
50
100
150
200
0
1
2
3
4
5
6
7
8

BM 25-INF

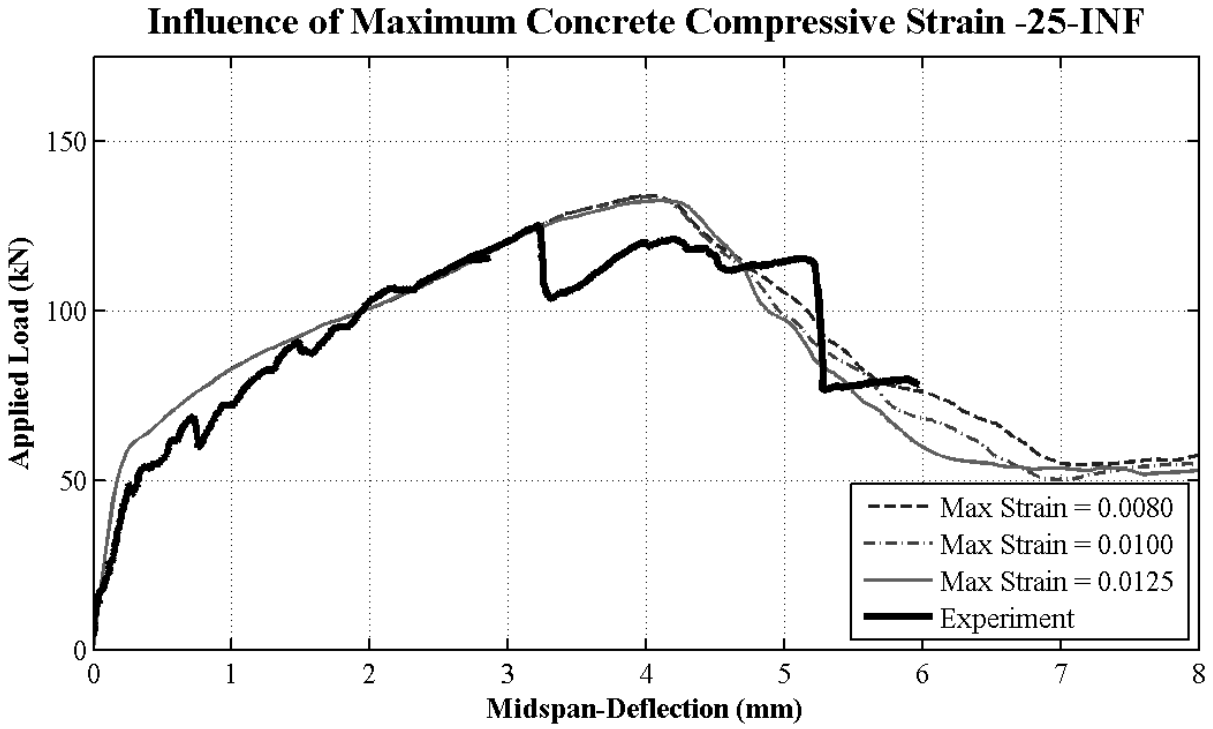
Influence of Maximum Concrete Compressive Strain -25-INF
Applied Load (kN)
Midspan-Deflection (mm)
Max Strain = 0.0080
Max Strain = 0.0100
Max Strain = 0.0125
Experiment

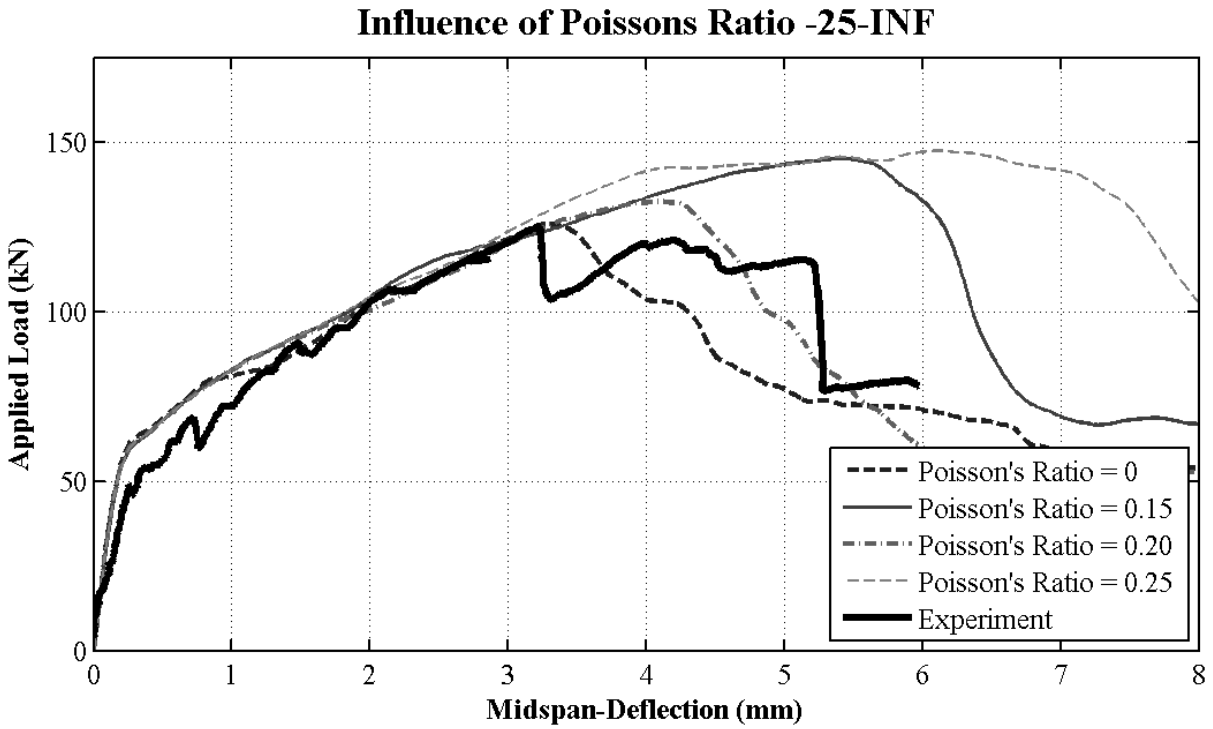
Influence of Poissons Ratio -25-INF
Applied Load (kN)
Midspan-Deflection (mm)
Poisson's Ratio = 0
Poisson's Ratio = 0.15
Poisson's Ratio = 0.20
Poisson's Ratio = 0.25
Experiment

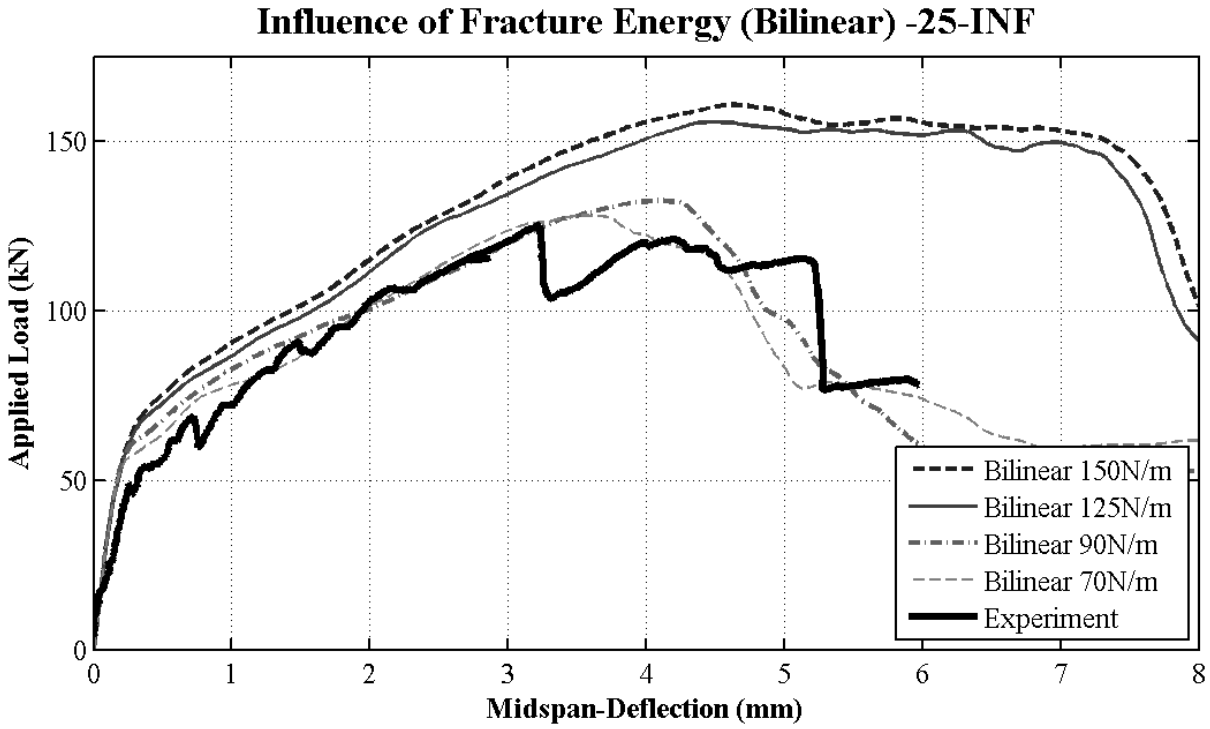
Influence of Fracture Energy (Bilinear) -25-INF
Applied Load (kN)
Midspan-Deflection (mm)
Bilinear 150N/m
Bilinear 125N/m
Bilinear 90N/m
Bilinear 70N/m
Experiment

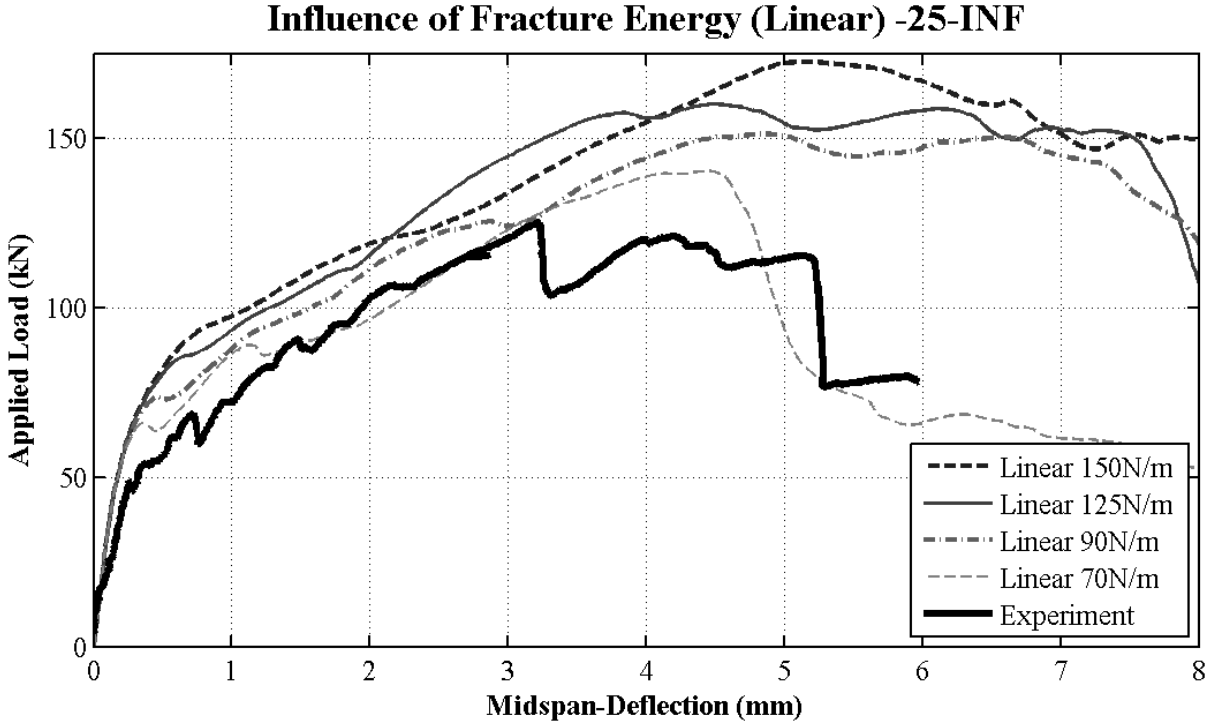
Influence of Fracture Energy (Linear) -25-INF
Applied Load (kN)
Midspan-Deflection (mm)
Linear 150N/m
Linear 125N/m
Linear 90N/m
Linear 70N/m
Experiment

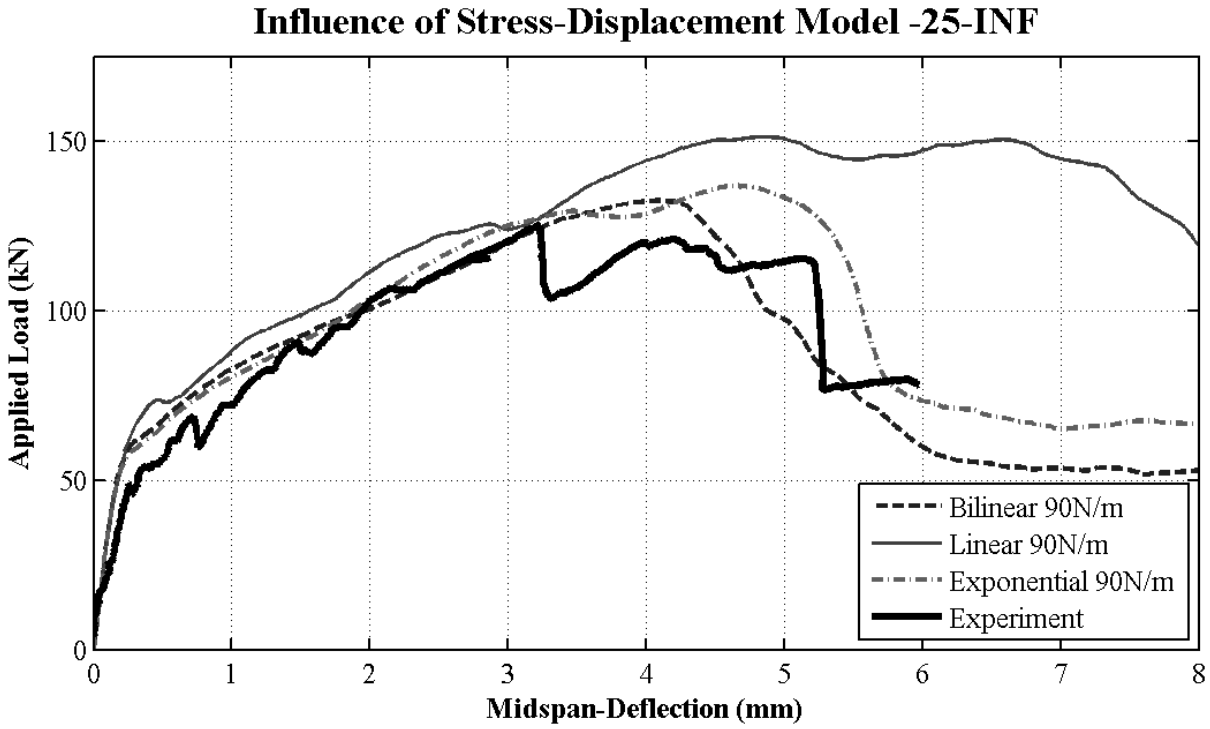
Influence of Stress-Displacement Model -25-INF
Applied Load (kN)
Midspan-Deflection (mm)
Bilinear 90N/m
Linear 90N/m
Exponential 90N/m
Experiment

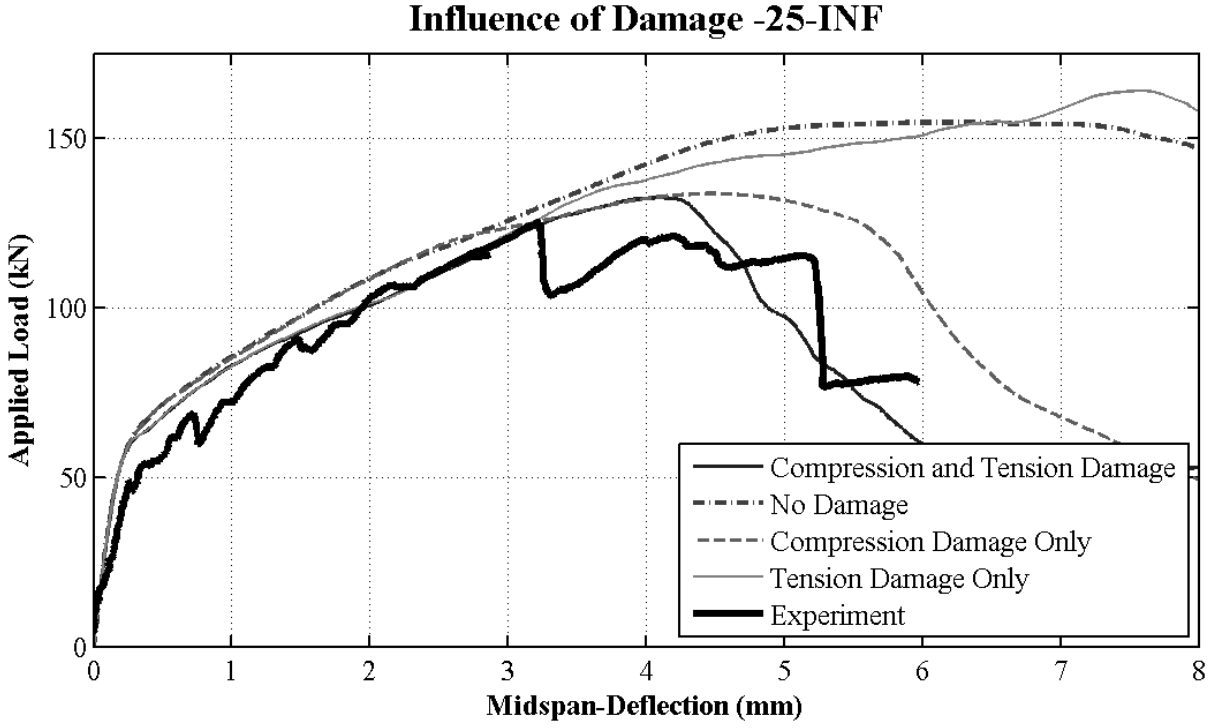
Influence of Damage -25-INF
Applied Load (kN)
Midspan-Deflection (mm)
Compression and Tension Damage
No Damage
Compression Damage Only
Tension Damage Only
Experiment

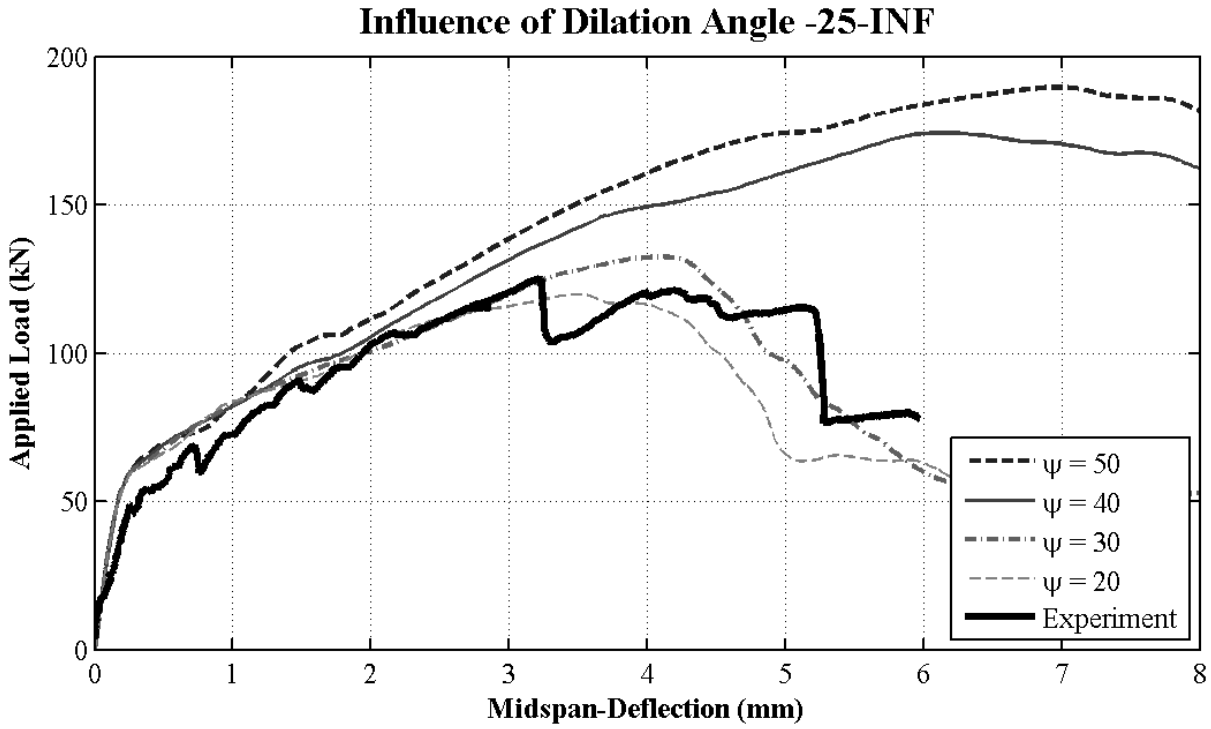
Influence of Dilation Angle -25-INF
Applied Load (kN)
Midspan-Deflection (mm)
ψ = 50
ψ = 40
ψ = 30
ψ = 20
Experiment

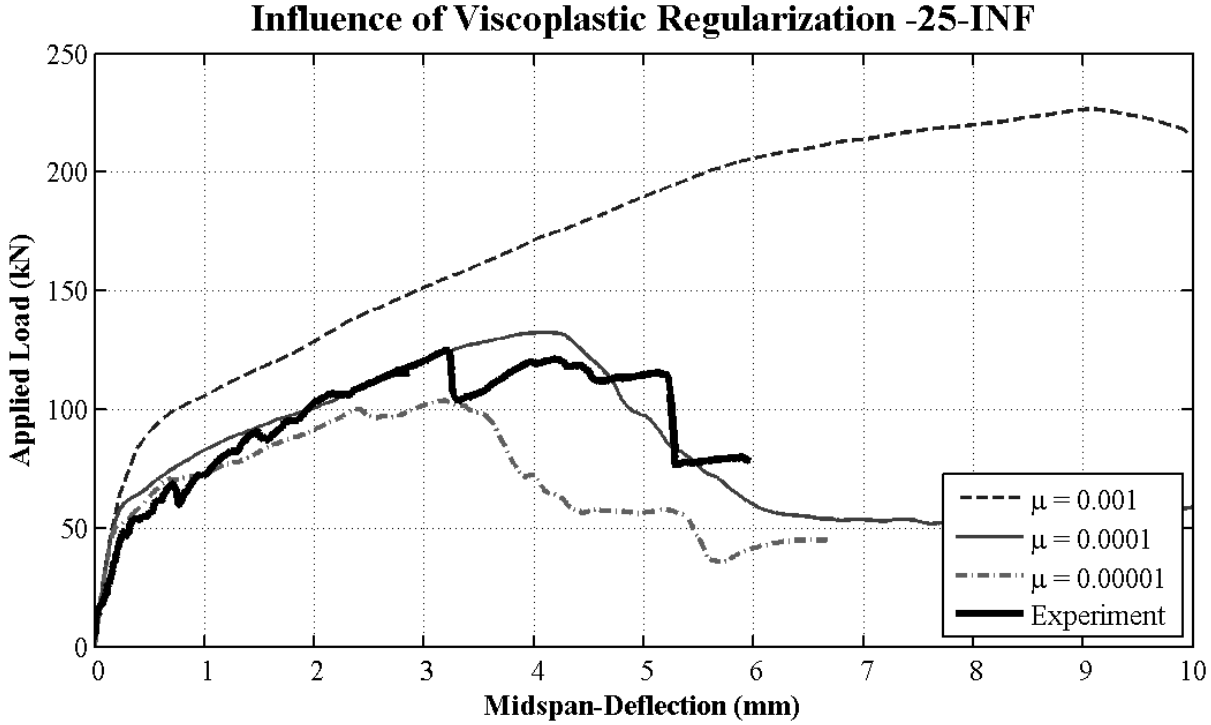
Influence of Viscoplastic Regularization -25-INF
Applied Load (kN)
Midspan-Deflection (mm)
μ = 0.001
μ = 0.0001
μ = 0.00001
Experiment

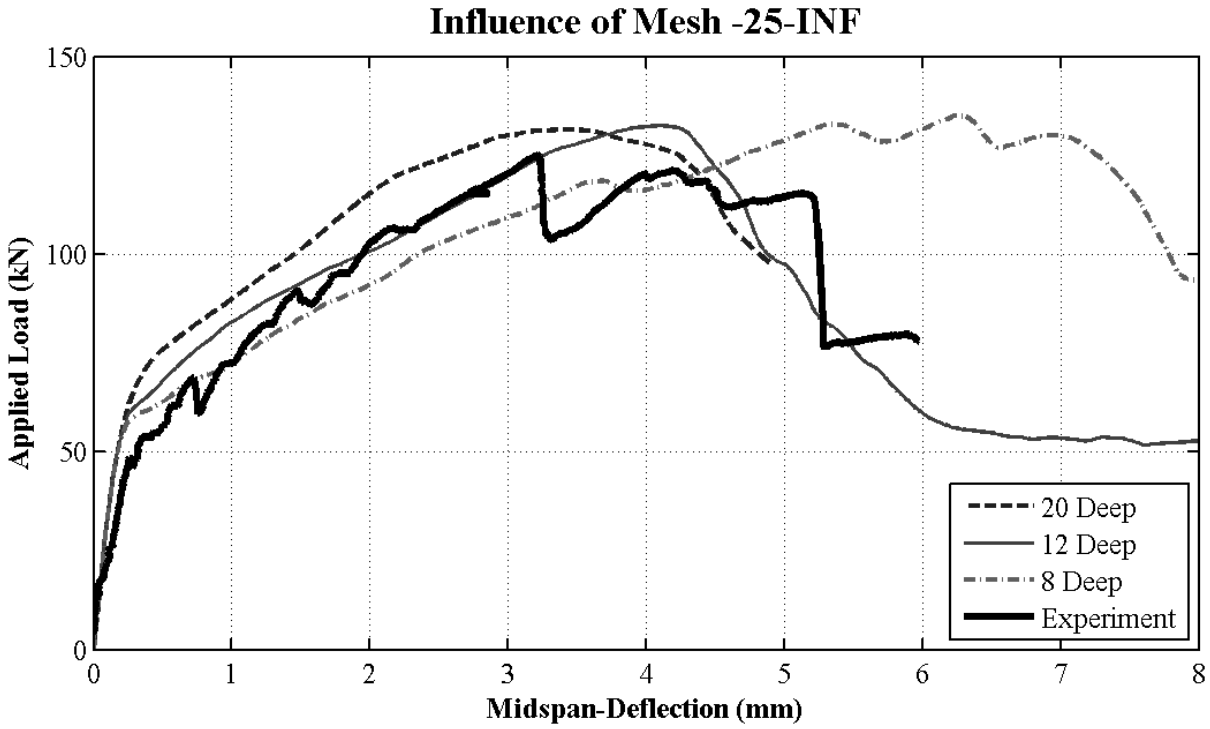
Influence of Mesh -25-INF
Applied Load (kN)
Midspan-Deflection (mm)
20 Deep
12 Deep
8 Deep
Experiment

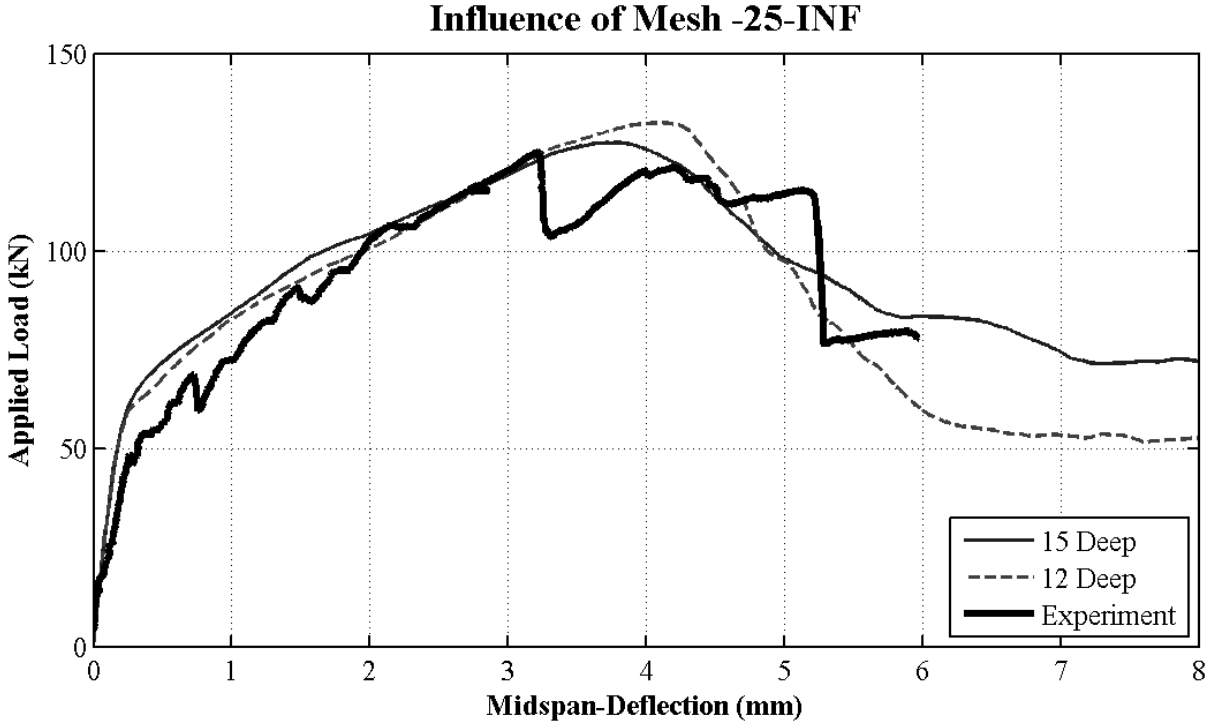
Influence of Mesh -25-INF
Applied Load (kN)
Midspan-Deflection (mm)
15 Deep
12 Deep
Experiment

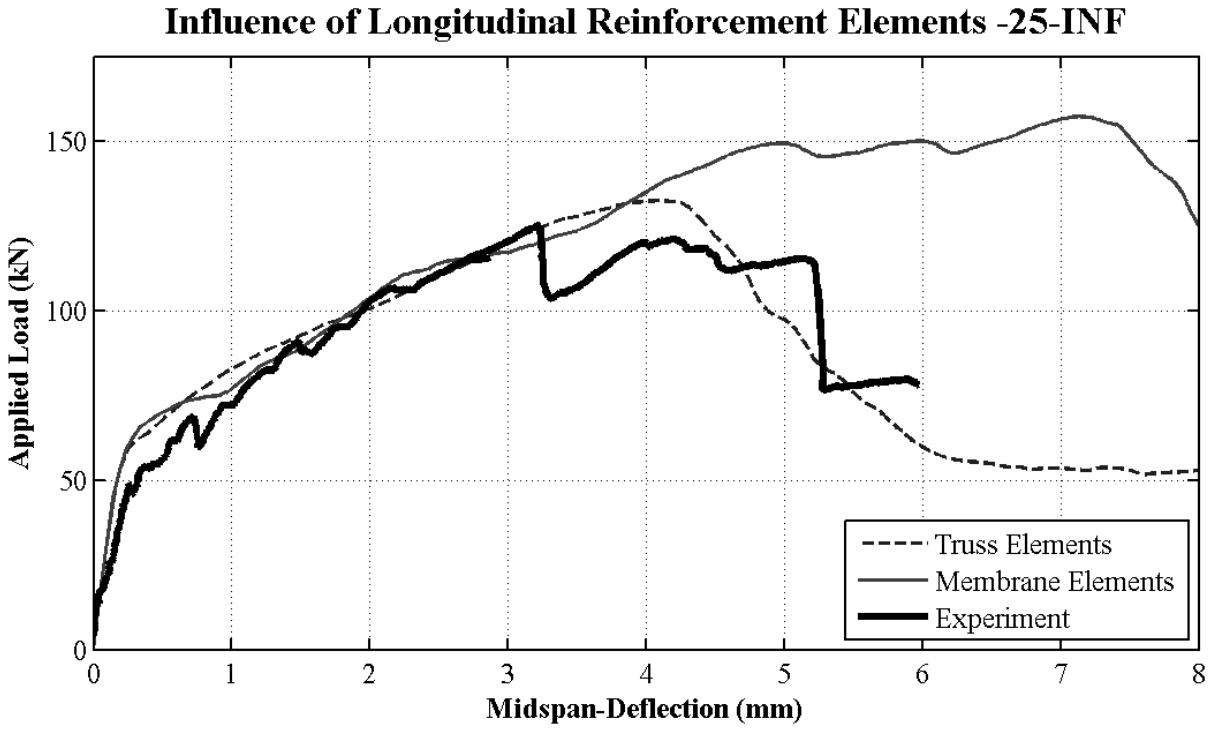
Influence of Longitudinal Reinforcement Elements -25-INF
Applied Load (kN)
Midspan-Deflection (mm)
0
50
100
150
0
1
2
3
4
5
6
7
8
Truss Elements
Membrane Elements
Experiment

Appendix C

Beams with Stirrups

This Appendix provides the results of all analyses performed for beams with stirrups spaced at 150mm and 220mm. Unless stated otherwise, the parameters summarized in Table C.1 were used in all analyses presented in this appendix.

Table C.1: Parameters Used for the Modelling of Beams with Stirrups

Compression Model:	Modified Hognestad Parabola
Maximum Compressive Strain:	0.015
Tension Model:	Bilinear Stress-Displacement
Fracture Energy, G_f:	90 N/m
Damage:	Tension and Compression Included
Poisson's Ratio, v:	0.2
Dilation Angle, ψ:	50°
σ_{bo}/σ_{co}:	1.16
Eccentricity, ϵ:	0.1
K_c:	2/3
Viscosity Parameter, μ:	0.0001
Mesh Refinement:	12 Deep
Longitudinal Reinforcement:	Linear Truss Sections
Stirrup Reinforcement:	Reinforced Membrane Sections

BM 12-150

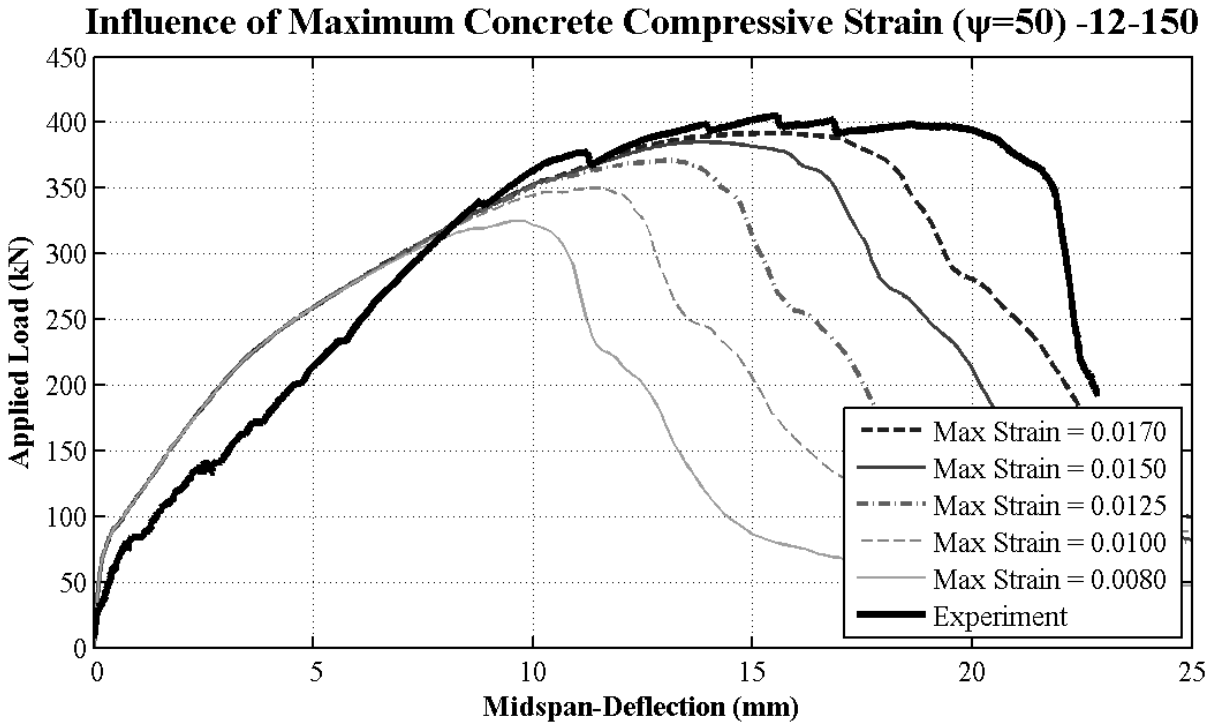
Influence of Maximum Concrete Compressive Strain (ψ=50) -12-150
Applied Load (kN)
Midspan-Deflection (mm)
Max Strain = 0.0170
Max Strain = 0.0150
Max Strain = 0.0125
Max Strain = 0.0100
Max Strain = 0.0080
Experiment

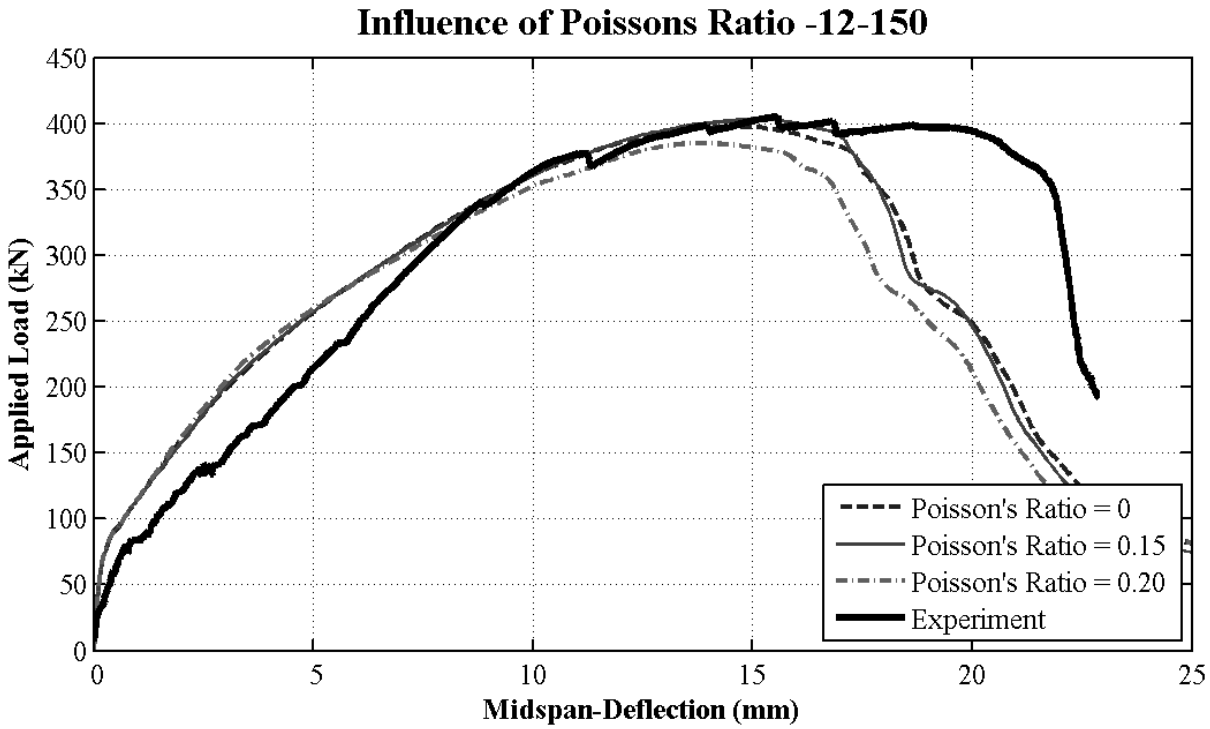
Influence of Poissons Ratio -12-150
Applied Load (kN)
Midspan-Deflection (mm)
Poisson's Ratio = 0
Poisson's Ratio = 0.15
Poisson's Ratio = 0.20
Experiment

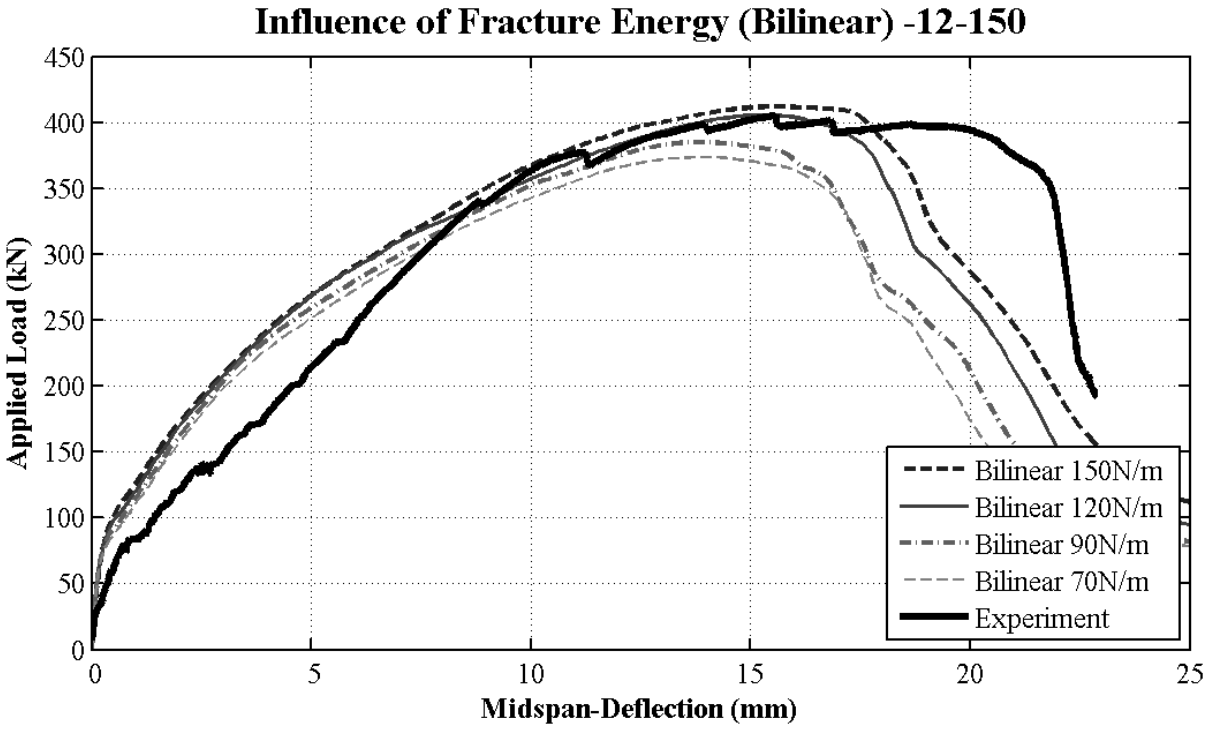
Influence of Fracture Energy (Bilinear) -12-150
Applied Load (kN)
Midspan-Deflection (mm)
Bilinear 150N/m
Bilinear 120N/m
Bilinear 90N/m
Bilinear 70N/m
Experiment

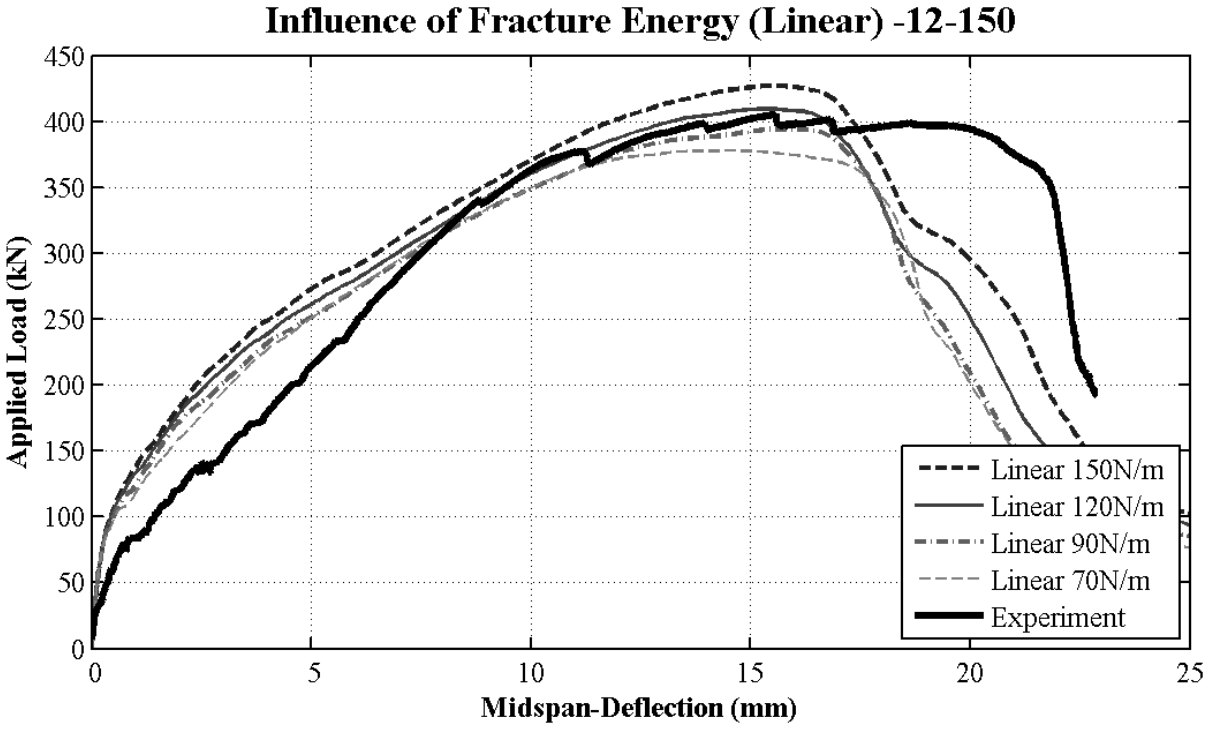
Influence of Fracture Energy (Linear) -12-150
Applied Load (kN)
Midspan-Deflection (mm)
Linear 150N/m
Linear 120N/m
Linear 90N/m
Linear 70N/m
Experiment

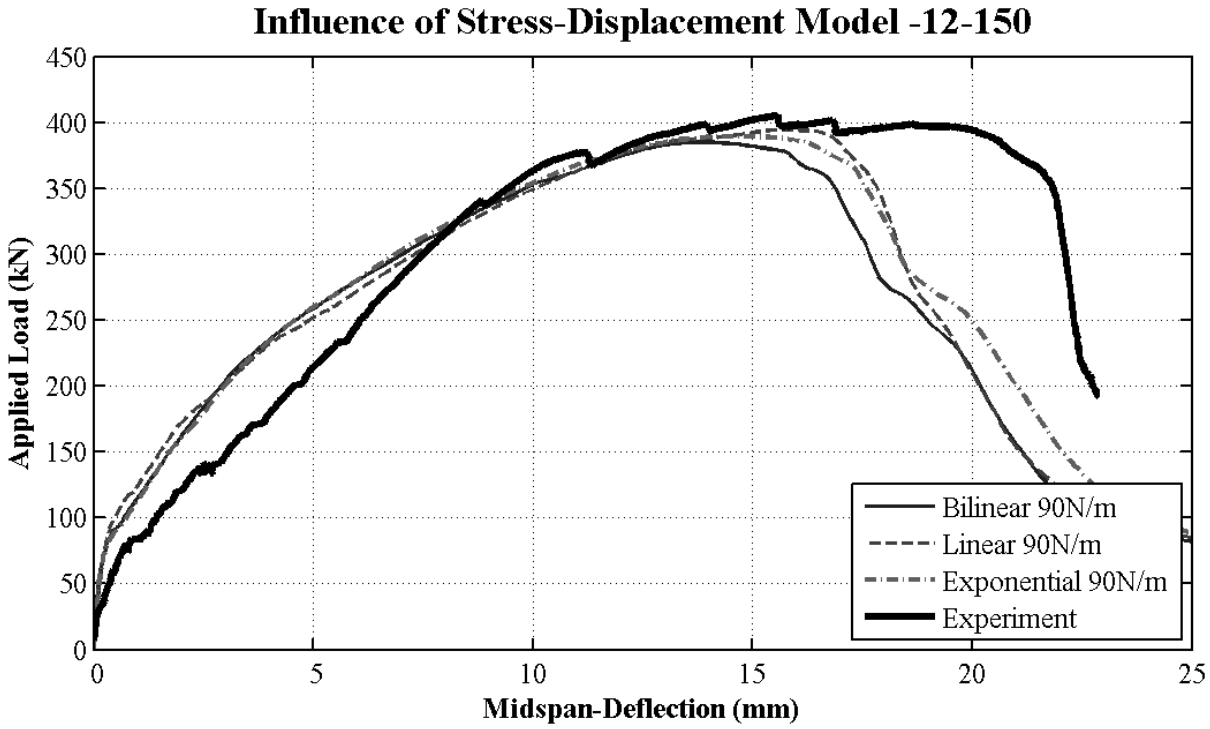
Influence of Stress-Displacement Model -12-150
Applied Load (kN)
Midspan-Deflection (mm)
Bilinear 90N/m
Linear 90N/m
Exponential 90N/m
Experiment

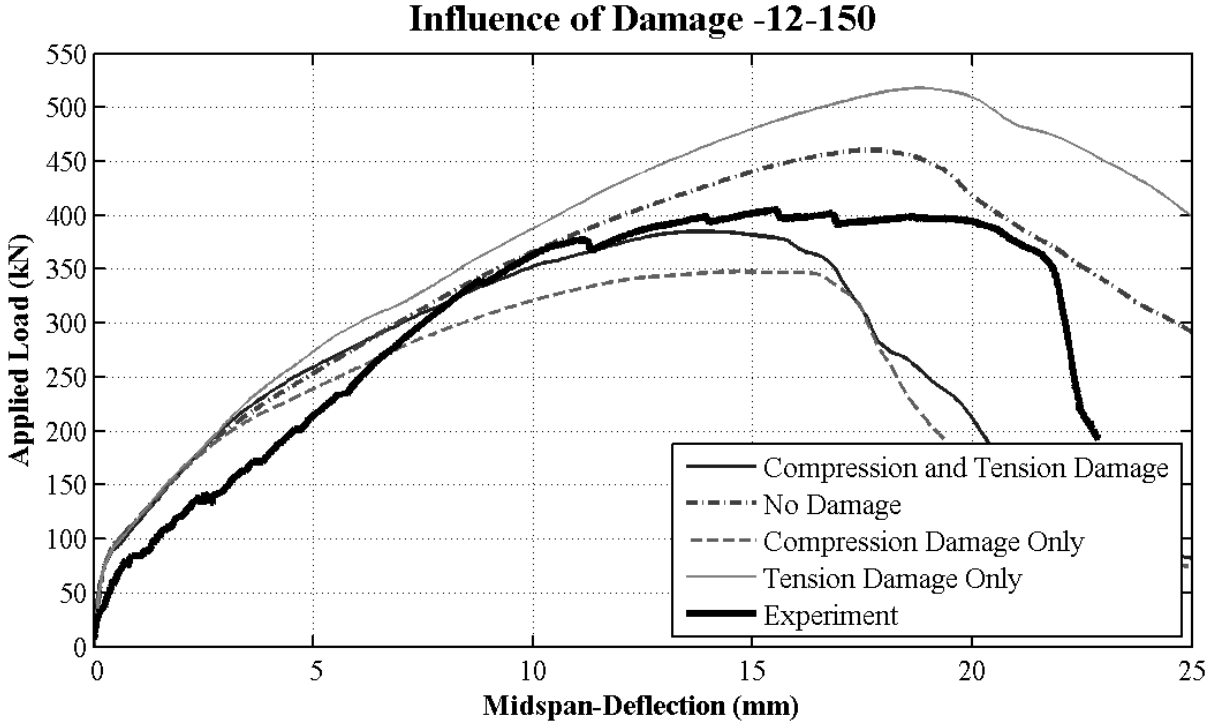
Influence of Damage -12-150
Applied Load (kN)
Midspan-Deflection (mm)
Compression and Tension Damage
No Damage
Compression Damage Only
Tension Damage Only
Experiment

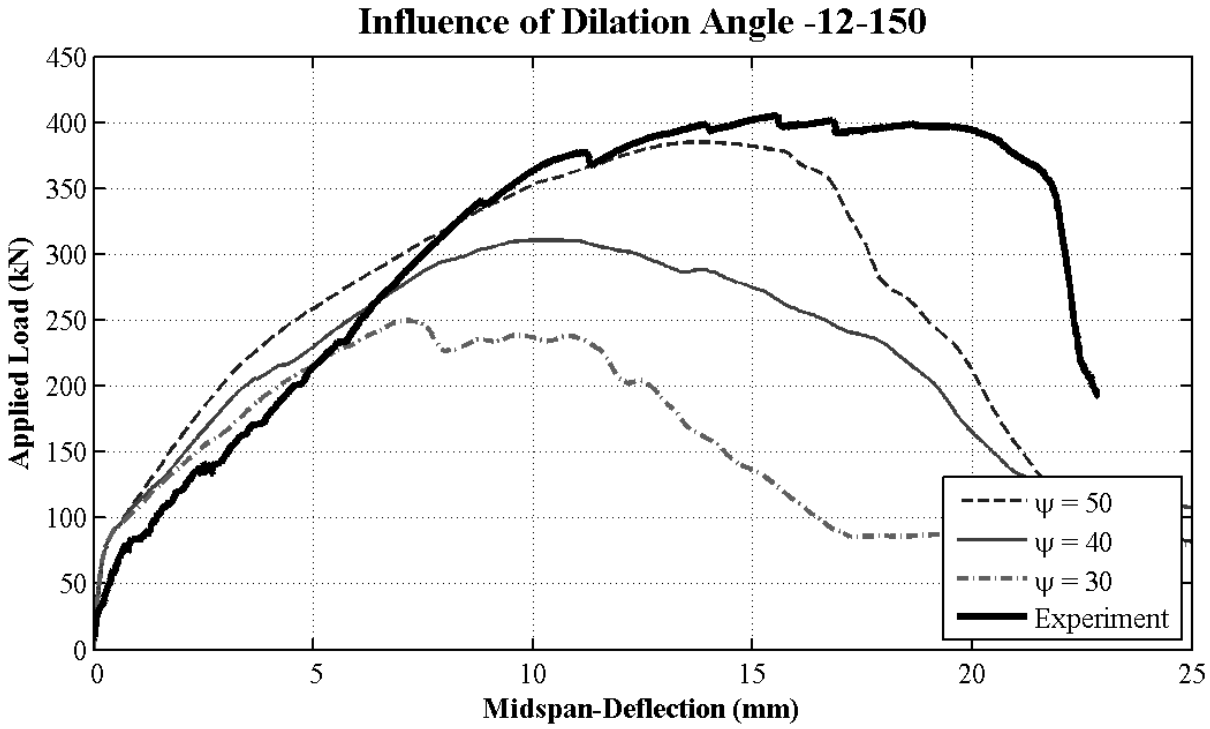
Influence of Dilation Angle -12-150
Applied Load (kN)
Midspan-Deflection (mm)
ψ = 50
ψ = 40
ψ = 30
Experiment

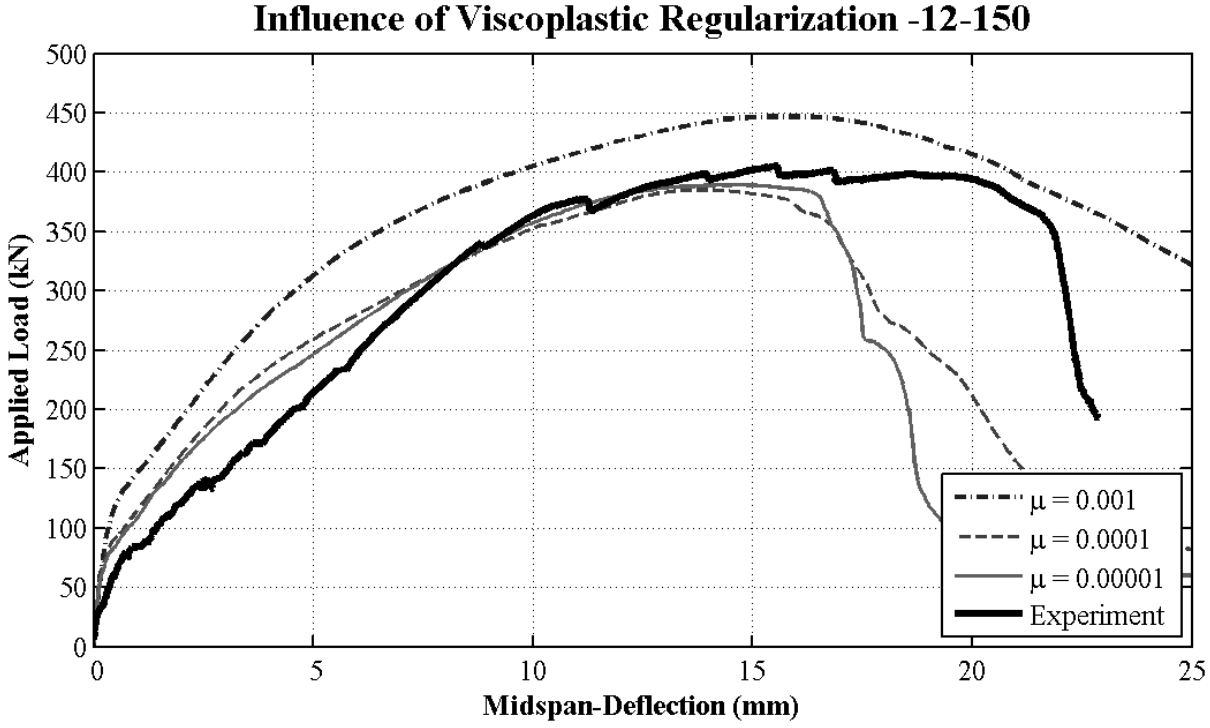
Influence of Viscoplastic Regularization -12-150
Applied Load (kN)
Midspan-Deflection (mm)
μ = 0.001
μ = 0.0001
μ = 0.00001
Experiment

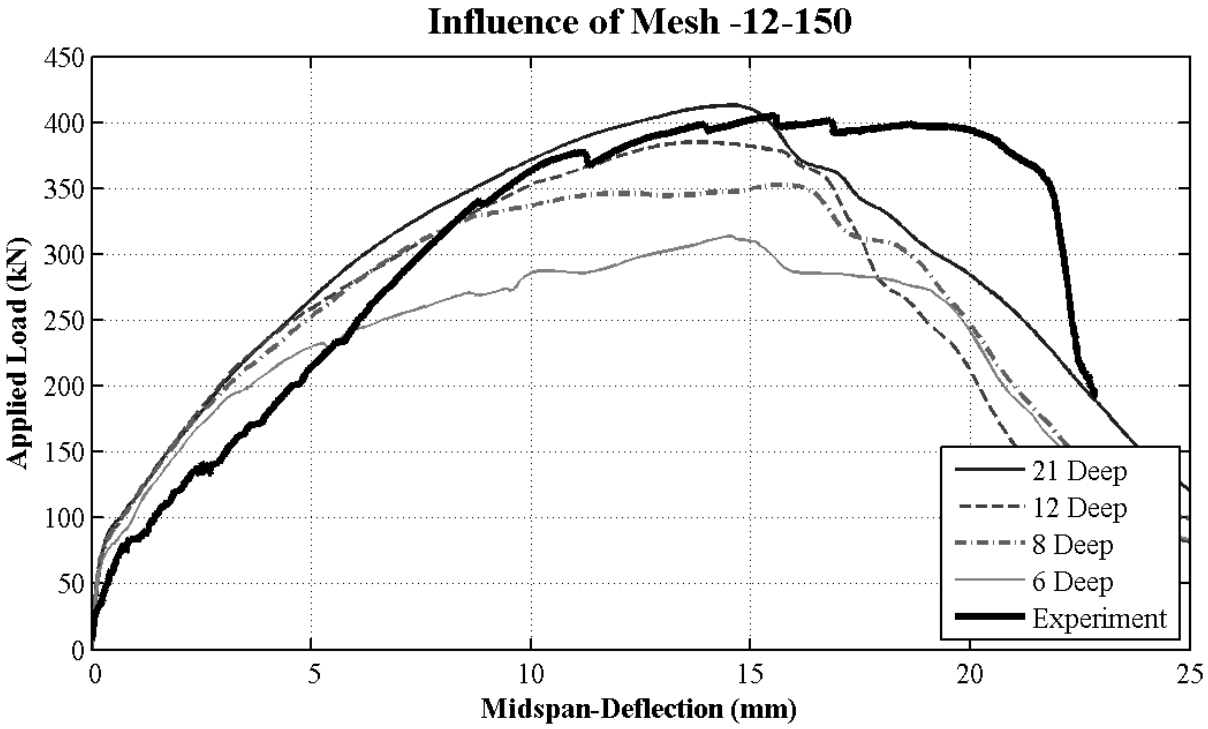
Influence of Mesh -12-150
Applied Load (kN)
Midspan-Deflection (mm)
21 Deep
12 Deep
8 Deep
6 Deep
Experiment

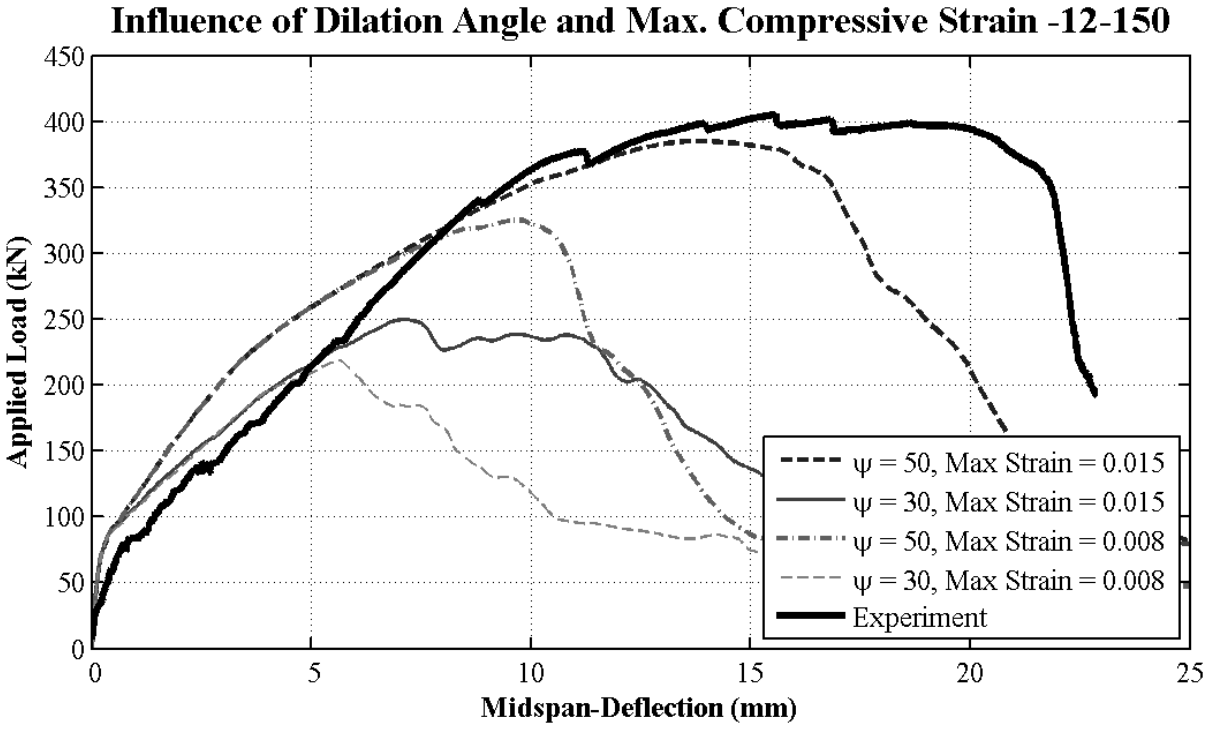
Influence of Dilation Angle and Max. Compressive Strain -12-150
Applied Load (kN)
Midspan-Deflection (mm)
ψ = 50, Max Strain = 0.015
ψ = 30, Max Strain = 0.015
ψ = 50, Max Strain = 0.008
ψ = 30, Max Strain = 0.008
Experiment

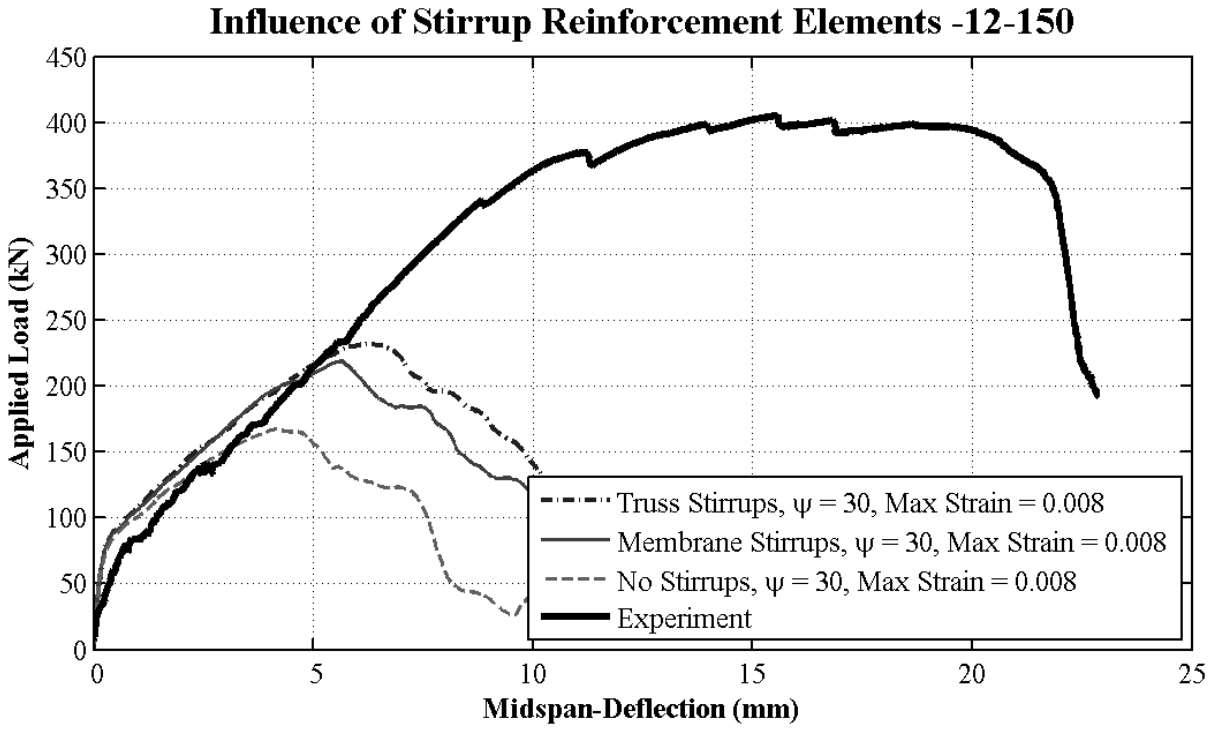
Influence of Stirrup Reinforcement Elements -12-150
Applied Load (kN)
Midspan-Deflection (mm)
Truss Stirrups, ψ = 30, Max Strain = 0.008
Membrane Stirrups, ψ = 30, Max Strain = 0.008
No Stirrups, ψ = 30, Max Strain = 0.008
Experiment

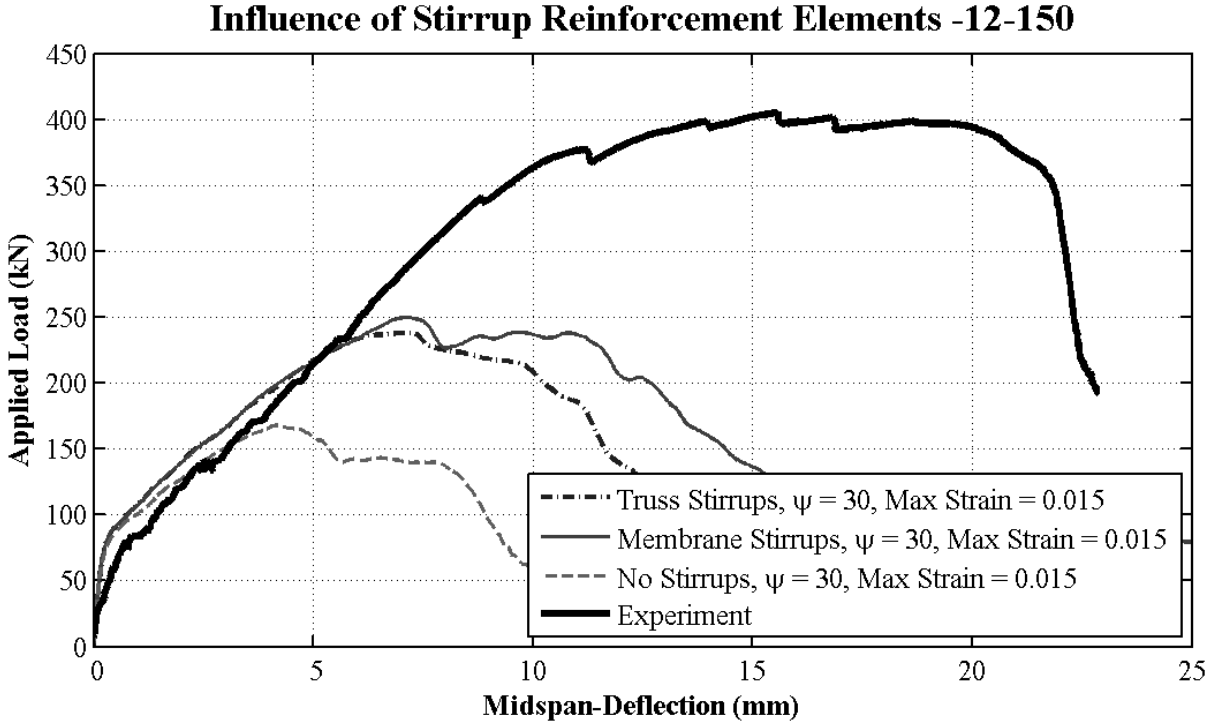
Influence of Stirrup Reinforcement Elements -12-150
Applied Load (kN)
Midspan-Deflection (mm)
Truss Stirrups, ψ = 30, Max Strain = 0.015
Membrane Stirrups, ψ = 30, Max Strain = 0.015
No Stirrups, ψ = 30, Max Strain = 0.015
Experiment

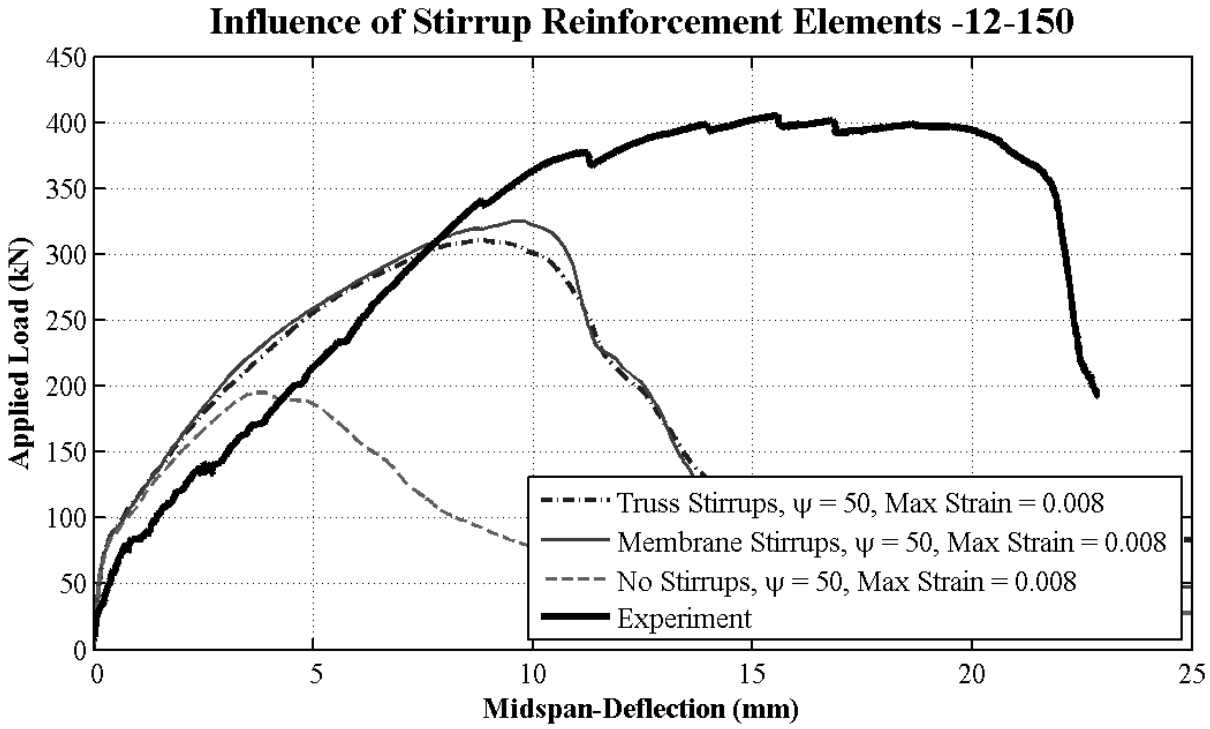
Influence of Stirrup Reinforcement Elements -12-150
Applied Load (kN)
Midspan-Deflection (mm)
Truss Stirrups, ψ = 50, Max Strain = 0.008
Membrane Stirrups, ψ = 50, Max Strain = 0.008
No Stirrups, ψ = 50, Max Strain = 0.008
Experiment

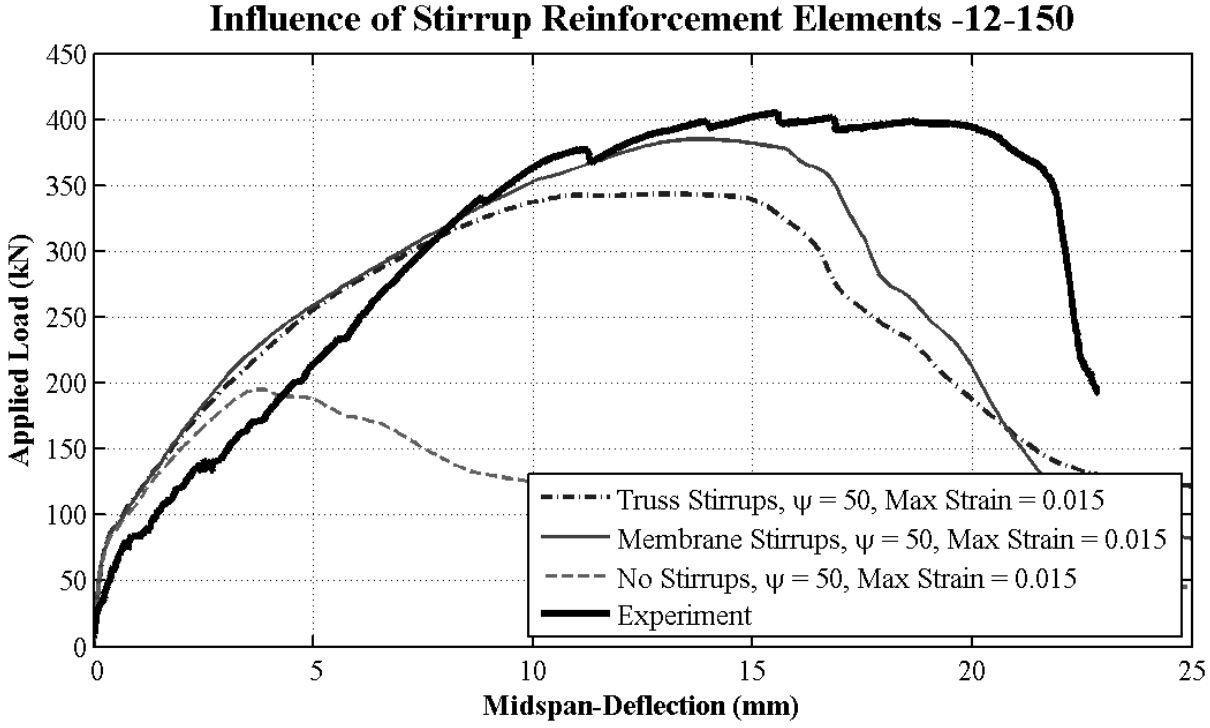
Influence of Stirrup Reinforcement Elements -12-150
Applied Load (kN)
Midspan-Deflection (mm)
Truss Stirrups, ψ = 50, Max Strain = 0.015
Membrane Stirrups, ψ = 50, Max Strain = 0.015
No Stirrups, ψ = 50, Max Strain = 0.015
Experiment

BM 16-150

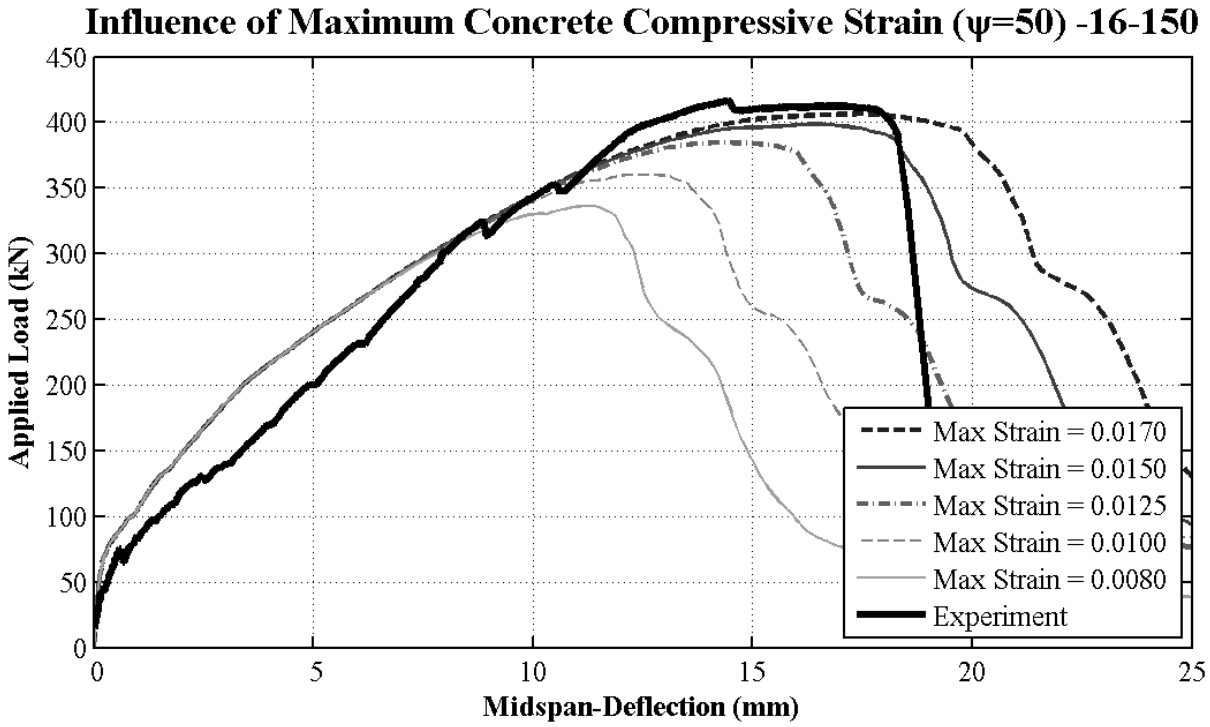
Influence of Maximum Concrete Compressive Strain (ψ=50) -16-150
Applied Load (kN)
Midspan-Deflection (mm)
Max Strain = 0.0170
Max Strain = 0.0150
Max Strain = 0.0125
Max Strain = 0.0100
Max Strain = 0.0080
Experiment

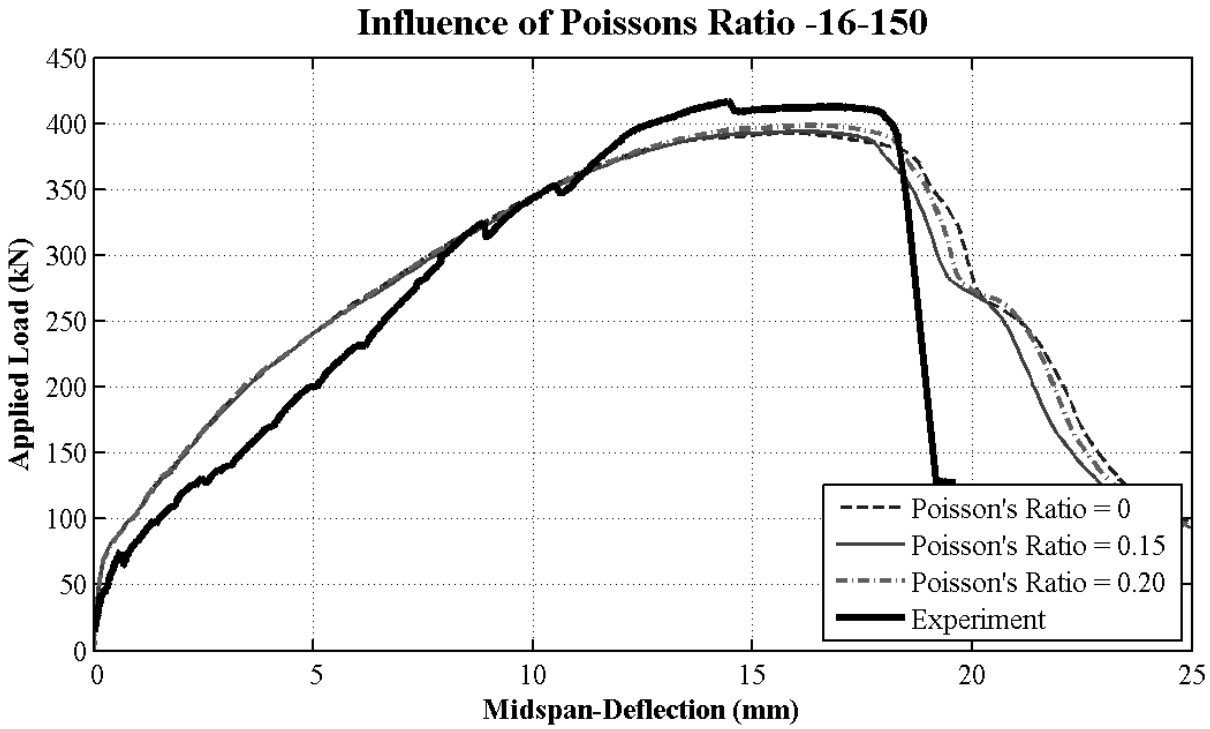
Influence of Poissons Ratio -16-150
Applied Load (kN)
Midspan-Deflection (mm)
Poisson's Ratio = 0
Poisson's Ratio = 0.15
Poisson's Ratio = 0.20
Experiment

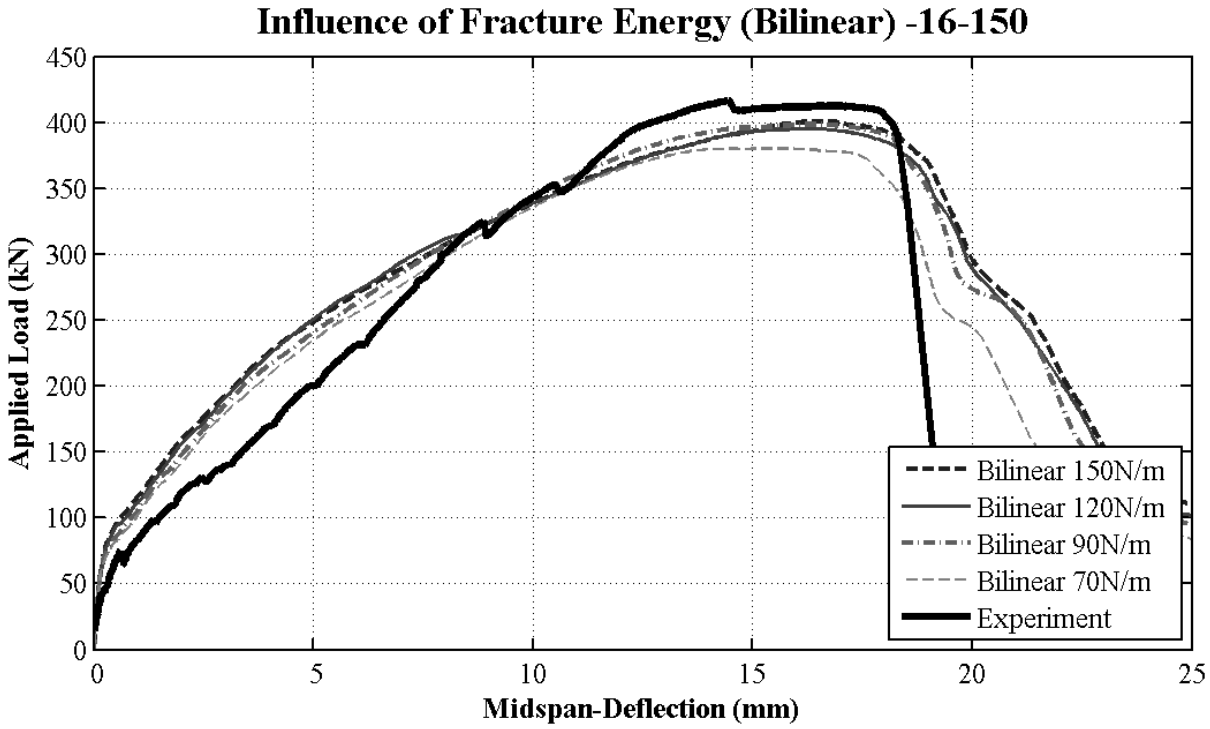
Influence of Fracture Energy (Bilinear) -16-150
Applied Load (kN)
Midspan-Deflection (mm)
Bilinear 150N/m
Bilinear 120N/m
Bilinear 90N/m
Bilinear 70N/m
Experiment

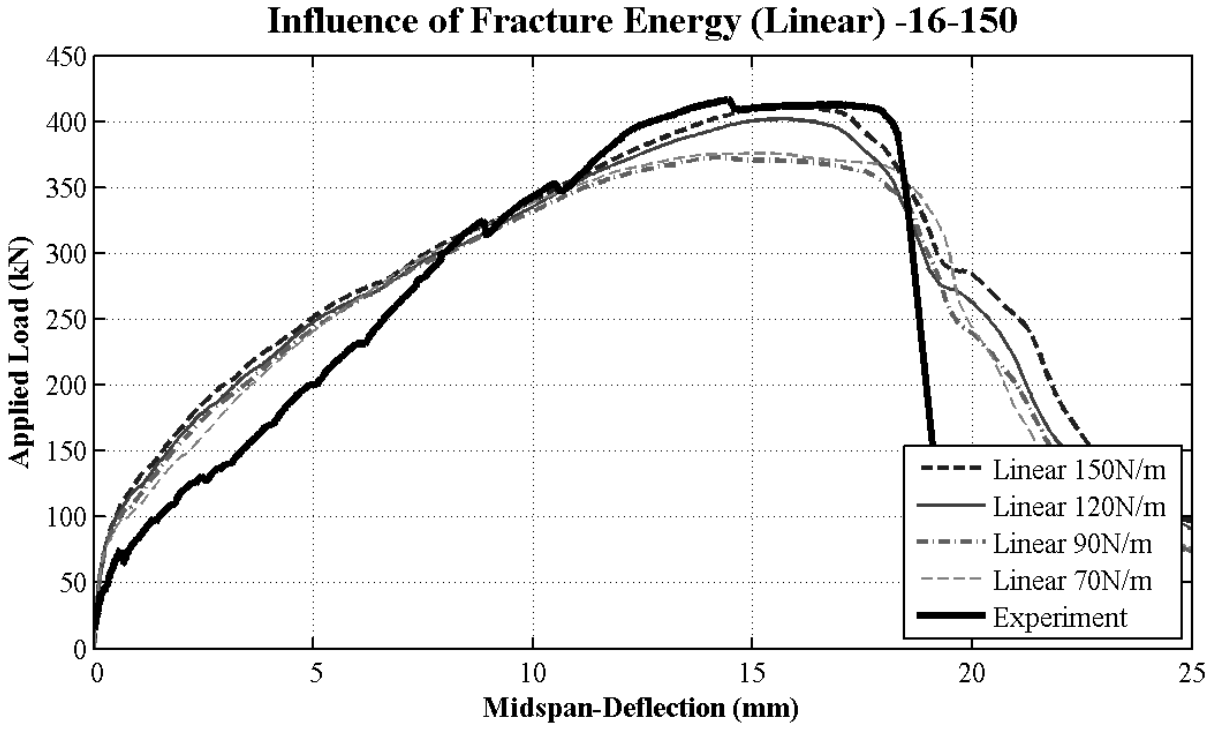
Influence of Fracture Energy (Linear) -16-150
Applied Load (kN)
Midspan-Deflection (mm)
Linear 150N/m
Linear 120N/m
Linear 90N/m
Linear 70N/m
Experiment

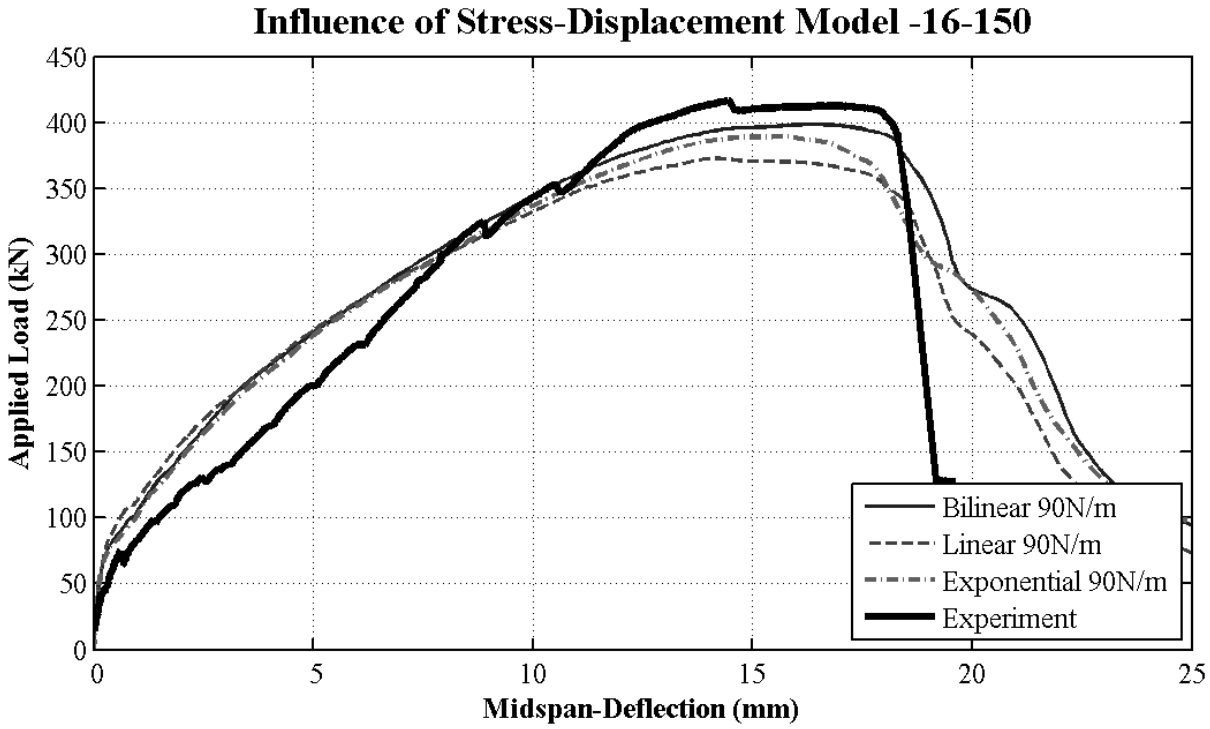
Influence of Stress-Displacement Model -16-150
Applied Load (kN)
Midspan-Deflection (mm)
Bilinear 90N/m
Linear 90N/m
Exponential 90N/m
Experiment

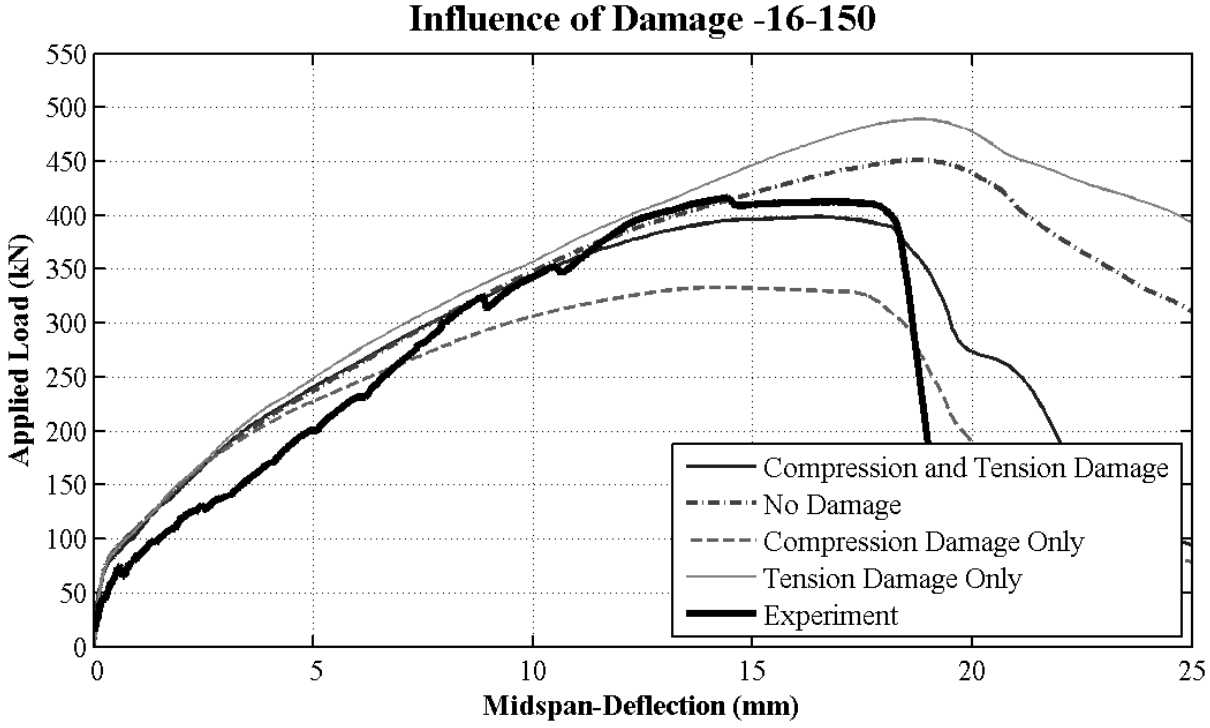
Influence of Damage -16-150
Applied Load (kN)
Midspan-Deflection (mm)
Compression and Tension Damage
No Damage
Compression Damage Only
Tension Damage Only
Experiment

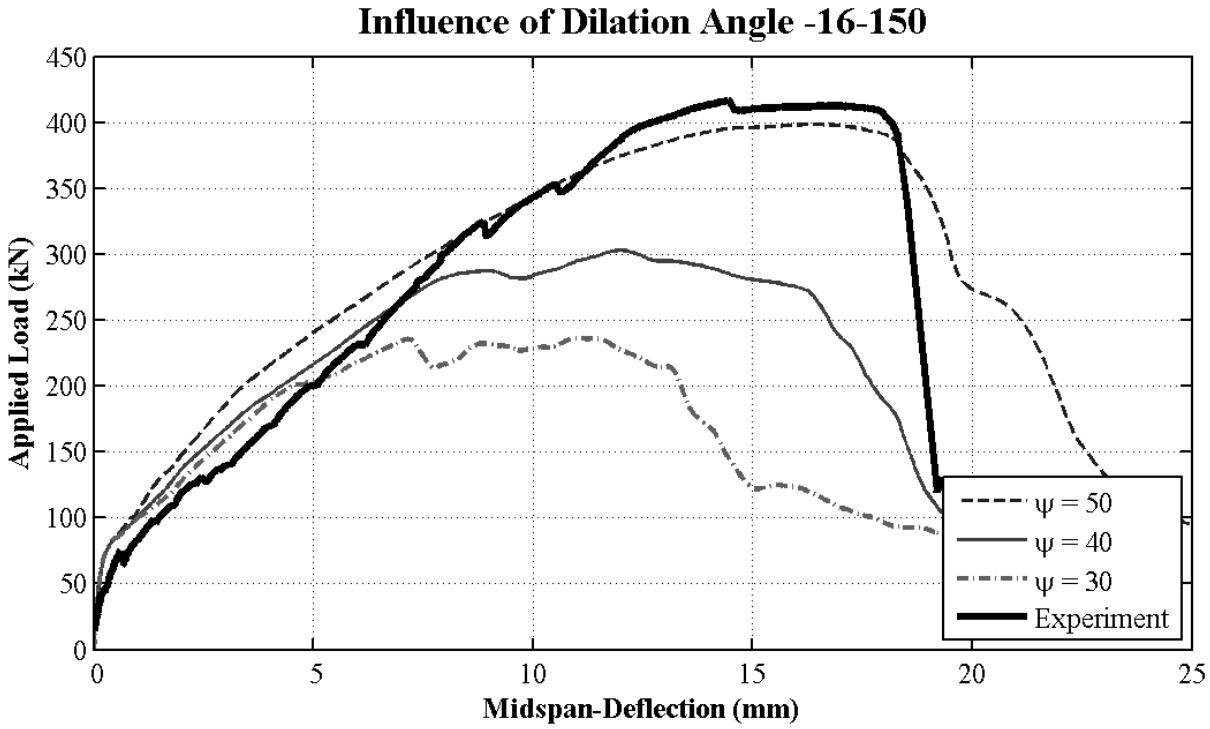
Influence of Dilation Angle -16-150
Applied Load (kN)
Midspan-Deflection (mm)
ψ = 50
ψ = 40
ψ = 30
Experiment

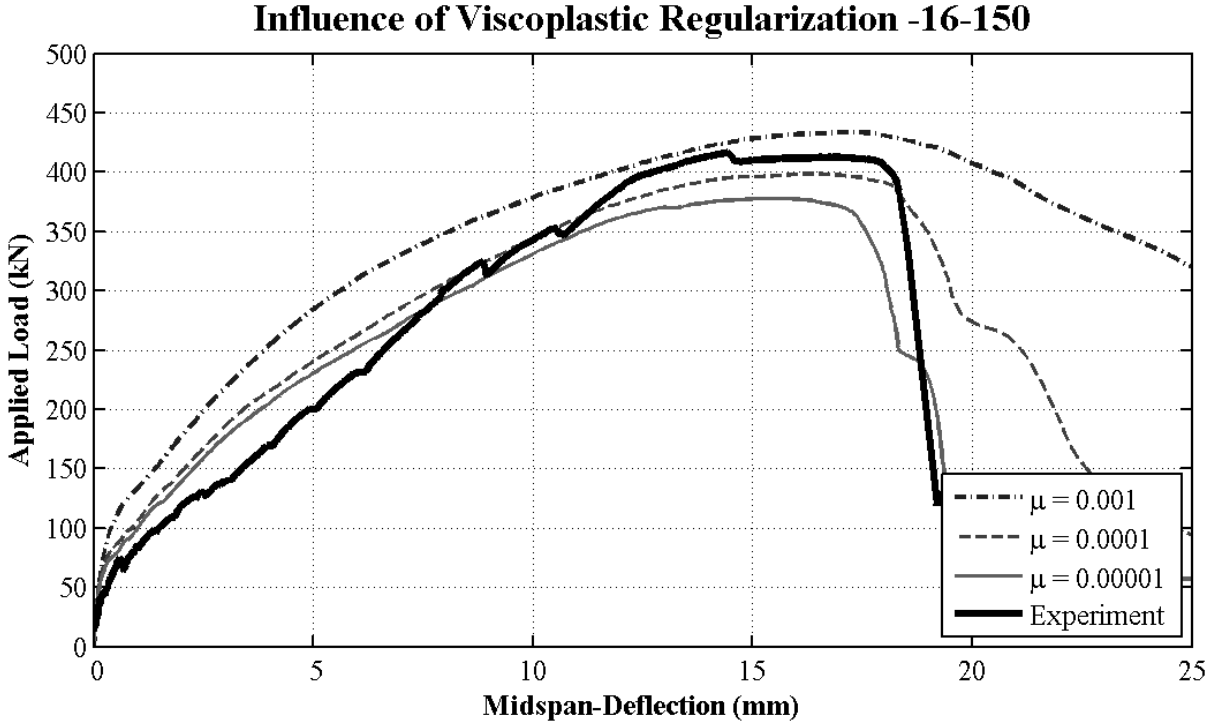
Influence of Viscoplastic Regularization -16-150
Applied Load (kN)
Midspan-Deflection (mm)
μ = 0.001
μ = 0.0001
μ = 0.00001
Experiment

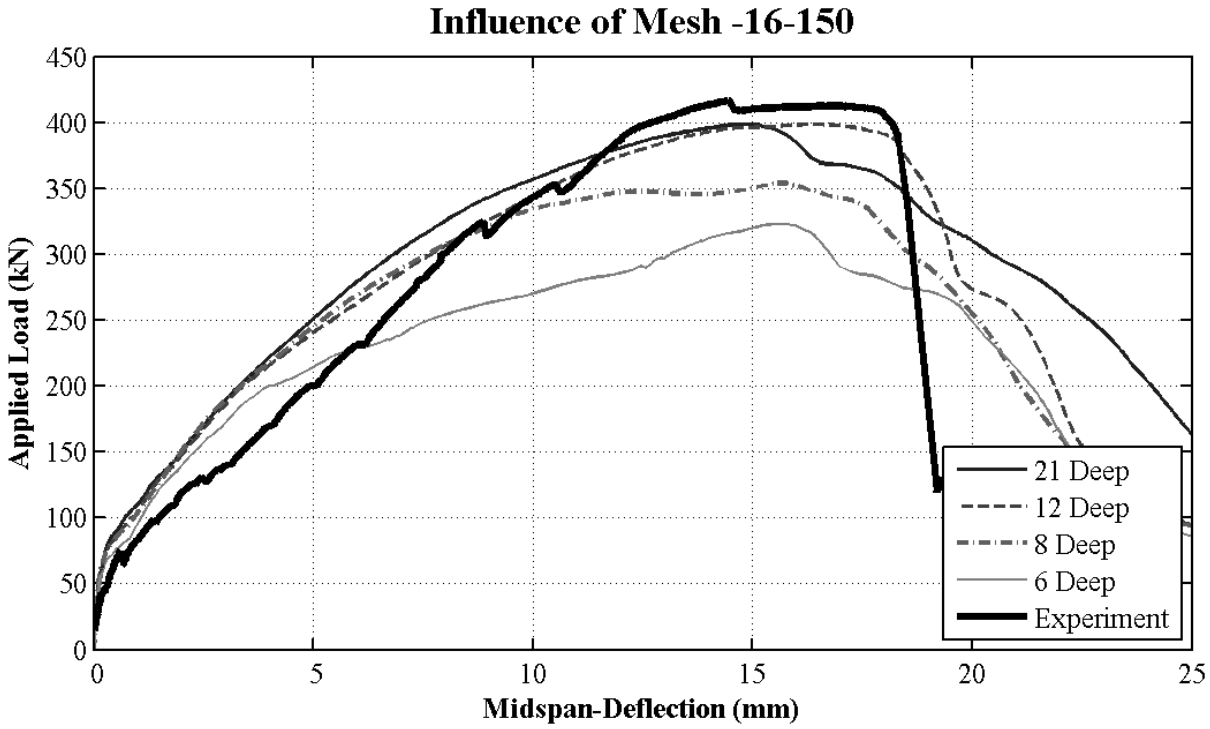
Influence of Mesh -16-150
Applied Load (kN)
Midspan-Deflection (mm)
21 Deep
12 Deep
8 Deep
6 Deep
Experiment

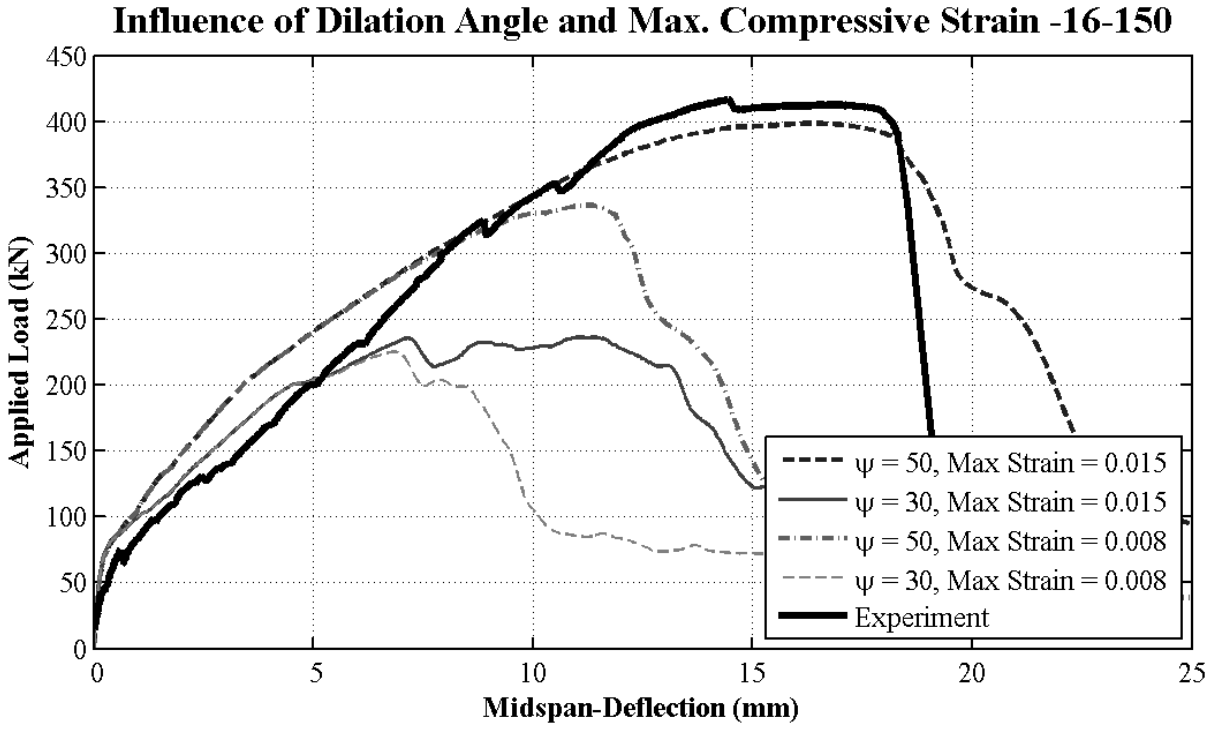
Influence of Dilation Angle and Max. Compressive Strain -16-150
Applied Load (kN)
Midspan-Deflection (mm)
ψ = 50, Max Strain = 0.015
ψ = 30, Max Strain = 0.015
ψ = 50, Max Strain = 0.008
ψ = 30, Max Strain = 0.008
Experiment

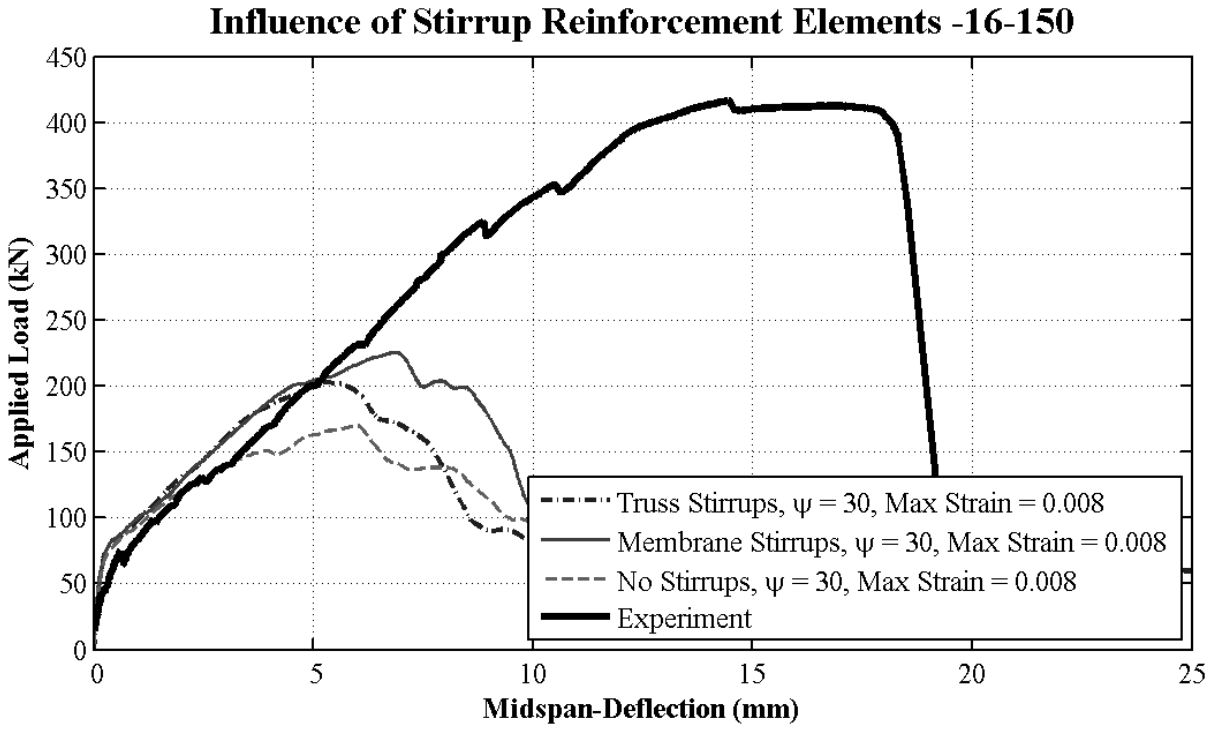
Influence of Stirrup Reinforcement Elements -16-150
Applied Load (kN)
Midspan-Deflection (mm)
Truss Stirrups, ψ = 30, Max Strain = 0.008
Membrane Stirrups, ψ = 30, Max Strain = 0.008
No Stirrups, ψ = 30, Max Strain = 0.008
Experiment

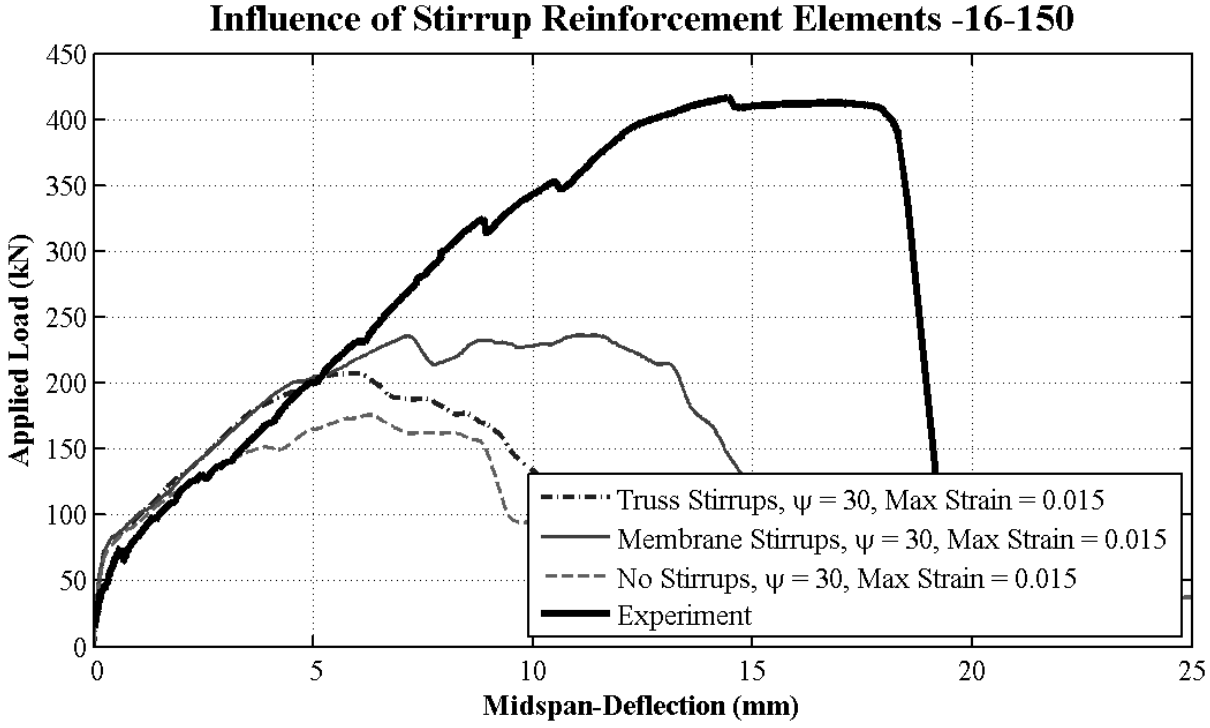
Influence of Stirrup Reinforcement Elements -16-150
Applied Load (kN)
Midspan-Deflection (mm)
Truss Stirrups, ψ = 30, Max Strain = 0.015
Membrane Stirrups, ψ = 30, Max Strain = 0.015
No Stirrups, ψ = 30, Max Strain = 0.015
Experiment

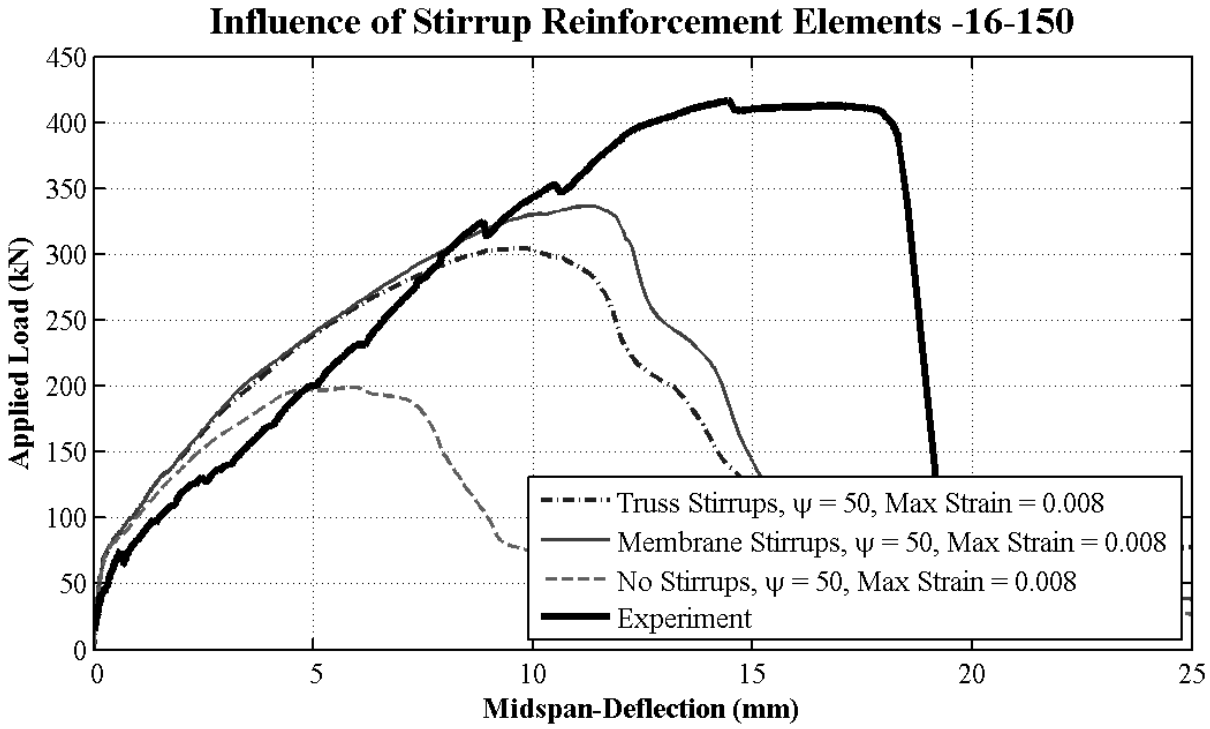
Influence of Stirrup Reinforcement Elements -16-150
Applied Load (kN)
Midspan-Deflection (mm)
Truss Stirrups, ψ = 50, Max Strain = 0.008
Membrane Stirrups, ψ = 50, Max Strain = 0.008
No Stirrups, ψ = 50, Max Strain = 0.008
Experiment

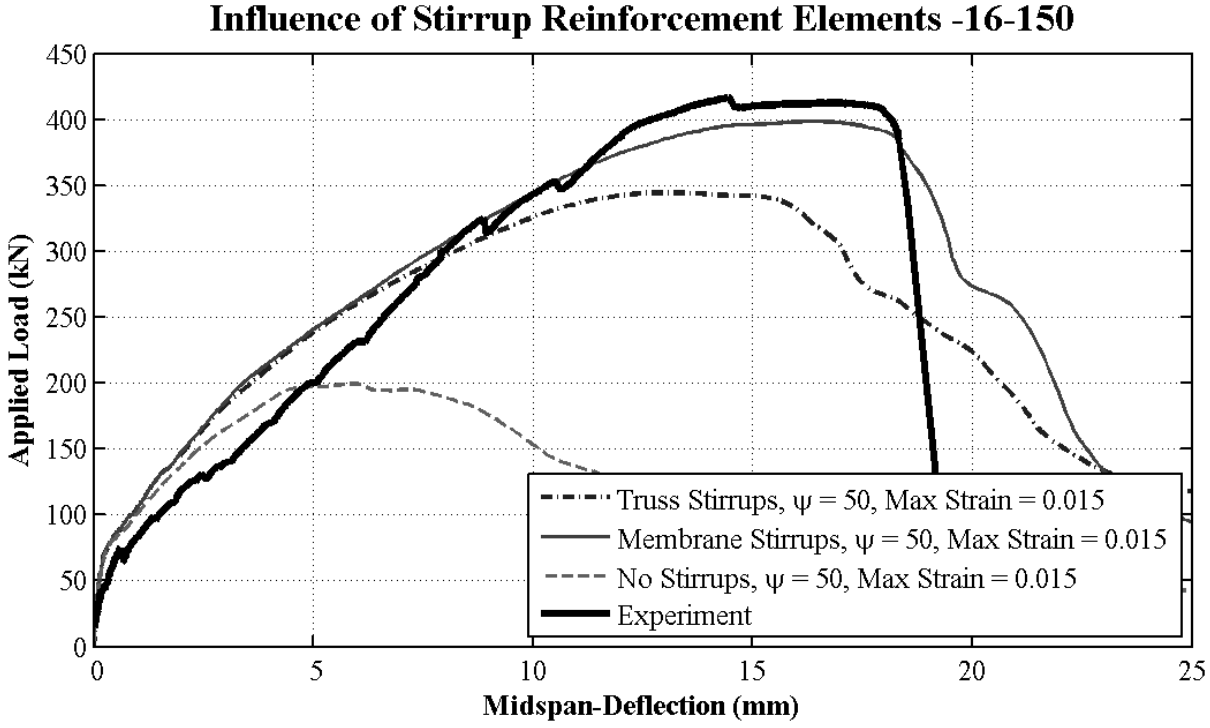
Influence of Stirrup Reinforcement Elements -16-150
Applied Load (kN)
Midspan-Deflection (mm)
Truss Stirrups, ψ = 50, Max Strain = 0.015
Membrane Stirrups, ψ = 50, Max Strain = 0.015
No Stirrups, ψ = 50, Max Strain = 0.015
Experiment

BM 25-150

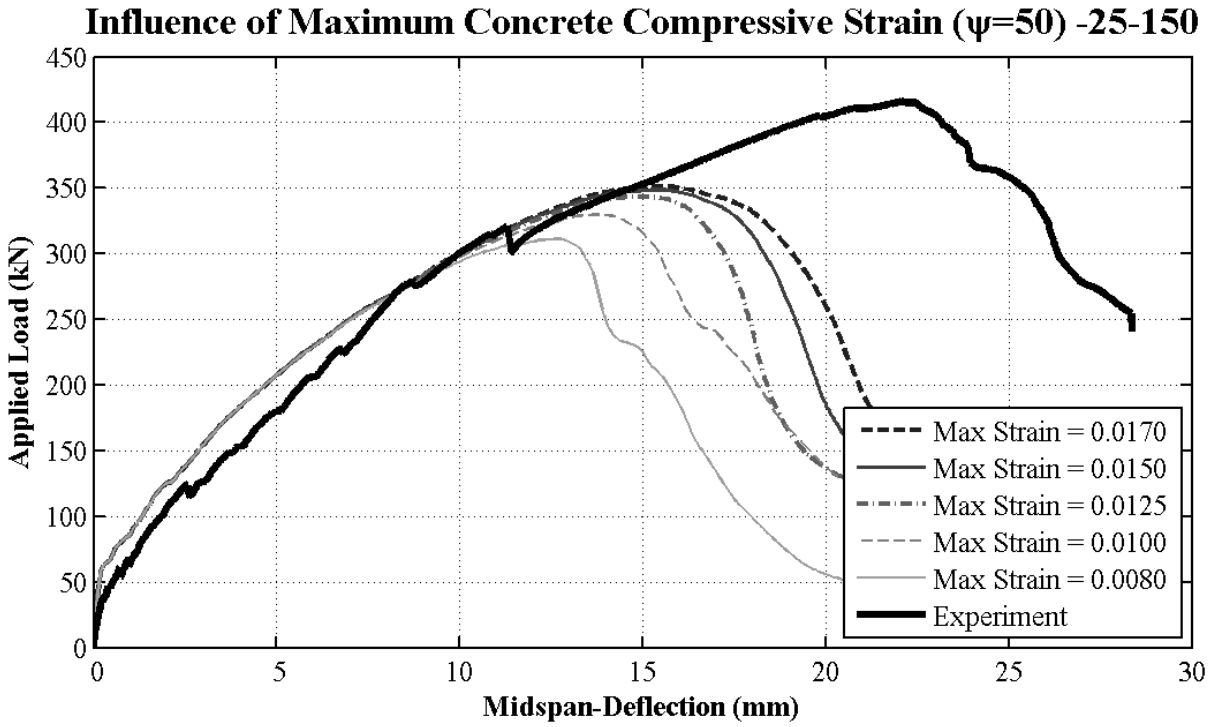
Influence of Maximum Concrete Compressive Strain (ψ=50) -25-150
Applied Load (kN)
Midspan-Deflection (mm)
Max Strain = 0.0170
Max Strain = 0.0150
Max Strain = 0.0125
Max Strain = 0.0100
Max Strain = 0.0080
Experiment

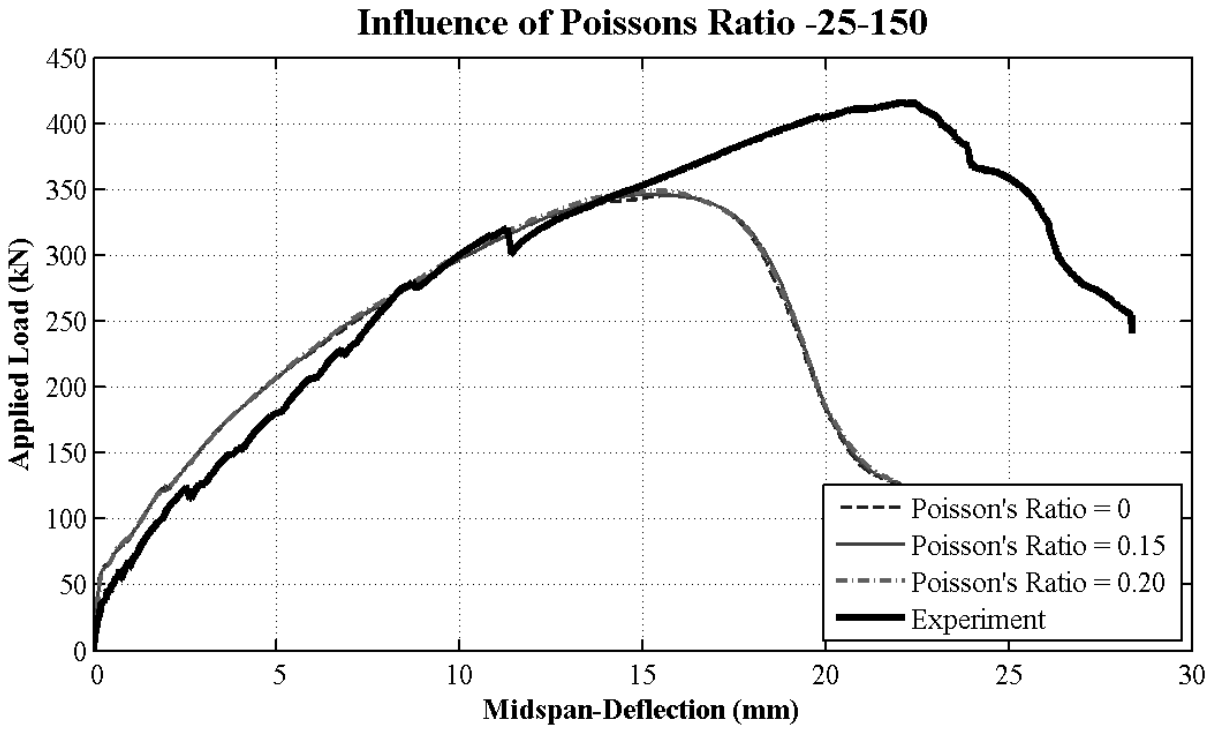
Influence of Poissons Ratio -25-150
Applied Load (kN)
Midspan-Deflection (mm)
Poisson's Ratio = 0
Poisson's Ratio = 0.15
Poisson's Ratio = 0.20
Experiment

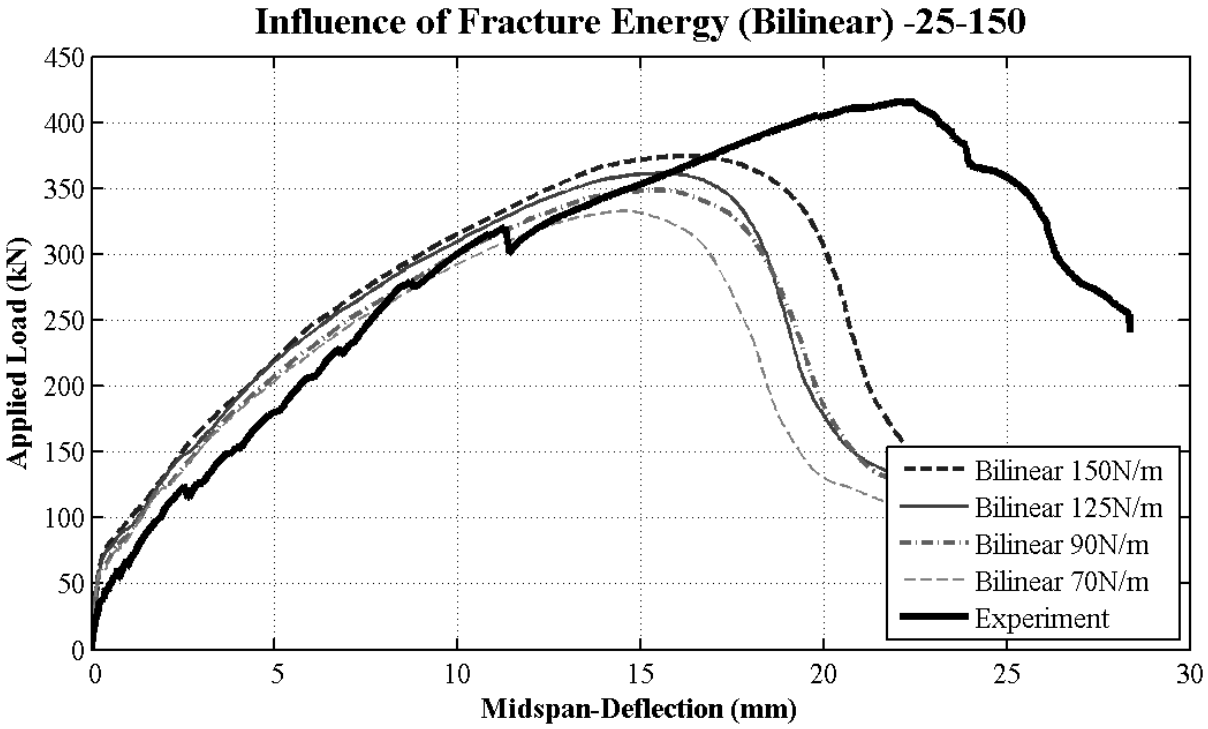
Influence of Fracture Energy (Bilinear) -25-150
Applied Load (kN)
Midspan-Deflection (mm)
Bilinear 150N/m
Bilinear 125N/m
Bilinear 90N/m
Bilinear 70N/m
Experiment

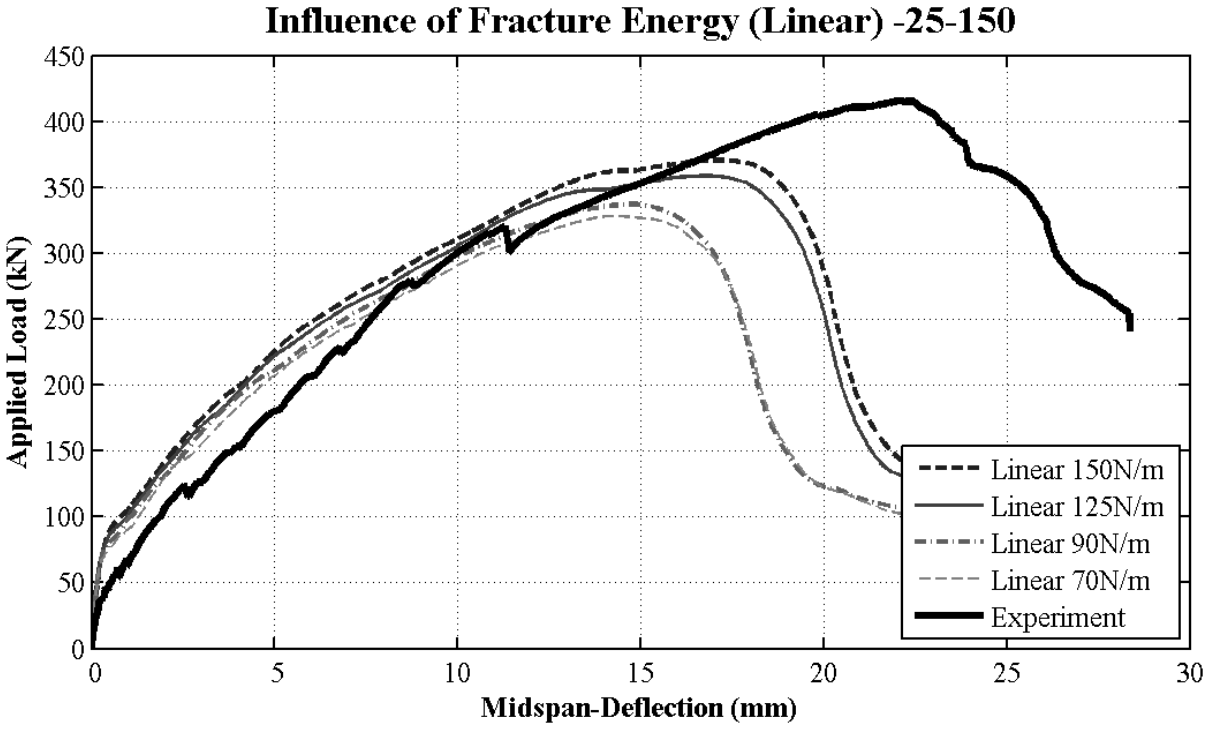
Influence of Fracture Energy (Linear) -25-150
Applied Load (kN)
Midspan-Deflection (mm)
Linear 150N/m
Linear 125N/m
Linear 90N/m
Linear 70N/m
Experiment

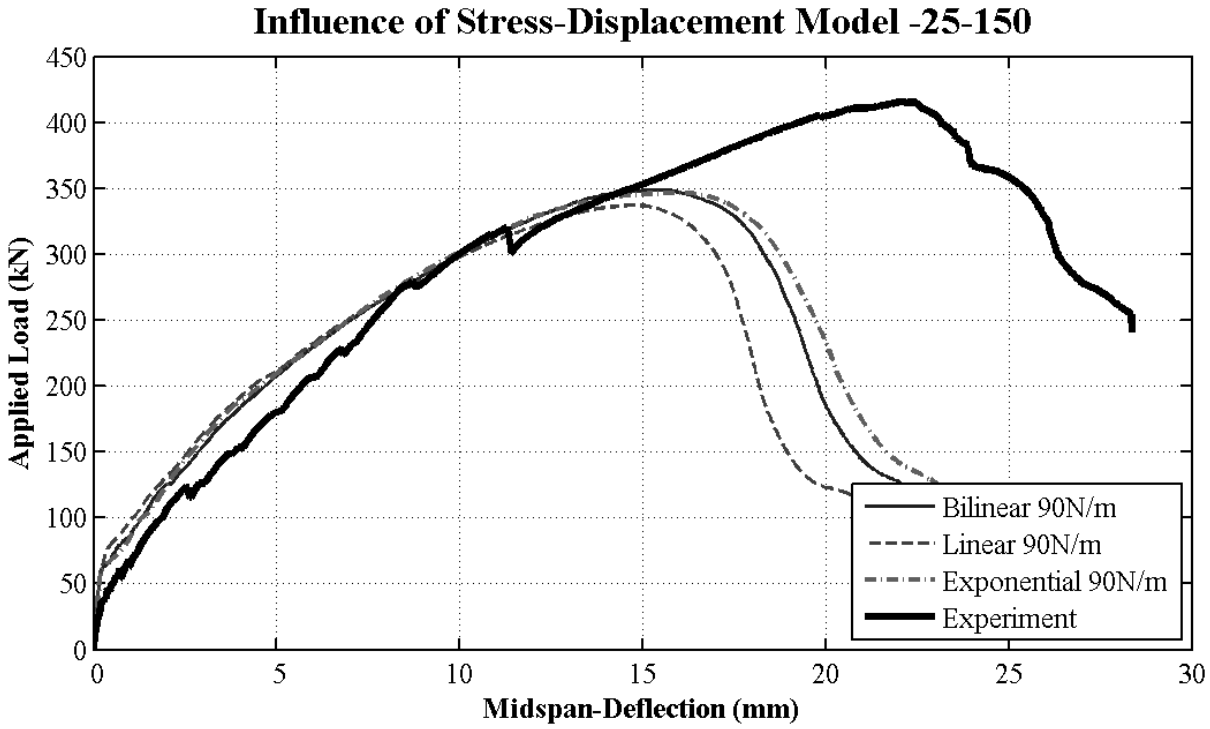
Influence of Stress-Displacement Model -25-150
Applied Load (kN)
Midspan-Deflection (mm)
Bilinear 90N/m
Linear 90N/m
Exponential 90N/m
Experiment

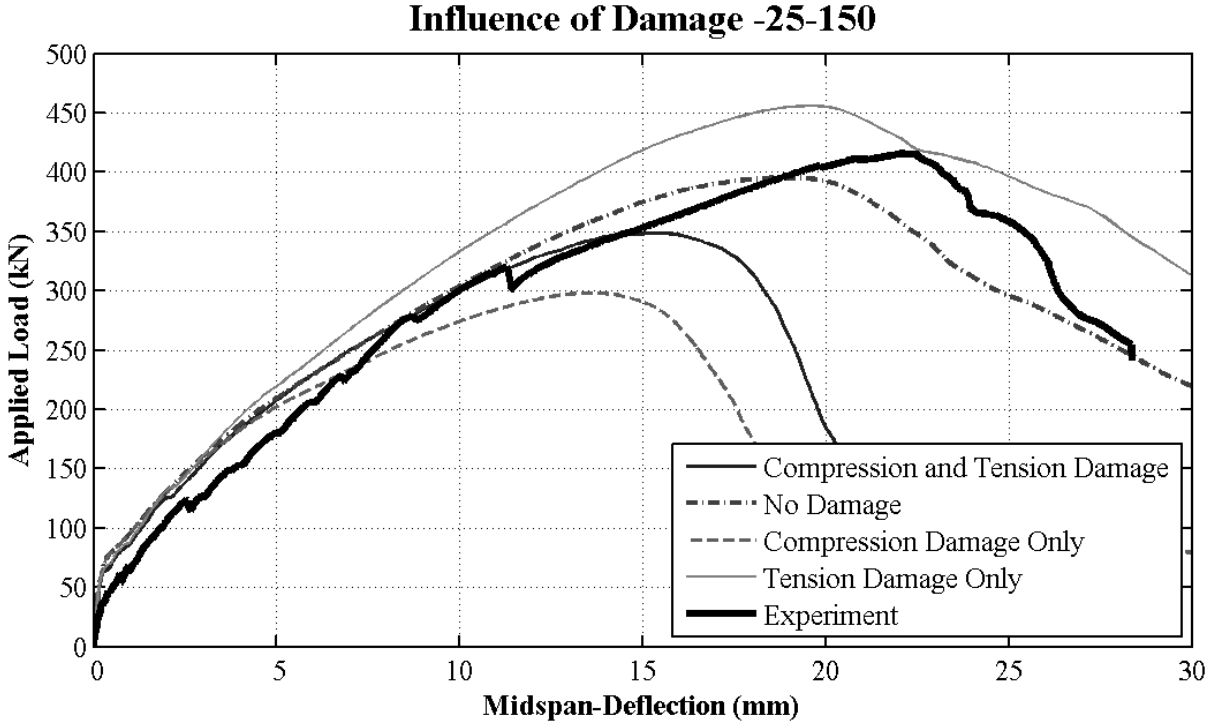
Influence of Damage -25-150
Applied Load (kN)
Midspan-Deflection (mm)
Compression and Tension Damage
No Damage
Compression Damage Only
Tension Damage Only
Experiment

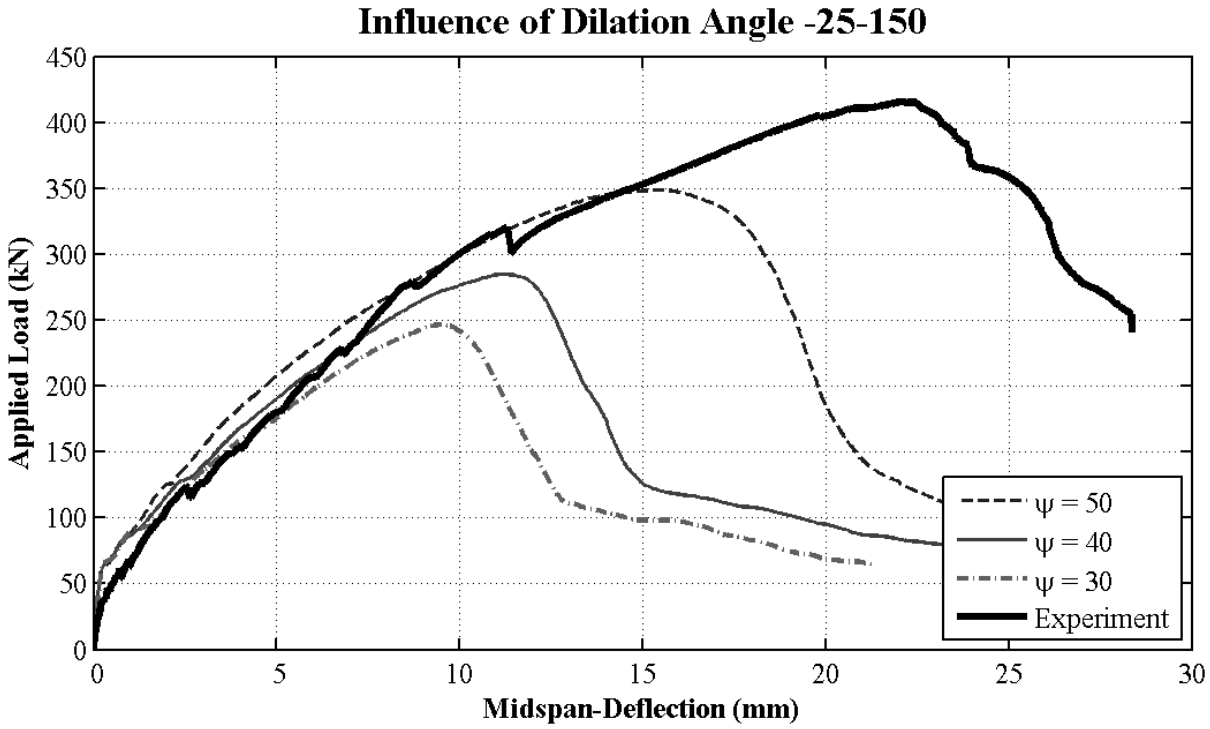
Influence of Dilation Angle -25-150
Applied Load (kN)
Midspan-Deflection (mm)
ψ = 50
ψ = 40
ψ = 30
Experiment

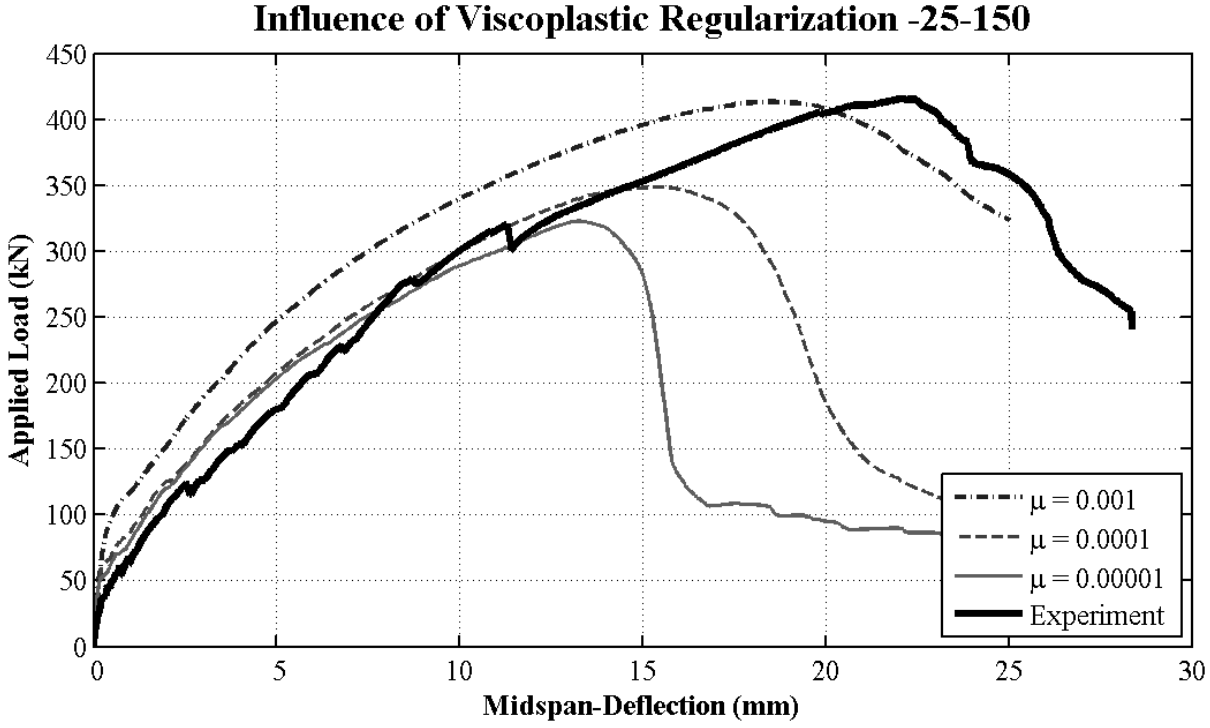
Influence of Viscoplastic Regularization -25-150
Applied Load (kN)
Midspan-Deflection (mm)
μ = 0.001
μ = 0.0001
μ = 0.00001
Experiment

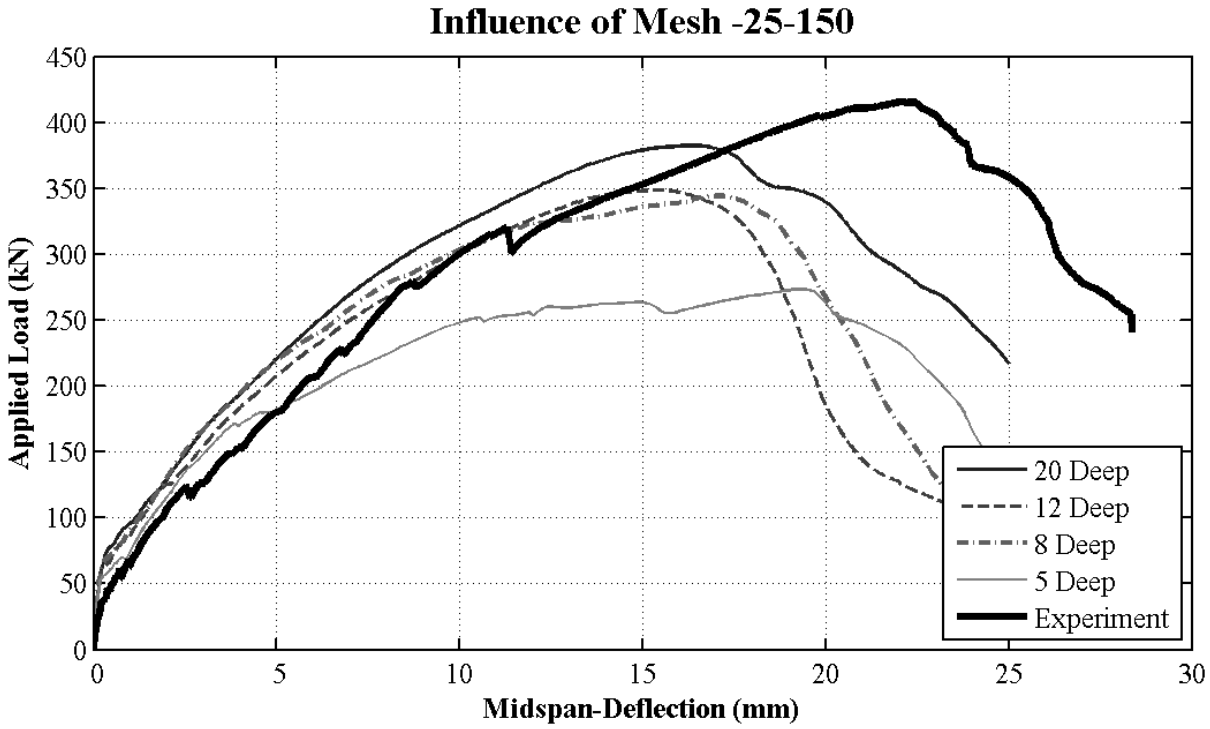
Influence of Mesh -25-150
Applied Load (kN)
Midspan-Deflection (mm)
20 Deep
12 Deep
8 Deep
5 Deep
Experiment

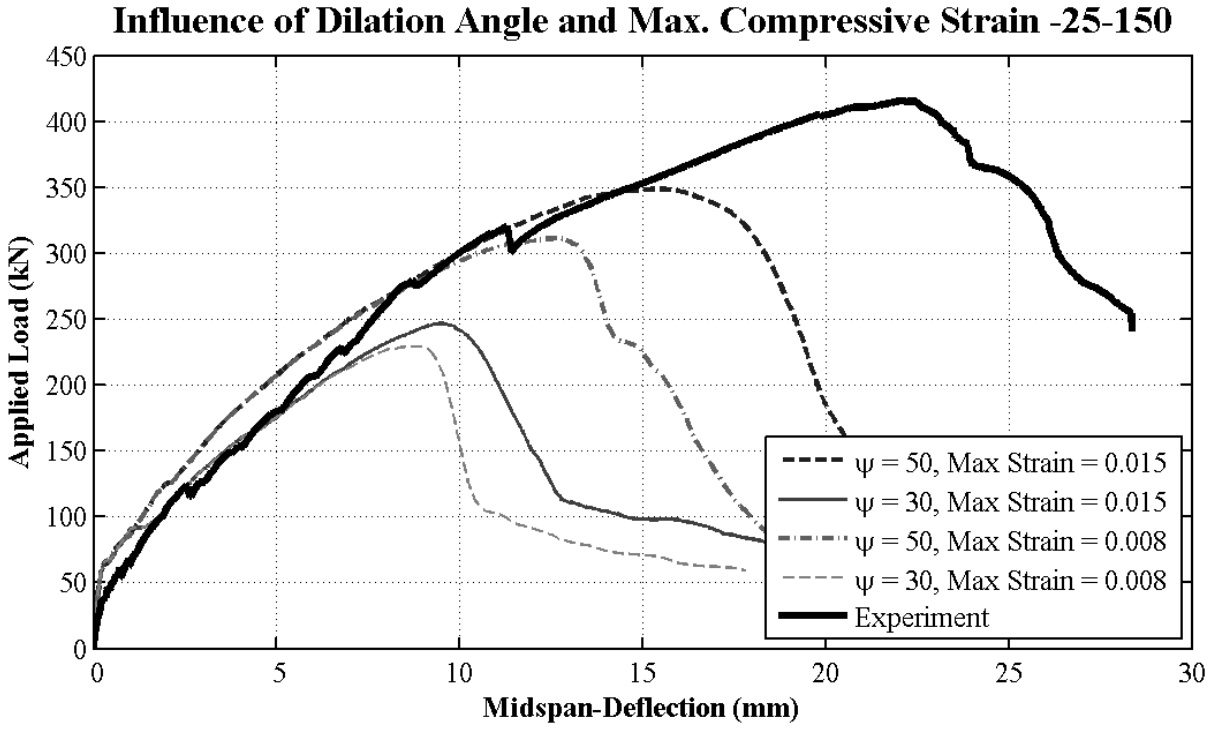
Influence of Dilation Angle and Max. Compressive Strain -25-150
Applied Load (kN)
Midspan-Deflection (mm)
ψ = 50, Max Strain = 0.015
ψ = 30, Max Strain = 0.015
ψ = 50, Max Strain = 0.008
ψ = 30, Max Strain = 0.008
Experiment

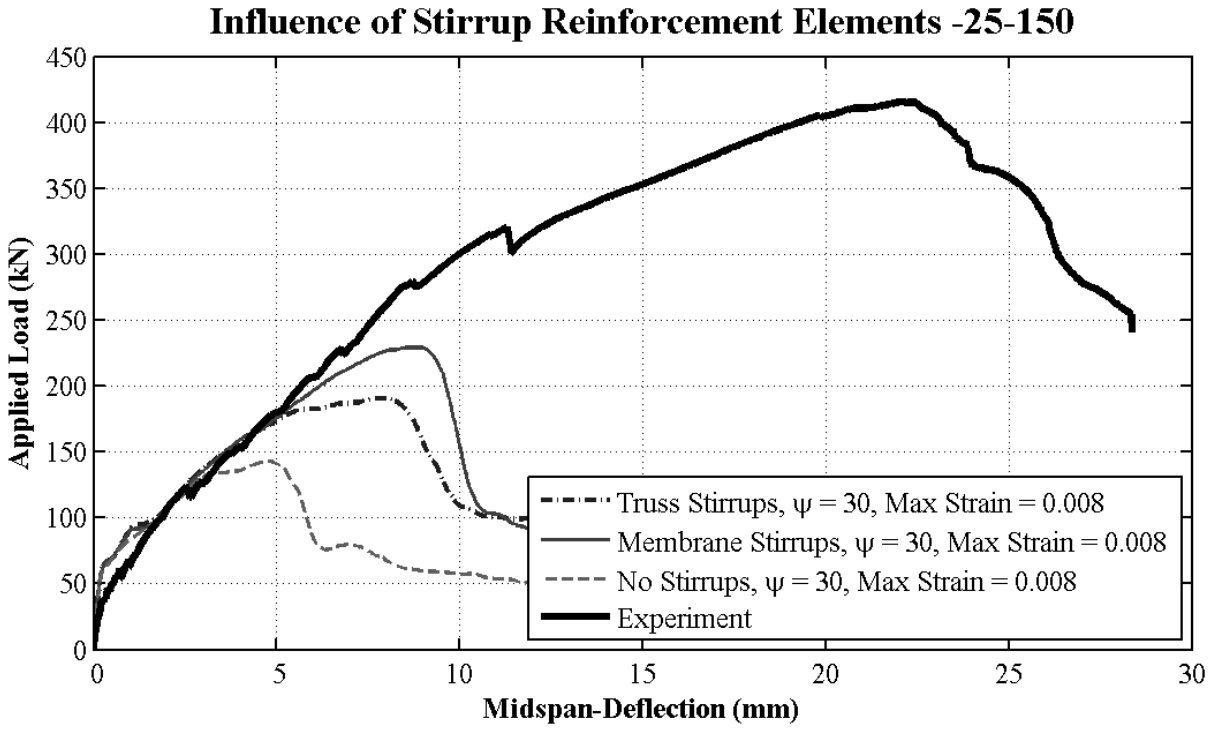
Influence of Stirrup Reinforcement Elements -25-150
Applied Load (kN)
Midspan-Deflection (mm)
Truss Stirrups, ψ = 30, Max Strain = 0.008
Membrane Stirrups, ψ = 30, Max Strain = 0.008
No Stirrups, ψ = 30, Max Strain = 0.008
Experiment

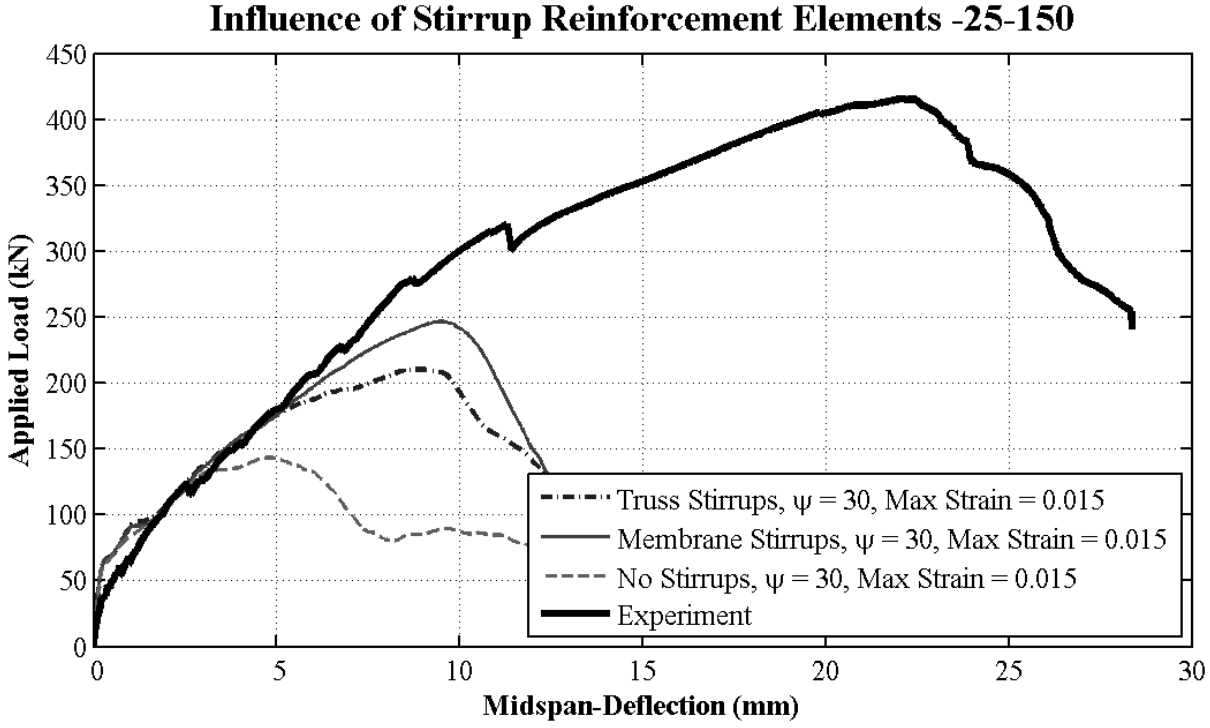
Influence of Stirrup Reinforcement Elements -25-150
Applied Load (kN)
Midspan-Deflection (mm)
Truss Stirrups, ψ = 30, Max Strain = 0.015
Membrane Stirrups, ψ = 30, Max Strain = 0.015
No Stirrups, ψ = 30, Max Strain = 0.015
Experiment

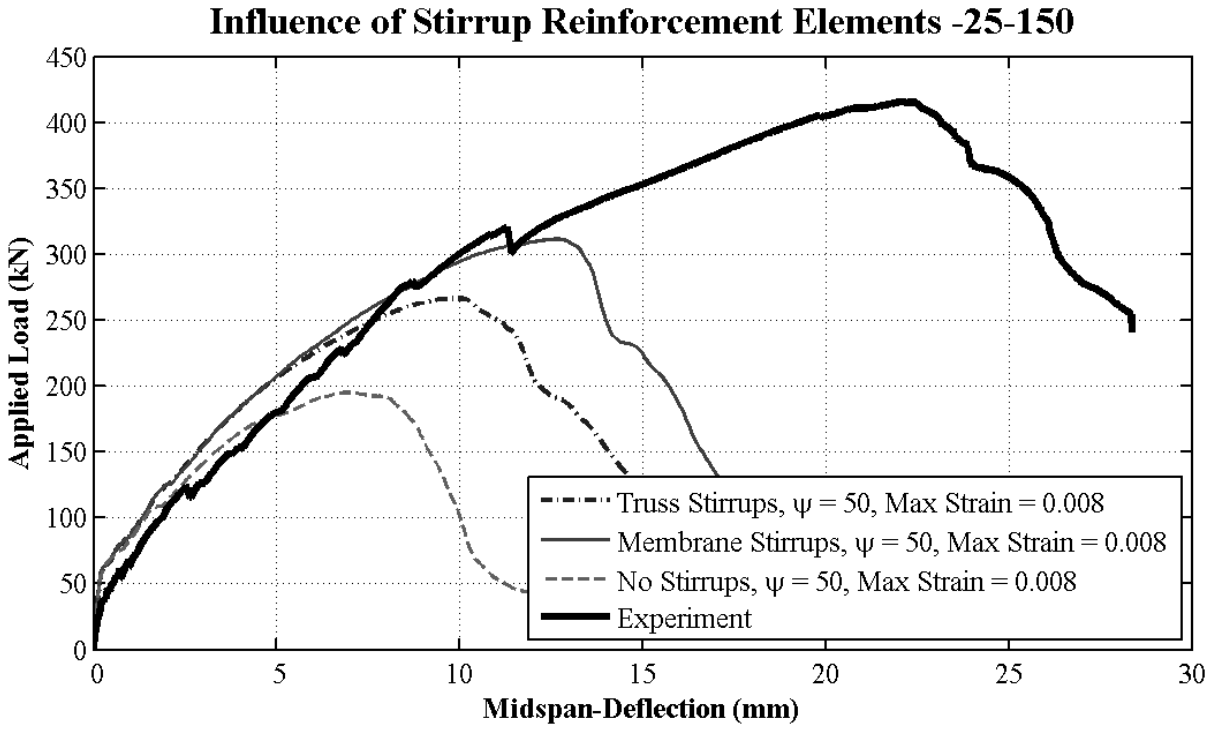
Influence of Stirrup Reinforcement Elements -25-150
Applied Load (kN)
Midspan-Deflection (mm)
Truss Stirrups, ψ = 50, Max Strain = 0.008
Membrane Stirrups, ψ = 50, Max Strain = 0.008
No Stirrups, ψ = 50, Max Strain = 0.008
Experiment

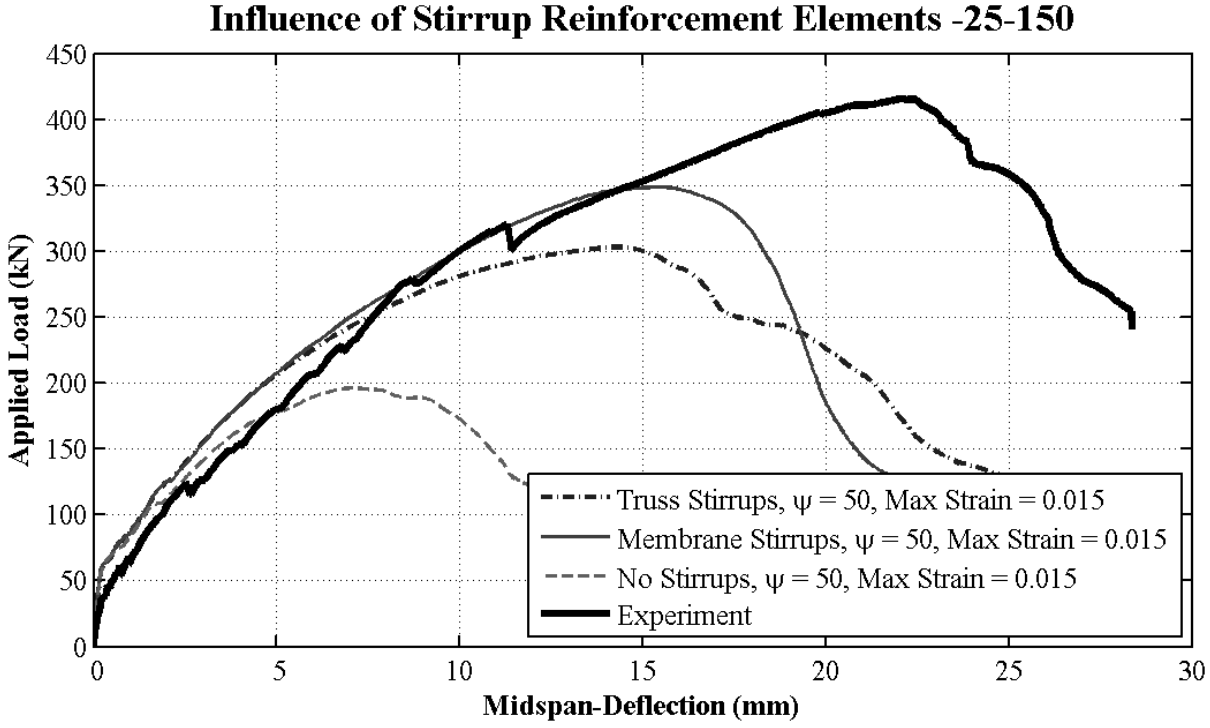
Influence of Stirrup Reinforcement Elements -25-150
Applied Load (kN)
Midspan-Deflection (mm)
Truss Stirrups, ψ = 50, Max Strain = 0.015
Membrane Stirrups, ψ = 50, Max Strain = 0.015
No Stirrups, ψ = 50, Max Strain = 0.015
Experiment

BM 12-220

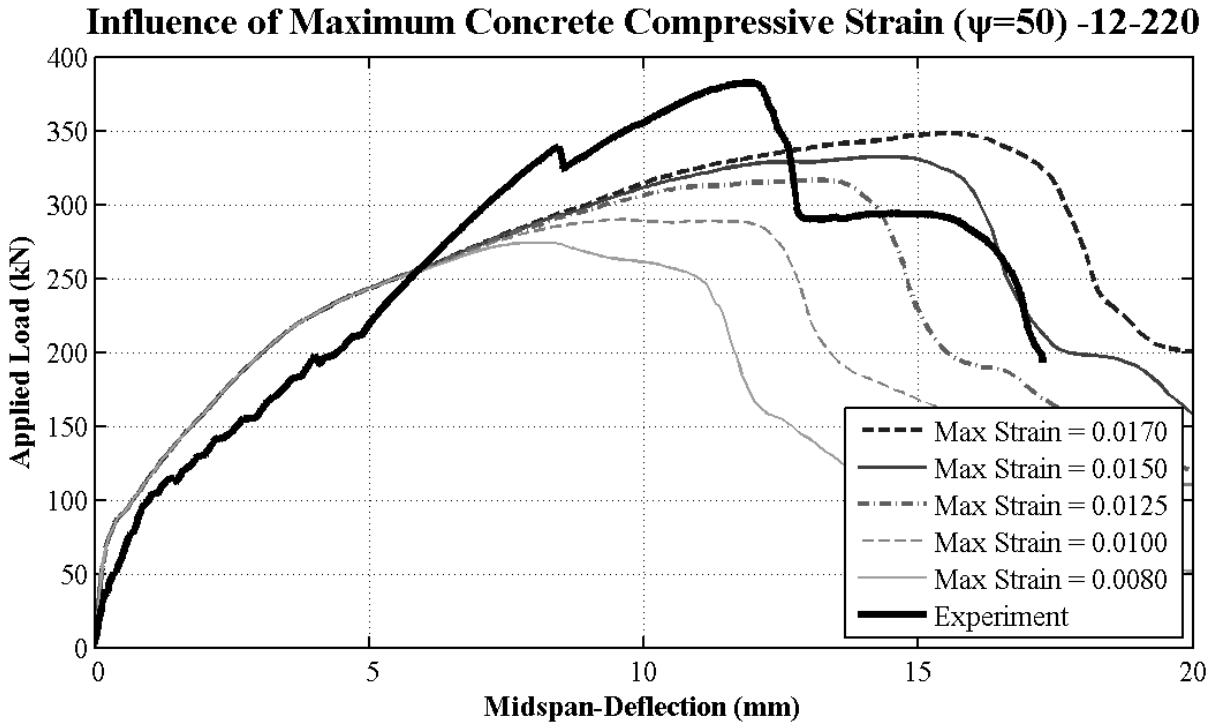
Influence of Maximum Concrete Compressive Strain (ψ=50) -12-220
Applied Load (kN)
Midspan-Deflection (mm)
0
50
100
150
200
250
300
350
400
0
5
10
15
20
Max Strain = 0.0170
Max Strain = 0.0150
Max Strain = 0.0125
Max Strain = 0.0100
Max Strain = 0.0080
Experiment

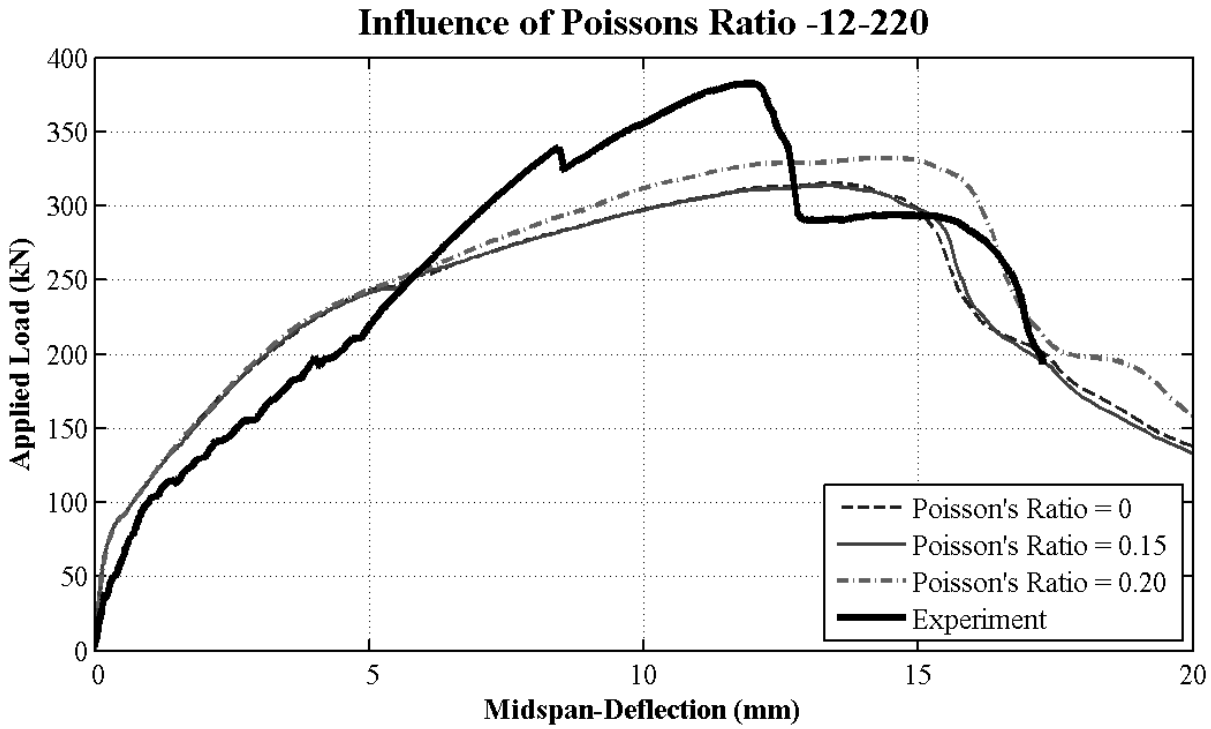
Influence of Poissons Ratio -12-220
Applied Load (kN)
Midspan-Deflection (mm)
0
50
100
150
200
250
300
350
400
0
5
10
15
20
Poisson's Ratio = 0
Poisson's Ratio = 0.15
Poisson's Ratio = 0.20
Experiment

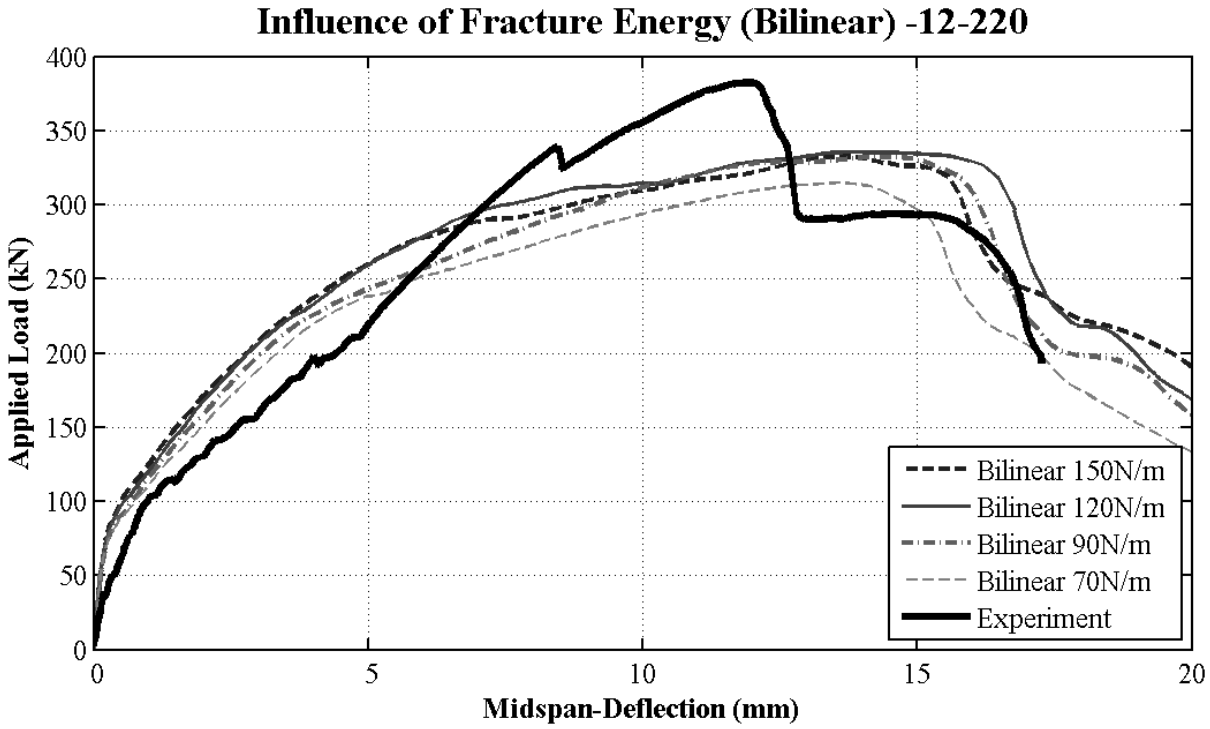
Influence of Fracture Energy (Bilinear) -12-220
Applied Load (kN)
Midspan-Deflection (mm)
Bilinear 150N/m
Bilinear 120N/m
Bilinear 90N/m
Bilinear 70N/m
Experiment
0
50
100
150
200
250
300
350
400
0
5
10
15
20

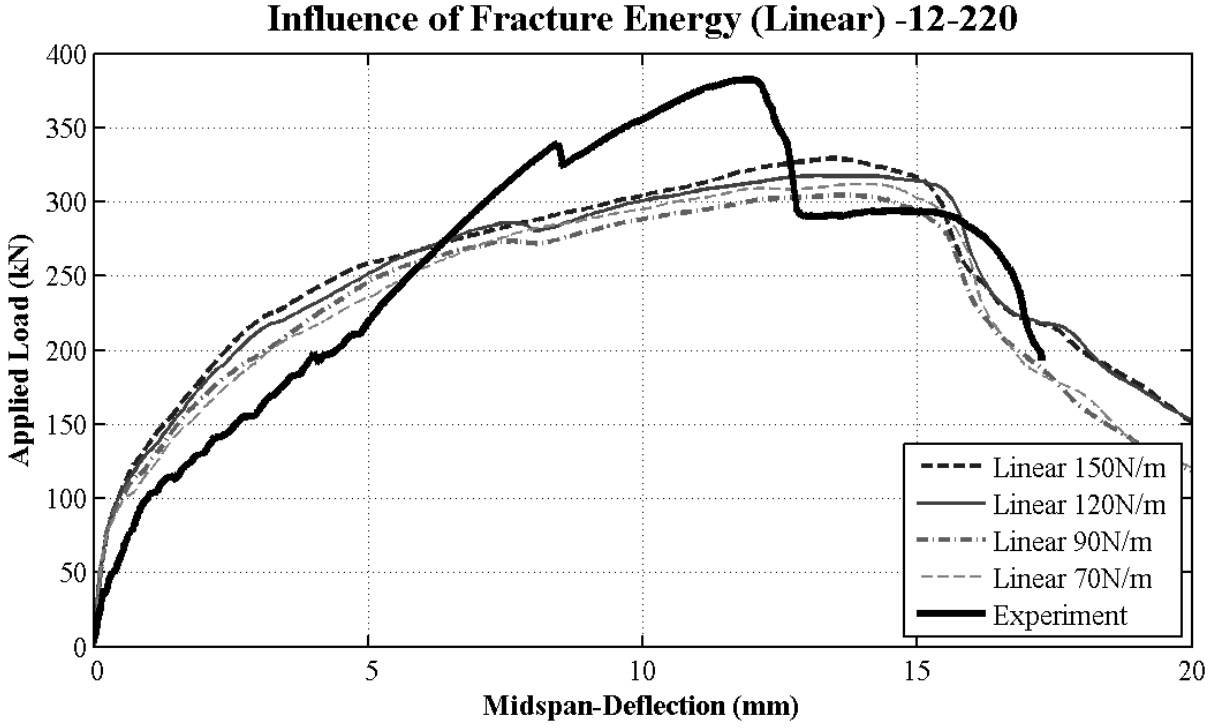
Influence of Fracture Energy (Linear) -12-220
Applied Load (kN)
Midspan-Deflection (mm)
Linear 150N/m
Linear 120N/m
Linear 90N/m
Linear 70N/m
Experiment
0
50
100
150
200
250
300
350
400
0
5
10
15
20

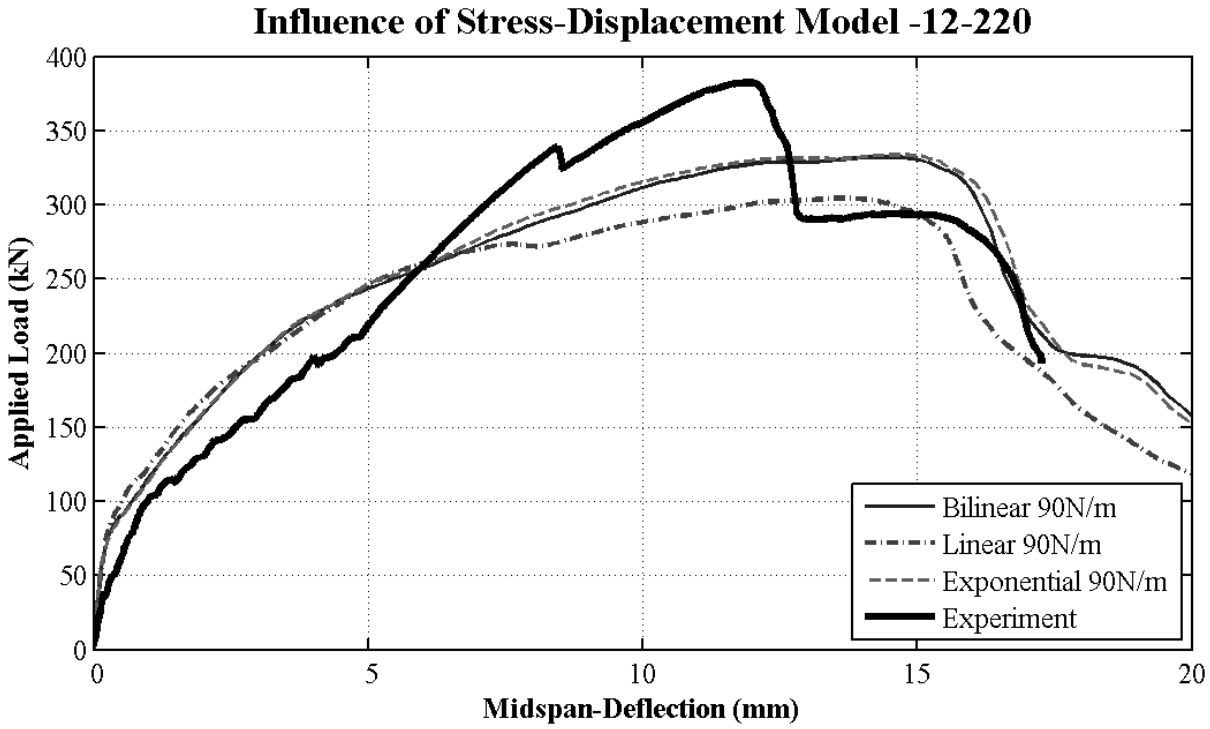
Influence of Stress-Displacement Model -12-220
Applied Load (kN)
Midspan-Deflection (mm)
Bilinear 90N/m
Linear 90N/m
Exponential 90N/m
Experiment

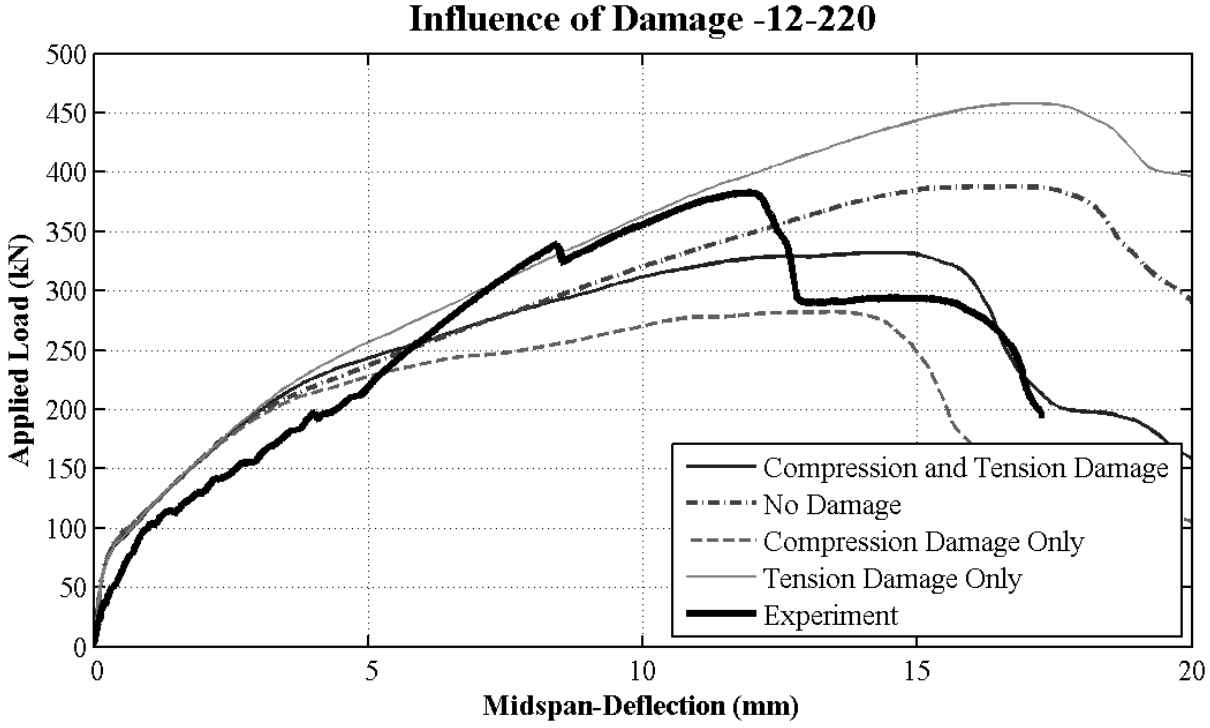
Influence of Damage -12-220
Applied Load (kN)
Midspan-Deflection (mm)
Compression and Tension Damage
No Damage
Compression Damage Only
Tension Damage Only
Experiment

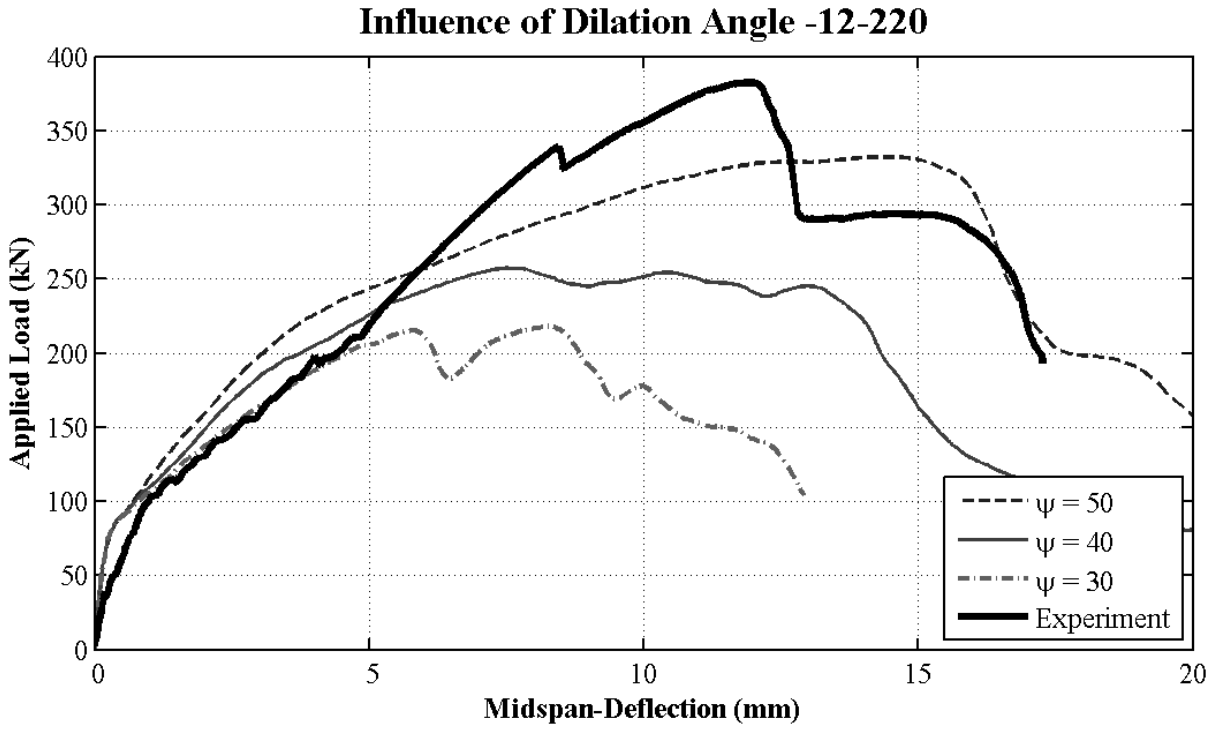
Influence of Dilation Angle -12-220
Applied Load (kN)
Midspan-Deflection (mm)
ψ = 50
ψ = 40
ψ = 30
Experiment

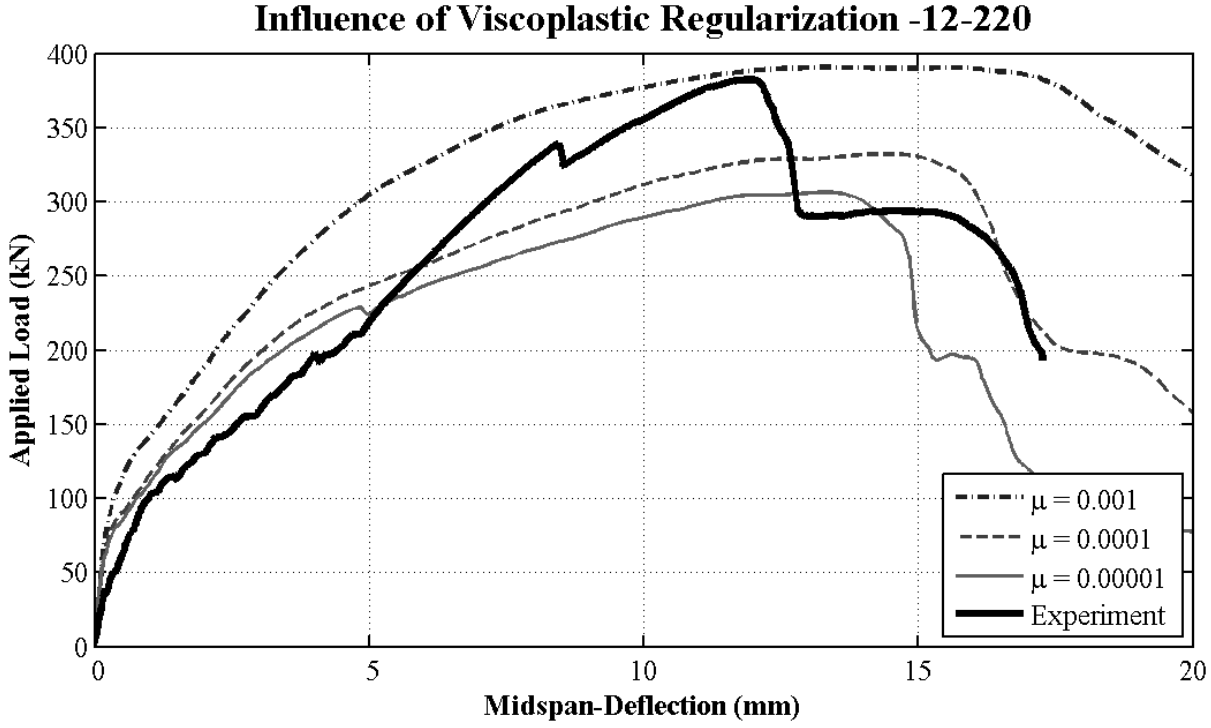
Influence of Viscoplastic Regularization -12-220
Applied Load (kN)
Midspan-Deflection (mm)
μ = 0.001
μ = 0.0001
μ = 0.00001
Experiment

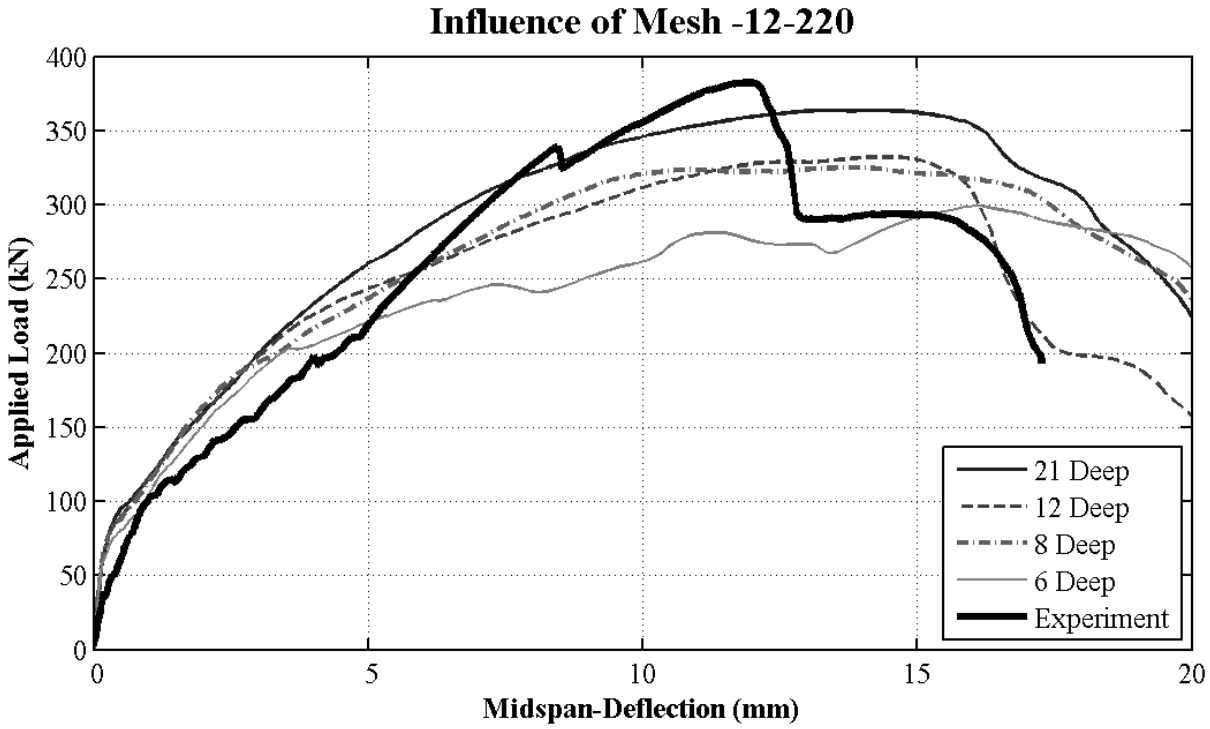
Influence of Mesh -12-220
Applied Load (kN)
Midspan-Deflection (mm)
21 Deep
12 Deep
8 Deep
6 Deep
Experiment

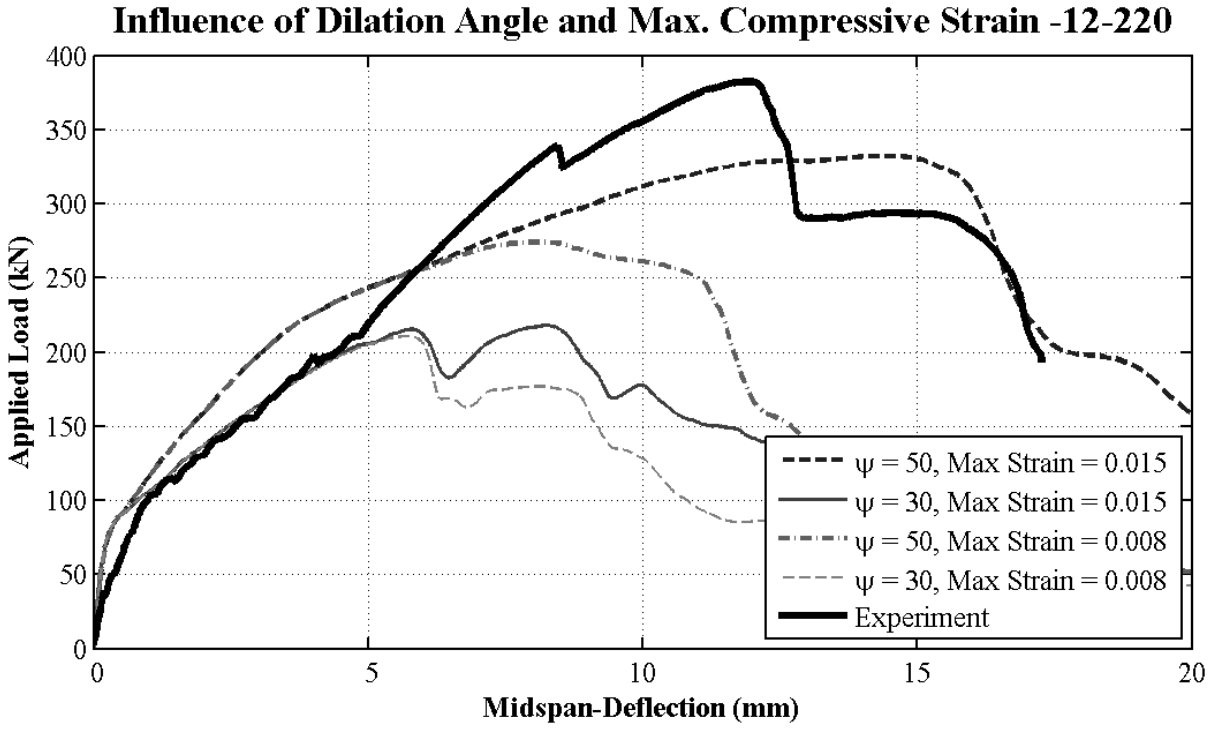
Influence of Dilation Angle and Max. Compressive Strain -12-220
Applied Load (kN)
Midspan-Deflection (mm)
ψ = 50, Max Strain = 0.015
ψ = 30, Max Strain = 0.015
ψ = 50, Max Strain = 0.008
ψ = 30, Max Strain = 0.008
Experiment

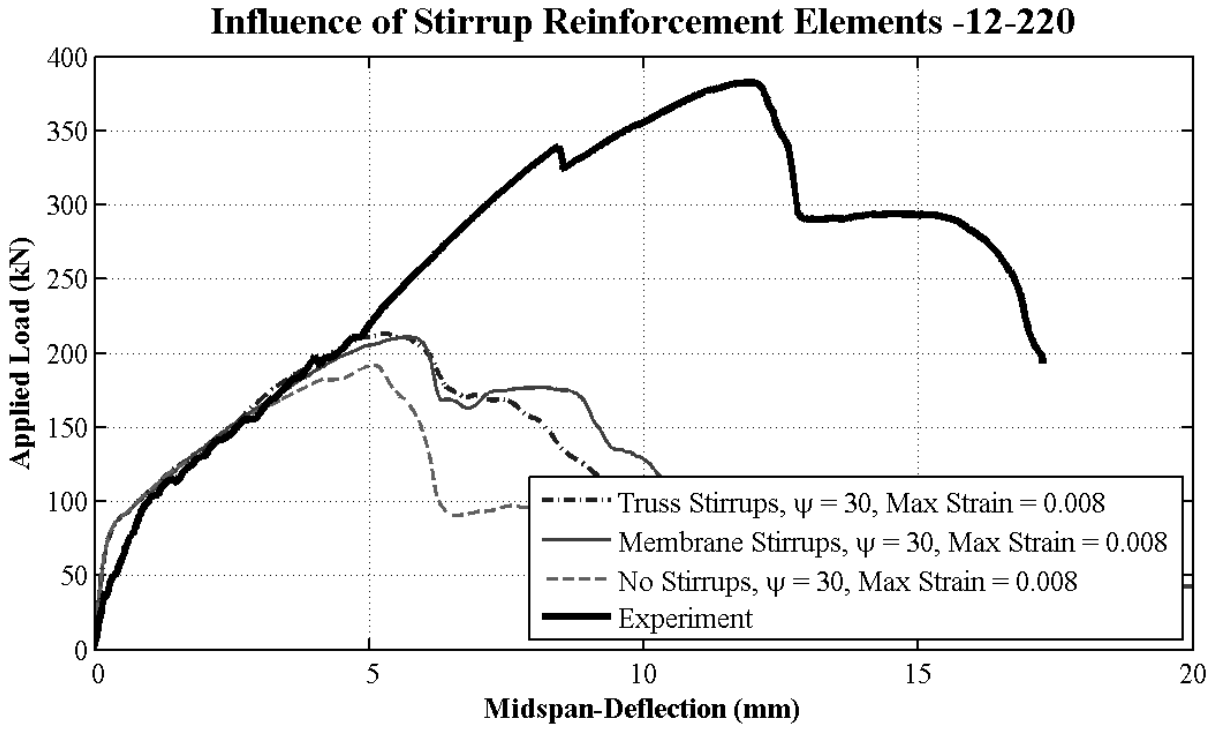
Influence of Stirrup Reinforcement Elements -12-220
Applied Load (kN)
Midspan-Deflection (mm)
Truss Stirrups, ψ = 30, Max Strain = 0.008
Membrane Stirrups, ψ = 30, Max Strain = 0.008
No Stirrups, ψ = 30, Max Strain = 0.008
Experiment

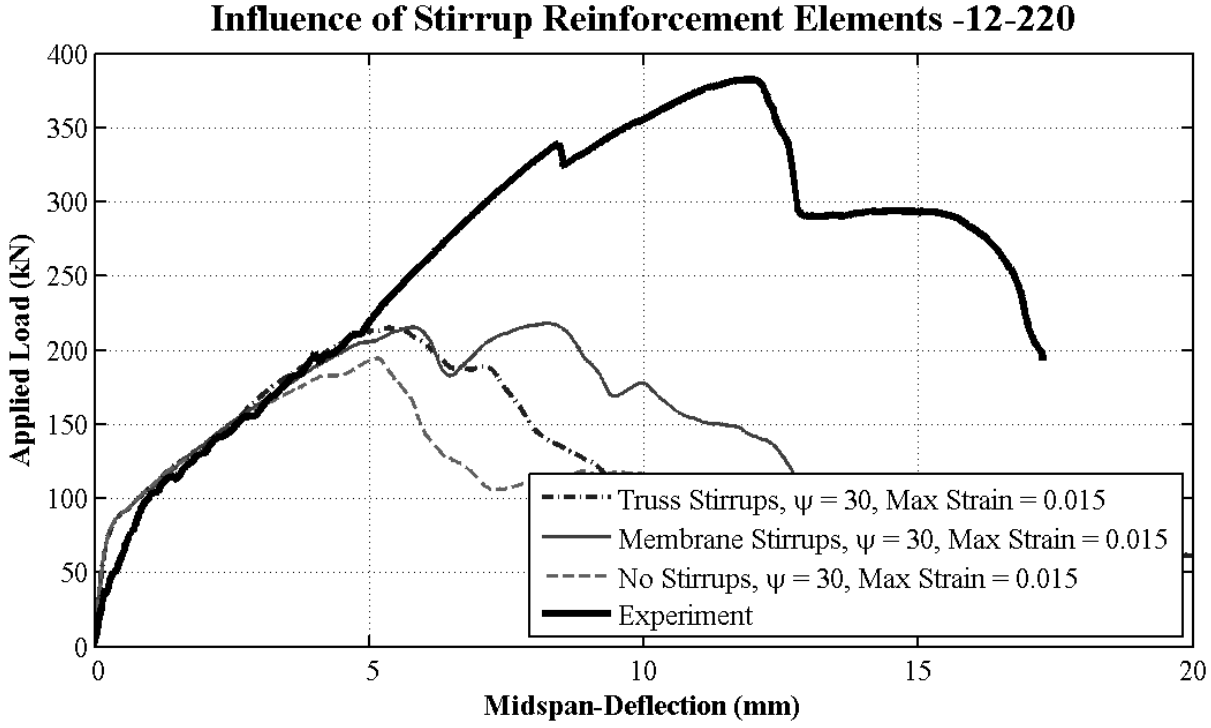
Influence of Stirrup Reinforcement Elements -12-220
Applied Load (kN)
Midspan-Deflection (mm)
Truss Stirrups, ψ = 30, Max Strain = 0.015
Membrane Stirrups, ψ = 30, Max Strain = 0.015
No Stirrups, ψ = 30, Max Strain = 0.015
Experiment

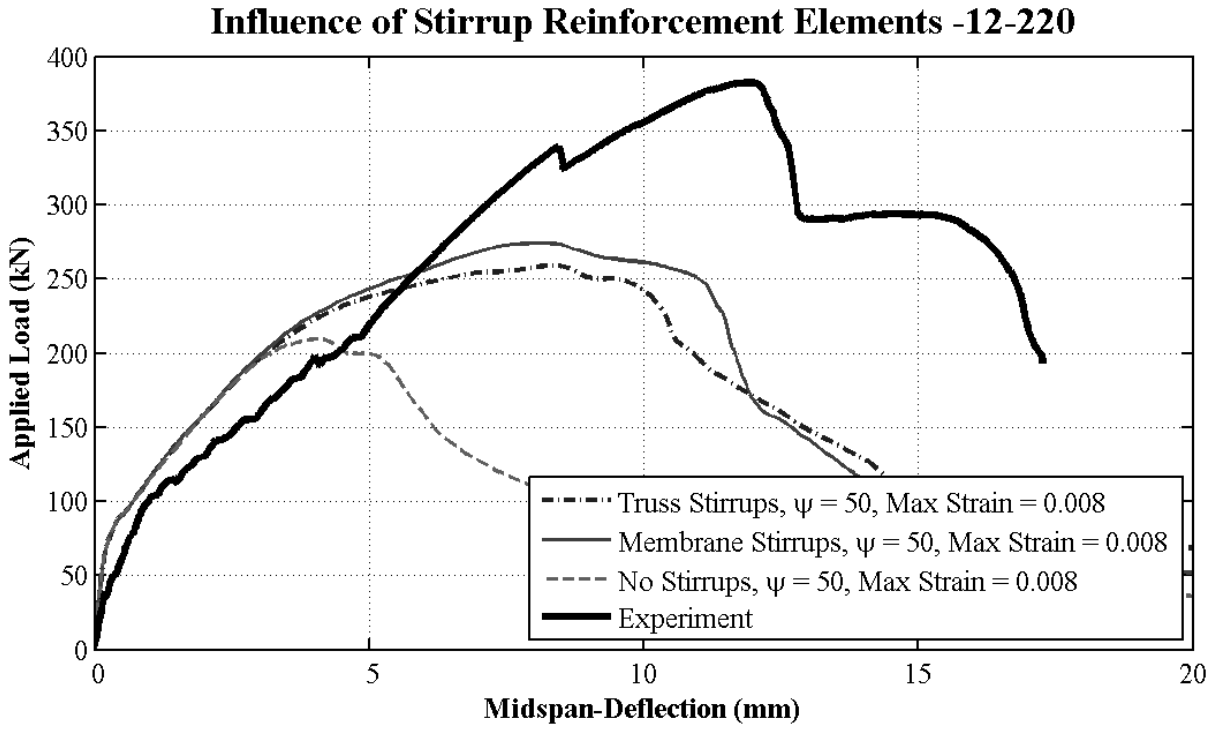
Influence of Stirrup Reinforcement Elements -12-220
Applied Load (kN)
Midspan-Deflection (mm)
Truss Stirrups, ψ = 50, Max Strain = 0.008
Membrane Stirrups, ψ = 50, Max Strain = 0.008
No Stirrups, ψ = 50, Max Strain = 0.008
Experiment

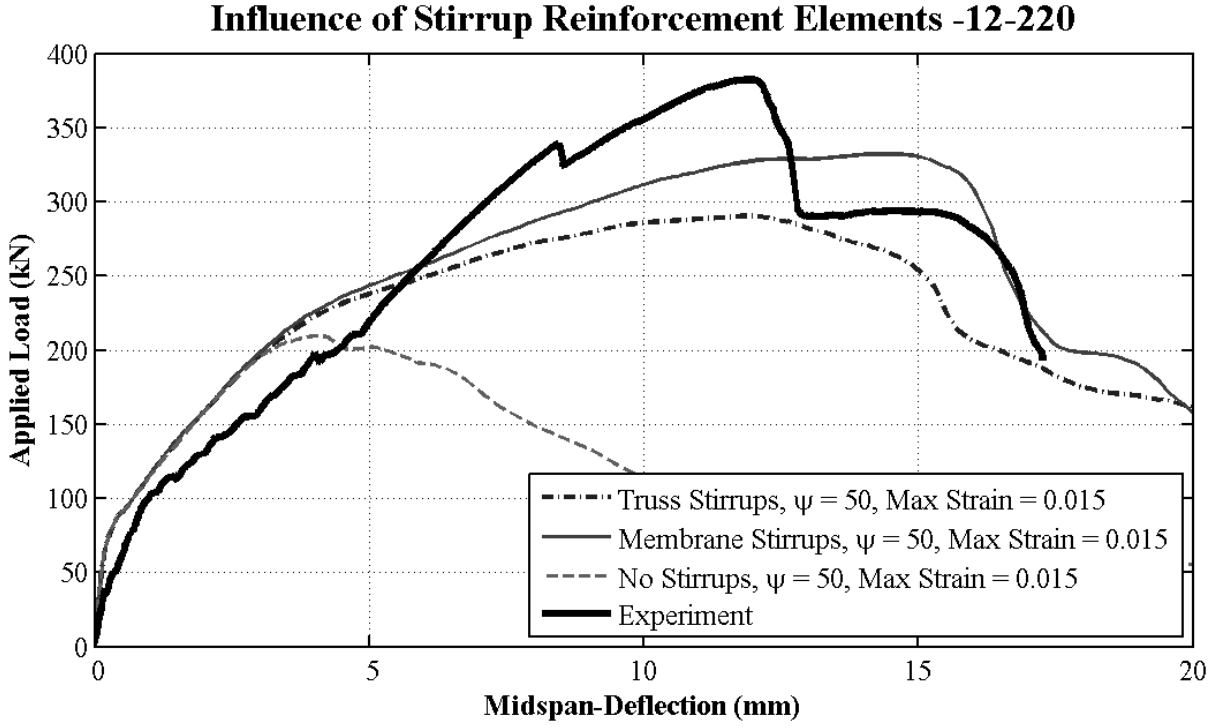
Influence of Stirrup Reinforcement Elements -12-220
Applied Load (kN)
Midspan-Deflection (mm)
Truss Stirrups, ψ = 50, Max Strain = 0.015
Membrane Stirrups, ψ = 50, Max Strain = 0.015
No Stirrups, ψ = 50, Max Strain = 0.015
Experiment

BM 16-220

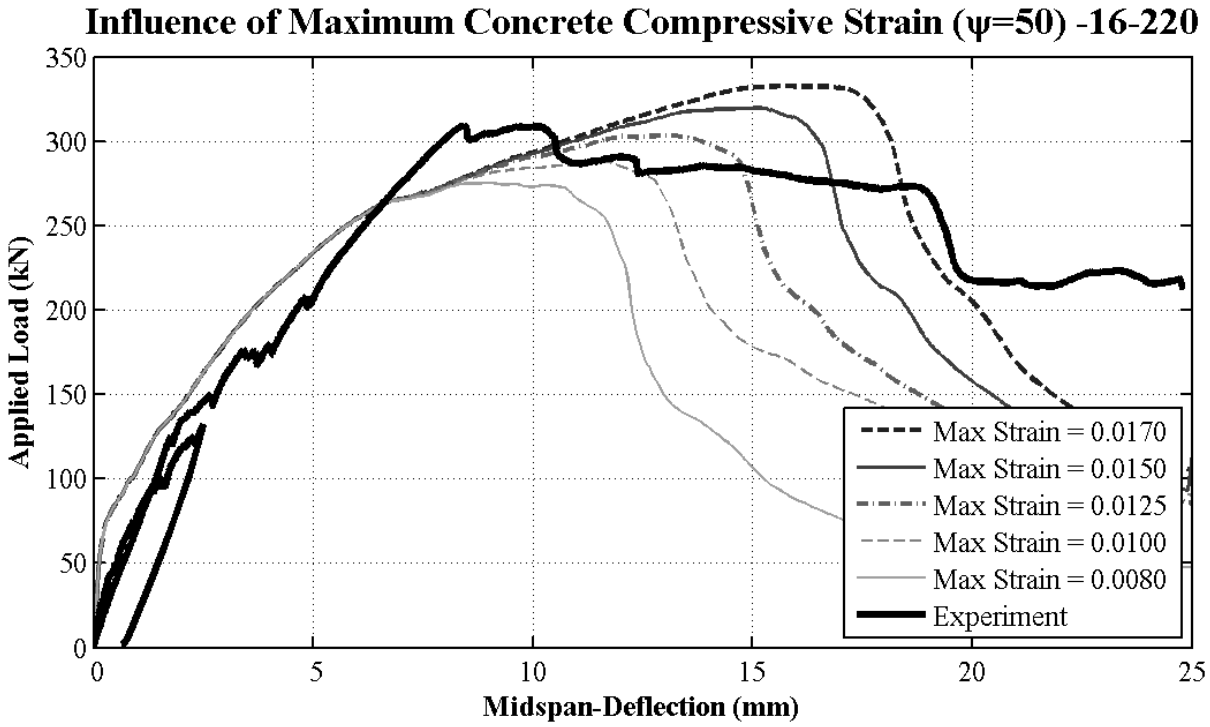
Influence of Maximum Concrete Compressive Strain (ψ=50) -16-220
Applied Load (kN)
Midspan-Deflection (mm)
0
50
100
150
200
250
300
350
0
5
10
15
20
25
Max Strain = 0.0170
Max Strain = 0.0150
Max Strain = 0.0125
Max Strain = 0.0100
Max Strain = 0.0080
Experiment

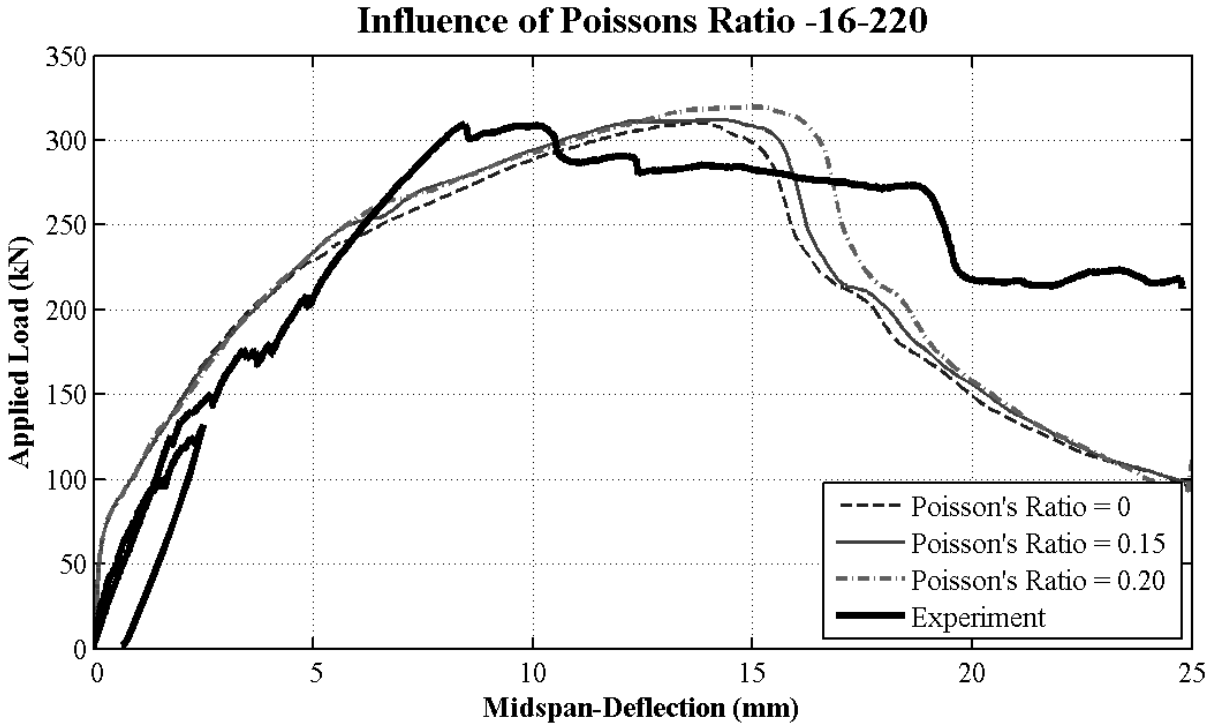
Influence of Poissons Ratio -16-220
Applied Load (kN)
Midspan-Deflection (mm)
0
50
100
150
200
250
300
350
0
5
10
15
20
25
Poisson's Ratio = 0
Poisson's Ratio = 0.15
Poisson's Ratio = 0.20
Experiment

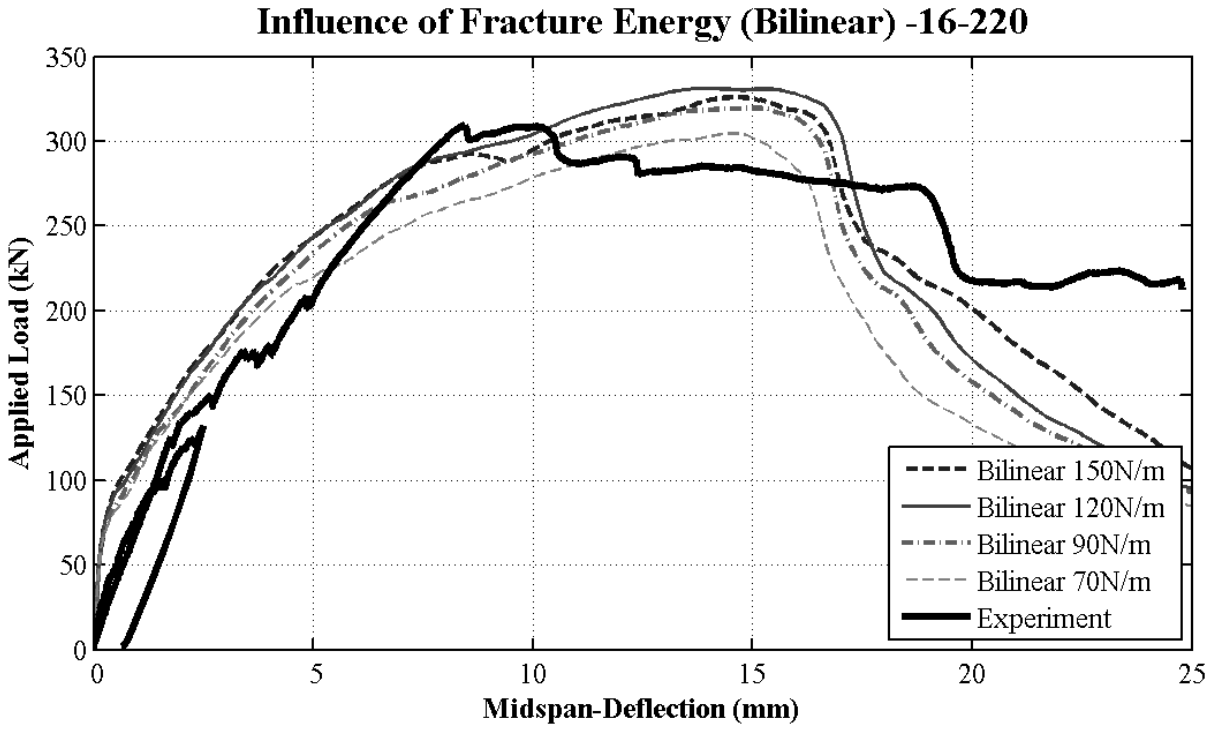
Influence of Fracture Energy (Bilinear) -16-220
Applied Load (kN)
Midspan-Deflection (mm)
0
50
100
150
200
250
300
350
0
5
10
15
20
25
Bilinear 150N/m
Bilinear 120N/m
Bilinear 90N/m
Bilinear 70N/m
Experiment

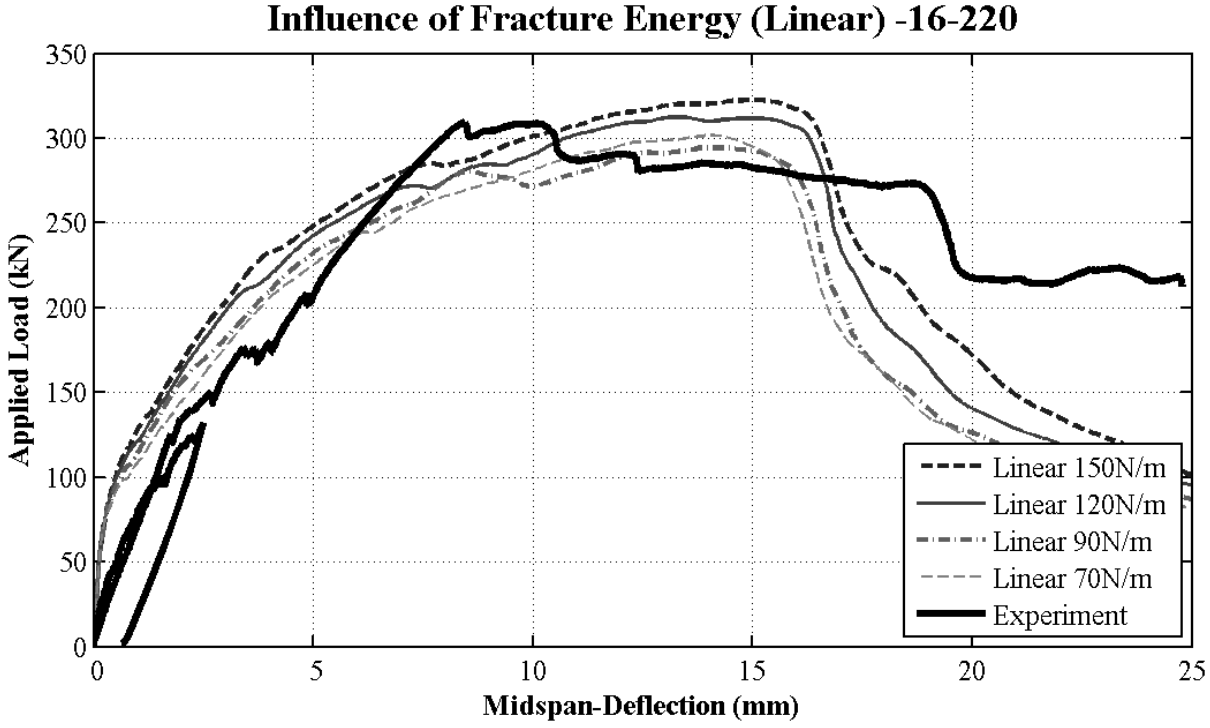
Influence of Fracture Energy (Linear) -16-220
Applied Load (kN)
Midspan-Deflection (mm)
0
50
100
150
200
250
300
350
0
5
10
15
20
25
Linear 150N/m
Linear 120N/m
Linear 90N/m
Linear 70N/m
Experiment

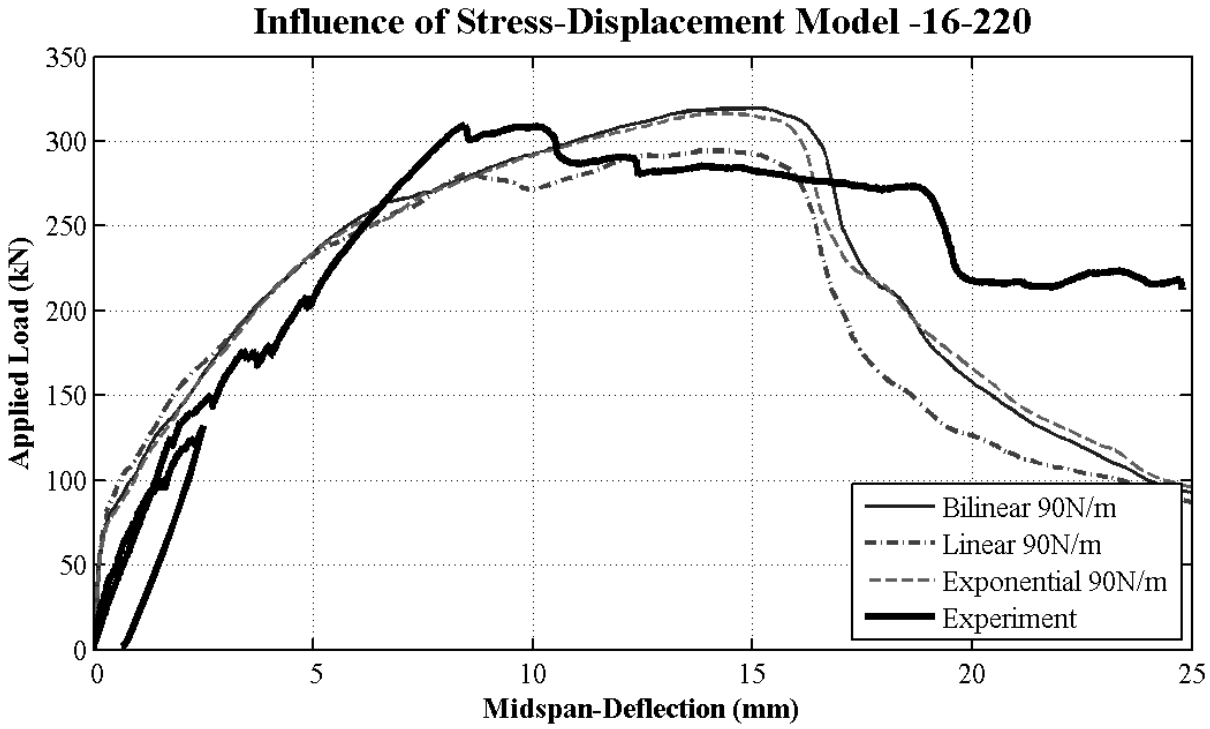
Influence of Stress-Displacement Model -16-220
Applied Load (kN)
Midspan-Deflection (mm)
Bilinear 90N/m
Linear 90N/m
Exponential 90N/m
Experiment

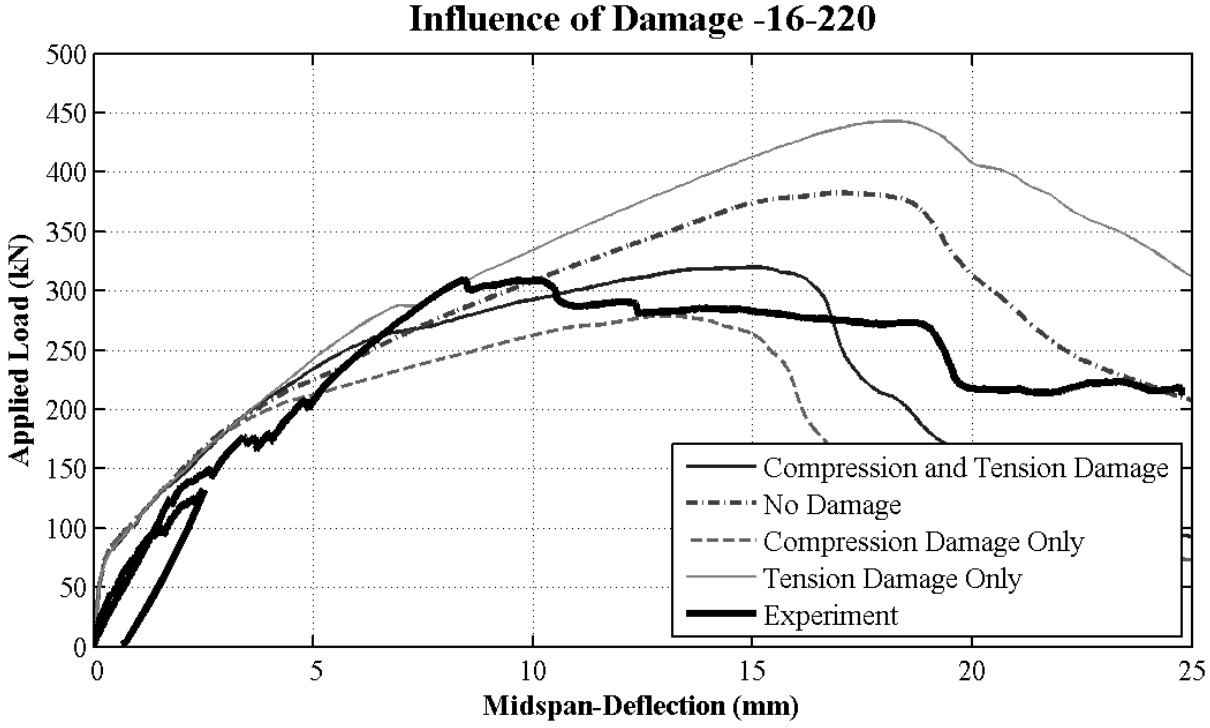
Influence of Damage -16-220
Applied Load (kN)
Midspan-Deflection (mm)
Compression and Tension Damage
No Damage
Compression Damage Only
Tension Damage Only
Experiment

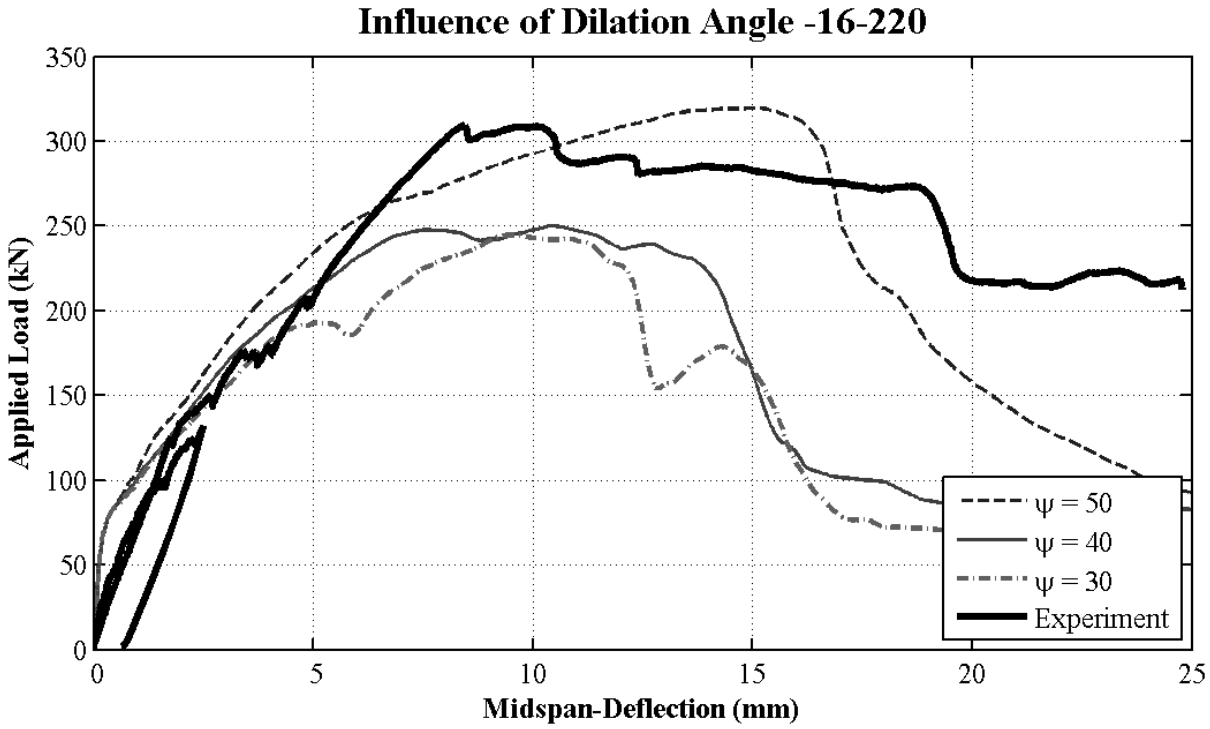
Influence of Dilation Angle -16-220
Applied Load (kN)
Midspan-Deflection (mm)
ψ = 50
ψ = 40
ψ = 30
Experiment

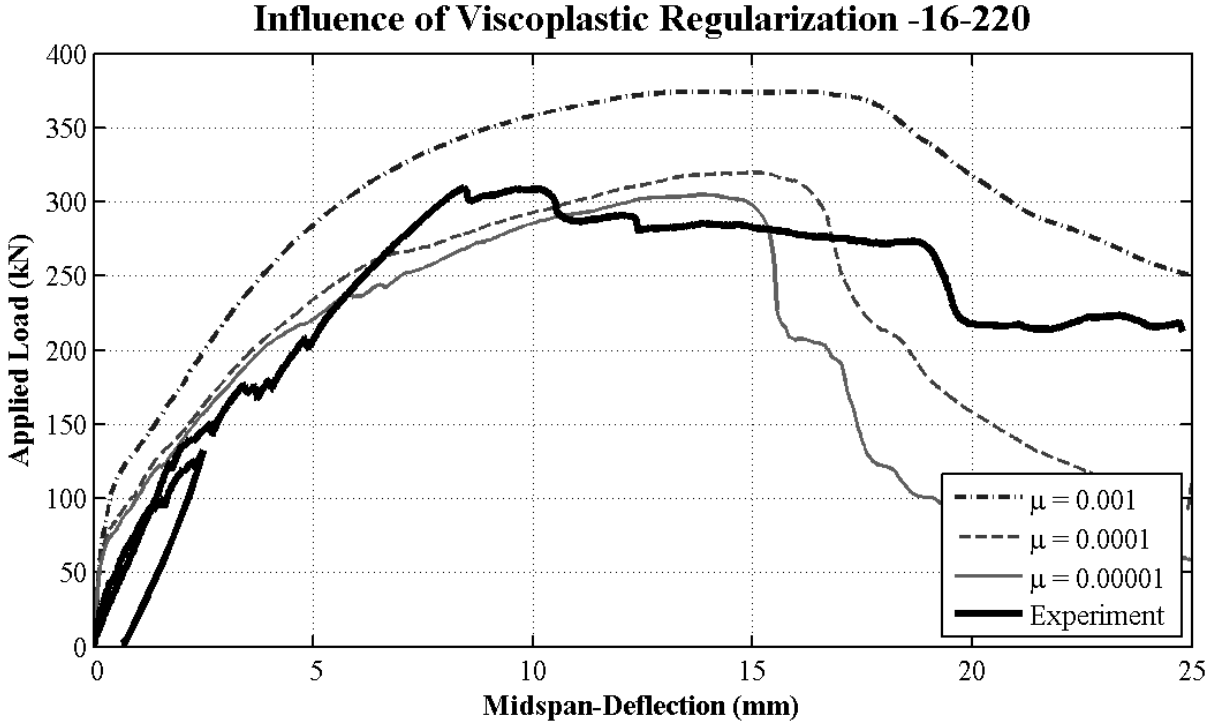
Influence of Viscoplastic Regularization -16-220
Applied Load (kN)
Midspan-Deflection (mm)
μ = 0.001
μ = 0.0001
μ = 0.00001
Experiment

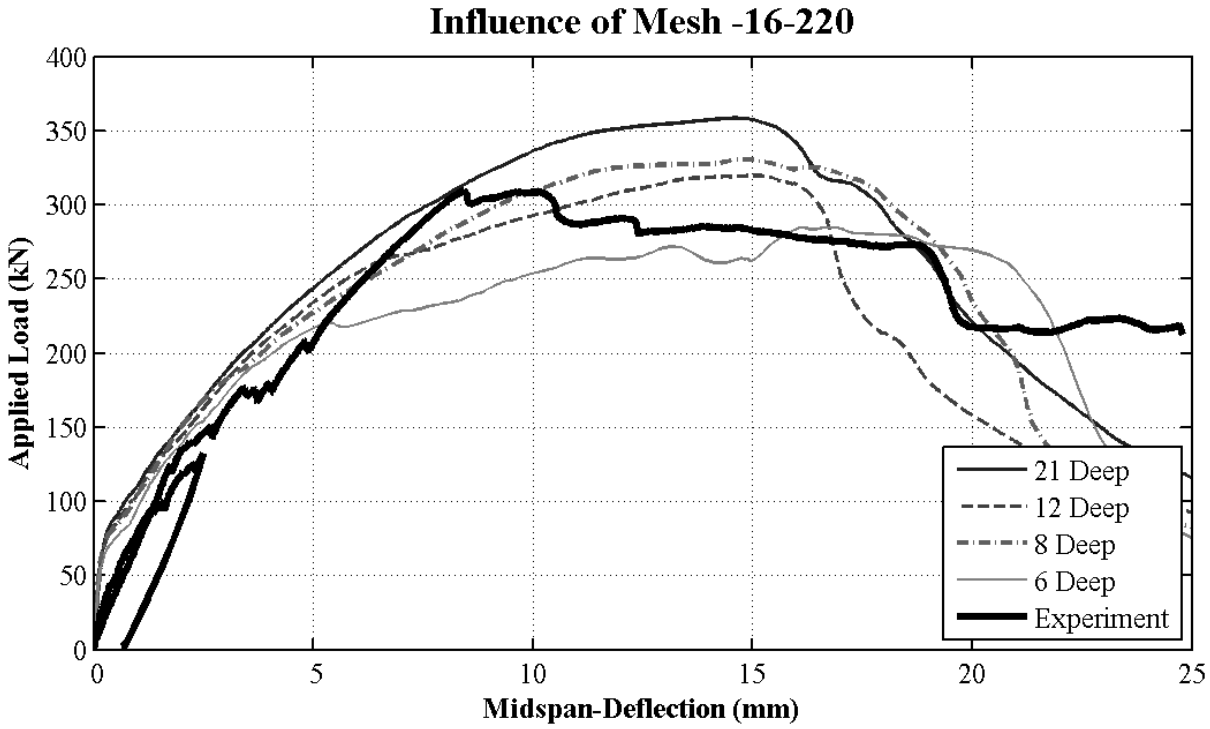
Influence of Mesh -16-220
Applied Load (kN)
Midspan-Deflection (mm)
21 Deep
12 Deep
8 Deep
6 Deep
Experiment

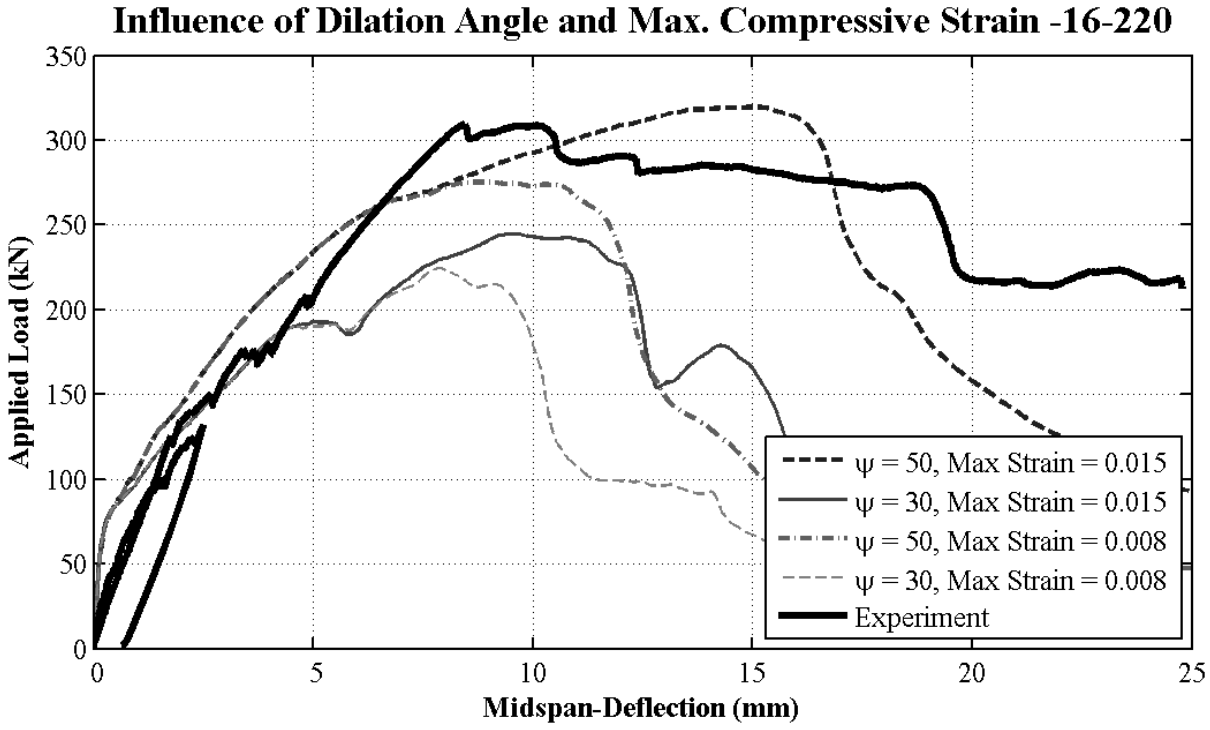
Influence of Dilation Angle and Max. Compressive Strain -16-220
Applied Load (kN)
Midspan-Deflection (mm)
ψ = 50, Max Strain = 0.015
ψ = 30, Max Strain = 0.015
ψ = 50, Max Strain = 0.008
ψ = 30, Max Strain = 0.008
Experiment

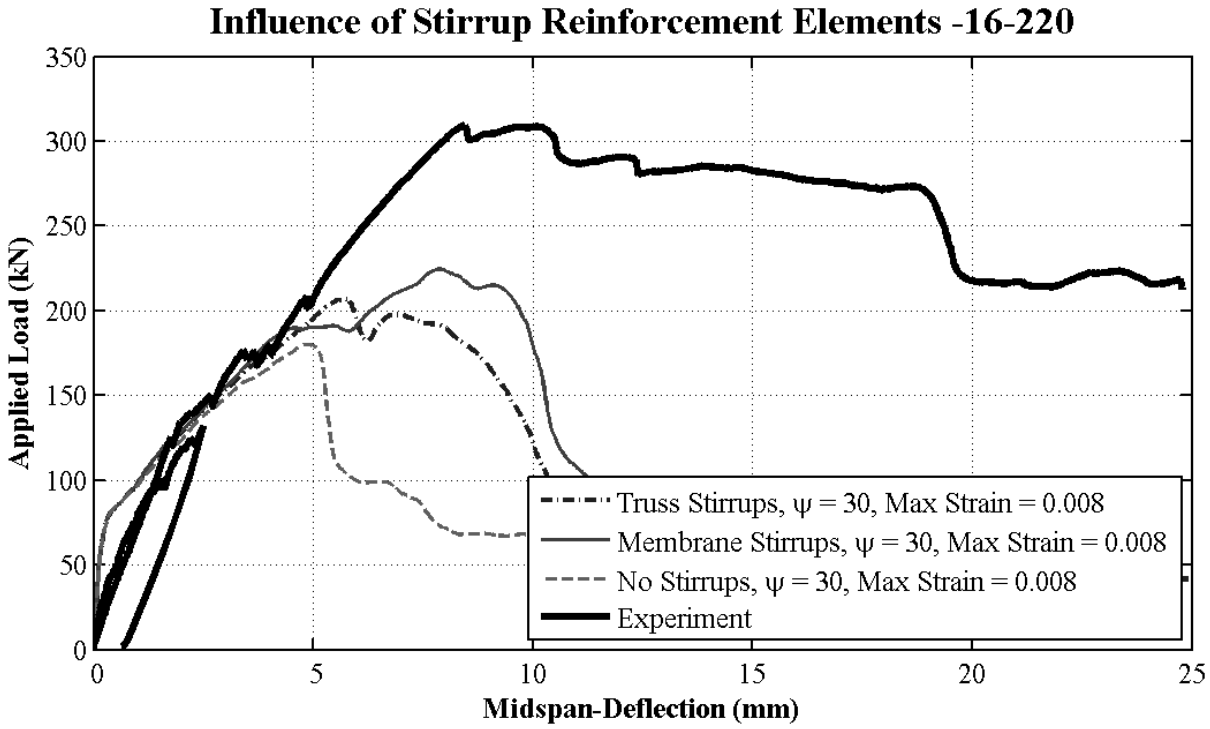
Influence of Stirrup Reinforcement Elements -16-220
Applied Load (kN)
Midspan-Deflection (mm)
Truss Stirrups, ψ = 30, Max Strain = 0.008
Membrane Stirrups, ψ = 30, Max Strain = 0.008
No Stirrups, ψ = 30, Max Strain = 0.008
Experiment

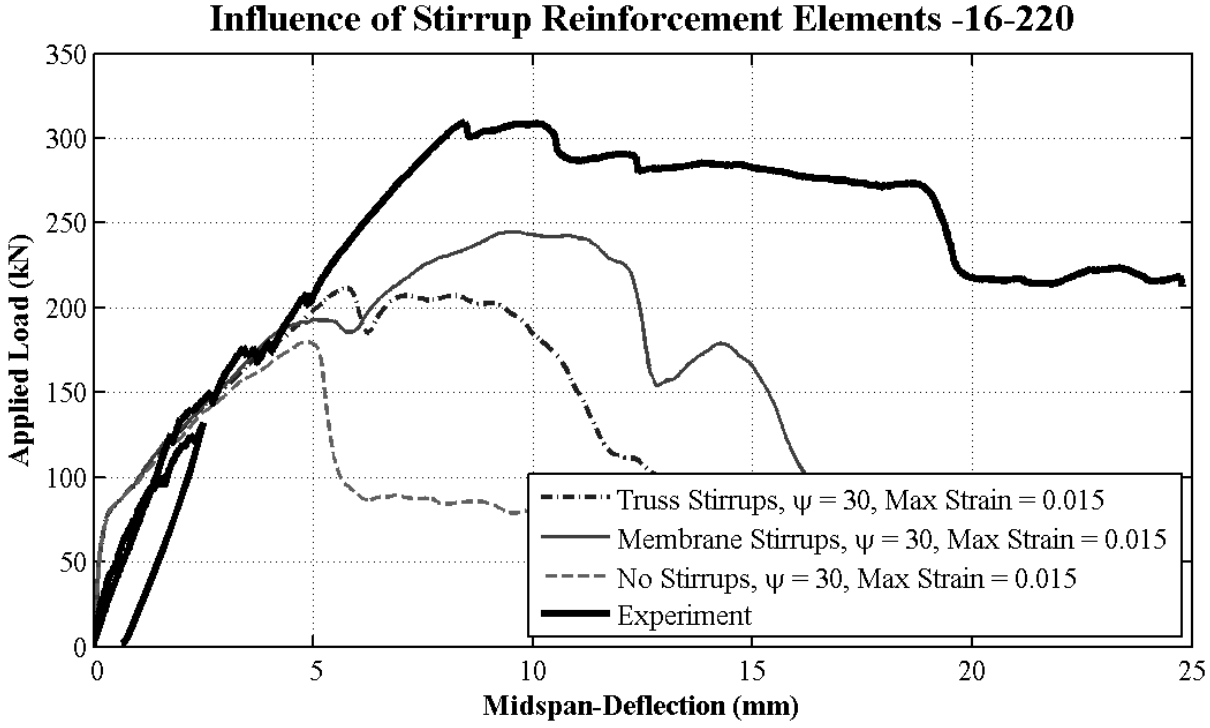
Influence of Stirrup Reinforcement Elements -16-220
Applied Load (kN)
Midspan-Deflection (mm)
Truss Stirrups, ψ = 30, Max Strain = 0.015
Membrane Stirrups, ψ = 30, Max Strain = 0.015
No Stirrups, ψ = 30, Max Strain = 0.015
Experiment

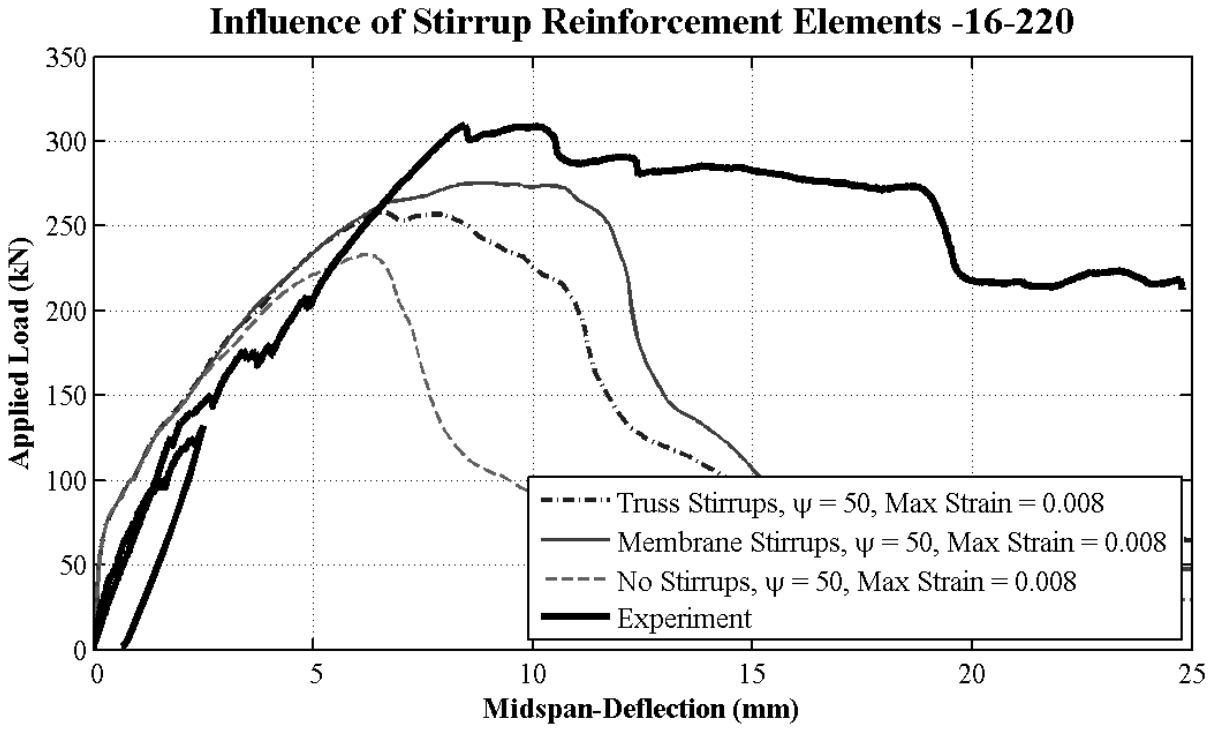
Influence of Stirrup Reinforcement Elements -16-220
Applied Load (kN)
Midspan-Deflection (mm)
Truss Stirrups, ψ = 50, Max Strain = 0.008
Membrane Stirrups, ψ = 50, Max Strain = 0.008
No Stirrups, ψ = 50, Max Strain = 0.008
Experiment

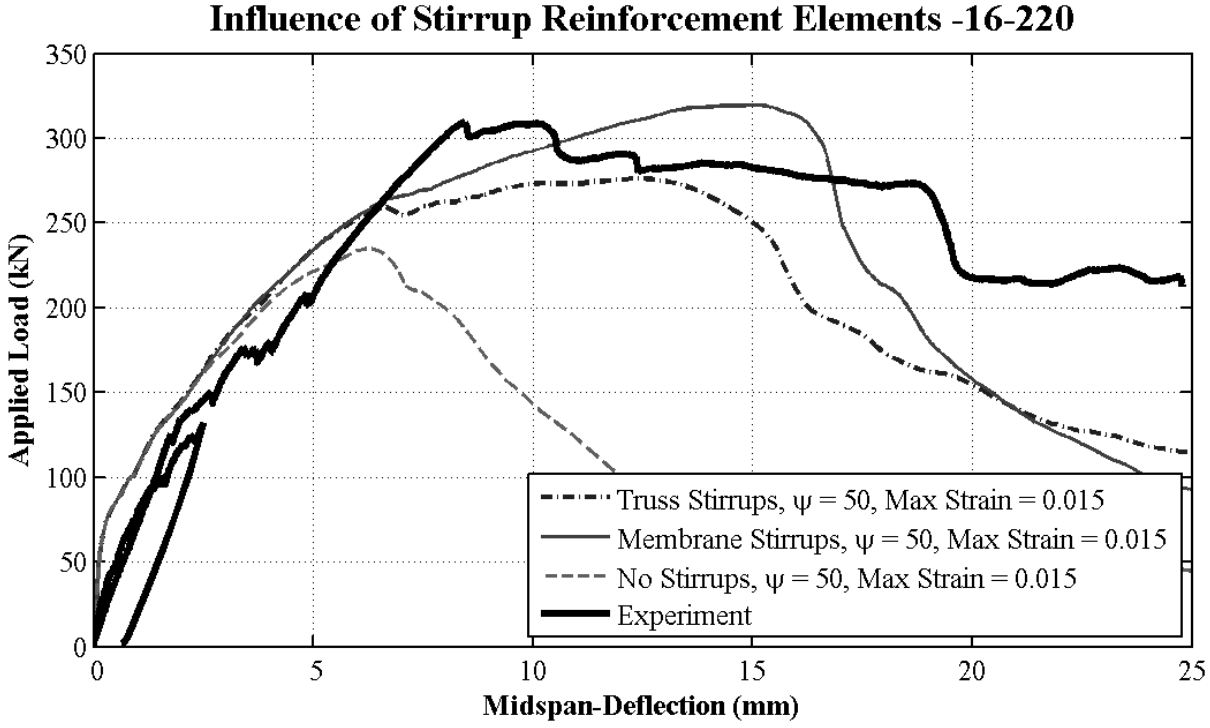
Influence of Stirrup Reinforcement Elements -16-220
Applied Load (kN)
Midspan-Deflection (mm)
Truss Stirrups, ψ = 50, Max Strain = 0.015
Membrane Stirrups, ψ = 50, Max Strain = 0.015
No Stirrups, ψ = 50, Max Strain = 0.015
Experiment

BM 25-220

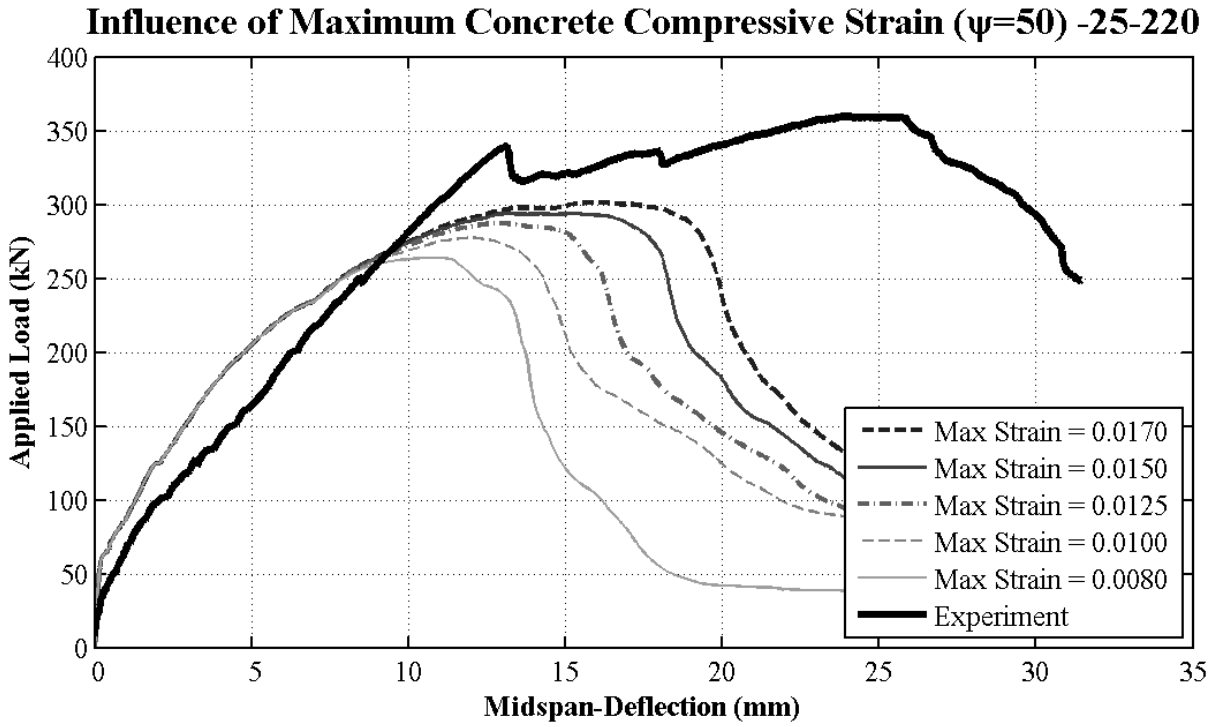
Influence of Maximum Concrete Compressive Strain (ψ=50) -25-220
Applied Load (kN)
Midspan-Deflection (mm)
Max Strain = 0.0170
Max Strain = 0.0150
Max Strain = 0.0125
Max Strain = 0.0100
Max Strain = 0.0080
Experiment

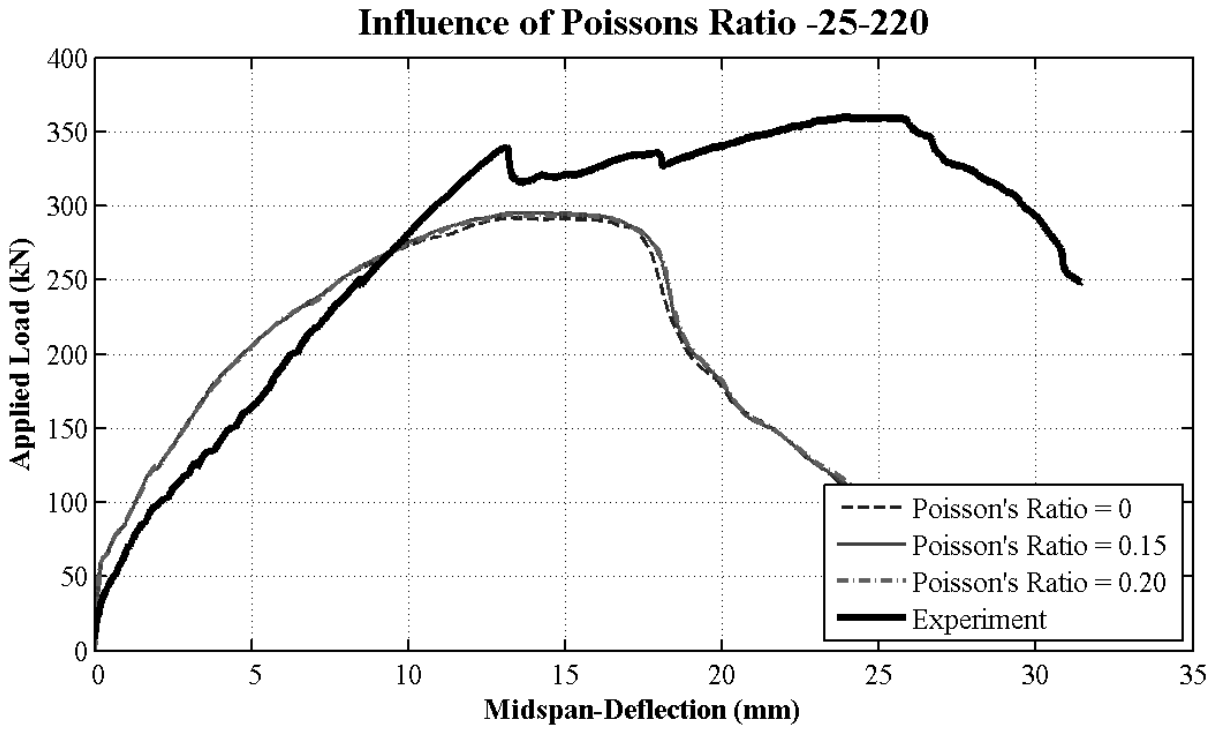
Influence of Poissons Ratio -25-220
Applied Load (kN)
Midspan-Deflection (mm)
Poisson's Ratio = 0
Poisson's Ratio = 0.15
Poisson's Ratio = 0.20
Experiment

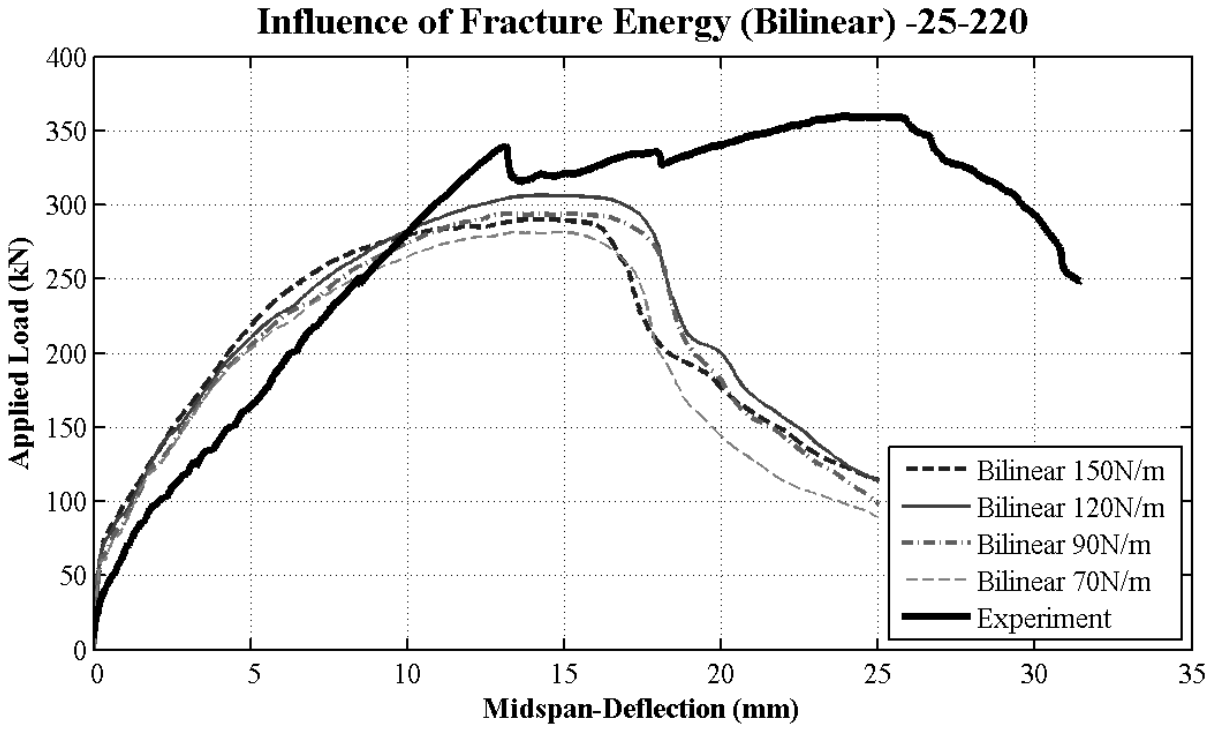
Influence of Fracture Energy (Bilinear) -25-220
Applied Load (kN)
Midspan-Deflection (mm)
Bilinear 150N/m
Bilinear 120N/m
Bilinear 90N/m
Bilinear 70N/m
Experiment

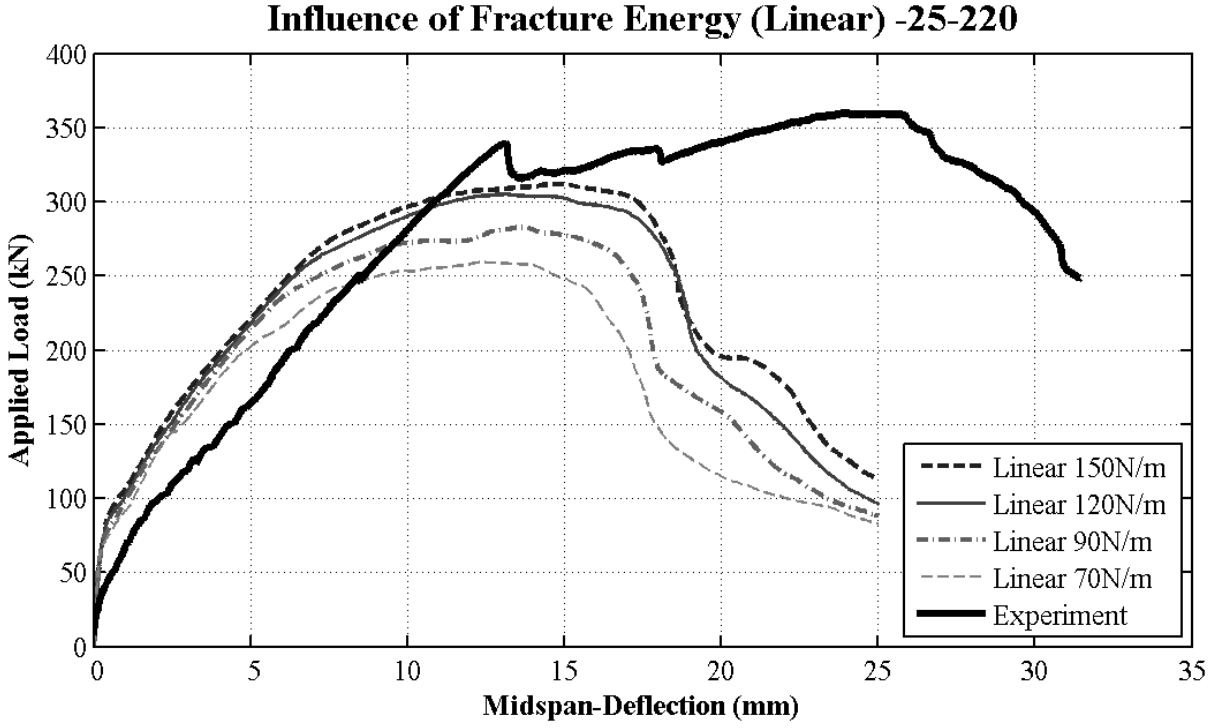
Influence of Fracture Energy (Linear) -25-220
Applied Load (kN)
Midspan-Deflection (mm)
Linear 150N/m
Linear 120N/m
Linear 90N/m
Linear 70N/m
Experiment

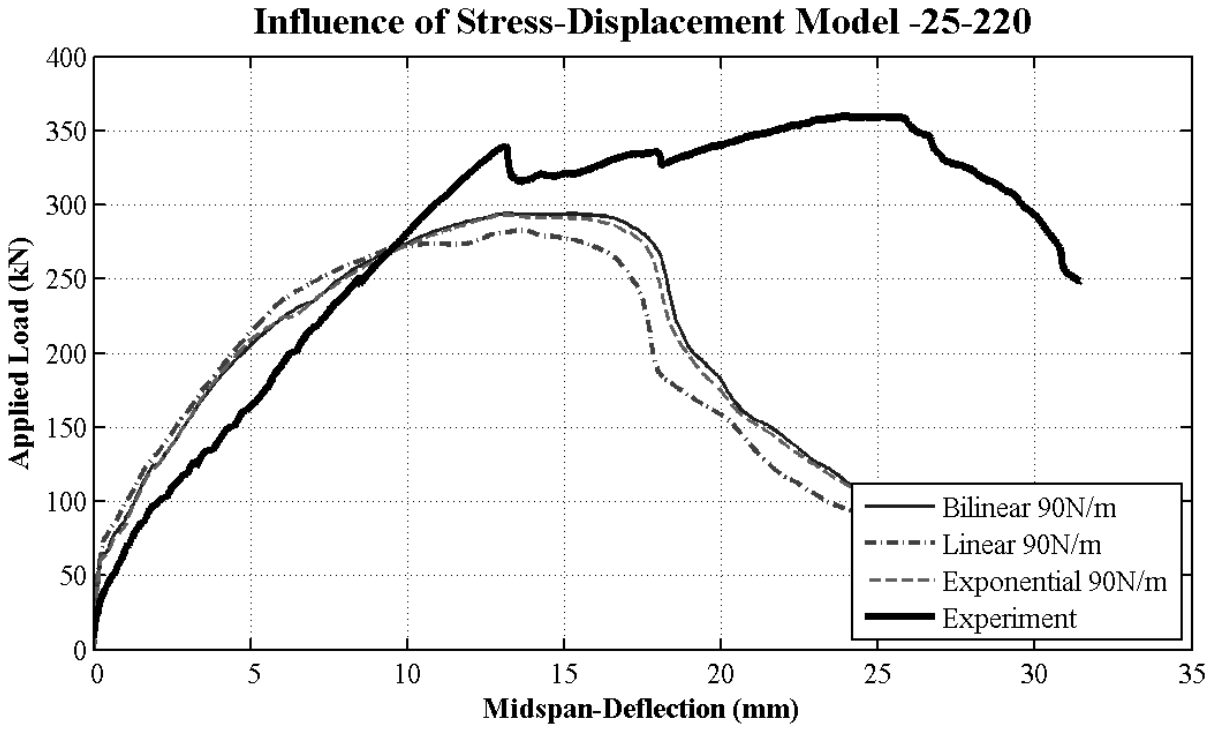
Influence of Stress-Displacement Model -25-220
Applied Load (kN)
Midspan-Deflection (mm)
Bilinear 90N/m
Linear 90N/m
Exponential 90N/m
Experiment

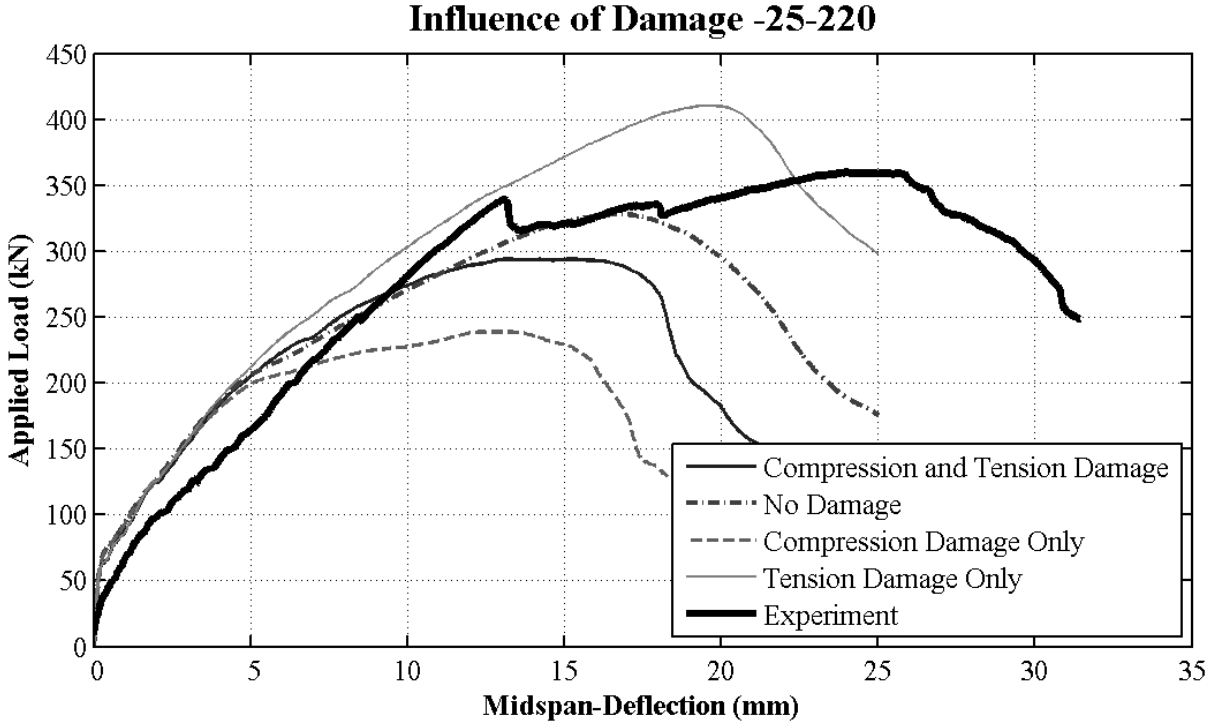
Influence of Damage -25-220
Applied Load (kN)
Midspan-Deflection (mm)
Compression and Tension Damage
No Damage
Compression Damage Only
Tension Damage Only
Experiment

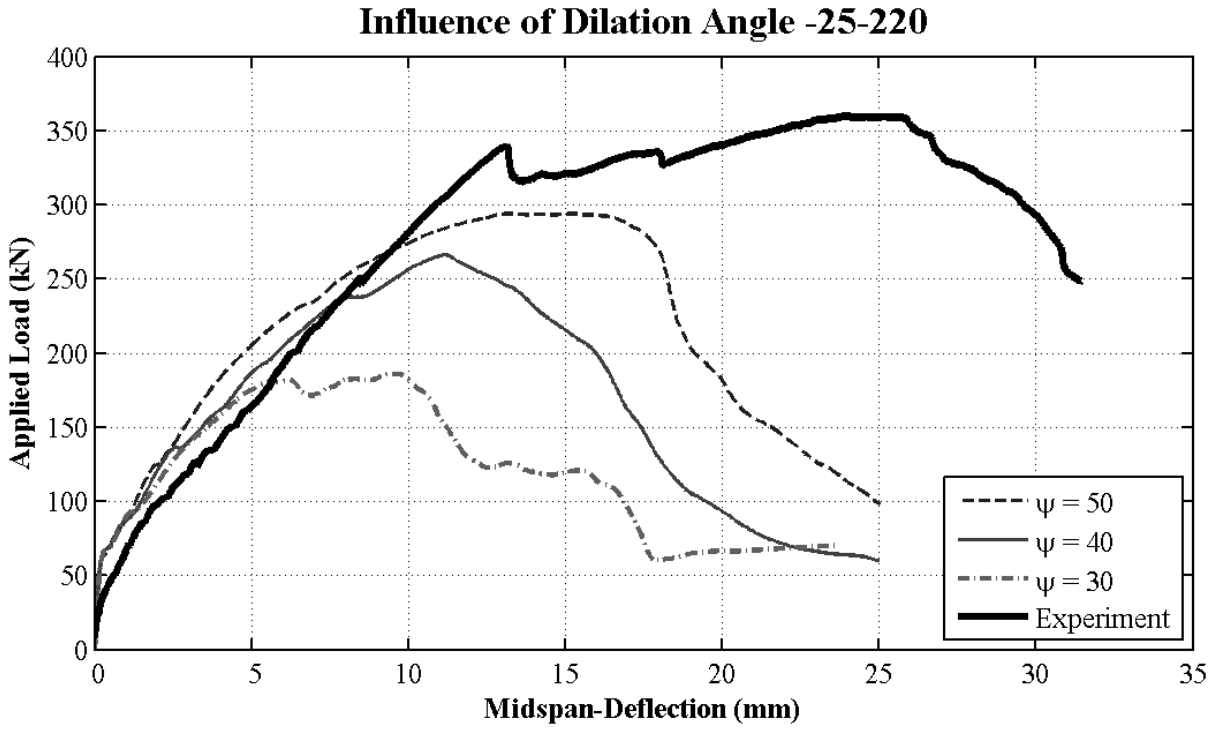
Influence of Dilation Angle -25-220
Applied Load (kN)
Midspan-Deflection (mm)
ψ = 50
ψ = 40
ψ = 30
Experiment

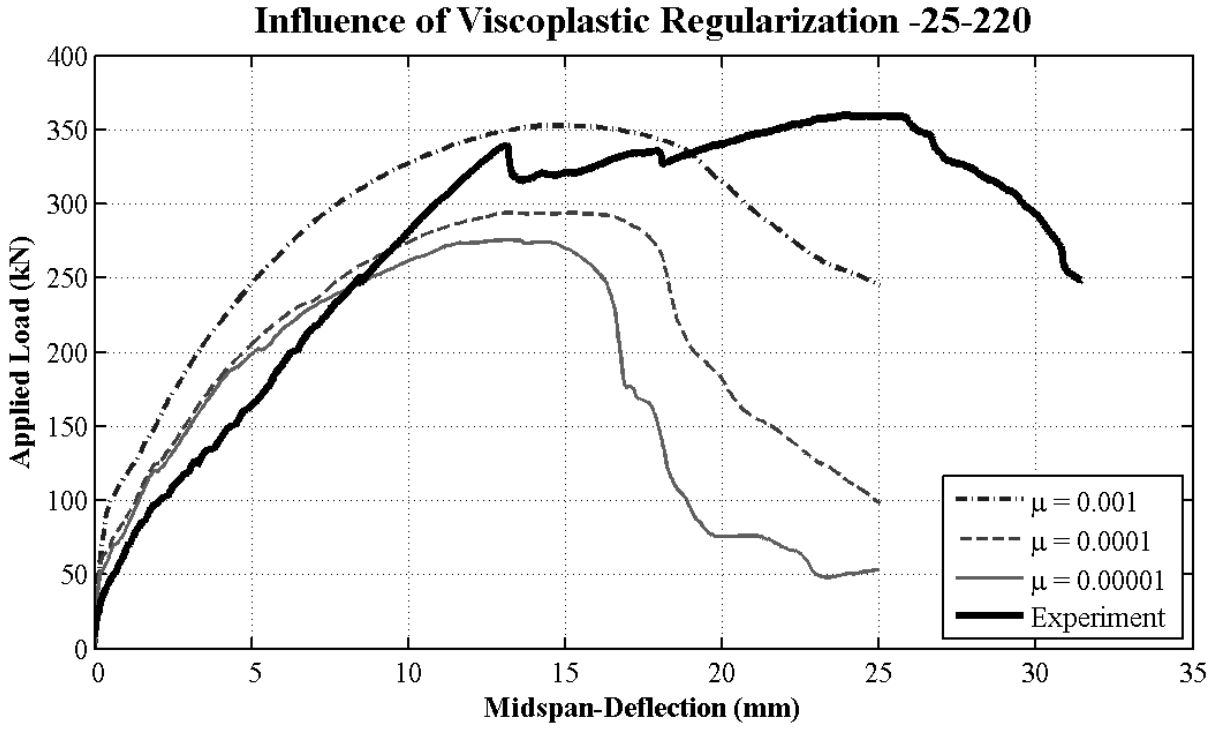
Influence of Viscoplastic Regularization -25-220
Applied Load (kN)
Midspan-Deflection (mm)
μ = 0.001
μ = 0.0001
μ = 0.00001
Experiment

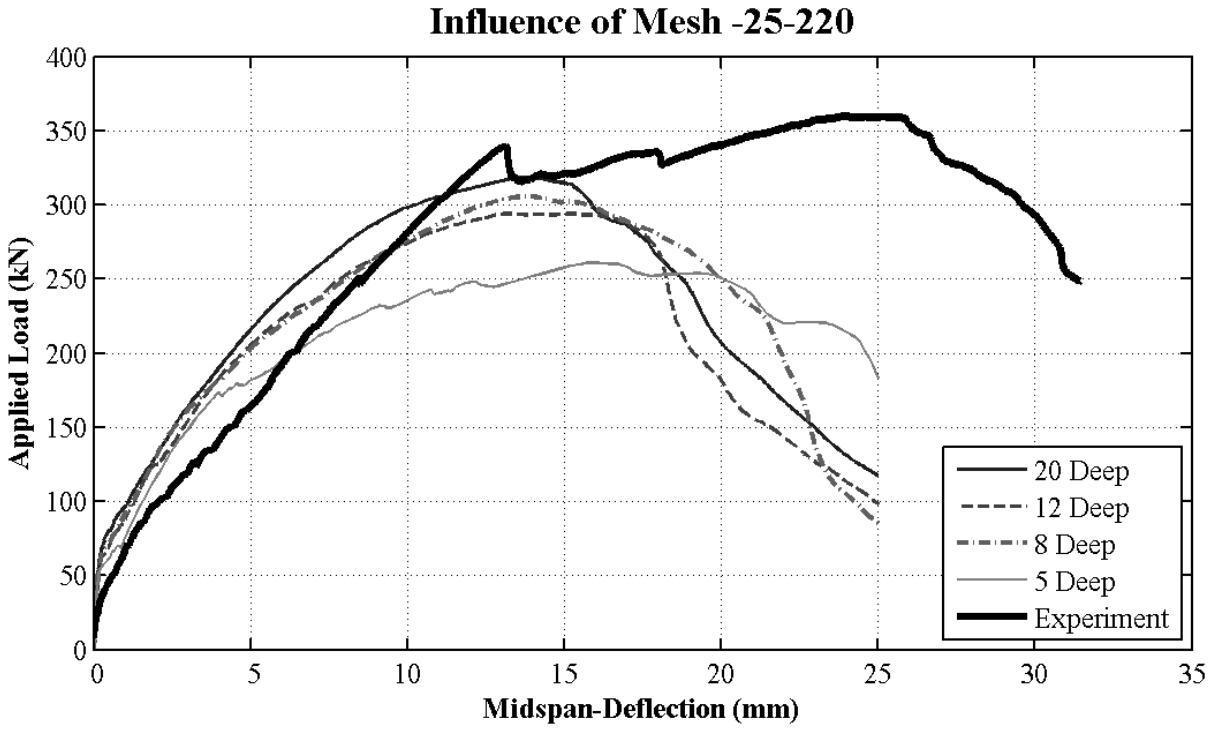
Influence of Mesh -25-220
Applied Load (kN)
Midspan-Deflection (mm)
20 Deep
12 Deep
8 Deep
5 Deep
Experiment

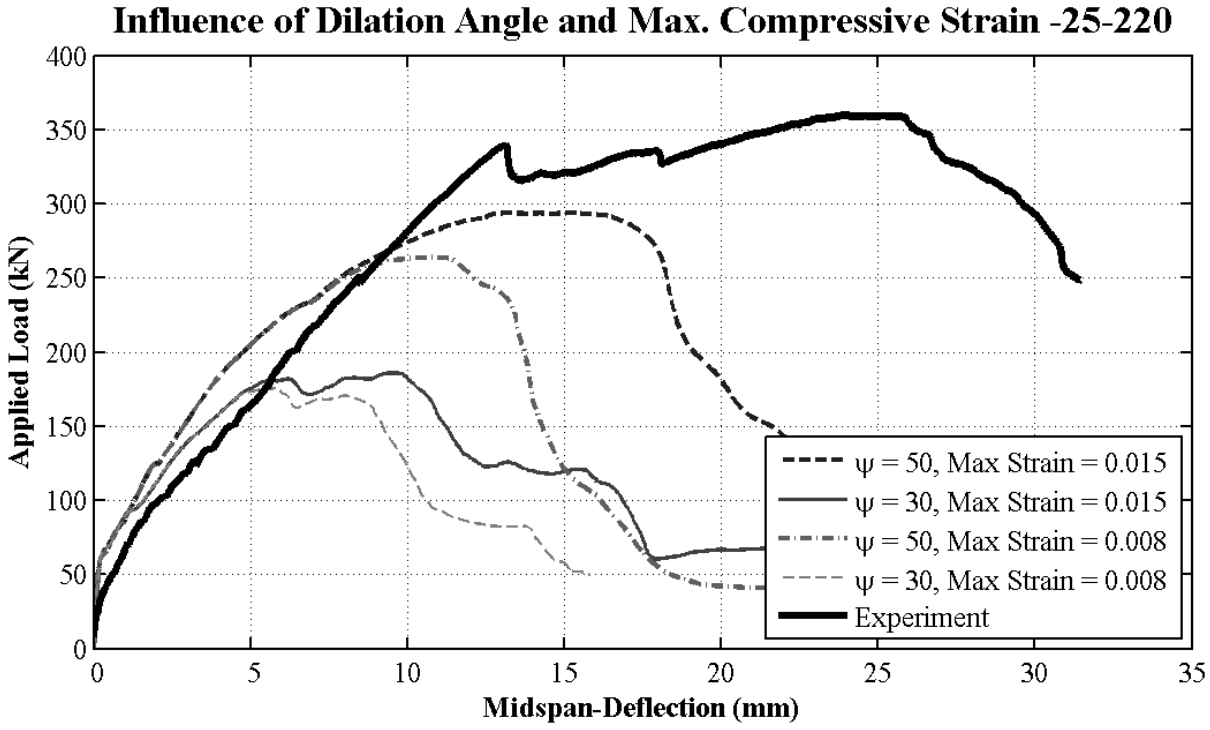
Influence of Dilation Angle and Max. Compressive Strain -25-220
Applied Load (kN)
Midspan-Deflection (mm)
ψ = 50, Max Strain = 0.015
ψ = 30, Max Strain = 0.015
ψ = 50, Max Strain = 0.008
ψ = 30, Max Strain = 0.008
Experiment

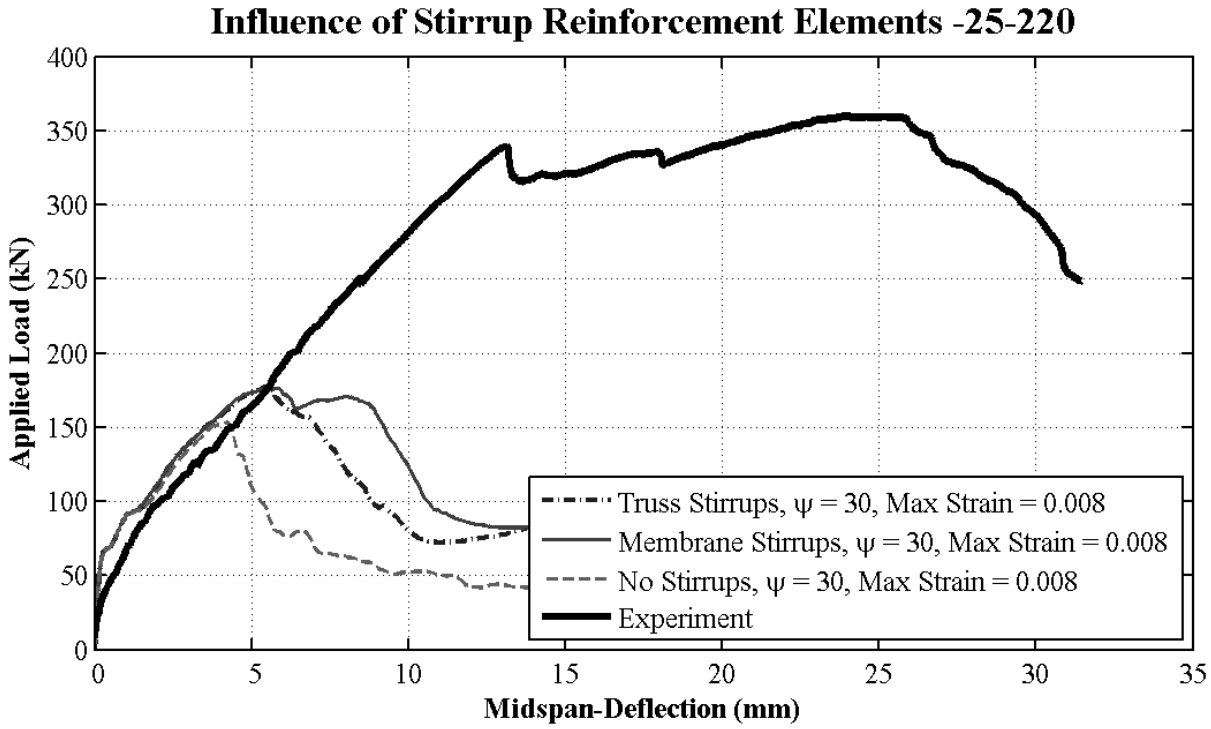
Influence of Stirrup Reinforcement Elements -25-220
Applied Load (kN)
Midspan-Deflection (mm)
Truss Stirrups, ψ = 30, Max Strain = 0.008
Membrane Stirrups, ψ = 30, Max Strain = 0.008
No Stirrups, ψ = 30, Max Strain = 0.008
Experiment

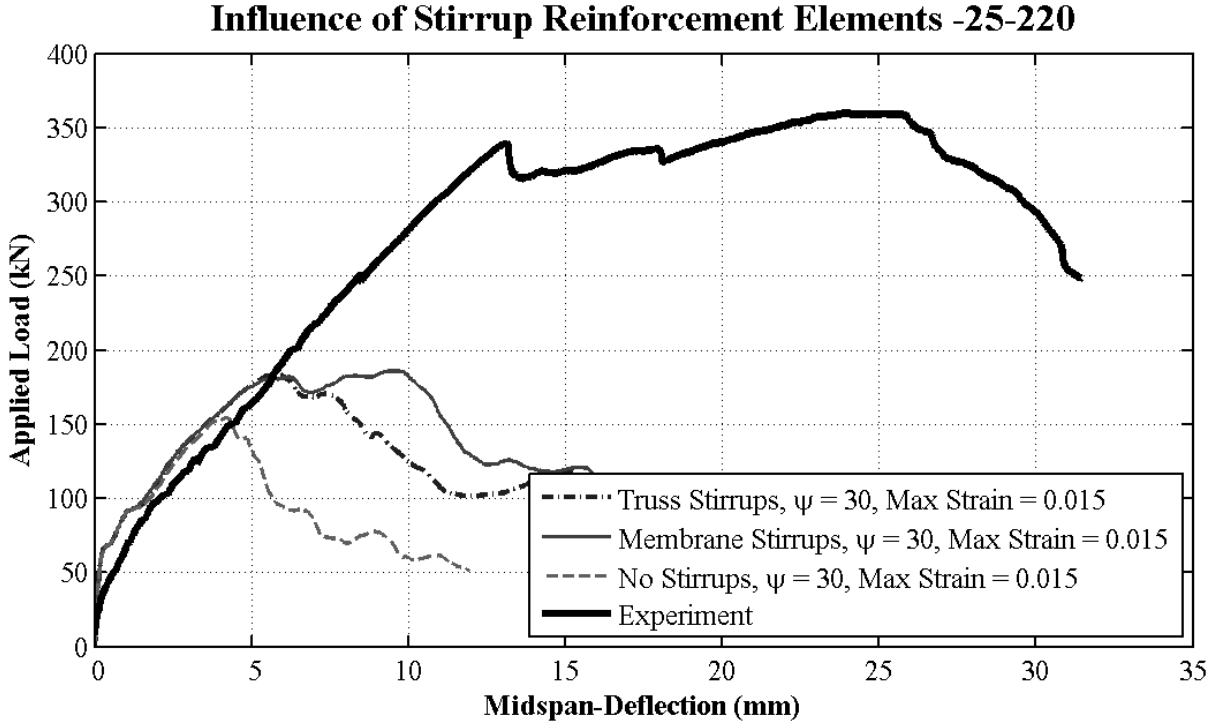
Influence of Stirrup Reinforcement Elements -25-220
Applied Load (kN)
Midspan-Deflection (mm)
Truss Stirrups, ψ = 30, Max Strain = 0.015
Membrane Stirrups, ψ = 30, Max Strain = 0.015
No Stirrups, ψ = 30, Max Strain = 0.015
Experiment

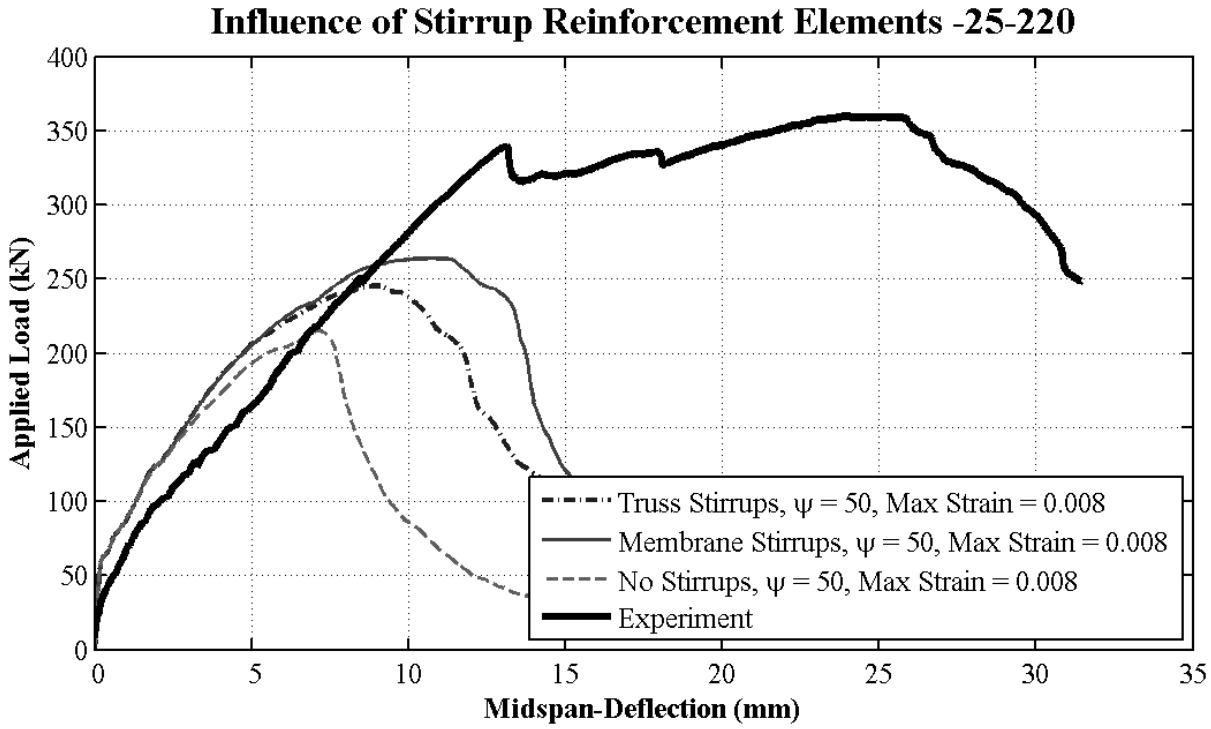
Influence of Stirrup Reinforcement Elements -25-220
Applied Load (kN)
Midspan-Deflection (mm)
Truss Stirrups, ψ = 50, Max Strain = 0.008
Membrane Stirrups, ψ = 50, Max Strain = 0.008
No Stirrups, ψ = 50, Max Strain = 0.008
Experiment

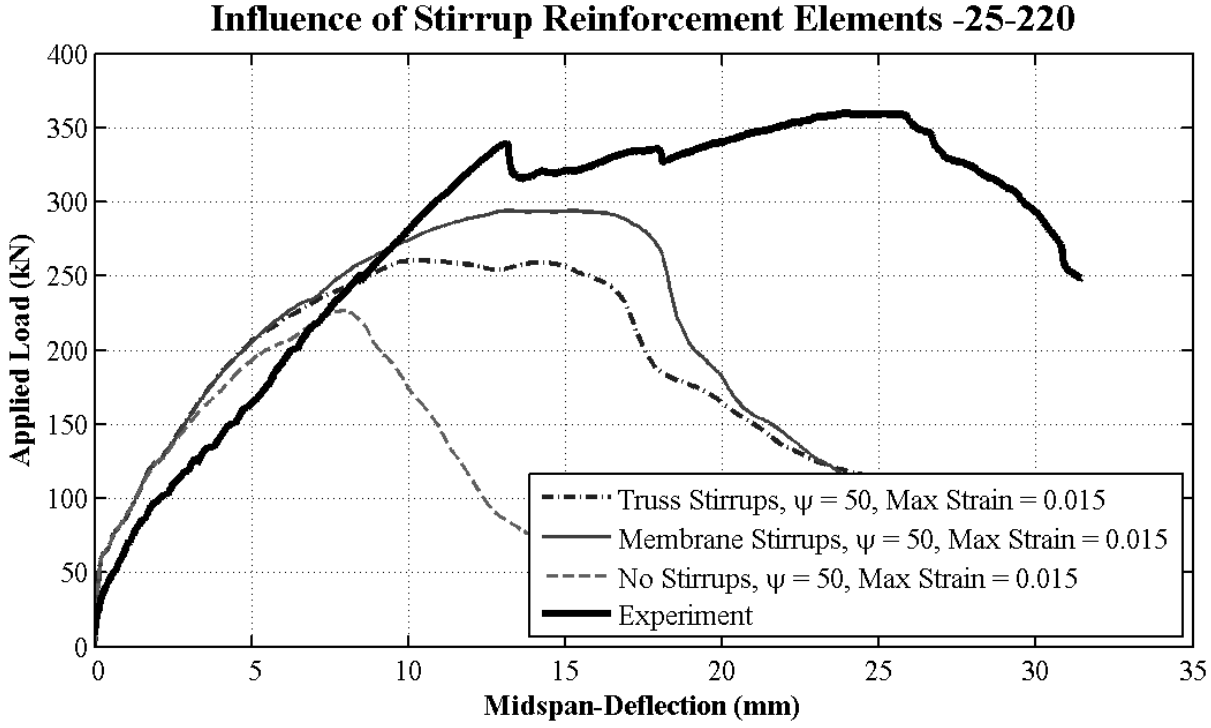
Influence of Stirrup Reinforcement Elements -25-220
Applied Load (kN)
Midspan-Deflection (mm)
Truss Stirrups, ψ = 50, Max Strain = 0.015
Membrane Stirrups, ψ = 50, Max Strain = 0.015
No Stirrups, ψ = 50, Max Strain = 0.015
Experiment

Appendix D

Parametric Study

This Appendix presents the results of the parametric study performed as discussed in Chapter 7. Table D.1 presents the ultimate load at failure, P, as determined by the proposed ABAQUS models and the corresponding bending moment, M, for each beam. The units for the applied loads and bending moments are kN and kN-m, respectively.

Table D.2 compares the ultimate loads predicted for beams with no stirrups. Tables D.3 to D.5 compare the ultimate loads predicted for beams with stirrups spaced at 150mm, 220mm, and 230mm, respectively. The comparisons presented are limited to the following:

1. Flexural strength provided by CSA S806-12
2. Shear strength provided by CSA S806-12 (with reduction factor of 0.4)
3. Shear strength provided by CSA S806-12 (with reduction factor of 1.0)
4. Shear strength model proposed by Nehdi et al., (2007)
5. Strength predicted by proposed ABAQUS models
6. Strength observed during experimental testing

For each beam, the load-deflection and moment-deflection responses are presented for each slenderness ratio (a/d) studied. The strength predictions are then plotted as a function of the slenderness ratio, and the proposed ABAQUS results are compared with the governing strength predictions.

Table D.1: Ultimate Loads and Moments

Beam		a/d					
		1.5	2.5	3.5	4.5	5.5	6.5
12-INF	P	217.3	169.4	133.3	100.0	83.3	85.8
	M	44.0	57.2	63.0	60.7	61.8	75.3
16-INF	P	215.0	142.3	110.3	90.5	83.3	72.5
	M	43.5	48.0	52.1	55.0	61.8	63.6
25-INF	P	198.1	128.6	105.0	83.8	71.8	69.9
	M	40.1	43.4	49.6	50.9	53.3	61.4
12-150	P	478.1	385.1	325.0	269.2	234.1	207.6
	M	96.8	130.0	153.5	163.6	173.8	182.2
16-150	P	469.9	393.9	316.2	262.5	227.4	192.3
	M	95.2	133.0	149.4	159.5	168.8	168.7
25-150	P	369.7	346.0	271.7	226.8	213.5	185.6
	M	74.9	116.8	128.4	137.8	158.5	162.8
12-220	P	395.5	332.2	269.3	234.9	203.7	186.1
	M	80.1	112.1	127.3	142.7	151.2	163.3
16-220	P	373.3	320.4	283.5	226.6	200.4	180.8
	M	75.6	108.1	133.9	137.7	148.8	158.6
25-220	P	345.8	294.1	255.8	218.6	196.0	175.3
	M	70.0	99.3	120.8	132.8	145.5	153.8
12-s230	P	526.5	422.5	364.9	285.2	247.8	218.7
	M	106.6	142.6	172.4	173.3	184.0	191.9
16-s230	P	542.2	391.8	343.6	277.9	239.9	207.6
	M	109.8	132.2	162.4	168.8	178.1	182.1
25-s230	P	440.2	368.1	301.1	257.3	221.1	198.2
	M	89.1	124.2	142.2	156.3	164.2	173.9

Note: All loads, P, have units of kN. All moments, M, have units kNm

Table D.2: Comparison of Ultimate Loads for Beams with No Stirrups (kN)

Beam	a/d	CSA Flexure	CSA Shear	Nehdi et al.	Model	Exp.
12-INF	1.5	719.9	271.6	283.7	217.3	-
	2.5	431.9	152.8	151.3	169.4	163.1
	3.5	308.5	129.1	140.1	133.3	-
	4.5	240.0	113.9	132.2	100.0	-
	5.5	196.3	103.0	126.2	83.3	-
	6.5	163.6	94.8	121.5	85.8	-
16-INF	1.5	683.8	266.2	275.4	215.0	-
	2.5	410.3	144.8	146.9	142.3	150.2
	3.5	293.1	122.3	136.0	110.3	-
	4.5	227.9	107.9	128.4	90.5	-
	5.5	186.5	97.6	122.6	83.3	-
	6.5	155.4	89.8	117.9	72.5	-
25-INF	1.5	620.8	256.9	261.0	198.1	-
	2.5	372.5	131.8	139.3	132.5	125.1
	3.5	266.1	111.4	128.9	105.0	-
	4.5	206.9	98.2	121.6	83.8	-
	5.5	169.3	88.9	116.2	71.8	-
	6.5	141.1	81.7	111.8	69.9	-

Table D.3: Comparison of Ultimate Loads for Beams with Stirrups at 150mm (kN)

Beam	a/d	CSA Flexure	CSA Shear, 0.4	CSA Shear, 1.0	Nehdi et al.	Model	Exp.
12-150	1.5	736.4	345.5	446.9	510.5	478.1	-
	2.5	441.9	226.2	300.8	376.7	385.1	405.2
	3.5	315.6	196.9	262.4	365.4	325.0	-
	4.5	245.5	177.2	235.1	357.4	269.2	-
	5.5	200.8	162.3	214.2	351.4	234.1	-
	6.5	167.4	150.6	205.8	346.6	207.6	-
16-150	1.5	703.3	336.2	407.4	502.8	469.9	-
	2.5	422.0	214.4	283.2	372.7	393.9	416.5
	3.5	301.4	186.4	246.1	361.6	316.2	-
	4.5	234.4	167.3	219.8	353.9	262.5	-
	5.5	191.8	153.0	207.5	348.0	227.4	-
	6.5	159.8	141.7	199.5	343.3	192.3	-
25-150	1.5	646.6	320.9	380.2	489.8	369.7	-
	2.5	388.0	195.4	254.4	365.7	346.0	415.8
	3.5	277.1	169.2	220.2	355.1	271.7	-
	4.5	215.5	151.3	206.6	347.7	226.8	-
	5.5	176.4	137.9	197.0	342.1	213.5	-
	6.5	147.0	127.3	189.7	337.7	185.6	-

Table D.4: Comparison of Ultimate Loads for Beams with Stirrups at 220mm (kN)

Beam	a/d	CSA Flexure	CSA Shear, 0.4	CSA Shear, 1.0	Nehdi et al.	Model	Exp.
12-220	1.5	736.4	325.7	384.9	470.8	395.5	-
	2.5	441.9	206.2	264.6	337.0	332.2	382.4
	3.5	315.6	178.9	231.1	325.6	269.3	-
	4.5	245.5	160.6	207.7	317.7	234.9	-
	5.5	200.8	147.1	189.9	311.7	203.7	-
	6.5	167.4	136.5	175.7	306.9	186.1	-
16-220	1.5	703.3	318.0	372.2	463.1	373.3	-
	2.5	422.0	195.7	250.0	333.0	320.4	309.3
	3.5	301.4	169.6	217.7	321.9	283.5	-
	4.5	234.4	152.1	195.1	314.1	226.6	-
	5.5	191.8	139.1	178.0	308.3	200.4	-
	6.5	159.8	128.9	165.1	303.6	180.8	-
25-220	1.5	646.6	305.6	351.1	450.1	345.8	-
	2.5	388.0	178.9	226.2	326.0	294.1	360.1
	3.5	277.1	154.6	195.9	315.4	255.8	-
	4.5	215.5	138.2	174.7	308.0	218.8	-
	5.5	176.4	126.1	163.4	302.4	196.0	-
	6.5	147.0	116.6	156.1	298.0	175.3	-

Table D.5: Comparison of Ultimate Loads for Beams with Stirrups at 230mm (kN)

Beam	a/d	CSA Flexure	CSA Shear, 0.4	CSA Shear, 1.0	Nehdi et al.	Model	Exp.
12-s230	1.5	806.6	442.0	552.7	626.8	526.5	-
	2.5	484.0	293.3	396.1	477.9	422.5	466.9
	3.5	345.7	255.4	357.8	465.2	364.9	-
	4.5	268.9	229.0	340.0	456.4	285.2	-
	5.5	220.0	209.0	327.3	449.7	247.8	-
	6.5	183.3	193.4	317.7	444.3	218.7	-
16-s230	1.5	770.0	427.6	532.9	618.3	542.2	-
	2.5	462.0	277.0	373.9	473.4	391.8	434.0
	3.5	330.0	240.5	347.7	461.0	343.6	-
	4.5	256.7	215.1	330.7	452.4	277.9	-
	5.5	210.0	196.1	318.7	445.9	239.9	-
	6.5	175.0	186.9	309.5	440.7	207.6	-
25-s230	1.5	706.7	395.7	510.7	604.0	440.2	-
	2.5	424.0	245.5	348.5	465.7	368.1	444.0
	3.5	302.9	211.9	324.9	454.0	301.1	-
	4.5	235.6	192.1	309.6	445.7	257.3	-
	5.5	192.7	181.3	298.7	439.5	221.1	-
	6.5	160.6	173.0	290.5	434.5	198.2	-

BM 12-INF

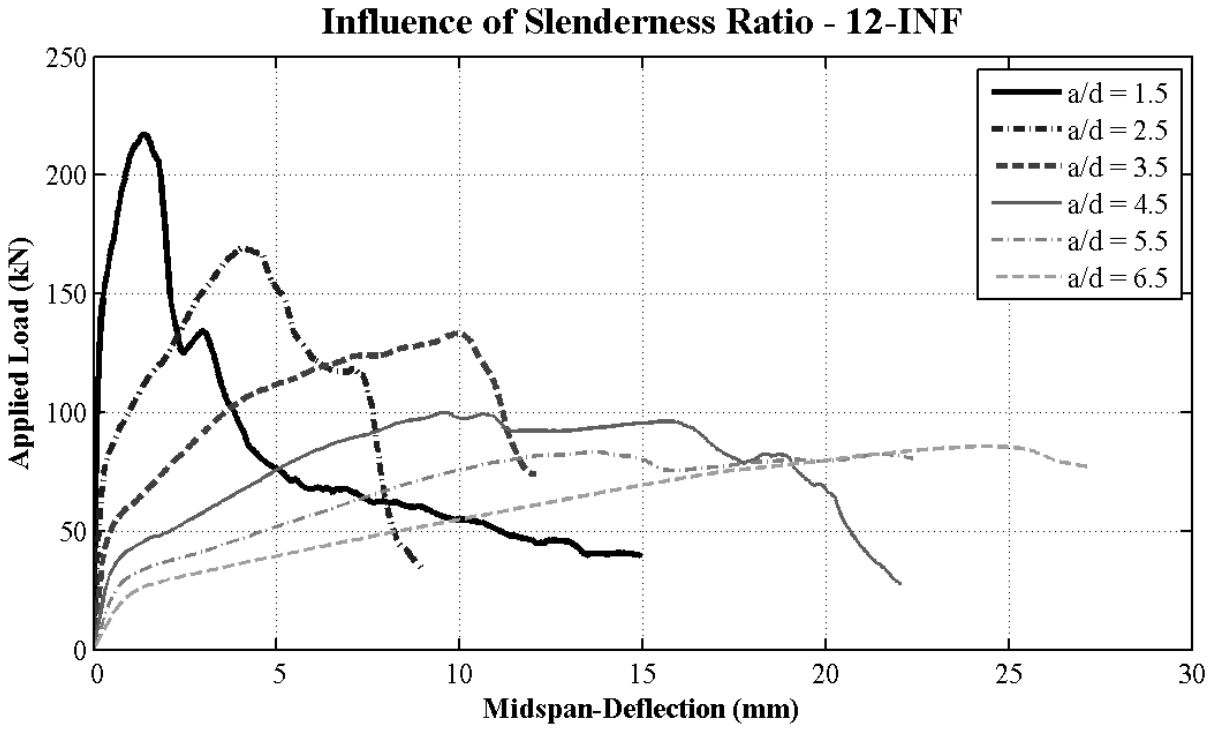
Influence of Slenderness Ratio - 12-INF
Applied Load (kN)
Midspan-Deflection (mm)
a/d = 1.5
a/d = 2.5
a/d = 3.5
a/d = 4.5
a/d = 5.5
a/d = 6.5
0
50
100
150
200
250
0
5
10
15
20
25
30

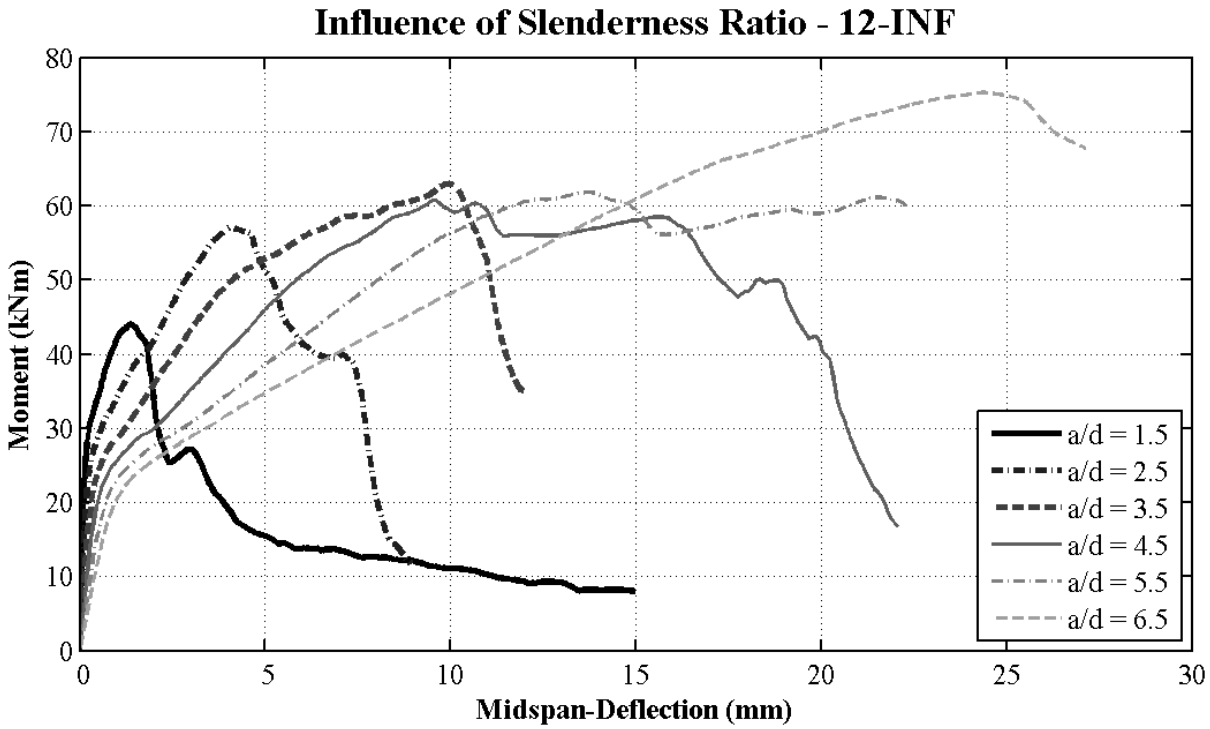
Influence of Slenderness Ratio - 12-INF
Moment (kNm)
Midspan-Deflection (mm)
a/d = 1.5
a/d = 2.5
a/d = 3.5
a/d = 4.5
a/d = 5.5
a/d = 6.5
0
10
20
30
40
50
60
70
80
0
5
10
15
20
25
30

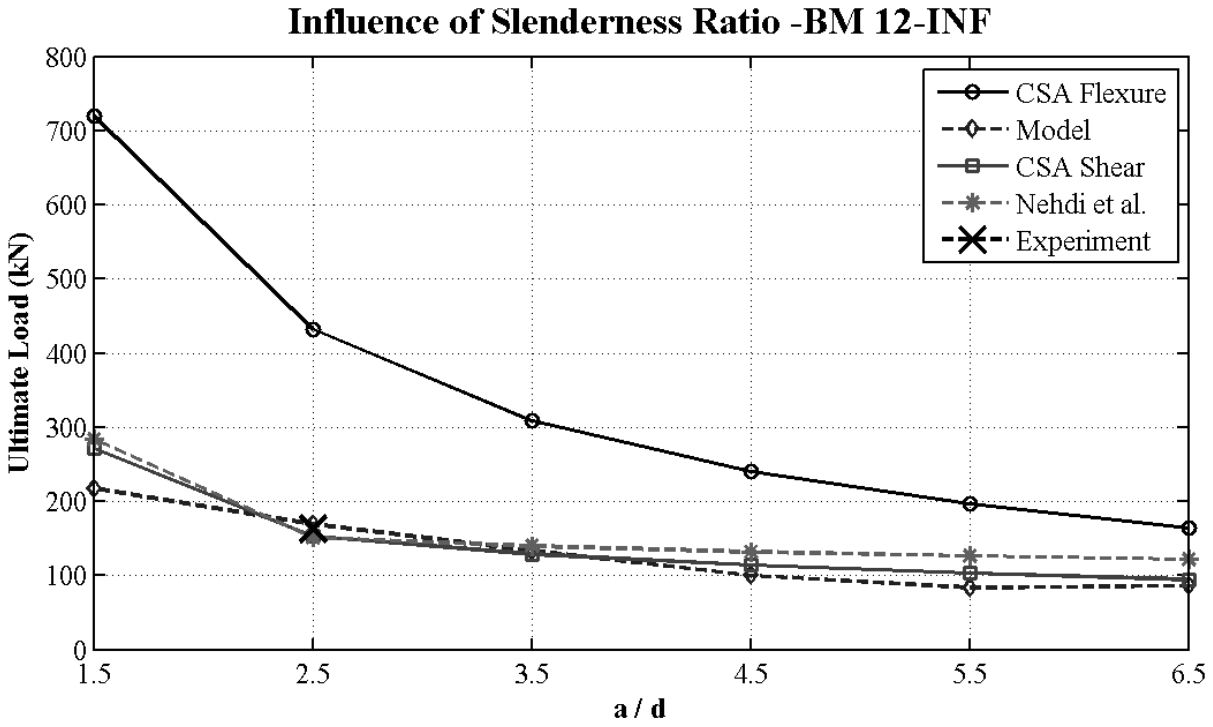
Influence of Slenderness Ratio -BM 12-INF
Ultimate Load (kN)
a / d
CSA Flexure
Model
CSA Shear
Nehdi et al.
Experiment
0
100
200
300
400
500
600
700
800
1.5
2.5
3.5
4.5
5.5
6.5

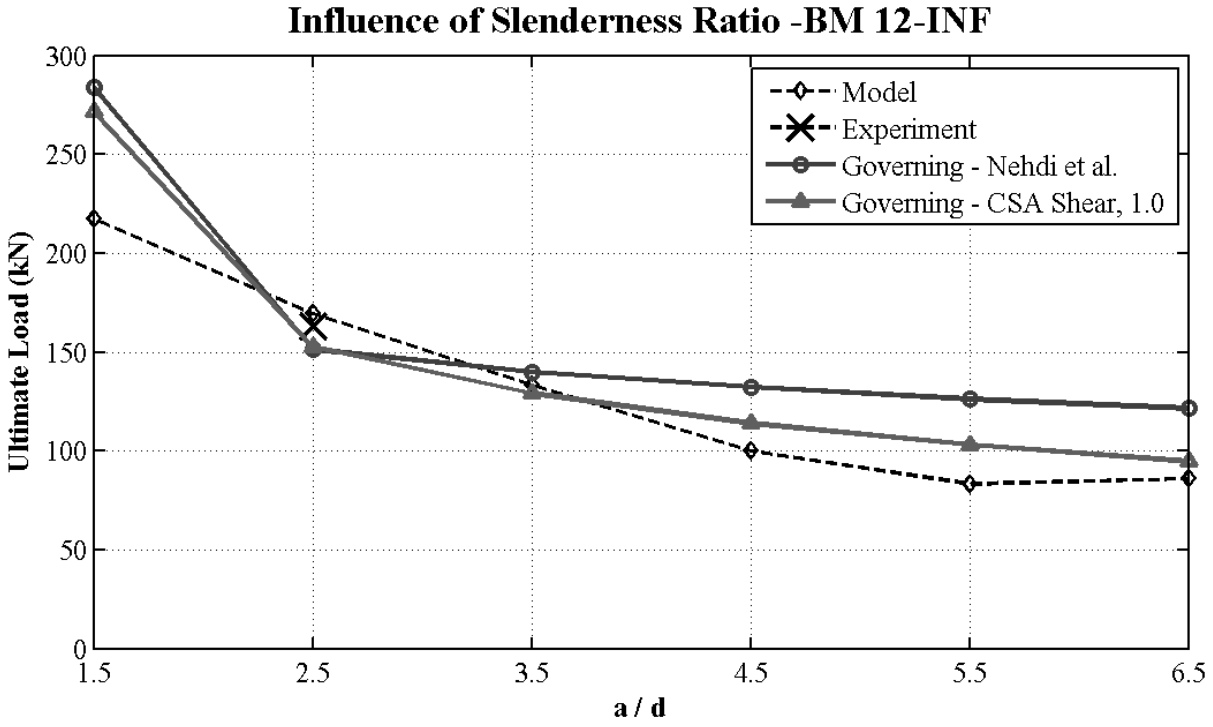
Influence of Slenderness Ratio -BM 12-INF
Ultimate Load (kN)
a / d
Model
Experiment
Governing - Nehdi et al.
Governing - CSA Shear, 1.0
0
50
100
150
200
250
300
1.5
2.5
3.5
4.5
5.5
6.5

BM 16-INF

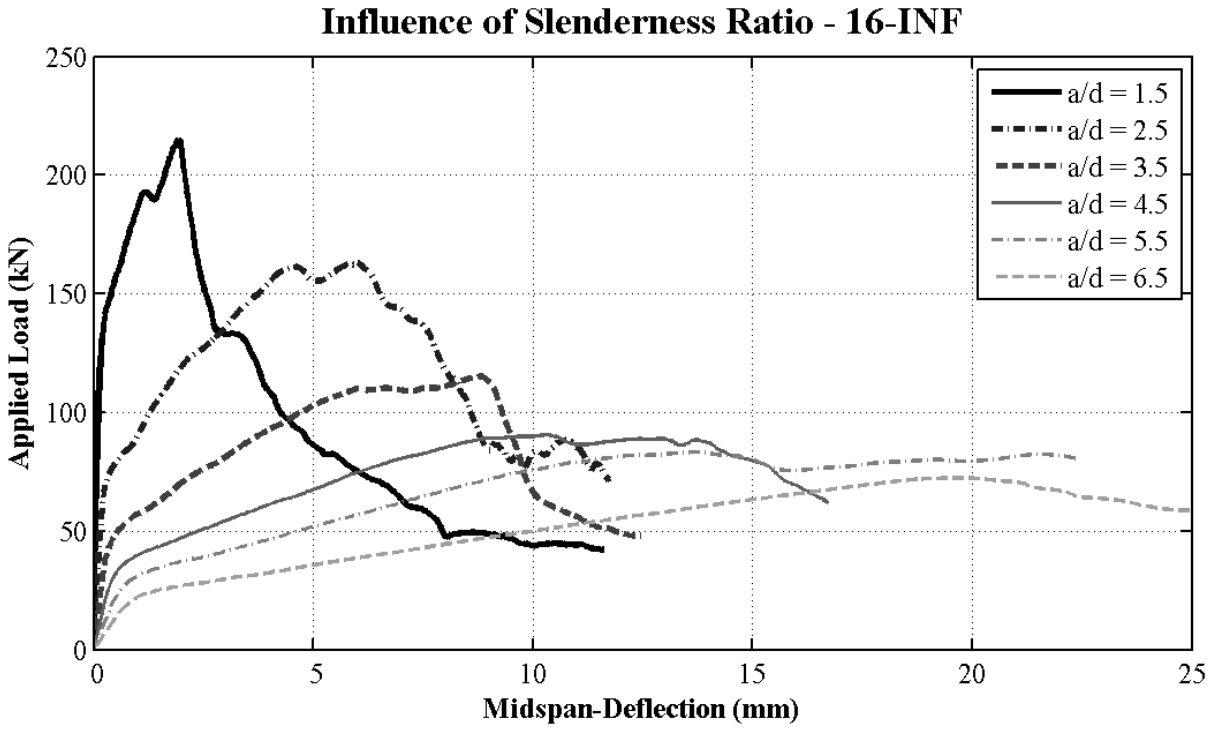
Influence of Slenderness Ratio - 16-INF
Applied Load (kN)
Midspan-Deflection (mm)
a/d = 1.5
a/d = 2.5
a/d = 3.5
a/d = 4.5
a/d = 5.5
a/d = 6.5
0
50
100
150
200
250
0
5
10
15
20
25

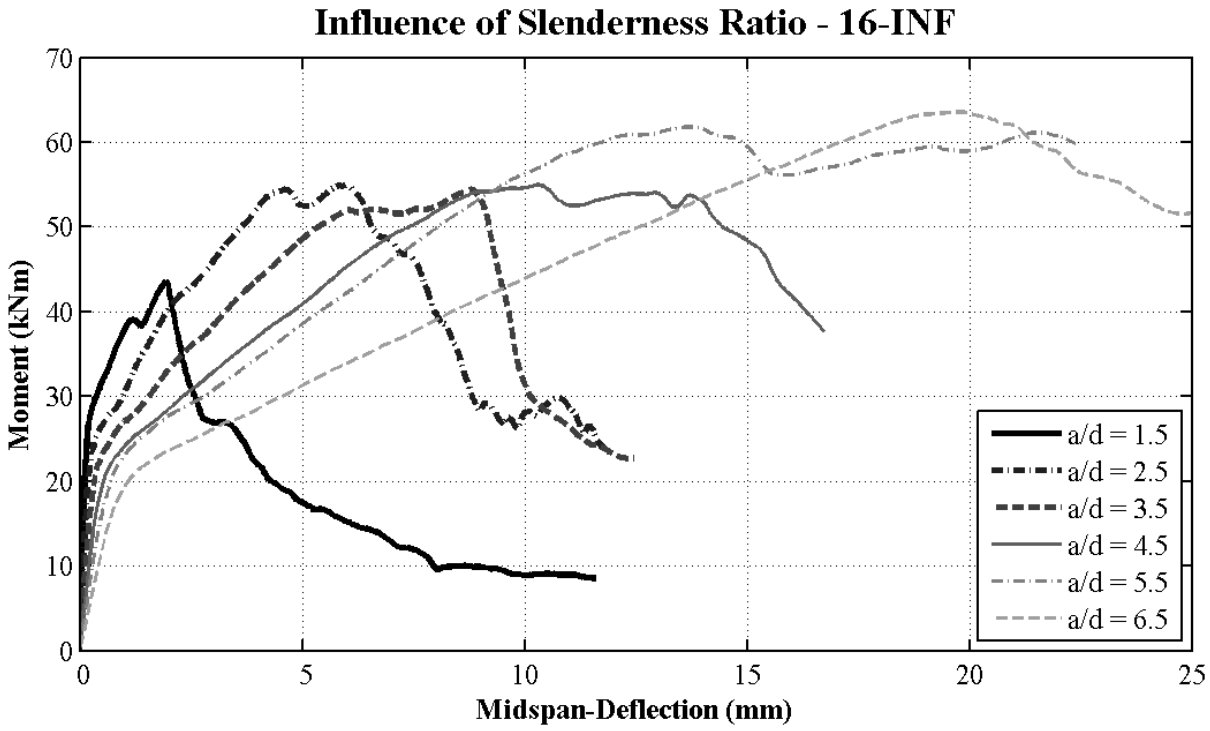
Influence of Slenderness Ratio - 16-INF
Moment (kNm)
Midspan-Deflection (mm)
a/d = 1.5
a/d = 2.5
a/d = 3.5
a/d = 4.5
a/d = 5.5
a/d = 6.5
0
10
20
30
40
50
60
70
0
5
10
15
20
25

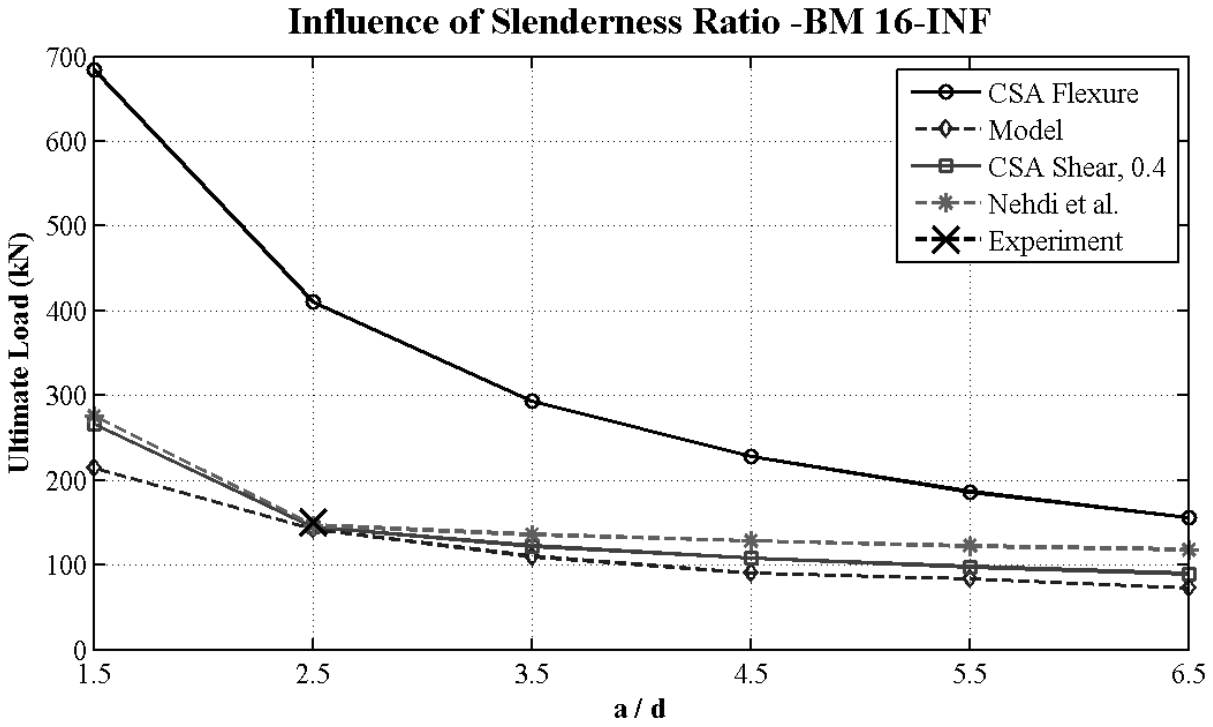
Influence of Slenderness Ratio -BM 16-INF
Ultimate Load (kN)
a / d
CSA Flexure
Model
CSA Shear, 0.4
Nehdi et al.
Experiment
0
100
200
300
400
500
600
700
1.5
2.5
3.5
4.5
5.5
6.5

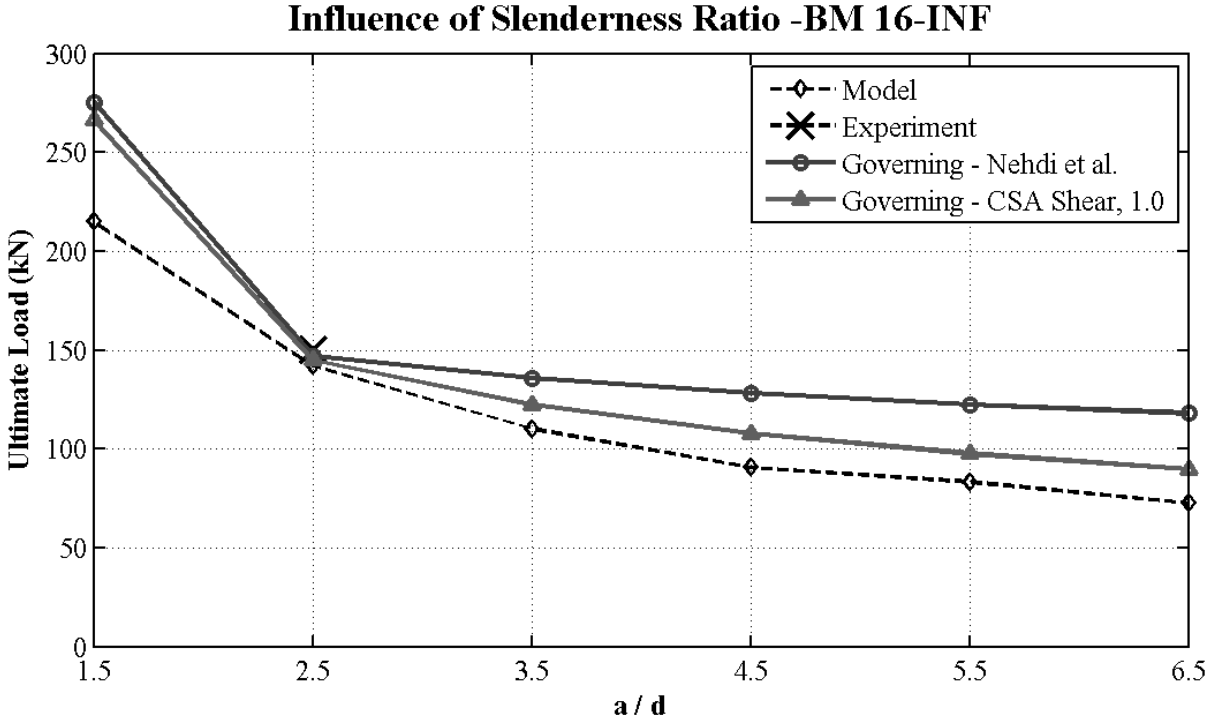
Influence of Slenderness Ratio -BM 16-INF
Ultimate Load (kN)
a / d
Model
Experiment
Governing - Nehdi et al.
Governing - CSA Shear, 1.0
0
50
100
150
200
250
300
1.5
2.5
3.5
4.5
5.5
6.5

BM 25-INF

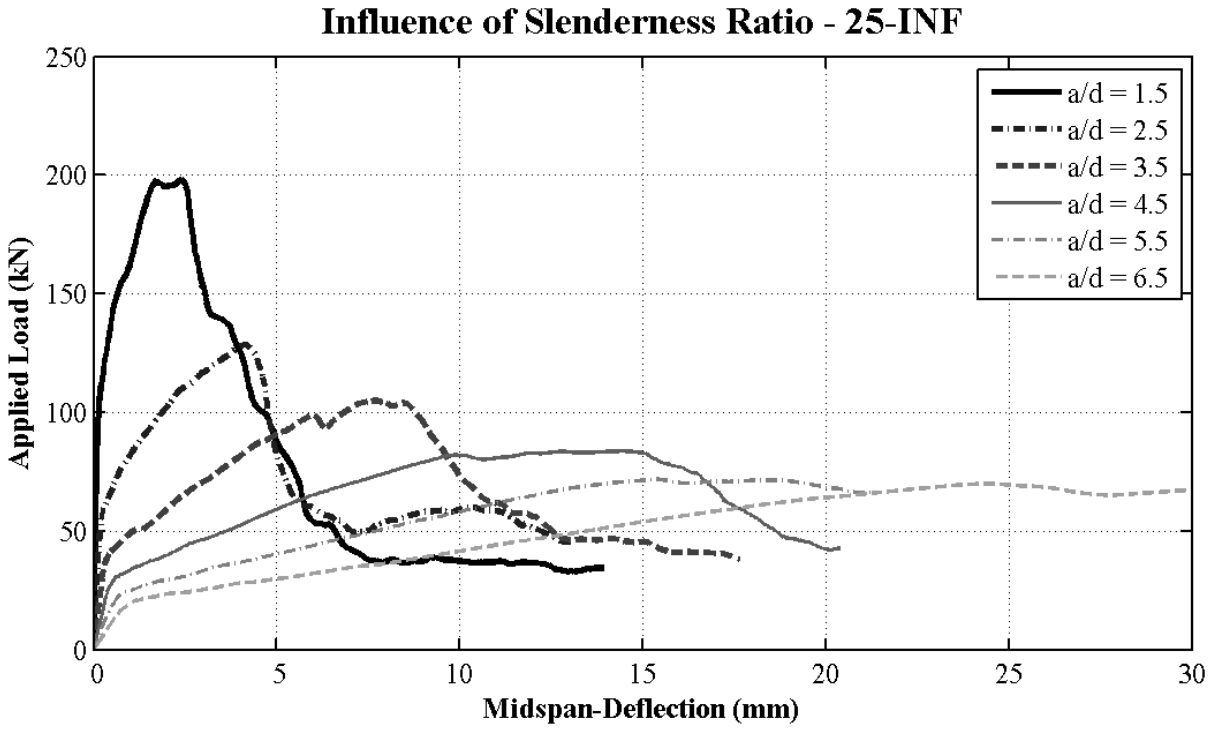
Influence of Slenderness Ratio - 25-INF
Applied Load (kN)
Midspan-Deflection (mm)
a/d = 1.5
a/d = 2.5
a/d = 3.5
a/d = 4.5
a/d = 5.5
a/d = 6.5
0
50
100
150
200
250
0
5
10
15
20
25
30

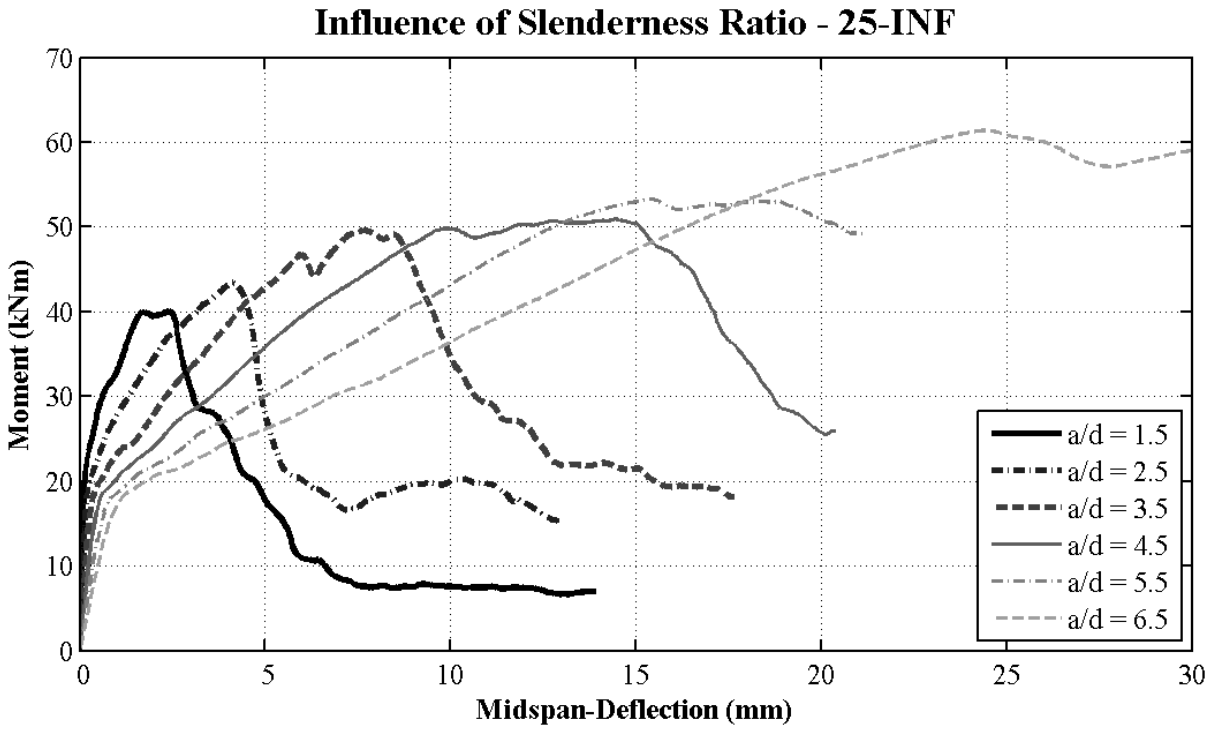
Influence of Slenderness Ratio - 25-INF
Moment (kNm)
Midspan-Deflection (mm)
a/d = 1.5
a/d = 2.5
a/d = 3.5
a/d = 4.5
a/d = 5.5
a/d = 6.5
0
10
20
30
40
50
60
70
0
5
10
15
20
25
30

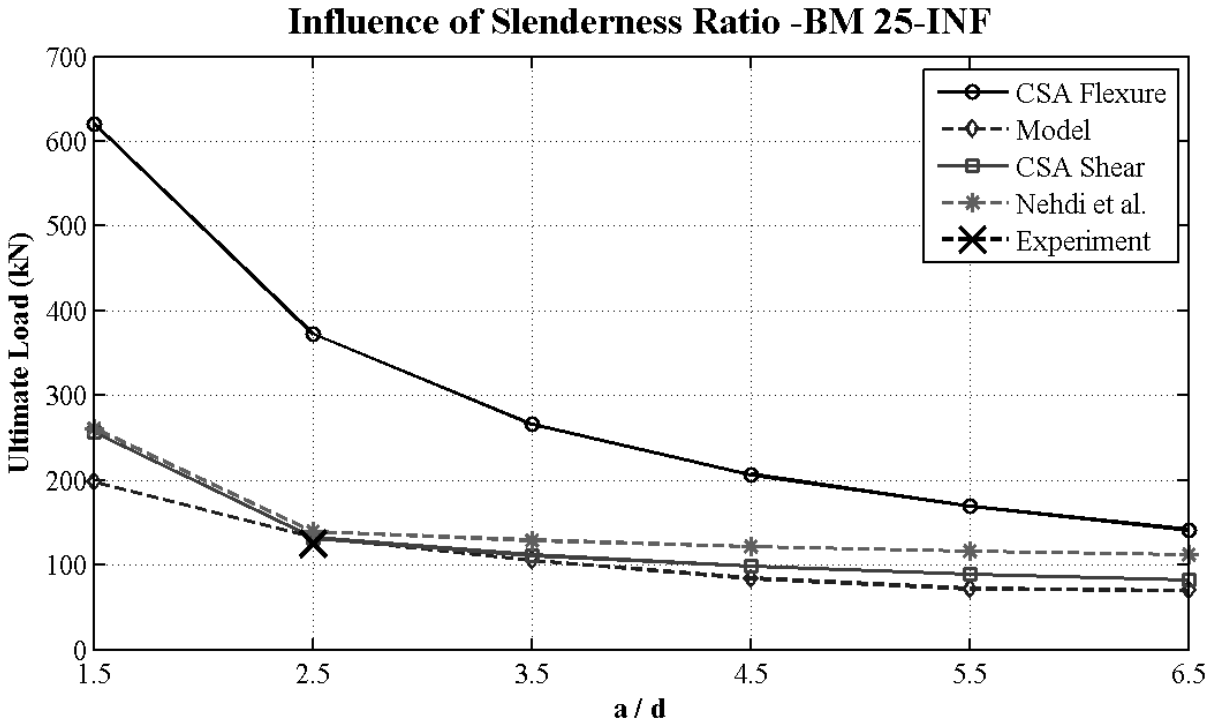
Influence of Slenderness Ratio -BM 25-INF
Ultimate Load (kN)
a / d
CSA Flexure
Model
CSA Shear
Nehdi et al.
Experiment
0
100
200
300
400
500
600
700
1.5
2.5
3.5
4.5
5.5
6.5

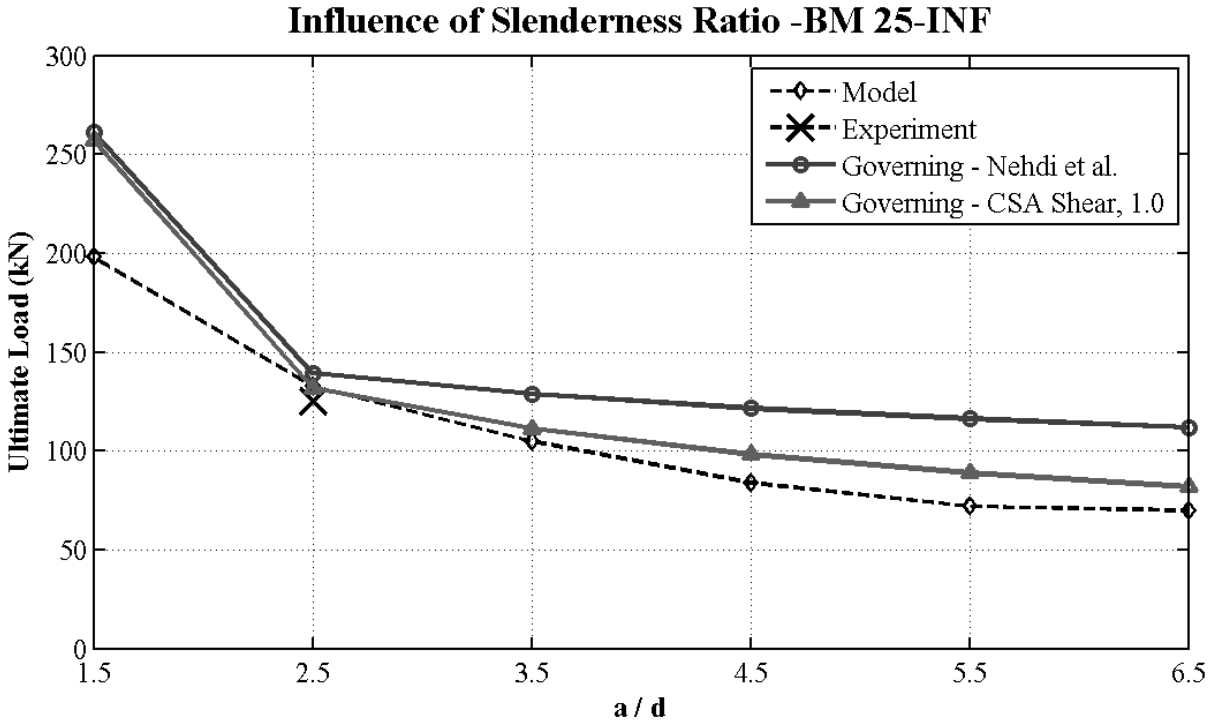
Influence of Slenderness Ratio -BM 25-INF
Ultimate Load (kN)
a / d
Model
Experiment
Governing - Nehdi et al.
Governing - CSA Shear, 1.0
0
50
100
150
200
250
300
1.5
2.5
3.5
4.5
5.5
6.5

BM 12-150

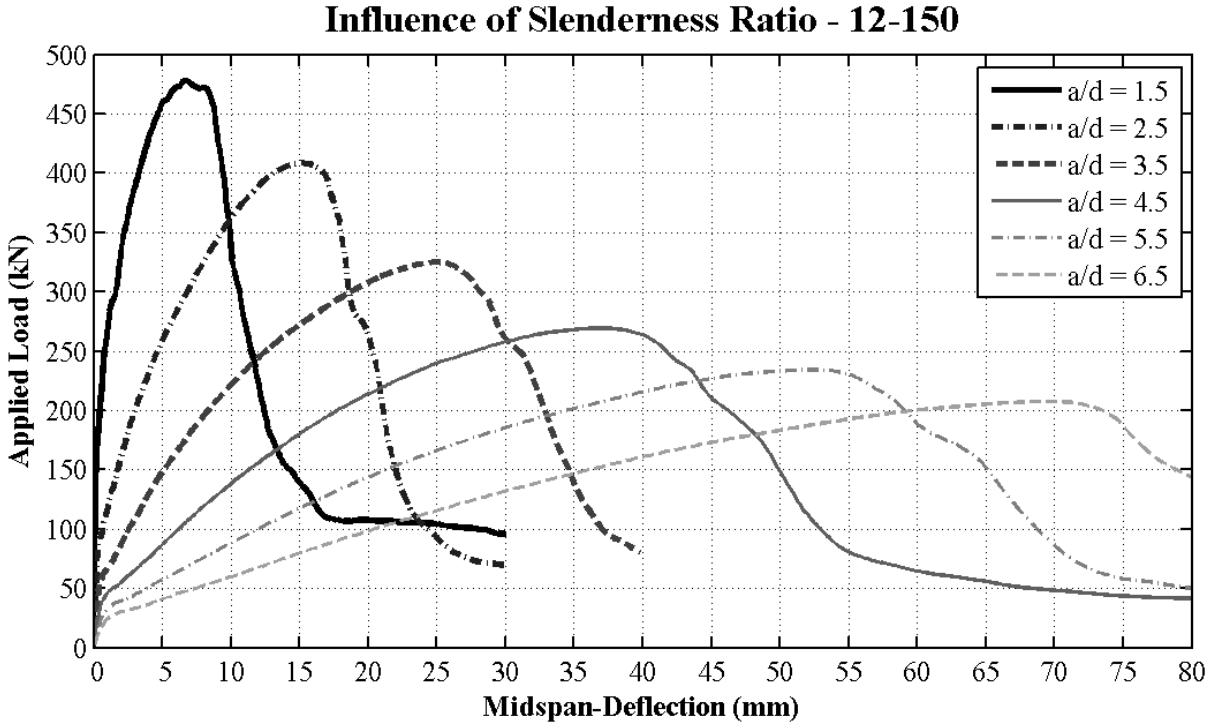
Influence of Slenderness Ratio - 12-150
Applied Load (kN)
Midspan-Deflection (mm)
a/d = 1.5
a/d = 2.5
a/d = 3.5
a/d = 4.5
a/d = 5.5
a/d = 6.5

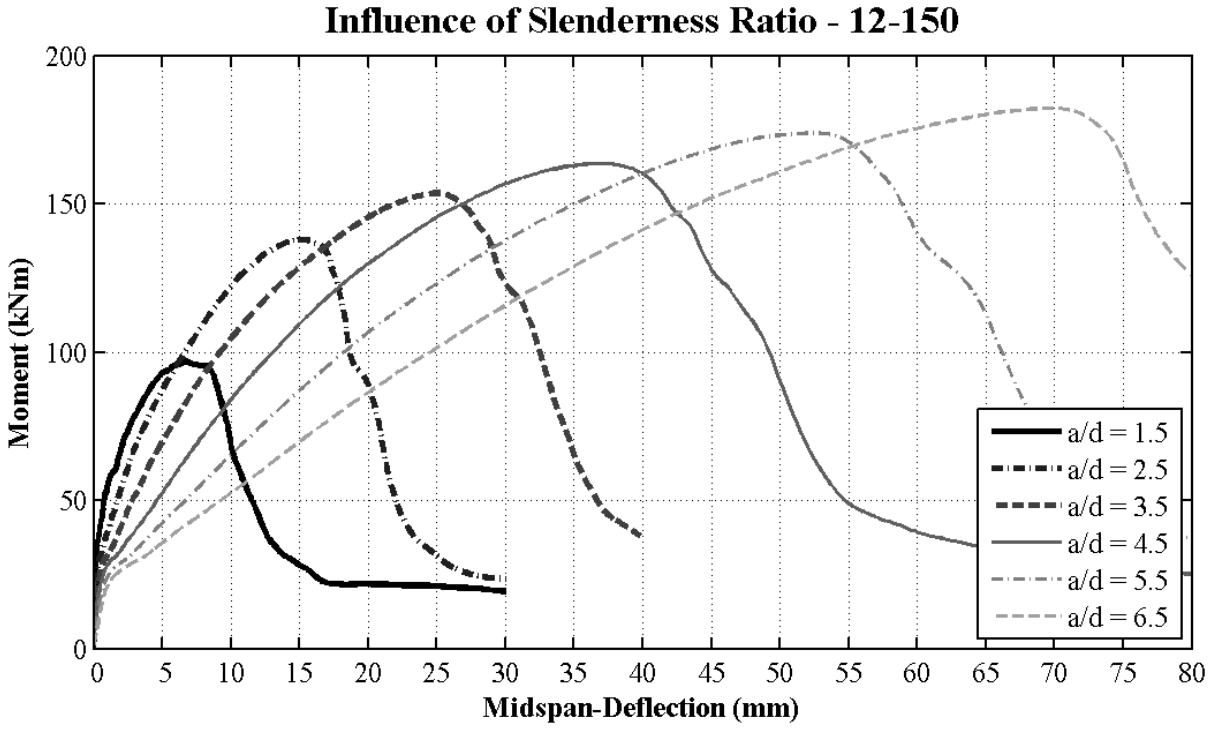
Influence of Slenderness Ratio - 12-150
Moment (kNm)
Midspan-Deflection (mm)
a/d = 1.5
a/d = 2.5
a/d = 3.5
a/d = 4.5
a/d = 5.5
a/d = 6.5

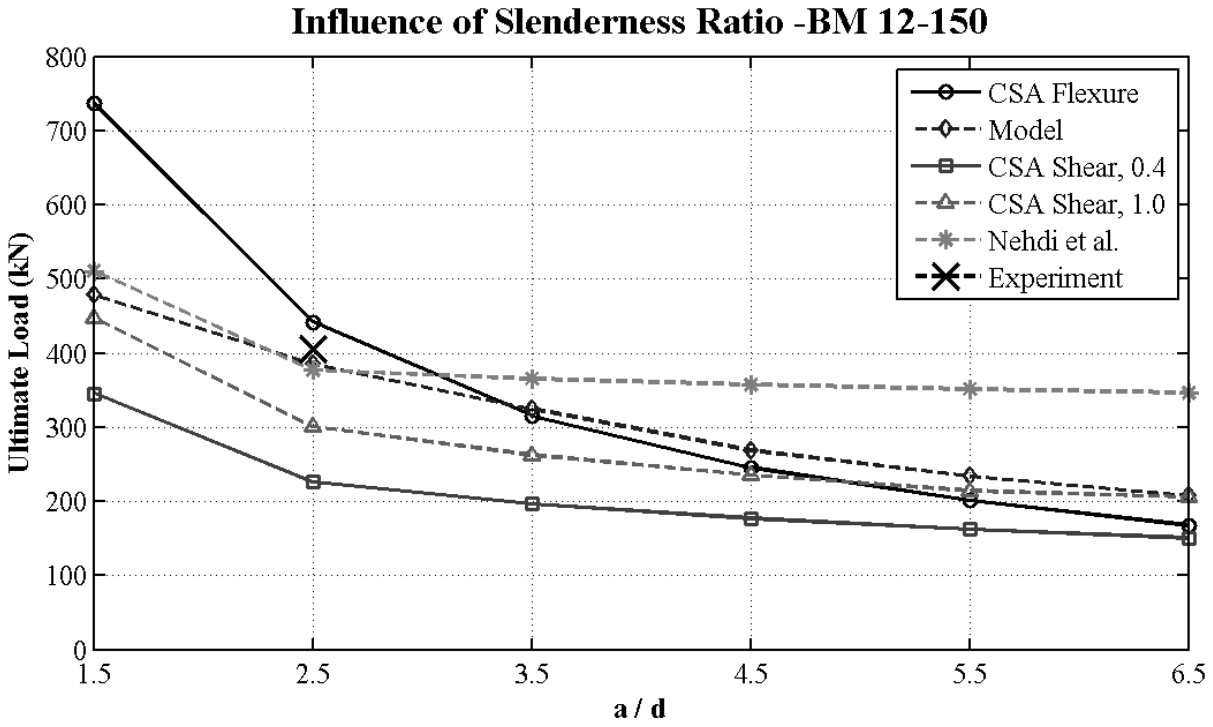
Influence of Slenderness Ratio -BM 12-150
Ultimate Load (kN)
a / d
CSA Flexure
Model
CSA Shear, 0.4
CSA Shear, 1.0
Nehdi et al.
Experiment
0
100
200
300
400
500
600
700
800
1.5
2.5
3.5
4.5
5.5
6.5

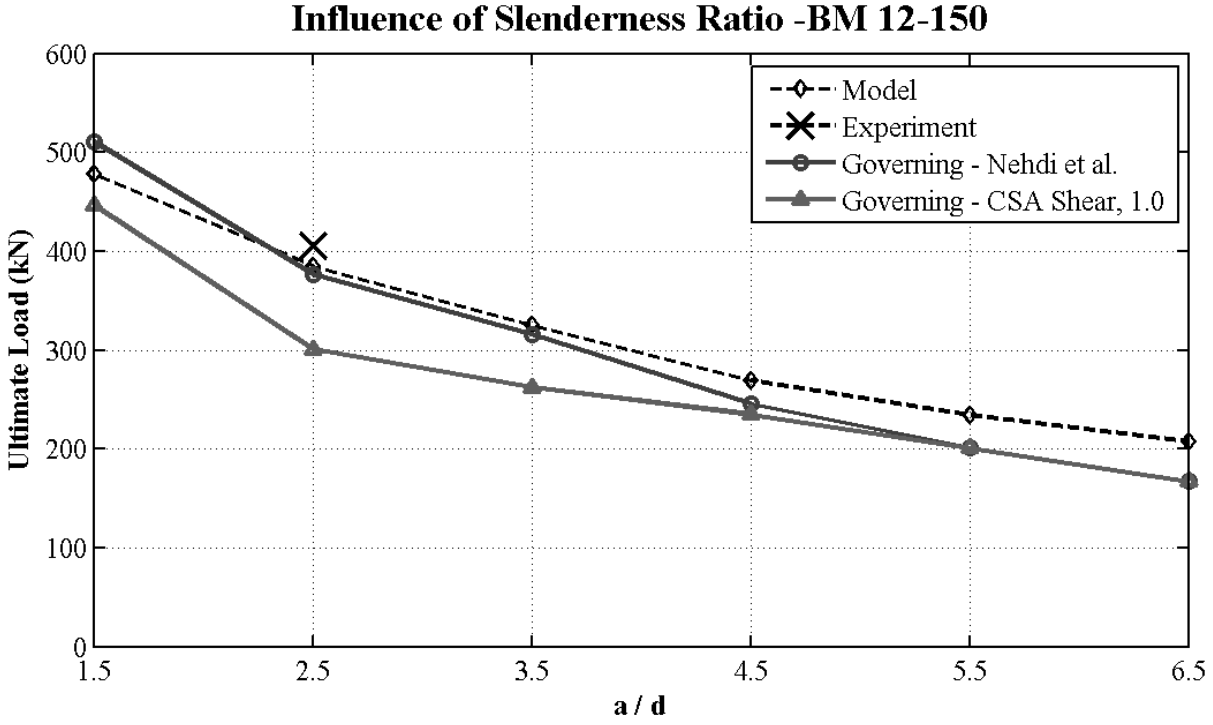
Influence of Slenderness Ratio -BM 12-150
Ultimate Load (kN)
a / d
Model
Experiment
Governing - Nehdi et al.
Governing - CSA Shear, 1.0
0
100
200
300
400
500
600
1.5
2.5
3.5
4.5
5.5
6.5

BM 16-150

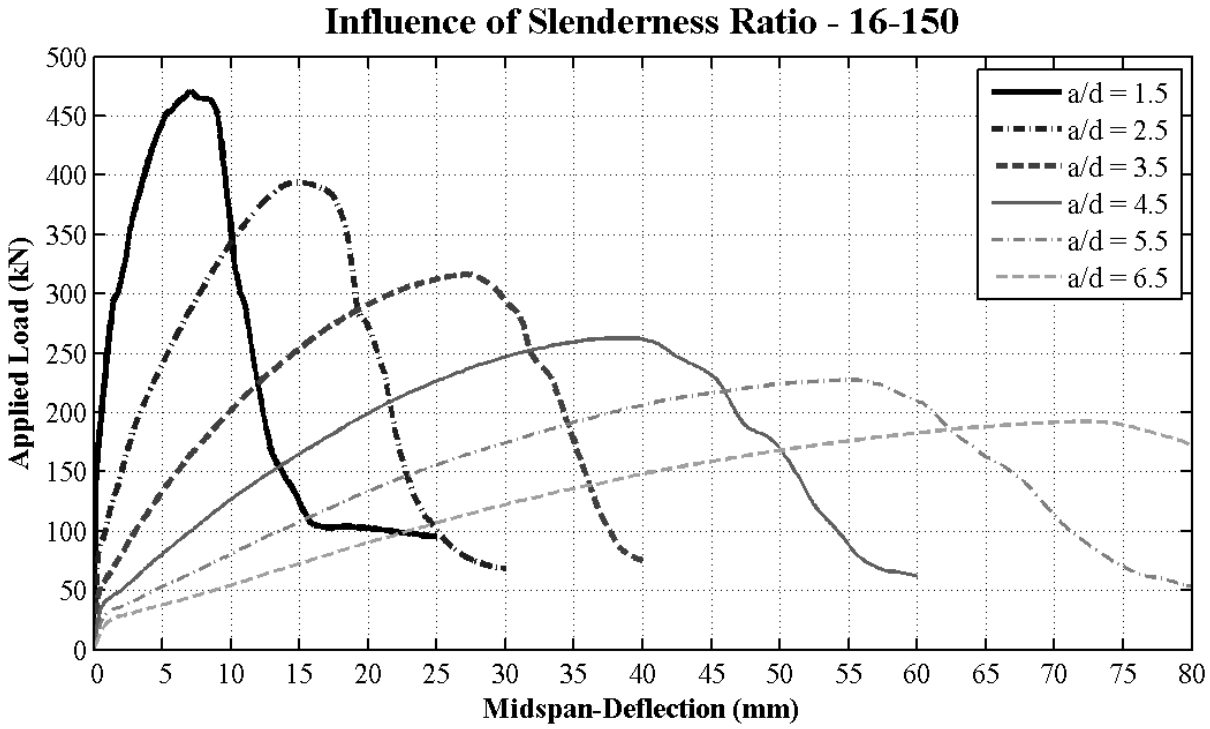
Influence of Slenderness Ratio - 16-150
Applied Load (kN)
Midspan-Deflection (mm)
a/d = 1.5
a/d = 2.5
a/d = 3.5
a/d = 4.5
a/d = 5.5
a/d = 6.5

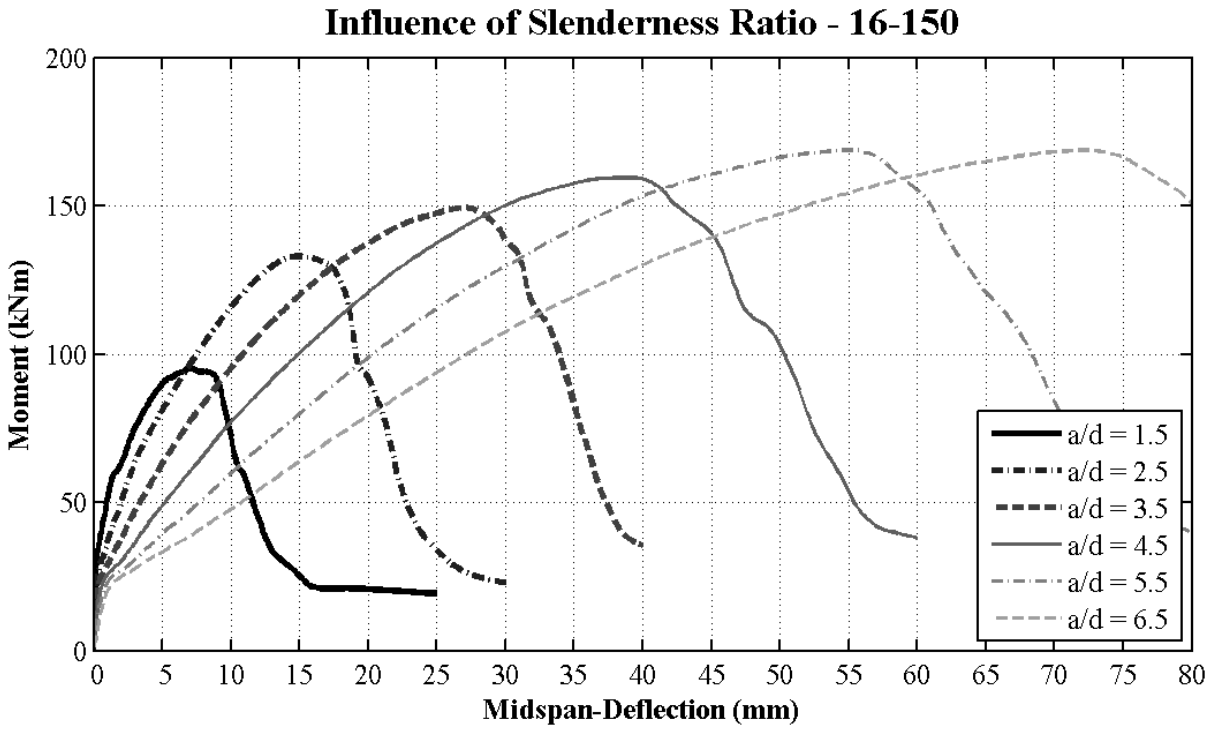
Influence of Slenderness Ratio - 16-150
Moment (kNm)
Midspan-Deflection (mm)
a/d = 1.5
a/d = 2.5
a/d = 3.5
a/d = 4.5
a/d = 5.5
a/d = 6.5

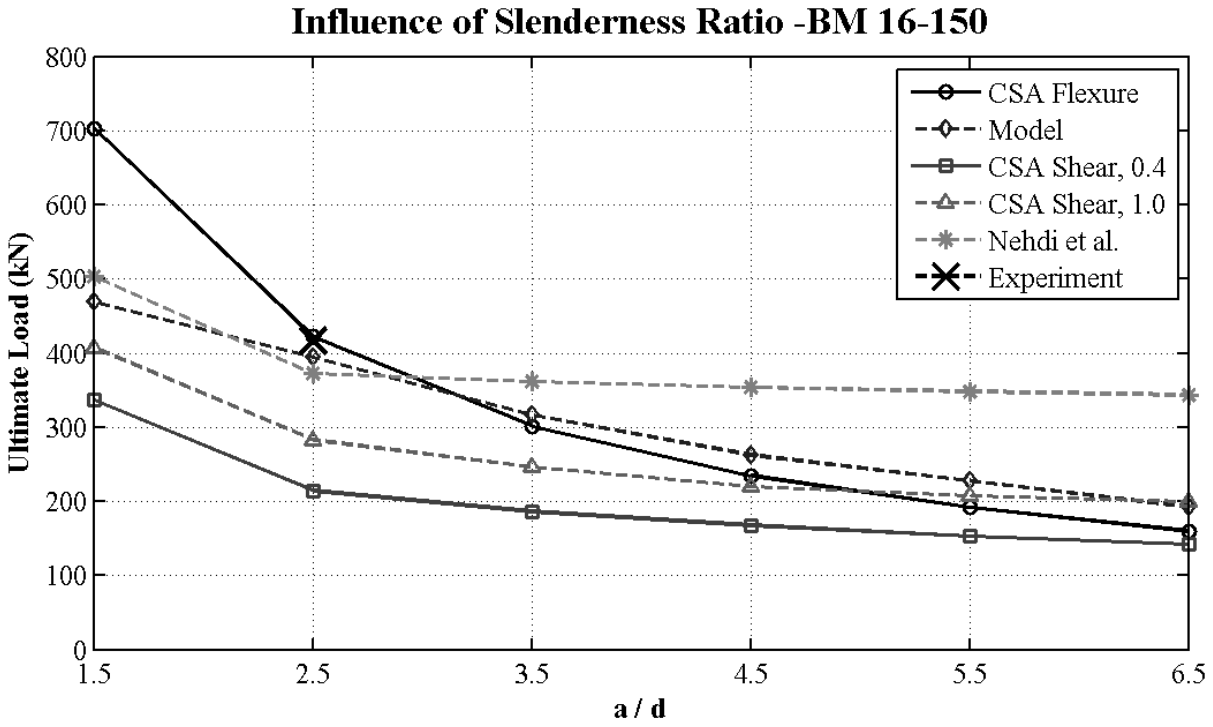
Influence of Slenderness Ratio -BM 16-150
Ultimate Load (kN)
a / d
CSA Flexure
Model
CSA Shear, 0.4
CSA Shear, 1.0
Nehdi et al.
Experiment
0
100
200
300
400
500
600
700
800
1.5
2.5
3.5
4.5
5.5
6.5

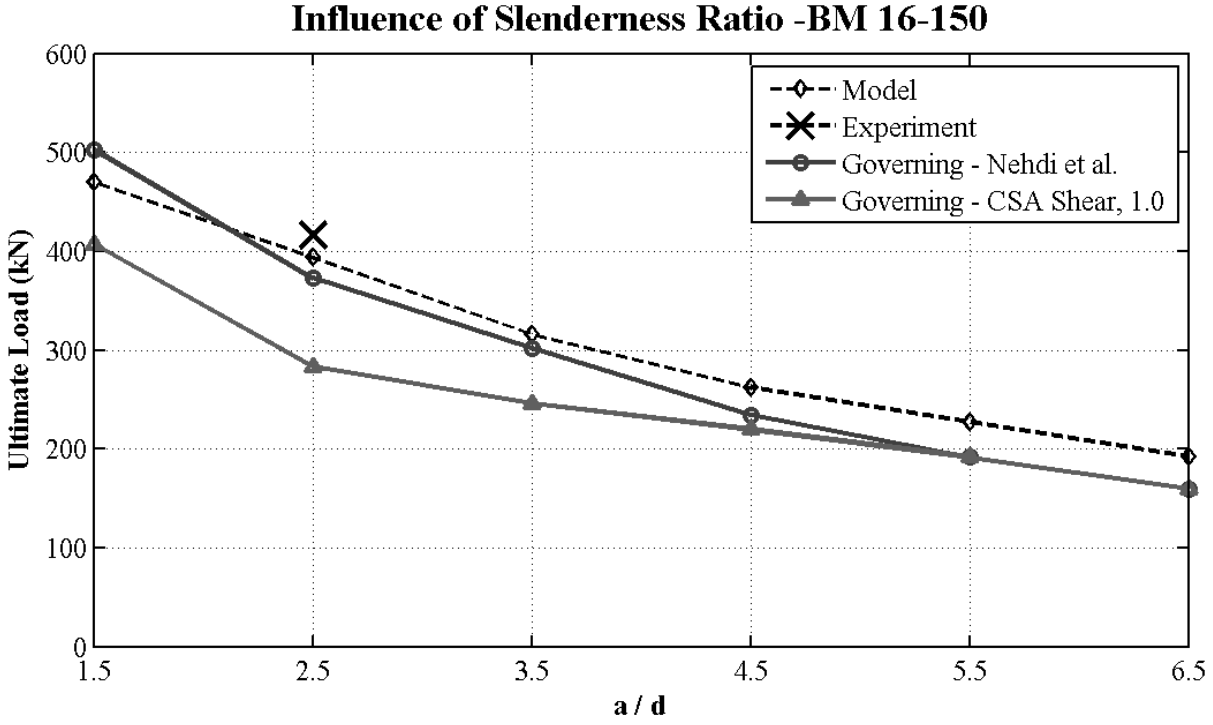
Influence of Slenderness Ratio -BM 16-150
Ultimate Load (kN)
a / d
Model
Experiment
Governing - Nehdi et al.
Governing - CSA Shear, 1.0
0
100
200
300
400
500
600
1.5
2.5
3.5
4.5
5.5
6.5

BM 25-150

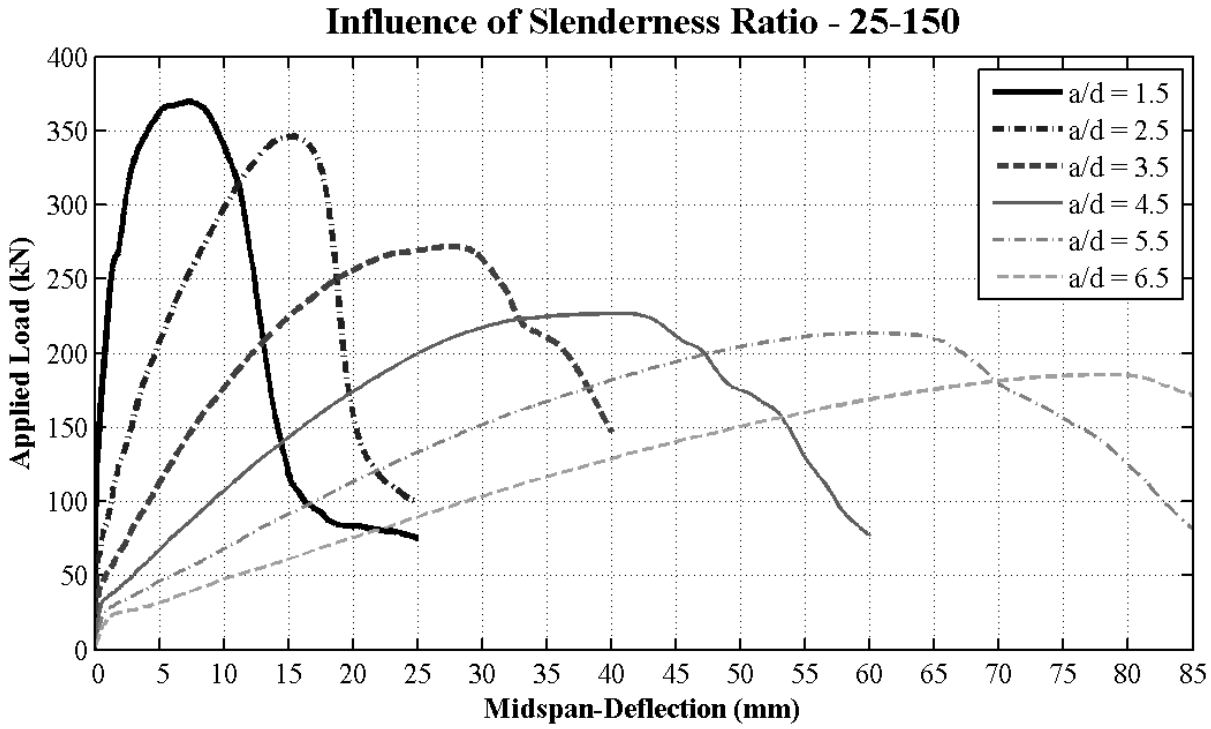
Influence of Slenderness Ratio - 25-150
Applied Load (kN)
Midspan-Deflection (mm)
a/d = 1.5
a/d = 2.5
a/d = 3.5
a/d = 4.5
a/d = 5.5
a/d = 6.5

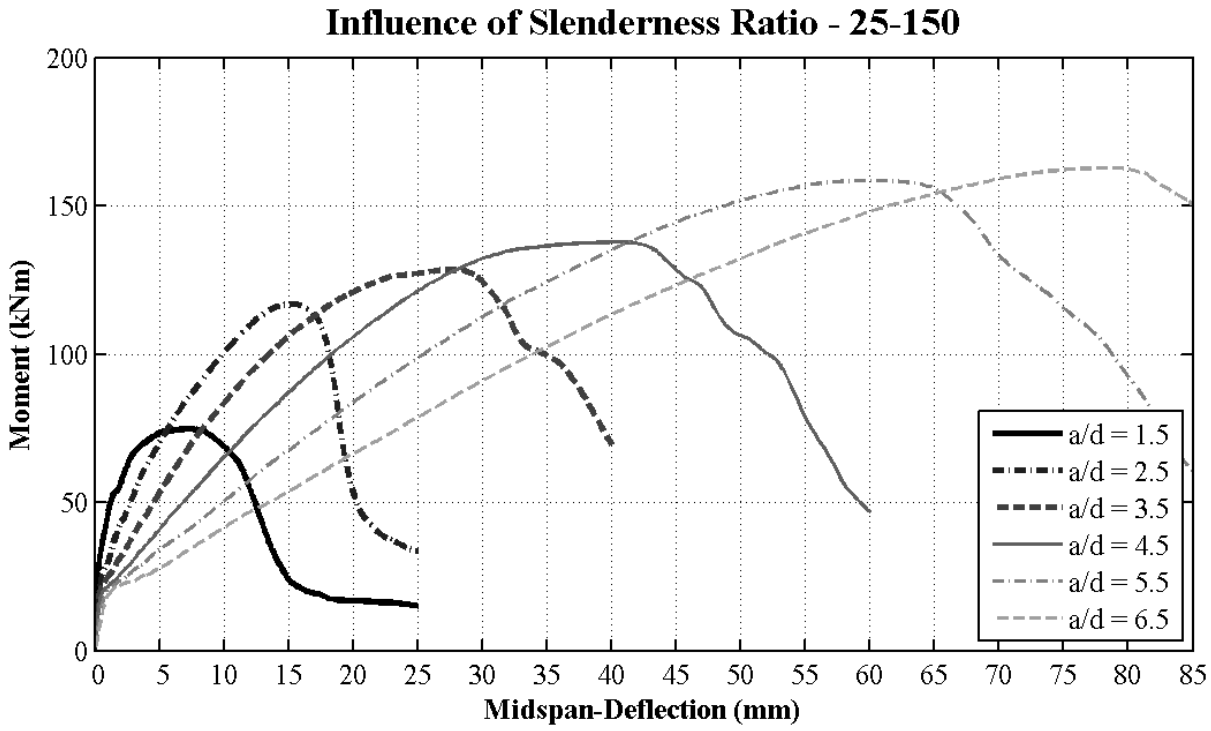
Influence of Slenderness Ratio - 25-150
Moment (kNm)
Midspan-Deflection (mm)
a/d = 1.5
a/d = 2.5
a/d = 3.5
a/d = 4.5
a/d = 5.5
a/d = 6.5

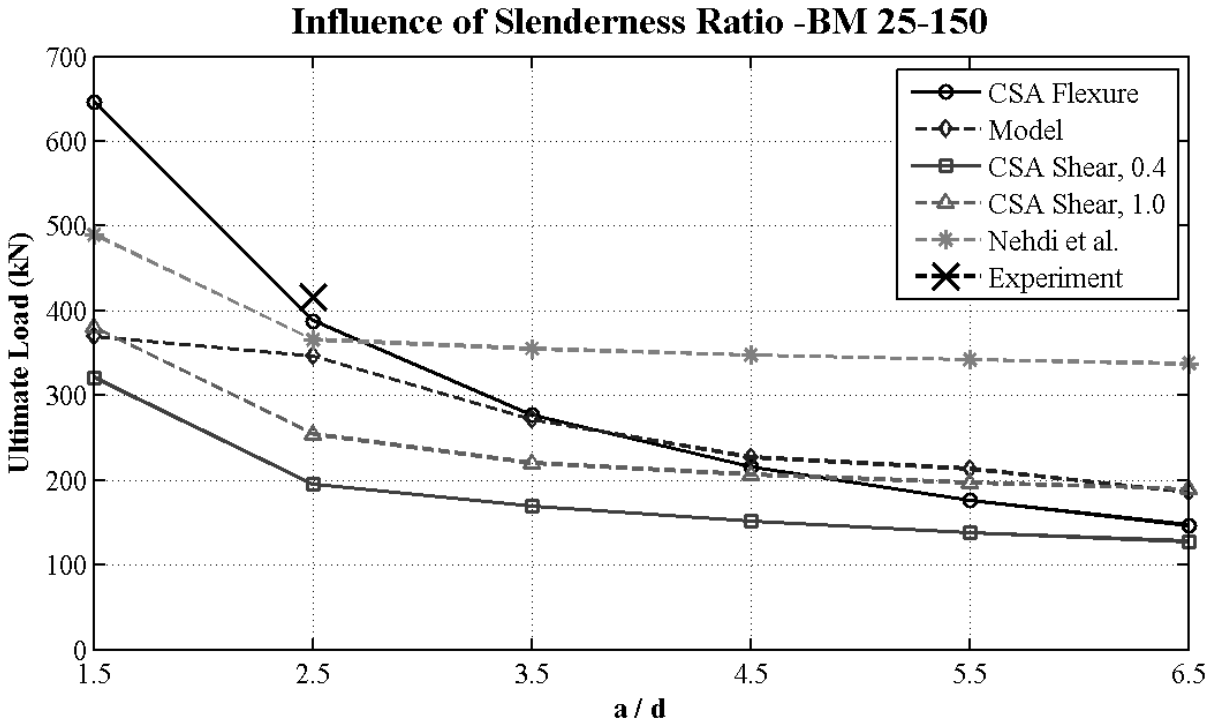
Influence of Slenderness Ratio -BM 25-150
Ultimate Load (kN)
a / d
CSA Flexure
Model
CSA Shear, 0.4
CSA Shear, 1.0
Nehdi et al.
Experiment
0
100
200
300
400
500
600
700
1.5
2.5
3.5
4.5
5.5
6.5

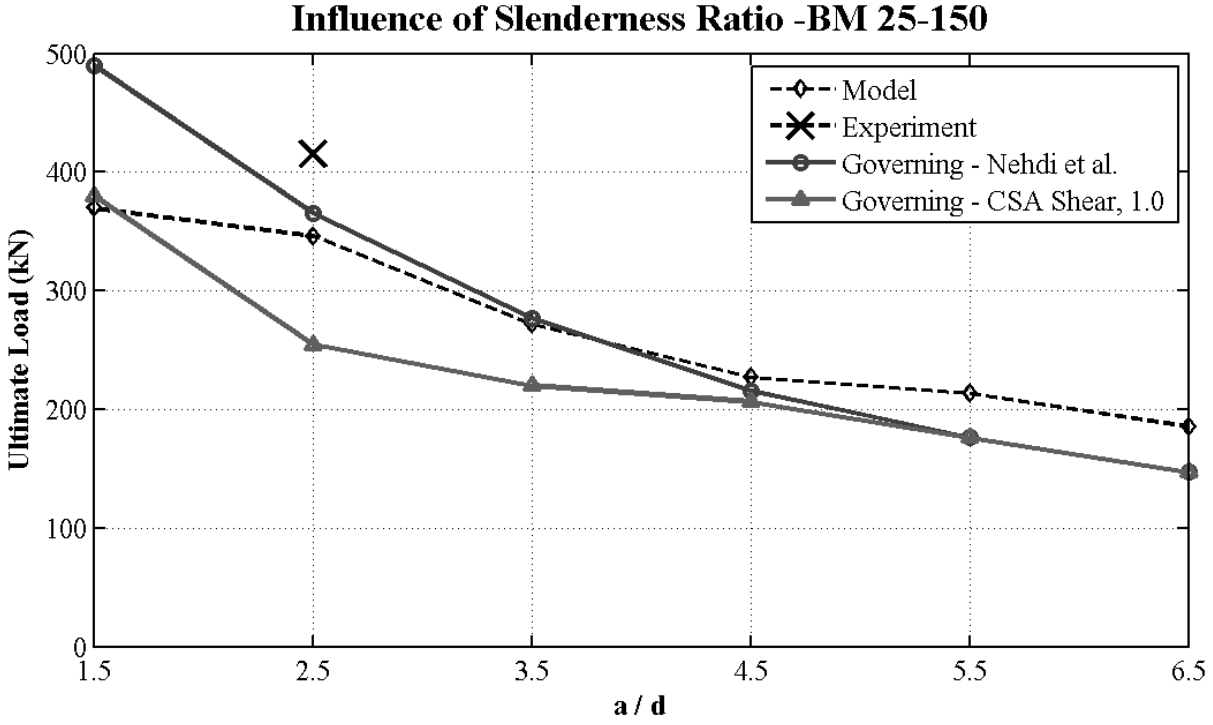
Influence of Slenderness Ratio -BM 25-150
Ultimate Load (kN)
a / d
Model
Experiment
Governing - Nehdi et al.
Governing - CSA Shear, 1.0
0
100
200
300
400
500
1.5
2.5
3.5
4.5
5.5
6.5

BM 12-220

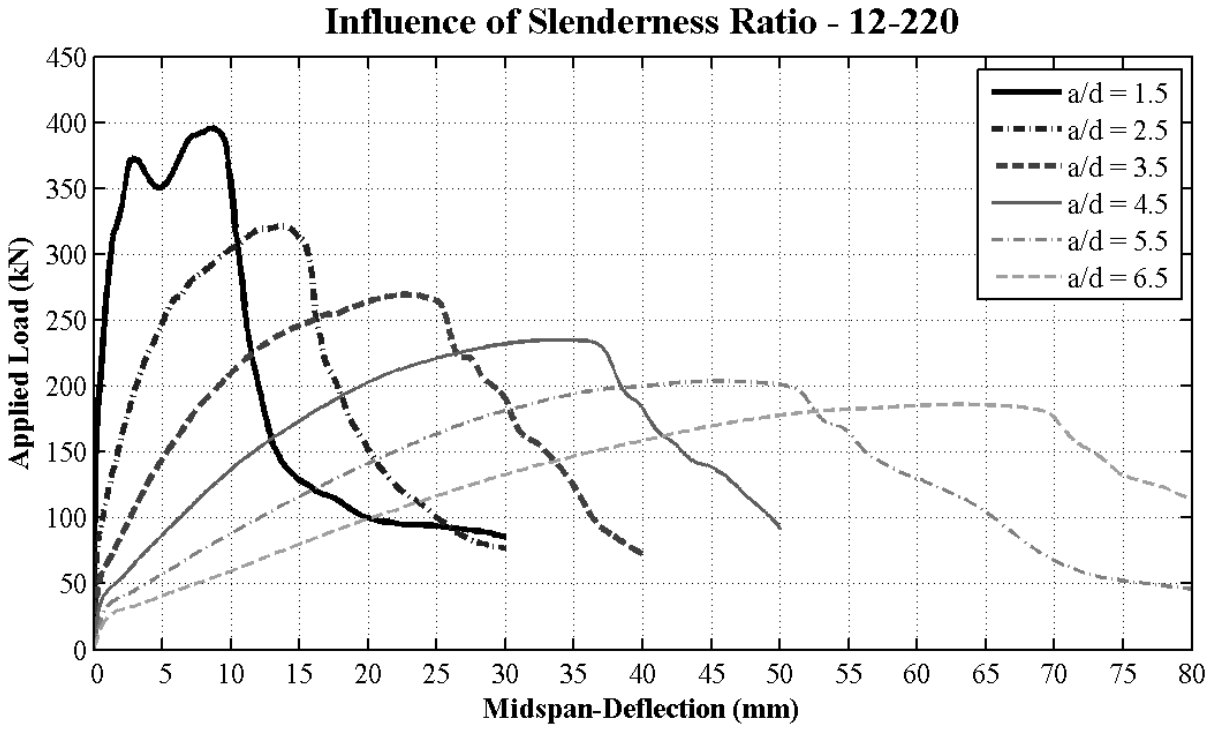
Influence of Slenderness Ratio - 12-220
Applied Load (kN)
Midspan-Deflection (mm)
a/d = 1.5
a/d = 2.5
a/d = 3.5
a/d = 4.5
a/d = 5.5
a/d = 6.5

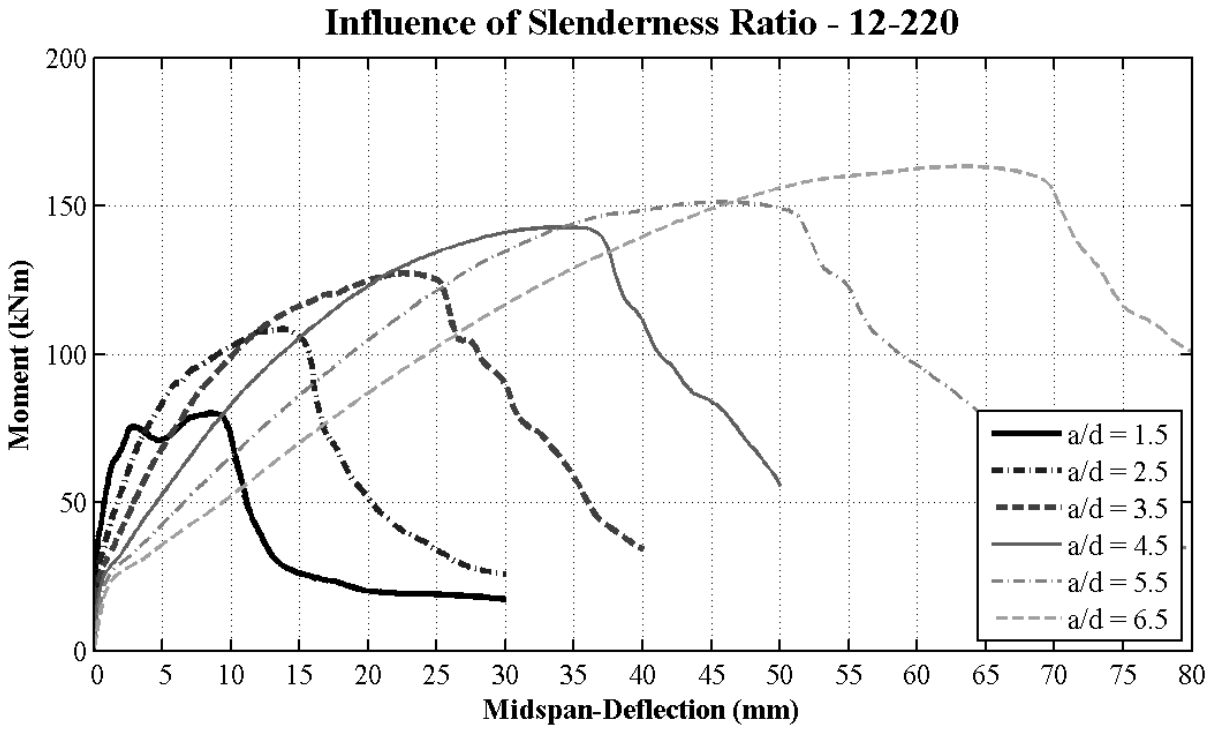
Influence of Slenderness Ratio - 12-220
Moment (kNm)
Midspan-Deflection (mm)
a/d = 1.5
a/d = 2.5
a/d = 3.5
a/d = 4.5
a/d = 5.5
a/d = 6.5

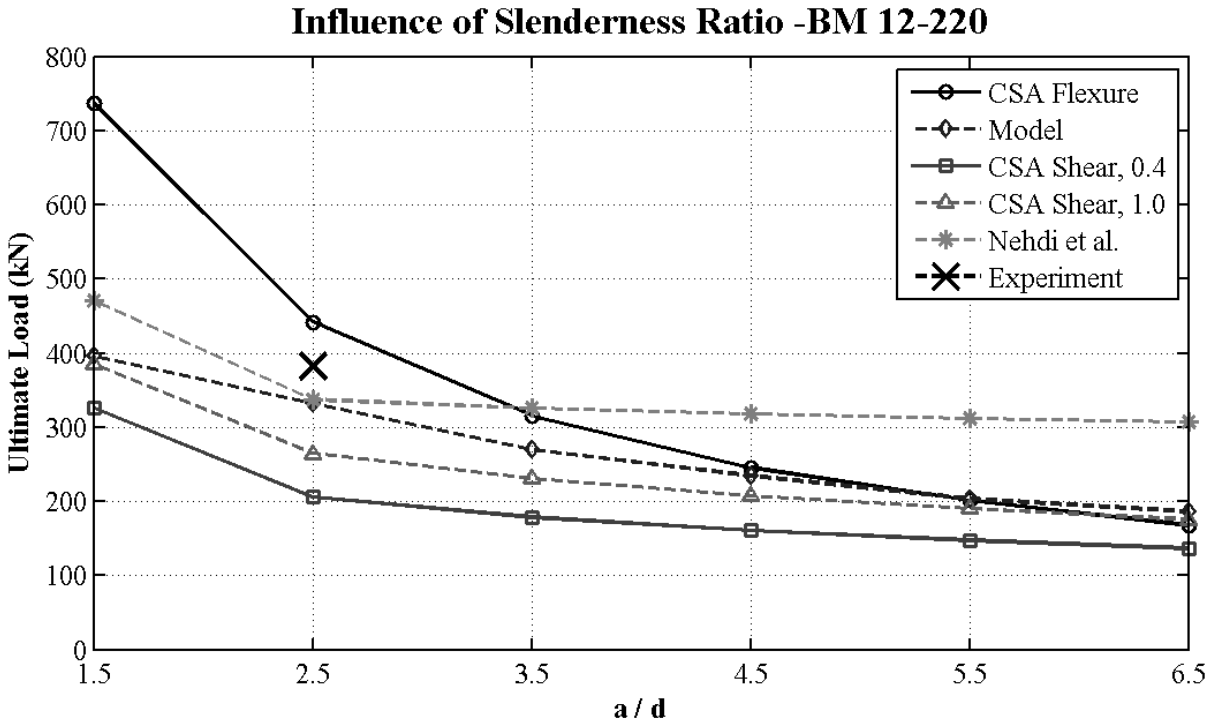
Influence of Slenderness Ratio -BM 12-220
Ultimate Load (kN)
a / d
CSA Flexure
Model
CSA Shear, 0.4
CSA Shear, 1.0
Nehdi et al.
Experiment
0
100
200
300
400
500
600
700
800
1.5
2.5
3.5
4.5
5.5
6.5

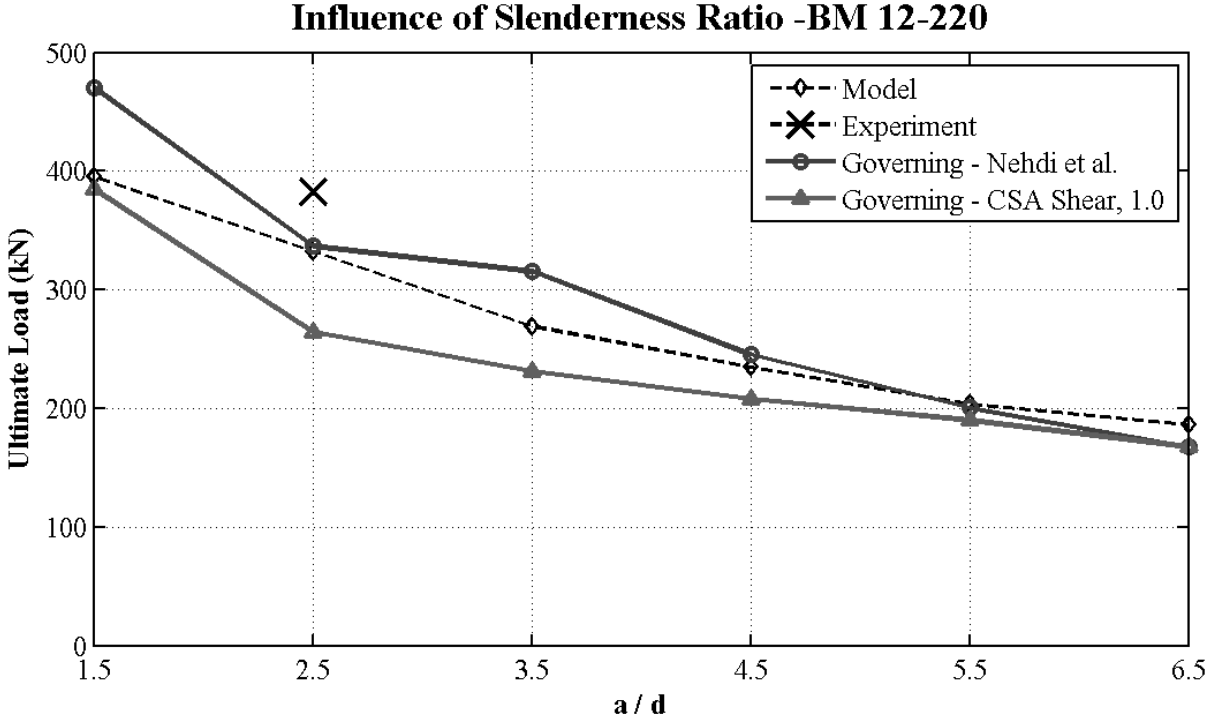
Influence of Slenderness Ratio -BM 12-220
Ultimate Load (kN)
a / d
Model
Experiment
Governing - Nehdi et al.
Governing - CSA Shear, 1.0
0
100
200
300
400
500
1.5
2.5
3.5
4.5
5.5
6.5

BM 16-220

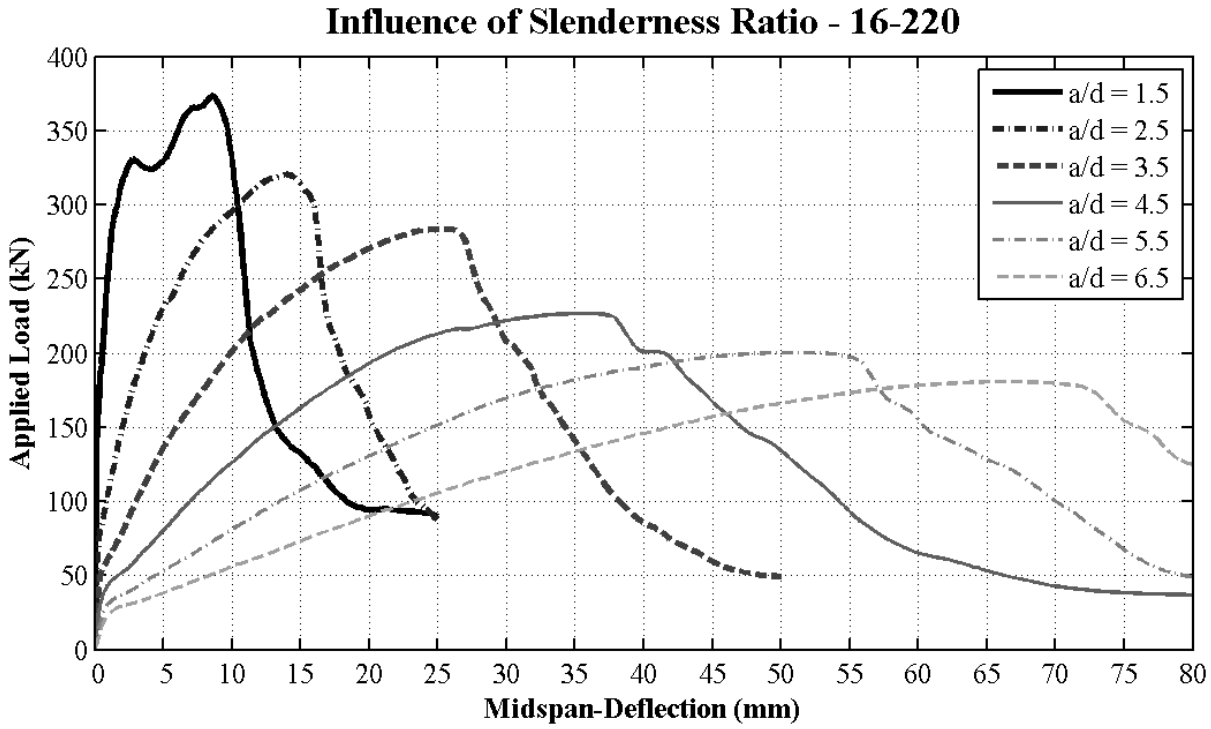
Influence of Slenderness Ratio - 16-220
Applied Load (kN)
Midspan-Deflection (mm)
a/d = 1.5
a/d = 2.5
a/d = 3.5
a/d = 4.5
a/d = 5.5
a/d = 6.5

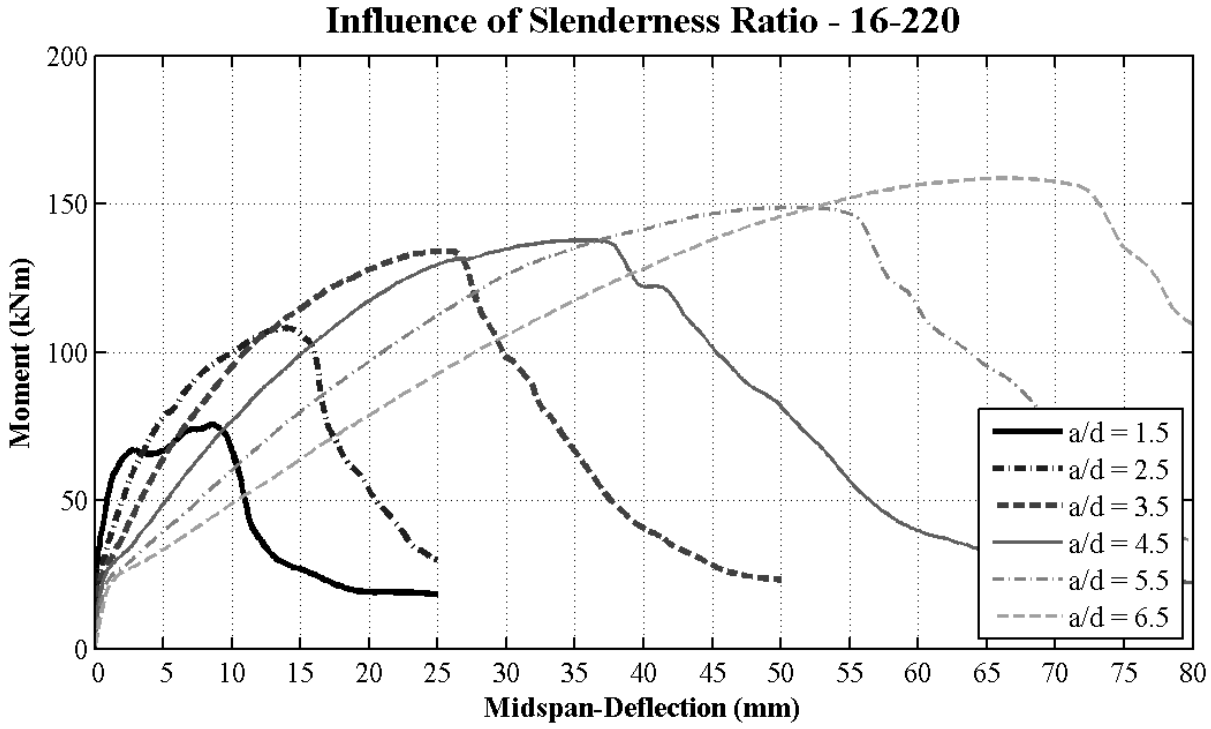
Influence of Slenderness Ratio - 16-220
Moment (kNm)
Midspan-Deflection (mm)
a/d = 1.5
a/d = 2.5
a/d = 3.5
a/d = 4.5
a/d = 5.5
a/d = 6.5

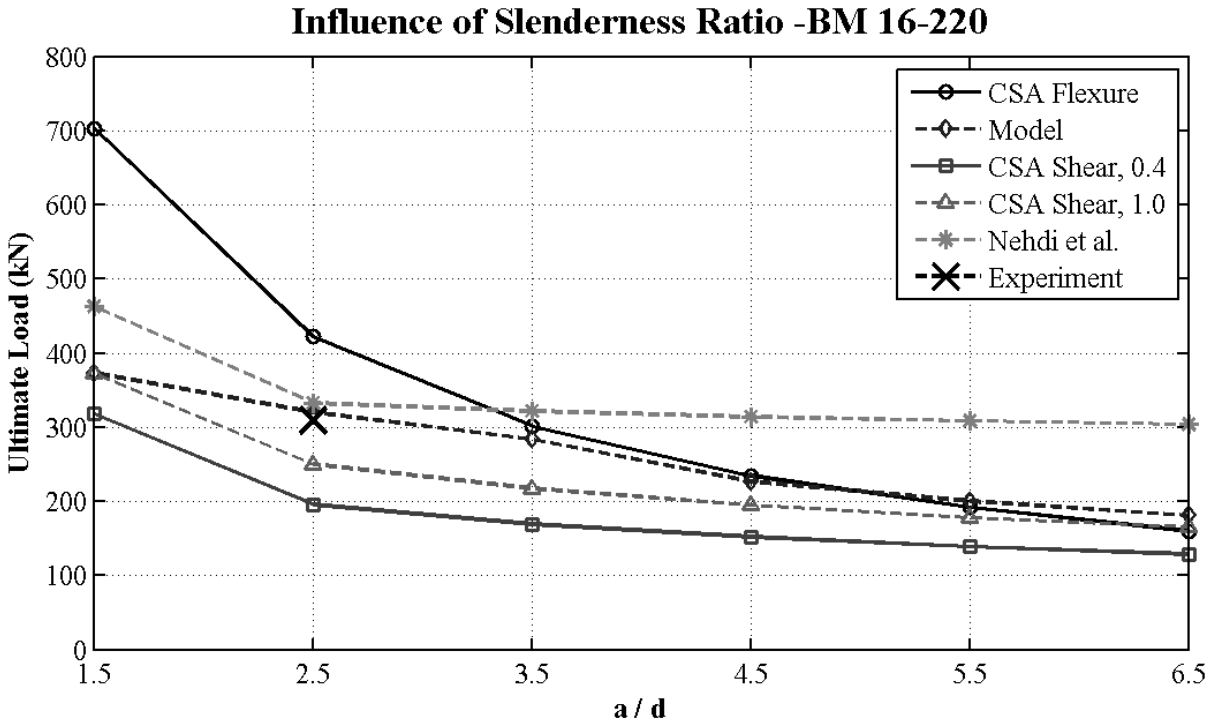
Influence of Slenderness Ratio -BM 16-220
Ultimate Load (kN)
a / d
CSA Flexure
Model
CSA Shear, 0.4
CSA Shear, 1.0
Nehdi et al.
Experiment
0
100
200
300
400
500
600
700
800
1.5
2.5
3.5
4.5
5.5
6.5

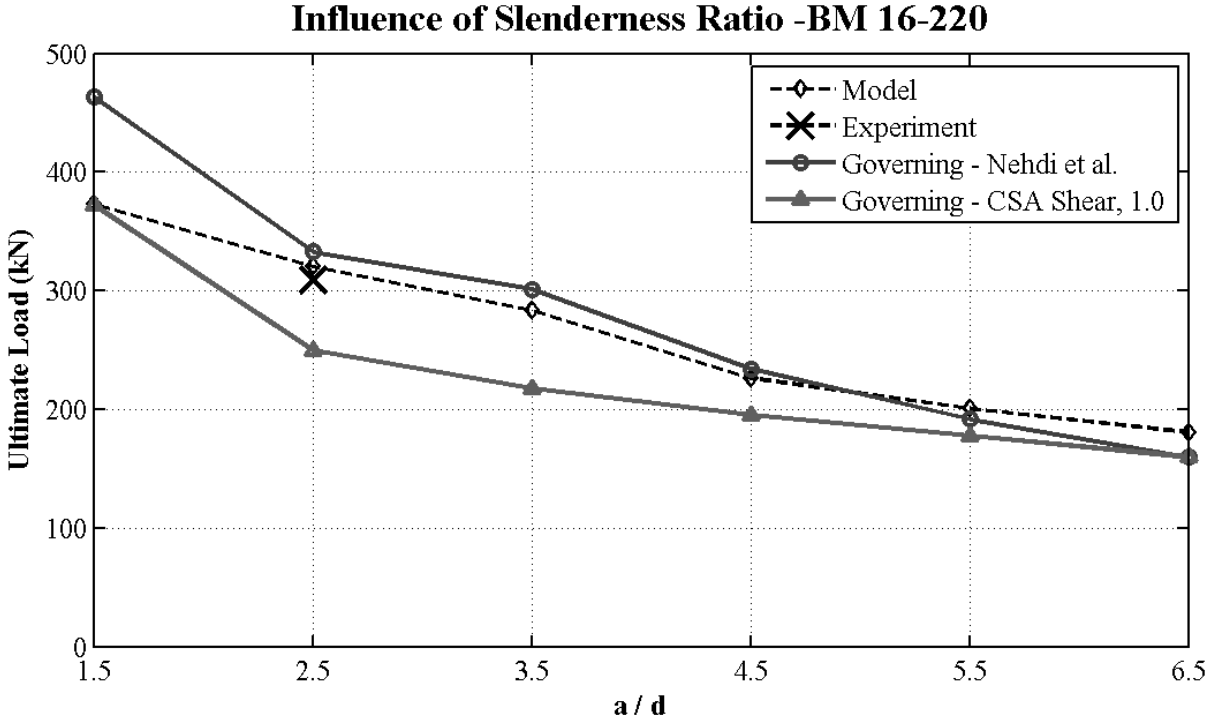
Influence of Slenderness Ratio -BM 16-220
Ultimate Load (kN)
a / d
Model
Experiment
Governing - Nehdi et al.
Governing - CSA Shear, 1.0
0
100
200
300
400
500
1.5
2.5
3.5
4.5
5.5
6.5

BM 25-220

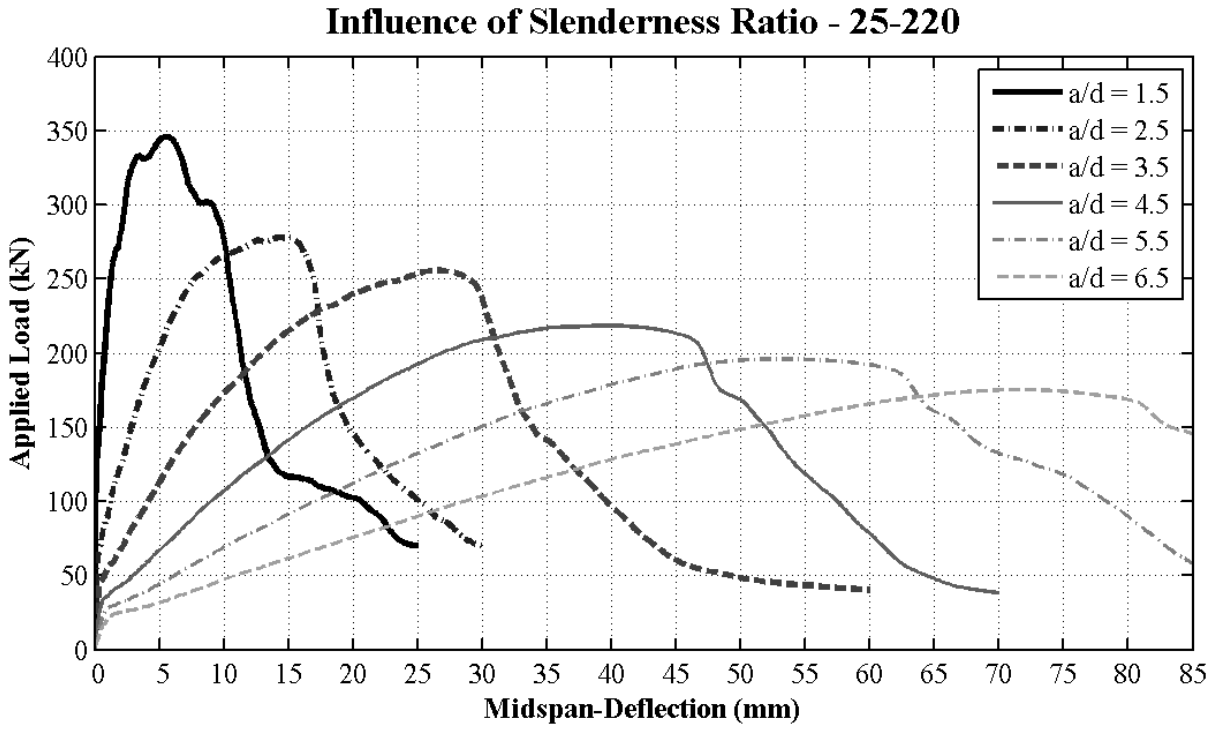
Influence of Slenderness Ratio - 25-220
Applied Load (kN)
Midspan-Deflection (mm)
a/d = 1.5
a/d = 2.5
a/d = 3.5
a/d = 4.5
a/d = 5.5
a/d = 6.5

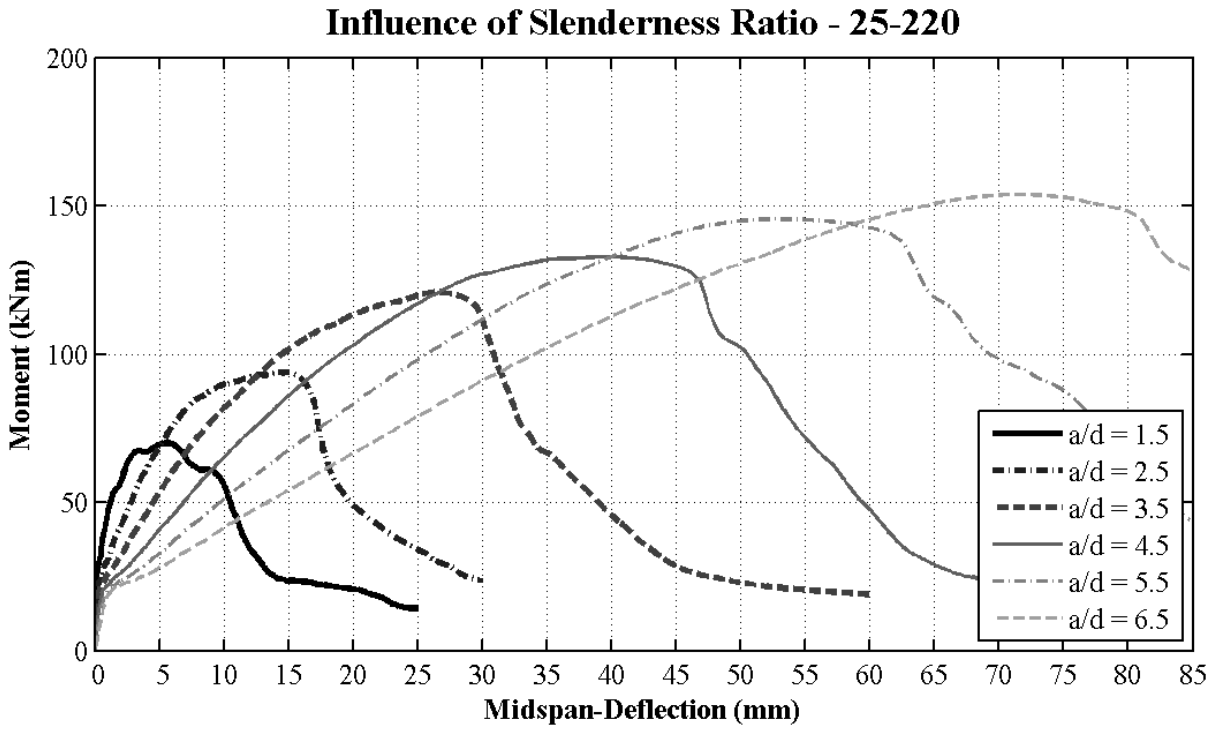
Influence of Slenderness Ratio - 25-220
Moment (kNm)
Midspan-Deflection (mm)
a/d = 1.5
a/d = 2.5
a/d = 3.5
a/d = 4.5
a/d = 5.5
a/d = 6.5

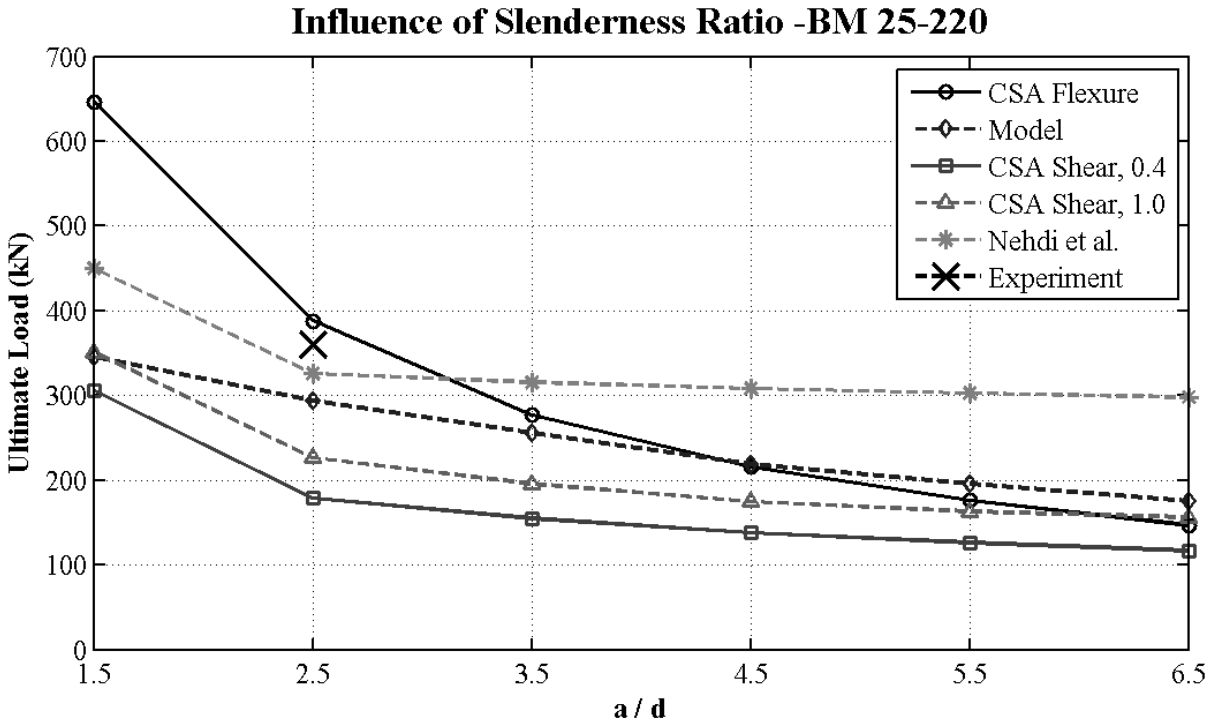
Influence of Slenderness Ratio -BM 25-220
Ultimate Load (kN)
a / d
CSA Flexure
Model
CSA Shear, 0.4
CSA Shear, 1.0
Nehdi et al.
Experiment
0
100
200
300
400
500
600
700
1.5
2.5
3.5
4.5
5.5
6.5

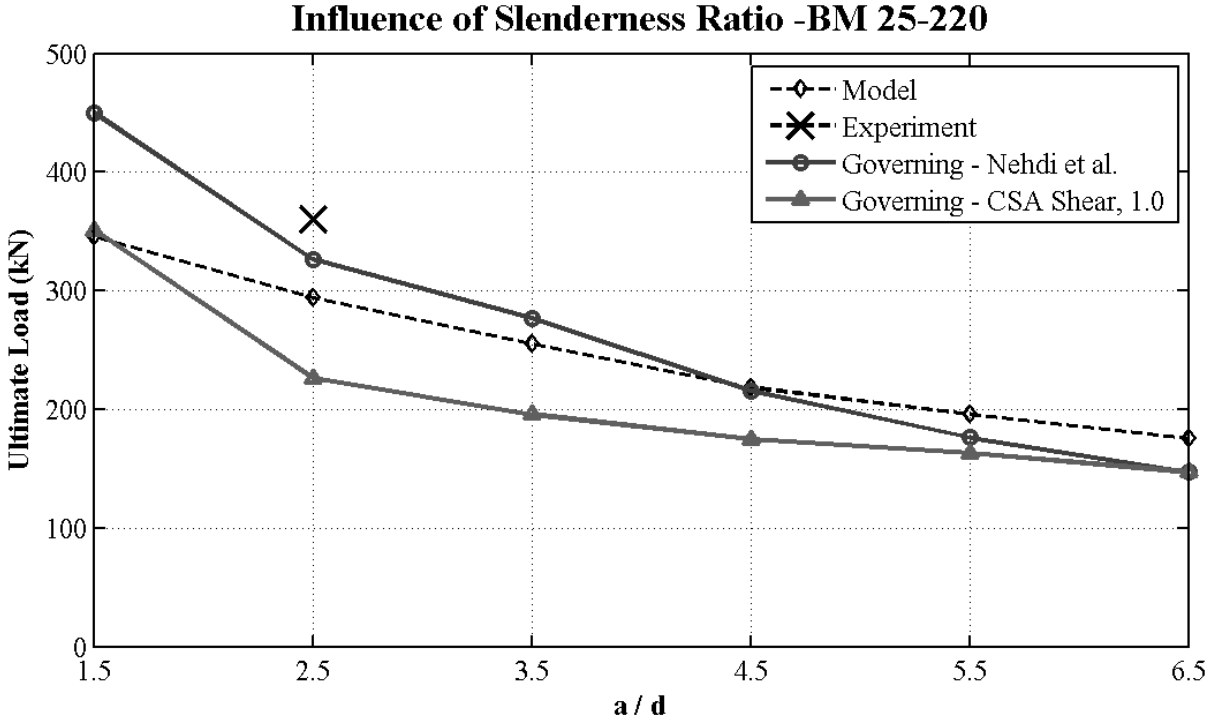
Influence of Slenderness Ratio -BM 25-220
Ultimate Load (kN)
a / d
Model
Experiment
Governing - Nehdi et al.
Governing - CSA Shear, 1.0
0
100
200
300
400
500
1.5
2.5
3.5
4.5
5.5
6.5

BM 12-s230

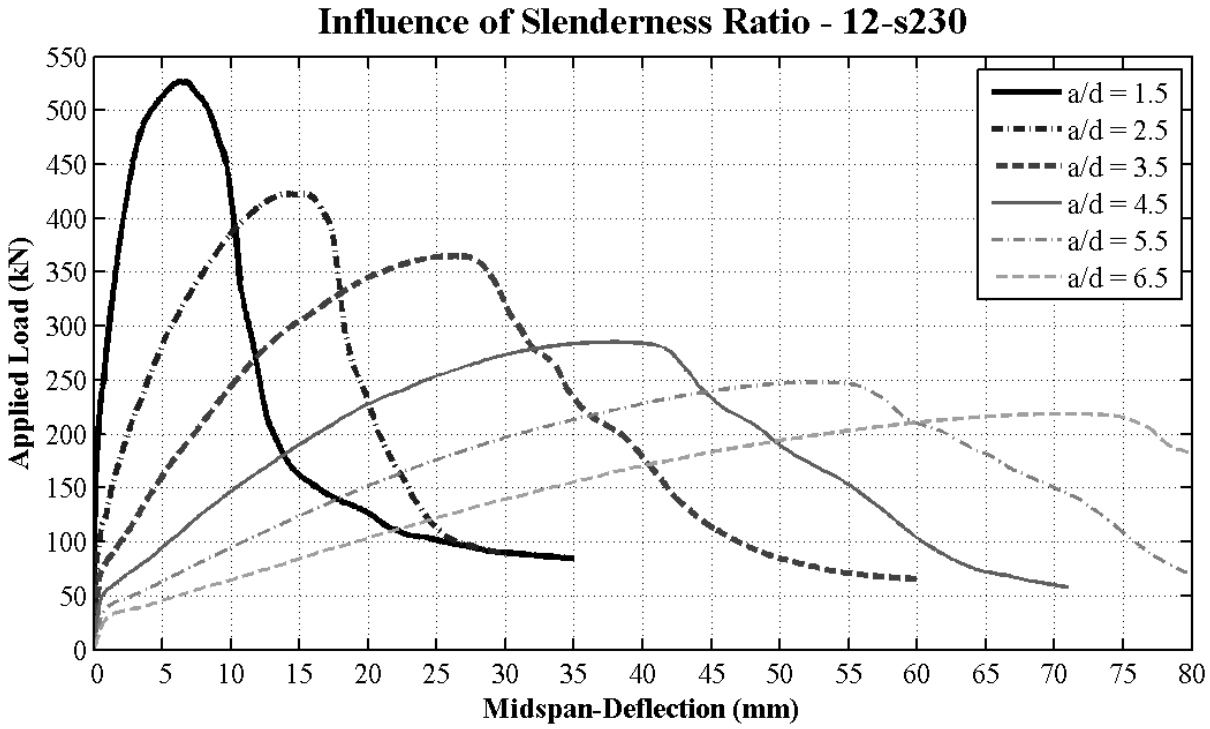
Influence of Slenderness Ratio - 12-s230
Applied Load (kN)
Midspan-Deflection (mm)
a/d = 1.5
a/d = 2.5
a/d = 3.5
a/d = 4.5
a/d = 5.5
a/d = 6.5

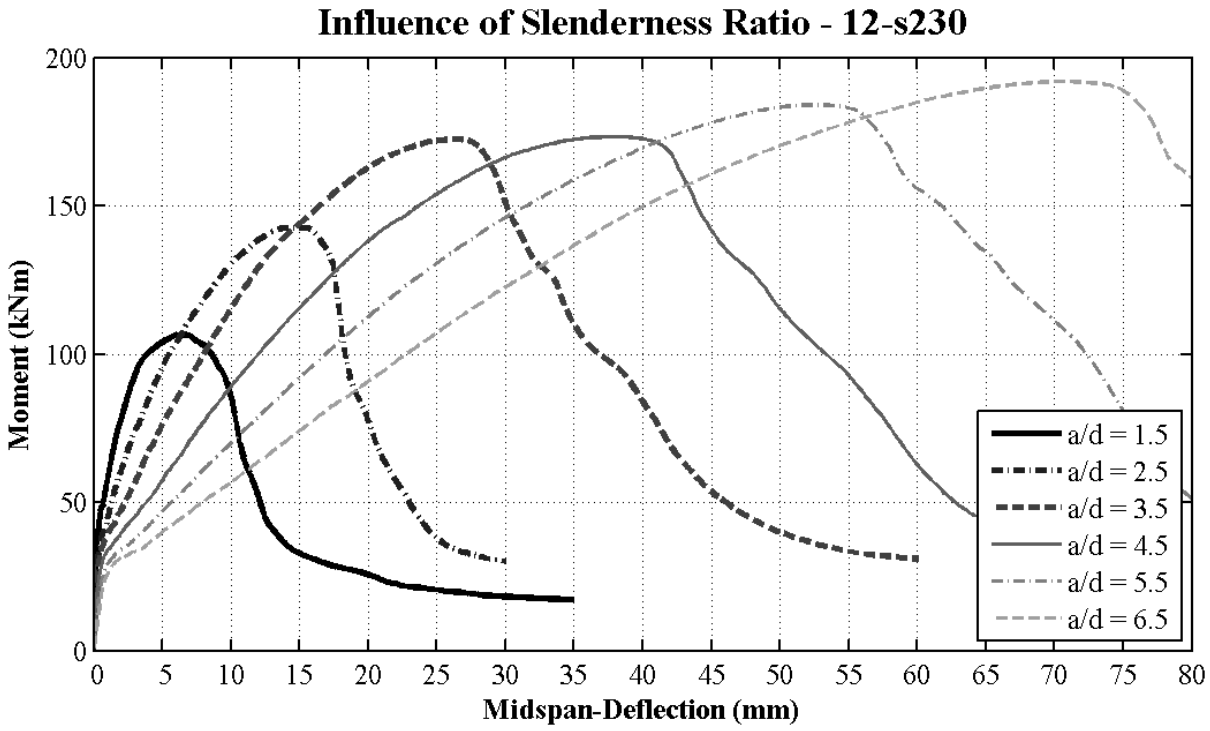
Influence of Slenderness Ratio - 12-s230
Moment (kNm)
Midspan-Deflection (mm)
a/d = 1.5
a/d = 2.5
a/d = 3.5
a/d = 4.5
a/d = 5.5
a/d = 6.5

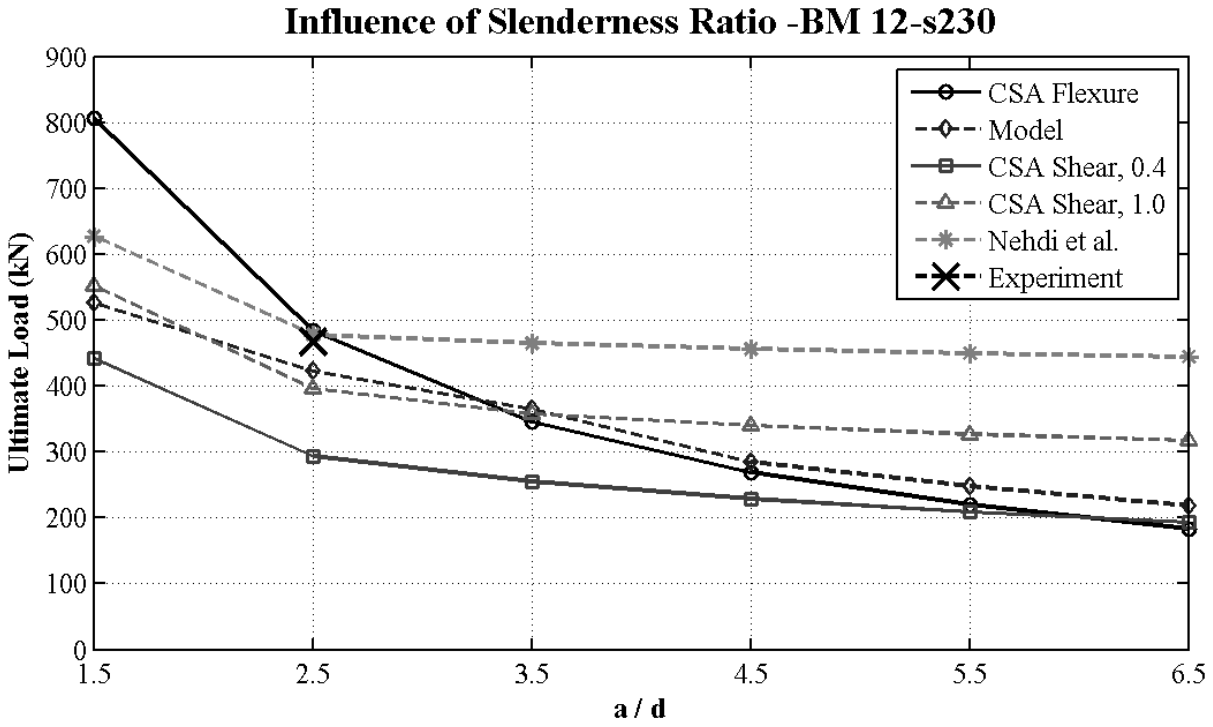
Influence of Slenderness Ratio -BM 12-s230
Ultimate Load (kN)
a / d
CSA Flexure
Model
CSA Shear, 0.4
CSA Shear, 1.0
Nehdi et al.
Experiment
0
100
200
300
400
500
600
700
800
900
1.5
2.5
3.5
4.5
5.5
6.5

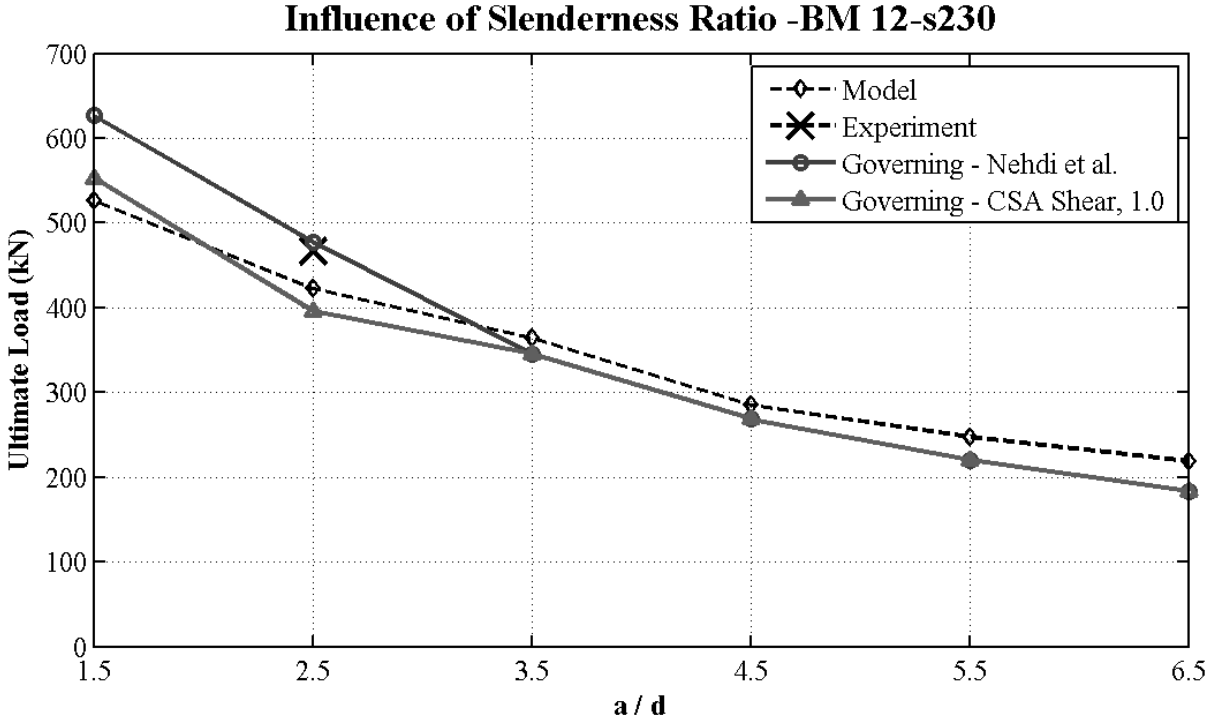
Influence of Slenderness Ratio -BM 12-s230
Ultimate Load (kN)
a / d
Model
Experiment
Governing - Nehdi et al.
Governing - CSA Shear, 1.0
0
100
200
300
400
500
600
700
1.5
2.5
3.5
4.5
5.5
6.5

BM 16-s230

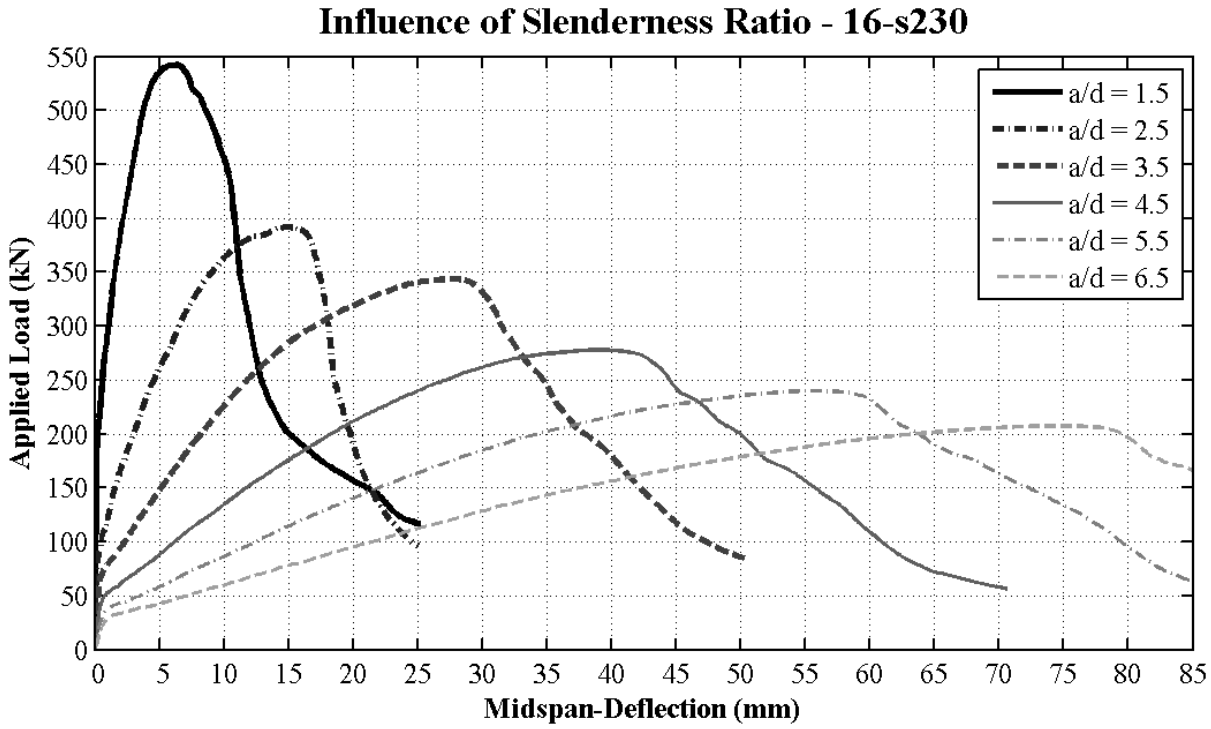
Influence of Slenderness Ratio - 16-s230
Applied Load (kN)
Midspan-Deflection (mm)
a/d = 1.5
a/d = 2.5
a/d = 3.5
a/d = 4.5
a/d = 5.5
a/d = 6.5

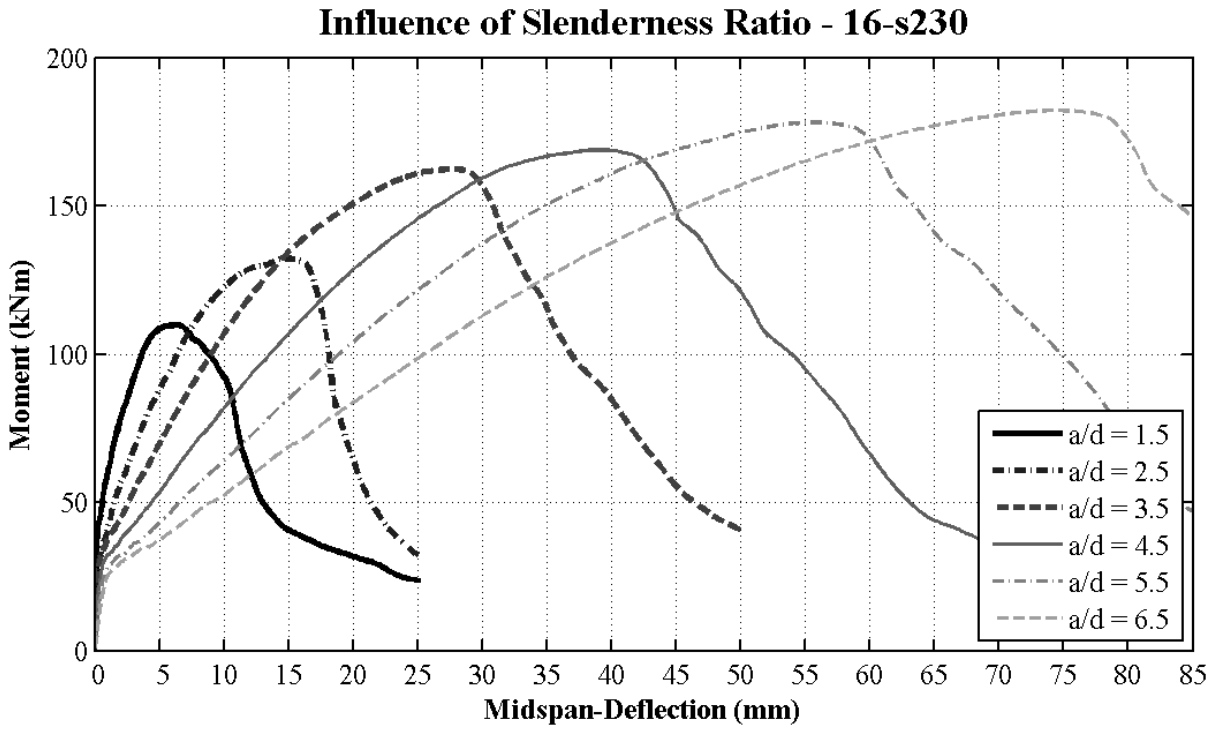
Influence of Slenderness Ratio - 16-s230
Moment (kNm)
Midspan-Deflection (mm)
a/d = 1.5
a/d = 2.5
a/d = 3.5
a/d = 4.5
a/d = 5.5
a/d = 6.5

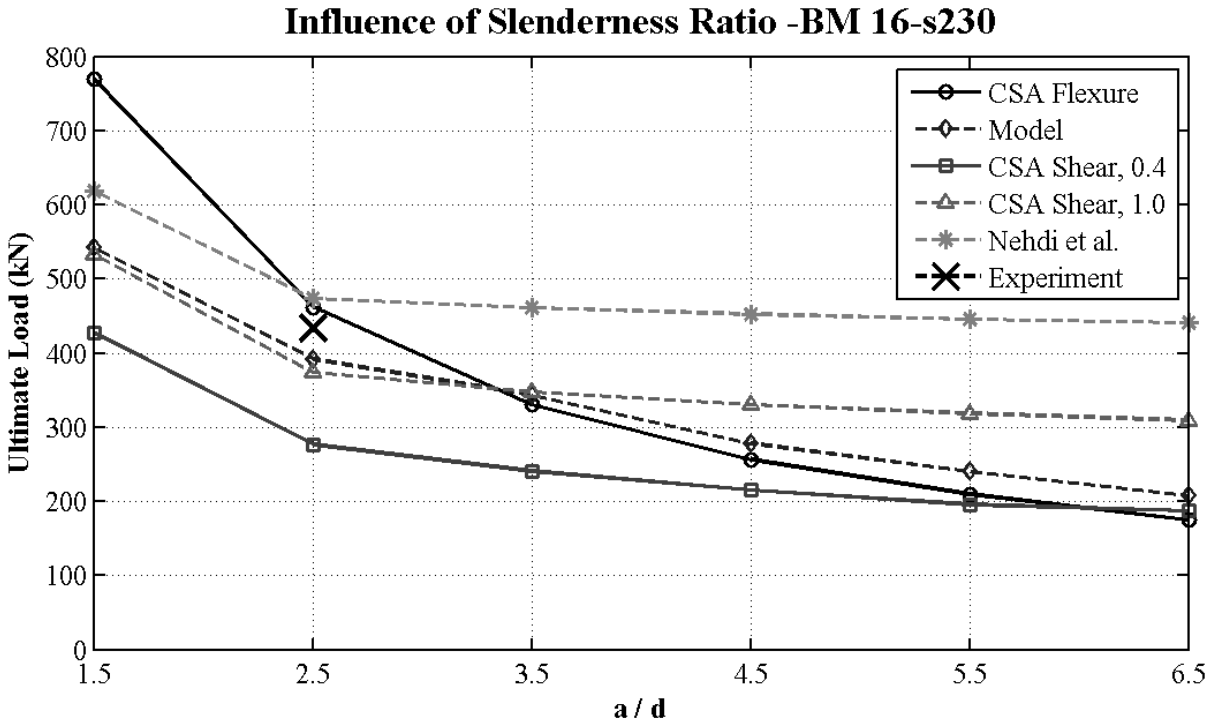
Influence of Slenderness Ratio -BM 16-s230
Ultimate Load (kN)
a / d
CSA Flexure
Model
CSA Shear, 0.4
CSA Shear, 1.0
Nehdi et al.
Experiment
0
100
200
300
400
500
600
700
800
1.5
2.5
3.5
4.5
5.5
6.5

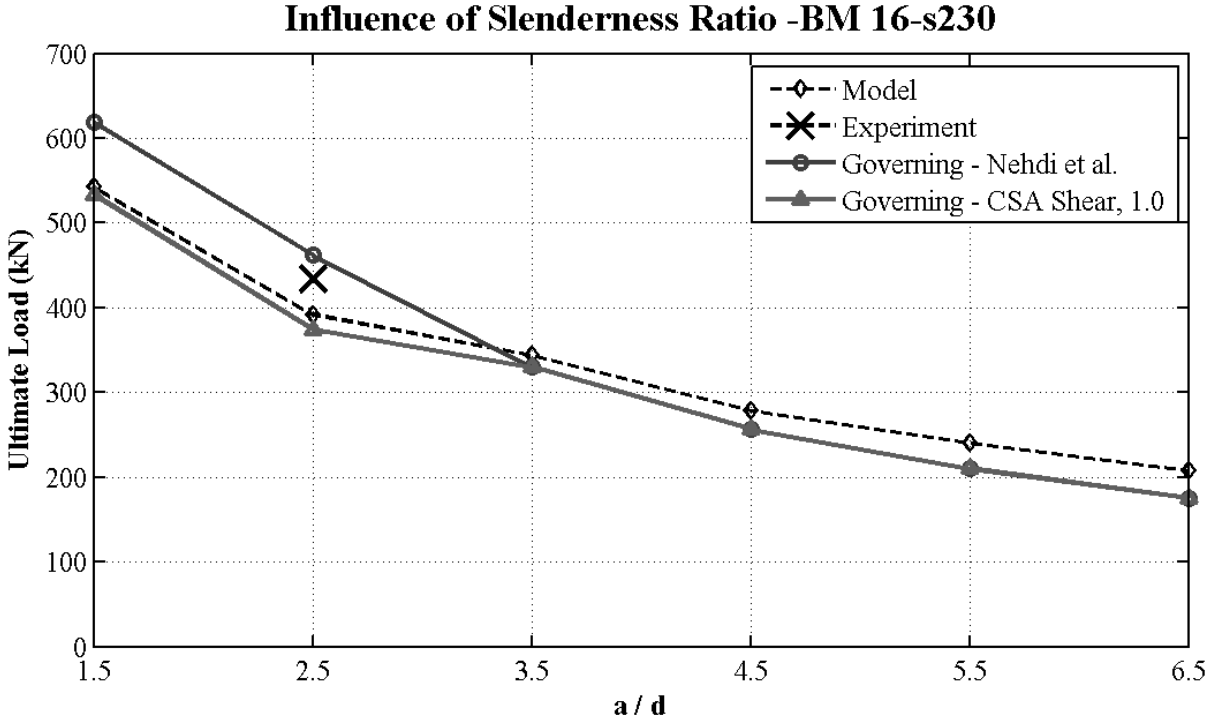
Influence of Slenderness Ratio -BM 16-s230
Ultimate Load (kN)
a / d
Model
Experiment
Governing - Nehdi et al.
Governing - CSA Shear, 1.0
0
100
200
300
400
500
600
700
1.5
2.5
3.5
4.5
5.5
6.5

BM 25-s230

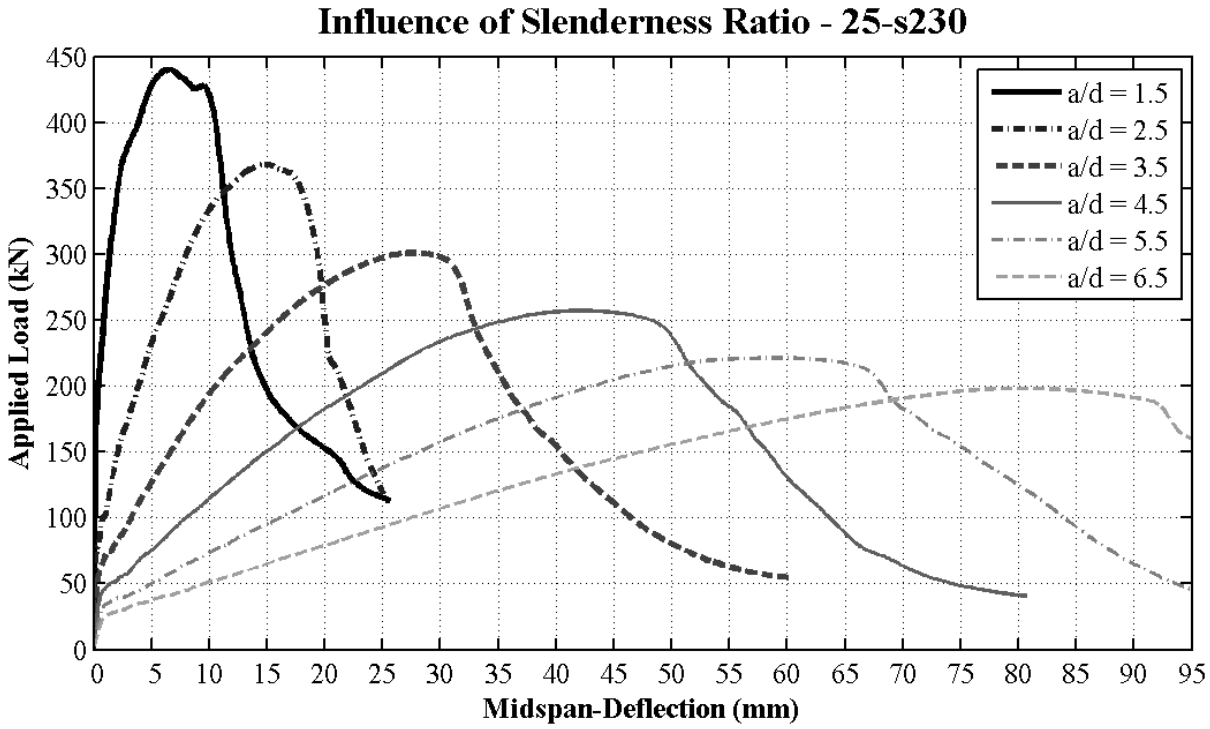
Influence of Slenderness Ratio - 25-s230
Applied Load (kN)
Midspan-Deflection (mm)
a/d = 1.5
a/d = 2.5
a/d = 3.5
a/d = 4.5
a/d = 5.5
a/d = 6.5

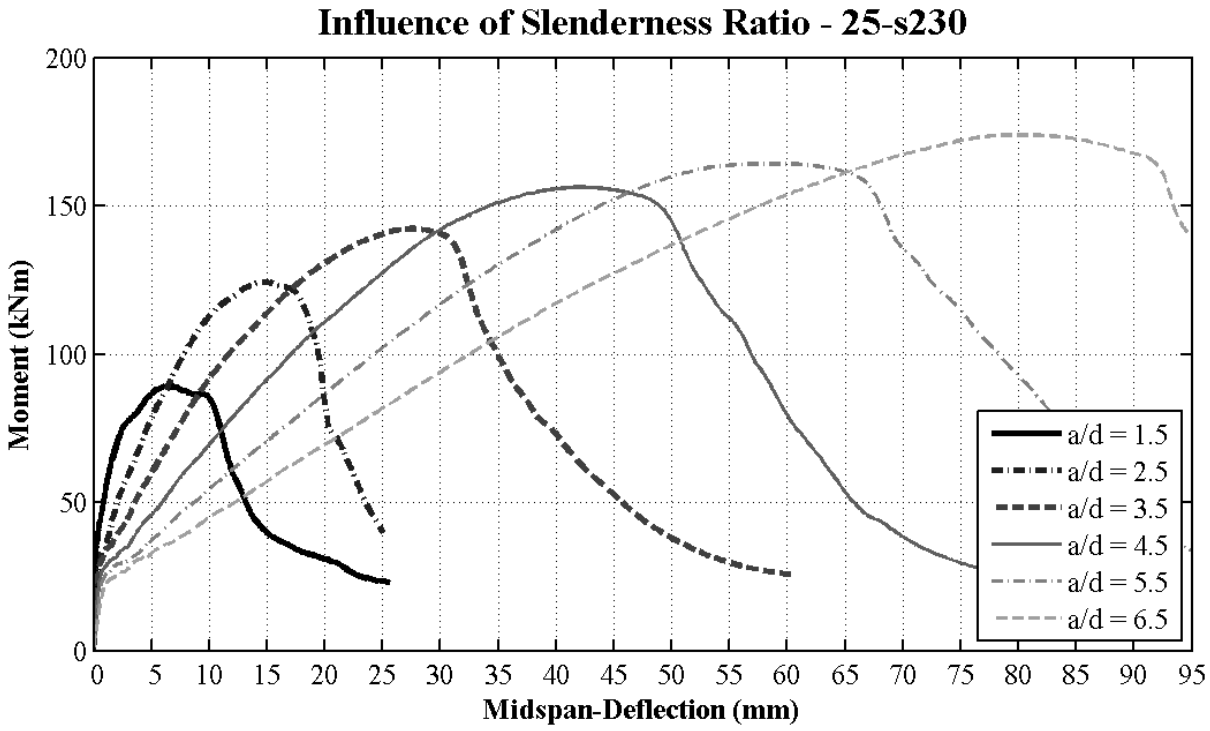
Influence of Slenderness Ratio - 25-s230
Moment (kNm)
Midspan-Deflection (mm)
a/d = 1.5
a/d = 2.5
a/d = 3.5
a/d = 4.5
a/d = 5.5
a/d = 6.5

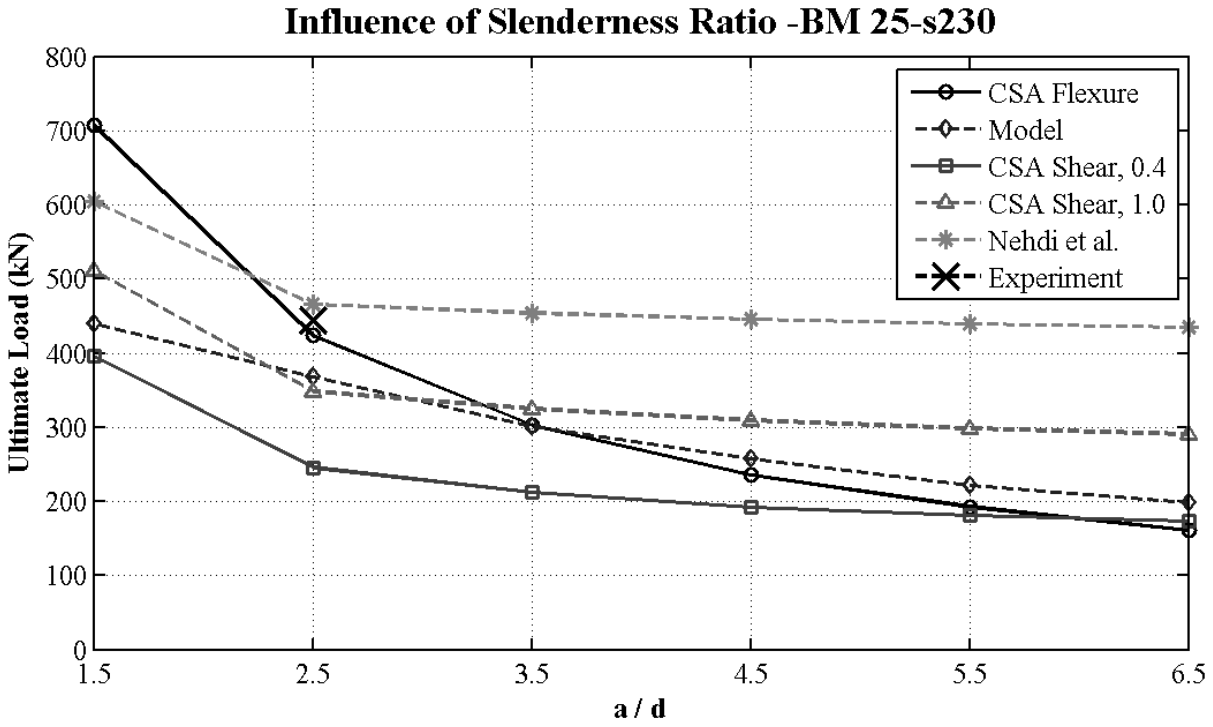
Influence of Slenderness Ratio -BM 25-s230
Ultimate Load (kN)
a / d
CSA Flexure
Model
CSA Shear, 0.4
CSA Shear, 1.0
Nehdi et al.
Experiment
0
100
200
300
400
500
600
700
800
1.5
2.5
3.5
4.5
5.5
6.5

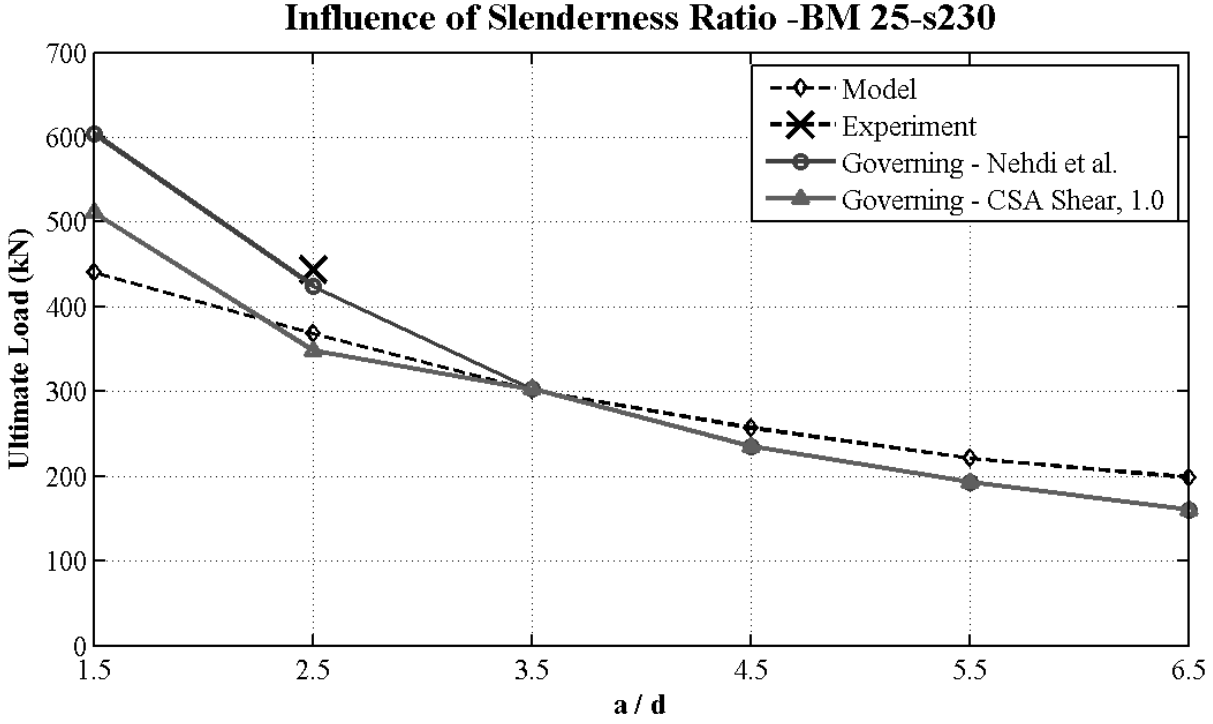
Influence of Slenderness Ratio -BM 25-s230
Ultimate Load (kN)
a / d
Model
Experiment
Governing - Nehdi et al.
Governing - CSA Shear, 1.0
0
100
200
300
400
500
600
700
1.5
2.5
3.5
4.5
5.5
6.5